AJNR

AMERICAN JOURNAL OF NEURORADIOLOGY

THE JOURNAL OF DIAGNOSTIC AND
INTERVENTIONAL NEURORADIOLOGY

Official Journal ASNR • ASFNR • ASHNR • ASPNR • ASSR
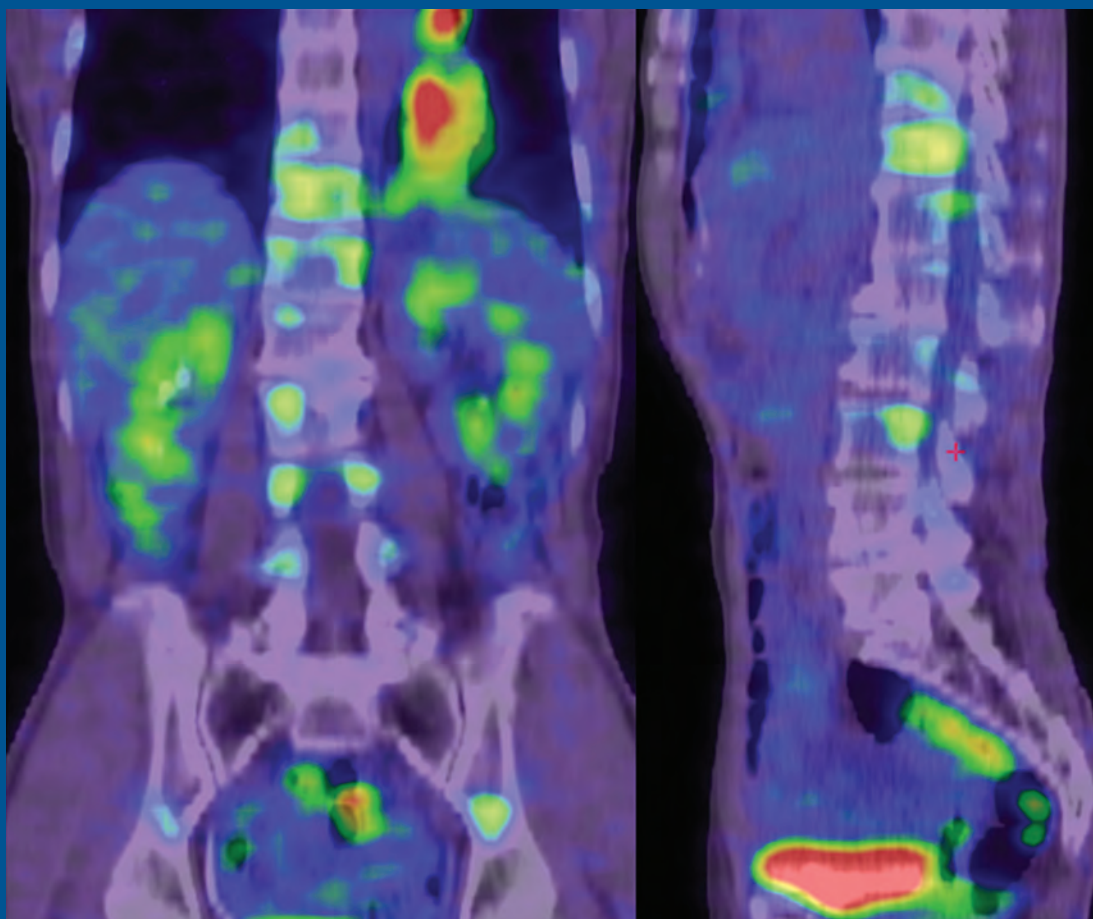
Advanced

by MicroVention

SOFTNESS ZONE

TRANSITION ZONE

SUPPORT ZONE

V-Trak®
Advanced
Coil System
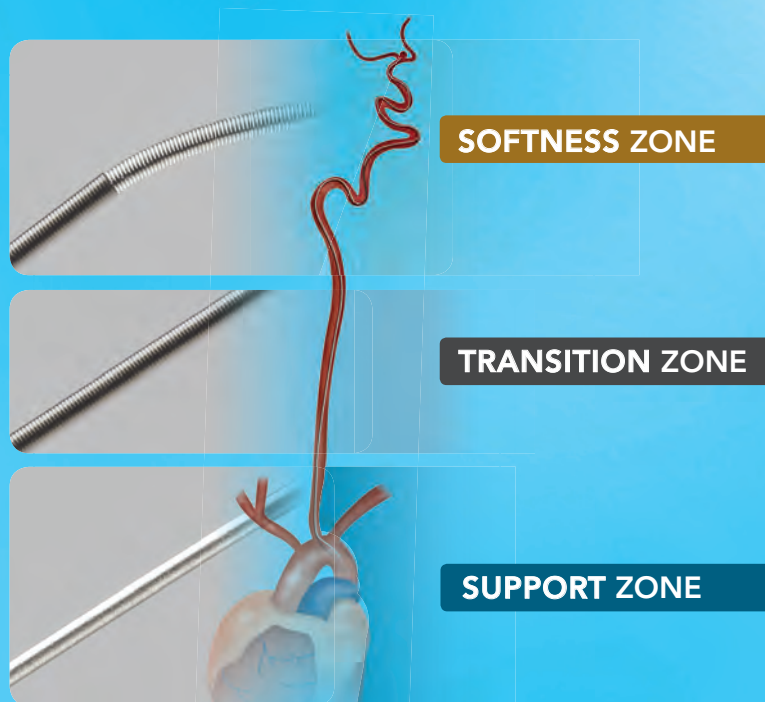
ENHANCED CONTROL TO MAXIMIZE COIL PERFORMANCE

The **V-Trak® Advanced Coil System**, the next generation to power the performance of our most technically advanced line of coils. Offering the optimal combination of support and flexibility.

microvention.com

BARRICADE™
COIL SYSTEM

PERFORMANCE AND VALUE DELIVERED

AJNR

AMERICAN JOURNAL OF NEURORADIOLOGY

Publication Preview at www.ajnr.org features articles released in advance of print. Visit www.ajnrblog.org to comment on AJNR content and chat with colleagues and AJNR's News Digest at http://ajnrdigest.org to read the stories behind the latest research in neuroimaging.

EDITORIAL

PERSPECTIVES

REVIEW ARTICLES

LEVEL 1 EBM EXPEDITED PUBLICATION

RESEARCH PERSPECTIVES

HEALTH CARE REFORM VIGNETTE

BRAIN

☆ Indicates Editor's Choices selection

〰 Indicates Fellows' Journal Club selection

O⚬ Indicates open access to non-subscribers at www.ajnr.org

☰ Indicates article with supplemental on-line table

◆ Indicates article with supplemental on-line photo

▶ Indicates article with supplemental on-line video

EBM1 Indicates Evidence-Based Medicine Level 1

EBM2 Indicates Evidence-Based Medicine Level 2
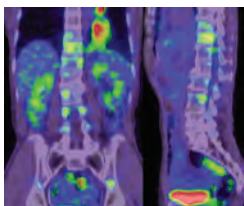
Hyperplastic hematopoietic marrow shows FDG uptake on PET.

Trevo® XP
PROVUE RETRIEVER

Take Control. Capture More.

The newly designed Trevo® XP ProVue Retriever takes proven Trevo Retriever performance to new levels for **easy delivery, easy placement,** and **easy visualization.**

When you're in control, it's amazing what you can capture.

stryker®
Neurovascular

Stroke: *Our Only Focus. Our Ongoing Promise.*

AJNR

CALL FOR AJNR EDITORIAL FELLOWSHIP CANDIDATES

ASNR and AJNR are pleased once again to join efforts with other imaging-related journals that have training programs on editorial aspects of publishing for trainees or junior staff (3–5 years after training), including Radiology (Olmsted fellowship), AJR (Figley and Rogers fellowships), and Radiologia.

2015 Candidate Information and Requirements

GOALS

- Increase interest in "editorial" and publication-related activities in younger individuals.
- Increase understanding and participation in the AJNR review process.
- Incorporate into AJNR's Editorial Board younger individuals who have previous experience in the review and publication process.
- Fill a specific need in neuroradiology not offered by other similar fellowships.
- Increase the relationship between "newer" generation of neuroradiologists and more established individuals.
- Increase visibility of AJNR among younger neuroradiologists.

ACTIVITIES OF THE FELLOWSHIP

- Serve as Editorial Fellow for one year. This individual will be listed on the masthead as such.
- Review at least one manuscript per month for 12 months. Evaluate all review articles submitted to AJNR.
- Access to our electronic manuscript review system will be granted so that the candidate can learn how these systems work.
- Be involved in the final decision of selected manuscripts together with the Editor-in-Chief.
- Participate in all monthly Senior Editor telephone conference calls.
- Participate in all meetings of the Editors and Publications Committee during the annual meetings of ASNR and RSNA as per candidate's availability. AJNR/ASNR will not provide funding for this activity but may offer a discounted fee for its annual meeting.
- Evaluate progress and adjust program to specific needs in biannual meeting or telephone conference with the Editor-in-Chief.
- Write at least one editorial for AJNR.
- Embark on an editorial scientific or bibliometric project that will lead to the submission of an article to AJNR or another appropriate journal as determined by the Editor-in-Chief. This project will be presented by the Editorial Fellow at the ASNR annual meeting.
- Serve as liaison between AJNR and ASNR's Young Professionals Network and the 3 YPs appointed to AJNR as special consultants. Participate in meetings and telephone calls with this group. Design one electronic survey/year polling the group regarding readership attitudes and wishes.
- Recruit trainees as reviewers as determined by the Editor-in-Chief.
- Participate in Web improvement projects.
- Potentially become a member of AJNR's Editorial Board at the end of the fellowship.
- Invite Guest Editors for AJNR's News Digest to cover a variety of timely topics.

QUALIFICATIONS

- Be a fellow in neuroradiology from North America, including Canada (this may be extended to include other countries).
- Be a junior faculty neuroradiology member (< 3 years) in either an academic and private environment.
- Provide an "end" of fellowship report to AJNR's Editor-in-Chief and ASNR's Publications Committee.
- Be an "in-training" or member of ASNR in any other category.

APPLICATION

- Include a short letter of intent with statement of goals and desired research project. CV must be included.
- Include a letter of recommendation from the Division Chief or fellowship program director. A statement of protected time to perform the functions outlined is desirable.
- Applications will be evaluated by AJNR's Senior Editors and the Chair of the Publications Committee prior to the ASNR meeting. The name of the selected individual will be announced at the meeting.
- Applications should be received by March 3, 2014 and sent to Ms. Karen Halm, AJNR Managing Editor, electronically at khalm@asnr.org.

ASNR 53rd Annual Meeting & The Foundation of the ASNR Symposium 2015

Getting Personal · Getting Personal · Getting Personal · Getting Personal

ASNR

CHICAGO ★ 2015

April 25-30, 2015

Sheraton Chicago Hotel & Towers

ASFNR ASHNR ASPNR ASSR SNIS

THE FOUNDATION OF THE ASNR

Abstract Deadline:

Friday, December 12, 2014
Please visit www.asnr.org/2015
for more information

ASNR 2015 Program Chair/President Elect
Laurie A. Loevner, MD

Programming developed in cooperation with the:

American Society of Functional Neuroradiology (ASFNR)
Pratik Mukherjee, MD, PhD

American Society of Head and Neck Radiology (ASHNR)
Richard H. Wiggins, III, MD

American Society of Pediatric Neuroradiology (ASPNR)
Thierry A.G.M. Huisman, MD

American Society of Spine Radiology (ASSR)
Adam E. Flanders, MD

American Society of Neuroradiology (ASNR)
Health Policy Committee
Robert M. Barr, MD, FACR

Society of NeuroInterventional Surgery (SNIS)
Donald F. Frei, Jr. MD

Request Programming and Registration Materials
for the ASNR 53rd Annual Meeting, Contact:

ASNR 53rd Annual Meeting
c/o American Society of Neuroradiology
800 Enterprise Drive, Suite 205
Oak Brook, Illinois 60523-4216
Phone: 630-574-0220
Fax: 630-574-0661
Email: meetings@asnr.org
Website: www.asnr.org/2015

Scan now to visit our website

AJNR

AMERICAN JOURNAL OF NEURORADIOLOGY

ACTI 2015

The 3rd Asian Congress of Thoracic Imaging
March 20-22, 2015, Taipei, Taiwan
Howard Civil Service International House

▶ **Invited Speaker**

Garry Choy	Kiyoshi Murata
Jin Mo Goo	Yoshiharu Ohno
Albert Hsiao	Santiago Rossi
Jung Gi Im	Zhonghua Sun
Takeshi Johkoh	Masashi Takahashi
Ki-Nam Lee	Charles S. White
Kyung Soo Lee	Carol Wu
Paul L. Molina	

▶ **Important Date**

Registration Open	2014/08/01
Early Registration Due	2014/12/31
Author Registration Due	2015/01/31
Abstract Submission Start	2014/08/01
Abstract Submission Close	2014/10/15
Acceptance Notice	2014/11/30
Congress Date	2015/03/20-22

▶ **Registration**

Category	Early bird Registration (Until 2014/12/31)	Standard Registration (2015/1/1~2015/2/28)	On-site (2015/3/1~2015/3/22)
Physician	USD 150	USD 200	USD 250
Trainee/Non-Physician	USD 75	USD 100	USD125
ACTI 2015 Congress Dinner	USD 30	USD 30	USD 60
Accompanying	USD 50	USD 50	USD 60

Hosted by   Asian Society of Thoracic Radiology (ASTR) / The Radiological Society of Republic of China (CTSR)
Chang Gung Memorial Hospital at Linkou / Chang Gung University

The Radiological Society of Republic of China (CTSR)
Add: 2F, No. 63, Sec. III, Chong-Qing N. Road, Taipei, 10362, Taiwan
Tel : +886-2-25865332   Fax : +886-2-25865330   Email : secretariat@acti2015.org   Web : www. acti2015.org

---

wfnrs The World Federation of Neuroradiological Societies
NRST Neuroradiological Society of Taiwan

www.snr2018.org

XXI Symposium Neuroradiologicum

The World Congress of Neuroradiology
March 19-24, 2018   Taipei Taiwan

One World One Family

Symposium President
Professor Wan-Yuo GUO, M.D., Ph.D.

Symposium Vice-Presidents
Professor Yukunori KOROGI, M.D., Ph.D. (Japan)
Professor Sang-Joon KIM, M.D., Ph.D. (Korea)
Professor Sandy CY CHEN, M.D. (Taiwan)
Professor Ho-Fai WONG, M.D. (Taiwan)

Welcome to TAIPEI

Taipei 101   Queen's Head of Yehliu   National Palace Museum   Sun Moon Lake

Simplify
the MOC Process

Manage
your CME Credits Online

CMEgateway.org

It's Easy and Free!

Log on to CME Gateway to:

- View or print reports of your CME credits from multiple societies from a single access point.
- Print an aggregated report or certificate from each participating organization.
- Link to SAMs and other tools to help with maintenance of certification.

American Board of Radiology (ABR) participation!

By activating ABR in your organizational profile, your MOC–fulfilling CME and SAM credits can be transferred to your own personalized database on the ABR Web site.

Sign Up Today!

go to CMEgateway.org

Available to Members of Participating Societies

American Board of Radiology (ABR)

American College of Radiology (ACR)

American Roentgen Ray Society (ARRS)

American Society of Neuroradiology (ASNR)

Commnission on Accreditation of Medical Physics Educational Programs, Inc. (CAMPEP)

Radiological Society of North America (RSNA)

Society of Interventional Radiology (SIR)

SNM

The Society for Pediatric Radiology (SPR)

Join us at the French Congress of Radiology !

JFR 2014

Diagnostique & Interventionnelle

jfr.radiologie.fr

October 17-20, Paris France

2014 Main Topic:
Emergency, MRI

JFR 2013

17,747	Attendees including
2,648	from 72 different countries
154	Exhibitors
157	Focused and Scientific Sessions
203	Hours of Conferences and Workshops

Posters:
Illustrate all aspects of patient care.
Interventional Village:
A unique space that brings together all those who want to familiarize themselves with the interventional activities.
Research :
A space of expression for exchange and discovery for all: juniors, radiologists, laboratories, research centers, manufacturers.
Books:
MRI in practice :
Factsheets to help the radiologist to establish protocols in his everyday practice.

SFR
sfr.radiologie.fr
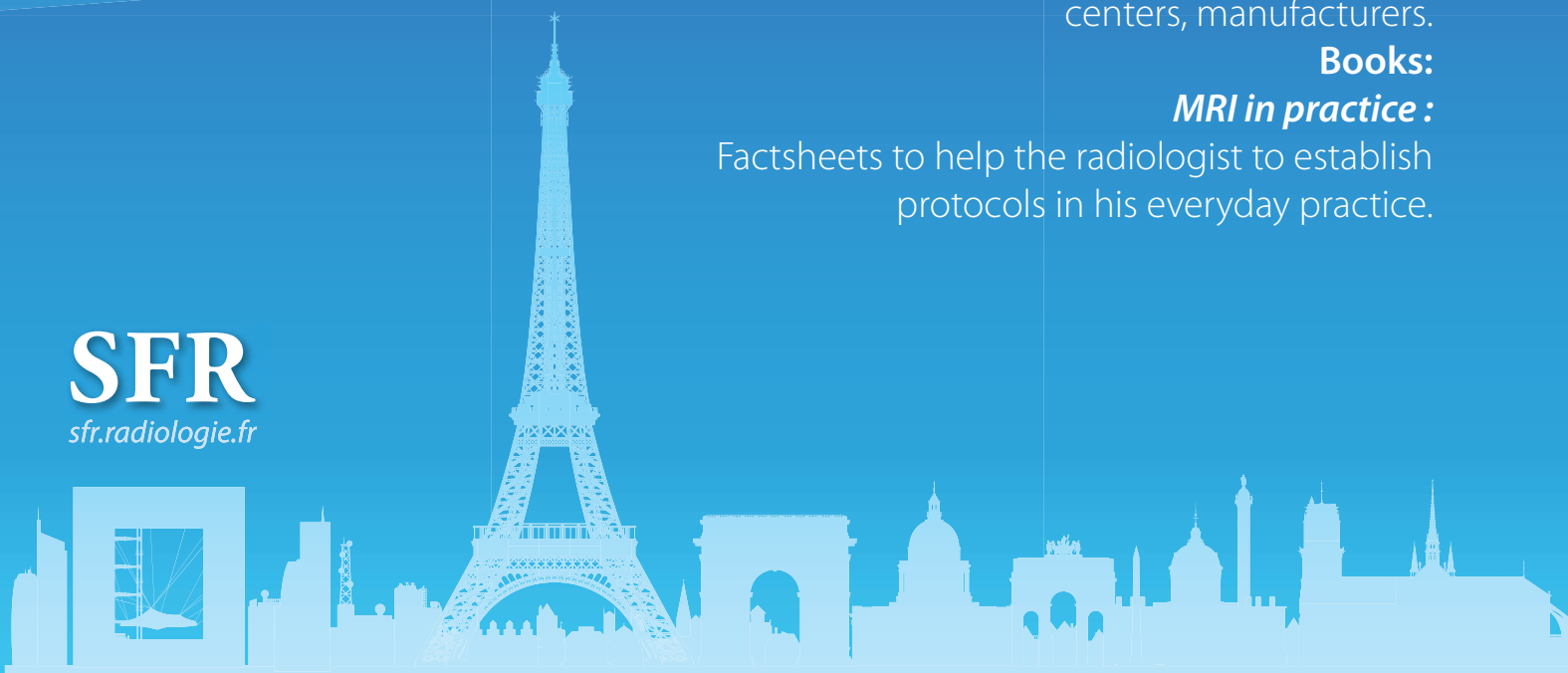
The Ins and Outs of Sexual Imaging

Golf and sex are the only two things you don't have to be good at to enjoy.

Kevin Costner in *Tin Cup*

M. Castillo, *Editor-in-Chief*

What happens inside the human body during sexual intercourse has fascinated artists, scientists, and the public since the start of humanity. Leonardo da Vinci (1452–1519) drew the internal anatomy of a couple engaged in intercourse in "The Copulation" and suggested that connections between the penis, the distal spinal cord, and the brain existed. In the Middle Ages and the Renaissance, the act of sex was not scientifically studied. The term "sexology" was first used in Victorian times to describe the relationship between men and women.[1] The idea of "sexual science" originated in Germany and Italy, and the term "sexual medicine" was not established until the 1970s. In the United States, the first physician who worked full-time in "diseases" of a sexual nature was Harry Benjamin, who studied mostly trans-sexualism. Perhaps one of the most common names associated with sexual medicine is Alfred Kinsey, who collected the sexual clinical histories of more than 18,000 patients (a story entertainingly told by T.C. Boyle in his novel *The Inner Circle,* Viking Adult, 2003). Kinsey was the first to quantitate a few aspects of sexual behavior. His legacy lives on at the Kinsey Institute (http://www.kinseyinstitute.org) at Indiana University in Bloomington. A few years after the apparition of the "Kinsey Report,"[2] Masters and Johnson began their studies of sexuality, all of which culminated with the creation of the International Society for Sexual Medicine, which now publishes the *Journal of Sexual Medicine* (Impact Factor: 3.55). Today, sexual medicine is a serious and mature specialty that incorporates physicians, psychiatrists, psychologists, and even neuroradiologists.

Sex has 2 goals: foremost reproduction and then pleasure. The main brain region controlling pleasure and thus orgasm is the medial preoptic area of the hypothalamus. In animals, stimulation of this region elicits pleasurable sexual responses via sympathetic (by way of the paraventricular hypothalamic nucleus) and parasympathetic mechanisms.[1] Axons from this region connect with the nucleus paragingantocellularis in the ventrolateral medulla, and axons from the latter extend down to the tip of the spinal cord (here it is curious to note that during the Renaissance, semen was thought to come down from the brain traveling by way of a canal in the spine and following a path that somewhat matches that of these axons). By way of the periaqueductal gray matter, the medial preoptic area may inhibit the hypothalamic nucleus, terminating the sensations of pleasure.

Direct observations of what occurs at the penis-vagina interface during sex were initially made by Masters and Johnson, who studied the mechanics of this activity by using an artificial penis (a funny episode in the popular TV series "Masters of Sex" recounts

the experiments done with this instrument). Sonography was first used to study copulation in 1999, but the images obtained were of poor quality by today's standards.[3] Later in 1999, MR imaging was used to study the state of the female genital and pelvic organs during sexual arousal in 8 couples during 13 "encounters."[4] In this study, in which one author was a radiologist, the main conclusion was that local responses were similar for pre- and post-menopausal women. The article contains no MR images of the act of coitus. In 2001, Faix et al[5] asked a couple to have sex in the MR imaging unit (in face-to-face or "missionary" position). The main observation, among many uninteresting measurements that were perhaps used to justify publishing such an article, was that in this position the contact between the penis and vagina occurs mostly at the anterior cul-de-sac and anterior vaginal wall. One year later the same authors asked a couple (the same one?) to have intercourse in the MR imaging unit again, also in missionary position, and images showed that the internal contact between the organs was different and occurred along the posterior cul-de-sac and posterior vaginal wall.[6] The images illustrating those articles are not too different from the original da Vinci drawing previously mentioned. The conclusions of this latter study were simply silly: "Initially the aim of the study was to 'copy' the genius of Leonardo da Vinci. We showed that an MR imaging scan of sexual intercourse in two positions is feasible and artistic but not as artistic as the images drawn by da Vinci."[6] I wonder whether today any reasonable scientific journal would publish a study with these conclusions!

MR imaging has also been used to map the spread of contraceptive gel during both simulated and real intercourse.[7] These experiments offer important information regarding the spread of intravaginal medications and how it relates to dosage (small or large doses do not appear to make a difference). Studies have found that gels spread evenly, covering the cervix and proving a good contraceptive barrier.

What happens during sex at a local level is, from a neuroradiologist's point of view, not too interesting and for purposes of this *Perspectives*, I will now attempt to summarize some of what presumably happens in our brains. Using fMRI, Meston et al[8] studied 6 women while being shown neutral and erotic films, and all reported moderate arousal to the latter. Areas that showed activation during sexual arousal included the inferior temporal lobes, anterior cingulate gyri, insular cortex, corpus callosum, thalami, caudate nuclei, globus pallidi, and inferior frontal lobes. In women, the activation was bilateral, while in men it was unilateral (mostly right-sided).[9] A different study in a larger number of men and women showed activations in the same regions and, in addition, in the medial prefrontal cortex, occipitotemporal cortex, and amygdalae, but only men showed significant activation of the hypothalamus.[10] Some of the cortical areas were also activated with other emotional stimuli and presentation of rewards. Thus, it seems that female and male brains respond to sex differently (to me, not surprising).

In males, stimuli leading to initial genital responses activate the left frontal operculum, probably related to imagining the forthcoming sexual act.[10] Then, anticipatory motor and somato-

sensory imagery activates the left supramarginal gyrus and Brodmann area 2, respectively. A positive feedback mechanism consequently increases the response of these brain areas, but the frontal lobes also have the ability to disrupt these pathways and stop related brain activations. During orgasm, prominent activation has been shown in the paraventricular hypothalamic nuclei, periaqueductal gray matter, hippocampus, and cerebellar cortex, confirming observations made previously in animal models. Stimulation of the posterior pituitary lobe with release of hormones such as oxytocin also occurs during orgasm in both animals and humans.

Because fMRI can shed light on what happens during normal sex, it has also been used to evaluate deviant sexual behaviors. It is curious (and somewhat scary) that pedophiles activate the same brain regions, albeit more intensively, than nonpedophile controls.[11,12] It seems that in sexually addicted individuals, the frontal brain loses its ability to stop the positive feedback mechanisms that recruit other brain regions, leading to widespread activations.[13] DTI has also shown low diffusivity in the superior frontal cortex in sexually addicted patients (similar results have been found in other behaviors with abnormal impulsivity such as kleptomania, gambling, and eating).[13] These observations suggest that neurons and axons are abnormal or abnormally organized in these regions in addicted individuals.

Because sex and love are related (not always, but fairly commonly), it is useful to explore what happens to the brain during love. There are 2 types of love: passionate (being in love with someone) and companionate (loving someone). The former is more intense and though both types occur simultaneously early in a relationship, they are different feelings that may not survive together in long-term unions (with time, passionate love becomes companionate). Passionate love is characterized by activations in all dopaminergic brain regions and decreased activity of brain areas associated with anxiety and fear.[14] Most studies have shown that the amygdalae tend to be deactivated during love, sex, and orgasm, decreasing fear and anxiety and contributing to the feeling of well-being experienced with love, sex, and orgasm.[15] Conversely, in deviant sexual behaviors such as pedophilia, the amygdalae activate abnormally.[12] The brains of pedophiles appear to be more severely impaired than those of other sexual offenders, including rapists, and some brain regions (such as the basal frontotemporal ones) are affected in these and other delinquents and criminals of a nonsexual nature.

Romantic love is also ruled by the dopaminergic systems of the brain. Love is primarily motivational and changes our habits to please the person who receives it. Central features that both love and sex share are intrusiveness and obsessive thinking, which are involuntary and difficult to control. In individuals sustaining long-term partners, the initial reward-value brain circuits remain activated similar to new love. Serotonin production is elevated with certain antidepressants, and this chemical must be present to feel love, so there is a chance that individuals taking these drugs may be unable to fall in love or have a tendency to fall out of it.

So, it seems that the mysteries of love and lust are starting to become clearer with fMRI. Although the study of sex has gone in and out of style many times, thanks to neuroimaging, it is definitively in now.

REFERENCES

1. Schultheiss D, Glina S. **Highlights from the history of sexual medicine.** *J Sex Med* 2010;7:2031–43
2. Kinsey AC. Pomeroy WB, Martin CE, et al. *Sexual Behavior in the Human Female*. 1st ed. Philadelphia: Saunders; 1953 (still available on Amazon.com)
3. Riley AJ, Less W, Riley EJ. **An ultrasound study of human coitus.** In: Bezemer W, Cohen-Kettenis P, Salob K, et al, eds. *Sex Matters*. Amsterdam: Elsevier; 1999:29–36
4. Schultz WW, van Andel P, Sabelis I, et al. **Magnetic resonance imaging of male and female genitals during coitus and female sexual arousal.** *BMJ* 1999;319:18–25
5. Faix A, Lapray JF, Courtieu C, et al. **Magnetic resonance imaging of sexual intercourse: initial experience.** *J Sex Marital Ther* 2001; 27:475–82
6. Faix A. Lapray JF, Callede O, et al. **Magnetic resonance imaging (MRI) of sexual intercourse: second experience in missionary position and initial experience in posterior position.** *J Sex Marital Ther* 2002;28:63–76
7. Pretorius ES, Timbers K, Malamud D, et al. **Magnetic resonance imaging to determine the distribution of a vaginal gel: before, during, and after both simulated and real intercourse.** *Contraception* 2002;66:443–51
8. Meston CM, Levin RJ, Sipski ML, et al. **Women's orgasm.** *Annu Rev Sex Res* 2004;15:796–97
9. Stoleru S, Gregoire MC, Gerard D, et al. **Neuroanatomical correlates of visually evoked sexual arousal in human males.** *Arch Sex Behav* 1999;28:1–12
10. Karama S, Lecours AR, Leroux JM, et al. **Areas of brain activation in males and females during viewing of erotic film excerpts.** *Human Brain Mapp* 2002;16:1–13
11. Schiffer B, Krueger T, Paul T, et al. **Brain response to visual stimuli in homosexual pedophiles.** *J Psychiatry Neurosci* 2008;33:23–33
12. Sartorious A, Ruf M, Kief C, et al. **Abnormal amygdala activation profile in pedophilia.** *Eur Arch Psychiatry Clin Neurosci* 2008; 258:271–77
13. Estellon V, Mouras H. **Sexual addiction: insights from psychoanalysis and functional neuroimaging.** *Socioaffectinve Neuroscience and Psychology* 2012;2:11814
14. Oritgue S, Bianchi-Demicheli F, Patel N, et al. **Neuroimaging of love: fMRI meta-analysis evidence towards new perspectives in sexual medicine.** *Sexual Med* 2010;7:3541–52
15. Dickinson RL. *Human Sex Anatomy: A Topographical Hand Atlas.* 2nd ed. London, UK: Balliere, Tyndall and Cox; 1949:84–109

CFD: Computational Fluid Dynamics or Confounding Factor Dissemination? The Role of Hemodynamics in Intracranial Aneurysm Rupture Risk Assessment

J. Xiang, V.M. Tutino, K.V. Snyder, and H. Meng

ABSTRACT

SUMMARY: Image-based computational fluid dynamics holds a prominent position in the evaluation of intracranial aneurysms, especially as a promising tool to stratify rupture risk. Current computational fluid dynamics findings correlating both high and low wall shear stress with intracranial aneurysm growth and rupture puzzle researchers and clinicians alike. These conflicting findings may stem from inconsistent parameter definitions, small datasets, and intrinsic complexities in intracranial aneurysm growth and rupture. In Part 1 of this 2-part review, we proposed a unifying hypothesis: both high and low wall shear stress drive intracranial aneurysm growth and rupture through mural cell–mediated and inflammatory cell–mediated destructive remodeling pathways, respectively. In the present report, Part 2, we delineate different wall shear stress parameter definitions and survey recent computational fluid dynamics studies, in light of this mechanistic heterogeneity. In the future, we expect that larger datasets, better analyses, and increased understanding of hemodynamic-biologic mechanisms will lead to more accurate predictive models for intracranial aneurysm risk assessment from computational fluid dynamics.

ABBREVIATIONS: CFD = computational fluid dynamics; IA = intracranial aneurysm; LSA = low shear-stress area; MWSS = maximum wall shear stress; OSI = oscillatory shear index; TAWSS = time-averaged wall shear stress; WSS = wall shear stress

Image-based computational fluid dynamics (CFD) holds a prominent position in the patient-specific evaluation of intracranial aneurysms (IAs). Hemodynamic parameters, particularly those related to aneurysmal wall shear stress (WSS), the frictional force of flowing blood on the vessel lumen, have been shown to correlate with IA growth[1-3] and rupture.[4,5] Consequently, the clinical community has taken an interest in not only the intuitive and esthetic aspects of CFD simulations (dubbed "color for doctors")[6] but also the enormous potential of CFD to provide objective, quantitative, and mechanism-based markers of aneurysm rupture risk.

In a recent *American Journal of Neuroradiology* editorial, Kallmes[7] raised concerns regarding the current status of CFD studies and their clinical utility in IA rupture risk assessments, asking if CFD should alternatively be interpreted as "confounding factor dissemination." This thought- and debate-provoking question reflects wide concerns over the growing number of hemodynamic parameters and conflicting findings reported in the current literature. Indeed, 3 other editorials published in the same journal[8-10] appeared shortly after Kallmes's editorial. Cebral and Meng[8] offered the first counterpoint, in which they commented that inconsistencies in hemodynamic parameter definitions and conflicting findings reflect exploratory efforts of isolated groups with small datasets; yet, more importantly, the conflicting findings could originate from the intrinsic complexity of aneurysm growth and rupture mechanisms and our scarce knowledge about them. Intracranial aneurysm has long been suspected to be a highly heterogeneous disease, containing several disease types.[10,11] As Strother and Jiang[10] pointed out in their editorial, IA may even be a spectrum of a disease or even multiple separate diseases.

Currently, conflicting results concerning aneurysmal WSS, the most frequently explored hemodynamic parameter of augmented rupture risk, puzzle the IA research and clinical communities. Both high and low WSS have been found to be correlated with IA growth and rupture.[1-5,12,13] Prompted by this "high-versus-low WSS" controversy, we published Part 1 of a 2-part review, in which we proposed a unified hypothesis regarding the roles of high and low WSS in IA growth and rupture.[11] That review aimed

From the Toshiba Stroke and Vascular Research Center (J.X., V.M.T., K.V.S., H.M.) and Departments of Neurosurgery (J.X.), Biomedical Engineering (V.M.T.), and Mechanical and Aerospace Engineering (H.M.), University at Buffalo, State University of New York, Buffalo, New York.

Grant support (H.M.) was provided by the National Institutes of Health (5R01NS064592) and Toshiba Medical Systems.

Please address correspondence to Hui Meng, PhD, Toshiba Stroke and Vascular Research Center, University at Buffalo, Clinical and Translational Research Center, 875 Ellicott St, Buffalo, NY 14203; e-mail: huimeng@buffalo.edu

○━ Indicates open access to non-subscribers at www.ajnr.org

▤ Indicates article with supplemental on-line tables

http://dx.doi.org/10.3174/ajnr.A3710

at providing new insight into the complex hemodynamic-biologic mechanisms underlying IA pathophysiology. In brief, we proposed that both high and low WSS could drive IA growth and rupture. On the basis of published studies on pathologic vascular responses to hemodynamics in IA genesis[14,15] and atherosclerosis,[16] we hypothesized that these 2 aberrant hemodynamic conditions could elicit different destructive vascular remodeling pathways, mediated by mural cells and inflammatory cell infiltrates, respectively. Such diversity in the driving hemodynamics and elicited biologic pathways may generate the observed heterogeneity of IA phenotypes. Understanding this intrinsic mechanistic complexity could help us to better characterize and converge inconsistent CFD findings.

To follow up, this work serves as Part 2 of this 2-part review. We delineate commonly used definitions of WSS and related parameters, provide a detailed survey on how WSS can be defined and used in image-based CFD studies, and describe how it has been related to IA growth and rupture. In conjunction with Part 1, we hope this review sheds light on the disparate CFD findings concerning the role of WSS in IA growth and rupture.

Current Status of Image-Based CFD Studies of Aneurysmal Hemodynamics

Hemodynamics plays a central role throughout IA natural history.[11] Because of a lack of appropriate animal models to study hemodynamic-biologic mechanisms, investigators have resorted to the use of CFD analysis of patient IA images[1-5,12,13,17-38] to identify hemodynamic characteristics and explore potential mechanisms associated with IA growth and rupture. The capability of image-based CFD to investigate detailed 3D aneurysmal hemodynamics, combined with the availability of segmentation tools such as the Vascular Modeling Toolkit (www.vmtk.org),[39] has contributed to an increasing number of hemodynamic IA studies over the past 2 decades. There have been several large, multi-nation projects that use image-based CFD to study aneurysms. For example, the @neurIST project, with a €17 million budget, gathered data from 28 public and private institutions in 12 European countries from 2006–2010.[40-42]

Over the past 10 years, the number of publications in this field has increased nearly exponentially,[9] as image-based CFD studies have grown broader and deeper. Simulations have steadily migrated from idealized geometries to patient-specific IA geometries, from steady-state flow to pulsatile flow, and from qualitative flow pattern descriptions[20,22,23,43] to sophisticated quantitative statistical analyses.[4,5,30] Furthermore, efforts to bolster statistical power have increased the number of patient-specific IA cases per hemodynamic study from 1 (in the year 2003)[44] to 210 (in the year 2011).[5] Worldwide interactions between engineers and clinicians, exemplified by the annual International Intracranial Stent Meeting (http://www.ics-meeting.net), have stressed the dire medical need for clinically relevant information, including rupture risk assessments.

The rising number of CFD studies has resulted in a growing number of proposed hemodynamic parameters related to IA growth and rupture. On-line Table 1 summarizes the most commonly defined hemodynamic parameters in these studies. Clearly, WSS has been the focus because it is a measurable biome-chanical factor (obtained from CFD calculation) that holds the promise of reporting and predicting IA development.

WSS in Aneurysm Development

WSS and Pressure in IA Pathologic Remodeling. Wall shear stress directly acts on the luminal surface of vascular endothelial cells to stimulate biologic responses through the main stages of IA natural history. As shown in Fig 2*A* of Part 1,[11] blood flow interacts with the IA wall by exerting both pressure and WSS. Blood pressure elicits tensile stresses in the wall, which, when unbalanced, stimulate medial cell–mediated collagen synthesis and cross-linking and collagen degradation.[45] Wall shear stress, on the other hand, is sensed by endothelial cells, which transduce this mechanical signal into biologic signals, activating biochemical pathways that maintain vascular homeostasis and regulate remodeling.[46] Aberrant levels of WSS elicit endothelial cell–mediated pathologic responses, including pro-inflammatory behavior,[16] matrix metalloproteinase activation,[47] cell death,[48] extracellular matrix degradation, and destructive remodeling.[15,49,50]

Although both tensile stress and WSS can affect aneurysmal pathobiology, the current exploration of WSS-mediated effects appears to offer a greater clinical utility for the following reasons: 1) Patient-specific in vivo flow dynamic simulation, that is, CFD, and WSS analyses can be routinely performed from existing medical imaging modalities (DSA, CTA, MRA). Conversely, tensile stress calculation requires knowledge of patient-specific, in vivo wall thickness and material properties, which are unavailable from current imaging capabilities. 2) The simplified analyses of tensile stress–mediated pathways involve collagen turnover in response to imbalanced wall stresses. Theoretically, this process should reduce the imbalance and ultimately lead to IA stabilization, not to unbound growth or rupture.[51] The rupture event itself, a catastrophe that results when wall stress exceeds wall strength, is precipitated by a local weakening of the IA wall resulting from pathologic remodeling.[45] Without the means to monitor wall stress and wall strength, it is impossible to predict when an IA will rupture. However, because pathologic remodeling is partially mediated by abnormal WSS, which can persist throughout IA natural history, WSS may be a suitable for clinical application at this stage.

Various Definitions of WSS. By definition, WSS is a mechanical stress that acts tangential to the vessel lumen. For unsteady flow (which is always the case for patient aneurysms), instantaneous WSS can change its magnitude and direction with space and time. Motivated by different hypotheses regarding the hemodynamic conditions driving IA progression, CFD researchers have explored different variations of WSS definitions.

To reflect the hypothesis that lasting exposure to abnormal WSS potentiates wall weakening, WSS has been most commonly reported as the time-averaged magnitude of WSS (the mathematical definition is given in the first row of On-line Table 1), or TAWSS. Time-averaged wall shear stress is defined point-wise on the lumen of the vessel and plotted as a surface distribution. Unless explicitly stated otherwise, time-averaging over 1 cardiac cycle is usually implied. Occasionally, however, instantaneous WSS at a

certain time point in the cardiac cycle, such as peak systole or diastole, is used instead of TAWSS.

To compare the overall level of WSS among different aneurysms for risk stratification, TAWSS is sometimes further spatially averaged over the entire aneurysm sac, such that each aneurysm has one average aneurysmal WSS value.[5,30,31] Alternatively, some authors prefer to examine the spatial maximum (MWSS in On-line Table 1) of TAWSS in an aneurysm. Both values require identification of the IA neck and an objective method to isolate the aneurysm.[52,53]

To remove the dependence of WSS values on the inlet flow condition, the time- and space-averaged aneurysmal WSS can be normalized by the average parent vessel WSS value to become a nondimensional number[4] (second row in On-line Table 1). It has been suggested that normalized WSS is more reliable than the absolute WSS when used to stratify IA rupture risk,[4] especially when patient-specific inlet flow conditions are unavailable and CFD simulations are carried out under assumed inlet flow conditions. When surrogate (assumed) inlet flow boundary conditions are used, the CFD-generated absolute aneurysmal WSS values are not meaningful; only relative values are meaningful. Normalization by parent vessel WSS generated from the same CFD simulation minimizes the dependence on inlet conditions. Furthermore, this normalized ratio compares the pathologic IA wall with the healthy parent vessel wall, as a baseline. In parallel to such approaches in hemodynamic studies, recent morphologic studies have shown that to better inform rupture risk, aneurysm size should be evaluated relative to the parent vessel diameter (thus generating an important new morphologic metric, size ratio).[54] Size ratio is potentially better at predicting IA rupture risk than aneurysm size only.[4,54-56] Similarly, aneurysmal WSS values might be better evaluated against a healthy baseline from the individual at a specific location, for example, WSS values from the parent vessel.

Besides responding to TAWSS directly, endothelial cells respond to temporal oscillations and spatial gradients of WSS.[16,57,58] The hypothesis that directional variations of WSS induce pathologic endothelial cell responses (as in atherogenesis) is reflected by the oscillatory shear index (OSI), a dimensionless metric of directional changes in WSS[59] (third row in On-line Table 1). Oscillatory shear index is often used to describe the disturbance of a flow field. Additionally, spatial WSS gradient, the derivative of WSS along the flow direction, is also considered in some studies.[4] Variations of these factors, for example, low shearstress area (LSA)[4] and gradient oscillatory number factor (GON factor),[60] are summarized in On-line Table 1.

It is important to recognize that instantaneous WSS is a vector. During a cardiac cycle, the unsteady aneurysmal flow leaves imprints of flickering, swirling, and dancing WSS vectors on the luminal surface, forming various patterns such as sources, sinks, or streets. The definitions of WSS-derived hemodynamic factors above are degenerated forms that account only for the magnitude of WSS (as in TAWSS) or the magnitude of the cycle-averaged vector (as in OSI). How endothelial cells respond to various patterns of instantaneous WSS vectors is unknown but could play an important role in the pathologic remodeling leading to IA growth and rupture. When new evidence indicates such roles, new hemo-

dynamic parameters capturing these characteristics may need to be defined.

Currently, a plethora of WSS definitions and other flow parameters are confusing to both the clinical and engineering communities.[7-10] Findings from different studies correlating WSS to IA progression are not converging: both high and low WSS are correlated to growth and rupture. To gain a better understanding of these divergent findings, we systematically review the current literature on hemodynamic studies correlating high and low WSS to IA growth and rupture in the following 2 sections.

CFD Studies of High and Low WSS in Aneurysm Growth
The investigation of IA growth requires longitudinally following patients with 3D imaging. Because of a lack of reliable risk assessment systems, discovered IAs are often defensively treated, leaving only a small number of aneurysms for conservative observation and periodic imaging.[1,2,17] These IAs tend to be small or have no clear, safe surgical options.[1,2,17] Thus, only a limited number of studies have been able to investigate the hemodynamics of growing IAs.

In On-line Table 2, we summarize 5 published studies that investigated patient-specific hemodynamics during IA growth.[1-3,17,19] The number of patients in these studies ranged from 1 to 25. Impressively, 4[1-3,17] of the 5 studies used patient-specific inlet boundary conditions (velocity from phase-contrast MRA), which is more accurate for CFD simulation than the widely used, assumed inlet flow conditions.

Three of these studies found a correlation between IA growth and low aneurysmal WSS. Jou et al[1] demonstrated this correlation in their CFD analysis of 2 aneurysms. Additionally, a serial study containing baseline imaging and 4 follow-ups by Acevedo-Bolton et al[2] found that the region of maximal growth in a giant basilar trunk IA consistently had the lowest WSS (Fig 1A).[2] The same group analyzed 7 growing aneurysms in a follow-up study and found a linear correlation between the local displacement of the IA wall (that is, enlargement) and low WSS, as shown in Fig 1B.[17]

Studies by Sugiyama et al[3] and Sforza et al,[19] however, found that both low WSS and high WSS were associated with aneurysm growth. Sugiyama et al[3] reported 2 adjacent growing aneurysms in 1 patient, each with different hemodynamic characteristics and growing patterns. They found that the distal growing aneurysm was associated with low and oscillatory WSS in the entire aneurysm sac, whereas the proximal aneurysm was subjected to local high flow in the growing lobe.[3] In the other study, Sforza et al[19] followed several growing aneurysms. The growth of 3 aneurysms was correlated with high WSS impingement at the dome, whereas the growth of 2 aneurysms was correlated with low WSS at the dome.

These inconsistent findings may be attributed to a limited number of cases and thus selection biases. However, we believe that these contradictions may stem from the intrinsic mechanistic complexity of IAs. As hypothesized in Part 1,[11] both high and low WSS could drive IA progression. To confirm this, future investigations of IA growth would need to collect a larger volume of longitudinal data despite the inherent difficulties in building large, unskewed databases of unruptured growing IAs. One possible solution would be to implement population-based screening
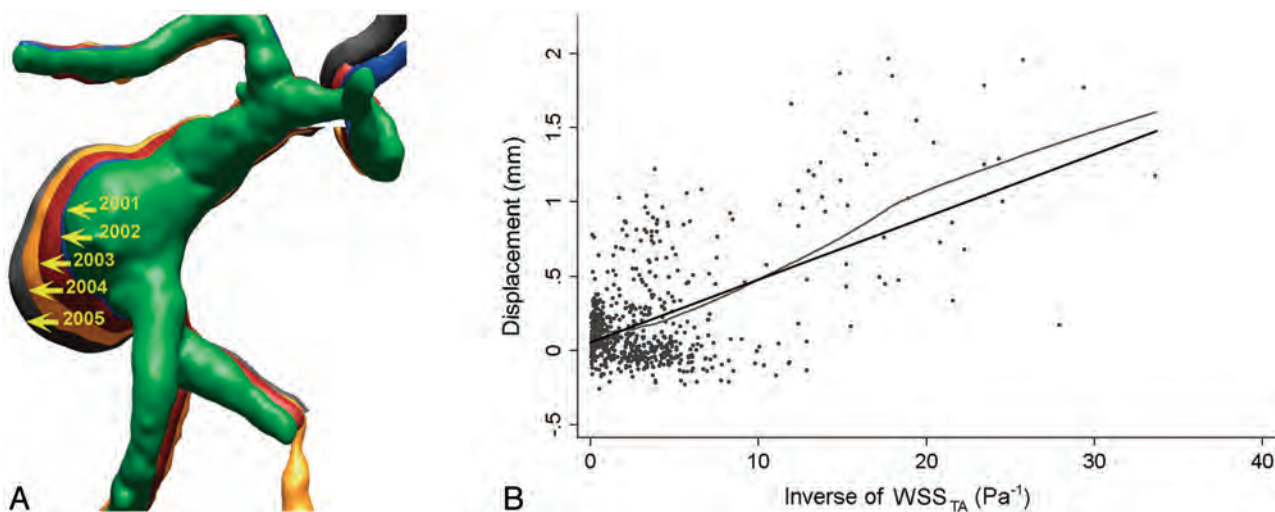
FIG 1. Longitudinally followed aneurysms show correlation between growth and low WSS. *A,* Overlying 3D images of a basilar-trunk aneurysm from consecutive years show dramatic size increase in the direction of the lowest WSS.[2] *B,* Linear correlation between local displacement of IA wall (IA enlargement) and inverse of time-averaged WSS ($P < .001$) in a follow-up study analyzing 7 growing IAs by the same group.[17] Reproduced with permission from Acevedo-Bolton G, Jou LD, Dispensa BP, et al. Estimating the hemodynamic impact of interventional treatments of aneurysms: numerical simulation with experimental validation: technical case report. *Neurosurgery* 2006;59:E429–30 and Boussel L, Rayz V, McCulloch C, et al. Aneurysm growth occurs at region of low wall shear stress: patient-specific correlation of hemodynamics and growth in a longitudinal study. *Stroke* 2008;39:2997–3002.

methods. For example, in Japan, screening of the population to detect and monitor IAs has provided the opportunity to longitudinally follow unruptured aneurysms. However, these conservatively followed IAs tend to be small, because large and giant IAs are probably treated rather than monitored.[28,31]

CFD Studies of High and Low WSS in Aneurysm Rupture

Whereas longitudinal data are needed to study aneurysm growth, cross-sectional data have been used to study IA rupture, accounting for a larger number of rupture risk assessment studies. By extracting hemodynamic features of ruptured IAs and comparing them with those of unruptured IAs, these studies implicitly assume that unruptured aneurysms resembling ruptured aneurysms are at higher risk of rupture than those that do not. Thus, hemodynamic parameters that significantly distinguish ruptured from unruptured IAs have been explored and suggested as potential markers for rupture risk.

In On-line Table 3, we chronologically summarize 24 studies that performed CFD on patient-specific aneurysm geometries in search of correlations between aneurysmal hemodynamics and rupture. The number of aneurysm cases in each study ranged from 6–210. Whereas all 24 studies included pulsatile CFD simulations, none used patient-specific flow waveforms at inlet boundaries. As for the specification of inlet flow magnitude, different authors adopted different assumptions across different cases, namely the same flow velocity,[12,27,33,34] the same flow rate,[4,13,20,28,30,31,35] or the same WSS.[5,22-26,43,61] The specified values were either taken from the literature or measured from one subject. Because the inlet boundary condition specified in this way is not patient-specific, absolute levels of physical quantities, such as WSS, calculated from CFD are not accurate. However, the distributions and relative levels of these hemodynamic quantities and flow patterns should not be significantly influenced by the inlet condition.[5,13]

Although many hemodynamic parameters have been proposed and analyzed, most of these studies have focused on WSS. Published results regarding whether aneurysmal WSS can significantly distinguish ruptured from unruptured aneurysms are conflicting. These findings typically fall into 4 categories: 1) high spatial mean WSS is correlated with rupture[5]; 2) low spatial mean WSS is correlated with rupture[4,27,29]; 3) high maximum WSS is correlated with rupture[22,23]; and 4) WSS is not correlated with rupture.[13,28,30] Examples of low WSS correlated with aneurysm rupture are presented in Fig 2.[4] Caution is required when interpreting results from these studies because many were based on small datasets and consequently have inherent selection bias.

Below, we discuss 2 notable studies that investigated a large number of IAs but produced inconsistent findings.[4,5] Xiang et al[4] published the first study that comprehensively examined multiple IA hemodynamic factors (as well as morphologic factors) in a large dataset. The authors analyzed 119 aneurysms and found that among the 7 hemodynamic parameters examined, 6 were significantly correlated with ruptured IAs. These were lower WSS, lower maximum WSS (MWSS), higher relative residence time, higher OSI, higher LSA, and larger number of vortices. Only 1 parameter, WSS gradient, showed no significance. Further multivariate logistic regression reduced the list of significant parameters to 2 independently significant parameters: WSS and OSI. The odds of an IA being ruptured can be estimated by use of a prediction model, which is an exponential function with ($-$WSS) and OSI in the exponent. According to this result, aneurysms with lower WSS and higher OSI have a larger chance of being ruptured.[4]

The essential finding that low WSS and high OSI are correlated with IA rupture is consistent with recent clinical results by Omodaka et al.[35] By intraoperatively identifying rupture points of
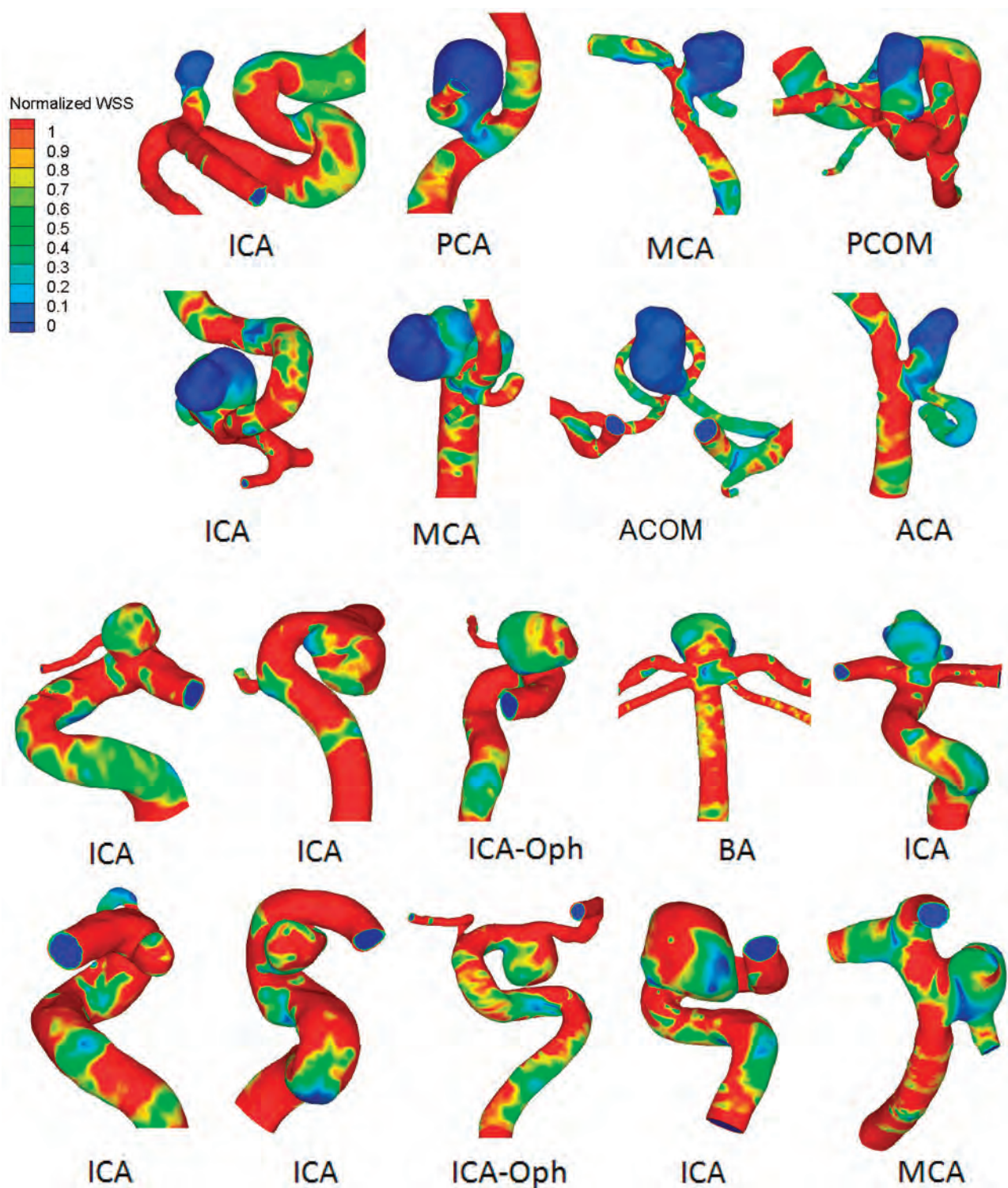
FIG 2. Examples of WSS distributions in ruptured (top 2 rows) and unruptured aneurysms (bottom 2 rows) from a study of 119 aneurysms by Xiang et al.[4] Ruptured aneurysms were associated with lower aneurysmal WSS ($P < .0001$). Reproduction with permission from Xiang J, Natarajan SK, Tremmel M, et al. Hemodynamic-morphologic discriminants for intracranial aneurysm rupture. *Stroke* 2011;42:144 –52

6 MCA IAs and then performing retrospective CFD analysis, they found that rupture points were located in regions of lower WSS and higher OSI, compared with surrounding areas. Interestingly, they found that by numerically removing blebs within the IA, areas of bleb formation were associated with flow impaction and were subjected to higher WSS than surrounding areas. Although

the number of cases in this study was relatively small, their findings support the hypothesis that low WSS could be causing the wall to weaken at rupture points.

Another large study, however, arrived at different conclusions. Cebral et al[5] analyzed 210 aneurysms and investigated 7 hemodynamic parameters. From univariate statistical analysis, they found

that 4 of the 7 parameters, that is, larger MWSS, larger inflow concentration index and larger shear concentration index, and lower viscous dissipation ratio, were significantly correlated with ruptured IAs. The other 3 hemodynamic parameters, that is, LSA, kinetic energy ratio, and low shear index, did not achieve statistical significance. By simulating these 210 aneurysms with different inlet flow conditions (2 different pulsatile conditions and 3 steady-flow conditions), the authors further demonstrated that though the values of hemodynamic quantities changed with different inlet flow conditions, the statistical differences or ratios between their mean values over the ruptured and unruptured IAs were maintained.

In the above-mentioned large studies (Xiang et al[4] and Cebral et al[5]), findings regarding LSA and MWSS, the only overlapping parameters analyzed, were contradictory. Low shear stress area significantly separated ruptured from unruptured IAs in the Xiang et al[4] study but not in the Cebral et al[5] study. This difference could partially be attributed to the different definitions of LSA used by these authors. Xiang et al[4] used 10% of parent vessel WSS value as the threshold for low WSS in LSA calculation, whereas Cebral et al[5] used a threshold below 1 standard deviation of parent vessel WSS. The conflicting results could also reflect different hemodynamic mechanisms dominating these 2 IA cohorts. Overall, their inconsistent LSA definitions make it difficult to compare their results.

In the case of MWSS, which had consistent definitions in both studies, the reported opposite associations of MWSS with rupture might suggest something more fundamental. Xiang et al[4] found that low MWSS along with low (average) WSS were significantly correlated with ruptured IAs. Furthermore, Xiang et al[4] found that in most of their IAs, the MWSS was located near the aneurysm neck. However, Cebral et al[5,20,22,23] found that high MWSS correlated with ruptured IAs and was mostly located in the IA dome. This raises an important question: did these 2 cohorts contain vastly different types of aneurysms, which might have been subjected to different flow and rupture mechanisms?

In a recent editorial, Strother and Jiang[10] suggested that IA may not be one single disease but may be a spectrum of a disease or even multiple diseases. In Part 1 of our 2-part review,[11] we hypothesized that there are 3 principal IA phenotypes: Type I, typically small IAs with thin, translucent walls, dominated by high WSS and impinging flow; Type II, typically large IAs with thick and atherosclerotic walls, dominated by low WSS and disturbed flow; and a third type, a combination of Type I and Type II, containing both high and low WSS. We proposed that both high and low WSS can drive IA growth and rupture by different biologic mechanisms: high WSS may trigger a mural cell–mediated destructive remodeling pathway, akin to the process of IA genesis[14,15] or bleb formation,[26,29] whereas low WSS may trigger an inflammatory cell–mediated destructive remodeling pathway, akin to atherosclerotic (aortic aneurysm) development. The 2 hypothesized pathways can dominate different phases of IA development (including rupture) or even different parts of the same aneurysm sac at a given time.

Given such heterogeneity in aneurysmal hemodynamic-biologic mechanisms and manifestation, studies with a limited number of samples could be skewed to one side of the spectrum or the other. Overall, however, we think that after the aneurysm initiation phase (which has been determined to be driven by high WSS

and high, positive WSS gradient[14,15]), aneurysm sac enlargement tends to continuously lower WSS, allowing inflammation to dominate the rest of IA development. Still, a smaller set of aneurysms may be continuously dominated by impinging flow because of their geometry; thus, their growth and rupture may be driven by high WSS through the noninflammatory pathway.

Summary
Collaborative efforts between computational researchers and clinicians have thrust image-based CFD to the forefront of emerging patient-specific IA evaluations. WSS-based hemodynamic metrics are promising predictors of IA growth and rupture. However, the rapid growth of this field has also generated inconsistent hemodynamic parameters and at times produced conflicting results, raising concerns of the clinical utility of image-based CFD.

The "high-versus-low WSS" controversy represents the pinnacle of this unsettling issue. Although it is not surprising to see inconsistent results from studies that are based on small datasets (typically 1–30 IA cases),[8] it is disconcerting that larger studies with consistent WSS definitions have produced opposite results concerning the correlation of WSS with IA rupture. This suggests that perhaps the mechanistic heterogeneity underlying IA growth and rupture leads to different characteristics within IA datasets collected at different centers, thereby producing the inconsistent findings reported in the current literature.

We believe that the intrinsic complexity of aneurysm growth and rupture mechanisms could be a major cause of inconsistent findings. As elaborated on in Part 1,[11] high and low WSS can elicit different hemodynamic-biologic pathways of pathologic remodeling, driving IA growth and rupture and accounting for heterogeneous aneurysm phenotypes. As such, IA heterogeneity may need to be taken into account in future large-scale correlative hemodynamic IA studies. Computational fluid dynamics is not "confounding factor dissemination"; rather, it enables us to appreciate the complexity of IA pathophysiology driven by hemodynamics. To close the gap between CFD research and clinical utility, however, we must perform CFD more thoughtfully. We expect that both larger databases and better ways of categorizing and analyzing IAs, along with increased knowledge of the hemodynamic-mechanobiology of IA, will continue to define the role of hemodynamics in IA growth and rupture, leading to more accurate rupture risk assessments and improved clinical utility of CFD analyses.

Future Directions
Going forward, the heterogeneity of IA presentation and the proposed underlying hemodynamic mechanisms should be addressed in large, multi-center, CFD studies. Large databases could help to consolidate contradictory WSS findings, form conceptual models of IA pathophysiology, and build a foundation for more accurate clinical risk stratification models.

To facilitate the creation of such databases, CFD researchers should begin to standardize and unify aneurysm modeling procedures and hemodynamic variable definitions.[8] Once these procedures are standardized, it will be possible to combine and compare datasets from different centers with assured consistency, which is required to conduct studies of aneurysm rupture risk that

are valid across centers and populations. A common framework, available across the entire aneurysm research community, on which to study the connections between hemodynamics and aneurysm growth and rupture, will help accomplish this goal. On the other hand, we should also advance the clinical integration of user-friendly, streamlined computational tools at the point of care. Such clinically oriented IA analysis tools will enable clinicians to gain first-hand experience with CFD modeling, sharpen their intuition of treatment decisions and planning on the basis of flow visualization, and rapidly provide sorely needed constructive feedback and guidance to computational researchers.[8]

Mechanistic heterogeneity implies that different datasets, or subsets of datasets, could be dominated by different mechanisms of IA growth and rupture. Thus, whereas larger databases could increase the statistical prowess of predictive metrics, they also could produce more divergence. More sophisticated data mining and analytic methods will be required to categorize aneurysms. In accordance with the hypothesis that both high and low WSS can drive aneurysm growth and rupture through different biologic mechanisms,[11] integrative hemodynamic parameters capturing both mechanisms could be explored as potentially better risk predictors. Alternatively, aneurysms could be categorized by location or type for the extrapolation of separate predictive markers. These foreseeable developments are expected to not only produce more accurate predictors of IA growth and rupture, but also consolidate the large number of predictive metrics suggested in the literature.

Modeling and analytic efforts must be directed by a better understanding of hemodynamic-biologic and mechanobiological mechanisms of IA growth and rupture. Ideally, both hemodynamic-biologic and mechanobiological mechanisms at play during IA natural history should be tested in experimental models, but endogenous models of IA growth and rupture do not currently exist. At the present time, efforts can be made to follow different types of IAs (eg, Type I and Type II, see Part 1[11]) in patients when possible, so that specific hemodynamic-biologic pathways related to aneurysm growth and rupture can be identified. Furthermore, study of the mechanobiology of the IA wall, for example, the interaction of aneurysm biology and wall mechanics, will help researchers better understand the mechanisms of IA growth and rupture that cannot be explained wholly by hemodynamics.[9]

It is important to recognize that most aneurysm datasets obtained clinically are composed of cross-sectional data. Bringing computational tools to the bedside can improve our ability to follow and analyze aneurysm hemodynamics and natural history longitudinally. Such data are vital not only for the validation of predictive models built from cross-sectional data but also for the development of new models that incorporate the progression of time. As proposed in Part 1,[11] hemodynamics may change roles throughout IA natural history. The advancement of IA wall mechanobiological measurements, combined with longitudinal aneurysm datasets, could enable a new class of computational tools, for example, fluid-solid-growth models, to simulate IA progression.[45] Such longitudinal models could provide a general framework upon which researchers might explore aneurysm evolution and test hypotheses related to aneurysm growth and rupture, leading to more robust rupture risk assessments.[9,45] Fur-

thermore, by incorporating hemodynamics, mechanobiological wall mechanics, and geometry changes throughout IA natural history, fluid-solid-growth models could allow researchers to infer changing mechanisms during growth and rupture.

We hope that this review not only helps to delineate the current CFD literature to clarify the WSS controversy but also calls for worldwide interactions among CFD researchers and clinicians. Collaborative efforts will converge discrepancies in the field and ultimately lead to a greater understanding of the complex aneurysm pathophysiology, more robust risk predictors, and better patient care outcomes.

REFERENCES
1. Jou LD, Wong G, Dispensa B, et al. **Correlation between lumenal geometry changes and hemodynamics in fusiform intracranial aneurysms.** *AJNR Am J Neuroradiol* 2005;26:2357–63
2. Acevedo-Bolton G, Jou LD, Dispensa BP, et al. **Estimating the hemodynamic impact of interventional treatments of aneurysms: numerical simulation with experimental validation: technical case report.** *Neurosurgery* 2006;59:E429–30
3. Sugiyama SI, Meng H, Funamoto K, et al. **Hemodynamic analysis of growing intracranial aneurysms arising from a posterior inferior cerebellar artery.** *World Neurosurg* 2012;78:462–68
4. Xiang J, Natarajan SK, Tremmel M, et al. **Hemodynamic-morphologic discriminants for intracranial aneurysm rupture.** *Stroke* 2011;42:144–52
5. Cebral JR, Mut F, Weir J, et al. **Quantitative characterization of the hemodynamic environment in ruptured and unruptured brain aneurysms.** *AJNR Am J Neuroradiol* 2011;32:145–51
6. Steinman DA. **Computational modeling and flow diverters: a teaching moment.** *AJNR Am J Neuroradiol* 2011;32:981–83
7. Kallmes DF. **Point: CFD— computational fluid dynamics or confounding factor dissemination.** *AJNR Am J Neuroradiol* 2012;33:395–96
8. Cebral JR, Meng H. **Counterpoint: realizing the clinical utility of computational fluid dynamics— closing the gap.** *AJNR Am J Neuroradiol* 2012;33:396–98
9. Robertson AM, Watton PN. **Computational fluid dynamics in aneurysm research: critical reflections, future directions.** *AJNR Am J Neuroradiol* 2012;33:992–95
10. Strother CM, Jiang J. **Intracranial aneurysms, cancer, x-rays, and computational fluid dynamics.** *AJNR Am J Neuroradiol* 2012;33:991–92
11. Meng H, Tutino VM, Xiang J, et al. **High WSS or low WSS? Complex interactions of hemodynamics with intracranial aneurysm initiation, growth, and rupture: toward a unifying hypothesis.** *AJNR Am J Neuroradiol* 2014;35:1254–62
12. Shojima M, Oshima M, Takagi K, et al. **Magnitude and role of wall shear stress on cerebral aneurysm: computational fluid dynamic study of 20 middle cerebral artery aneurysms.** *Stroke* 2004;35:2500–05
13. Jou LD, Lee DH, Morsi H, et al. **Wall shear stress on ruptured and

unruptured intracranial aneurysms at the internal carotid artery. *AJNR Am J Neuroradiol* 2008;29:1761–67

14. Meng H, Wang Z, Hoi Y, et al. **Complex hemodynamics at the apex of an arterial bifurcation induces vascular remodeling resembling cerebral aneurysm initiation.** *Stroke* 2007;38:1924–31

15. Metaxa E, Tremmel M, Natarajan SK, et al. **Characterization of critical hemodynamics contributing to aneurysmal remodeling at the basilar terminus in a rabbit model.** *Stroke* 2010;41:1774–82

16. Malek AM, Alper SL, Izumo S. **Hemodynamic shear stress and its role in atherosclerosis.** *JAMA* 1999;282:2035–42

17. Boussel L, Rayz V, McCulloch C, et al. **Aneurysm growth occurs at region of low wall shear stress: patient-specific correlation of hemodynamics and growth in a longitudinal study.** *Stroke* 2008;39:2997–3002

18. Tateshima S, Tanishita K, Omura H, et al. **Intra-aneurysmal hemodynamics during the growth of an unruptured aneurysm: in vitro study using longitudinal CT angiogram database.** *AJNR Am J Neuroradiol* 2007;28:622–27

19. Sforza DM, Putman CM, Tateshima S, et al. **Hemodynamics characteristics of growing and stable aneurysms.** *ASME Summer Bioengineering Conference,* Fajardo, Puerto Rico, June 20–23, 2012

20. Cebral JR, Castro MA, Burgess JE, et al. **Characterization of cerebral aneurysms for assessing risk of rupture by using patient-specific computational hemodynamics models.** *AJNR Am J Neuroradiol* 2005;26:2550–59

21. Hassan T, Timofeev EV, Saito T, et al. **A proposed parent vessel geometry-based categorization of saccular intracranial aneurysms: computational flow dynamics analysis of the risk factors for lesion rupture.** *J Neurosurg* 2005;103:662–80

22. Castro M, Putman C, Radaelli A, et al. **Hemodynamics and rupture of terminal cerebral aneurysms.** *Acad Radiol* 2009;16:1201–07

23. Castro MA, Putman CM, Sheridan MJ, et al. **Hemodynamic patterns of anterior communicating artery aneurysms: a possible association with rupture.** *AJNR Am J Neuroradiol* 2009;30:297–302

24. Chien A, Castro MA, Tateshima S, et al. **Quantitative hemodynamic analysis of brain aneurysms at different locations.** *AJNR Am J Neuroradiol* 2009;30:1507–12

25. Chien A, Tateshima S, Sayre J, et al. **Patient-specific hemodynamic analysis of small internal carotid artery-ophthalmic artery aneurysms.** *Surg Neurol* 2009;72:444–50

26. Cebral JR, Sheridan M, Putman CM. **Hemodynamics and bleb formation in intracranial aneurysms.** *AJNR Am J Neuroradiol* 2010;31:304–10

27. Lu G, Huang L, Zhang XL, et al. **Influence of hemodynamic factors on rupture of intracranial aneurysms: patient-specific 3D mirror aneurysms model computational fluid dynamics simulation.** *AJNR Am J Neuroradiol* 2011;32:1255–61

28. Qian Y, Takao H, Umezu M, et al. **Risk analysis of unruptured aneurysms using computational fluid dynamics technology: preliminary results.** *AJNR Am J Neuroradiol* 2011;32:1948–55

29. Zhang Y, Mu S, Chen J, et al. **Hemodynamic analysis of intracranial aneurysms with daughter blebs.** *Eur Neurol* 2011;66:359–67

30. Goubergrits L, Schaller J, Kertzscher U, et al. **Statistical wall shear stress maps of ruptured and unruptured middle cerebral artery aneurysms.** *J R Soc Interface* 2012;9:677–88

31. Takao H, Murayama Y, Otsuka S, et al. **Hemodynamic differences between unruptured and ruptured intracranial aneurysms during observation.** *Stroke* 2012;43:1436–39

32. Hoi Y, Meng H, Woodward SH, et al. **Effects of arterial geometry on aneurysm growth: three-dimensional computational fluid dynamics study.** *J Neurosurg* 2004;101:676–81

33. Shojima M, Oshima M, Takagi K, et al. **Role of the bloodstream impacting force and the local pressure elevation in the rupture of cerebral aneurysms.** *Stroke* 2005;36:1933–38

34. Valencia A, Morales H, Rivera R, et al. **Blood flow dynamics in patient-specific cerebral aneurysm models: the relationship between wall shear stress and aneurysm area index.** *Med Eng Phys* 2008;30:329–40

35. Omodaka S, Sugiyama S, Inoue T, et al. **Local hemodynamics at the rupture point of cerebral aneurysms determined by computational fluid dynamics analysis.** *Cerebrovasc Dis* 2012;34:121–29

36. Kawaguchi T, Kanamori M, Takazawa H, et al. **Flow dynamics analysis in patients with a ruptured middle cerebral artery aneurysm: a case report.** *No Shinkei Geka* 2011;39:281–86

37. Miura Y, Ishida F, Umeda Y, et al. **Low wall shear stress is independently associated with the rupture status of middle cerebral artery aneurysms.** *Stroke* 2013;44:519–21

38. Xu J, Yu Y, Wu X, et al. **Morphological and hemodynamic analysis of mirror posterior communicating artery aneurysms.** *PloS One* 2013;8:e55413

39. Antiga L, Piccinelli M, Botti L, et al. **An image-based modeling framework for patient-specific computational hemodynamics.** *Med Biol Eng Comput* 2008;46:1097–112

40. Geers AJ, Larrabide I, Radaelli AG, et al. **Patient-specific computational hemodynamics of intracranial aneurysms from 3D rotational angiography and CT angiography: an in vivo reproducibility study.** *AJNR Am J Neuroradiol* 2011;32:581–86

41. Morales HG, Kim M, Vivas EE, et al. **How do coil configuration and packing density influence intra-aneurysmal hemodynamics?** *AJNR Am J Neuroradiol* 2011;32:1935–41

42. Marzo A, Singh P, Larrabide I, et al. **Computational hemodynamics in cerebral aneurysms: the effects of modeled versus measured boundary conditions.** *Ann Biomed Eng* 2011;39:884–96

43. Cebral JR, Mut F, Weir J, et al. **Association of hemodynamic characteristics and cerebral aneurysm rupture.** *AJNR Am J Neuroradiol* 2011;32:264–70

44. Steinman DA, Milner JS, Norley CJ, et al. **Image-based computational simulation of flow dynamics in a giant intracranial aneurysm.** *AJNR Am J Neuroradiol* 2003;24:559–66

45. Humphrey JD, Taylor CA. **Intracranial and abdominal aortic aneurysms: similarities, differences, and need for a new class of computational models.** *Annu Rev Biomed Eng* 2008;10:221–46

46. Nixon AM, Gunel M, Sumpio BE. **The critical role of hemodynamics in the development of cerebral vascular disease.** *J Neurosurg* 2010;112:1240–53

47. Ota R, Kurihara C, Tsou TL, et al. **Roles of matrix metalloproteinases in flow-induced outward vascular remodeling.** *J Cereb Blood Flow Metab* 2009;29:1547–58

48. Frosen J, Tulamo R, Paetau A, et al. **Saccular intracranial aneurysm: pathology and mechanisms.** *Acta Neuropathol* 2012;123:773–86

49. Wang Z, Kolega J, Hoi Y, et al. **Molecular alterations associated with aneurysmal remodeling are localized in the high hemodynamic stress region of a created carotid bifurcation.** *Neurosurgery* 2009;65:169–77

50. Kolega J, Gao L, Mandelbaum M, et al. **Cellular and molecular responses of the basilar terminus to hemodynamics during intracranial aneurysm initiation in a rabbit model.** *J Vasc Res* 2011;48:429–42

51. Watton PN, Selimovic A, Raberger NB, et al. **Modelling evolution and the evolving mechanical environment of saccular cerebral aneurysms.** *Biomech Modeling Mechanobiol* 2011;10:109–32

52. Cardenes R, Pozo JM, Bogunovic H, et al. **Automatic aneurysm neck detection using surface Voronoi diagrams.** *IEEE Trans Med Imaging* 2011;30:1863–76

53. Larrabide I, Cruz Villa-Uriol M, Cardenes R, et al. **Three-dimensional morphological analysis of intracranial aneurysms: a fully automated method for aneurysm sac isolation and quantification.** *Med Physics* 2011;38:2439–49

54. Dhar S, Tremmel M, Mocco J, et al. **Morphology parameters for intracranial aneurysm rupture risk assessment.** *Neurosurgery* 2008;63:185–96

55. Rahman M, Smietana J, Hauck E, et al. **Size ratio correlates with intracranial aneurysm rupture status: a prospective study.** *Stroke* 2010;41:916–20

56. Ma D, Tremmel M, Paluch RA, et al. **Size ratio for clinical assessment of intracranial aneurysm rupture risk.** *Neurol Res* 2010; 32:482–86

57. Dolan JM, Meng H, Singh S, et al. **High fluid shear stress and spatial shear stress gradients affect endothelial proliferation, survival, and alignment.** *Ann Biomed Eng* 2011;39:1620–31

58. LaMack JA, Friedman MH. **Individual and combined effects of shear stress magnitude and spatial gradient on endothelial cell gene expression.** *Am J Physiol Heart Circ Physiol* 2007;293: H2853–59

59. He X, Ku DN. **Pulsatile flow in the human left coronary artery bifurcation: average conditions.** *J Biomech Eng* 1996;118:74–82

60. Shimogonya Y, Ishikawa T, Imai Y, et al. **Can temporal fluctuation in spatial wall shear stress gradient initiate a cerebral aneurysm? A proposed novel hemodynamic index, the gradient oscillatory number (GON).** *J Biomech* 2009;42:550–54

61. Chien A, Tateshima S, Castro M, et al. **Patient-specific flow analysis of brain aneurysms at a single location: comparison of hemodynamic characteristics in small aneurysms.** *Med Biol Eng Comput* 2008;46:1113–20

62. Kawaguchi T, Nishimura S, Kanamori M, et al. **Distinctive flow pattern of wall shear stress and oscillatory shear index: similarity and dissimilarity in ruptured and unruptured cerebral aneurysm blebs.** *J Neurosurg* 2012;117:774–80

Review of Transcranial Doppler Ultrasound to Detect Microemboli during Orthopedic Surgery

B.S. Silbert, L.A. Evered, D.A. Scott, S. Rahardja, R.P. Gerraty, and P.F. Choong

ABSTRACT

SUMMARY: Transcranial Doppler ultrasonography has been used to detect microemboli in the middle cerebral artery during orthopedic surgery. We conducted a comprehensive systematic literature review of transcranial Doppler ultrasonography in orthopedic surgery to evaluate its status in this setting. Fourteen studies were selected for qualitative analysis. The highest number of patients studied was 45; emboli were detected in all studies, occurring in 20%–100% of patients. Most embolic counts were below 10, but some high counts were noted. No study reported all the technical parameters of the transcranial Doppler ultrasonography. All studies assessed neurologic status, and 6 studies evaluated cognitive function postoperatively. No study identified an association between postoperative cognitive function and embolic count. Six studies sought the presence of right-to-left shunts.

ABBREVIATIONS: HITS = high-intensity transient signals; PFO = patent foramen ovale; TCD = transcranial Doppler ultrasonography; TEE = transesophageal echocardiography

Transcranial Doppler uses sonography to study cerebral blood flow velocity and can be used to detect microembolic material in the cerebral circulation. In orthopedic surgery, sonography was originally introduced to detect fat embolism in the venous system after long bone fracture[1-3] and subsequently to detect microemboli in the middle cerebral artery.[4] In general, microemboli that enter the venous circulation are largely filtered out by the pulmonary circulation but, in some cases, may cross into the systemic circulation by either pulmonary shunts or a right-to-left shunt within the heart.

In addition to fat, it is believed that other solid particles such as thrombus, tissue, and cement may pass into the circulation as microemboli during orthopedic surgery. Gas microemboli have also been noted during orthopedic surgery,[5] though the exact source is open to conjecture. Air may enter blood vessels in the surgical field, originate in the intravenous solutions, or arise from agitation during surgical manipulation.

Transcranial Doppler ultrasonography (TCD) has been used in orthopedic surgery to count these microemboli that are detected as high-intensity transient signals in (HITS) the MCA. In addition to counting the number of microemboli in the cerebral circulation, investigators have also sought to identify which specific surgical manipulations lead to microemboli entering the cerebral circulation and thus potentially placing the patient at risk.[6,7]

Large emboli in the arterial circulation that reach the brain may cause overt neurologic symptoms (ie, stroke). Smaller microemboli may cause more subtle neurologic damage manifesting as postoperative cognitive dysfunction.[8] Several studies have sought to identify whether neurologic or cognitive change is related to the number of HITS (microemboli) detected in the MCA.

The use of TCD requires technical expertise and accurate interpretation of the signal. Differences in criteria used for signal identification originally caused confusion and led a Consensus Committee in 1995 to recommend the criteria for identification of HITS (Table 1).[9] The Consensus Committee suggested that investigators specify ultrasonic frequency, dynamic range, gain settings, and identification criteria for classifying HITS. A subsequent International Consensus Group recommended that specific parameters of the ultrasonic device be reported (Table 2) in addition to the detection criteria and also stated that automatic emboli detection did not have the required sensitivity and specificity for clinical use.[10]

We systematically reviewed studies that used TCD intraoperatively in orthopedic surgery to detect cerebral emboli with the following specific aims:

From the Department of Anaesthesia (B.S.S., L.A.E., D.A.S., S.R.), Centre for Anaesthesia and Cognitive Function, St. Vincent's Hospital, Melbourne, Australia; Department of Anaesthesia (B.S.S., L.A.E., D.A.S.), Perioperative and Pain Medicine Unit, Melbourne Medical School, and Department of Surgery (P.F.C.), University of Melbourne, Melbourne, Australia; Epworth Healthcare (R.P.G.), Richmond, Victoria, Australia; and Department of Medicine (R.P.G.), Epworth HealthCare, Monash University, Melbourne, Australia.

Please address correspondence to Brendan Silbert, MD, Department of Anaesthesia, St. Vincent's Hospital Melbourne, PO Box 2900, Fitzroy, Victoria, Australia; e-mail: brendan.silbert@svhm.org.au

○⊷ Indicates open access to non-subscribers at www.ajnr.org

▤ Indicates article with supplemental on-line tables.

http://dx.doi.org/10.3174/ajnr.A3688

Table 1: Criteria for identification of high-intensity transient signals

Criteria
1) Doppler microembolic signal is transient, usually lasting <300 ms
2) The amplitude is usually at least 3 dB higher than the background blood flow
3) A signal is unidirectional within the Doppler velocity spectrum
4) Microembolic signal is accompanied by an audible output

Table 2: Recommended parameters to be reported for transcranial Doppler ultrasound

Parameters
1) Ultrasound device
2) Transducer type
3) Insonated artery
4) Insonation depth
5) Algorithms for signal-intensity measurement
6) Scale settings
7) Detection threshold
8) Axial extension of sample volume
9) Fast Fourier transformation size (no. of points used)
10) Fast Fourier transformation length (time)
11) Fast Fourier transformation overlap
12) Transmitted ultrasound frequency
13) High-pass filter settings
14) Recording time

1) To identify whether the investigators have documented the features of the TCD device and detection criteria (as recommended)

2) To determine the number of emboli released during orthopedic surgery.

We also recorded whether the studies also sought to identify right-to-left shunts as an explanation for the cerebral emboli count or measure neurologic or cognitive change as a result of the cerebral emboli count.

MATERIALS AND METHODS
Eligibility Criteria
Eligibility criteria for article selection were any publication from 1965 through 2012 that used TCD during orthopedic surgery to detect HITS in the MCA. The publications must have been in the English language and contain surgical reports of intraoperative patient data of microemboli in the cerebral arteries in >1 case (ie, single case reports were excluded, but case series were included).

Study Identification
Electronic searches of MEDLINE and EMBASE were performed with results limited to the English language from 1965 to August 2012 inclusive. Three broad categories were combined to find appropriate articles for review. The categories were Doppler transcranial ultrasonography, orthopedic surgery, and embolism. The specific search strategies used in each data base are listed below.

Full-text articles were retrieved for any citations that were considered potentially relevant. Additional articles were sought by searching bibliographies of previous articles and review articles. Relevant journal and conference proceedings were also hand-searched. Inclusion criteria were English language, prospective,

intraoperative, orthopedic surgery, and use of TCD. Exclusion criteria were the use of TCD preoperatively or postoperatively, Doppler used other than transcranially, and nonorthopedic surgery. Reports of single cases were excluded, but case series consisting of multiple cases were included.

MEDLINE (Searched on www.EBSCOhost.com)
A combination of MeSH terms and keywords were used as follows: [{(MH "Ultrasonography, Doppler" OR MH "Blood Flow Velocity" OR "blood flow velocity" OR "Doppler") AND "transcranial"} OR MH "Ultrasonography, Doppler, Transcranial" OR "high-intensity transient signals"] AND [MH "Orthopedic Procedures +" OR "orthopedic*" OR "orthopedic*" OR "arthroplasty" OR "fracture*" OR MH "Musculoskeletal Diseases+/SU"] AND [MH "Intracranial Embolism" OR MH "Embolism" OR MH "Embolism, Fat+" OR "embol*" or "microembol*" or "micro-embol*"].

Twenty-nine results were selected from the MEDLINE search.

www.EMBASE.com
A combination of EMTREE terms and keywords were used as follows: [("Doppler echography"/de OR "Doppler" OR "high-intensity transient signals" OR "blood flow velocity" OR "blood flow velocity"/de) AND "transcranial"] AND ["orthopedic surgery"/exp OR "orthopedic*" OR "orthopedic*" OR "arthroplasty" OR "fracture*"] AND ["embolism"/de OR "fat embolism"/de OR "embol*" OR "microembol*" OR "microembolism"].

Thirty results were selected from the EMBASE search.

Fifty-nine articles were identified; screening removed 19 duplicates, leaving 40 eligible articles for review by 2 independent researchers. Fourteen articles satisfied the selection criteria (vide supra) for both researchers and were included for qualitative synthesis. Both independent researchers selected these 14 articles, so there was no need for an adjudication process. The reasons for eliminating articles are shown in Fig 1.

Of the 2 articles by Rodriguez et al in 2001,[11,12] the first describes 13 adolescents and the second describes 4 adolescents who appear to be a subset of the first article but have been included because they additionally underwent transesophageal echocardiography (TEE). Similarly, the 12 patients included by Patel et al[13] were also described in the subsequent article as part of a larger study[7]; both articles have been included because cognitive decline was sought in the larger study but not in the former study.

Although the primary search related to the use of TCD to detect microemboli in the cerebral circulation, we also noted whether the studies additionally sought the presence of a patent foramen ovale (PFO) or assessed the neurologic or cognitive changes postoperatively.

RESULTS
We found 14 publications that satisfied the inclusion criteria (Table 3). Ten of these publications additionally investigated the presence of PFO by using echocardiography or TCD after intravenous injection of agitated saline. All 14 publications made some comment on postoperative neurologic status, ranging from the
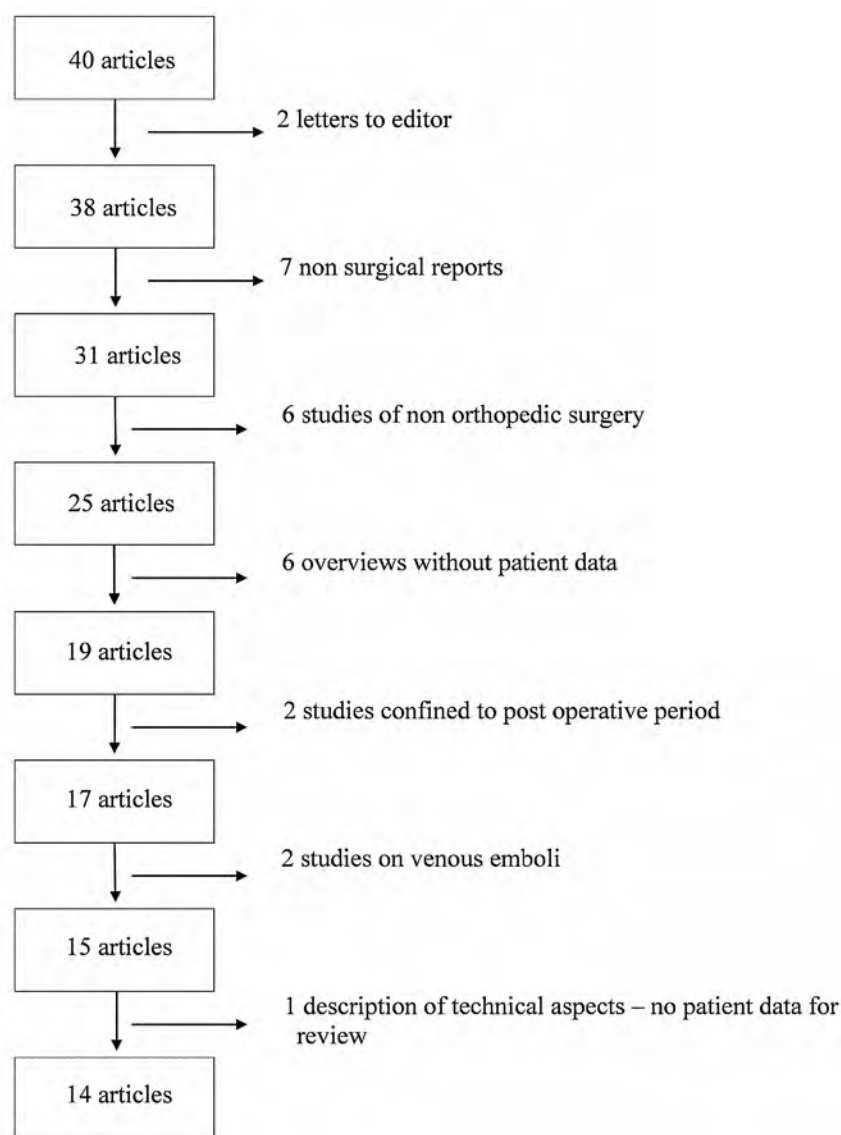
FIG 1. Reasons for exclusion of articles after selection.

Table 3: Studies selected for review

Study No.	Study Name	Year	No. of Patients Studied
1	Forteza et al[4]	1999	5
2	Sulek et al[20]	1999	22
3	Edmonds et al[17]	2000	23
4	Rodriguez et al[11]	2001	13
5	Rodriguez et al[12]	2001	4
6	Riding et al[15]	2004	41
7	Rodriguez et al[19]	2005	37
8	Kalairajah et al[18]	2006	24
9	Koch et al[8]	2007	24
10	Barak et al[5]	2008	22
11	Gray et al[6]	2008	20
12	Gray et al[22]	2009	20
13	Patel et al[13]	2009	24
14	Patel et al[7]	2010	45

presence or absence of neurologic complications to more subtle cognitive changes.

On-line Tables 1 and 2 contain a description of each study

included and whether the 14 specifications of the TCD used to detect HITS as recommended by the Consensus Committee[10] were documented. Ideally, each of the 14 points should be made available in accordance with the consensus article. However, as evident from On-line Tables 1 and 3, none of the studies documented all 14 requirements.

For each study, On-line Table 3 shows the type of surgery, the number of patients, the criteria for emboli detection, the method of counting HITS, and monitoring of either unilateral or bilateral MCAs. Ten studies conformed to the recommended detection criteria, 3 studies raised the threshold amplitude >3 dB higher than background flow, and 1 study reduced the duration to <100 ms. On-line Table 4 lists the emboli count for each study and whether a PFO was sought and neurologic or cognitive change was identified. Emboli were detected in all 14 studies and ranged from 20% to 100% of patients (Fig 2). Most counts were low (<10), but high counts were present in some patients.

On-line Table 4 also lists whether a right-to-left shunt was sought. The passage of microemboli from the venous into the arterial circulation can be confirmed by 2 methods either before or after surgery. Air microbubbles in an intravenous injection of agitated saline may pass into the arterial circulation via either cardiac or pulmonary communications and can be detected by TCD in the MCA as HITS. The early appearance of microemboli (eg, within the first 6 heart beats after injection[14]) suggests a cardiac communication (eg, functional or anatomic PFO) rather than a pulmonary communication (arteriovenous shunt). In the 2 studies by Patel et al,[7,13] the diagnostic time window for microemboli was 25 seconds. Riding et al[15] used a time window of 12 cardiac cycles, which is still arbitrary and open to challenge. Koch et al[8] used contrast agents with microbubbles, which do not survive pulmonary passage.[16]

The second method involves the use of echocardiography (either TEE or transthoracic echocardiography) to identify right-to-left intracardiac shunts. This is also achieved by an intravenous injection of agitated saline. Echocardiography is then used to track these bubbles as they pass into the left atrium or ventricle as opposed to detecting them in the MCA. Unlike the detection of a right-to-left shunt by using TCD, which may not clearly distinguish cardiac from pulmonary communications, TEE definitively identifies cardiac communications. On-line Table 4 suggests that
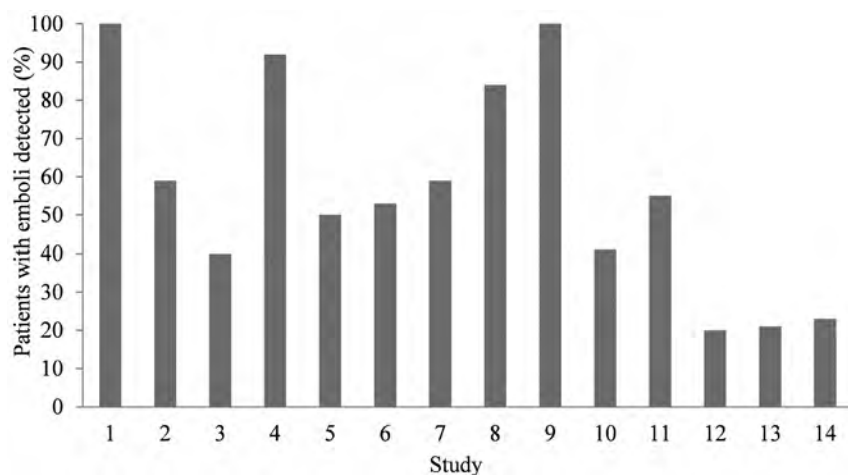
FIG 2. The percentage of patients with emboli detected in each of the 14 studies listed in Table 3.

when TEE identifies a PFO, emboli counts may be high, but pulmonary communications also account for the appearance of HITS. No definitive conclusions can be drawn from these studies on the size and number of microemboli originating from cardiac or pulmonary communications.

Finally, On-line Table 4 lists whether the presence of neurologic or cognitive change was sought and whether any such change was related to the number of emboli.

The 14 articles spanned the 13 years from 1999 to 2010. Five studies were on hip replacements, 3 on knee replacements, 2 on both operations, 2 on fractured long bones, and 2 on scoliosis corrections in adolescents. Among the adult studies, the number of patients in each study ranged from 5 to 45. Two of the articles[5,17] did not conform to the consensus criteria for detection of microemboli.[9] Despite the use of automatic HITS counting, 13 articles reviewed the HITS count off-line. One article neither conformed to the consensus criteria nor stated how the emboli count was undertaken.[18]

Echocardiography was used to detect PFO in 6 studies (transthoracic echocardiography in 1 study, transthoracic echocardiography and TEE together in 1 study, and TEE in the remaining 4 studies). TCD was used to detect arteriovenous shunts in 3 studies and both TEE and TCD in 1 study.[19] In general, higher counts were found in the presence of arteriovenous shunts.

All studies commented on the presence or absence of neurologic changes postoperatively. This appears to be assessed as part of routine follow-up, though 1 study specifically undertook neurologic examinations.[20] Six studies measured cognitive function, and 1 study measured quality of life postoperatively as a proxy for cognition.[13] No study found an association between neurologic or cognitive change and embolic count.

DISCUSSION

Articles that described the use of TCD to detect microemboli during orthopedic surgery were sought and reviewed for the accuracy of reporting and the number of microemboli counted. Additionally, we recorded whether the detection of right-to-left shunts was sought and whether any neurologic or postoperative cognitive changes were noted. Fourteen articles were included for qualitative synthesis, and the largest number of patients in a single study

was 45. The data for this important topic are thus limited, and this review highlights the need for larger and better reported studies in this area.

There are limitations on the quality of the reports. Few investigators explicitly stated all the features of the sonographic device used, particularly the 14 parameters recommended by the consensus statement.[10] Settings that were consistently included were the insonated artery (MCA), insonation depth (40–60 mm), and sonographic frequency (2 MHz). The specific device, sample volume, threshold, and recording time were all inconsistent and poorly reported.

Once data have been recorded, it is common practice to use an independent observer to count the HITS. The criteria for classification of HITS should be documented to allow comparisons of studies. The Consensus Committee of the Ninth International Cerebral Hemodynamic Symposium addressed this concern in 1995 and recommended the criteria for classification.[21] The results in On-line Tables 1 and 2 show that all studies stated the criteria for emboli detection, though 4 articles adjusted the threshold or duration from the recommended criteria. Additionally, while 12 of 14 articles included the guidelines used to count microemboli, the studies by Edmonds et al[17] and Kalairajah et al[18] did not specify how microemboli were counted. The validity of the results of these articles is of concern because the reliability of the TCD detection remains operator-dependent. Without independent analysis and strict classification guidelines, recorded data run the risk of including TCD signals which, in fact, are not real microemboli. Rodriguez et al[11] noted that diathermy created interference that could easily be misinterpreted as HITS (especially by automatic detection), but this was not mentioned by other authors.

This review of the literature confirms that microemboli are detectable in the MCA during orthopedic surgery for the specific procedures identified. The embolic count may be absent but is more commonly present in small numbers (<10) or high numbers (>100), the highest reported being 550 for the unifrequency probe.[6] A multifrequency probe detected 464 solid and 479 gas emboli in 1 patient,[5] but counting was automatic with off-line verification by the same operator. The count distribution appears bimodal, and there is evidence that the high counts are associated with PFO when this has been sought by TEE (On-line Table 4). There is no apparent relationship between the type of surgery and the embolic count. Patient factors obviously play a role in addition to surgical factors. Rather than a specific surgical operation being implicated, any operation involving bone and intramedullary instrumentation is most likely to lead to embolic events.[22]

Of the 6 studies that tested for cognitive change, 1 did not explicitly describe the cognitive tests used, simply referring to a mental test score without describing the tests.[18] The other 5 studies used a battery of neuropsychological tests at various time intervals before and after surgery. The definition of cognitive

change is controversial.[23,24] One study calculated the incidence of cognitive change by using the 20% rule (a decrease in cognitive score of 20% in 20% of the tests)[25] and showed that the number of emboli was not different in patients with and without cognitive change.[8] Three studies used group analyses to calculate the mean change in cognitive scores and showed that there was no difference in cognitive change between patients with and without detectable HITS.[6,7,22] Only 1 study converted a cognitive score to a standardized score by using normative means and SDs[19] but still found no association between the incidence of postoperative cognitive dysfunction and HITS count. Despite the use of highly differing methods of analysis, no study has found any association between HITS and neurologic or cognitive change.

This lack of association between embolic count and neuropsychological change brings into question the concept that microemboli released in orthopedic surgery may lead to cognitive changes. Even the patient with the highest embolic count ($>$500) was discharged with no detectable cognitive dysfunction.[6]

The early concern regarding microembolism to the brain during cardiac surgery being a cause of postoperative cognitive dysfunction[26,27] has not been confirmed in more recent studies[28] and systematic reviews.[29,30] Liu et al[31] reported a median embolic count of 430 (range, 155–2088) in patients undergoing cardiac surgery with cardiopulmonary bypass against a median embolic count of 2 (range, 0–66) in off-pump surgery but could show no difference in cognitive outcome. While the number of microemboli seen during cardiac surgery is much greater than that during orthopedic surgery, these are more likely to be predominantly gaseous. Cardiac surgical postoperative cognitive dysfunction has more recently been considered to be multifactorial.[32,33]

Several studies have used MR imaging and diffusion-weighted imaging after cardiac surgery to identify the relationship of new cerebral lesions to quantitative microemboli counts.[34,35] None of the studies in this review used MR imaging or diffusion-weighted imaging to explore the incidence of cerebral lesions in relation to microemboli count.

CONCLUSIONS

Studies using TCD to detect cerebral microemboli in orthopedic surgery have used small numbers of patients. Many of these studies have not disclosed the full details of the TCD machine specifications, though most have used the recommended detection criteria. TCD often detects microemboli in the MCA during orthopedic surgery, in which the counts are frequently low but may be high in approximately 20% cases. High counts appear to be associated with right-to-left shunts when verified by agitated saline detected in the MCA by using TCD or when visualized by using TEE or transthoracic echocardiography. There is no evidence that these microemboli are associated with cognitive change after surgery. A study with high patient numbers, accurate reporting of TCD machine specifications, and criteria for emboli detection, together with comprehensive cognitive testing and analysis, is required to definitively confirm these conclusions.

REFERENCES

1. Gurd AR. **Fat embolism: an aid to diagnosis.** *J Bone Joint Surg Br* 1970;52:732–37
2. Kelly GL, Dodi G, Eiseman B. **Ultrasound detection of fat emboli.** *Surg Forum* 1972;23:459–61
3. Herndon JH, Bechtol CO, Crickenberger DP. **Use of ultrasound to detect fat emboli during total hip replacement.** *Acta Orthop Scand* 1975;46:108–18
4. Forteza AM, Koch S, Romano JG, et al. **Transcranial Doppler detection of fat emboli.** *Stroke* 1999;30:2687–91
5. Barak M, Kabha M, Norman D, et al. **Cerebral microemboli during hip fracture fixation: a prospective study.** *Anesthe Analg* 2008;107:221–25
6. Gray AC, Torrens L, Howie CR, et al. **Cognitive function and cerebral emboli after primary hip arthroplasty.** *Hip Int* 2008;18:40–45
7. Patel RV, Stygall J, Harrington J, et al. **Cerebral microembolization during primary total hip arthroplasty and neuropsychologic outcome: a pilot study.** *Clin Orthop Relat Res* 2010;468:1621–29
8. Koch S, Forteza A, Lavernia C, et al. **Cerebral fat microembolism and cognitive decline after hip and knee replacement.** *Stroke* 2007;38:1079–81
9. **Basic identification criteria of Doppler microembolic signals: Consensus Committee of the Ninth International Cerebral Hemodynamic Symposium.** *Stroke* 1995;26:1123
10. Ringelstein EB, Droste DW, Babikian VL, et al. **Consensus on microembolus detection by TCD: International Consensus Group on Microembolus Detection.** *Stroke* 1998;29:725–29
11. Rodriguez RA, Letts M, Jarvis J, et al. **Cerebral microembolization during pediatric scoliosis surgery: a transcranial Doppler study.** *J Pediatr Orthop* 2001;21:532–36
12. Rodriguez RA, Sinclair B, Weatherdon D, et al. **Patent foramen ovale and brain microembolization during scoliosis surgery in adolescents.** *Spine (Phila Pa 1976)* 2001;26:1719–21
13. Patel R, Stygall J, Harrington J, et al. **Intra-operative cerebral microembolisation during primary hybrid total hip arthroplasty compared with primary hip resurfacing.** *Acta Orthop Belg* 2009;75:671–77
14. Klötzsch C, Janssen G, Berlit P. **Transesophageal echocardiography and contrast-TCD in the detection of a patent foramen ovale: experiences with 111 patients.** *Neurology* 1994;44:1603–06
15. Riding G, Daly K, Hutchinson S, et al. **Paradoxical cerebral embolization: an explanation for fat embolism syndrome.** *J Bone Joint Surg Br* 2004;86:95–98
16. Droste DW, Lakemeier S, Wichter T, et al. **Optimizing the technique of contrast transcranial Doppler ultrasound in the detection of right-to-left shunts.** *Stroke* 2002;33:2211–16
17. Edmonds CR, Barbut DM, Hager D, et al. **Intraoperative cerebral arterial embolization during total hip arthroplasty.** *Anesthesiology* 2000;93:315–18
18. Kalairajah Y, Cossey AJ, Verrall GM, et al. **Are systemic emboli reduced in computer-assisted knee surgery? A prospective, randomised, clinical trial.** *J Bone Joint Surg Br* 2006;88:198–202
19. Rodriguez RA, Tellier A, Grabowski J, et al. **Cognitive dysfunction after total knee arthroplasty: effects of intraoperative cerebral embolization and postoperative complications.** *J Arthroplasty* 2005;20:763–71
20. Sulek CA, Davies LK, Enneking FK, et al. **Cerebral microembolism diagnosed by transcranial Doppler during total knee arthroplasty: correlation with transesophageal echocardiography.** *Anesthesiology* 1999;91:672
21. Ringelstein EB. **Skepticism toward carotid ultrasonography: a virtue, an attitude, or fanaticism?** *Stroke* 1995;26:1743–46
22. Gray AC, Torrens L, Christie J, et al. **Cerebral emboli and cognitive**

function after intramedullary fracture fixation. *Injury* 2009;40: 742–45

23. Rasmussen LS, Larsen K, Houx P, et al. **The assessment of postoperative cognitive function.** *Acta Anaesthesiol Scand* 2001;45:275–89

24. Lewis M, Maruff P, Silbert B. **Statistical and conceptual issues in defining post-operative cognitive dysfunction.** *Neurosci Biobehav Rev* 2004;28:433–40

25. Lewis MS, Maruff P, Silbert BS, et al. **The sensitivity and specificity of three common statistical rules for the classification of post-operative cognitive dysfunction following coronary artery bypass graft surgery.** *Acta Anaesthesiol Scand* 2006;50:50–57

26. Fearn SJ, Pole R, Wesnes K, et al. **Cerebral injury during cardiopulmonary bypass: emboli impair memory.** *J Thoracic Cardiovasc Surg* 2001;121:1150–60

27. Braekken SK, Reinvang I, Russell D, et al. **Association between intraoperative cerebral microembolic signals and postoperative neuropsychological deficit: comparison between patients with cardiac valve replacement and patients with coronary artery bypass grafting.** *J Neurol Neurosurg Psychiatry* 1998;65:573–76

28. Stroobant N, Van Nooten G, Van Belleghem Y, et al. **Relation between neurocognitive impairment, embolic load, and cerebrovascular reactivity following on- and off-pump coronary artery bypass grafting.** *Chest* 2005;127:1967–76

29. Martin KK, Wigginton JB, Babikian VL, et al. **Intraoperative cerebral high-intensity transient signals and postoperative cognitive function: a systematic review.** *Am J Surg* 2009;197:55–63

30. Kruis RW, Vlasveld FA, Van Dijk D. **The (un)importance of cerebral microemboli.** *Semin Cardiothorac Vasc Anesth* 2010;14:111–18

31. Liu YH, Wang DX, Li LH, et al. **The effects of cardiopulmonary bypass on the number of cerebral microemboli and the incidence of cognitive dysfunction after coronary artery bypass graft surgery.** *Anesth Analg* 2009;109:1013–22

32. Selnes OA, McKhann GM. **Neurocognitive complications after coronary artery bypass surgery.** *Ann Neurol* 2005;57:615–21

33. Grocott HP, Homi HM, Puskas F. **Cognitive dysfunction after cardiac surgery: revisiting etiology.** *Semin Cardiothorac Vasc Anesth* 2005;9:123–29

34. Restrepo L, Wityk RJ, Grega MA, et al. **Diffusion- and perfusion-weighted magnetic resonance imaging of the brain before and after coronary artery bypass grafting surgery.** *Stroke* 2002;33:2909–15

35. Knipp SC, Matatko N, Wilhelm H, et al. **Evaluation of brain injury after coronary artery bypass grafting: a prospective study using neuropsychological assessment and diffusion-weighted magnetic resonance imaging.** *Eur J Cardiothorac Surg* 2004;25:791–800

Spinal Fluid Biomechanics and Imaging: An Update for Neuroradiologists

V. Haughton and K.-A. Mardal

ABSTRACT

SUMMARY: Flow imaging with cardiac-gated phase-contrast MR has applications in the management of neurologic disorders. Together with computational fluid dynamics, phase-contrast MR has advanced our understanding of spinal CSF flow. Phase-contrast MR is used to evaluate patients with Chiari I malformation who are candidates for surgical treatment. In theory, abnormal CSF flow resulting from the abnormal tonsil position causes syringomyelia and other neurologic signs and symptoms in patients with Chiari I. CSF flow imaging also has research applications in syringomyelia and spinal stenosis. To optimize MR acquisition and interpretation, neuroradiologists must have familiarity with healthy and pathologic patterns of CSF flow. The purpose of this review is to update concepts of CSF flow that are important for the practice of flow imaging in the spine.

ABBREVIATION: PCMR = phase-contrast MR

In the spinal canal, oscillatory CSF flow results primarily from the displacement of approximately 1.5 mL of fluid[1] from the cranial cavity as intracranial blood vessels expand in arterial systole (Monro-Kellie doctrine). CSF in the spinal canal moves caudally when the systolic pulse wave reaches the brain and cephalad during diastole. Caudal CSF flow has greater velocities and shorter duration than cephalad flow (Fig 1). The fluid entering the spinal canal displaces blood from the epidural venous plexus in the spine. CSF flow and the venous displacement diminish progressively from the cephalic end of the cervical canal to the caudal end of the thoracic canal. CSF oscillations are coupled to CSF pressure oscillations that, in the healthy adult, are approximately 90° out of phase with the velocity fluctuations.[2] Elastic properties of the tissues surrounding the subarachnoid space theoretically induce pressure waves, which to date are not fully characterized.[3] With contrast media or radionuclides in the spinal subarachnoid space, a slow convection of fluid is observed resulting from the continuous oscillation of CSF.[4]

Viscous and inertial properties, together with the complex anatomy of the subarachnoid space, determine CSF flow patterns. Viscosity creates a laminar pattern of flow, which can be thought of as layers of flowing fluid with no disruption between the layers.

Laminar CSF flow means that fluid moves with greater velocity in the center of a channel and with lesser velocity near a boundary resulting from frictional effects (Fig 2). Inertial forces resulting from the mass and velocity of CSF produce other effects in CSF flow. Acceleration and deceleration in CSF require the application of pressure. When a pressure gradient is applied to a laminar flow, the resulting velocities depend in part on the initial velocity of the fluid. Pressure gradients change flow velocities and affect flow
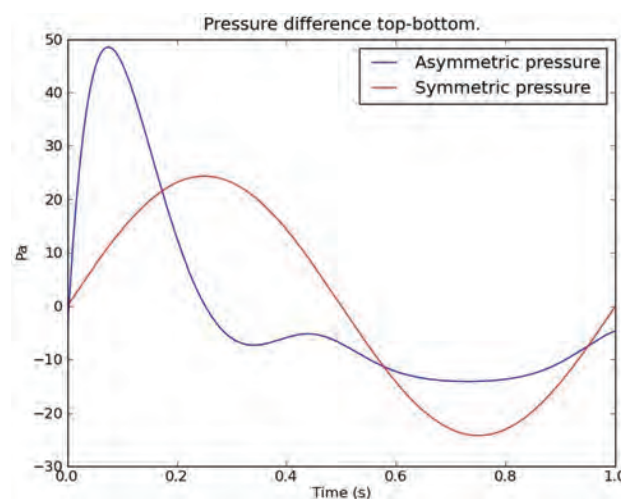
FIG 1. Plot of CSF velocity through the cardiac cycle (blue) and for comparison a sinusoid (red). CSF flow has greater velocity in the positive direction (systolic flow) than in the negative direction (diastolic flow). Systolic flow has shorter duration than diastolic flow. Flow volume in the 2 directions is equal.

From the Department of Radiology (V.H.), University of Wisconsin, Madison, Wisconsin; and Center for Biological Computing (K.-A.M.), Simula, Lysaker, Norway.

Please address correspondence to Victor Haughton, Department of Radiology, University of Wisconsin, 600 Highland Ave, Madison, WI 53792; e-mail: haughtonvictor@gmail.com
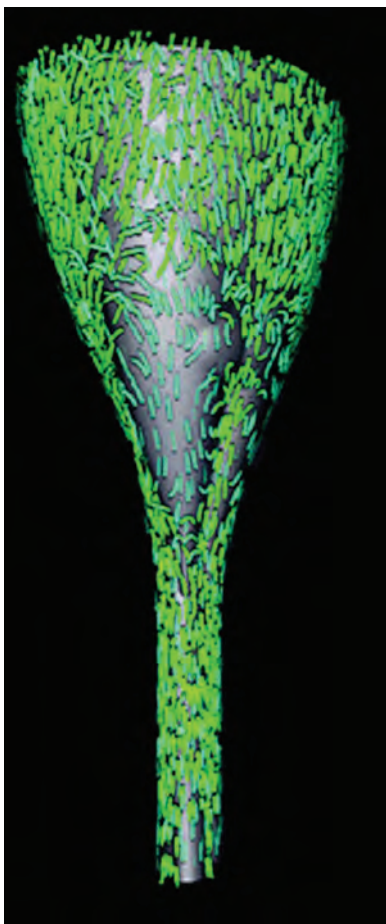
FIG 2. A 3D representation of CSF velocities in an idealized model of the posterior fossa and spinal canal of a patient with Chiari I. It displays the subarachnoid space posteriorly. It shows the direction and magnitude of flow throughout the space at one moment in the cardiac cycle by the direction and length of arrows. Flow velocities and flow directions vary from one region to another. The flow is more rapid at the cervical spine below the tonsils than at the craniovertebral junction. Flow predominates in the long axis of the model but has evidence of vortices in some areas.

near the dura and pia differently than flow in the middle of the channel. As flow oscillates between craniad and caudad directions, flow direction reverses throughout the subarachnoid space at slightly different times with the result that, for short periods of time, CSF flows in both craniad and caudad directions (synchronous bidirectional flow, Fig 3).[5] This synchronous bidirectional flow does not appear in phase-contrast MR (PCMR) studies of healthy human subjects because of the limited temporal and spatial resolution of the MR method. Inertial properties of fluid may in some geometries create a pattern of flow called "flow separation," which results in eddy currents and vortices (Fig 4).[6] Flow not aligned with the spinal axis can be demonstrated by computational fluid dynamics (Fig 5)[7] and by PCMR when multiple gradient directions are used.[6]

The anatomy of the subarachnoid space increases the complexity of CSF flow patterns in the spine. The flow velocities in any axial section of the spine have nonuniform distributions throughout the cardiac cycle, as PCMR and flow simulations show (Figs 6 and 7). PCMR images demonstrate flow jets anterolateral to the spinal cord and lower velocities elsewhere. Flow patterns differ
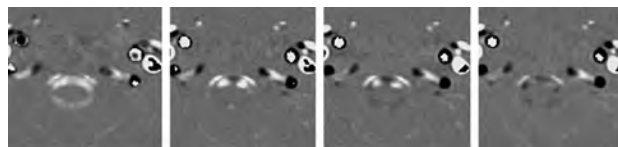
FIG 3. Four consecutive PCMR images of the 14 images obtained during one cardiac cycle in the upper cervical spine demonstrating flow in the subarachnoid space and in cervical arteries and veins. The first image shows flow anterior and posterior to the spinal cord has a positive sign (caudad direction). The second image shows flow anterolateral to the cord remains positive whereas flow in the midline anterior to the cord has a negative sign (cephalad). The third image shows more voxels with cephalad flow and fewer with caudad flow. The fourth image shows predominantly cephalad flow with little caudad flow detected. The 2 vessels anterolateral to the subarachnoid space have caudad flow in each of the 4 images.
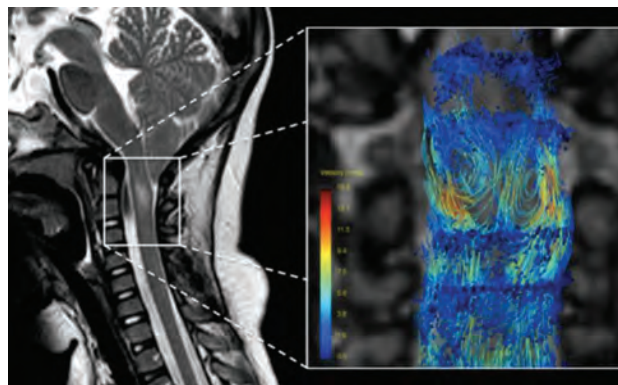
FIG 4. Sagittal T2-weighted MR image and coronal slab obtained with 4D PCMR acquisition method. The streamlines in PCMR image shows some flow along the spinal axis and some flow in vortices. Reproduced with permission from: Bunck AC, Kröger JR, Jüttner A, et al. Magnetic resonance 4D flow characteristics of cerebrospinal fluid at the craniocervical junction and the cervical spinal canal. *Eur Radiol* 2011;21:1788–96.
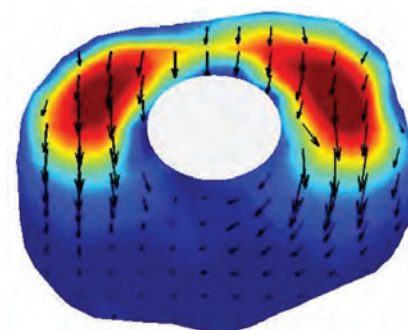
FIG 5. Computer graphic from a flow simulation showing flow along the spinal axis by red-blue-green color coding and in-plane flow by arrows in which velocity is coded by the dimensions of the arrows. Longitudinal flow predominates anterolateral to the cord (top of image) and in-plane flow predominates in a posterior direction. Modified from Roldan et al.[7]

from one spinal level to another. Peak CSF velocities increase progressively from C1 to C4 due to the tapering of this portion of the spinal canal. Systolic CSF velocities normally range up to 5 cm/s in the foramen magnum and up to 10 cm/s at C4 (Fig 8).[8] Diastolic CSF velocities also vary with level. Simulations in patient-specific models show the progressive increase in systolic and
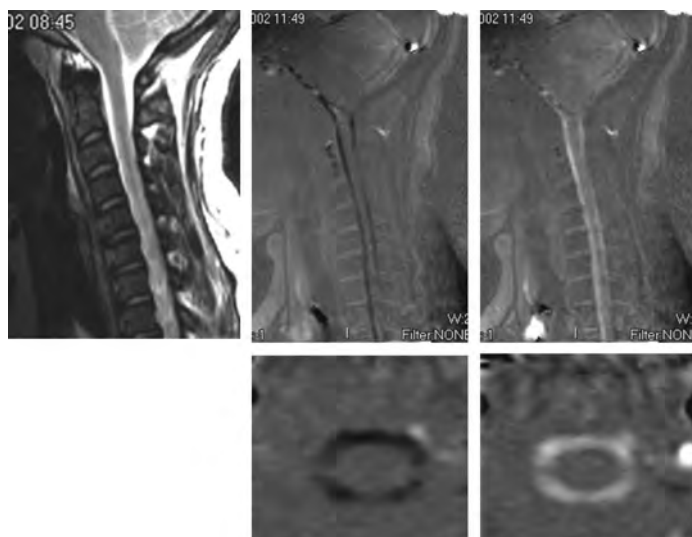
FIG 6. PCMR images in sagittal (upper row) and axial (lower row) views showing flow in one systolic and one diastolic phase of the cycle and for reference (top left) the sagittal T2-weighted image in the patient. These demonstrate more flow anterior to the cord than posterior. On careful inspection, the axial images show more flow anterolateral to the cord than posterior to it. Reproduced with permission from Hofkes SK, Iskandar BJ, Turski PA, et al. Differentiation between symptomatic Chiari I malformation and asymptomatic tonsilar ectopia by using cerebrospinal fluid flow imaging: initial estimate of imaging accuracy. *Radiology* 2007;245:532–40.
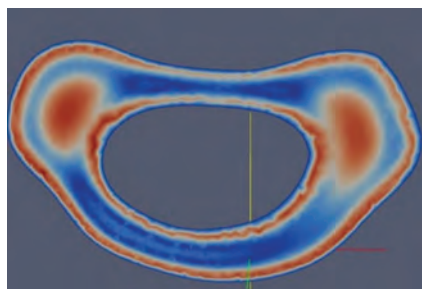
FIG 7. Graphic illustrating simulated flow in a patient-specific model of the subarachnoid space to illustrate the inhomogeneity of CSF flow. Flow velocity, in red-blue-green color coding, shows the greatest velocities anterolateral to the spinal cord. Modified from Rutkowska et al.[9]

diastolic velocities between the upper and midcervical spine (Fig 9).[9]

In fluid mechanics, the relative effects of inertia and viscosity on fluid can be inferred from the Reynolds and Womersley numbers. The Reynolds number, the ratio of inertial to viscous forces, differs little between CSF and blood in large arteries. The Womersley number, which quantifies the transient inertial forces in proportion to viscous effects, has a slightly lower value for CSF than for blood in large arteries. On the basis of the Reynolds and Womersley numbers, the oscillating spinal CSF flow has in theory some of the flow patterns observed in the arterial blood, though these are perhaps more complex because the surface has a more complex geometry.

Velocity fluctuations in the spinal fluid are associated with pressure fluctuations (Fig 10). In the healthy adult, spinal velocity and pressure fluctuations have an approximately 90° phase difference. In the presence of obstruction, the phase difference narrows.[2] Pressure fluctuations in the CSF produce transient pressure waves and gradients in the spinal cord. In portions of the

spinal cord with a persistent central canal, pressure on the external surface of the cord may produce radial pressure gradients in the cord.[10] In computational models of the spinal cord with realistic anatomic properties such as the central canal, the anterior median fissure, and white matter with anisotropic properties, pressure waves produce complex patterns of fluid movement in the cord.[11] Further studies may clarify the role of these fluid movements in the pathogenesis of syringomyelia.

CSF Flow in Different Physiologic States

Age, heart rate, blood pressure, intrathoracic pressure, and other physiologic parameters may factor in CSF flow patterns. The cervical spinal canal tends to taper more steeply in adults than in children.[12] Children have greater CSF velocities than adults; this is likely because of a greater expansion of cerebral blood vessels during systole and age-related tapering of the cervical spinal canal.[13] Physical exertion, which may trigger symptoms in patients with Chiari I, may hypothetically produce clinically important changes in CSF flow. Because of methodologic limitations, studies of CSF flow under nonresting physiologic conditions are infrequent. In CSF flow simulations in idealized models of a patient with Chiari and a healthy adult, increasing the pulse rate decreases the duration of the diastolic phase of CSF flow, increases the peak diastolic velocity, increases the magnitude of synchronous bidirectional flow, and doubles the pressure load on the spinal cord.[14] In vivo, Bhadelia et al[15,16] used a pencil beam MR technique to show that the Valsalva maneuver transiently reduces CSF velocity. Cough raises pressures in the CSF, to a greater extent in patients with Chiari I than in healthy controls.[17] Williams[18] used manometry in vivo to show that a Valsalva maneuver slows the passage of a pressure wave from the cranial vault to the lumbar spinal CSF. More studies are needed to understand the effect of physiologic factors on CSF flow.

CSF Flow in the Chiari I Malformation

Patients with Chiari commonly develop syringomyelia. The ectopic cerebellar tonsils in the upper cervical spinal canal in patients with Chiari I increase the complexity of flow patterns, the peak CSF velocities, and the magnitude of synchronous bidirectional flow. Flow velocities in the foramen magnum reach 12 cm/s in patients with Chiari I[19,20] or more[6] compared with 5 cm/s in healthy adults.[20] Both peak systolic and diastolic velocities are elevated in Chiari I. In Chiari I, CSF velocities along the spinal axis are greater than in healthy subjects when subjected to the same pressure drop. PCMR demonstrates greater complexity of flow with larger jets and increased flow inhomogeneity in patients with Chiari I[19] (Fig 9). Simulations of CSF flow in patient-specific models of the subarachnoid spaces in patients with Chiari

Velocities and PC Images by Region in a Chiari I Patient
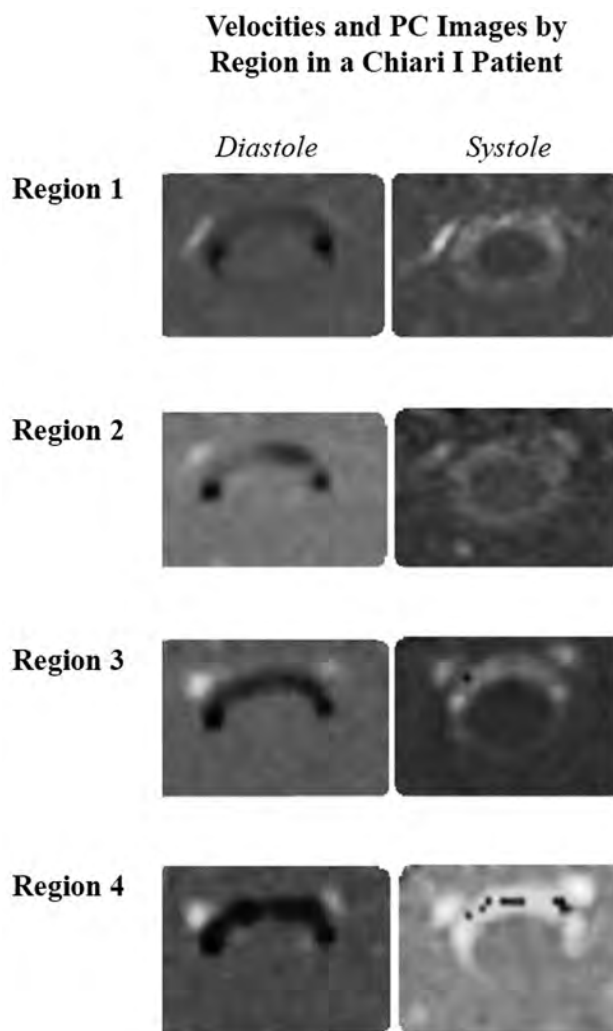
FIG 8. PCMR images of diastolic flow (left column) and systolic flow (right column) in successively lower levels of the upper cervical spinal canal in a patient with Chiari I. CSF velocities increase from region 1 near the tonsils to region 4 near the C4 level. At C4, aliasing produces negative flow voxels (black) scattered among the voxels with positive flow (white voxels). Modified from Shah et al.[8]
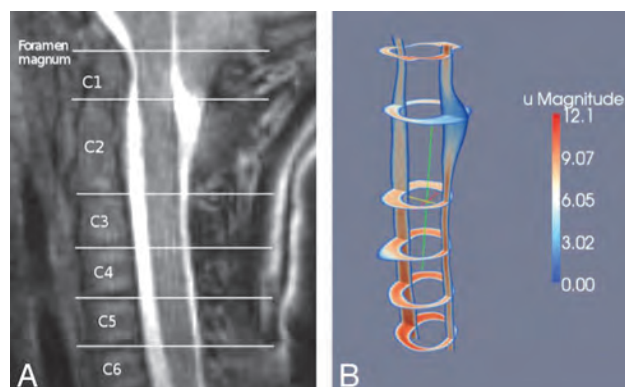
FIG 9. Sagittal T2-weighted image in a patient with a Chiari I malformation and graphic showing simulated flow velocities in the same patient by sagittal and multiple axial sections. The flow simulations show inhomogeneous flow patterns, greatest flow anterolateral to the cord, and increasing velocities between C1 and C4. Reproduced from Rutkowska et al.[9]
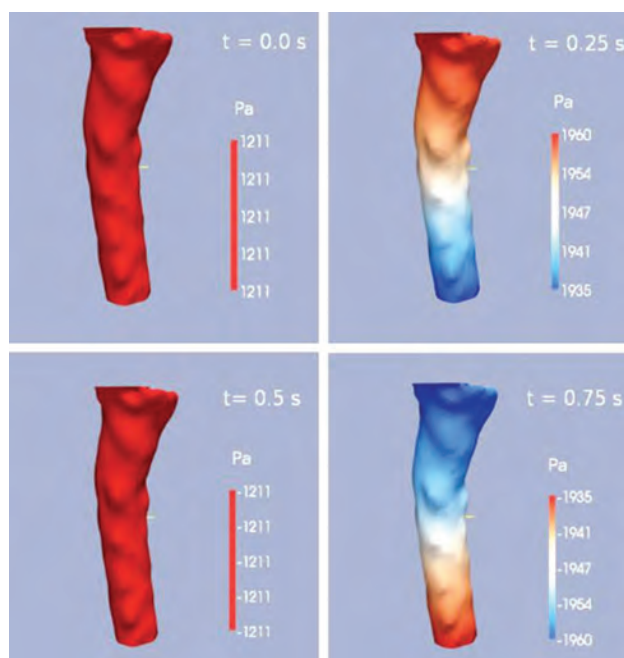
FIG 10. Graphic showing pressure gradients along the cervical spinal canal at 4 phases of the cardiac cycle. Pressure is coded by the red-blue-green scale. At one phase, pressure decreases from C1 to C7; at one phase it increases from C1 to C7, and at 2 phases in the cycle, no gradient is present. The pressure oscillates between these pressure patterns during the cycle. Velocities peak approximately 90° out of phase with the pressure in healthy adults. Modified from Roldan et al.[7]

document increased synchronous bidirectional flow.[5,9] In symptomatic patients with Chiari, PCMR demonstrates flow simultaneously in a caudad and cephalad direction (synchronous bidirectional flow) for 15–20% of the cardiac cycle, that is 2 or 3 phases in a typical 14-phase PCMR acquisition[19] (Fig 3) and not in asymptomatic patients with Chiari or controls.[21] Other differences between patients with Chiari and controls were reported, including different durations of systole and shifts in phase between velocity and pressure.[22] Although incompletely studied, transitional or turbulent CSF flow may occur in patients with Chiari I. Simulations in a model of a typical patient with Chiari I showed flow instabilities that may develop into turbulent flow though did not show self-sustained turbulence.[23]

The clinical objective of most PCMR imaging is to help distinguish patients who are symptomatic from the Chiari malformation from those whose symptoms are not related to their ectopic tonsil position. Readers interpreting PCMR images have an accuracy of 60–70% in differentiating symptomatic from asymptomatic cases.[21] Symptomatic cases of Chiari I typically have evidence of synchronous bidirectional flow and asymptomatic cases do not.

Cervical spinal canal dimensions, which affect local CSF velocities, differ between patients with Chiari and controls. The cervical spinal canal tapers less steeply in patients with Chiari with the result that peak CSF velocities, though more elevated in the foramen magnum, increase less rapidly than in healthy adults.[12,24] Spinal canal tapering in patients with Chiari with a syrinx differs from those without a syrinx (A. Thompson, unpublished data, 2014). Tapering affects CSF pressures and pressure gradients in the upper cervical spinal canal. Pressures and pressure gradients

Pressure Gradient for the Chiari, Normal and Post-operative Models
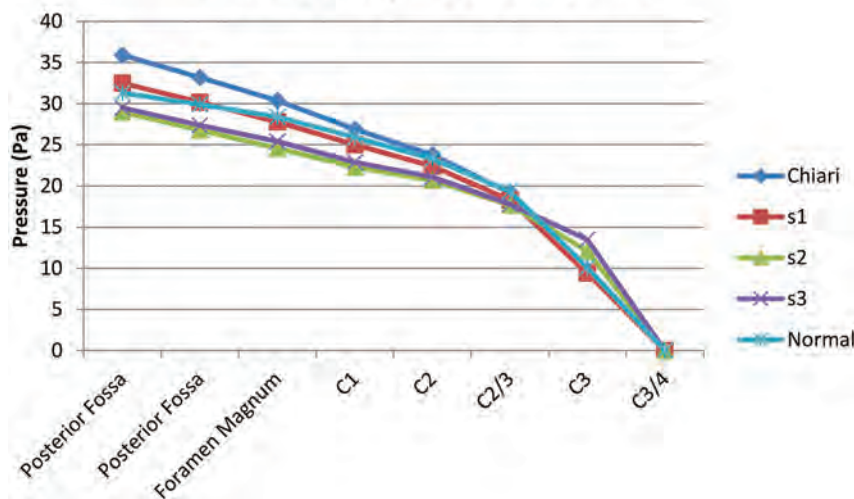
FIG 11. Plot of relative pressure against position from the midposterior fossa to the C3/4 level in 5 computational models: an idealized healthy model, an idealized patient with Chiari I, and 3 models showing the Chiari model with various amounts of craniovertebral decompression. At this phase of the cycle, pressure decreases from posterior fossa to C3/4. The gradients are steepest in the Chiari I model and least steep in the healthy model. The 3 degrees of craniovertebral decompression appear to lower pressures in the foramen magnum and to normalize pressures at the C3/4 level.

increase in proportion to the tapering in patients with Chiari I without and with syrinx. The role of spinal canal tapering in the pathogenesis of syringomyelia requires more study.

Craniovertebral decompression and removal of a portion of the inferior posterior calvaria and the posterior part of C1 to modify CSF flow usually reverses the growth of syrinx and relieves neurologic signs and symptoms in the patient with Chiari I. This surgical procedure reduces CSF velocities in the foramen magnum but not to healthy levels.[25] Simulations show that a craniovertebral surgical defect normalizes velocities in the midcervical spine and reduces them in the upper cervical spine[26] (Fig 11). It also lowers the pressures to which the spinal cord is subjected. Determining how the changes in pressure gradients lead to resolution of a syrinx requires additional simulations.

CSF Flow in Other Spinal Pathologies

CSF flow dynamics in idiopathic syringomyelia, arachnoiditis, and cervical spinal stenosis have been investigated.

PCMR imaging shows hyper kinetic flow in idiopathic syringomyelia.[27] This suggests that pathogenetic mechanisms in the condition may be similar to those in Chiari I. The term Chiari 0 is sometimes used to describe idiopathic syringomyelia because idiopathic syringomyelia and Chiari I have similar symptoms and signs except for tonsilar ectopia. Like a Chiari I malformation, idiopathic syringomyelia has smaller than normal posterior fossa dimensions.[28] The spine in patients with idiopathic syringomyelia tapers more like patients with Chiari I with syrinx than patients with Chiari I without syrinx or healthy adults (A. Struck, unpublished data, 2014).

Arachnoiditis, characterized by thickening and stiffening of

the membrane lining the subarachnoid space has, in CSF flow simulations, higher than normal pressure pulses.[29] Investigators hypothesize that elevated CSF pressure may be a significant factor in the pathogenesis of syringomyelia that may accompany arachnoiditis.

Syringomyelia may occur below an obstruction of the cervical spinal canal secondary to osteochondrosis.[30] Laminectomy at the level of the stenosis effectively treats the syrinx in these patients.[31]

CONCLUSIONS

Spinal CSF has complex oscillatory flow patterns resulting from the displacement of cranial CSF. MR flow imaging shows cyclic changes in spinal fluid flow related to the cardiac cycle, spinal fluid flow jets related to the complex spinal anatomy, and flow vortices. It shows hyperdynamic CSF flow in the presence of tonsilar ectopia. Simulations show these complex flow patterns and provide measurements of the CSF pressure gradients through the cardiac cycle. Engineering calculations suggest that the inertial and viscous forces in CSF have similar proportions to blood flowing in the aorta. Ongoing studies suggest how CSF flow may have a role in the development of syringomyelia and how surgical management may be optimized.

REFERENCES

1. Gupta S, Soellinger M, Grzybowski DM, et al. **Cerebrospinal fluid dynamics in the human cranial subarachnoid space: an overlooked mediator of cerebral disease. I. Computational model.** *J R Soc Interface* 2010;7:1195–204
2. Støverud KH, Langtangen HP, Haughton V, et al. **CSF pressure and velocity in obstructions of the subarachnoid spaces.** *Neuroradiol J* 2013;26:218–26
3. Shaffer N, Martin BA, Rocque B, et al. **Cerebrospinal fluid flow impedance is elevated in Type I Chiari malformation.** *J Biomech Eng* 2014;136:021012
4. Greitz D, Hannerz JA. **Proposed model of cerebrospinal fluid circulation: observations with radionuclide cisternography.** *AJNR Am J Neuroradiol* 1996;17:431–38
5. Linge SO, Haughton V, Løvgren AE, et al. **Effect of tonsillar herniation on cyclic CSF flow studied with computational flow analysis.** *AJNR Am J Neuroradiol* 2011;32:1474–81
6. Bunck AC, Kroeger JR, Juettner A, et al. **Magnetic resonance 4D flow analysis of cerebrospinal fluid dynamics in Chiari I malformation with and without syringomyelia.** *Eur Radiol* 2012;22:1860–70
7. Roldan A, Wieben O, Haughton V, et al. **Characterization of CSF hydrodynamics in the presence and absence of tonsillar ectopia by computational flow analysis.** *AJNR Am J Neuroradiol* 2009;30:941–46
8. Shah S, Haughton V, del Río AM. **CSF flow through the upper cervical spinal canal in Chiari I malformation.** *AJNR Am J Neuroradiol* 2011;32:1149–53
9. Rutkowska G, Haughton V, Linge S, et al. **Patient-specific 3D simulation of cyclic CSF flow at the craniocervical region.** *AJNR Am J Neuroradiol* 2012;33:1756–62

10. Drøsdal IN, Mardal K-A, Støverud K, et al. **Effect of the central canal in the spinal cord on fluid movement within the cord.** *Neuroradiol J* 2013;26:585–90

11. Støverud K. **Relation between the Chiari I malformation and syringomyelia from a mechanical perspective.** http://folk.uio.no/kent-and/thesis-5.pdf. Accessed May 18, 2014

12. Hammersley J, Haughton V, Wang Y, et al. **Tapering of the cervical spinal canal in patients with scoliosis with and without the Chiari I malformation.** *AJNR Am J Neuroradiol* 2012;33:1752–55

13. Iskandar BJ, Haughton V. **Age-related variations in peak cerebrospinal fluid velocities in the foramen magnum.** *J Neurosurg* 2005;103(6 suppl):508–11

14. Linge SO, Mardal K-A, Haughton V, et al. **Simulating CSF flow dynamics in the normal and the Chiari I subarachnoid space during rest and exertion.** *AJNR Am J Neuroradiol* 2013; 34:41–45

15. Bhadelia RA, Frederick E, Patz S, et al. **Cough-associated headache in patients with Chiari I malformation: CSF flow analysis by means of cine phase-contrast MR imaging.** *AJNR Am J Neuroradiol* 2011;32:739–42

16. Bhadelia RA, Madan N, Zhao Y, et al. **Physiology-based MR imaging assessment of CSF flow at the foramen magnum with a Valsalva maneuver.** *AJNR Am J Neuroradiol* 2013;34:1857–62

17. Sansur CA, Heiss JD, DeVroom HL, et al. **Pathophysiology of headache associated with cough in patients with Chiari I malformation.** *J Neurosurg* 2003;98:453–58

18. Williams B. **Cerebrospinal fluid pressure changes in response to coughing.** *Brain* 1976;99:331–46

19. Quigley MF, Iskandar B, Quigley ME, et al. **Cerebrospinal fluid flow in foramen magnum: temporal and spatial patterns at MR imaging in volunteers and in patients with Chiari I malformation.** *Radiology* 2004;232:229–36

20. Hofmann E, Warmuth-Metz M, Bendszus M, et al. **Phase-contrast MR imaging of the cervical CSF and spinal cord: volumetric motion analysis in patients with Chiari I malformation.** *AJNR Am J Neuroradiol* 2000;21:151–58

21. Hofkes SK, Iskandar BJ, Turski PA, et al. **Differentiation between symptomatic Chiari I malformation and asymptomatic tonsilar ectopia by using cerebrospinal fluid flow imaging: initial estimate of imaging accuracy.** *Radiology* 2007;245:532–40

22. Stoodley Bilston LE, Stoodley MA, Fletcher DF. **The influence of the relative timing of arterial and subarachnoid space pulse waves on spinal perivascular cerebrospinal fluid flow as a possible factor in syrinx development.** *J Neurosurg* 2010;112:808–13

23. Helgeland A, Mardal K-A, Haughton V, et al. **Numerical simulations of the pulsating flow of cerebrospinal fluid flow in the cervical spinal canal of a Chiari patient.** *J Biomech* 2014;47:1082–90

24. Hirano M, Haughton V, Munoz del Rio A. **Tapering of the cervical spinal canal in patients with Chiari I malformations.** *AJNR Am J Neuroradiol* 2012;33:1326–30

25. Dolar MT, Haughton VM, Iskandar BJ, et al. **Effect of craniocervical decompression on peak CSF velocities in symptomatic patients with Chiari I malformation.** *AJNR Am J Neuroradiol* 2004;25:142–45

26. Linge SO, Mardal KA, Helgeland A, et al. **Effect of craniovertebral decompression on CSF dynamics in Chiari malformation Type I studied with computational fluid dynamics.** *J Neurosurg Spine* 2014; Aug 1. [Epub ahead of print]

27. Struck AF, Haughton VM. **Idiopathic syringomyelia: phase-contrast MR of cerebrospinal fluid flow dynamics at level of foramen magnum.** *Radiology* 2009;253:184–90

28. Bogdanov EI, Heiss JD, Mendelevich EG, et al. **Clinical and neuroimaging features of "idiopathic" syringomyelia.** *Neurology* 2004;62:791–94

29. Cheng S, Stoodley MA, Wong J, et al. **The presence of arachnoiditis affects the characteristics of CSF flow in the spinal subarachnoid space: a modelling study.** *J Biomech* 2012;45:1186–91

30. Lee JH, Chung CK, Kim HJ. **Decompression of the spinal subarachnoid space as a solution for syringomyelia without Chiari malformation.** *Spinal Cord* 2002;40:501–06

31. Kato N, Tanaka T, Nagashima H, et al. **Syrinx disappearance following laminoplasty in cervical canal stenosis associated with Chiari malformation–case report.** *Neurol Med Chir (Tokyo)* 2010;50:172–74

Effect of the CT Table Strap on Radiation Exposure and Image Quality during Cervical Spine CT

P.G. Kranz, J.D. Wylie, J.K. Hoang, and A.S. Kosinski

ABSTRACT

BACKGROUND AND PURPOSE: The CT table strap may impair shoulder lowering during cervical spine CT. The purpose of this investigation was to evaluate the effect of the CT table strap on radiation exposure and image quality during CT of the cervical spine.

MATERIALS AND METHODS: Patients undergoing cervical spine CT were prospectively randomized to having the CT table strap placed around the torso and arms (control group) or around the torso only (intervention group). Radiation exposure, shoulder position, and image quality were evaluated. Potential confounders, including neck diameter and scan length, were also assessed.

RESULTS: Fifty-eight patients were enrolled and randomized, and 51 subjects were included in the final study population. There was a 21% decrease in radiation exposure in the intervention group compared with the control group (mean dose-length product, 540 ± 152 versus 686 ± 200 mGy $\times$ cm, $P = .005$). Subjects in the intervention group achieved shoulder lowering of an average of >1 vertebral body lower than the control group (mean shoulder level, 7.7 ± 1.3 versus 6.5 ± 1.3, $P = .001$). Subjective image quality, determined by the lowest level of spinal cord visibility, was also better in the intervention group (mean cord visibility level, 6.9 ± 1.3 versus 5.9 ± 1.3, $P = .006$). No differences in neck diameter ($P = .28$) or scan length ($P = .55$) were observed between groups.

CONCLUSIONS: The CT table strap inhibits shoulder lowering during CT of the cervical spine. Placement of the patient's arms outside the CT table strap results in decreased radiation exposure and increased image quality compared with patients whose arms are placed inside the strap.

ABBREVIATIONS: DLP = dose-length product; $CTDI_{vol}$ = volume CT dose index; SSDE = size-specific dose estimate

In recent years, increasing radiation exposure from CT has prompted attention to dose-reduction strategies, both in the medical literature and by various professional societies.[1,2] Several techniques to reduce the dose have been developed by the CT manufacturers, including tube current modulation, iterative reconstruction, and organ-based dose modulation. Many dose-reduction strategies involve trade-offs, however, including factors related to image quality, such as increased image noise or subjective alterations in image appearance, and financial impacts related to product cost and supporting hardware requirements.[3-5] Dose-reduction strategies that minimize these trade-offs are, therefore, clearly desirable.

One method for reducing radiation exposure without compromising image quality or increasing cost is through optimization of patient positioning. We have observed in practice, for example, that image quality in the lower cervical spine is dependent on the degree to which patients are able to lower their shoulders (Fig 1), because removal of the patient's shoulders from the imaged region decreases attenuation of the radiation beam. When automated tube current modulation is used, shoulder lowering also results in a reduction in the required tube current and, therefore, decreased radiation exposure. Our experience further suggests that 1 factor that affects shoulder lowering is the placement of the CT table strap. When the arms are placed within the strap, they may be constrained medially against the torso, causing the shoulders to elevate, thereby reversing previously performed shoulder-lowering maneuvers, and may impair further effort to shift the shoulders downward out of the imaging FOV.

The purpose of this study was to evaluate the effect of the table

FIG 1. Effect of shoulder position on image quality in the lower cervical spine. Axial CT scan obtained in a 55-year-old man before (*A*) and following (*B*) shoulder lowering, demonstrating substantial improvement in image quality. The images were acquired only a few minutes apart, as part of an interventional procedure, by using otherwise identical scan techniques (CT fluoroscopy; 120 kVp; 60 mA; 2.5-mm section thickness; 1-second rotation time; display FOV, 12 cm).
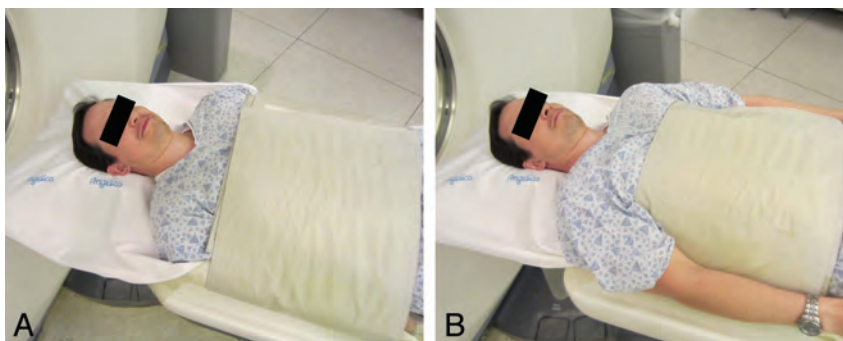
FIG 2. Position of the CT table strap relative to the arms in the control (*A*) and intervention (*B*) groups. Images were obtained by using an asymptomatic volunteer.

strap on radiation exposure during CT of the cervical spine. We hypothesized that by placing the arms outside the strap, patients would be able to increase shoulder lowering compared with patients whose arms remained inside the strap, resulting in decreased radiation exposure and improved image quality.

MATERIALS AND METHODS

This investigation was a prospective, randomized trial comparing cervical spine CTs obtained in patients referred from the emergency department by using 2 different positions of the CT table strap. The control group had the strap placed in the standard fashion, with the arms inside the strap, and the intervention group had the strap placed around the torso only, with the arms outside the strap (Fig 2). The study was approved by the local institutional review board and was compliant with Health Insurance Portability and Accountability Act regulations.

Subjects

Patients referred from the emergency department for cervical spine imaging with a study indication of suspected or observed trauma were eligible to participate if they met the following inclusion criteria: a conscious patient 1) able to follow commands and cooperate with instructions, 2) able to provide informed consent, 3) in a hard cervical collar, 4) male or nonpregnant females, and 5) 18 years of age or older. Patients who were unconscious, had

sustained significant upper extremity injury (including, but not limited to, fractures of the shoulder or arm), had sustained significant injury to other internal organs or were otherwise unable to cooperate with instructions regarding shoulder lowering, were not in cervical collars, or were undergoing contrast examinations before the cervical spine CT were excluded. Patients were recruited during normal daytime hours on the basis of the availability of study personnel and were, therefore, not necessarily consecutive.

Imaging Technique

Eligible patients who consented to participation were randomized by using a predetermined simple randomization schedule. Subjects were all given the same instructions by the CT technologist and the study staff regardless of assigned study group. Subjects were first positioned on the CT table with shoulders lowered as much as possible per the standard imaging protocol. The CT technologist then placed the table strap according to the subject's randomized assignment. The strap was secured according to the technologist's standard practice, and no special instructions were provided regarding how securely it should be applied. The subject was told that he or she would receive further instructions regarding shoulder lowering and that he or she should maintain that position throughout the scan. Immediately before obtaining the scout images, the subject was verbally instructed to again lower his or her shoulders as much as possible. No immediate attempt was made to judge the degree of compliance with the instructions, and the instructions were not repeated or otherwise emphasized unless the subject indicated that he or she did not hear or understand the instructions.

All subjects were scanned by using 1 of two 64-section multidetector row CT scanners in the emergency department (Light-Speed VCT; GE Healthcare, Milwaukee, Wisconsin). After the scout image was obtained, the technologist prescribed the z-axis coverage according to the standard protocol. Before scanning, a study radiologist reviewed the z-axis coverage to ensure coverage from the clivus through the T1 vertebral body, reducing or increasing the z-axis coverage as necessary, to ensure that only the area of interest was scanned and that the scan coverage was as homogeneous as possible throughout the study population as a whole. The same scan protocol was used for all patients, by using the following parameters: 120 kV(peak); automatic tube current modulation (tube current minimum, 150 mA; maximum, 440 mA); noise index, 10; axial scan mode; rotation time, 0.5 seconds; display FOV, 12 cm; large-body scan FOV. Images were acquired at 0.625 mm and were reconstructed in the sagittal and coronal planes at 2-mm thickness by using a bone algorithm.

FIG 3. Determination of shoulder level. The level was defined on the anteroposterior scout image as the intersection of a line connecting the acromion processes with the spinal axis.

FIG 4. Method for grading spinal cord visibility. The level was defined as the lowest spinal level where the margins of the spinal cord were distinguishable from the adjacent CSF (*arrow*).

Outcome Measures

The primary outcome measure for the investigation was radiation exposure, measured by dose-length product (DLP). Secondary outcome measures included the anatomic level of the shoulders and subjective image quality, determined by visibility of the spinal cord.

Data Analysis

Image analysis was performed by a board-certified radiologist who held a Certificate of Added Qualification in neuroradiology and by a board-certified radiologist who was a fellow in neuroradiology. At the time of image analysis, the radiologists were blinded to the study group assignment. To ensure homogeneous scan lengths, subsequent to enrollment, subjects were excluded if the anatomic coverage of the scan extended below the T2–3 disk

space or if a substantial portion of the T1 vertebral body (>25% total volume) was excluded from the scan.

DLP and volume CT dose index ($CTDI_{vol}$) were recorded from the automated dose report generated by the scanner. A size-specific dose estimate (SSDE) was calculated for each subject according to the methods outlined in the American Association of Physicists in Medicine Report 204 by using the following equation:

$$SSDE = f_{size}^{32,Lat} \times CTDI_{vol}^{32}$$

where $f_{size}^{32,Lat}$ is the size-specific conversion factor for the lateral diameter measured on the scout image for a 32-cm polymethylmethacrylate phantom and $CTDI_{vol}^{32}$ is the volume CTDI recorded from the patient's automated dose report.[6]

Shoulder level was determined by creating a straight line on the anteroposterior scout image connecting the acromion processes bilaterally and evaluating the level where this line intersected the spine (Fig 3). A numeric value was assigned, depending on where the intersection occurred, with the superior endplate of the vertebral body assigned an integer value and fractional values assigned for lower portions of the vertebral body (eg, the superior endplate of C7 would be assigned 7.0; the midportion of C7, 7.5; the superior endplate of T1, 8.0; and so forth).

Subjective image quality was measured on the sagittal reconstructions of the CT scan with a standard soft-tissue window/level setting (window: 342/level: 56) as the lowest spinal level where the spinal cord could be discriminated from the CSF, by using the same numeric scoring system as that used for shoulder position (Fig 4).

To control for body habitus, we measured a potential confounder, neck size, by using the minimum transverse diameter of the neck on the anteroposterior scout image (Fig 5). Because scan length contributes to DLP, the total scan length was assessed for each subject by multiplying the total number of axial images acquired by the section thickness.

Image noise was measured by creating a standard-sized region of interest (20 ± 1 mm^2) in the tracheal air column on the 0.625-mm axial CT source images at 3 different vertebral levels: 1 above the expected location of the shoulders (C4) and 2 closer to the expected shoulder level (C7 and T1). The noise was measured as the SD of the Hounsfield units within the

FIG 5. Determination of neck diameter based on the shortest transverse diameter measured on the anteroposterior scout image.

RESULTS

Fifty-eight subjects were enrolled. After evaluation of the images, 3 patients from the control group and 4 from the intervention group were excluded due to excessive or inadequate anatomic coverage, resulting in a final cohort of 51 subjects, including 26 men and 25 women. Demographic characteristics and scan lengths are presented in Table 1. There were no differences in sex ($P = 1.0$) or age ($P = .87$) between the control and intervention groups. The mean neck diameter was 13.2 ± 1.4 cm for the control group and 12.7 ± 1.3 cm for the intervention group, which was not significantly different ($P = .28$). There was no difference in scan length between the 2 groups, with a mean scan length of 19.3 ± 1.1 cm for the control group and 19.1 ± 1.4 cm for the intervention group ($P = .55$).

Comparison of radiation exposure and the estimated dose between the control and intervention groups is illustrated in Fig 6. Statistically significant decreases were observed in all metrics of radiation exposure in the intervention group compared with the control group: DLP decreased by 21% (mean DLP, 540 ± 152 versus 686 ± 200, $P = .005$), $CTDI_{vol}$ decreased by 28% (mean $CTDI_{vol}$, 25.0 ± 8.8 versus 34.7 ± 10.4 mGy, $P = .026$), and SSDE decreased by 17% (mean SSDE, 69.6 ± 21.0 versus 83.5 ± 24.1 mGy, $P = .032$).

Subjects in the intervention group were able to lower their shoulders an average of >1 vertebral body segment lower than subjects in the control group, with a mean shoulder level of 6.5 ± 1.3 in the control group and 7.7 ± 1.3 in the intervention group ($P = .001$). Subjective image quality was better in the lower portions of the spine as well, with visualization of the spinal cord an average of 1 vertebral segment lower in the intervention group compared with the control group, evidenced by a mean cord visibility level of 5.9 ± 1.3 in the control group versus 6.9 ± 1.3 in the intervention group ($P = .006$). These results are illustrated in Fig 7.

Image noise at the various spinal levels is shown in Table 2. Noise was not statistically different between the 2 groups at any of the measured levels, though there was a trend toward decreasing P values in the more inferior levels of the spine (P values at C4, C7, and T1 = .60, .49, and .11, respectively). Mean image noise was higher at the inferior vertebral levels, with a mean noise of 26.1 ± 6.7, 28.9 ± 9.6, and 36.8 ± 12.7 at the C4, C7, and T1 levels, respectively.

Table 1: Patient characteristics and scan length

	Control Group (n = 25)	Intervention Group (n = 26)	P Value
Age (yr)			
Mean	49.2 ± 21.8	49.9 ± 20.4	
Median	47	46	.87[a]
Range	18–90	19–88	
Sex			
Male (No.) (%)	13 (52.0)	13 (50.0)	
Female (No.) (%)	12 (48.0)	13 (50.0)	1.0[b]
Scan length (cm)			
Mean	19.3 ± 1.1	19.1 ± 1.4	
Median	20	20	.55[a]
Range	16–20	16–22	
Neck width (cm)			
Mean	13.2 ± 1.4	12.7 ± 1.3	
Median	13.0	12.5	.28[a]
Range	11.1–17.8	10.2–14.7	

[a] Based on the 2-sample Wilcoxon test.
[b] Based on the Fisher exact test.

region of interest.[7] At each level, the measurement was obtained 3 times by using the same region of interest and an average noise was calculated. Demographic information (age and sex) was also collected.

Statistical Analysis

An enrollment target of 58 patients was selected so that the study would have a power of 80% to detect a difference in DLP values of 120 mGy × cm (a 20% difference, assuming a mean DLP of 600 mGy × cm and $\sigma = 175$ for both groups), with a 2-sided $\alpha = .05$.

The Shapiro-Wilk test was performed to determine the normality of the data and supported a normal distribution for the primary and secondary outcome measures, as well as $CTDI_{vol}$ and SSDE (P values = >.05); a 2-tailed Student t test was therefore used to compare these data. Patient age, neck width, scan length, and image noise were not normally dis-

FIG 6. Box-and-whisker plots showing differences in DLP (*A*), CTDI$_{vol}$ (*B*), and SSDE (*C*) values in the control and intervention groups.
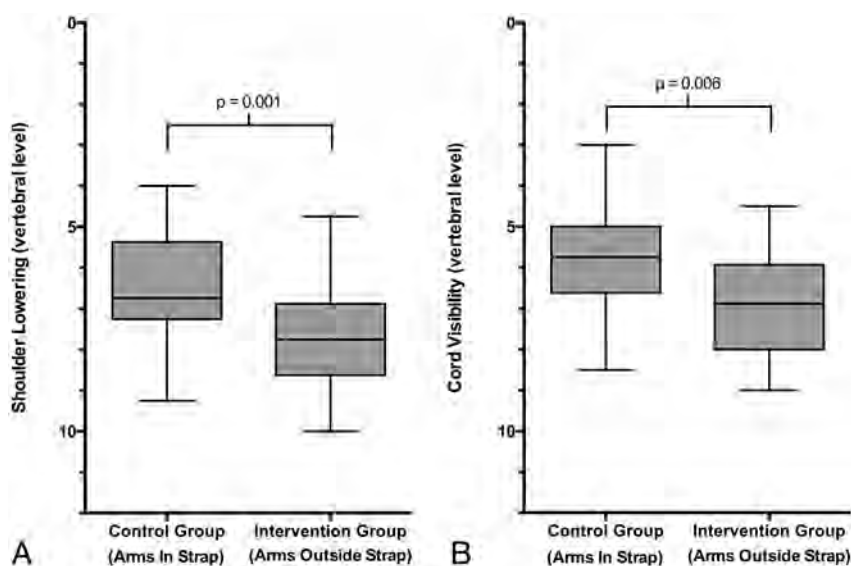
FIG 7. Box-and-whisker plots showing differences in shoulder lowering (*A*) and spinal cord visibility (*B*) in the control and intervention groups. Note that the vertical axis has been reversed to correspond with the anatomic orientation of the vertebral levels.

DISCUSSION

Our investigation found that in patients undergoing cervical spine CT, shoulder lowering is impaired by placing the patient's arms inside the CT table strap and that improved shoulder lowering can easily be achieved by placing the strap around only the torso, allowing the arms to remain free. This simple modification resulted in a decrease in radiation exposure of >20% in our study. Additionally, we found a subjective improvement in image quality in the lower cervical spine as well. This technique can be easily implemented into routine practice when scanning cooperative patients without the addition of any financial cost or logistic complexity.

DLP was used in this investigation as the primary outcome measure. DLP is a reflection of the total amount of radiation used in a CT examination that takes into account scan length, but it does not reflect the individual patient dose.[8] It is derived by taking

the product of CTDI$_{vol}$ and scan length. To ensure homogeneous scan lengths between groups, two potential sources of variability required attention in our investigation. First, there may be anatomic variability, with taller patients requiring a longer scan length to cover the same anatomy compared with shorter patients. Second, scan length is manually designated by the scanner operator and may therefore demonstrate scan-to-scan variation, depending on the operator.

We attempted to control for these potential confounders by using several methods, both before and following data acquisition. First, the study design was prospective, permitting randomization to reduce the effect of variations in individual subject anatomy. Second, at the scanner, z-axis coverage was manually determined for each subject by 1 of 2 study radiologists, according to predefined anatomic criteria to reduce interoperator variability. Finally, subsequent to data acquisition, scans were reviewed to make sure underscanning or overscanning had not occurred, and subjects whose scans showed anatomic coverage outside predetermined parameters were excluded. These measures were ultimately effective in ensuring equal scan lengths between the 2 study groups.

CTDI$_{vol}$, a component of DLP, is a reflection of scanner radiation output.[9] CTDI$_{vol}$ estimates are based on uniform phantoms; thus, these do not take variations in individual body habitus into account. As a result, CTDI$_{vol}$ can underestimate dose by 40%–70%, depending on age and body size.[10] Size-specific doses have been proposed that rely on corrections to CTDI$_{vol}$ based on direct anatomic measurements of individual patients being scanned to minimize inaccuracies related to habitus.[6] These SSDEs have been shown to more accurately represent the

Table 2: Comparison of image noise by vertebral level

Image Noise	Control Group	Intervention Group	P Value[a]
At C4			
Mean	26.8 ± 6.2	25.4 ± 7.1	
Median	27.9	26.5	.60
Range	14.4–37.8	5.7–34.3	
At C7			
Mean	30.2 ± 10.7	27.7 ± 8.3	
Median	29.9	26.4	.49
Range	13.8–58.3	15.9–48.9	
At T1			
Mean	39.0 ± 9.8	34.7 ± 14.9	
Median	37.6	32.6	.11
Range	24.1–66.4	7.3–70.1	

[a] Based on the 2-sample Wilcoxon test.

absorbed dose compared with $CTDI_{vol}$.[10] In our investigation, both $CTDI_{vol}$ and SSDE were lower in the intervention group, with a 28% reduction in $CTDI_{vol}$ and a 17% reduction in SSDE observed. Furthermore, we found no difference in body habitus, as determined by transverse neck diameter, between our study groups. Together with the DLP reductions, these data demonstrate that the observed decreases in radiation exposure and dose metrics in the intervention group are attributable to the study intervention (eg, placement of the CT table strap) rather than to other factors such as variation in scan length or habitus.

In addition to differences in radiation, we also found differences in image quality between groups, with improved visibility of the lower spinal cord in the intervention group. This finding was despite the fact that automated tube current modulation should function to maintain image quality when attenuation of the x-ray beam by soft tissue increases, such as in elevated shoulders. To quantitatively examine this finding, we measured image noise at several spinal levels both above and at the expected level of the shoulders, to determine the degree to which automated tube current modulation was effectively compensating for increased soft tissue around the cervicothoracic junction. We observed a nonsignificant trend toward increasing noise at the C7 and T1 levels in the control group. This observation is likely explained by the fact that the control group had a higher average shoulder level than the intervention group, resulting in a greater likelihood of reaching the maximum tube current during scanning at the lower cervical and upper thoracic levels, beyond which automated tube current modulation would no longer keep image noise constant.

Although there are no prior studies that evaluate the effect of shoulder positioning during cervical spine CT, it is well-known that arm position should be up for CT of the chest and down for CT of the neck or cervical spine, to reduce streak artifacts and dose when automated tube current modulation is used. A previous retrospective study of patients undergoing thoracoabdominal CT imaging in the setting of trauma investigated the effect of raising the arms outside the imaged volume.[11] This investigation found that while image quality was tolerable with the arms down, raising the arms had the effect of improving image quality and reducing dose, with the trade-off of requiring longer scanner time because it necessitated a second-pass scan to image above the cervicothoracic junction. The magnitude of dose reduction in this study was 18%–45%, depending on whether 1 or both arms were raised.

Another investigation advocated that a swimmers position be used during CT to improve visualization of the lower cervical spine.[12] Because this technique required a second scan with the modified arm positioning as well, the authors recommended that the technique be used only as a problem-solving tool in select cases. Unlike these investigations, however, placement of the patient's arms outside the CT table strap does not increase scan time or require repeat scanning and can be routinely implemented for most patients undergoing cervical CT.

Our investigation has several limitations. First, the assessment of image quality in this investigation was based on visualization of the spinal cord, a feature that may not directly reflect the diagnostic performance of the scan in the detection of fractures, which is the primary purpose of obtaining cervical spine CT in the setting of trauma. However, the incidence of fractures, especially those of the lower cervical spine whose visualization may be impaired by the position of the shoulders, would be expected to be very low in light of the widespread use of cervical CT as the first-line imaging technique when screening patients with trauma, and a very large number of subjects would be needed to find enough fractures to sufficiently compare performance between groups. Nevertheless, the primary purpose of this investigation was to evaluate radiation exposure; therefore, the study size was selected to evaluate this end point. Second, we evaluated 1 scanner type with 1 model of table strap. Although different table strap configurations may be available from other vendors, including straps of varying widths or shapes, we would expect the effect on shoulder lowering to be similar in all straps that constrain the arms against the torso, regardless of strap shape. Third, this investigation was performed at 1 center, and though we do not have normative data for neck diameter for the population in general, our study group may include patients with a larger body habitus than at other centers. This could potentially overestimate the effect of dose reduction compared with a population of thinner patients because the ability to voluntarily lower one's shoulders when the arms are placed inside the restraint strap may be less inhibited in patients with a small body habitus.

Next, we used transverse neck diameter rather than body mass index to assess the homogeneity of body habitus between groups, to evaluate the effectiveness of our randomization, because body mass index was not available in all patients. However, it has been previously shown that transverse neck diameter correlates well with image quality and radiation dose during routine multidetector row CT scanning when automated tube current modulation is used and that region-specific measurements are better indicators of habitus than body mass index when optimizing cross-sectional imaging.[13] Finally, SSDE measurements were developed for use in the torso, where anatomic geometry is less complex than at the cervicothoracic junction,[6] and transverse neck diameter was used to calculate the SSDE, which may result in increased variability compared with a combination of transverse and anteroposterior measurements.[10]

CONCLUSIONS

In summary, our investigation has demonstrated that the CT table strap inhibits shoulder lowering during CT of the cervical spine. Placement of the patient's arms outside the strap facilitates shoul-

der lowering, resulting in decreased radiation exposure and increased image quality. This simple change in positioning provides a mechanism for dose reduction that can be easily implemented when scanning cooperative patients and results in increased image quality without requiring data postprocessing or increasing cost.

REFERENCES

1. Costello JE, Cecava ND, Tucker JE, et al. **CT radiation dose: current controversies and dose reduction strategies.** *AJR Am J Roentgenol* 2013;201:1283–90
2. Goske MJ, Applegate KE, Boylan J, et al. **The Image Gently campaign: working together to change practice.** *AJR Am J Roentgenol* 2008;190:273–74
3. Hara AK, Paden RG, Silva AC, et al. **Iterative reconstruction technique for reducing body radiation dose at CT: feasibility study.** *AJR Am J Roentgenol* 2009;193:764–71
4. Silva AC, Lawder HJ, Hara A, et al. **Innovations in CT dose reduction strategy: application of the adaptive statistical iterative reconstruction algorithm.** *AJR Am J Roentgenol* 2010;194:191–99
5. Yu L, Bruesewitz MR, Thomas KB, et al. **Optimal tube potential for radiation dose reduction in pediatric CT: principles, clinical implementations, and pitfalls.** *Radiographics* 2011;31:835–48
6. Boone JM, Strauss KJ, Cody DD, et al. *Size-Specific Dose Estimates (SSDE) in Pediatric and Adult Body CT Examinations: Report of AAPM Task Group 204.* College Park, Maryland: American Association of Physicists in Medicine; 2011
7. Schindera ST, Nelson RC, Toth TL, et al. **Effect of patient size on radiation dose for abdominal MDCT with automatic tube current modulation: phantom study.** *AJR Am J Roentgenol* 2008;190: W100–05
8. Huda W, Mettler FA. **Volume CT dose index and dose-length product displayed during CT: what good are they?** *Radiology* 2011; 258:236–42
9. McCollough CH, Leng S, Yu L, et al. **CT dose index and patient dose: they are not the same thing.** *Radiology* 2011;259:311–16
10. Brady SL, Kaufman RA. **Investigation of American Association of Physicists in Medicine Report 204 size-specific dose estimates for pediatric CT implementation.** *Radiology* 2012;265:832–40
11. Brink M, de Lange F, Oostveen LJ, et al. **Arm raising at exposure-controlled multidetector trauma CT of thoracoabdominal region: higher image quality, lower radiation dose.** *Radiology* 2008;249: 661–70
12. Kane AG, Reilly KC, Murphy TF. **Swimmer's CT: improved imaging of the lower neck and thoracic inlet.** *AJNR Am J Neuroradiol* 2004;25:859–62
13. Hoang JK, Gafton AR, Eastwood JD, et al. **Correlation of cross-sectional diameter with image quality and radiation exposure in MDCT examinations of the neck.** *AJR Am J Roentgenol* 2011;197: W904–09

Neurointerventional Research between 2003 and 2012: Slow Growth, High Interdisciplinary Collaboration, and a Low Level of Funding

J.Y. Lee, D.Y. Yoon, S.D. Yoon, S.A. Nam, and B.M. Cho

ABSTRACT

BACKGROUND AND PURPOSE: Neurointerventional therapy of cerebrovascular disease is a greatly expanding field across many specialty disciplines. The goal of this study was to analyze the characteristics and trends of scientific publications that focused on neurointervention during the past decade.

MATERIALS AND METHODS: A bibliometric evaluation of neurointerventional research published between 2003 and 2012 was conducted by using the PubMed data base. Analyzed parameters included the year of publication, type of document, language of the article, topic, declared funding, country of origin, type of collaboration between disciplines, the first author's specialty, and subject category and the Impact Factor of the publishing journal.

RESULTS: Between 2003 and 2012, a total of 2123 articles were published, of which 1107 (52.1%) were original articles, 1948 (91.8%) were written in English, 192 (9.0%) received funding, 661 (31.1%) were published by the United States, and 1060 (49.9%) resulted from interdisciplinary collaboration. Neurosurgery departments produced the most articles ($n = 910$, 42.9%), followed by radiology ($n = 747$, 35.2%) and neurology ($n = 270$, 12.7%). The time-trend analysis in the number of publications demonstrated slow growth from 2003 to 2012, with an average annual growth rate of +6.0%.

CONCLUSIONS: The fields of neurosurgery, radiology, and neurology have contributed substantially to neurointervention research. Slow growth, high interdisciplinary collaboration, and a low level of funding are peculiar characteristics of research in this field.

ABBREVIATION: IF = Impact Factor

Cerebrovascular disease (stroke) is the second leading cause of death worldwide after ischemic heart disease. According to the most recent World Health Organization data, deaths from cerebrovascular disease were an estimated 6.2 million in 2011.[1] Conservative and surgical treatment has been the standard. In recent years, however, cerebral endovascular treatment (neurointervention) has become a useful therapeutic option for patients with cerebrovascular disease.[2]

Bibliometric analysis is a quantitative method of evaluating scientific productions for different authors, countries, journals, and publications related to a specific topic.[3] Many investigators from various disciplines have published articles on neurointervention, reflecting the broader application of the techniques to a wider variety of cerebrovascular conditions. To our knowledge, however, there has been no bibliometric analysis of characteristics and trends of research within the field.

We performed a bibliometric analysis of the characteristics and trends of scientific publications that focused on neurointervention during the past decade.

MATERIALS AND METHODS

This study was a retrospective analysis of a publicly available data base and was exempt from institutional review board approval.

Article Search

The PubMed data base of the National Library of Medicine (www.ncbi.nlm.nih.gov/Pubmed) was used as the primary source of data for this study. The search strategy was built by inputting first the following anatomic terms: "central nervous system" in [Medical Subject Heading Major Topic], carotid, cerebral, cerebellar, basilar, vertebral, or communicating artery in [Title/Abstract]; and second, the following procedural terms: angioplasty, embolisation*, embolization*, endovascular, intra-arterial therapy, neuroendovascular, neurointervention*, recanalize*, stroke

therapy, thrombectomy, thromboly*, balloon*, coil*, flow diverter*, or stent* in [Title/Abstract]. We limited the period of publication from 2003 to 2012, and we downloaded the data on July 26, 2013. This search resulted in 14,859 publications.

We restricted our analysis to research that was directly related to endovascular treatment for cerebrovascular disease. Therefore, articles on interventional procedures of the common carotid artery, cervical portion of the internal carotid artery, external carotid artery, or aorta ($n = 9347$); and articles related to the pathophysiology, hemodynamics, imaging, conservative management, and surgery of cerebrovascular disease ($n = 3239$) were excluded. Moreover, some types of documents (eg, editorial materials, letters, commentary, and author's reply) ($n = 30$); articles for which the full text was not available from on-line or off-line sources ($n = 71$); articles that were e-published ahead of print, but not yet included in a finalized printed issue from 2003 to 2012 ($n = 31$); and articles for which the authors' specialties were not clear ($n = 18$) were also excluded. Therefore, 2123 articles were finally included in our study.

Parameters Evaluated

For the analysis, the following information was obtained from each article: 1) year of publication, 2) type of document (original article, case report, review, or technical note), 3) language of the article, 4) topic (endovascular treatment of aneurysm, stent or angioplasty for vascular stenosis, endovascular treatment of arteriovenous malformation or arteriovenous fistula, thrombolysis or thrombectomy, vasospasm, tumor embolization, or miscellaneous), 5) declared funding, 6) country of origin, 7) type of collaboration between disciplines (no collaboration, corresponding author from other department, or coauthors from other department), 8) the first author's specialty (neurosurgery, radiology, neurology, or miscellaneous specialties), and 9) subject category (neuroscience journal, radiology journal, or others) and the Impact Factor (IF) of the publishing journal. We also evaluated the relationships between the first author's specialty and evaluated parameters.

Original articles were defined as reports that investigated clearly stated objectives or hypotheses and contained specifically articulated methods and results sections. If information about the authors' departments was not available or was ambiguous (such as Department of Neurologic Sciences, Stroke Center, or Neurovascular Research Unit) from the MEDLINE data base, we searched the Internet home page of the institution to obtain additional information. For the purpose of our research, the country of the first author was considered the country of origin of the article. If the first author was affiliated with >1 country, the corresponding author's country was considered the country of origin of the article.

The journals in which articles were published were classified as neuroscience journals, radiology journals, and journals related to other medical specialties (including multidisciplinary journals). Neuroscience journals were considered those that were included under the subject category "Clinical Neurology" or "Neurosciences" on the Web of Knowledge Journal Citation Reports: Science Edition 2012.[4] The journals included under the subject category "Radiology, Nuclear Medicine and Medical Imaging" or "Neuro-

imaging" were classified as radiology journals. According to the Journal Citation Reports, several journals were listed under >1 subject category, depending on the content of the journal. Journals that fell into >1 category were manually reviewed and assigned to only 1 category on the basis of the title of the journal, information contained in "Instructions to Authors," and the table of contents in a sample issue. For example, the American Journal of Neuroradiology was listed under "Clinical Neurology," "Neuroimaging," and "Radiology, Nuclear Medicine and Medical Imaging" subject categories and was assigned to the radiology journal category.

The IF of each journal was retrieved for the year of publication from the Journal Citation Reports. The IF of a journal for a given year is calculated by the number of citations that year of all articles published in the preceding 2 years divided by the number of articles published in that journal during the same period.[5] Of note, several journals were not indexed in the Science Citation Index or Science Citation Index (Expanded) and did not have IFs; therefore, any articles from these journals were excluded from the IF analysis.

Four study investigators (J.Y.L, D.Y.Y., S.D.Y., and S.A.N.) initially reviewed the same 200 articles independently to ensure consistency of data abstraction. Any disagreements were resolved by a consensus meeting. After initial pilot abstraction, the total number of articles was divided randomly into 4 samples and was manually reviewed by investigators. Questionable cases were decided by consensus of the all study investigators.

Analyses

The data were downloaded into a spreadsheet for analysis by using Excel software (Microsoft, Redmond, Washington). The present study adopted a descriptive research approach by bibliometric analysis. Relationships between the first author's specialty (radiology, neurosurgery, neurology, or miscellaneous specialties) and evaluated parameters were evaluated by using χ^2 or ANOVA tests.

Statistical analyses were performed by using the Statistical Package for the Social Sciences software (Version 12.0 for Windows; IBM, Armonk, New York), and a P value <.05 was considered statistically significant.

RESULTS

Total Publications

There were 2123 neurointervention-related articles in the PubMed data base between 2003 and 2012. Our examination of the trend in the number of publications demonstrated slow growth from 2003 to 2012, with an average annual growth rate during the period of +6.0% (Fig 1).

Type of Documents, Language, Topic, and Funding

The most frequent type of document was original article ($n = 1107$, 52.1%). Case reports and review articles numbered 762 (35.9%) and 162 (7.6%), respectively. The language of most articles was English ($n = 1948$, 91.8%), followed by Japanese ($n = 57$, 2.7%), Chinese ($n = 32$, 1.5%), and German ($n = 22$, 1.0%). The most frequent topic was endovascular treatment of aneurysm ($n = 941$, 44.3%), followed by stent or angioplasty for vascular stenosis ($n = 362$, 17.1%). During the study period, 192 (9.0%) articles received funding (Table 1). Original articles (168 of 1107,

15.2%) were funded more often than other article types such as technical notes (4 of 92, 4.3%), reviews (6 of 162, 3.7%), and case reports (14 of 762, 1.8%).

Journals

The 2123 articles were published in 245 journals. Most articles were published in neuroscience journals ($n = 1106$, 52.1%), followed by radiology journals ($n = 703$, 33.1%) (Table 1). Table 2 shows the top 20 journals containing articles that focused on neurointervention. The mean journal IF of 1830 articles published in Scientific Citation Index (Expanded) journals was 2.193.

The mean journal IF of publications from neurology (3.645) was significantly higher than that observed for radiology (2.103) and neurosurgery (1.806) (Table 3).

Country of Origin and Collaboration

Researchers from 48 countries published at least 1 article. Researchers from the United States published the most articles ($n = 661$, 31.1%), followed by Japan ($n = 287$, 13.5%), China ($n = 184$, 8.7%), and South Korea ($n = 170$, 8.0%) (Table 4). A total of 1060 articles (49.9%) resulted from collaboration with authors from different departments. Among them, 43 articles were the result of collaboration with a corresponding author from another department and 1017 articles were the result of collaboration with coauthors from other departments (Table 5).

First Author's Specialty and Its Relationship to Other Parameters

With regard to specialty contribution, neurosurgery departments produced the most articles ($n = 910$, 42.9%), followed by radiology ($n = 747$, 35.2%) and neurology ($n = 270$, 12.7%) (Table 1). The average annual growth of publications from neurology (+17.3%) was higher than that observed for publications from
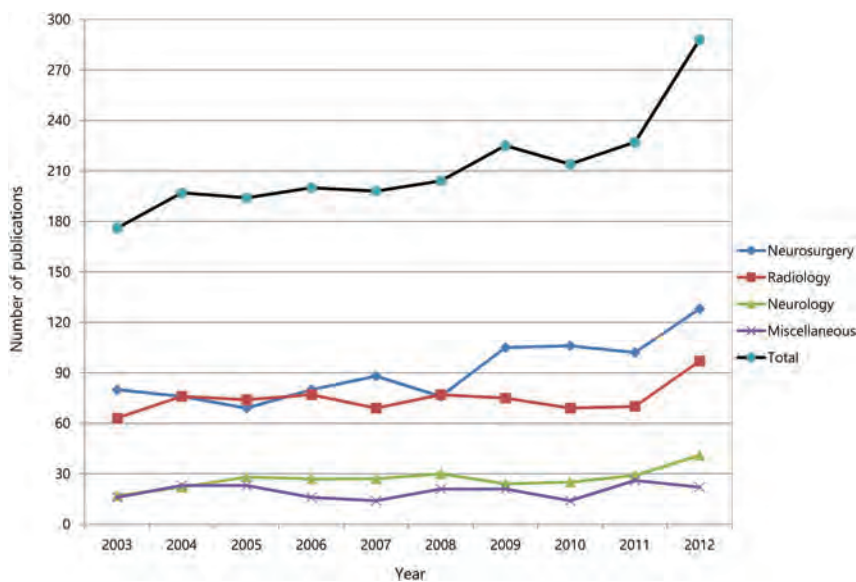
FIG 1. Annual amount of neurointerventional research between 2003 and 2012.

Table 1: Characteristics of neurointerventional research between 2003 and 2012[a]

	Department of the First Author				
	Neurosurgery ($n = 910$)	Radiology ($n = 747$)	Neurology ($n = 270$)	Miscellaneous ($n = 196$)	Total ($n = 2123$)
Document type					
Original article	436 (47.9)	429 (57.4)[b]	140 (51.9)	102 (52.1)	1107 (52.1)
Case report	360 (39.6)[c]	236 (31.6)	93 (34.4)	73 (37.2)	762 (35.9)
Review	59 (6.5)	49 (6.6)	35 (13.0)[d]	19 (9.7)	162 (7.6)
Technical note	55 (6.0)[e]	33 (4.4)	2 (0.7)	2 (1.0)	92 (4.4)
Journal					
Neuroscience journal	636 (69.9)[f]	245 (32.8)	176 (65.2)[f]	49 (25.0)	1106 (52.1)
Radiology journal	194 (21.3)	432 (57.8)[g]	48 (17.8)	29 (14.8)	703 (33.1)
Other or multidisciplinary journal	80 (8.8)	70 (9.4)	46 (17.0)	118 (60.2)[g]	314 (14.8)
Topic					
Endovascular treatment of aneurysm	481 (52.9)[g]	357 (47.8)	39 (14.4)	64 (32.7)	941 (44.3)
Stent or angioplasty for vascular stenosis	120 (13.2)	111 (14.9)	72 (26.7)[d]	59 (30.1)[d]	362 (17.1)
Endovascular treatment of AVM or AVF	174 (19.2)[e]	145 (19.4)[e]	13 (4.8)	23 (11.6)	355 (16.7)
Thrombolysis or thrombectomy	65 (7.1)	93 (12.4)	131 (48.5)[g]	26 (13.3)	315 (14.8)
Vasospasm	23 (2.5)	15 (2.0)	3 (1.1)	7 (3.6)	48 (2.3)
Tumor embolization	23 (2.5)	6 (0.8)	1 (0.4)	2 (1.0)	32 (1.5)
General or miscellaneous	24 (2.6)	20 (2.7)	11 (4.1)	15 (7.7)[d]	70 (3.3)
Declared funding					
Funded	62 (6.8)	65 (8.7)	41 (15.2)[d]	24 (12.2)	192 (9.0)
Not funded	848 (93.2)	682 (91.3)	229 (84.8)	172 (87.8)	1931 (91.0)

[a] Numbers in parentheses are percentages.
[b] Significantly different from the value for neurosurgery.
[c] Significantly different from the value for radiology.
[d] Significantly different from the values for departments of neurosurgery and radiology.
[e] Significantly different from the values for departments of neurology and miscellaneous.
[f] Significantly different from the values for departments of radiology and miscellaneous.
[g] Significantly different from the values for all other departments.

neurosurgery (+7.4%) and radiology (+5.9%) (Fig 1).

The document type varied slightly from specialty to specialty. Neurosurgeons published more case reports than did radiologists and more technical notes than neurologists and miscellaneous researchers. Radiologists published more original articles than neurosurgeons did, whereas neurologists published more review articles than neurosurgeons and radiologists. Three major departments published more than half (57.8%–69.9%) of the articles in their own specialty journals (Table 1).

Contributions from departments also differed widely according to the country of origin. For instance, neurosurgery was the most productive department for research in the top 4 most productive countries (United States, Japan, China, and South Korea). In most other countries, however, radiologists were the greatest contributors (Table 4).

Table 5 shows the pattern of collaboration among departments. Departments of neurology (65.6%) demonstrated significantly higher rates of interdisciplinary collaboration than departments of radiology (53.1%) and neurosurgery (41.3%).

Table 2: Top 20 journals with the highest amount of neurointerventional research between 2003 and 2012

Rank	Journal	Mean Journal IF[a]	No. of Articles
1	American Journal of Neuroradiology	2.778	233
2	Interventional Neuroradiology	0.341	173
3	Neurosurgery	2.802	165
4	Neuroradiology	2.064	109
5	Journal of Neurosurgery	2.511	104
6	Stroke	5.971	84
7	Journal of Neurointerventional Surgery	1.123[b]	71
8	Surgical Neurology or World Neurosurgery[c]	1.195	57
9	Neurologia Medico-Chirurgica (Tokyo)	0.548	43
10	No Shinkei Geka (Japanese)	–	42
11	Acta Neurochirurgica (Wien)	1.323	41
12	Journal of Clinical Neuroscience	0.973	39
13	Journal of Neuroimaging	1.421	31
14	Journal of Korean Neurosurgical Society	0.481[d]	28
15	Neurosurgical Focus	2.567[b]	27
16	Neurology India	0.696	23
16	Zhonghua Nei Ke Za Zhi (Chinese)	–	23
16	Neurological Research	1.432	23
19	Journal of Vascular and Interventional Radiology	2.133	21
19	Minimally Invasive Neurosurgery	0.731	21

[a] Mean journal Impact Factor between 2003 and 2012.
[b] Mean journal Impact Factor between 2010 and 2012.
[c] *Surgical Neurology* (2003–2009) is the former name of *World Neurosurgery* (2010–2012).
[d] Mean journal Impact Factor between 2009 and 2011.

DISCUSSION

The field of neurointerventional therapy was developed originally in 1960 when Lussenhop, a neurosurgeon, and Spence[6] described the technique of intravascular embolization of brain AVMs by injecting Silastic spheres (Dow Corning, Auburn, Michigan) through a surgically exposed carotid artery. After this monumental effort, neurointerventional therapy has made tremendous progress in recent years. This progress is attributable to continuing advances in imaging modalities, catheters and other devices, and interventional techniques, coupled with recent pharmaceutical and basic science knowledge. At least until the end of the 1990s, there was a bitter turf war regarding which of 3 specialties, neurosurgery, neuroradiology, and neurology, had the right to practice the neurointerventional procedures.

In the future, however, the most appropriate type of physician to perform the procedure in this evolving subspecialty may become less relevant with the ultimate goal of optimized patient care. In 2006, the Accreditation Council for Graduate Medical Education announced the revised program requirements in the United States for fellowship education in endovascular surgical neuroradiology.[7] Endovascular surgical neuroradiology occupies a unique niche in the area of neurovascular interventions among neuroradiology, neurosurgery, and neurology. In 2007, after much work, the Society of Neurointerventional Surgery (formerly the American Society of Interventional and Therapeutic Neuroradiology) was formed, comprising all specialists interested in neurointervention.[8] At present, in many neurointerventional centers throughout the world, clinical practice and research are performed by the collaborative effort among physicians with different backgrounds of training.

Given the relatively less invasive nature, rapid technical advances, and the large number of patients, neurointerventional therapy of cerebrovascular disease promises to be a greatly expanding field across many specialty disciplines such as neurosurgery, radiology, and neurology. Therefore, determining the group of physicians most appropriate to perform this specific endovascular procedure is becoming more difficult.[9-11]

The results of our study show that the total number of publications has slightly increased from 2003 to 2012. This increase in publications seems to be related to the increasing worldwide prevalence of cerebrovascular diseases and the increasing interest in the neurointerventional treatment from multiple disciplines. The most active discipline was neurosurgery, but we also observed increases in publications from radiology and neurology.

Despite these achievements, there were 2 disappointing features in the publications that focused on the neurointerventional

Table 3: Impact Factor of journals that published neurointerventional research between 2003 and 2012

	Department of the First Author			
	Neurosurgery	**Radiology**	**Neurology**	**Miscellaneous**
No. of articles published in SCI(E)-indexed journals	760	688	240	142
No. of SCI(E)-indexed journals	150	59	30	54
Mean journal IF	1.806 ± 1.549	2.103 ± 2.027	3.645 ± 5.259[a]	2.245 ± 1.826
25th Percentile Journal IF	0.645	1.069	1.378	1.057
50th Percentile (median) journal IF	1.274	1.990	2.244	2.135
75th Percentile journal IF	2.517	2.629	4.900	2.856

Note:—SCI(E) indicates Scientific Citation Index (Expanded).
[a] Significantly different from values for all other departments.

therapy of cerebrovascular diseases. First, only approximately half of the publications were in the form of original articles. This disproportionately low number of original articles suggests that increases in publication may not necessarily be accompanied by an equivalent increase in the growth of the global scientific impact. Second, only 9.0% of all publications received funding. It is possible that the preponderance of case reports and review articles are reducing the percentage of funded articles because these articles are not usually funded. When examining the original articles specifically, 15.2% of published original articles received funding. This funding rate is substantially lower than that in several other specialties, such as interventional radiology (23.0%)[12] and general radiology (26.9%).[13] These findings are alarming, given that a positive relationship between funding and research productivity has been well established.[14]

The United States was the leading country in producing articles on neurointervention, contributing 31.1% of the publications. This relative contribution of the United States is less than that in radiology literature (45.5%).[13] However, our figure is similar to the productivity in neurosurgery (31.7%) and stroke (27.2%) research of the United States.[15,16] Three Far East Asian countries—Japan, China, and South Korea—collectively accounted for 30.2% of publications. Although the cause of the high research productivity from these countries is likely multifactorial, state-of-the-art equipment and high standard training and education programs in these countries are possible key forces in this achievement.

An interesting feature of our study was that 3 major departments published a relatively small portion (57.8%–69.9%) of articles in their own specialty journals. We surmise that most journals related to neurointervention have an open spirit, providing a publication opportunity for researchers from other disciplines. One of the current trends in scientific publication is publication across disciplines. Several recent studies have addressed the evolution of the departmental affiliations of primary authors in many disciplines.[17-19]

Another interesting finding of the study was that half of the publications were the result of interdisciplinary collaboration. Although little attention has been paid to interdisciplinary collaboration in medical research, research on the neurointerventional therapy of cerebrovascular disease can be classified as a high-collaboration area at the specialty level. Many possible explanations exist for this interesting finding. First, some of these authors might even have multiple backgrounds or different specialties. The senior or corresponding author is often the person who plays the most important role on the research team. Second, interdisciplinary collaboration in research may reflect interdisciplinary collaboration in clinical practice for the neurointerventional therapy of cerebrovascular disease. However, it is unclear how many neurointerventional procedures are currently performed by each specialty. Finally, the size of the research group is increasing on all levels—the total number of authors, departments, institutions, and countries. The large research group has clear advantages for funding and other resources in biomedical research.[20]

Although the results of our study revealed that neurosurgeons, radiologists, and neurologists contributed in important ways to publications relating to neurointervention, we found several in-

Table 4: Share of neurointerventional research for 20 top-ranking countries between 2003 and 2012[a]

| Country | Department of the First Author | | | | |
	Neurosurgery	Radiology	Neurology	Miscellaneous	Total
United States	298	165	120	78	661 (31.1)
Japan	240	24	9	14	287 (13.5)
China[b]	121	46	15	2	184 (8.7)
South Korea	90	68	7	5	170 (8.0)
Germany	18	85	24	9	136 (6.4)
France	12	56	10	6	84 (4.0)
Italy	11	28	6	11	56 (2.6)
Canada	12	27	5	8	52 (2.5)
Turkey	8	31	1	7	47 (2.2)
United Kingdom	14	21	4	3	42 (2.0)
Spain	3	18	12	5	38 (1.8)
Taiwan	3	23	6	3	35 (1.6)
The Netherlands	0	30	3	1	34 (1.6)
Switzerland	2	20	10	1	33 (1.6)
India	1	17	2	7	27 (1.3)
Australia	6	10	6	3	25 (1.2)
Brazil	7	12	2	3	24 (1.1)
Poland	7	12	1	4	24 (1.1)
Belgium	5	12	2	2	21 (1.0)
Israel	11	1	4	2	18 (0.8)

[a] Data in parentheses are percentages. Data do not add up to 100% because shares of other countries are not included.
[b] Includes articles originating from Hong Kong.

Table 5: Collaboration with other disciplines in neurointerventional research between 2003 and 2012[a]

| | Department of the First Author | | | | |
Collaboration Type	Neurosurgery (n = 910)	Radiology (n = 747)	Neurology (n = 270)	Miscellaneous (n = 196)	Total (n = 2123)
Collaboration with other disciplines	376 (41.3)	397 (53.1)	177 (65.6)[b]	110 (56.1)	1060 (49.9)
Corresponding author from other disciplines	17 (1.9)	7 (0.9)	10 (3.7)	9 (4.6)	43 (2.0)
1) Coauthors from neurosurgery, radiology, and/or neurology disciplines	264 (29.0)	287 (38.4)	107 (39.6)	65 (33.2)	723 (34.1)
2) Coauthors from other disciplines	57 (6.3)	52 (7.0)	26 (9.6)	25 (12.8)	160 (7.5)
1 + 2	38 (4.2)	51 (6.8)	34 (12.6)	11 (5.6)	134 (6.3)
No collaboration with other disciplines	534 (58.7)	350 (46.9)	93 (34.4)	86 (43.9)	1063 (50.1)

[a] Data in parentheses are percentages.
[b] Significantly different from values for all other departments.

teresting differences in the publication pattern among specialties.

First, radiologists produced more original articles, neurosurgeons published more case reports and technical notes, and neurologists published more review articles. In addition, neurologists published their findings in journals with higher Impact Factors. Although it may be tempting to conclude that neurologists' research is superior to that of radiologists and neurosurgeons and, thus, is accepted by more prestigious journals, an alternative explanation is that neurologists published more articles in multidisciplinary journals that have more readers and higher journal IFs. Second, the funding rate of neurology (15.2%) was significantly higher than that observed for radiology (8.7%) and neurosurgery (6.8%). The exact cause of this disparity in funding is unclear and is likely multifactorial. Third, the specialty of the authors who published articles on this topic varied according to the country of origin. For instance, most articles originating from the top 4 most productive countries were published by neurosurgeons. Different national patterns of research output may indicate different clinical practice patterns if research precedes clinical adoption. Last, our results showed more collaboration in publications by first authors affiliated with departments of neurology (65.6%) than those affiliated with departments of radiology (53.1%) and neurosurgery (41.3%). A possible explanation for this finding may relate to the staff composition of neurointerventional centers. Neurologists may be a rather small group in the research team or may have a less prominent role in clinical research.

Several limitations in interpreting the results of this bibliometric study should be kept in mind. First, this study is limited to only articles indexed within the PubMed data base, which does not index all research. While PubMed is generally considered a comprehensive and trusted resource, any bias in PubMed indexing of articles could have potentially influenced the results. Second, it is difficult to identify publications that focus on neurointervention because of its broad nature and varied terminology. Consequently, some articles pertaining to the neurointerventional treatment of cerebrovascular disease may have been excluded accidentally. However, the goal of this study was not to capture all neurointerventional research but rather to examine a large representative sample. Finally, the assignment of the clinical specialty and country was based on the affiliation of the first author. Many publications in our data are the product of a collaborative effort among different specialties or countries, so assigning articles to 1 specialty or country is inherently difficult. However, several studies[21,22] have determined that first authors make the greatest contributions to the research and are considered the best means of assigning credit.

CONCLUSIONS

Even though the bibliometric methodology used may present some limitations, our bibliometric analysis provides a pivotal tool to evaluate the characteristics and trends of the publications related to the neurointerventional treatment of cerebrovascular diseases. Neurosurgery, radiology, and neurology have contributed substantially to research on neurointervention, though they each showed slightly different patterns of publication. Slow growth, high interdisciplinary collaboration, and a low level of funding are peculiar characteristics of research in this field.

REFERENCES

1. World Health Organization. Media Centre. The ten top causes of death. http://www.who.int/mediacentre/factsheets/fs310/en/index.html. Accessed October 15, 2013
2. Wakhloo AK, Deleo MJ 3rd, Brown MM. **Advances in interventional neuroradiology.** *Stroke* 2009;40:e305–12
3. Luukkonen T. **Bibliometrics and evaluation of research performance.** *Ann Med* 1990;22:145–50
4. Web of Science. *Journal Citation Reports: Science Edition 2012.* http://wokinfo.com/media/pdf/qrc/jcrqrc.pdf. Accessed October 20, 2013
5. Garfield E. **The history and meaning of the journal impact factor.** *JAMA* 2006;295:90–93
6. Lussenhop AJ, Spence WT. **Artificial embolization of cerebral arteries: report of use in a case of arteriovenous malformation.** *J Am Med Assoc* 1960;172:1153–55
7. Accreditation Council for Graduate Medical Education. ACGME Program Requirements for Graduate Medical Education in Endovascular Surgical Neuroradiology. http://www.acgme.org/acgmeweb/Portals/0/PFAssets/2013-PR-FAQ-PIF/163–182-422_endovascular_neuroradiology_07012013_1-YR.pdf. Accessed October 20, 2013
8. Society of Neurointerventional Surgery. http://www.snisonline.org/. Accessed October 20, 2013
9. Higashida RT. **Evolution of a new multidisciplinary subspecialty: interventional neuroradiology/neuroendovascular surgery.** *AJNR Am J Neuroradiol* 2000;21:1151–52
10. Levy EI, Rinaldi MJ, Howington JU, et al. **Should interventional cardiologists treat ischemic strokes? A global perspective.** *J Invasive Cardiol* 2002;14:646–51
11. Johnston SC. **Who belongs inside the carotid arteries?** *Neurology* 2005;64:188–89
12. Ray CE Jr, Gupta R, Blackwell J. **Changes in the American interventional radiology literature: comparison over a 10-year time period.** *Cardiovasc Intervent Radiol* 2006;29:599–604
13. Lim KJ, Yoon DY, Yun EJ, et al. **Characteristics and trends of radiology research: a survey of original articles published in AJR and Radiology between 2001 and 2010.** *Radiology* 2012;264:796–802
14. Lyubarova R, Itagaki BK, Itagaki MW. **The impact of National Institutes of Health funding on U.S. cardiovascular disease research.** *PLoS One* 2009;4:e6425
15. Hauptman JS, Chow DS, Martin NA, et al. **Research productivity in neurosurgery: trends in globalization, scientific focus, and funding.** *J Neurosurg* 2011;115:1262–72
16. Chow DS, Hauptman JS, Wong TT, et al. **Changes in stroke research productivity: a global perspective.** *Surg Neurol Int* 2012;3:27
17. Garg AX, Iansavichus AV, Kastner M, et al. **Lost in publication: half of all renal practice evidence is published in non-renal journals.** *Kidney Int* 2006;70:1995–2005
18. Donovan AJ, Tompkins RK. **Surgical research publication in a selection of research and surgical specialty journals.** *Surgery* 2010;147:5–12
19. Yun EJ, Yoon DY, Kim BY, et al. **Where do radiologists publish their work? A comparative analysis of publications by radiologists in nonradiology journals in 2000 and 2010.** *AJR Am J Roentgenol* 2013;200:W560–65
20. Engels TCE, Goos P, Dexters N, et al. **Group size, h-index, and efficiency in publishing in top journals explain expert panel assessments of research group quality and productivity.** *Res Eval* 2013;22:224–36
21. Slone RM. **Coauthors contributions to major papers published in the AJR: frequency of undeserved coauthorship.** *AJR Am J Roentgenol* 1996;167:571–79
22. Hwang SS, Song HH, Baik JH, et al. **Researcher contributions and fulfillment of ICMJE authorship criteria: analysis of author contribution lists in research articles with multiple authors published in radiology—International Committee of Medical Journal Editors.** *Radiology* 2003;226:16–23

Adding Value to Health Care: Where Radiologists May Contribute

R.A. Charalel, K.D. Hentel, R.J. Min, and P.C. Sanelli

National health care reform and scrutiny on rising health care costs have created a climate in which health care providers must improve the value, or quality per cost,[1] of patient care. Radiology in particular is at an important crossroads given the heavy use of imaging and the associated large percentage of health care expenditures.[2] At this critical juncture, it is important for radiologists to take responsibility for delivering the highest possible value of imaging and actively contribute to institutional and national solutions for providing the highest valued patient care.[3,4] Only with such active participation will radiologists be able to illustrate our role as an important cornerstone for health care delivery and secure our positions as decisive members of the health care team.

HOW RADIOLOGISTS CAN ADD VALUE

Value is a measure of quality efficiency and has been defined as quality per cost.[1] Quality in radiology may be defined as the ability to obtain the right imaging examination at the right time with accurate, readily available, and actionable interpretations. There are several steps of the imaging process at which radiologists have the opportunity to further improve patient care and health care efficiency, and serve as valued resources to patients and referring clinicians.[5] The following are examples of how radiologists can add value in their practice.

ACQUIRING QUALITY IMAGES

Most imaging orders are created by a referring physician who does not have imaging expertise. Thus, it is not surprising that the initial order may not always be the safest and most effective examination. As imaging experts, radiologists can insure that the right study gets done at the right time in the most effective way (ie, with or without contrast). This "consultation" occurs daily in many practices and is referred to as protocoling. For example, neuroradiologists add considerable value in developing and choosing between complex MR

imaging protocols to answer a targeted clinical question. These protocols differ when evaluating pathology in different central nervous system locations such as is seen with imaging neoplasms in the brain, skull base, spine, or head and neck. Despite the value of this service, most patients and referring physicians are not even aware of the radiologist's effort. This can be taken a step further by developing radiology consultation services,[6] thereby formalizing our role as specialist consultants, and facilitating access for both physicians and patients to the radiologist.

As imaging experts, radiologists also serve important institutional roles by contributing to equipment selection, technologist training, and the maintenance of quality metrics to help ensure that diagnostic quality images are produced. Furthermore, radiologists are responsible for developing new image protocols to reduce radiation dose, while still maintaining diagnostic quality. In addition, radiologists monitor radiation dosimetry for all patients, staff, and civilians, enforcing policies to reduce unnecessary exposure. As image experts, radiologists are critical to all aspects of developing a quality image.

IMAGE INTERPRETATION

Fee-for-service payment models have resulted in radiologists being rewarded for the efficient and accurate interpretation of imaging studies. However, value should not be measured on the basis of a single imaging study but rather considered in the context of the patient's medical condition. By using tools and information increasingly available to the radiologist at the time of image interpretation, the radiologist may create reports that not only describe the imaging study performed but increase value by guiding the care of the imaged patient. Radiologists must take into context the clinical scenario and put forth interpretations that are relevant with differential diagnoses that are plausible. The increasing availability of electronic medical records allows the radiologist to review images with the added context provided by operative notes, outpatient clinic notes, laboratory testing, and pathology results. Such context often results in a more informed and useful differential diagnosis; for example, identifying focal neurologic symptoms helps to focus the image interpretation of patients with acute stroke and may lead to the increased discovery of subtle findings such as a hyperattenuated vessel sign or early ischemic changes that may otherwise be overlooked. When ade-

quate information is not readily available in the medical record, consultations with the ordering physicians, other members of a patient's health care team, and the patient serve to acquire the necessary information and increase the visibility of the radiologist.

Furthermore, we can enhance the relevance of our interpretations by providing reports that synthesize all available imaging modalities across all organ systems, not just the most recent prior examination of a specific technique or body part. Subspecialization in radiology has led to nuanced reporting from expert imagers, particularly in the case of neuroradiology studies, which are largely interpreted by subspecialists in academic institutions and even in the community. However, it can also result in multiple reports for a single patient, even within the same care episode, leaving referring physicians to reconcile these multiple and potentially conflicting reports even though they may not have the expertise to understand the nuanced reports and the strengths and limitations of the used imaging modalities, or the ability to re-examine the images in a holistic patient context. Radiologists as imaging experts have the skills to do so, uniquely qualifying them to improve service and optimize care for our patients.

The greatest opportunity to provide value is when patients are new to a health care system and arrive with prior outside imaging. By facilitating the availability of such imaging to the new health care system and providing reports summarizing findings in a holistic patient context, repeat and often unnecessary studies can be reduced, ultimately allowing for more efficient and effective care of the patient.

BEYOND IMAGE INTERPRETATION

Still, providing more valuable reports is not enough. The value provided by the radiologist must be demonstrated to patients and the medical community. Failure to do so will risk the commoditization of imaging and places radiology in an unfavorable position as health care continues to transition to accountable, bundled care. Several opportunities for increased recognition exist in many of our practices. Multidisciplinary care conferences, including tumor boards and rounds, serve as an opportunity for radiologists to demonstrate their value within the overall care team by providing an opportunity to synthesize a patient's imaging history and suggest additional imaging studies as needed.

In addition, maintaining and developing technology for direct access to radiology reports and images through patient portals provides increased exposure. However, currently, most radiologists do not create reports with the patient audience in mind. Moving forward, radiologists and their reports must be cognizant of this new audience.[7] Finally, achieving the visibility needed will no doubt require radiologists to leave the reading room and directly interact with patients. In the new paradigm of decentralized reading rooms within clinics, patients and referring physicians may be more accessible than ever before.[8]

CONCLUSIONS

Although many clinicians, administrators, and patients may be relatively unaware of the radiologist's valuable role in delivering health care, the services radiologists provide in acquiring quality images, image interpretation, and consultation have been recognized as integral aspects of the physician work component in the Medicare resource-based relative value scale (RBRVS) payment system. Under the RBRVS system, a physician's work is measured by the technical skill, physical effort, required mental effort, judgment, stress due to the potential risk to the patient, and time it takes to perform the service.[9] However, many opportunities exist for radiologists to improve and demonstrate the value they provide to patients and the health care system. Recent and future changes to the health care environment, including increased emphasis on value and accountable care, provide unprecedented imperative and opportunity to do so.

REFERENCES

1. Porter ME. **What is value in health care?** *N Engl J Med* 2010; 363:2477–81
2. Rao VM, Levin DC. **The overuse of diagnostic imaging and the Choosing Wisely initiative.** *Ann Intern Med* 2012;157:574–76
3. Duszak R Jr. **Value: imaging's new wave imperative.** *J Am Coll Radiol* 2013;10:484–85
4. American College of Radiology. Imaging 3.0. http://www.acr.org/Advocacy/Economics-Health-Policy/Imaging-3. Accessed June 10, 2014
5. Patti JA, Berlin JW, Blumberg AL, et al. **ACR white paper: the value added that radiologists provide to the health care enterprise.** *J Am Coll Radiol* 2008;5:1041–53
6. Khorasani R, Silverman SG, Meyer JE, et al. **Design and implementation of a new radiology consultation service in a teaching hospital.** *AJR* 1994;163:457–59
7. Kuhlman M, Meyer M, Krupinski EA. **Direct reporting of results to patients: the future of radiology?** *Acad Radiol* 2012;19:646–50
8. Rosenkrantz AB, Lepor H, Taneja SS, et al. **Adoption of an integrated radiology reading room within a urologic oncology clinic: initial experience in facilitating clinician consultations.** *J Am Coll Radiol* 2014;11:496–500
9. American Medical Association. Overview of the RBRVS. http://www.ama-assn.org/ama/pub/physician-resources/solutions-managing-your-practice/coding-billing-insurance/medicare/the-resource-based-relative-value-scale/overview-of-rbrvs.page?. Accessed June 10, 2014

Decreased Infarct Volume and Intracranial Hemorrhage Associated with Intra-Arterial Nonionic Iso-Osmolar Contrast Material in an MCA Occlusion/Reperfusion Model

H. Morales, A. Lu, Y. Kurosawa, J.F. Clark, J. Leach, K. Weiss, and T. Tomsick

ABSTRACT

BACKGROUND AND PURPOSE: Infarct volume and intracranial hemorrhage after reperfusion with nonionic low-osmolar and iso-osmolar iodinated IRCM has not been previously compared. We postulated that iso-osmolar and low-osmolar iodinated contrast media exert varied effects on cerebral infarct after intra-arterial injection. We compared infarct volume and hemorrhagic changes following intra-arterial infusion of iodixanol, iopamidol, or normal saline in a rat MCA occlusion/reperfusion model.

MATERIALS AND METHODS: Infarct was induced in 30 rats by a previously validated method of MCA suture occlusion. Reperfusion was performed after 5 hours with either iodixanol ($n = 9$), iopamidol ($n = 12$), or saline ($n = 9$). MR images were obtained at both 6 and 24 hours after ischemia, followed by sacrifice. Infarct volume was measured with T2WI and DWI by semiautomatic segmentation. Incidence and area of hemorrhage were measured on brain sections postmortem.

RESULTS: T2WI mean infarct volumes were 242 ± 89, 324 ± 70, and 345 ± 92 mm^3 at 6 hours, and $341 \pm 147,470 \pm 91$, and 462 ± 71 mm^3 at 24 hours in the iodixanol, iopamidol, and saline groups, respectively. Differences in infarct volume among groups were significant at 6 hours ($P < .03$) and 24 hours ($P < .05$). In the iodixanol, iopamidol, and saline groups, mean areas for cortical intracranial hemorrhage were 0.8, 18.2, and 25.7 mm^2; and 28, 31, and 56.7 mm^2, respectively, for deep intracranial hemorrhage. The differences in intracranial hemorrhage area among groups were statistically significant for cortical intracranial hemorrhage ($P < .01$).

CONCLUSIONS: Intra-arterial infusion of nonionic iso-osmolar iodixanol showed reduced infarct volume and reduced cortical intracranial hemorrhage areas in comparison with nonionic low-osmolar iopamidol and saline. Our results may be relevant in the setting of intra-arterial therapy for acute stroke in humans, warranting further investigation.

ABBREVIATIONS: IA = intra-arterial; ICH = intracranial hemorrhage; IRCM = iodinated radiographic contrast material; HT = hemorrhagic transformation

U se of iodinated radiographic contrast material (IRCM) is inherent in the current diagnostic and therapeutic paradigm of stroke evaluation and therapy in humans, not only via intravenous infusion in CT angiography and CT perfusion but also via intra-arterial (IA) injection of IRCM during revascularization attempts. Data identifying CTP IRCM leakage as a predictor of subsequent hemorrhagic transformation (HT) and intracerebral hemorrhage (ICH) have accumulated.[1-3] Yet IRCM deposition in the brain as a sequela of IA revascularization in humans is a frequent phenomenon, commonly but not invariably associated with HT.[4]

Having identified relevant differences in ICH following IA infusion of nonionic low-osmolar IRCM in a rat reperfusion model, we postulated that potential clinical differences might also exist between low-osmolar and iso-osmolar IRCM with IA infusion.[5] Therefore, we evaluated nonionic iso-osmolar IRCM (iodixanol, 290 mOsmol) versus a nonionic low-osmolar IRCM (iopamidol, 616 mOsmol) on brain infarct and ICH in a rodent MCA occlusion/reperfusion stroke model. To the best of our knowledge, similar experimental studies evaluating potential differences of IA IRCM on these parameters have not been previously reported.

MATERIALS AND METHODS

The animal protocol was approved by the University Animal Care Committee and conformed to the National Institutes of Health *Guide for Care and Use of Laboratory Animals* (http://grants.nih.gov/grants/olaw/Guide-for-the-care-and-use-of-laboratory-animals.pdf). Male Sprague-Dawley rats had unrestricted access to food and water and were housed with a 12-hour light-dark cycle. Throughout the study, the investigators and veterinarian staff closely monitored the rats' health status.

This was a single blinded placebo-controlled study.

General Surgical Preparation

Thirty-four male Sprague-Dawley rats (body weight = 310.7 ± 12 g) were anesthetized with 3% isoflurane and maintained with 1.5% isoflurane in a mixture of 70% N_2 and 28.5% O_2. Rectal temperature was monitored and maintained at 37 ± 0.5°C with a feedback-controlled heating blanket. Four animals were excluded from the analysis due to failure of the surgical technique. They were not imaged, dying immediately following reperfusion. Subarachnoid hemorrhage was identified on postmortem analysis.

Stroke Model and Drug Injection

A previously validated method of MCA occlusion with intraluminal suture was used.[6] The left common carotid artery, external carotid artery, and internal carotid artery were isolated via a ventral midline incision. A 3/0 monofilament nylon suture was used to occlude the MCA.[7] The suture was inserted into the external carotid artery and advanced into the ICA until the tip occluded the junction of the MCA and anterior cerebral artery (approximately 20 mm beyond the carotid bifurcation until mild resistance was felt). The wound was closed temporarily, and the suture was kept in place for 5 hours. Rats were then re-anesthetized, and the ventral midline neck incision was again opened. Immediately after removal of the suture to allow reperfusion, a polyethylene-10 tube was placed into the external carotid artery with its tip at the ICA origin The ICA was not directly catheterized. All animals initially received a 10-minute intra-arterial saline infusion of 1 mL/kg. Next, either iodixanol (290 mOsmol/kg H_2O, Visipaque, 320 mg I/mL; GE Healthcare, Princeton, New Jersey), iopamidol (616 mOsmol/kg H_2O, Isovue, 300 mg I/mL; Bracco Diagnostics, Princeton, New Jersey), or normal saline (300 mOsmol/kg H_2O) was infused (1 mL/kg) for an additional 10 minutes. The external carotid artery was ligated, and the incisions were sutured. Thus, 3 groups were studied as follows: iso-osmolar iodixanol group (*n* = 9), low-osmolar iopamidol group, (*n* = 12), and saline group (*n* = 9).

Monitoring of Regional Cerebral Blood Flow

Before MCA occlusion, a small craniotomy near the vertex (5 mm lateral and 2 mm posterior to the bregma) was performed. This allowed cerebral blood flow estimation from the left MCA by using transcranial laser Doppler sonography perfusion measurements (PF-5001; Perimed, Järfälla, Sweden) before and after MCA occlusion and after reperfusion with saline and/or IRCM infusion.[8]

Neurologic Deficits and Mortality

Neurologic examinations at 45 minutes and 2, 12, and 24 hours after induction of ischemia were scored according to a 7-point scale modified from Zhang et al[9]: no neurologic deficit = 0, forelimb flexion = 1, circling to the right = 2, impaired or lame forelimbs = 3 and hind limbs = 4, inability to walk = 5, and animal death = 6. Average scores were calculated for each group. Mortality was expressed as the number of rats dying within 24 hours before euthanasia divided by the number in each group ×100.

MR Imaging Protocol

We used a custom-made single-channel coil (Resonance Innovations, Omaha, Nebraska) designed to fit a rat's head and optimized for use in a clinical 3T magnet (Signa Excite; GE Healthcare, Milwaukee, Wisconsin).

Following reperfusion at both 6 and 24 hours after ischemia, the animals were imaged in the coronal plane with the following protocol: T2WI (TR/TE: 2500/92 ms, section thickness: 2 mm, FOV: 6 cm, matrix: 256 × 256, NEX: 1), T1WI (TR/TE: 867/20 ms, section thickness: 2 mm, FOV: 6 cm, matrix: 256 × 256, NEX: 1), T2 FLAIR (TR/TE/TI: 12827/120/2250 ms, section thickness: 2 mm, FOV: 6 cm, matrix: 352 × 224, NEX: 1), gradient-recalled echo (TR/TE/flip angle: 550 ms/20 ms/20°, section thickness: 2 mm, FOV: 6 cm, matrix: 224 × 224, NEX: 2), and spin-echo DWI (*b* = 1000, FOV: 4 cm).

Infarct Identification and Volume Measurement

Infarct volume was measured in a randomized, blinded fashion at both 6 and 24 hours on T2WI and DWI, processed on a separate workstation with iPlan, Version 2.6 (BrainLab Software, Feldkirchen, Germany). Semiautomatic segmentation of the infarcted areas and of the entire brain was performed, and both the relative (volume of infarcted hemisphere / volume of total brain ×100) and the absolute volume were calculated.

Hemorrhage Identification and Measurement

After the 24-hour brain MR imaging, rats were sacrificed. The brain was sliced into six 2-mm coronal sections (12 faces). The sections were fixed in 4% paraformaldehyde for 15 minutes. A previously reported visual method was used to estimate the ICH area.[10-12] Both sides of the section were optically scanned. The incidence of hemorrhage was first calculated as number of rats with hemorrhage/total number of rats per group, then similar calculations were made regarding a distinct location of the hemorrhage in the basal ganglia or cortex. The hemorrhagic area on each section face was measured with the MCID imaging system (Imaging Research, St. Catherines, Ontario, Canada).[12] Finally, the total area for the 12 faces was obtained by summation of individual areas.

Statistical Analysis

Statistical analysis was performed with the Statistical Package for the Social Sciences for Windows, Version 16.0 (IBM, Armonk, New York). All data were described as mean ± SE. The difference among the 3 groups for quantitative variables of ischemia was assessed by using a 1-way ANOVA analysis. When statistical significance was obtained in the ANOVA analysis, a post hoc analysis between each of the 2 groups was assessed by using the Fisher Least Significant Difference test. The difference among the 3 groups for qualitative variables was assessed by using the χ^2 test or Kruskal-Wallis test.

The distribution of the quantitative variable "hemorrhagic area"

Table 1: Absolute and relative infarct volumes at 6 and 24 hours after ischemia

Group	Relative Infarct Volume (% Total Brain)		Absolute Infarct Volume: T2WI (mm³)		Absolute Infarct Volume: DWI (mm³)	
	6 hours	24 hours	6 hours	24 hours	6 hours	24 hours
Iodixanol	16.4 ± 6 (n = 9)	22.7 ± 10 (n = 8)	242 ± 89 (n = 9)	341 ± 147 (n = 8)	208 ± 90 (n = 7)	328 ± 144 (n = 7)
Iopamidol	22.8 ± 5.5 (n = 12)	32 ± 6.3 (n = 10)	324 ± 70 (n = 12)	470 ± 91 (n = 10)	309 ± 49 (n = 10)	438 ± 90 (n = 9)
Saline	24.4 ± 6.2 (n = 9)	32.4 ± 5.5 (n = 6)	345 ± 92 (n = 9)	462 ± 71 (n = 6)	331 ± 103 (n = 8)	468 ± 63 (n = 5)
Statistics (ANOVA)	P < .018	P < .028	P < .03	P < .047	P < .018	n.s.

Note:—n.s. indicates not significant.
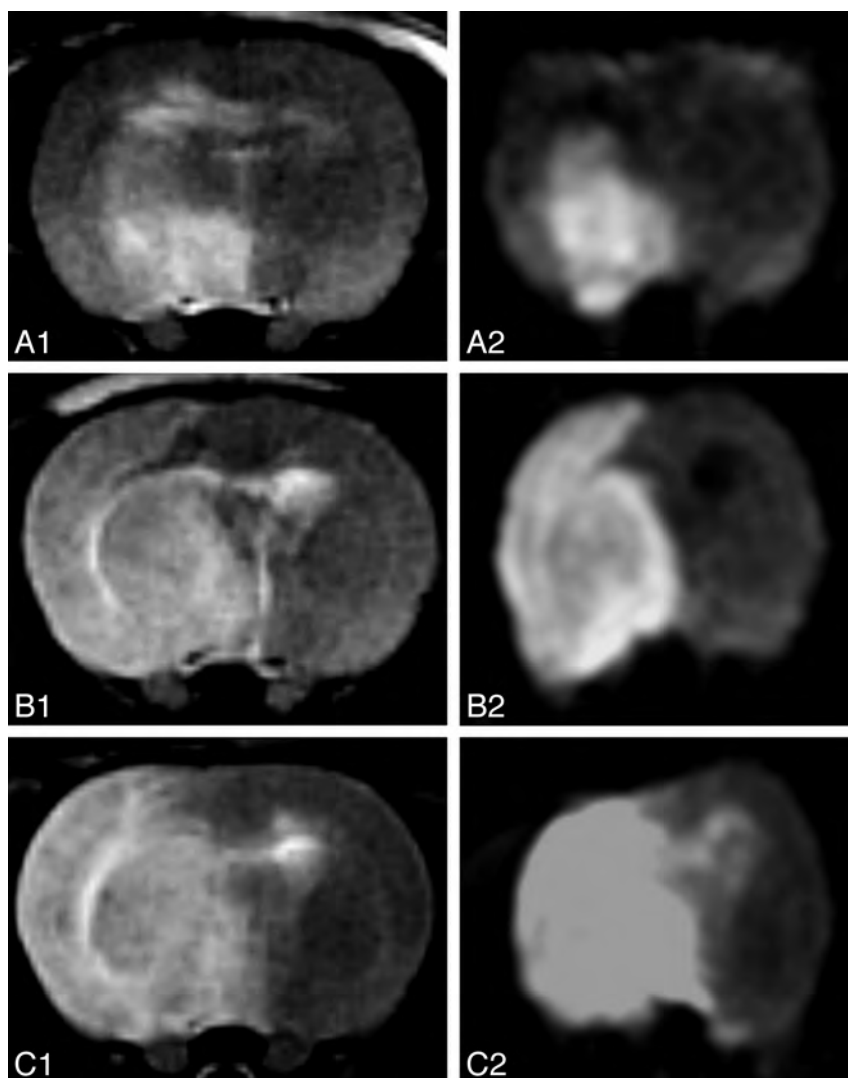
FIG 1. T2WI (*A1, B1, C1*) and DWI (*A2, B2, C2*) of 3 different rats at 24 hours after ischemia, corresponding to the iodixanol (*A1, A2*), iopamidol (*B1, B2*), and saline (*C1, C2*) groups, show decreased infarcted volume in the iodixanol group compared with iopamidol and saline groups.

was not normal; therefore, a nonparametric (Kruskal-Wallis) test was used to compare mean areas among groups. The difference among groups for categoric variables was assessed by using the exact test. The Pearson coefficient was used to correlate infarct volume and hemorrhagic area. Statistical significance was set at $P < .05$.

RESULTS

No statistically significant differences were found among groups in body weight, morphometric parameters, or physiologic parameters as measured during surgery, including body temperature (Celsius). Following occlusion before reperfusion, all animals showed hyperthermia, with similar average body temperatures (Celsius) in all 3 groups: 39.2 ± 0.9 (iodixanol), 39 ± 0.8 (iopamidol), and 39.3 ± 0.9 (saline).

CBF measured as the percentage perfusion after ischemia/before ischemia (39 ± 26%, 39 ± 17%, and 46 ± 22%) or as the percentage perfusion after IRCM/before ischemia (88 ± 14%, 90 ± 18%, and 78 ± 16%) for iodixanol, iopamidol, and saline, respectively, demonstrated no statistical difference among groups.

No statistical difference was found for the average neurologic score after 45 minutes and at 2, 12, and 24 hours among groups (3.9 ± 0.2, 3.6 ± 0.3, 3.4 ± 1, and 3.2 ± 1 in the iodixanol group; 3.7 ± 0.4, 3.5 ± 0.7, 3.9 ± 1.1, and 3.7 ± 1.3 in the iopamidol group; 4.1 ± 0.3, 3.3 ± 0.3, 4.3 ± 1.3, and 4.5 ± 1.8 in the saline group, respectively) (Kruskal-Wallis test). One animal in the iodixanol group (11%), 2 animals in the iopamidol group (17%), and 5 animals in the saline group (55%) died; 3, at 7 hours and 2 animals at 18 hours. Differences among groups for mortality were not statistically significant (exact test).

All animals developed T2 and FLAIR hyperintense signal and restricted diffusion in the MCA territory, including the basal ganglia, at 6 and 24 hours.[6,13] Both the relative and absolute infarct volumes after administration of iodixanol were significantly smaller than those in the other 2 groups at 6 and 24 hours (Table 1 and Fig 1). Differences in infarct volumes among groups were significant at 6 hours ($P < .03$) and 24 hours ($P < .05$) (Fig 2). Post hoc analysis for infarct volume differences between the iodixanol and iopamidol groups and between the iodixanol and saline groups was significant at 6 hours ($P < .03$ and $P < .01$, respectively) and 24 hours ($P < .02$ and $P < .008$, respectively).

Excessive DWI artifacts due to inadequate coil optimization were encountered in the first 4 animals at the 24-hour scan. The artifacts problem was resolved for the remainder of the study. Nevertheless, a strong trend for decreased DWI volume for the iodixanol group was identified when comparing the absolute DWI infarct volumes at 24 hours.

All animals showed HT, typically visualized on pathologic brain sections as macroscopic non-space-occupying red areas (Fig 3). The absolute cortical ICH in the iodixanol group was significantly smaller than that in the other 2 groups ($P < .01$) (Table 2). The incidence of cortical and deep (basal ganglia) ICH was not different among groups (exact test).

There was a positive but nonrobust linear scatterplot correlation between the MR imaging infarct volume and total hemorrhagic area on cut sections when all the groups were pooled (Pearson $r = 0.415$, $P < .023$; $r^2 = 0.17$). The correlations were positive for each group and fell into the moderate category as well: saline, $r = 0.365$, $P < .335$; iodixanol, $r = 0.449$, $P < .225$; and iopamidol, $r = 0.512$, $P < .089$ (Fig 4).

DISCUSSION

Both IV and IA IRCM injection may increase the permeability of the blood-brain barrier under normal conditions in animals.[14-16] Theoretically, it is possible that large IV or IA doses of IRCM (as used in therapeutic revascularization procedures) may contribute to a BBB opening, edema, and HT.[16,17] Following ischemia in humans, additional leakage of IRCM across the damaged BBB has been reported under a variety of circumstances. Contrast deposition during CT perfusion in the acute ischemic setting has been noted to be a marker of subsequent ICH.[1-3] It remains unclear whether this is both cause and effect. Lummel et al[4] recently constructed a nexus between hyperattenuated cerebral lesions and IRCM deposition immediately after mechanical revascularization preceded by CTA/CTP, suggesting that early hyperattenuated lesions were IRCM-volume related with a higher risk of secondary HT, but they did not find them necessarily predictive of reduced clinical functional outcome.

A variety of IRCM has been used clinically in human stroke evaluation and therapy, and IRCM differs in its effects on and potential for passage across the injured BBB. Variable passage across the BBB may modulate infarct edema and the risk of ICH. Ionic hyperosmolar IRCM (~1200 mOsm) has been abandoned for IA use due to increased neurotoxicity compared with the low-osmolar IRCM (~700 mOsm). Doerfler et al[18] showed decreased infarct volume following IV nonionic low-osmolar IRCM (770 mOsm) versus ionic hyperosmolar iothalamate (2520 mOsm) in a rodent permanent occlusion stroke model, and they suggested that osmolarity, at least in part, explained the effect. Newer iso-osmolar IRCM is theoretically less cytotoxic due to lower osmolarity (similar to plasma, ~300 mOsm), compared with low-osmolar IRCM.[19,20] However, complex mechanisms other than osmolarity alone are acting as well.

IRCM effects on infarct volume and ICH may be due to osmotic, direct neurotoxic, hydrostatic, or vascular occlusive effects. The belief that IRCM hyperosmolarity is responsible for several adverse effects of IRCM via toxic ionic load conflicts with data suggesting a beneficial osmotic tonicity effect of intravascular IRCM on the extravascular, extracellular space based on molecular size.[21-23] The molecule size of dimeric iodixanol (1000 d, approximately 6 times larger than mannitol) is approximately twice as large as monomeric iopamidol (500 d); it may be less
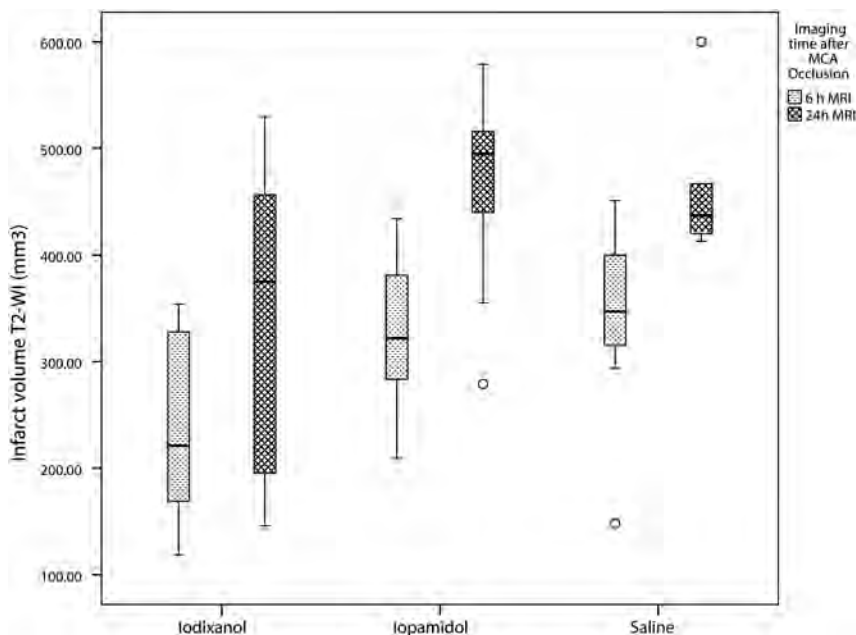
FIG 2. Boxplot analysis of absolute infarct volume per group and at 2 different times after ischemia (6 hours and 24 hours). There is increased volume of infarct in the iopamidol and saline groups compared with the iodixanol group.
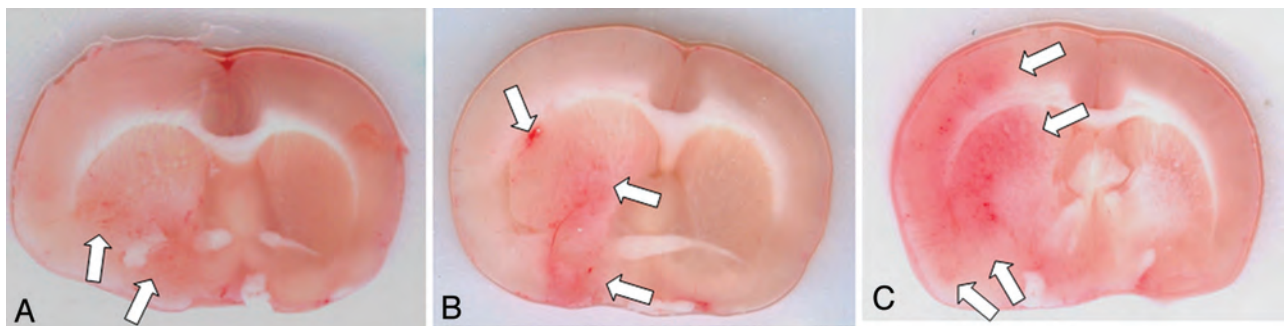
FIG 3. Hemorrhagic transformation on sample animals. *A*, Iodixanol group. *B*, Iopamidol group. *C*, Saline group. Note the small amount of hemorrhage in the iodixanol rat (*arrows* in *A*) compared with larger areas in the other 2 animals (*arrows* in *B* and *C*).

Table 2: Incidence and area of cortical and deep intracranial hemorrhage on cut-section inspection

Group	Cortex		Deep (Basal Ganglia)		Total	
	Incidence[b]	Area (mm^2)[a]	Incidence	Area (mm^2)[b]	Incidence	Area (mm^2)[b]
Iodixanol ($n = 9$)	5 (56%)	0.8 ± 1.5	9 (100%)	28 ± 23	9 (100%)	28.8 ± 23.3
Iopamidol ($n = 12$)	9 (75%)	18.2 ± 31	12 (100%)	31 ± 24.6	12 (100%)	49.2 ± 50.3
Saline ($n = 9$)	8 (89%)	25.7 ± 39.7	9 (100%)	56.7 ± 29.3	9 (100%)	82.5 ± 62.7

[a] $P < .01$.
[b] Not significant.
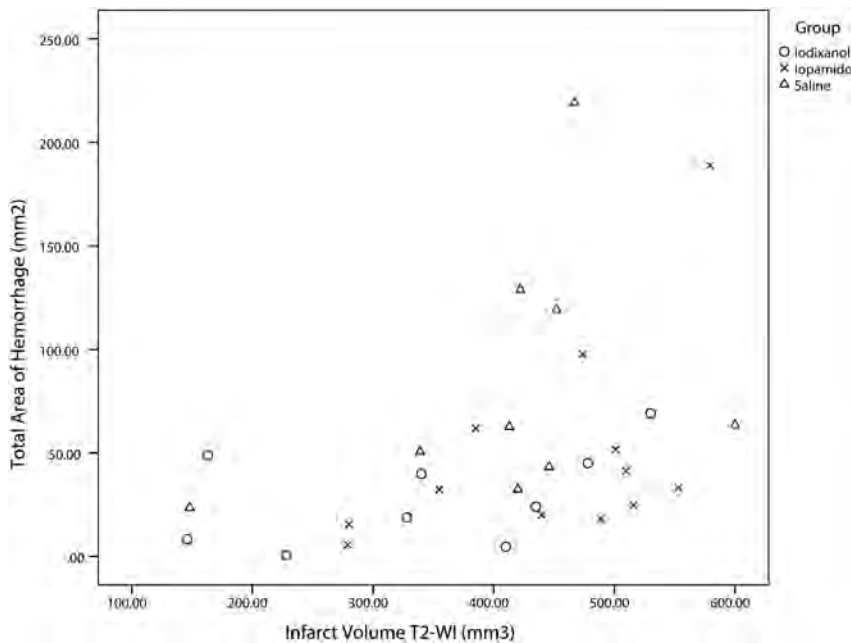
FIG 4. Scatterplot shows positive linear correlation between infarct volume and hemorrhagic transformation in all groups. The correlation is mild ($r = 0.415$), and in some cases, large infarct volumes were not associated with large hemorrhagic areas.

able to traverse early damage to the blood-brain barrier to exert adverse osmotic or direct toxic effects in the extracellular space. Conversely, iopamidol may ultimately more easily traverse the damaged membrane to increase edema, rather than decrease it, by osmotic effect.

Endothelial cell morphology and function may be directly affected variably by IRCM injection, contributing to IRCM and fluid passage beyond the arterial lumen.[24] There is conflicting evidence regarding increased neurotoxicity once the IRCM has crossed the BBB in animals and humans.[17,25-29] Heinrich et al[30] compared the direct cytotoxic effects of dimeric iso-osmolar and monomeric iso-osmolar IRCM on renal tubular cells in vitro and found that dimeric IRCM have stronger direct cytotoxic effects, postulating a mechanism independent from osmolarity.[30]

Molecular chemotoxicity, related to the chemical structure of the molecule, decreases as the number of carboxyl groups decreases and the number of hydroxyl groups increases. Increasing the number of hydroxyl groups also increases the solubility of the agent, thus reducing its tendency to bind to tissues and proteins.[31] Agents with no carboxyl groups and a number of hydroxyl groups evenly distributed around the main molecule have a reduced propensity for neurotoxicity.[32] Iodixanol has an increased number of hydroxyl groups compared with low-osmolar IRCM.

Hydrolysis of iodixanol in vitro can produce a derivative of propylene glycol (2,3-dihydroxy-1-propylamine HOCH$_2$-CH (OH)-CH$_2$-NH$_2$). Propylene glycol when injected intra-arterially in an ischemic brain model of rats has been found to decrease BBB dysfunction by a "sealing" effect, with subsequent decreased permeability and infarct size.[33] Although iodixanol has no biotransformation after intravenous injection, a similar "sealing" effect in the BBB is possible.[34,35]

Clot formation and coagulation interactions by IRCM also have impact on infarct volume and ICH.[36] Mechanisms and effects may be paradoxical, with equilibrium among thrombotic, antiplatelet, and fibrinolytic properties resulting in a dominant state, which varies among different IRCM. Specifically, iodixanol has been found to have a less thrombotic effect than iopamidol.[37] However, no Doppler-measured CBF differences were identified postreperfusion in our animals that could reasonably explain an effect of persistent reduced blood flow on infarct volume in the iodixanol group. Even in the absence of coagulation-mediated oligemic effects, increased hemoglobin binding attributed to IRCM may exert a circulatory hypoxic effect, promoting neurotoxicity via reduced oxygen delivery to tissue.[38]

Physical properties such as viscosity differ among IRCM and can exert a hydrostatic effect.[39] Iodixanol has increased viscosity (11.8 cP) compared with iopamidol (4.7 cP) at 37°C. The reduced hydrostatic effect across an injured BBB may account for the reduced infarct edema volume measured compared with saline or a less viscous low-osmolar contrast. Differences in infusion duration were not encountered in our study. Higher viscosity fluid may reduce antegrade reperfusion and reduce hydrostatic infarct edema. If so, reduced viscosity-related antegrade reperfusion may represent a new therapeutic option for further exploration.

Changes in the environment, such as decreased pH or increased temperature in the hypoxic brain tissue, can cause changes in the physicochemical properties of IRCM as well. The role these differences play in our particular results is difficult to postulate.

We observed a trend toward increased mortality and worse neurologic score in the saline group compared with iodixanol and iopamidol. It is likely that significant damage of the BBB had already occurred by the time of reperfusion 5 hours after ischemia. Reperfusion itself caused an inflammatory cytotoxic effect, with increased edema and ICH. Reperfusion increases levels of reactive oxygen species, including the superoxide radical and nitric oxide.[40,41] Oxidative radicals trigger activation of metallopro-

teinases, which disrupt permeability barriers and, in turn, potentiate injury to microvasculature and neural cells during ischemia and reperfusion.[42,43] Larger infarcts and increased HT occur in the reperfusion of MCA occlusion compared with permanent occlusion, and metalloproteinases are particularly increased after reperfusion compared with models of permanent occlusion.[12]

Aquaporin-4 has been linked to the severity of infarct volume but not with HT.[44] Therefore, the mechanism of HT, though linked to mechanisms affecting reperfusion, infarct volume, and edema previously discussed, might have a separate and different pathophysiologic pathway after reperfusion in acute ischemic stroke in humans and animals.[45]

The contributions of hemorrhagic changes, typically petechial in the rat, might also increase differences in apparent, measurable secondary infarct edema. However, on the basis of our pilot work, more hemorrhagic changes were anticipated in the IRCM group, as opposed to lesser areas with iodixanol. In contrast to our pilot work, in which 37% of saline-infused and 75% of iohexol-infused rats exhibited HT, all animals in the current study exhibited HT, most frequent and voluminous in the saline and iopamidol groups. The higher percentage of ICH in all groups can be attributed to the additional burden of postreperfusion transportation, anesthesia, MR imaging, recovery, and delay before sacrifice, likely contributing to stress-induced infarct volume and HT. Nevertheless, we identified decreased HT in the iodixanol group. Thus, we might indeed be identifying a direct or indirect effect of iodixanol, whose exact mechanisms and significance remain to be clarified.

There are a number of limitations of our methods, analyses, findings, and hypotheses regarding the IRCM effect on infarct volume and ICH. First, our data for infarct volume as measured by DWI are inconclusive at 24 hours, mainly due to field inhomogeneity artifacts precluding 4 early cases from adequate evaluation. The role of ADC for prediction of HT in our population is yet to be explored further.[46-48] The 5-hour time window is later than typically used in ischemic rat models. Knight et al[49] reported no T2 signal changes early after reperfusion in a model of 2–4 hours of transient ischemia. Thus, the late time was chosen to guarantee maximal ischemic potential.

The large volume and concentration of prolonged IA IRCM injection was chosen not only to avoid overlooking any potential adverse effect not obvious with lower volumes but also to more closely simulate the effect of frequent, repetitive injections in the setting of prolonged occlusion, as is commonly used in human stroke intervention, in the timeframe when intervention is most typically applied and when benefits of revascularization are expected to be diminishing.

Another limitation is the lack of images before reperfusion. Any proposed protective effect of iodixanol might have been demonstrated by different rates of increase, or reduction, of infarct edema volume between prereperfusion and postreperfusion scans. With surgery performed remote from the scanner site, imaging during occlusion was impractical at this stage of investigation.

Differences in infarct volume and ICH might be attributed to inadequate MCA occlusion or reduced reperfusion effect in the iodixanol group. However, Doppler CBF showed no statistical differences among groups, with overall no indication of inadequate occlusion or differences in reperfusion. In addition, we have found spontaneous hyperthermia useful in estimating successful occlusion of the MCA territory in our model, with direct correlation between the body temperature and infarct size.[50] All animals showed hyperthermia with similar average body temperatures before reperfusion in all 3 groups. Therein, we have no evidence that the infarct development before reperfusion was different in all 3 groups.

Nevertheless, further investigation with a larger number of animals could improve the consistency of late DWI measurements; if possible, MR imaging before reperfusion could help to confirm our results.

CONCLUSIONS

In our MCA occlusion/reperfusion rat model, iso-osmolar iodixanol perfusion demonstrated reduced infarct volume and cortical ICH area compared with both low-osmolar iopamidol and saline perfusion. The responsible mechanism for these findings is not clear. Multiple mechanisms are certainly possible, including not only physical-chemical or coagulation-related effects but also antioxidative or other antitoxic effects at the BBB and/or in the brain parenchyma. Although different low-osmolar IRCM can have distinct effects in the infarcted brain, a potential direct or indirect effect of iodixanol might be postulated. Further investigation is warranted.

ACKNOWLEDGMENTS

REFERENCES

1. Hom J, Dankbaar JW, Soares BP, et al. **Blood-brain barrier permeability assessed by perfusion CT predicts symptomatic hemorrhagic transformation and malignant edema in acute ischemic stroke.** *AJNR Am J Neuroradiol* 2011;32:41–48
2. Aviv RI, d'Esterre CD, Murphy BD, et al. **Hemorrhagic transformation of ischemic stroke: prediction with CT perfusion.** *Radiology* 2009;250:867–77
3. Lin K, Kazmi KS, Law M, et al. **Measuring elevated microvascular permeability and predicting hemorrhagic transformation in acute ischemic stroke using first-pass dynamic perfusion CT imaging.** *AJNR Am J Neuroradiol* 2007;28:1292–98
4. Lummel N, Schulte-Altedorneburg G, Bernau C, et al. **hyperattenuated intracerebral lesions after mechanical recanalization in acute stroke.** *AJNR Am J Neuroradiol* 2014;35:345–51
5. Kurosawa Y, Lu A, Khatri P, et al. **Intra-arterial iodinated radiographic contrast material injection administration in a rat middle cerebral artery occlusion and reperfusion model: possible effects on intracerebral hemorrhage.** *Stroke* 2010;41:1013–17
6. Koizumi A, Yoshida Y, Nakazawa T, et al. **Experimental studies of ischemic brain edema: a new experimental model of cerebral em-**

bolism in rats in which recirculation can be introduced in the ischemic area. *Jpn J Stroke* 1986;8:1–8

7. Longa EZ, Weinstein PR, Carlson S, et al. **Reversible middle cerebral artery occlusion without craniectomy in rats.** *Stroke* 1989;20:84–91

8. Nestler U, Seifner S, Greschus S, et al. **Doppler ultrasonographic measurement of blood flow velocities in major cerebral arteries of the rat using triplex mode.** *Neurol Res* 2006;28:877–80

9. Zhang RL, Chopp M, Zhang ZG, et al. **A rat model of focal embolic cerebral ischemia.** *Brain Res* 1997;766:83–92

10. Lapchak PA, Chapman DF, Zivin JA. **Metalloproteinase inhibition reduces thrombolytic (tissue plasminogen activator)-induced hemorrhage after thromboembolic stroke.** *Stroke* 2000;31:3034–40

11. Lapchak PA, Araujo DM, Song D, et al. **The nonpeptide glycoprotein IIb/IIIa platelet receptor antagonist SM-20302 reduces tissue plasminogen activator-induced intracerebral hemorrhage after thromboembolic stroke.** *Stroke* 2002;33:147–52

12. Lu A, Clark JF, Broderick JP, et al. **Mechanical reperfusion is associated with post-ischemic hemorrhage in rat brain.** *Exp Neurol* 2009;216:407–12

13. Edvinsson L, MacKenzie ET, McCulloch J. **General and comparative anatomy of the cerebral circulation.** In: Edvinsson L, MacKenzie ET, McCulloch J. *Cerebral Blood Flow and Metabolism.* New York: Raven Press; 1993:3–39

14. Aulie Michelet A. **Effects of intravascular contrast media on blood-brain barrier: comparison between iothalamate, iohexol, iopentol and iodixanol.** *Acta Radiol* 1987;28:329–33

15. Sage MR, Wilson AJ, Scroop R. **Contrast media and the brain: the basis of CT and MR imaging enhancement.** *Neuroimaging Clin N Am* 1998;8:695–707

16. Sage MR, Wilcox J, Evill CA, et al. **Comparison of blood-brain barrier disruption by intracarotid iopamidol and methylglucamine iothalamate.** *AJNR Am J Neuroradiol* 1983;4:893–95

17. Hayakawa K, Morris TM, Katzberg RW. **Opening of the blood-brain barrier by intravenous contrast media in euvolemic and dehydrated rabbits.** *Acta Radiol* 1989;30:439–44

18. Doerfler A, Engelhorn T, von Kummer R, et al. **Are iodinated contrast agents detrimental in acute cerebral ischemia? An experimental study in rats.** *Radiology* 1998;206:211–17

19. Pannu N, Wiebe N, Tonelli M. **Prophylaxis strategies for contrast-induced nephropathy.** *JAMA* 2006;295:2765–79

20. Fountaine H, Harnish P, Andrew E, et al. **Safety, tolerance, and pharmacokinetics of iodixanol injection, a nonionic, isosmolar, hexa-iodinated contrast agent.** *Acad Radiol* 1996(3 suppl 3):S475–84

21. Finley Caulfield A, Wijman CA. **Management of acute ischemic stroke.** *Neurol Clin* 2008;26:345–71, vii

22. Diringer MN, Zazulia AR. **Osmotic therapy: fact and fiction.** *Neurocrit Care* 2004;1:219–33

23. Qureshi AI, Wilson DA, Traystman RJ. **Treatment of elevated intracranial pressure in experimental intracerebral hemorrhage: comparison between mannitol and hypertonic saline.** *Neurosurgery* 1999;44:1055–63, discussion 1063–64

24. Franke RP, Fuhrmann R, Hiebl B, et al. **Influence of various radiographic contrast media on the buckling of endothelial cells.** *Microvasc Res* 2008;76:110–13

25. Wilcox J, Wilson AJ, Evill CA, et al. **A comparison of blood-brain barrier disruption by intracarotid iohexol and iodixanol in the rabbit.** *AJNR Am J Neuroradiol* 1987;8:769–72

26. Macdougall NJ, McVerry F, Baird S, et al. **Iodinated contrast media and cerebral hemorrhage after intravenous thrombolysis.** *Stroke* 2011;42:2170–74

27. Khatri P, Broderick JP, Khoury JC, et al. **Microcatheter contrast injections during intra-arterial thrombolysis may increase intracranial hemorrhage risk.** *Stroke* 2008;39:3283–87

28. Leong S, Fanning NF. **Persistent neurological deficit from iodinated contrast encephalopathy following intracranial aneurysm coiling: a case report and review of the literature.** *Interv Neuroradiol* 2012;18:33–41

29. Hayman LA, Evans RA, Bastion FO, et al. **Delayed high dose contrast CT: identifying patients at risk of massive hemorrhagic infarction.** *AJR Am J Roentgenol* 1981;136:1151–59

30. Heinrich MC, Kuhlmann MK, Grgic A, et al. **Cytotoxic effects of ionic high-osmolar, nonionic monomeric, and nonionic iso-osmolar dimeric iodinated contrast media on renal tubular cells in vitro.** *Radiology* 2005;235:843–49

31. McClennan BL, Stolberg HO. **Intravascular contrast media: ionic versus nonionic—current status.** *Radiol Clin North Am* 1991;29:437–54

32. Dooley M, Jarvis B. **Iomeprol: a review of its use as a contrast medium.** *Drugs* 2000;59:1169–86

33. Sood R, Taheri S, Estrada EY, et al. **Quantitative evaluation of the effect of propylene glycol on BBB permeability.** *J Magn Reson Imaging* 2007;25:39–47

34. Jacobsen PB, Larsen A, Konarboland R, et al. **Biotransformation of nonionic x-ray contrast agents in vivo and in vitro.** *Drug Metab Dispos* 1999;27:1205–13

35. Spencer CM, Goa KL. **Iodixanol: a review of its pharmacodynamic and pharmacokinetic properties and diagnostic use as an x-ray contrast medium.** *Drugs* 1996;52:899–927

36. Aspelin P, Stacul F, Thomsen HS, et al. **Effects of iodinated contrast media on blood and endothelium.** *Eur Radiol* 2006;16:1041–49

37. Georgakis A, Ener RA, Jin J, et al. **Risk of thrombogenicity among nonionic radiocontrast agents.** *J Invasive Cardiol* 2008;20:349–53

38. Kim SJ, Salem MR, Joseph NJ, et al. **Contrast media adversely affect oxyhemoglobin dissociation.** *Anesth Analg* 1990;71:73–76

39. Wilcox J, Sage MR. **Is viscosity important in the production of blood-brain barrier disruption by intracarotid contrast media?** *Neuroradiology* 1984;26:511–13

40. Dirnagl U, Lindauer U, Them A, et al. **Global cerebral ischemia in the rat: online monitoring of oxygen free radical production using chemiluminescence in vivo.** *J Cereb Blood Flow Metab* 1995;15:929–40

41. Kumura E, Yoshimine T, Iwatsuki KI, et al. **Generation of nitric oxide and superoxide during reperfusion after focal cerebral ischemia in rats.** *Am J Physiol* 1996;270:C748–52

42. Rosell A, Foerch C, Murata Y, et al. **Mechanisms and markers for hemorrhagic transformation after stroke.** *Acta Neurochir Suppl* 2008;105:173–78

43. Lu A, Clark JF, Broderick JP, et al. **Reperfusion activates metalloproteinases that contribute to neurovascular injury.** *Exp Neurol* 2008;210:549–59

44. Zador Z, Stiver S, Wang V, et al. **Role of aquaporin-4 in cerebral edema and stroke.** *Handb Exp Pharmacol* 2009:159–70

45. Simard JM, Kent TA, Chen M, et al. **Brain oedema in focal ischaemia: molecular pathophysiology and theoretical implications.** *Lancet Neurol* 2007;6:258–68

46. Kim EY, Na DG, Kim SS, et al. **Prediction of hemorrhagic transformation in acute ischemic stroke: role of diffusion-weighted imaging and early parenchymal enhancement.** *AJNR Am J Neuroradiol* 2005;26:1050–55

47. Tong DC, Adami A, Moseley ME, et al. **Prediction of hemorrhagic transformation following acute stroke: role of diffusion- and perfusion-weighted magnetic resonance imaging.** *Arch Neurol* 2001;58:587–93

48. Hoehn-Berlage M, Norris DG, Kohno K, et al. **Evolution of regional changes in apparent diffusion coefficient during focal ischemia of rat brain: the relationship of quantitative diffusion NMR imaging to reduction in cerebral blood flow and metabolic disturbances.** *J Cereb Blood Flow Metab* 1995;15:1002–11

49. Knight RA, Barker PB, Fagan SC, et al. **Prediction of impending hemorrhagic transformation in ischemic stroke using magnetic resonance imaging in rats.** *Stroke* 1998;29:144–51

50. Reglodi D, Somogyvari-Vigh A, Maderdrut JL, et al. **Postischemic spontaneous hyperthermia and its effects in middle cerebral artery occlusion in the rat.** *Exp Neurol* 2000;163:399–407

Collateral Score Complements Clot Location in Predicting the Outcome of Intravenous Thrombolysis

J.T. Saarinen, H. Rusanen, and N. Sillanpää

ABSTRACT

BACKGROUND AND PURPOSE: Collateral circulation is an important determinant of stroke outcome. We studied the impact of leptomeningeal collateral circulation with respect to the location of the thrombus in predicting the clinical outcome of patients treated with intravenous thrombolytic therapy (<3 hours) in a retrospective cohort.

MATERIALS AND METHODS: Anterior circulation thrombus was detected with CT angiography in 105 patients. Baseline clinical and imaging information was collected, and the site of the occlusion was recorded. Collaterals were assessed by using a 5-grade collateral score and were entered into logistic regression analysis to predict favorable clinical outcome (3-month modified Rankin Scale score of 0–2).

RESULTS: Two-thirds of patients with a proximal occlusion displayed poor collateral filling (collateral score 0–1), whereas in more distal clot locations, approximately one-third had poor collaterals. Only 36% of patients with a proximal occlusion and good collaterals experienced favorable clinical outcome. In multivariate analysis, both clot location and collateral score were highly significant ($P = .003$ and $P = .001$) and independent predictors of favorable clinical outcome. Good collateral status increased the odds of favorable clinical outcome about 9-fold (OR = 9.3; 95% CI, 2.4–35.8). After dichotomization, a distal clot location had a larger odds ratio (OR = 13.3; 95% CI, 3.0–60.0) compared with the odds ratio of good collaterals (OR = 5.9; 95% CI, 1.8–19.0).

CONCLUSIONS: A proximal occlusion in the anterior circulation is associated with poorer collateral status compared with a more distal occlusion. Both the clot location and collateral score are important and independent predictors of favorable clinical outcome of hyperacute stroke treated with intravenous thrombolysis. The location of the clot is a stronger determinant of the outcome than the collateral score.

ABBREVIATIONS: CS = collateral score; HIS = hyperacute ischemic stroke; IVT = intravenous thrombolytic therapy; M1D = distal M1 segment of the MCA; M1P = proximal M1 segment of the MCA

Ischemic stroke results from occlusion of an artery, with subsequent reduction in regional cerebral blood flow. The ischemic penumbra can remain viable for hours because some degree of blood flow is sustained through the leptomeningeal collateral supply. An important aspect of the work-up of patients with acute neurovascular syndrome is imaging of cervical and intracranial vasculature to detect the location of the occluding clot and evaluate the integrity of the collateral circulation. Both of these potentially influence decision-making for revascularization thera-

pies. Patients with proximal occlusions have a poor prognosis, even if treated with intravenous thrombolytic therapy (IVT).[1] Patients with good collateral status have larger penumbra[2] and respond better to both IVT and intra-arterial interventions,[2-5] whereas diminished or absent collaterals are associated with increased stroke severity, faster progression, and worse outcome.[6-8] Unfortunately, it appears that patients with a more proximal clot more frequently have worse collateral status.[9]

The purpose of our study was to analyze the impact of leptomeningeal collateral circulation with respect to the location of the clot in predicting 24-hour imaging findings and the 3-month clinical outcome of hyperacute ischemic stroke (HIS) in patients treated with IVT (<3 hours). We discuss the interplay between the location of the clot and the collateral circulation.

MATERIALS AND METHODS
Study Population
Our retrospective observational cohort study was approved by the Tampere University Hospital ethics committee. Altogether 315

patients with anterior or posterior circulation HIS were treated with IVT from January 2004 to December 2007 and had a 3-month follow-up after thrombolysis at the department of neurology of the Tampere University Hospital. CT angiography had been performed at admission in 285 (90%) of these patients. CTA was not performed because of previously known contrast agent hypersensitivity, chronic renal failure, or imminent closure of the 3-hour time window. Inclusion criteria for the study were acute anterior circulation vessel occlusion confirmed with CTA and treatment with a standard IVT administration protocol. The thrombolytic therapy protocol used was in line with the American Heart Association guidelines.[10]

Participants and Variables

Baseline clinical characteristics were collected from patient records. The National Institutes of Health Stroke Scale score at the time of administration of rtPA had been prospectively stored. Follow-up noncontrast-enhanced CT and NIHSS scoring were performed for all patients 24 hours after the administration of the thrombolytic agent. The modified Rankin Scale score 3 months after the stroke was the primary outcome measure. The 3-month mRS score was prospectively recorded on the basis of a follow-up visit to a neurologist or a phone interview by a neurologist.

Imaging Parameters

CT scans were obtained by using 2 different multidetector scanners: LightSpeed 16-detector row (GE Healthcare, Milwaukee, Wisconsin) and Brilliance 64-detector row (Philips Healthcare, Best, the Netherlands). CTA was performed from the C2 vertebra to the vertex. The imaging parameters were the following: 120 kV; 212 mAs (dynamic tube-current modulation); collimation, 64 × 0.625 mm; rotation, 0.75 seconds; pitch factor, 0.923 (64-detector row); or 120 kV; 160 mAs; collimation, 16 × 0.625 mm; rotation, 0.8 seconds; pitch factor, 0.938 (16-detector row). Contiguous sections were reconstructed to 0.9-mm thickness by using 0.45-mm overlap (64-detector row) or 1.25-mm thickness (16-detector row). The contrast agent (iobitridol, Xenetix, 350 mg I/mL; Guerbet, Aulnay-sous-Bois, France) was administered through an antecubital 18-ga cannula by using a double-piston power injector with a flow rate of 4 mL/s by using 70 mL of contrast agent followed by a 50-mL saline flush. Manual bolus triggering was used. NCCT was performed as described in our previous report.[11]

Image Analysis

The Alberta Stroke Program Early CT Score was assessed from admission and follow-up NCCT images, and CTA studies were interpreted as described in our previous article.[11] Infarcts with a volume of ≤10 mL in the 24-hour NCCT were defined as minor infarcts and those ≥100 mL were considered extensive infarcts. The location of the clot was recorded on the basis of the most proximal position of the occlusion. The M1 segment of the middle cerebral artery was divided into 2 parts of equal length: the proximal and the distal halves (designated as M1P and M1D). The status of the leptomeningeal collateral circulation was evaluated by using the scoring system devised by Souza et al.[8] In short, the collateral score (CS) was determined from MIP images according to the following rules: 0 = absent collaterals in >50% of an M2

branch territory; 1 = diminished collaterals in >50% of an M2 branch territory; 2 = diminished collaterals in <50% of an M2 branch territory; 3 = collaterals equal to the contralateral hemisphere; and 4 = increased collaterals.

The clot location was determined and CS was scored independently by 2 radiologists. In cases in which the scoring or the assignment differed, a consensus opinion was agreed on. The intraclass correlation coefficient between a staff radiologist and an experienced neuroradiologist for a test sample ($n = 20$) for CS was 0.87. Cohen κ was 0.94 for the location of the clot and 0.68 for the CS (0.90 after dichotomization).

Statistics

The data were analyzed with the Statistical Package for the Social Sciences, Version 19 (IBM, Armonk, New York). Group comparisons were performed by using the Student t test, the χ^2 test, the Fisher exact test, the Mann-Whitney U test, and the Kruskal-Wallis test. Patients with collateral scores from 2 to 4 had good collateral vessel filling. Patients who had 3-month mRS ≤ 2 had favorable clinical outcome. Binary logistic regression modeling by using this outcome measure as the dependent variable was repeated for single covariates of interest and their combinations. An odds ratio with a 95% CI was calculated for each covariate. The calibration of the models was evaluated with the Hosmer-Lemeshow test, and the discrimination, with the C statistic.

RESULTS

Baseline Characteristics

We studied 105 consecutive patients who met the inclusion criteria: acute anterior circulation vessel occlusion followed by IVT. The demographic and baseline characteristics of the study population have been described in depth in our previously published work.[1] The main baseline and other characteristics are summarized in Table 1. Fifty-four (52%) patients experienced favorable clinical outcome (mRS ≤ 2) at 3 months. One patient could not be reached with telephone or by other means for evaluation of mRS. Thirty-eight (36%) patients had a proximally located (distal ICA and/or proximal half of the M1 segment of MCA) occlusion, and 58 (55%) patients had good collateral status (CS 2–4). Overall, 29 (28%), 18 (17%), 20 (19%), 36 (34%), and 2 (2%) patients had CSs of 0, 1, 2, 3, and 4, respectively. The differences in baseline characteristics between patients with good and poor collateral status, proximal and distal occlusions, and favorable and unfavorable clinical outcome are given in Table 1. Poor collateral circulation was associated with more severe strokes according to admission NIHSS (15 versus 11, $P = .02$), more extensive ischemic changes in the admission NCCT ($P < .001$), worse clinical and imaging outcomes 24 hours after the treatment ($P < .001$), and somewhat shorter onset-to-treatment times (124 minutes versus 138 minutes, $P = .008$).

Collateral Score and Clinical Outcome in Different Clot Locations

The distribution of CSs in different clot locations is depicted in Fig 1, where CS 3–4 has been pooled into 1 group. In the 2 most proximal clot locations (ICA and M1P), approximately two-thirds of the patients (59% and 66%, respectively) displayed poor

Table 1: Demographic and baseline characteristics of all patients and by good collateral status, the locus of the thrombus, and 3-month outcome

Characteristic	All Patients (n = 105)	Collateral Score 0–1 (n = 47)	Collateral Score 2–4 (n = 58)	P₁	mRS ≤2 at Day 90 (n = 54)	mRS 3–6 at Day 90 (n = 50)	P₂	Proximal Thrombus (ICA+M1P, n = 38)	Distal Thrombus (M1D+M2+M3, n = 67)	P₃
Age (yr) (mean) (SD)	68.8 (13.5)	70.1 (14.4)	67.8 (12.7)	.38	66.4 (13.1)	71.3 (13.6)	.06	66.0 (15.1)	70.4 (12.3)	.11
Male (%)	60 (57)	29 (62)	31 (53)	.40	32 (59)	28 (56)	.74	27 (71)	33 (49)	.03
NIHSS score before treatment (median) (IQR)	13 (10)	15 (7)	11 (12)	.02	9 (10)	17 (7)	<.001	18 (7)	11 (10)	<.001
NIHSS score 24 hours after thrombolysis (median) (IQR)	6 (14)	14 (14)	3 (7)	<.001	2 (4)	16 (11)	<.001	15 (10)	3 (7)	<.001
ASPECTS at admission CT (median) (IQR)	10 (2)	8 (3)	10 (0)	<.001	10 (1)	9 (2)	.20	9 (3)	10 (2)	.07
ASPECTS at 24 hours after CT (median) (IQR)	7 (5)	5 (4)	8.5 (3)	<.001	9 (3)	5 (4)	<.001	4 (5)	8 (4)	<.001
Collateral score (median) (IQR)	2 (3)	0 (1)	3 (1)	<.001	3 (1)	1 (2)	<.001	1 (3)	2 (2)	.01
Onset-to-treatment time (min) (mean) (SD)	132 (27)	124 (26)	138 (27)	.008	133 (26)	129 (29)	.46	131 (31)	132 (25)	.85
Hypertension (No.) (%)	69 (65.7)	31 (66)	38 (66)	.96	36 (66.7)	33 (66.0)	.94	22 (57.9)	47 (70.1)	.20
Diabetes (No.) (%)	17 (16.2)	9 (19)	8 (14)	.46	6 (11.1)	11 (22.0)	.13	8 (21.1)	9 (13.4)	.31
Atrial fibrillation (No.) (%)	41 (39.0)	19 (40)	22 (38)	.79	23 (42.6)	18 (36.0)	.49	12 (31.6)	29 (43.3)	.24
Coronary artery disease (No.) (%)	35 (33.3)	19 (40)	16 (28)	.17	12 (22.2)	23 (46.0)	.01	16 (42.1)	19 (28.4)	.15

Note:—P₁ indicates a P value between poor and good collateral status; P₂, P value between mRS ≤ 2 and mRS > 2 groups; P₃, P value between the proximal and distal thrombus groups; IQR, interquartile range; min, minutes.
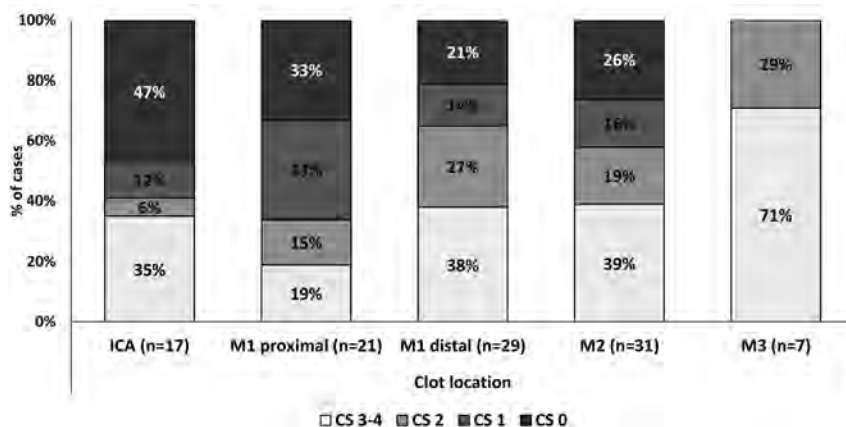
FIG 1. The distribution of collateral scores in different clot locations. Collateral scores 3 and 4 are pooled into same group.

(CS 0–1) collateral filling, whereas in the 2 more distal clot locations (M1D and M2), only about one-third (35% and 42%, respectively) had poor collaterals. In the most distant clot location studied (M3), all patients had good collateral status. The distribution of the CS was significantly different across the studied clot locations (P = .04). When adjoining clot locations (ICA-M1P, M1P-M1D, M1D-M2, M2-M3) were compared in pairs, only the difference in the distribution of CS between M1P and M1D yielded statistical significance (P = .05).

To assess the prognostic value of CS in different clot locations, we dichotomized the CS as described above and cross-tabulated it with the dichotomized 3-month mRS score (mRS ≤ 2) in different clot locations. Overall, poor collateral status was associated with unfavorable clinical outcome, especially in the proximal clot locations: Not a single patient with acute occlusion of the ICA and having poor collaterals experienced favorable clinical outcome (P < .001). However, the association between good collaterals and favorable clinical outcome was less pronounced in the proximal locations, 29% in ICA and 43% in the M1P. When individual

clot locations were considered, only M1D showed statistically significant differences with 70% of those with poor collaterals experiencing unfavorable outcome and 74% of those with good collaterals experiencing favorable outcome (P = .05).

On the basis of these results, location was dichotomized by using M1P-M1D as the dividing point and cross-tabulation was repeated. A proximal clot was more strongly associated with unfavorable outcome than poor collateral status (Fig 2). However, good collaterals were associated with improved outcome in both proximal and distal clot locations (P = .08 and P = .004, respectively).

To further assess the prognostic value of CS and its interplay with the clot location, we performed binary logistic regression analysis by using the dichotomized 3-month mRS score as the dependent variable. The CS was analyzed with the model we used in our previous article.[1] When the site of the occlusion was included in the model as a covariate, onset-to-treatment times, sex, diabetes, hypertension, atrial fibrillation, and coronary heart disease, tested one at a time, were not statistically significant covariates. Age, NIHSS score, CS, sex, and onset-to-treatment times were kept in the final multivariate regression model. The latter 2 variables were included for theoretic reasons, though they did not reach statistical significance in the preliminary analysis. The resulting model (Table 2) displayed satisfying fit and calibration (Hosmer-Lemeshow test, P = .95; C statistic = 0.92). The model was also tested with an interaction term (CS*clot location) that proved not to be statistically significant. Both the clot location and the CS were highly significant (P = .003 and P = .001, respectively) independent predictors of favorable clinical outcome in the presence of the NIHSS score (Table 2). Good collateral status increased the odds of favorable clinical out-

distal clot and good collaterals (n=43): 16% | 84%
distal clot and poor collaterals (n=23): 52% | 48%
proximal clot and good collaterals (n=14): 64% | 36%
proximal clot and poor collaterals (n=24): 92% | 8%

90 days mRS 0-2 shaded box vs. 3-6 shaded box

■ mRS at 90 days 3 - 6   □ mRS at 90 days 0 - 2
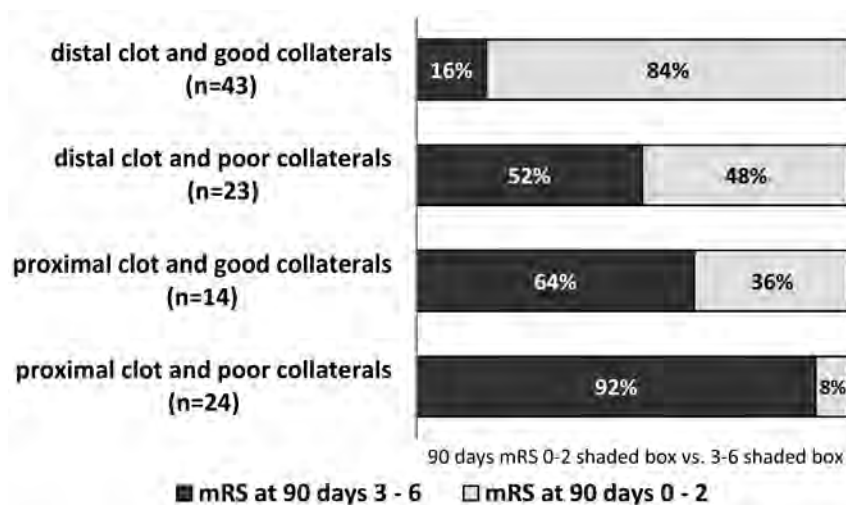
FIG 2. Collateral score and the site of the occlusion predict the clinical outcome. A proximal clot (ICA or M1P) is more strongly associated with unfavorable outcome than poor collateral status (CS 0–1).

Table 2: Logistic regression analysis for favorable clinical outcome[a]

	mRS ≤2 at 2 Months		
	Odds Ratio	95% CI	P Value
Clot location	–	–	.003
ICA	ref	ref	–
M1 proximal	10.1	0.74–140	.08
M1 distal	33.8	2.9–428	.007
M2 and M3	115.8	7.7–1737	.001
Onset-to-treatment time	0.99	0.97–1.02	.44
Sex	0.34	0.09–1.3	.11
Age	0.95	0.90–0.99	.02
Admission NIHSS score	0.81	0.71–0.92	.001
Favorable CS (2–4)	9.3	2.4–35.8	.001

Note:—ref indicates reference location; –, not applicable.
[a] Odds ratios are per minute for onset-to-treatment time, per year for age, and per 1 point for NIHSS.

come about 9-fold (OR = 9.3; 95% CI, 2.4–35.8). The OR for favorable clinical outcome increased in a graded fashion when moving from a proximal vessel position to a more distal one. A higher NIHSS score and advanced age were significantly associated with worse outcome. Finally, clot location was dichotomized similar to that in Fig 2 (cut-point at M1P/M1D), and the model was recalculated. A distal clot location had a larger odds ratio (OR = 13.3; 95% CI, 3.0–60.0) compared with that of good collateral status (OR = 5.9; 95% CI, 1.8–19.0).

Collateral Score Identifies Patients at Risk of Developing an Extensive Infarct

When cross-tabulated with dichotomized CS, 79% of patients with minor infarcts (≤10 mL) in the 24-hour follow-up NCCT had good collaterals, whereas 61% of patients with larger-than-minor infarcts (>10 mL) had poor collateral circulation (P < .001). Good collateral circulation was associated with minor infarcts, especially in the distal clot positions. Ninety-two percent of patients with a clot in the M1D and a minor infarct had good collaterals (P = .02); 72% of patients with M2 occlusion and a minor infarct had good collaterals (P = .08). Some patients (17%, 18 of 105) had an extensive infarct (≥100 mL). Two-thirds (12 of

18) of these had a proximal (ICA/M1P) occlusion. Most (89%, 16 of 18) patients with an extensive infarct had poor collaterals according to the CS (P < .001).

DISCUSSION

We studied the interplay between the location of the clot and the collateral status with regard to the 3-month clinical and the 24-hour imaging outcomes in a HIS cohort treated with IVT.

The tendency of patients with more proximal thrombi and larger clot burden to have poorer collateral status has been observed recently.[9] In our study, the proportion of patients with HIS with good collateral status doubled when the location of the occlusion moved from the proximal half of the M1 segment to the distal half. When the clot was found in the M3 segment, the collateral status was always good; this outcome can be expected from the definition of CS based on vascular territories supplied by the M2 segment arteries. The differential distribution of the CS in different clot locations may be due to proximal thrombi and poor collaterals sharing common risk factors, such as advanced atherosclerosis, old age, and hypertension.[12,13] However, an obvious mechanism explaining this observation is that the more proximal the occlusion and the more extensive the volume of the ischemic brain parenchyma and the more profound the reduction of cerebral blood flow in the ischemic core, the more easily is the capacity of the collateral vessels overwhelmed, resulting in a lower CS.

In the multivariate analysis, both the clot location and the CS proved to be highly significant and independent predictors of favorable clinical outcome, a finding that is in line with previous studies.[1-3,5-8,14-17] The cohorts of these studies were heterogeneous as to the use and types of revascularization therapies and onset-to-treatment times. Two of these studies analyzed cohorts consisting exclusively of patients undergoing IVT and/or intra-arterial thrombolysis, and they found that a high degree of collateralization predicted a good response to IVT.[3,5] However, these studies did not include the location of the clot as a covariate in their multivariate models, or the location of the clot was not a statistically significant predictor. By using a multivariate model, Lima et al[15] found that both the site of the intracranial occlusion and the pattern of leptomeningeal collateral circulation predicted the functional outcome of patients with anterior circulation stroke when all treatment modalities were considered. When only patients without revascularization therapy were analyzed, the site of the occlusion was not a significant determinant. In our cohort, adding the CS to a model already containing the location of the clot and NIHSS score resulted in better model fit (C statistic, 0.92 versus 0.90). Good collateral status increased the odds of favorable clinical outcome about 9-fold, and the odds of favorable clinical outcome increased substantially when the clot location was more distal. The site of the occlusion proved to be a stronger determinant of the outcome; good collaterals combined with IVT

managed to save only about one-third (36%) of the patients with a proximal clot from functional dependence or death at 3 months.

Poor collateral circulation is a major risk factor for already having developed an extensive infarct volume at admission.[8] The combination of a proximal thrombus and poor collaterals is referred to as a "malignant profile."[8] Supporting this concept, in our study, 89% of patients who had an extensive (>100 mL) infarct in the 24-hour follow-up NCCT had poor collateral filling. These findings emphasize the importance of timely and correct therapeutic decision-making in this patient subgroup and may have a role in avoiding futile recanalization.[18]

Selection bias related to the retrospective design is a potential limitation of this study. Direct data on vessel recanalization or reperfusion were not available. Even so, a low ASPECTS at 24-hour NCCT is intimately related to delayed or failed recanalization/reperfusion and can be used as a surrogate. CTA has limitations in the evaluation of collateral circulation. It provides a snapshot of the filling of collaterals at the time of image acquisition. It has been shown that this may lead to underestimation of the collateral circulation because of late vessel filling.[19] Finally, the impact of the CS or clot location on clinical outcome may vary according to treatment variables beyond consideration of this study, such as rehabilitation or withdrawal of care after severe stroke.

CONCLUSIONS

The results of this study show that a proximal site of occlusion in the anterior circulation is associated with poorer collateral status compared with a more distal occlusion. Both the location of the clot and the CS are important, independent predictors of the 3-month clinical outcome in the context of HIS treated with IVT. The location of the clot is a more powerful determinant of clinical outcome than the CS. However, poor collateral circulation is closely associated with extensive infarct volumes.

ACKNOWLEDGMENTS

We thank Jari Hakomäki, MD, for image interpretation.

REFERENCES

1. Saarinen JT, Sillanpaa N, Rusanen H, et al. **The mid-M1 segment of the middle cerebral artery is a cutoff clot location for good outcome in intravenous thrombolysis.** *Eur J Neurol* 2012;19:1121–27
2. Miteff F, Levi CR, Bateman GA, et al. **The independent predictive utility of computed tomography angiographic collateral status in acute ischaemic stroke.** *Brain* 2009;132:2231–38
3. Calleja AI, Cortijo E, Garcia-Bermejo P, et al. **Collateral circulation on perfusion-computed tomography-source images predicts the response to stroke intravenous thrombolysis.** *Eur J Neurol* 2013; 20:795–802
4. Christoforidis GA, Mohammad Y, Kehagias D, et al. **Angiographic assessment of pial collaterals as a prognostic indicator following intra-arterial thrombolysis for acute ischemic stroke.** *AJNR Am J Neuroradiol* 2005;26:1789–97
5. Kucinski T, Koch C, Eckert B, et al. **Collateral circulation is an independent radiological predictor of outcome after thrombolysis in acute ischaemic stroke.** *Neuroradiology* 2003;45:11–18
6. Bang OY, Saver JL, Buck BH, et al. **Impact of collateral flow on tissue fate in acute ischaemic stroke.** *J Neurol Neurosurg Psychiatry* 2008;79:625–29
7. Maas MB, Lev MH, Ay H, et al. **Collateral vessels on CT angiography predict outcome in acute ischemic stroke.** *Stroke* 2009;40:3001–05
8. Souza LC, Yoo AJ, Chaudhry ZA, et al. **Malignant CTA collateral profile is highly specific for large admission DWI infarct core and poor outcome in acute stroke.** *AJNR Am J Neuroradiol* 2012; 33:1331–36
9. Tan IY, Demchuk AM, Hopyan J, et al. **CT angiography clot burden score and collateral score: correlation with clinical and radiologic outcomes in acute middle cerebral artery infarct.** *AJNR Am J Neuroradiol* 2009;30:525–31
10. Adams HP Jr, Brott TG, Furlan AJ, et al. **Guidelines for thrombolytic therapy for acute stroke: a supplement to the guidelines for the management of patients with acute ischemic stroke—a statement for healthcare professionals from a Special Writing Group of the Stroke Council, American Heart Association.** *Circulation* 1996; 94:1167–74
11. Sillanpaa N, Saarinen JT, Rusanen H, et al. **CT perfusion ASPECTS in the evaluation of acute ischemic stroke: thrombolytic therapy perspective.** *Cerebrovasc Dis Extra* 2011;1:6–16
12. Arsava EM, Vural A, Akpinar E, et al. **The detrimental effect of aging on leptomeningeal collaterals in ischemic stroke.** *J Stroke Cerebrovasc Dis* 2014;23:421–26
13. Shuaib A, Butcher K, Mohammad AA, et al. **Collateral blood vessels in acute ischaemic stroke: a potential therapeutic target.** *Lancet Neurol* 2011;10:909–21
14. Bang OY, Saver JL, Kim SJ, et al. **Collateral flow predicts response to endovascular therapy for acute ischemic stroke.** *Stroke* 2011; 42:693–99
15. Lima FO, Furie KL, Silva GS, et al. **The pattern of leptomeningeal collaterals on CT angiography is a strong predictor of long-term functional outcome in stroke patients with large vessel intracranial occlusion.** *Stroke* 2010;41:2316–22
16. Menon BK, Smith EE, Modi J, et al. **Regional leptomeningeal score on CT angiography predicts clinical and imaging outcomes in patients with acute anterior circulation occlusions.** *AJNR Am J Neuroradiol* 2011;32:1640–45
17. Sillanpää N, Saarinen JT, Rusanen H, et al. **Location of the clot and outcome of perfusion defects in acute anterior circulation stroke treated with intravenous thrombolysis.** *AJNR Am J Neuroradiol* 2013;34:100–06
18. Liebeskind DS, Sanossian N. **How well do blood flow imaging and collaterals on angiography predict brain at risk?** *Neurology* 2012;79:S105–09
19. Smit EJ, Vonken EJ, van Seeters T, et al. **Timing-invariant imaging of collateral vessels in acute ischemic stroke.** *Stroke* 2013;44:2194–99

Computer-Aided Diagnosis Improves Detection of Small Intracranial Aneurysms on MRA in a Clinical Setting

I.L. Štepán-Buksakowska, J.M. Accurso, F.E. Diehn, J. Huston, T.J. Kaufmann, P.H. Luetmer, C.P. Wood, X. Yang, D.J. Blezek, R. Carter, C. Hagen, D. Hořínek, A. Hejčl, M. Roček, and B.J. Erickson

ABSTRACT

BACKGROUND AND PURPOSE: MRA is widely accepted as a noninvasive diagnostic tool for the detection of intracranial aneurysms, but detection is still a challenging task with rather low detection rates. Our aim was to examine the performance of a computer-aided diagnosis algorithm for detecting intracranial aneurysms on MRA in a clinical setting.

MATERIALS AND METHODS: Aneurysm detectability was evaluated retrospectively in 48 subjects with and without computer-aided diagnosis by 6 readers using a clinical 3D viewing system. Aneurysms ranged from 1.1 to 6.0 mm (mean = 3.12 mm, median = 2.50 mm). We conducted a multireader, multicase, double-crossover design, free-response, observer-performance study on sets of images from different MRA scanners by using DSA as the reference standard. Jackknife alternative free-response operating characteristic curve analysis with the figure of merit was used.

RESULTS: For all readers combined, the mean figure of merit improved from 0.655 to 0.759, indicating a change in the figure of merit attributable to computer-aided diagnosis of 0.10 (95% CI, 0.03–0.18), which was statistically significant ($F_{1,47} = 7.00$, $P = .011$). Five of the 6 radiologists had improved performance with computer-aided diagnosis, primarily due to increased sensitivity.

CONCLUSIONS: In conditions similar to clinical practice, using computer-aided diagnosis significantly improved radiologists' detection of intracranial DSA-confirmed aneurysms of ≤6 mm.

ABBREVIATIONS: CAD = computer-aided diagnosis; FOM = figure of merit

Intracranial aneurysms are abnormal dilations of the cerebral arteries that may rupture and result in subarachnoid hemorrhage, a condition associated with high morbidity and mortality. The estimated prevalence of unruptured intracranial aneurysms in the population varies between 0.2% and 9% according to different postmortem and angiographic studies,[1] with most estimates in the 2%–3% range. The estimates of the risk of rupture of aneurysms are controversial,[2-5] but two-thirds of patients with aneurysm rupture either die or have serious morbidity.[6]

While DSA remains the criterion standard for the detection of intracranial aneurysms, MRA is widely accepted as a noninvasive diagnostic tool. In recent years, due to the increasing use and availability of MRA, incidental unruptured aneurysms are detected more frequently than in the past.[1,7] Older studies specifically evaluating the detectability of untreated aneurysms by using MRA compared with DSA showed a sensitivity from 67%–89%,[8,9] but only 35%–56% for aneurysms <5 mm[9-11]; more recent studies have shown a sensitivity as high as 96.7%, which is comparable with that of DSA.[12-14]

It is often difficult to detect small (<5–7 mm) or very small (<3 mm) aneurysms[15-17] on maximum-intensity-projection images due to overlap of the aneurysm with adjacent arteries and to flow patterns that reduce signal. Aneurysms often occur at arterial branch points, where there is greater likelihood of vessel overlap. Additionally, TOF-MRA, the most common technique in clinical

practice, is often limited by low signal intensity within the aneurysm due to irregular or slow flow.

We have developed an algorithm that is capable of identifying regions that are suspicious for intracranial aneurysms on TOF-MRA with high sensitivity.[18] It can be considered automated because no human input is required to produce its results. Previous computer-aided diagnosis (CAD) algorithms were evaluated on a few cases from a single MR imaging scanner, or they were not fully automatic.[19,20] In other studies, CAD did not detect small or fusiform types of aneurysms,[21] or its effectiveness was not tested with a proper reader performance study.[22] Although there have been several performance studies on CAD schemes described by Arimura et al[19,23] by using receiver operating characteristic curve analysis,[20,24] none of these studies used DSA as a standard of reference for the presence or absence of aneurysms; therefore, the true CAD accuracy remains unknown.

We examined the practical use of our automated CAD scheme for detecting aneurysms by using DSA as the reference standard. We performed a retrospective multireader observer performance study by using MRA data from a variety of clinical sites with variable image quality.

MATERIALS AND METHODS
Design of the Present Study
After review by the institutional review board, the present study was determined to be of minimal risk, and the requirement for consent was waived. We queried the radiology information system to find all TOF-MRA examinations of the brain that were performed for clinical purposes 0–30 days before DSA. This short time span increased the diagnostic reliability. Fifty cases were randomly chosen from the 312 cases in our data base, with the only requirements being that aneurysms must be ≤7 mm and the patients have no previously treated aneurysms. The cases were retrieved from the image archive, with protected health information removed and subject identifiers inserted. Ninety-one percent of these examinations were performed on 1.5T scanners: Signa Excite MR imaging (46%) (GE Healthcare, Milwaukee, Wisconsin); Genesis Signa (25%) (GE Healthcare); Magnetom Espree (10%) (Siemens, Erlangen, Germany); Signa HDx (8%) (GE Healthcare); Magnetom Avanto (2%) (Siemens). Six percent of examinations were performed on 3T scanners (Signa Excite MR imaging [4%]; Signa HDx [2%]). For all the examinations, standard protocols were used with gradient-echo TOF-MRA sequences (short TR, 512 × 512 in-plane resolution).

Two neuroradiologists then reviewed all MRAs and confirmed the number and location of aneurysms by using DSA as the reference standard for the presence and size of aneurysms. The location from DSA for each aneurysm was then mapped to a location in the MRA dataset by a radiologist.

CAD Algorithm
In a previous article, we described in detail the fully automatic CAD scheme for detecting aneurysms on 3D TOF-MRA images.[18] Briefly, it applies an automatic-segmentation algorithm based on global thresholding and region-growing schemes that generate separate 3D regions (representing a group of connected vessels). Next, it calculates the centerline of each 3D region, resulting in 3D

thinned vessel representations, which are later transformed into vector representations, which we refer to as "trunks." It uses an inner tangent sphere-testing method to calculate the radius of the vessel at each trunk. Subsequently, it applies a single-point seeded distance transformation algorithm and radius-fitting to detect the change in the radii of vessels. On the basis of these calculations, initial points of interest are created.

The algorithm also uses 2 other supplementary methods we found useful in case of incomplete segmentation to collect initial points of interest. One is based on subtracting the segmented vessels from the raw image and collecting the points of interest from the difference image (floater points of interest); in the other method, we apply a dot-enhancement filter to the raw image and collect points of interest from the filtered images (dot points of interest). These steps are necessary because of signal drop-out sometimes seen on 3D TOF images. The series of empirically predetermined filtering rules remove most (about 99%) of the initial points of interest, and the remaining points of interest are then assigned a score (ranging from 0 to 1) and are output as aneurysm suspects. Clusters of suspect points of interest are combined to eliminate overlapping detections.

Image Review
The CAD algorithm was applied to all 50 cases, and the results were represented as a DICOM-structured report that was sent to a 3D viewing system used in our clinical practice (Aquarius iNtuition; TeraRecon, San Mateo, California). The algorithm allowed a configurable number of suspicious regions, or hits, per examination. In this study, we limited that number to a maximum of 10, and for this set of 50 cases, the mean number of hits was 7.2. The study used a multireader, multicase, double-crossover, free-response design. Six experienced radiologists (hereafter referred to as readers) participated in this study, including 5 Certificate of Added Qualification–certified neuroradiologists and 1 general radiologist (range of 4–22 years on staff), trained on the TeraRecon system and the CAD algorithm. All cases were presented to readers twice, once with CAD and once without CAD, with 5 weeks' separation. Half of the cases (determined by random selection) were presented first without CAD. Each presentation used a unique identifier, so the readers were blinded to all other imaging studies and clinical data for each subject.

The 50 cases of the first set were made available to readers for 5 weeks. The readers were aware neither of the number of DSA-confirmed aneurysms nor of the size range. Readers were allowed to freely mark suspected regions, recording the coordinates (x, y, z in millimeters) and assigning a level of certainty (from 1 to 5) to all suspected regions that might represent an aneurysm for each dataset. The certainty scale used reflected clinical decision-making as follows: 1) no aneurysm detected; 2) probably not, follow-up MRA in 6 months; 3) probably, use CTA to confirm; 4) likely, use DSA to confirm, and possibly treat; 5) unequivocal. Readers were able to view the study images by using interactive multiplanar, maximum-intensity-projection, and volume-rendering methods, according to their preferences. The actual CAD results were depicted as blue dots on the rendering (they could be hidden if preferred) (Fig 1). Each suspicious point could be centered in the rendering view by using a clickable list (Fig 2). In the

FIG 1. Example of examination visualization in a patient without an intracranial aneurysm. The CAD outputs are depicted as blue dots on different MRA projections (shown here as *gray dots*).
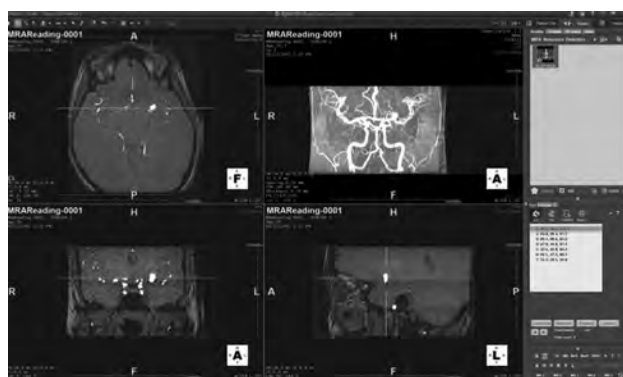
FIG 2. Rendering showing the algorithm implemented in a 3D viewing system with the suspicious point centered in the rendering view by using a clickable list.

Table 1: Location and size of 11 aneurysms[a]

No.	Size (mm)	Location
1	3.6	Left middle cerebral artery (M1)
2	2.5	Right posterior communicating artery
3	4.2	Right internal carotid artery terminus
4	2.1	Right distal anterior cerebral artery (A1)
5	2.1	Right supraclinoid internal carotid
6	2.2	Left pericallosal artery aneurysm (A2)
7	1.1	Left middle cerebral artery (M1)
8	6.0	Right proximal cavernous internal carotid artery
9	4.0	Left superior cerebellar artery
10	4.0	Left internal carotid artery proximal to ophthalmic
11	2.5	Left middle cerebral artery (M1)

[a] The sizes shown are the greatest dimension based on the DSA images.
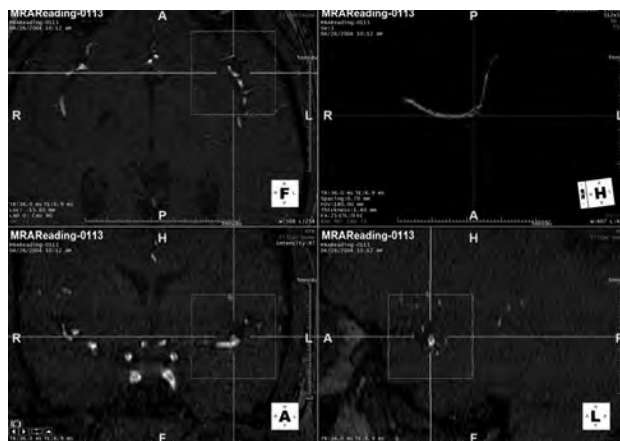
FIG 3. The smallest aneurysm (1.1 mm).

final step, an independent adjudication (I.L.Š.B. and B.J.E.) determined whether marked regions of interest were correct, denoted as lesion localization, or incorrect, denoted as nonlesion localization. A mark within 1 cm of the true location was considered a correct localization.

Statistical Analysis

Of the 50 cases selected, 2 were rejected after ratings were obtained but before statistical analysis: 1 with 9 aneurysms, which made confident identification of reader markings too challenging; and another in which the DSA did not include injection of 1 of the carotid arteries. The remaining 48 cases (39 with no aneurysm; 9 with ≥1 aneurysm) were included for analysis.

The lesion localization and nonlesion localization ratings were combined to produce the alternative free-response receiver operating characteristic curve with the figure of merit (FOM), which is the area under the alternative free-response receiver operating characteristic curve.[25,26] The marked-pair data were analyzed by using jackknife alternative free-response operating characteristic curve analysis software (Version 4.1a; http://www.devchakraborty.com).[25-27] The nonlesion localizations on cases with at least 1 aneurysm were not used in the analysis. The Dorfman-Berbaum-Metz mixed-model method[28] was used for significance testing. A

fixed-reader random-case model was used for the primary analysis because the selected radiologists were not considered a random sampling of radiologists.

Sensitivity, specificity, and accuracy rates were computed for CAD and no CAD for each reader; SAS 9.3 (SAS Institute, Cary, North Carolina) was used for this analysis. For these calculations, a rating of ≥3 on any case was considered a detection (the highest rating a reader assigned for each case was used, regardless of location). Because the goal was to improve clinical care, any patient with at least 1 suspected aneurysm would typically go to DSA; therefore, we collapsed cases with at least 1 rating of 3, 4, or 5 into positive cases.

RESULTS

For the 48 cases analyzed, there were 9 cases with aneurysms (11 aneurysms) and 39 cases without aneurysm. Table 1 highlights the size and location of the 11 aneurysms. The mean aneurysm size was <5 mm (mean = 3.12 mm, median = 2.50 mm, minimum = 1.1, maximum = 6). Ninety-one percent of the aneurysms (10/11) were detected by our CAD algorithm, including the 1.1-mm aneurysm (Fig 3). The aneurysm that was not detected was actually larger than average (4.2 mm) but had a rather vessel-like appearance, which likely accounts for the false-negative (Fig 4).

Impact of CAD on Reader Figure of Merit

The mean number of suspicious regions per patient was 7.2 when using CAD. Overall there were 393 lesion localizations and 237
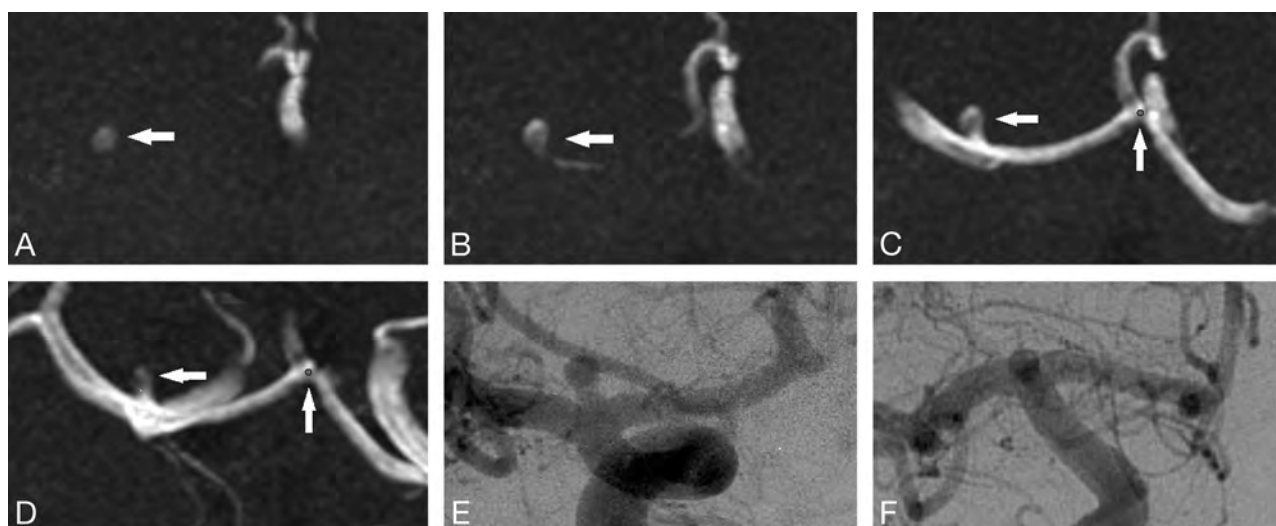
FIG 4. This aneurysm was missed by the CAD algorithm. We believe that the error was because the aneurysm had a relatively consistent diameter up to the dome, thus not meeting the curvature criteria. This was detected by all radiologists with and without CAD.

Table 2: Estimated figure of merit by reader and method[a]

| | Estimated FOM | | | | |
	CAD–	CAD+	Difference	95% CI	P Value
Reader 1	0.667	0.726	0.060	(−0.184–0.304)	.62
Reader 2	0.660	0.842	0.182	(0.021–0.344)	.028
Reader 3	0.789	0.892	0.103	(−0.071–0.276)	.24
Reader 4[b]	0.594	0.746	0.152	(−0.042–0.347)	.12
Reader 5	0.514	0.717	0.203	(−0.158–0.564)	.26
Reader 6	0.707	0.630	-0.077	(−0.371–0.217)	.60
Overall	0.655	0.759	0.104	(0.025–0.183)	.011

[a] For all except reader 6, there was a definite increase in the FOM when CAD results were available, though the difference was statistically significant for only 1 reader (reader 2).
[b] General radiologist; all other readers are neuroradiologists.

nonlesion localizations among the 6 readers. Of true-negative cases (cases in which DSA showed no aneurysm), 20.5% were correctly marked as negative for aneurysm by all readers without CAD, and 20.5%, by all readers with CAD.

No aneurysm was missed by all readers with CAD. Five aneurysms (45.5%) were found by all readers only when CAD was used (mean size = 3.59 mm, median = 4 mm). Every aneurysm was missed by at least 1 reader without CAD. Five of the 6 readers achieved higher FOMs by using CAD, whereas 1 reader did not. For each of those 5 readers, the FOM improved. For 1 reader (reader 6), the FOM decreased. For all readers combined, the mean FOM improved from 0.655 to 0.759, a mean change in the FOM attributable to using CAD of 0.10 (95% CI, 0.03–0.18). This improvement was statistically significant ($F_{1,47} = 7.00$, $P = .011$). These results are depicted in Table 2 and Fig 5.

Impact of CAD on Reader Sensitivity, Specificity, and Accuracy

The mean sensitivity value for all readers without CAD was $70.40 \pm 10.47\%$, and this improved to a mean of $83.35 \pm 8.48\%$ with CAD. Five of 6 readers demonstrated higher sensitivity with CAD, and 1 reader improved the sensitivity from 77.8% to 100%. The mean specificity without CAD was $79.50 \pm 3.31\%$ and $75.65 \pm 4.37\%$ with CAD. The mean accuracy without CAD was
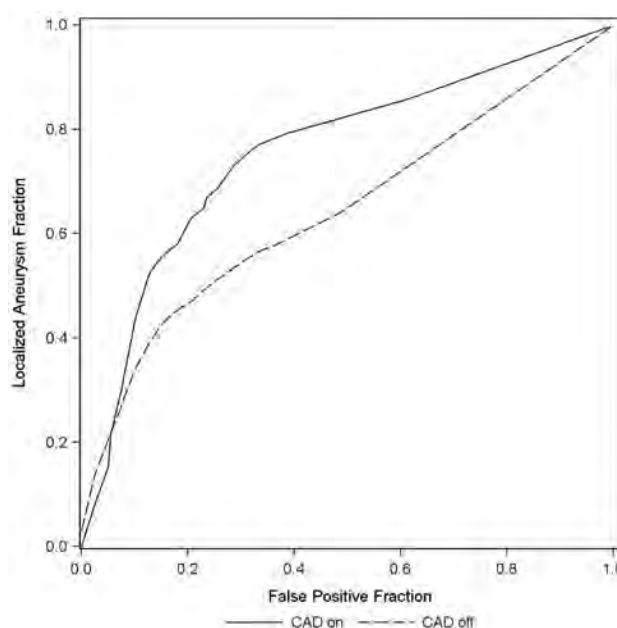
FIG 5. A free-response receiver operating characteristic curves aneurysm fraction.

$77.78 \pm 3.94\%$ and $77.10\% \pm 4.64\%$ with CAD. Sensitivity, specificity, and accuracy for each reader are depicted in Table 3.

DISCUSSION

This report studies the value of CAD in an image-viewing environment that is similar to that in clinical practice. The performance in detecting intracranial aneurysms was significantly improved with CAD. Most important, in comparison with previous studies, we used DSA as a criterion standard for all cases, and we included cases that had multiple and small aneurysms (mean size = 3.2 mm).

In the present study, the overall performance of the pool of 5 neuroradiologists and 1 general radiologist was significantly improved when using the CAD algorithm because the mean FOM increased from 0.655 to 0.759. The absolute numbers (both with

Table 3: Individual reader performance results

	Sensitivity (95% CI)	Specificity (95% CI)	Accuracy (95% CI)
Reader 1			
CAD−	55.6% (5/9) (26.7%–81.1%)	76.9% (30/39) (61.7%–87.4%)	72.9% (35/48) (59.0%–83.4%)
CAD+	77.8% (7/9) (45.3%–93.7%)	66.7% (26/39) (51.0%–79.4%)	68.8% (33/48) (54.7%–80.1%)
Reader 2			
CAD−	66.7% (6/9) (35.4%–87.9%)	74.4% (29/39) (58.9%–85.4%)	72.9% (35/48) (59.0%–83.4%)
CAD+	88.9% (8/9) (56.5%–98.0%)	79.5% (31/39) (64.5%–89.2%)	81.3% (39/48) (68.1%–89.8%)
Reader 3			
CAD−	77.8% (7/9) (45.3%–93.7%)	84.6% (33/39) (70.3%–92.8%)	83.3% (40/48) (70.4%–91.3%)
CAD+	100% (9/9) (70.1%–100.0%)	79.5% (31/39) (64.5%–89.2%)	83.3% (40/48) (70.4%–91.3%)
Reader 4[a]			
CAD−	66.7% (6/9) (35.4%–87.9%)	82.1% (32/39) (67.3%–91.0%)	79.2% (38/48) (65.7%–88.3%)
CAD+	77.8% (7/9) (45.3%–93.7%)	76.9% (30/39) (61.7%–87.4%)	77.1% (37/48) (63.5%–86.7%)
Reader 5			
CAD−	88.9% (8/9) (56.5%–98.0%)	79.5% (31/39) (64.5%–89.2%)	81.3% (39/48) (68.1%–89.8%)
CAD+	77.8% (7/9) (45.3%–93.7%)	74.4% (29/39) (58.9%–85.4%)	75% (36/48) (61.2%–85.1%)
Reader 6			
CAD−	66.7% (6/9) (35.4%–87.9%)	79.5% (31/39) (64.5%–89.2%)	77.1% (37/48) (63.5%–86.7%)
CAD+	77.8% (7/9) (45.3%–93.7%)	76.9% (30/39) (61.7%–87.4%)	77.1% (37/48) (63.5%–86.7%)

[a] General radiologist, all other readers are neuroradiologists.

and without CAD) were lower than analogous data seen in previous studies. In the 2-reader performance studies evaluating the algorithm of Arimura et al,[19,23] the average areas under the receiver operating characteristic analysis curve were improved from 0.931 to 0.983 (sensitivity and specificity values were not given)[20,29] and from 0.851 to 0.903 (with a sensitivity of 82.7% and a specificity of 88.6%).[24] However, in previous studies, readers were informed that there was either zero or 1 aneurysm per case (making false-positives less likely), DSA was not used as the criterion standard imaging method, the mean aneurysm size was larger, and the non-CAD images were presented first with CAD presented after them.

We tested using the criterion standard of DSA, which is important because 3D TOF can have artifacts causing signal to be lost in the region of an aneurysm. In cases in which there might be signal loss on the 3D TOF, the prior studies might conclude that an MRA is negative for aneurysm. Similarly, artifacts on MRA that falsely gave the appearance of an aneurysm might have been incorrectly counted as an aneurysm without DSA to deny its presence.

In the present study, we did see overall sensitivity increased significantly (from the range of 55.6%–88.9% to the range of 77.8%–100%), suggesting that with proper interpretation of the CAD results, 100% sensitivity is possible and was achieved by 1 individual. We noted also a mild decrease in specificity from the range of 74.4%–84.6% to 66.7%–79.5% and a slight decrease in accuracy from 77.78% to 77.10%. This was seen in other CAD reports[30,31] and was not surprising because the improved sensitivity is typically accompanied by an increase in the average number of false-positive results. We designed our study to be like clinical practice, and the higher number of negative cases may account for the lower apparent performance.

Other reports suggest that CAD increases the performance of nonspecialists, approaching that of specialists but with no significant benefit to specialists,[20,24] but we did not observe that. Tables 1 and 2 show the improved performance of the general radiologist (marked with a footnote). This is contrary to the results of Kakeda et al[24] but similar to those of Hirai et al.[20] Unlike the above-mentioned observer performance studies, our readers did not know a priori how many aneurysms were present in each case and therefore searched for any suspicious areas and marked them together with the confidence level. Conventional receiver operating characteristic analysis with the FOM as the area under the receiver operating characteristic curve has limited value, with the rating of the highest rated mark in the image only, without taking into account the aneurysm locations. In contrast, free-response operating characteristic analysis is considered more sensitive and enables more precise evaluation of the performance of radiologists (with greater statistical power) by using multiple responses, each with information on both the confidence level and location.[32] The estimated FOM is, therefore, interpretable as the probability that the rating of the highest rated and correct detection on an aneurysm case exceeds the rating of the highest-rated detection mark on a normal case. The higher statistical power for this approach is an important issue in observer performance studies because it determines the probability of detecting a true difference between modalities/groups while controlling the probability of detecting nonexisting differences.[33]

Our CAD algorithm turned out to be efficient in terms of the workflow; though we did not specifically focus on measuring the time of reader evaluations, the algorithm implemented in a clinical rendering viewing system enabled them to efficiently review the regions of concern. Therefore, the overall time spent on the evaluation did not change.

Improved CAD-attributable efficiency at aneurysm detection has clinical impact when making further diagnostic and management decisions. Most interesting, treatment guidelines are different worldwide, and this difference is valid particularly for smaller aneurysms (early invasive treatment after detection versus follow-up). The higher detection rate would, therefore, directly influence the decision-making process. Increasing the level of reader confidence for equivocal cases would also provide better guidance with further diagnostic possibilities (CTA versus DSA).

Our study had a number of limitations. We had only 1 general radiologist in the study group, which limits our ability to determine whether there is a difference in the value of CAD for special-

ists versus nonspecialists. In many CAD applications, there is a much greater benefit to general radiologists than specialists, but in this study, we found a benefit for both specialists and generalists. Additionally, the cases in this study were randomly selected and were of variable quality. Only 6% of examinations were conducted on a 3T scanner. Some MRA examinations, particularly older ones, had lower signal-to-noise and more intensity variation. It is possible that the CAD algorithm could see through these problems and that the benefit may be greater with older technologies than with current MR imaging scanners. It is also possible that CAD does better with newer examinations where more vessels are visualized, increasing the superimposition problem.

CONCLUSIONS

A CAD algorithm significantly improved the performance of radiologists (specialists and general) in detecting intracranial aneurysms ≤6 mm in conditions that are similar to those in clinical practice.

REFERENCES

1. Jeon TY, Jeon P, Kim KH. **Prevalence of unruptured intracranial aneurysm on MR angiography.** *Korean J Radiol* 2011;12:547–53
2. Wiebers DO, Whisnant JP, Huston J 3rd, et al. **Unruptured intracranial aneurysms: natural history, clinical outcome, and risks of surgical and endovascular treatment.** *Lancet* 2003;362:103–10
3. Juvela S, Porras M, Poussa K. **Natural history of unruptured intracranial aneurysms: probability and risk factors for aneurysm rupture**. *Neurosurg Focus* 2000;8:Preview 1
4. Rinkel GJ. **Natural history, epidemiology and screening of unruptured intracranial aneurysms.** *J Neuroradiol* 2008;35:99–103
5. White PM, Wardlaw J. **Unruptured intracranial aneurysms: prospective data have arrived.** *Lancet* 2003;362:90–91
6. Seibert B, Tummala RP, Chow R, et al. **Intracranial aneurysms: review of current treatment options and outcomes.** *Front Neurol* 2011;2:45
7. Horikoshi T, Akiyama I, Yamagata Z, et al. **Retrospective analysis of the prevalence of asymptomatic cerebral aneurysm in 4518 patients undergoing magnetic resonance angiography: when does cerebral aneurysm develop?** *Neurol Med Chir (Tokyo)* 2002;42:105–12, discussion 113
8. Ross JS, Masaryk TJ, Modic MT, et al. **Intracranial aneurysms: evaluation by MR angiography.** *AJR Am J Roentgenol* 1990;155:159–65
9. White PM, Teasdale EM, Wardlaw JM, et al. **Intracranial aneurysms: CT angiography and MR angiography for detection prospective blinded comparison in a large patient cohort.** *Radiology* 2001; 219:739–49
10. Korogi Y, Takahashi M, Mabuchi N, et al. **Intracranial aneurysms: diagnostic accuracy of MR angiography with evaluation of maximum intensity projection and source images.** *Radiology* 1996;199:199–207
11. Okahara M, Kiyosue H, Yamashita M, et al. **Diagnostic accuracy of magnetic resonance angiography for cerebral aneurysms in correlation with 3D-digital subtraction angiographic images: a study of 133 aneurysms.** *Stroke* 2002;33:1803–08
12. Shahzad R, Younas F. **Detection and characterization of intracranial aneurysms: magnetic resonance angiography versus digital subtraction angiography.** *J Coll Physicians Surg Pak* 2011;21:325–29
13. Wrede KH, Dammann P, Monninghoff C, et al. **Non-enhanced MR imaging of cerebral aneurysms: 7 Tesla versus 1.5 Tesla.** *PLoS One* 2014;9:e84562
14. Cirillo M, Scomazzoni F, Cirillo L, et al. **Comparison of 3D TOF-MRA and 3D CE-MRA at 3T for imaging of intracranial aneurysms.** *Eur J Radiol* 2013;82:e853–59
15. Kashiwazaki D, Kuroda S. **Size ratio can highly predict rupture risk in intracranial small (<5 mm) aneurysms.** *Stroke* 2013;44:2169–73
16. Chien A, Liang F, Sayre J, et al. **Enlargement of small, asymptomatic, unruptured intracranial aneurysms in patients with no history of subarachnoid hemorrhage: the different factors related to the growth of single and multiple aneurysms.** *J Neurosurg* 2013;119: 190–97
17. Jagadeesan BD, Delgado Almandoz JE, Kadkhodayan Y, et al. **Size and anatomic location of ruptured intracranial aneurysms in patients with single and multiple aneurysms: a retrospective study from a single center.** *J Neurointerv Surg* 2014;1;6:169–74
18. Yang X, Blezek DJ, Cheng LT, et al. **Computer-aided detection of intracranial aneurysms in MR angiography.** *J Digit Imaging* 2011;24: 86–95
19. Arimura H, Li Q, Korogi Y, et al. **Automated computerized scheme for detection of unruptured intracranial aneurysms in three-dimensional magnetic resonance angiography.** *Acad Radiol* 2004; 11:1093–104
20. Hirai T, Korogi Y, Arimura H, et al. **Intracranial aneurysms at MR angiography: effect of computer-aided diagnosis on radiologists' detection performance.** *Radiology* 2005;237:605–10
21. Kobashi S, Kondo K, Hata Y. **Computer-aided diagnosis of intracranial aneurysms in MRA images with case-based reasoning.** *IEICE T Inf Syst* 2006;E89d:340–50
22. Uchiyama Y, Ando H, Yokoyama R, et al. **Computer-aided diagnosis scheme for detection of unruptured intracranial aneurysms in MR angiography.** *Conf Proc IEEE Eng Med Biol Soc* 2005;3:3031–34
23. Arimura H, Li Q, Korogi Y, et al. **Computerized detection of intracranial aneurysms for three-dimensional MR angiography: feature extraction of small protrusions based on a shape-based difference image technique.** *Med Phys* 2006;33:394–401
24. Kakeda S, Korogi Y, Arimura H, et al. **Diagnostic accuracy and reading time to detect intracranial aneurysms on MR angiography using a computer-aided diagnosis system.** *AJR Am J Roentgenol* 2008;190:459–65
25. Chakraborty DP, Berbaum KS. **Observer studies involving detection and localization: modeling, analysis, and validation.** *Med Phys* 2004; 31:2313–30
26. Chakraborty DP. **Maximum likelihood analysis of free-response receiver operating characteristic (FROC) data.** *Med Phys* 1989;16: 561–68
27. Chakraborty DP. **A brief history of free-response receiver operating characteristic paradigm data analysis.** *Acad Radiol* 2013;20:915–19
28. Dorfman DD, Berbaum KS, Metz CE. **Receiver operating characteristic rating analysis: generalization to the population of readers and patients with the jackknife method.** *Invest Radiol* 1992;27:723–31
29. Doi K. **Computer-aided diagnosis in medical imaging: historical review, current status and future potential.** *Comput Med Imaging Graph* 2007;31:198–211
30. Chabi ML, Borget I, Ardiles R, et al. **Evaluation of the accuracy of a computer-aided diagnosis (CAD) system in breast ultrasound according to the radiologist's experience.** *Acad Radiol* 2012;19:311–19
31. Sahiner B, Chan HP, Roubidoux MA, et al. **Malignant and benign breast masses on 3D US volumetric images: effect of computer-aided diagnosis on radiologist accuracy.** *Radiology* 2007;242:716–24
32. Wagner RF, Metz CE, Campbell G. **Assessment of medical imaging systems and computer aids: a tutorial review.** *Acad Radiol* 2007; 14:723–48
33. Chakraborty DP. **Validation and statistical power comparison of methods for analyzing free-response observer performance studies.** *Acad Radiol* 2008;15:1554–66

Value of 4D MR Angiography at 3T Compared with DSA for the Follow-Up of Treated Brain Arteriovenous Malformation

S. Soize, F. Bouquigny, K. Kadziolka, C. Portefaix, and L. Pierot

ABSTRACT

BACKGROUND AND PURPOSE: Four-dimensional, contrast-enhanced MRA is a useful technique for the diagnosis and classification of brain AVM. The purpose of this study was to evaluate its usefulness in the follow-up of treated brain AVM.

MATERIALS AND METHODS: Patients with treated brain AVM (embolization, radiosurgery, and/or surgery) were investigated with both DSA (the "gold standard") and 4D MRA. Four-dimensional MRA was performed at 3T using a 4D sequence, combining contrast-enhanced timing-robust angiography, keyhole, and sensitivity encoding techniques. Examinations were evaluated by 2 independent readers and disagreements were resolved by a third reader. Interobserver and intermodality agreement with respect to residual nidus, residual venous drainage, and brain AVM patency were determined.

RESULTS: Between May 2008 and February 2013, 37 patients with a median age of 45 years (interquartile range = 26−55) were prospectively included. Examinations were acquired 36 months (IQR = 10−45.5) after the last treatment. Interobserver agreement for brain AVM patency was very good for both 4D MRA (κ 0.82, 95% CI .67−.98) and DSA (κ 0.84, 95% CI .69−.98). After consensus reading, intermodality agreement for the evaluation of brain AVM patency was good (κ 0.73, 95% CI .55−.90). Diagnostic accuracy of 4D MRA for residual brain AVM compared with DSA, reached a sensitivity of 73.7%, specificity 100%, positive predictive value 100%, and negative predictive value 78.3%. Agreements by technique of treatment are also detailed.

CONCLUSIONS: Four-dimensional MRA is a useful radiation-free technique for the follow-up of patients with treated brain AVM, especially patients treated by radiosurgery. However, given its actual limitations it is not sufficient to assert the cure; DSA remains mandatory for this purpose.

ABBREVIATIONS: 4D-MRA = 4D contrast-enhanced MRA; bAVM = brain AVM; CENTRA = contrast-enhanced timing-robust angiography; SENSE = sensitivity encoding

Brain AVMs (bAVMs) are rare developmental disorders (prevalence of 0.01%−0.52%) composed of a network of channels (nidus) interposed between feeding arteries and draining veins.[1] They are often revealed by spontaneous intracranial hemorrhages with high morbidity and mortality.[2,3] They are often diagnosed in young, otherwise healthy patients and carry a life-long bleeding risk ranging between 1.5% and 4.0% per year.[4,5] There are several treatment options, including surgical resection, endovascular embolization, and radiosurgery, that can be attempted to achieve a cure.[6-10] The risk of bleeding persists as long as an anatomic cure is not completely achieved.[5,6] Therefore, it is necessary to confirm

an AVM cure after the treatment. When the AVM is treated by surgery and/or embolization, imaging is performed a few weeks or months after the end of the treatment to evaluate the AVM occlusion status (complete occlusion or residual AVM). When AVM is treated with radiosurgery (alone or after embolization and/or surgery), occlusion is usually achieved after a few years, and a regular imaging follow-up is conducted every 6 or 12 months.[5,6]

Despite several disadvantages, such as radiation exposure, iodinated contrast agent injection risks (including allergy and nephrotoxicity), and neurologic procedural risks (0.30%−2.63%),[11-13] DSA is the reference method to evaluate AVM occlusion status because of posttreatment modifications. Indeed, it has a very good spatial and especially temporal resolution allowing for a precise evaluation of potential residual nidus and residual venous drainage. To reduce these risks, several noninvasive cross-sectional imaging techniques like 3D TOF-MRA and 3D contrast-enhanced MRA were used.[14-16] The diagnostic accuracy of these techniques was quite good, but not enough to replace DSA be-

cause they suffered from a poor temporal resolution that limited analysis of the angioarchitecture and hemodynamics.[14-16] Four-dimensional contrast-enhanced MRA (4D-MRA) was conceived to solve this problem and to provide a better temporal resolution while also preserving spatial resolution. However, the first examinations were not efficient enough; by incorporating progressive new technologies such as parallel imaging and intelligent sampling of the k-space, it became an emergent imaging technique with the advantage of a dynamic "DSA-like" evaluation of the AVM that allows for the definition of arterial feeders, nidus, and draining veins in the same examination.[17] Actually, 4D-MRA permits the effective diagnosis and classification of bAVM.[17-20] The value of 4D-MRA for the follow-up of patients with a treated bAVM has been rarely evaluated.[21,22] The purpose of this study was to evaluate the performance of 4D-MRA at 3T for the follow-up of patients with a treated bAVM. In other words, this study will try to answer the 2 following questions: is 4D-MRA enough to assert the cure? Is 4D-MRA useful for the follow-up of treated bAVM?

MATERIALS AND METHODS

Study Design
Institutional review board approval was obtained and informed consent was waived according to the design of the study. All patients treated for a bAVM in our academic department were prospectively included in a data base. Since May 2008, all patients receiving MR imaging in our department for a bAVM underwent a 4D-MRA. For the purpose of the present study, patients imaged between May 2008 and February 2013 were included if they met the following criteria: 1) they had a bAVM treated at least by 1 of the following modalities (embolization, radiosurgery, or surgery), 2) they were imaged during the follow-up with both 4D-MRA at 3T and DSA, 3) both examinations were performed at least 1 month after the last treatment, 4) both examinations were performed in a time interval less than 1 month and without treatment in between, and 5) image datasets were of sufficient quality. For patients who underwent several sets of examinations, only the last set was taken into account to avoid redundant data.

Treatment Strategy
For all patients analyzed in this study, indication and strategy of treatment was based on multidisciplinary decisions involving neurologists, neurosurgeons, radiotherapists, and neuroradiologists.

MR Imaging
Examinations were performed on a 3T whole-body MR imaging system (Achieva; Philips Health Care, Best, the Netherlands), using an 8-channel sensitivity encoding (SENSE) head coil that allows for parallel imaging. A dose of 0.2 mL/kg of gadoterate meglumine (Dotarem; Guerbet, Aulnay-sous-Bois, France) was injected at a flow rate of 1.5 mL/s using an automated power injector (Spectris; Medrad, Indianola, Pennsylvania), followed by a saline flush of 30 mL injected at the same flow rate (1.5 mL/s).

The 4D-MRA was performed with 20 dynamic sagittal acquisitions using a 3D, T1-weighted, fast-field echo sequence. Imaging parameters were as follows: TE, 1.50 ms; TR, 2.9 ms; flip angle, 20°; section thickness, 1 mm; acquisition bandwidth, 1350 Hz;

FOV: 270 × 126 × 150 mm³, covering all of the brain; acquisition matrix, 264 × 200 mm²; and reconstruction matrix, 400 mm. A total of 160 thin sagittal 2-mm sections with a 1-mm overlap between sections were acquired with an acceleration SENSE factor of 2 in the selection direction and a SENSE factor of 2.7 in the phase-encoding direction, yielding a total acceleration factor of 5.4 (2.7 × 2).[23] Half-Fourier imaging was used, skipping 25% of k-space data, yielding an acceleration factor of 1.33. For further acceleration, we used combined contrast-enhanced timing-robust angiography (CENTRA)-keyhole k-space filling with a percentage factor of 18% and the last dynamic scan as reference, yielding an acceleration factor of 5.55.[17,24] Combining these techniques, the 4D-MRA yielded a total acceleration factor of 40 [5.4 (SENSE) × 5.55 (18% keyhole) × 1.33 (half scan factor)] compared with standard contrast enhanced-MR angiography without such techniques. In total, 20 dynamic acquisitions were achieved with a temporal resolution of 1.4 seconds per volume, combined with a reference scan of 7.8 seconds, for a total acquisition time of 34.8 seconds, with a spatial resolution at acquisition of 1.02 × 1.13 × 2 mm³ and after interpolation a voxel size of 0.68 × 0.68 × 1 mm³.

Conventional Angiography
DSA was performed on a biplane angiography unit (Axiom Artis; Siemens, Erlangen, Germany) with a 5-Fr catheter using a femoral artery approach and selective contrast injection of the internal carotid artery, external carotid, and vertebral arteries. A temporal resolution of 3 images per second was used, in standard orthogonal anteroposterior and lateral projections and oblique projections, if necessary. Anteroposterior images had a matrix of 720 × 720 mm² and FOV of 32 cm. Lateral projections had a matrix of 960 × 960 mm² and FOV of 25 cm. Three-dimensional rotational angiography was not systematically performed and these data were not used in this study. Bolus injections of iodinated contrast material (iodixanol, Visipaque 320; GE Healthcare, Vélizy-Villacoublay, France) were 6 mL at a flow rate of 2 mL/s for the external carotid, 8 mL at a flow rate of 4 mL/s for the internal carotid, and 10 mL at a flow rate of 5 mL/s for the vertebral artery using an automated power injector (Angiomat Illumena; Liebel-Flarsheim Medical System, Cincinnati, Ohio).

Image Analysis
A first reader (4 years of experience in diagnostic and interventional neuroradiology) evaluated the 4D-MRA overall image quality before image analysis using a practical 5-point grading system formerly used by Hadizadeh et al.[19] Examinations were considered of sufficient quality if the score was ≥3. Examinations with a score lower than 3 were excluded.

Two independent readers (11 and >20 years of experience in diagnostic and interventional and neuroradiology, respectively) reviewed 4D-MRA and DSA examinations randomly. Readers were blinded to baseline and follow-up clinical data and were only aware of the bAVM location and the received treatments. They determined if there was a residual nidus and/or residual venous drainage for each examination. Results for each reader were recorded separately and used to determine interobserver and intermodality agreement. For studies where the 2 readers disagreed,
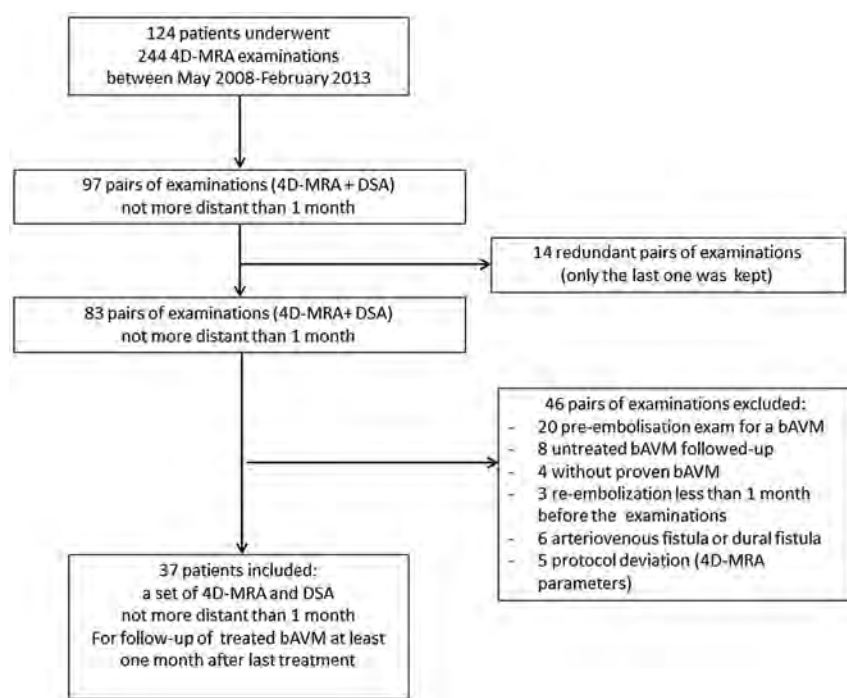
FIG 1. Patient flow chart. DF indicates dural fistula.

Table 1: Characteristics of the 37 patients

Demographics	
Age, years	45.0 [26.0–55.0]
Sex, male	22 (59.5%)
Type of treatment	
Embolization then radiosurgery	14 (37.8%)
Embolization	8 (21.6%)
Radiosurgery	8 (21.6%)
Surgery	3 (8.1%)
Surgery then radiosurgery	3 (8.1%)
Surgery then embolization	1 (2.7%)
bAMV location	
Supratentorial	33 (89.2%)
Infratentorial	4 (10.8%)
Time intervals	
Delay between last treatment and images, months	36 [10–45.5]
Delay between DSA and 4D-MRA, days	1 [0.5–1]
Presentation	
Hemorrhage	16 (45.7%)
Seizure	8 (22.9%)
Headache	6 (17.1%)
Neurologic symptoms	4 (11.4%)
Incidental	1 (2.9%)

Note:—Continuous variables were presented by proportion and percentage, categoric variables were described with median, first, and third quartiles. Presentation mode was available for 35 of 37 patients.

consensus for each imaging technique was performed by a third reader (>20 years of experience in diagnostic and interventional neuroradiology), who was blinded from the results of the first readings and used to determine intermodality agreement. A residual bAVM was defined as the presence of a residual venous drainage associated or not with a residual nidus.

All MRA and DSA data were transferred to the local PACS and were randomly reviewed on separate workstations using the medical viewer. For 4D-MRA visualization, subtracted data with MIP

reconstructions were used. The software enabled the enlargement of regions of interest in any 3D direction, with the possibility of viewing the progress of the contrast injection. For DSA visualization, each stored run was composed of a loop of 6 images, which enabled the readers to appreciate the contrast filling with discrimination of arterial, capillary, and venous phases. Enlargement of the regions of interest was permitted by the software as for MRA images.

Statistical Analysis

Quantitative variables were described as mean and standard deviation, whereas qualitative variables were described as numbers and percentages. Interobserver agreement for 4D-MRA and DSA and intermodality agreement with respect to the presence of residual nidus, residual early venous drainage, and bAVM patency were determined using the κ statistic test. Results were displayed as percentages and 95% CI. Strength of agreement was defined as $\kappa \leq 0.20$: poor; κ 0.21–0.40: fair; κ 0.41–0.60: moderate; κ 0.61–0.80: good; κ 0.81–0.90: very good; and $\kappa \geq 0.91$: excellent, including 95% CI. In addition, the exact number and percentage of results from the 2 readers and the 2 modalities that were in exact agreement were provided. A P value of less than .05 was considered statistically significant. Sensitivity, specificity, and positive and negative predictive values were then calculated. All statistical analyses were performed with MedCalc statistical software (11.4.3.0; MedCalc Software, Mariakerke, Belgium).

RESULTS

Between May 2008 and February 2013, 37 patients fulfilled the inclusion criteria (Fig 1). Their demographic data, different types of treatment, bAVM location, time intervals (between the last treatment and images, and between both imaging modalities), and presentation mode are detailed in Table 1. For patients who underwent radiosurgery, mean time between images and irradiation was 3.7 ± 2.0 years (extremes: 24–144 months).

Image Quality

Image quality scores ranged between 3 (adequate for diagnosis) and 5 (excellent), with a mean quality score of 3.6 ± 0.5 on the 5-point grading scale. All examinations were judged to be of adequate quality for diagnosis.

Interobserver Agreement

For 4D-MRA examinations, the 2 observers were in agreement for residual nidus in 35 of 37 (94.6%) bAVMs, resulting in good interobserver agreement (κ 0.78, 95% CI .57–.98). The 2 disagreements concerned small (<1 cm) and heterogeneous residual nidus in patients treated by embolization. The readers matched for
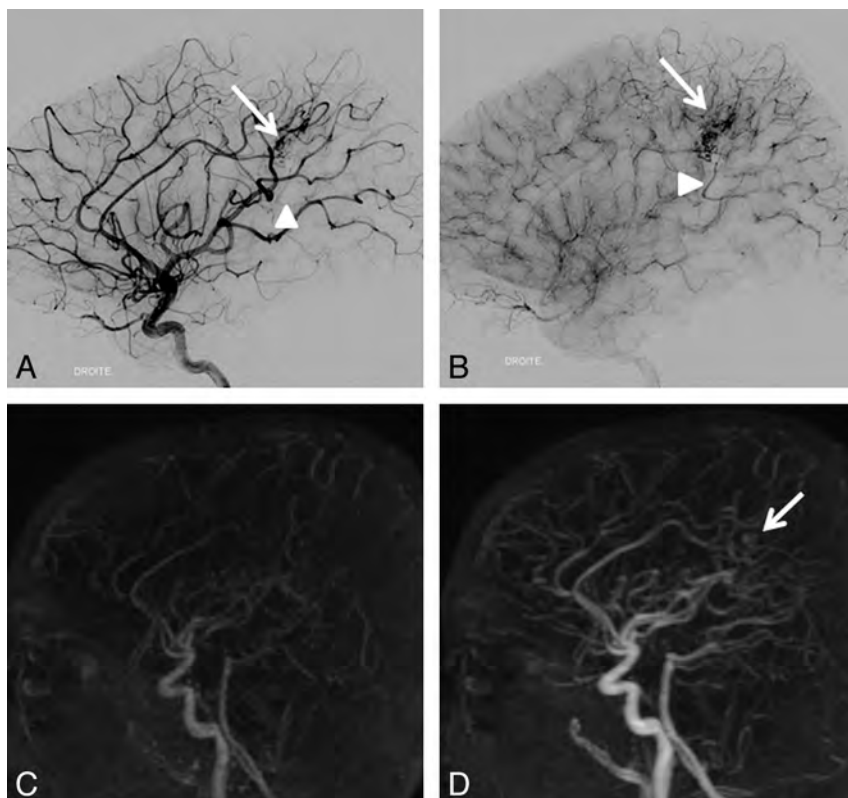
FIG 2. An 11-year-old boy with a right pericallosal AVM revealed by hemorrhage and treated 11 months ago by surgery. Residual nidus (*arrow*) and venous drainage (*arrowhead*) are seen on DSA (*A, B*) but not on 4D-MRA (*C, D*) by both readers. Retrospectively, a part of the nidus may be visible (*arrow*).

FIG 3. A 32-year-old woman with a left frontal-parietal AVM revealed by seizures and treated by embolization then radiosurgery more than 4 years ago. Residual nidus (*arrow*) and venous drainage (*arrowhead*) are seen on DSA (*A*) but not on 4D-MRA (*B*) by both readers. Retrospectively, the draining vein is visible (*arrowhead*) on 4D-MRA, but is not dilated and appears during the venous phase (indistinguishable from cortical veins).

residual venous drainage in 34 of 37 (91.9%) bAVMs, also resulting in good interobserver agreement (κ 0.68, 95% CI .44–.91). The 3 disagreements concerned small veins, of which 1 was visible early and 2 were visible only since the capillary phase. When taking into account only the patency of the bAVM (residue or cured), agreement was very good (κ 0.82, 95% CI .67–.98).

For DSA examinations, observers were in agreement for residual nidus in 35 of 37 (94.6%) bAVMs, yielding good interobserver agreement (κ 0.80, 95% CI .61–.99). Two patients had a very small residual

nidus masked by a large cast of Onyx not seen by 1 of the readers. The observers matched in 34 of 37 (91.9%) bAVMs for residual venous drainage, also resulting in good interobserver agreement (κ 0.68, 95% CI .48–.92). Disagreements concerned 3 patients with veins that were visible during the capillary phase and interpreted as normal by 1 reader. Taking into account only AVM patency (residue or cured), agreement was very good (κ 0.84, 95% CI .69–.98).

Intermodality Agreement
Consensus readings for 4D-MRA and DSA showed agreement regarding residual nidi in 33 of 37 (89.2%) bAVMs, resulting in moderate intermodality agreement (κ 0.60, 95% CI .35–.85). The unseen nidi were small (4 of 4, 100%) and heterogeneous (3 of 4, 75%), which is often seen when the AVM has been embolized (4 of 4, 100%). Figures 2 and 3 show examples of nidi and veins undiagnosed with 4D-MRA. For residual venous drainage, consensus readings showed agreement in 32 of 37 (86.48%) bAVMs, also resulting in moderate agreement (κ 0.51, 95% CI .25–.78). Concerning the unseen venous drainage, 4D-MRA had a worse accuracy when veins were not dilated (3 of 5, 60%) and seen only during the capillary phase on DSA (3 of 5, 60%). In addition, unseen residual venous drainage on MRA was always masked by a large cast of Onyx that was not completely transparent and diminished the visibility of pathologic veins. In contrast, when the drainage was early, the vein dilated, and the nidus compact, depiction was easier (Fig 4). When taking into account only the patency of the bAVM, the agreement was good (κ 0.73, 95% CI .55–.92).

Diagnostic Value of 4D-MRA Compared with DSA
The diagnostic accuracy of 4D-MRA reached a sensitivity of 73.7%, specificity 100%, positive predictive value 100%, and negative predictive value 78.3%.

Agreement for Patients Treated by Radiosurgery or Embolization
Among patients treated by radiosurgery alone (8/37, 21.7%), the diagnostic accuracy reached a sensitivity of 100%, specificity 100%, positive predictive value 100%, and negative predictive value 100%. Among patients treated by embolization alone (8/37,
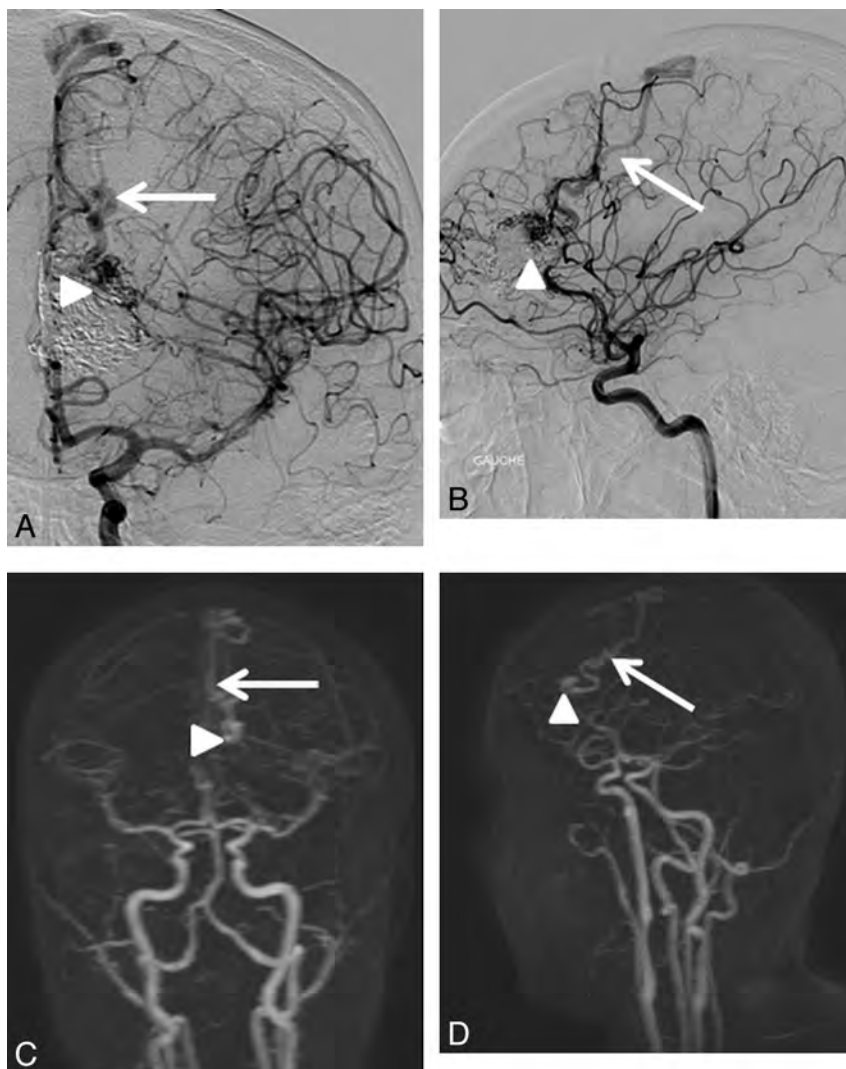
FIG 4. A 16-year-old adolescent girl with a left frontal AVM revealed by transitory neurologic symptoms; treated by embolization then radiosurgery 2 years and 10 months earlier. When the drainage is early, the vein dilated, and the nidus compact, depiction is easy. The residual nidus (*arrowhead*) and venous drainage (*arrow*) were visualized by both readers in DSA (*A, B*) and 4D-MRA (*C, D*).

Table 2: Agreement for patients treated by radiosurgery or embolization

Parameters by Modality of Treatment	Residual Nidus	Residual Venous Drainage
Radiosurgery alone (*n* = 8)		
Interobserver agreement for 4D-MRA	1.00 (1.00–1.00)	1.00 (1.00–1.00)
Interobserver agreement for DSA	1.00 (1.00–1.00)	1.00 (1.00–1.00)
Intermodality agreement between 4D-MRA and DSA	1.00 (1.00–1.00)	1.00 (1.00–1.00)
Embolization then radiosurgery (*n* = 14)		
Interobserver agreement for 4D-MRA	0.75 (0.43–1.00)	0.75 (0.43–1.00)
Interobserver agreement for DSA	0.50 (0.08–0.92)	0.75 (0.43–1.00)
Intermodality agreement between 4D-MRA and DSA	0.49 (0.06–0.92)	0.50 (0.08–0.92)
Embolization alone (*n* = 8)		
Interobserver agreement for 4D-MRA	0.50 (0.00–1.00)	1.00 (1.00–1.00)
Interobserver agreement for DSA	0.50 (0.00–1.00)	0.20 (0.00–0.81)
Intermodality agreement between 4D-MRA and DSA	0.50 (0.00–1.00)	0.50 (0.00–1.00)

Note:—Data are given as percent (95% CI).

tic accuracy reached a sensitivity of 66.7%, specificity 100%, positive predictive value 100%, and negative predictive value 62.5%. Interobserver and intermodality agreements for these 3 groups of patients are detailed in Table 2.

Patient Outcomes

On follow-up DSA, 18 of 37 (48.6%) patients had a residual AVM and the remaining 19 patients had no residual AVM. In the group treated by embolization, 8 of 22 (36.4%) were cured. Eight patients (21.7%) who were treated by embolization and complementary radiosurgery had small residuals followed-up (pending the effectiveness of radiosurgery); 2 patients (5.4%) had a new embolization attempt; 3 patients (8.1%) had additional radiosurgery; 1 patient (2.7%) had a second session of complementary radiosurgery; and 3 patients (8.1%) refused further treatment. In the group treated by radiosurgery alone, 6 of 8 (75.0%) were cured. Moreover, in the surgery group, 5 of 7 (71.4%) were cured.

DISCUSSION

Four-dimensional contrast-enhanced MRA is increasingly used in bAVM assessment as it shows high efficacy to make a diagnosis and anatomic analysis of bAVM, with good interobserver and intermodality agreements compared with DSA. It is actually an emerging noninvasive imaging technique to assess bAVM and can potentially help to reduce the number of postinterventional invasive diagnostic DSAs. However, its role in posttreatment follow-up is actually not well-defined. The present study evaluated the accuracy of 4D-MRA at 3T for detecting residual bAVM after treatment. The results showed that 4D-MRA had good interobserver agreement (κ 0.78, 95% CI .57–.98 for residual nidus and κ 0.68, 95% CI .44–.91 for residual venous drainage), moderate intermodality agreement with DSA (κ 0.60, 95% CI .35–.85 for residual nidus and κ 0.51, 95% CI .25–.78 for residual venous drainage), and good overall agreement (κ 0.73, 95% CI .55–.92), yielding to a sensitivity of 73.7%,

21.7%), the diagnostic accuracy reached a sensitivity of 75.0%, specificity 100%, positive predictive value 100%, and negative predictive value 80.0%. Furthermore, for patients treated by embolization combined with radiosurgery (14/37, 37.8%), diagnos- specificity 100%, positive predictive value 100%, and negative predictive value 78.3%.

Although it has good diagnostic accuracy, given its actual limitations, a negative 4D-MRA cannot assert the AVM is cured with

certainty. Subgroup analysis showed that the diagnostic accuracy seemed to be better in patients treated by radiosurgery alone than those who underwent embolization (alone or in combination with radiosurgery). The excellent agreement (κ 1.00, 95% CI 1.00–1.00) for patients treated after radiosurgery could compete with DSA for the follow-up of these patients. These results are consistent with the study of Lim et al,[22] which focused on the diagnostic accuracy of 4D-MRA after radiosurgery and found a diagnostic accuracy of 86.1%, with a sensitivity of 79.6% and 64.3% (reader 1 and 2), a specificity of 90.9% and 100%, a positive predictive value of 84.6% and 100%, and a negative predictive value of 90% and 81.5%. Furthermore, even if 4D-MRA cannot depict all the residual bAVM, its very high sensitivity and positive predictive value make it a very reliable test in case of positivity. This means that if it detects a residual bAVM, there is no risk of a false-positive and it can potentially help avoid some unnecessary DSA examinations, especially for patients followed-up after radiosurgery (see agreements for patients treated by radiosurgery or embolization).

Hadizadeh et al[21] recently concluded an excellent correlation between 4D-MRA and DSA regarding pre- and postoperative evaluation of bAVM, suggesting that 4D-MRA could be substituted for DSA in these 2 indications. However, in this series, of the 25 patients who had been followed-up after treatment, only 1 patient presented residual venous drainage. In our study, the proportion of residual bAVM detected with DSA was higher; 18 of 37 (48.6%), of which 12 of 18 (66.7%) were correctly depicted by 4D-MRA. Our results are consistent with the study of Lim et al,[22] which focused on the follow-up after radiosurgery. However, this study, compared with the present study, had the limitation of a large delay (up to 6 months) between the realization of 4D-MRA and DSA images. In contrast to the absence of false-positives in our study, Lim et al[22] reported 1 in their series where a normal vein was interpreted as pathologic. Indeed, sometimes it is difficult to differentiate if a vein is normal or pathologic. To avoid subjective disagreements on the physiopathology of pathologic veins, in our study, veins were considered pathologic by both readers when they appeared early (ie, during the arterial or capillary phase). Despite this, during the capillary phase, there are many superimpositions that can lead readers to miss some pathologic veins because of the lack of temporal and spatial resolution. This is particularly true for 4D-MRA but can also be seen in some cases with DSA.

The interobserver agreement on DSA was very good but a bit less than at 4D-MRA because of difficult cases (very small residual AVM) in which 4D-MRA was negative for both readers, whereas the residual AVM was sometimes seen by 1 reader on DSA leading to more disagreement. The third reader who made consensus determined that there was no false-positive case and disagreements were based on missed veins and/or nidus that were particularly difficult to depict. This problem was particularly true for patients treated by embolization with a large cast of Onyx and a small residual AVM. Indeed, there were 2 disagreements on DSA related to 2 small residual AVMs that were very difficult to identify (they were not seen on 4D-MRA by both readers) and missed by 1 reader on DSA; these 2 difficult cases did not cause disagreement on 4D-MRA but were responsible of disagreement for DSA. The

results of the subgroup analysis should be interpreted with caution for this reason and because the number of patients was small in each group so that any disagreement may strongly vary the result.

Four-dimesional contrast-enhanced MRA showed moderate agreement with DSA regarding the depiction of residual nidus and venous drainage. However, unseen residues were either small and heterogeneous nidus or veins appearing on capillary time. In our study, residual bAVMs unseen with 4D-MRA were difficult to diagnose and concerned mainly patients who were treated by embolization followed by gamma knife. Five patients benefited from a new treatment after the results of 1 set of examinations: 2 embolization attempts, 2 additional treatments by gamma knife in patients previously treated by embolization, and 1 patient treated with a second session of radiosurgery. There is, therefore, a diagnostic and therapeutic impact in properly monitoring these patients.

After radiosurgery, obliteration of bAVM is progressive and achieved after 2 to 5 years.[25] Given that these patients need repeated examinations during a long-term follow-up, an annual 4D-MRA can be proposed until it becomes negative (ie, until there is no residual AVM visible). Then a final DSA examination can be done to assert the cure. In contrast, if 4D-MRA shows a residual bAVM after a long follow-up (maybe 4 or 5 years, the delay in discussing the failure of radiosurgery treatment is still controversial), a DSA examination will be needed to decide on future therapeutic options (new radiosurgery or other treatments can be considered).[26] For follow-up after radiosurgery, this scheme accords with the conclusion of Khandanpour et al[27] (except that they used TOF-MRA instead of 4D-MRA). After surgery, the bAVM is most often cured, but sometimes removal is incomplete. In these cases, DSA seems to be the appropriate method to assert the cure or to plan new treatments (in case of incomplete surgery). After embolization, given its actual limitations and strengths, 4D-MRA has a limited place. When the bAVM is not cured after the last embolization, there is a need to do a DSA for evaluation before future treatment. When the bAVM seems to be cured at the end of the last embolization session, it can be useful to use 4D-MRA for the follow-up. If it is positive (ie, residual bAVM is visible), then DSA will be performed with a new attempt at embolization, and, if it is negative, a late DSA will be performed to assert the cure.

Recently, several publications described new tools that can further improve the efficacy of 4D-MRA, opening new prospects for bAVM assessment before treatment. Four-dimensional flow MRA techniques provide velocity measures and even color-encoded flow maps to aid in understanding the angioarchitecture.[28,29] In addition, the contribution of selective arterial spin-labeling, in addition to 4D-MRA, provided supplementary functional or anatomic information in 25% of the cases.[30] These techniques have not been evaluated in the posttreatment population.

It is also important to specify the limits of our study. First, the same technique developed in 2008 was used during the study period. However, although this technique is actually currently used and accords to recent publications, there is still the possibility of further improving the spatiotemporal resolution of this technique. Indeed, a way of improving our sequence could be to per-

form hemi-encephalic imaging, with the advantage of a better temporal resolution while minimizing vessel superimpositions. In addition, temporal and spatial resolution can be further improved up to an acceleration factor of 60 by optimizing the use of intelligent k-space sampling techniques (ie, CENTRA, parallel imaging, and partial Fourier imaging), whereas our examinations had an acceleration factor of 40, equivalent to other recent publications.[17,19-21,28,31] Second, the interobserver agreement for DSA was not as high as expected compared with 4D-MRA, though it was very good (κ 0.84, 95% CI .69–.98 and κ 0.82, 95% CI .67–.98, respectively) for the reasons explained above.

CONCLUSIONS

Four-dimensional contrast-enhanced MRA is a useful noninvasive technique for the follow-up of treated bAVM, especially in patients treated by radiosurgery. However, given its actual limitations it is not sufficient to assert the cure. DSA remains mandatory for this purpose.

REFERENCES

1. Cognard C, Spelle L, Pierot L. **Pial arteriovenous malformations.** In: Forsting M, ed. *Intracranial Malformations and Aneurysms.* Berlin/New York: Springer-Verlag; 2004:39–100
2. Choi JH, Mohr JP. **Brain arteriovenous malformations in adults.** *Lancet Neurol* 2005;4:299–308
3. Da Costa L, Wallace MC, Ter Brugge KG, et al. **The natural history and predictive features of hemorrhage from brain arteriovenous malformations.** *Stroke* 2009;40:100–05
4. Kondziolka D, McLaughlin MR, Kestle JR. **Simple risk predictions for arteriovenous malformation hemorrhage.** *Neurosurgery* 1995;37:851–55
5. Pierot L, Cognard C, Spelle L. **Cerebral arteriovenous malformations: evaluation of the hemorrhagic risk and its morbidity.** *J Neuroradiol* 2004;31:369–75
6. Novakovic RL, Lazzaro MA, Castonguay AC, et al. **The diagnosis and management of brain arteriovenous malformations.** *Neurol Clin* 2013;31:749–63
7. Pierot L, Januel AC, Herbreteau D, et al. **Endovascular treatment of brain arteriovenous malformations using Onyx: preliminary results of a prospective, multicenter study.** *Interventional Neuroradiology* 2005;11(suppl 1):159–64
8. Pierot L, Januel AC, Herbreteau D, et al. **Endovascular treatment of brain arteriovenous malformations using Onyx: results of a prospective, multicenter study.** *J Neuroradiol* 2009;36:147–52
9. Pierot L, Cognard C, Herbreteau, et al. **Endovascular treatment of brain arteriovenous malformations using a liquid embolic agent: results of a prospective, multicentre study (BRAVO).** *Eur Radiol* 2013;23:2838–45
10. Pierot L, Kadziolka K, Litré F, et al. **Combined treatment of brain AVMs with use of Onyx embolization followed by radiosurgery.** *AJNR Am J Neuroradiol* 2013;34:1395–400
11. Kaufmann TJ, Huston J, III, Mandrekar JN, et al. **Complications of diagnostic cerebral angiography: evaluation of 19,826 consecutive patients.** *Radiology* 2007;243:812–19
12. Fifi JT, Meyers PM, Lavine SD, et al. **Complications of modern diagnostic cerebral angiography in an academic medical center.** *J Vasc Interv Radiol* 2009;20:442–47
13. Thiex R, Norbash AM, Frerichs KU. **The safety of dedicated-team catheter-based diagnostic cerebral angiography in the era of advanced noninvasive imaging.** *AJNR Am J Neuroradiol* 2010;31:230–34
14. Heidenreich JO, Schilling AM, Unterharnscheidt F, et al. **Assessment of 3D-TOF-MRA at 3.0 Tesla in the characterization of the angioarchitecture of cerebral arteriovenous malformations: a preliminary study.** *Acta Radiol* 2007;48:678–86
15. Unlu E, Temizoz O, Albayram S, et al. **Contrast-enhanced MR 3D angiography in the assessment of brain AVMs.** *Eur J Radiol* 2006;60:367–78
16. Lee KE, Choi CG, Choi JW, et al. **Detection of residual brain arteriovenous malformations after radiosurgery: diagnostic accuracy of contrast-enhanced three-dimensional time of flight MR angiography at 3.0 Tesla.** *Korean J Radiol* 2009;10:333–39
17. Taschner CA, Gieseke J, Le Thuc V, et al. **Intracranial arteriovenous malformation: time-resolved contrast-enhanced MR angiography with combination of parallel imaging, keyhole acquisition, and k-space sampling techniques at 1.5 T.** *Radiology* 2008;246:871–79
18. Parmar H, Ivancevic MK, Dudek N, et al. **Neuroradiologic applications of dynamic MR angiography at 3 T.** *Magn Reson Imaging Clin N Am* 2009;17:63–75
19. Hadizadeh DR, von Falkenhausen M, Gieseke J, et al. **Cerebral arteriovenous malformation: Spetzler-Martin classification at subsecond-temporal-resolution four-dimensional MR angiography compared with that at DSA.** *Radiology* 2008;246:205–13
20. Machet A, Portefaix C, Kadziolka K, et al. **Brain arteriovenous malformation diagnosis: value of time-resolved contrast-enhanced MR angiography at 3.0 T compared to DSA.** *Neuroradiology* 2012;54:1099–108
21. Hadizadeh DR, Kukuk GM, Steck DT, et al. **Noninvasive evaluation of cerebral arteriovenous malformations by 4D-MRA for preoperative planning and postoperative follow-up in 56 patients: comparison with DSA and intraoperative findings.** *AJNR Am J Neuroradiol* 2012;33:1095–101
22. Lim HK, Choi CG, Kim SM, et al. **Detection of residual brain arteriovenous malformations after radiosurgery: diagnostic accuracy of contrast-enhanced four-dimensional MR angiography at 3.0 T.** *Br J Radiol* 2012;85:1064–69
23. Weiger M, Pruessmann KP, Kassner A, et al. **Contrast-enhanced 3D MRA using SENSE.** *J Magn Reson Imaging* 2000;12:671–77
24. Willinek WA, Gieseke J, Conrad R, et al. **Randomly segmented central k-space ordering in high-spatial-resolution contrast-enhanced MR angiography of the supraaortic arteries: initial experience.** *Radiology* 2002;225:583–88
25. Steiner L, Lindquist C, Adler JR, et al. **Clinical outcome of radiosurgery for cerebral arteriovenous malformations.** *J Neurosurg* 1992;77:1–8
26. Maesawa S, Flickinger JC, Kondziolka D, et al. **Repeated radiosurgery for incompletely obliterated arteriovenous malformations.** *J Neurosurg* 2000;92:961–70
27. Khandanpour N, Griffiths P, Warren D, et al. **Prospective comparison of late 3T MRI with conventional angiography in evaluating the patency of cerebral arteriovenous malformations treated with stereotactic radiosurgery.** *Neuroradiology* 2013;55:683–87
28. Ansari SA, Schnell S, Carroll T, et al. **Intracranial 4D flow MRI: toward individualized assessment of arteriovenous malformation hemodynamics and treatment-induced changes.** *AJNR Am J Neuroradiol* 2013;34:1922–28
29. Illies T, Forkert ND, Ries T, et al. **Classification of cerebral arteriovenous malformations and intranidal flow patterns by color-encoded 4D-hybrid-MRA.** *AJNR Am J Neuroradiol* 2013;34:46–53
30. Kukuk GM, Hadizadeh DR, Boström A, et al. **Cerebral arteriovenous malformations at 3.0 T: intraindividual comparative study of 4D-MRA in combination with selective arterial spin labeling and digital subtraction angiography.** *Invest Radiol* 2010;45:126–32
31. Willinek WA, Hadizadeh DR, von Falkenhausen M, et al. **4D time-resolved MR angiography with keyhole (4D-TRAK): more than 60 times accelerated MRA using a combination of CENTRA, keyhole, and SENSE at 3.0 T.** *J Magn Reson Imaging* 2008;27:1455–60

Extensive White Matter Dysfunction in Cognitively Impaired Patients with Secondary-Progressive Multiple Sclerosis

P.L. Francis, T.L. Chia, R. Jakubovic, P. O'Connor, L. Lee, A. Feinstein, and R.I. Aviv

ABSTRACT

BACKGROUND AND PURPOSE: Cognitive impairment is a common, disabling symptom of MS. We investigated the association between cognitive impairment and WM dysfunction in secondary-progressive multiple sclerosis using DTI.

MATERIALS AND METHODS: Cognitive performance was assessed with a standard neuropsychological battery, the Minimal Assessment of Cognitive Function in Multiple Sclerosis. Cognitive impairment was defined as scoring >1.5 standard deviations below healthy controls on ≥2 subtests. Fractional anisotropy maps were compared against cognitive status using tract-based spatial statistics with threshold-free cluster enhancement.

RESULTS: Forty-five patients with secondary-progressive multiple sclerosis (median age: 55 years, female/male: 27/18, median Expanded Disability Status Scale Score: 6.5) were prospectively recruited. Cognitively impaired patients (25/45) displayed significantly less normalized global GM and WM volumes ($P = .001$, $P = .024$), more normalized T2-weighted and T1-weighted WM lesion volumes ($P = .002$, $P = .006$), and lower WM skeleton fractional anisotropy ($P < .001$) than non-impaired patients. Impaired patients also had significantly lower fractional anisotropy ($p_{corr} < .05$) in over 50% of voxels within every major WM tract. The most extensively impinged tracts were the left posterior thalamic radiation (100.0%), corpus callosum (97.8%), and right sagittal stratum (97.5%). No WM voxels had significantly higher fractional anisotropy in patients with cognitive impairment compared with their non-impaired counterparts ($p_{corr} > .05$). After the inclusion of confounders in a multivariate logistic regression, only fractional anisotropy remained a significant predictor of cognitive status.

CONCLUSIONS: Cognitively impaired patients with secondary-progressive multiple sclerosis exhibited extensive WM dysfunction, though preferential involvement of WM tracts associated with cognition, such as the corpus callosum, was apparent. Multivariate analysis revealed that only WM skeleton fractional anisotropy was a significant predictor of cognitive status.

ABBREVIATIONS: CC = corpus callosum; EDSS = Expanded Disability Status Scale; FA = fractional anisotropy; MNI = Montreal Neurological Institute; RRMS = relapsing-remitting MS; SPMS = secondary-progressive MS; TBSS = tract-based spatial statistics; WML = white matter lesion

Cognitive impairment is a prevalent symptom of MS and has been estimated to occur in 43%–65% of patients.[1] Those with secondary-progressive multiple sclerosis (SPMS) exhibit the highest frequency of impairment.[2] Prior neuroimaging studies have almost exclusively investigated such impairment by assessing discrete cognitive domains, such as information processing speed or working memory, with neuropsychological tests that have established domain specificity. Such an approach is apparent in studies that examined both brain and lesion volumetry[3-6] and WM integrity.[7-11] Domain-specific cognitive tests are powerful tools that can assess the impact of MS pathology on individual cognitive domains and specific neuronal pathways, but cannot investigate cognition as a multidomain entity. Few studies of cognitive impairment in MS have adopted this broader perspective, and patients with MS with multiple domain impairment may exhibit considerably different structural brain damage from their counterparts with single domain impairment.

MS has been traditionally viewed as a disease predominantly affecting WM, though only modest associations between T2-weighted hyperintense or T1-weighted hypointense white matter lesion (WML) load and cognitive test performance have been reported.[12] Normal-appearing white matter is being increasingly examined, particularly through DTI techniques.[7-11,13,14] These studies have most frequently used fractional anisotropy (FA) as

their primary outcome,[8-11,13,14] whereas mean diffusivity has been investigated to a lesser extent.[7] Radial diffusivity and axial diffusivity have been examined as secondary outcomes.[11,14] Given the recent emphasis on the role of GM pathology both in the etiology of MS and related cognitive dysfunction, FA was considered in the context of GM volume using multivariate regression.[15-17] Normal-appearing white matter has also been investigated using magnetization transfer ratio.[18]

Tract-based spatial statistics (TBSS) is being increasingly utilized in DTI studies of MS and cognition.[8,9,11,13] TBSS has improved on traditional voxel-based morphometry by thinning WM to invariant tracts common to all patients.[19] The voxel-based morphometry approach suffers from deficiencies related to spatial alignment and smoothing, which are mitigated by TBSS. Several prior TBSS studies have concluded that cognitive impairment in MS is because of the selective disruption of specific WM tracts associated with cognition, such as the cingulum and corpus callosum (CC).[8,9,11] It should be noted that this spatial specificity has a physiologic basis and is not mediated by the cognitive nature of these tracts. These studies correlated FA values with performance on individual cognitive tests and examined cohorts primarily or solely comprising patients with relapsing-remitting MS (RRMS). DTI outcomes in patients with SPMS with and without cognitive impairment have not been well investigated, yet 65% of patients with RRMS will progress to SPMS.[20] While WM injury is initially selective for specific tracts associated with impaired cognition in RRMS, DTI abnormalities are expected to become significantly more widespread and generalized with greater impairment and disease severity progression.

We hypothesized that patients with SPMS with impairment spanning multiple cognitive domains should exhibit extensive WM dysfunction not restricted to tracts implicated in cognition, such as the cingulum and CC.

MATERIALS AND METHODS

Patients
This study was approved by the research ethics boards of Sunnybrook Health Sciences Centre and St. Michael's Hospital. Patients with SPMS were prospectively recruited during a 1-year period from 2 tertiary referral MS clinics. SPMS diagnosis was based on the opinion of a senior neurologist with specialist practice in MS (20 years' experience). Charts of potential participants were screened by the same senior neurologist before recruitment to ensure eligibility. Exclusion criteria were: history of drug/alcohol abuse, use of disease-modifying drugs or steroids within the past 6 months, premorbid (ie, pre-MS) psychiatric history, head injury with loss of consciousness, concurrent medical diseases (eg, cerebrovascular disease), and contraindication to MR imaging. Clinical data included: age, sex, education level, and disease duration. MR imaging acquisition, neurologic examination, and Expanded Disability Status Scale (EDSS) assessment[21] were completed on the same day.

Cognitive Testing
The Minimal Assessment of Cognitive Function in Multiple Sclerosis was administered under the supervision of a senior neuropsychiatrist.[22] This standard MS cognitive battery is a compre-

hensive assessment tool consisting of 7 neuropsychological tests: Paced Auditory Serial Addition Test (working memory), Symbol Digit Modalities Test (processing speed), California Verbal Learning Test, 2nd Edition (verbal memory), Brief Visuospatial Memory Test, Revised (visuospatial memory), Delis-Kaplan Executive Function System (executive function), Controlled Word Association Test (verbal fluency), and Judgement of Line Orientation (visuospatial perception). Impairment on an individual test was defined as scoring more than 1.5 standard deviations below normative data of healthy controls.[23] Patients with 2 or more test impairments were designated as having cognitive impairment.[23] Beck Depression Inventory scores were also obtained because of the association between depression and cognitive impairment in patients with MS.[4]

MR Imaging Acquisition
MR imaging scanning was performed on a 3T scanner (Philips Healthcare, Best, the Netherlands) with a 16-channel phased array coil. The following sequences were acquired: 1) T1 3D (TR/TE: 9.5 ms/2.3 ms, resolution: $0.71 \times 0.71 \times 1.4$ mm^3); 2) proton density/T2 (TR/TE: 2900 ms/10.7 ms, resolution: $0.45 \times 0.45 \times 3$ mm^3); 3) DTI (TR/TE: 8966 ms/57 ms, resolution: $2.95 \times 2.95 \times 3$ mm^3, 50 sections, b-value: 1000 seconds/mm^2, single b = 0 scan, 32 gradient directions, 2 sequential scans [co-registered and averaged off-line]).

Image Processing
The structural scans were processed to generate global GM, WM, T2-weighted WML, and T1-weighted WML tissue volumes normalized to total intracranial volume as previously reported.[17] Briefly, regions of GM and WM were delineated algorithmically, and T2-weighted hyperintensities and T1-weighted hypointensities were hand traced using Medical Image Processing, Analysis, and Visualization version 4.0 (National Institutes of Health, Bethesda, Maryland). The FMRIB Software Library (FSL, http://www.fmrib.ox.ac.uk/fsl) processed the DTI scans.[24] The FSL FLIRT tool co-registered the 2 sequential DTI scans per patient by using a 12-parameter affine transform, and the co-registered scans were averaged using Fslutils (http://fsl.fmrib.ox.ac.uk/fsl/fslwiki/Fslutils). This approach avoids averaging on the scanner, which is inappropriate because of EPI susceptibility artifacts.[25] The FSL Diffusion Toolbox corrected the co-registered, averaged scans for motion and eddy current distortions before fitting the diffusion tensors and calculating the FA maps. The acquisition space FA maps were normalized to Montreal Neurological Institute (MNI) space using the FSL FNIRT tool. The mean MNI space FA map for all patients was computed and thinned to invariant WM tracts common to every patient. This mean MNI space FA skeleton was thresholded at 0.2 before being applied as a mask to skeletonise the MNI space FA map for each individual patient to exclude non-WM voxels.

Statistical and Image Analysis
Clinical data were compared between patients with and without cognitive impairment using the Wilcoxon rank sum test for continuous variables or Pearson χ^2 test for dichotomous variables. Results for continuous variables were expressed as median (inter-
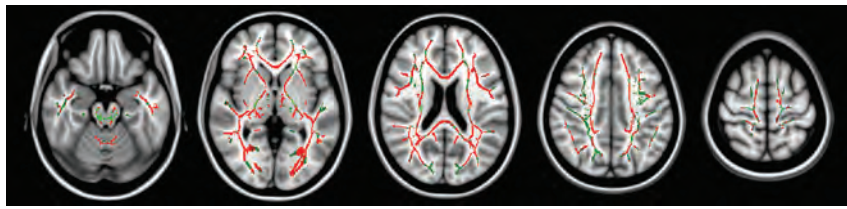
FIG 1. Significantly reduced WM FA values in cognitively impaired patients with SPMS. Inferior to superior arrangement of axial sections with 2 different color overlays. The red overlay represents voxels of significantly reduced FA in cognitively impaired patients with SPMS within the WM skeleton. The green overlay represents the remainder of the WM skeleton where no such significant association was identified.

Table 1: Clinical and radiologic characteristics of patients with SPMS

	Without Cognitive Impairment (n = 20)	With Cognitive Impairment (n = 25)	P Value
Age (y)	54.5 (49.3−62.3)	55.0 (47.5−61.5)	.954[a]
Sex (F/M)	11/9	16/9	.540[b]
Education level (y)	15.5 (13.0−17.8)	14.0 (13.0−17.0)	.619[a]
Disease duration (y)	18.5 (10.5−20.8)	19.0 (12.0−28.5)	.192[a]
EDSS (score)	6.0 (6.0−6.5)	6.5 (6.0−6.5)	.249[a]
BDI (score)	6.5 (5.0−11.8)	9.0 (7.5−13.5)	.067[a]
Normalized GM volume (%)	41.8 (41.5−42.9)	40.5 (38.7−41.6)	.001[a]
Normalized WM volume (%)	34.2 (33.9−35.1)	33.8 (33.3−34.3)	.024[a]
Normalized T2-weighted WML volume (%)	0.40 (0.08−0.94)	1.05 (0.63−1.78)	.002[a]
Normalized T1-weighted WML volume (%)	0.12 (0.03−0.32)	0.44 (0.13−0.67)	.006[a]
WM skeleton FA (mean)	0.37 (0.34−0.38)	0.33 (0.28−0.34)	<.001[a]

Note:— EBSS indicates Expanded Disability Status Scale; BDI, Beck Depression Inventory.
[a] Wilcoxon rank-sum test (median [interquartile range]).
[b] Pearson χ^2 test.

quartile range), and results for dichotomous variables were expressed as proportions.

The normalized global tissue volumes were analyzed with respect to cognitive status as previously described.[17] The skeletonized FA maps were compared between patients with and without cognitive impairment using FSL's Randomise tool, which conducts permutation-based nonparametric testing while correcting for multiple comparisons across space.[26] To be conservative and assumption free, voxelwise group analysis was conducted with 5000 permutations and threshold-free cluster enhancement (p_{corr} < .05). Threshold-free cluster enhancement is a recent advance in TBSS methodology that eliminates the need for an arbitrarily chosen cluster size threshold.[27] The results appeared as images with voxel values consisting of corrected P values. The WM parcellation map based on the MNI space ICBM-DTI-81 atlas provides stereotaxic delineation of every major WM tract in the brain and was employed as an region of interest template.[28] This WM tract region of interest template was applied as an overlay on the results images, and both the total voxel count and number of significant voxels were algorithmically extracted for every region of interest. ROIs found to contain less than 100 voxels when superimposed on the mean FA skeleton were excluded from subsequent analyses. A list of included ROIs is provided in Table 2. Mean FA values for the WM skeleton of each patient were also calculated. A multivariate logistic regression model was used to identify factors predictive of cognitive status. Putative factors submitted to multivariate analysis were those demonstrating a P < .1 association with cognition in univariate analysis.

RESULTS

Clinical and Radiologic Characteristics

Of 45 patients with SPMS prospectively recruited, 25 (55.6%) were classified as being cognitively impaired. The clinical characteristics, including age, sex, education level, disease duration, and EDSS score, were not significantly different between patients with and without cognitive impairment (P > .05) (Table 1). There was a trend toward higher Beck Depression Inventory scores in impaired patients, but this did not reach clinical significance (P = .07). Impaired patients displayed significantly reduced normalized global GM volume (P = .001), significantly lower normalized global WM volume (P = .024), significantly higher normalized T2-weighted WML volume (P = .002), significantly greater normalized T1-weighted WML volume (P = .006), and significantly lower WM skeleton FA (P < .001) than patients without cognitive impairment. No significant difference in normalized global WM volume was found (P > .05) (Table 1). Following multivariate analysis, WM skeleton FA was the only factor that remained a significant predictor of cognitive status (P = .03).

WM Integrity and Cognition

Patients with cognitive dysfunction had significantly lower FA values in over 50% of the voxels within every major WM tract compared with those without (p_{corr} < .05) (Fig 1, Table 2). The most extensively affected WM tracts were the left posterior thalamic radiation (100.0%), CC (97.8%), right sagittal stratum (includes inferior fronto-occipital fasciculus and inferior longitudinal fasciculus, 97.5%), right posterior thalamic radiation (96.1%), and left sagittal stratum (95.4%). Only 1 other region (right medial lemniscus) had greater than 90% alteration (90.8%). These findings illustrate that although WM dysfunction is predominantly generalized with respect to cognitive status, preferential involvement of specific WM tracts was apparent. No WM voxels had significantly higher FA in patients with cognitive impairment compared with their nonimpaired counterparts (p_{corr} > .05).

DISCUSSION

Cognitively impaired patients with SPMS in the present series exhibited significantly reduced normalized global GM and WM volumes, significantly increased normalized T2-weighted and T1-weighted WML volumes, and significantly lower WM skeleton FA consistent with the assertion that cognitive impairment is associated with more advanced disease. Multivariate analysis of factors predicting cognitive status demonstrated that only WM skeleton FA was significant. Our results demonstrate that in advanced MS

Table 2: Tract-based spatial statistics group analysis identifying WM tracts with significantly lower FA values in patients with cognitive impairment compared with patients without cognitive impairment

	Total Voxels	Significant Voxels	% Significant
Middle cerebellar peduncle	2608	2068	79.3%
Corpus callosum	7044	6891	97.8%[a]
R corticospinal tract	134	72	53.7%
L corticospinal tract	208	154	74.0%
R medial lemniscus	174	158	90.8%
L medial lemniscus	209	171	81.8%
R cerebellar peduncle	476	331	69.5%
L cerebellar peduncle	414	294	71.0%
R cerebral peduncle	575	502	87.3%
L cerebral peduncle	600	415	69.2%
R internal capsule	2219	1728	77.9%
L internal capsule	1659	1308	78.8%
R corona radiata	3935	3267	83.0%
L corona radiata	3142	2486	79.1%
R posterior thalamic radiation	1086	1044	96.1%[a]
L posterior thalamic radiation	554	554	100.0%[a]
R sagittal stratum	652	636	97.5%[a]
L sagittal stratum	345	329	95.4%[a]
R external capsule	1115	993	89.1%
L external capsule	565	437	77.3%
R cingulum	526	397	75.5%
L cingulum	319	220	69.0%
R superior longitudinal fasciculus	1614	1363	84.4%
L superior longitudinal fasciculus	1338	840	62.8%

Note:—R indicates right; L, left.[br /]
[a] Regions with greater than 95% WM impingement.

disease characterized by SPMS, multiple domain cognitive dysfunction is the result of diffuse WM injury with regional predilections present in the CC, posterior thalamic radiation, and sagittal stratum. Of these 3 regions only the CC is traditionally associated with cognition,[29] though a recent study implicated the posterior thalamic radiation in intellectual performance.[30] Thalamocortical circuit integrity has additionally been found to differentiate normal aging from mild cognitive impairment.[31] This suggests that thalamic radiations are implicated in a wide range of cognitive tasks. Furthermore, significantly reduced FA was recently reported in the inferior longitudinal fasciculus, a component of the sagittal stratum, of patients with mild cognitive impairment.[32]

The observed differences in the spatial extent of WM dysfunction between the present SPMS study and those investigating RRMS allow for inference regarding the interplay of disease progression, WM integrity, and cognitive impairment. The SPMS cohort enrolled in the present study had a median EDSS score of 6.5, which is higher than prior TBSS studies that were all primarily or solely composed of patients with RRMS with a median EDSS score of 3 or less.[8,9,11] Generalized WM injury predominated in the present SPMS cohort with cognitive impairment, though preferential involvement of specific WM tracts was evident. Interestingly, prior studies of cognitive dysfunction in patients with RRMS primarily reported selective degradation of WM pathways associated with cognition but also showed widespread WM tract alteration.[8,9,11] This inverted symmetry suggests that disease progression in cognitively impaired patients with MS, as demonstrated by EDSS score and MS subtype classification, is associated with evolution from a more tract specific imaging pattern to a more generalized imaging pattern.

Yu et al[11] highlighted the significant correlations between reduced FA values and lower cognitive test scores in cognitively relevant tracts. However, significant correlations also occurred within all association fibers, commissural fibers, and projection fibers. This suggests that while WM abnormalities were principally tract selective, they appeared on a background of generalized WM alteration. Strikingly, the most extensively impaired WM regions in that study were the posterior thalamic radiation, CC, and sagittal stratum. Those results mirror our findings of diffuse WM dysfunction with residua of tract selectivity in the presence of greater disease severity.

We propose that even though WM dysfunction initially favors tracts associated with cognition, abnormalities become significantly more extensive and generalized as more domains are impaired and disease severity progresses. This suggests that cognitive impairment in patients with MS with progressive disease is a sequela of diffuse, nonspecific WM dysfunction. Such a pattern of WM alteration in turn raises the possibility that the underlying disease pathology itself is diffuse and nonspecific during the progressive phase, which aligns with the findings of a landmark postmortem study that investigated a variety of MS subtypes and found diffuse normal-appearing white matter injury to be a characteristic hallmark of progressive phase MS.[33]

Disease duration and disease severity were greater in our cognitively impaired patients than their nonimpaired counterparts, which suggests that cognitive dysfunction is associated with more advanced disease, though the findings did not reach statistical significance. Similarly, a recent study that also dichotomized patients according to performance on multiple cognitive tests demonstrated significantly higher EDSS scores in patients with MS with cognitive impairment.[34] It has also been shown that patients with benign MS with cognitive impairment did not significantly differ from patients with SPMS with respect to normalized brain volume, global WML load, or GM mean diffusivity.[35] In contrast, benign patients without cognitive impairment demonstrated significant differences.

Possible limitations of this study include sample size. The present cohort of patients with SPMS is relatively well populated ($n = 45$), but larger DTI studies of cognition in MS have been performed using different analytic approaches ($n = 82$).[34] It is also possible that fatigue may have impacted the cognitive testing as it was not assessed. In addition, TBSS is a semi-automated technique that relies on a somewhat arbitrary FA threshold of 0.2 to define WM. In terms of cognition, we chose to solely focus on global cognitive impairment dichotomized based on the findings of a standard neuropsychological battery, instead of investigating individual subtests. This decision was motivated by the dearth of MS neuroimaging studies examining cognition as a multidomain entity, though this method is not without its own inherent limitations. Without the use of individual subtests, we were not able to fully establish a damage-response relationship where incremental changes in cognition can be correlated with incremental neuronal dysfunction.

Another potential limitation is our choice of SPMS as a disease subtype to investigate. RRMS is an earlier form of the disease and has been investigated much more frequently than SPMS. Our decision to examine patients with SPMS with cognitive impair-

ment means that our results are therefore not directly comparable with previous DTI studies of MS and cognition.[8-11,13,34] However, our data do demonstrate structural differences between patients with SPMS with and without cognitive impairment and provide insight into the diffuse WM tract disturbances that occur with disease progression. Differences between impaired and nonimpaired patients with SPMS may also provide a potential surrogate marker for new therapeutic interventions to forestall the onset of cognitive impairment even in advanced disease.

CONCLUSIONS

This study sought to examine MR imaging correlates of multiple domain cognitive impairment in patients with SPMS with an emphasis on WM integrity. Impaired patients exhibited extensive WM dysfunction that severely disrupted every major tract in the brain while retaining predilection for pathways associated with cognition, such as the CC. These findings strongly suggest that cognitive impairment in patients with MS with advanced disease progression is predominantly the result of diffuse WM injury superimposed on a background of cognition-specific tract damage sustained during earlier stages of the disease. While impaired patients with SPMS also displayed significantly reduced global GM and WM volumes and significantly increased T2-weighted and T1-weighted WML loads, multivariate analysis revealed that only WM skeleton FA was a significant predictor of cognitive status.

REFERENCES

1. Rao SM, Leo GJ, Bernardin L, et al. **Cognitive dysfunction in multiple sclerosis. I. Frequency, patterns, and prediction.** *Neurology* 1991;41:685–91
2. Huijbregts SC, Kalkers NF, de Sonneville LM, et al. **Differences in cognitive impairment of relapsing remitting, secondary, and primary progressive MS.** *Neurology* 2004;63:335–39
3. Sperling RA, Guttmann CR, Hohol MJ, et al. **Regional magnetic resonance imaging lesion burden and cognitive function in multiple sclerosis: a longitudinal study.** *Arch Neurol* 2001;58:115–21
4. Benedict RH, Weinstock-Guttman B, Fishman I, et al. **Prediction of neuropsychological impairment in multiple sclerosis: comparison of conventional magnetic resonance imaging measures of atrophy and lesion burden.** *Arch Neurol* 2004;61:226–30
5. Houtchens MK, Benedict RH, Killiany R, et al. **Thalamic atrophy and cognition in multiple sclerosis.** *Neurology* 2007;69:1213–23
6. Papadopoulou A, Muller-Lenke N, Naegelin Y, et al. **Contribution of cortical and white matter lesions to cognitive impairment in multiple sclerosis.** *Mult Scler* 2013;19:1290–96
7. Rovaris M, Iannucci G, Falautano M, et al. **Cognitive dysfunction in patients with mildly disabling relapsing-remitting multiple sclerosis: an exploratory study with diffusion tensor MR imaging.** *J Neurol Sci* 2002;195:103–09
8. Dineen RA, Vilisaar J, Hlinka J, et al. **Disconnection as a mechanism for cognitive dysfunction in multiple sclerosis.** *Brain* 2009;132:239–49
9. Roosendaal SD, Geurts JJ, Vrenken H, et al. **Regional DTI differences in multiple sclerosis patients.** *Neuroimage* 2009;44:1397–403
10. Warlop NP, Achten E, Fieremans E, et al. **Transverse diffusivity of cerebral parenchyma predicts visual tracking performance in relapsing-remitting multiple sclerosis.** *Brain Cogn* 2009;71:410–15
11. Yu HJ, Christodoulou C, Bhise V, et al. **Multiple white matter tract abnormalities underlie cognitive impairment in RRMS.** *Neuroimage* 2012;59:3713–22
12. Filippi M, Rocca MA, Benedict RH, et al. **The contribution of MRI in assessing cognitive impairment in multiple sclerosis.** *Neurology* 2010;75:2121–28
13. Hawellek DJ, Hipp JF, Lewis CM, et al. **Increased functional connectivity indicates the severity of cognitive impairment in multiple sclerosis.** *Proc Natl Acad Sci USA* 2011;108:19066–71
14. Hulst HE, Steenwijk MD, Versteeg A, et al. **Cognitive impairment in MS: impact of white matter integrity, gray matter volume, and lesions.** *Neurology* 2013;80:1025–32
15. Lucchinetti CF, Popescu BF, Bunyan RF, et al. **Inflammatory cortical demyelination in early multiple sclerosis.** *N Engl J Med* 2011;365:2188–97
16. Aviv RI, Francis PL, Tenenbein R, et al. **Decreased frontal lobe gray matter perfusion in cognitively impaired patients with secondary-progressive multiple sclerosis detected by the bookend technique.** *AJNR Am J Neuroradiol* 2012;33:1779–85
17. Francis PL, Jakubovic R, O'Connor P, et al. **Robust perfusion deficits in cognitively impaired patients with secondary-progressive multiple sclerosis.** *AJNR Am J Neuroradiol* 2013;34:62–67
18. Khalil M, Enzinger C, Langkammer C, et al. **Cognitive impairment in relation to MRI metrics in patients with clinically isolated syndrome.** *Mult Scler* 2011;17:173–80
19. Smith SM, Jenkinson M, Johansen-Berg H, et al. **Tract-based spatial statistics: voxelwise analysis of multi-subject diffusion data.** *Neuroimage* 2006;31:1487–505
20. Compston A, Coles A. **Multiple sclerosis.** *Lancet* 2008;372:1502–17
21. Kurtzke JF. **Rating neurologic impairment in multiple sclerosis: an expanded disability status scale (EDSS).** *Neurology* 1983;33:1444–52
22. Benedict RH, Fischer JS, Archibald CJ, et al. **Minimal neuropsychological assessment of MS patients: a consensus approach.** *Clin Neuropsychol* 2002;16:381–97
23. Benedict RH, Cookfair D, Gavett R, et al. **Validity of the minimal assessment of cognitive function in multiple sclerosis (MACFIMS).** *J Int Neuropsychol Soc* 2006;12:549–58
24. Smith SM, Jenkinson M, Woolrich MW, et al. **Advances in functional and structural MR image analysis and implementation as FSL.** *Neuroimage* 2004;23(suppl 1):S208–19
25. Smith SM, Johansen-Berg H, Jenkinson M, et al. **Acquisition and voxelwise analysis of multi-subject diffusion data with tract-based spatial statistics.** *Nat Protoc* 2007;2:499–503
26. Nichols TE, Holmes AP. **Nonparametric permutation tests for functional neuroimaging: a primer with examples.** *Hum Brain Mapp* 2002;15:1–25
27. Smith SM, Nichols TE. **Threshold-free cluster enhancement: addressing problems of smoothing, threshold dependence and localisation in cluster inference.** *Neuroimage* 2009;44:83–98
28. Mori S, Oishi K, Jiang H, et al. **Stereotaxic white matter atlas based on diffusion tensor imaging in an ICBM template.** *Neuroimage* 2008;40:570–82
29. Hines M, Chiu L, McAdams LA, et al. **Cognition and the corpus callosum: verbal fluency, visuospatial ability, and language lateralization related to midsagittal surface areas of callosal subregions.** *Behav Neurosci* 1992;106:3–14
30. Chiang MC, Barysheva M, Shattuck DW, et al. **Genetics of brain fiber architecture and intellectual performance.** *J Neurosci* 2009;29:2212–24
31. Cantero JL, Atienza M, Gomez-Herrero G, et al. **Functional integrity of thalamocortical circuits differentiates normal aging from mild cognitive impairment.** *Hum Brain Mapp* 2009;30:3944–57

32. Cho H, Yang DW, Shon YM, et al. **Abnormal integrity of corticocortical tracts in mild cognitive impairment: a diffusion tensor imaging study.** *J Korean Med Sci* 2008;23:477–83

33. Kutzelnigg A, Lucchinetti CF, Stadelmann C, et al. **Cortical demyelination and diffuse white matter injury in multiple sclerosis.** *Brain* 2005;128:2705–12

34. Mesaros S, Rocca MA, Kacar K, et al. **Diffusion tensor MRI tractography and cognitive impairment in multiple sclerosis.** *Neurology* 2012;78:969–75

35. Rovaris M, Riccitelli G, Judica E, et al. **Cognitive impairment and structural brain damage in benign multiple sclerosis.** *Neurology* 2008;71:1521–26

Phase White Matter Signal Abnormalities in Patients with Clinically Isolated Syndrome and Other Neurologic Disorders

J. Hagemeier, M. Heininen-Brown, T. Gabelic, T. Guttuso Jr, N. Silvestri, D. Lichter, L.E. Fugoso, N. Bergsland, E. Carl, J.J.G. Geurts, B. Weinstock-Guttman, and R. Zivadinov

ABSTRACT

BACKGROUND AND PURPOSE: Identifying MRI biomarkers that can differentiate multiple sclerosis patients from other neurological disorders is a subject of intense research. Our aim was to investigate phase WM signal abnormalities for their presence, prevalence, location, and diagnostic value among patients with clinically isolated syndrome and other neurologic disorders and age-, sex-, and group-matched healthy controls.

MATERIALS AND METHODS: Forty-eight patients with clinically isolated syndrome and 30 patients with other neurologic diseases and a healthy control group ($n = 47$) were included in the study. Subjects were scanned at 3T by using SWI-filtered phase and T2WI, with WM signal abnormalities $\geq$3 mm being classified.

RESULTS: Patients with clinically isolated syndrome had significantly more phase and T2 WM signal abnormalities than healthy controls ($P < .001$). Phase WM signal abnormalities were more prevalent among patients with clinically isolated syndrome compared with patients with other neurologic disorders (4:1 ratio), whereas T2 WM signal abnormalities were more ubiquitous with a 2:1 ratio. The presence of phase WM signal abnormalities was sensitive for clinically isolated syndrome (70.8%) and achieved a moderate-to-high specificity for differentiating patients with clinically isolated syndrome and healthy controls, patients with other neurologic disorders, and patients with other neurologic disorders of other autoimmune origin (specificity, 70%–76.7%). Combining the presence of $\geq$2 phase lesions with the McDonald 2005 and 2010 criteria for dissemination in space improved the specificity (90%), but not the accuracy, in differentiating patients with clinically isolated syndrome from those with other neurologic disorders. In subanalyses among patients with clinically isolated syndrome who converted to clinically definite multiple sclerosis versus those who did not within a 3-year follow-up period, converters had significantly more phase ($P = .008$) but not T2 or T1 WM signal abnormalities.

CONCLUSIONS: Phase WM signal abnormalities are prevalent among patients with clinically isolated syndrome. The presence of (multiple) phase WM signal abnormalities tended to be more predictive of conversion to clinically definite multiple sclerosis and was specific in differentiating patients with clinically isolated syndrome and other neurologic disorders, compared with T2 WM signal abnormalities; however, the accuracy remains similar to that of the current McDonald criteria.

ABBREVIATIONS: CDMS = clinically definite MS; CIS = clinically isolated syndrome; DIS = dissemination in space; HC = healthy control; OND = other neurologic disorders; ROC = receiver operating characteristic; SA = signal abnormality

The occurrence of WM signal abnormalities (SAs) is a hallmark feature of multiple sclerosis, yet the clinical relevance of the pathologic substrate of WM-SAs is disappointing.[1-4] WM-SAs observed on T2WI and T1WI represent focal pathology and are thought to be caused by inflammation, edema, demyelination, or gliosis.[2] They are usually secondary to active inflammation, imaged by using postcontrast T1WI gadolinium-enhanced scanning.[5] Even though T2 WM-SAs are present at the first demyelinating episode, the poor specificity of conventional MR imaging[1,6] and comparable MR imaging features at disease onset compared with ischemic, autoimmune diseases or aging limits their predictive value.

Indicates open access to non-subscribers at www.ajnr.org

Indicates article with supplemental on-line tables.

http://dx.doi.org/10.3174/ajnr.A3969

Previously, differential diagnosis between MS and other conditions was considered by using brain and spinal cord MR imaging and incorporating number, location, and morphology of T2 WM-SAs in the diagnostic criteria of MS[7] or by using different nonconventional MR imaging techniques.[6,8-10] It is important to further investigate the value of nonconventional MR imaging techniques in the MS differential diagnosis, for example by using SWI-filtered phase to identify early focal brain pathology indicative of MS, especially in patients with clinically isolated syndrome (CIS).

Recent studies have confirmed histologically that WM-SAs visible on MR imaging phase and R^{2*} correspond to focal iron deposits, whereas T2 and T1 WM-SAs are influenced by water content.[11] A substantial subset of MS WM-SAs has phase shifts[11,12] and morphologic differences.[11-15] However, factors other than nonheme iron may influence the observed WM-SA signal, such as changes in myelin, deoxyhemoglobin, and inflammation.[11,16-19] Therefore, because there are a multitude of effects, it is not fully known to what extent they each individually influence SWI-filtered phase changes.

Phase changes may signal early WM-SA development[17,20] in that these phase WM-SAs may appear initially but then disappear as the pathology advances.[17] Considering that the distinct pathologies influencing phase shift (eg, cellular/myelin destruction, iron levels, microstructural changes) in WM-SAs are most likely intricately related and are observed in MS and related disorders,[12,14,15,21-23] the inquiry into pathology visible on SWI-filtered phase remains important regardless of the causative factors.

SWI-filtered phase work has mostly focused on patients with MS,[11,13-15,24] high-field-strength imaging,[11,13,24] or histologically validating phase WM-SAs.[11,25] Regardless of what pathology phase WM-SAs represent, it is imperative to identify whether their presence has diagnostic value. In the present study, we assessed WM-SAs visible on T2WI and SWI-filtered phase among patients with CIS and patients with other neurologic disorders (OND) to investigate their prevalence, location, and ability to differentiate disease groups.

MATERIALS AND METHODS
Subjects
This study used data from an ongoing prospective study of genetic and environmental risk factors in MS.[26,27] One-hundred twenty-five subjects satisfied the inclusion criteria: CIS, OND, or healthy control (HC) and having an MR imaging scan obtained with an SWI sequence. Forty-eight patients were diagnosed with CIS (disease duration = 2.8 ± 3.9 years), while 47 HCs were age- and sex-matched to the patients with CIS and OND. From the 48 patients with CIS, subanalyses were performed on 20 patients who underwent a second clinical attack within a 3-year follow-up period (clinically definite multiple sclerosis [CDMS]), 12 remained clinically stable (non-CDMS), while no follow-up was available for 16 patients with CIS. Presented analyses are based on baseline data because the follow-up MR imaging protocols were not standardized. In addition, 30 patients with OND were also included. HCs were recruited from volunteers who had normal neurologic examination findings without a history of any neurologic or psychiatric disorders. Patients with CIS were recruited from the MS

clinic if they had no relapse and were not treated with steroids within the month preceding study entry. The OND group was recruited from the Department of Neurology specialized clinics and consisted of a heterogeneous assortment of neurologic patients that included degenerative ($n = 10$, 33.3%), autoimmune ($n = 10$, 33.3%), and vascular ($n = 10$, 33.3%) disorders. Participants underwent full neurologic assessment and were excluded if they had pre-existing medical conditions or were pregnant. Written informed consent was obtained, and the study protocol was approved by our institutional review board.

MR Imaging Acquisition
Scans were acquired on a 3T Signa Excite HD 12.0 (GE Healthcare, Milwaukee, Wisconsin) by using a multichannel head and neck coil. We acquired the following sequences: 3D flow-compensated gradient-echo for SWI, T2WI and proton attenuation, FLAIR, and T1WI spoiled gradient-echo with magnetization-prepared inversion recovery pulse. Imaging parameters are presented in On-line Table 1.

Image Analysis and White Matter Signal-Abnormality Classification
SWI-filtered phase images were reconstructed, processed, and analyzed as described previously.[12,15] Each subject's images and WM-SA maps were coregistered into a subject-specific up-sampled FLAIR image space ($576 \times 768 \times 64$) with $0.33 \times 0.33 \times 2$ mm voxels. The FMRIB Linear Image Registration Tool software[28] (http://www.fmrib.ox.ac.uk/) was used to determine the optimal 6 df (rigid-body) registration. Images were resampled by using trilinear interpolation, and WM-SA maps were resampled with nearest neighbor interpolation by using the registration matrix of their associated images. Identification of WM-SAs was done by using a semiautomated edge-detection contouring/thresholding technique.[29]

The classification of phase WM-SAs was previously determined to be reproducible by using the same methodology and rater.[12] Image analyses were performed by a single operator blinded to the clinical status. The operator had 4 years of experience in phase WM-SA identification. WM-SAs were identified separately on T2/proton-attenuation/FLAIR and SWI-filtered phase maps in a blinded manner without a priori knowledge of where the WM-SAs were located with respect to the other technique. Round/oval WM-SAs ≥3 mm were included in the study (Fig 1). In addition, a subset of WM-SAs was visible on both SWI-filtered phase and T2/proton-attenuation/FLAIR; these were identified a posteriori as overlapping when ≥1 voxel overlapped, after unblinding was performed. Location of both T2 and phase WM-SAs was determined and divided into periventricular, juxtacortical, infratentorial, and deep WM regions according to anatomic location. T2 WM-SAs were classified according to the McDonald 2005[30] and 2010[7] criteria for dissemination in space (DIS).

Global and tissue-specific brain volumes were acquired on 3D T1WI by using SIENAX, Version 2.6, in FMRIB.[15] Normalized volume measures of the whole brain, gray matter, white matter, and lateral ventricles were calculated.
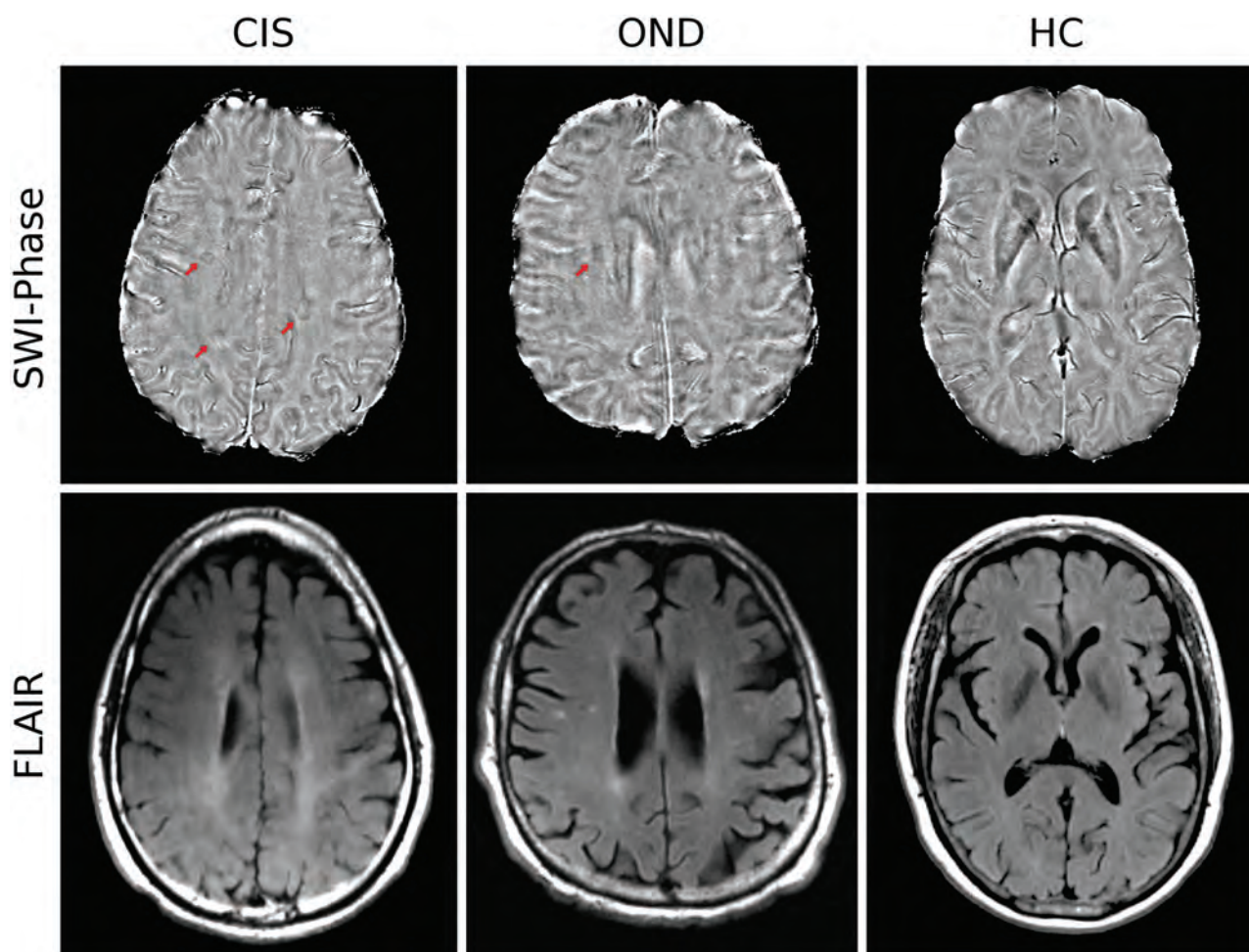
FIG 1. Phase (top) and FLAIR imaging (bottom) WM signal abnormalities in patients with clinically isolated syndrome, other neurologic diseases, and healthy controls. *Red arrows* indicate a hypointense ring on nodular-phase WM-SAs on SWI. Note the presence of phase WM-SA in the right periventricular region in the patient with CIS, which is not present on FLAIR.

Statistical Analysis

Analyses were conducted by using the Statistical Package for the Social Sciences 20.0 (IBM, Armonk, New York) and R for Windows 2.15.2 (R-project; http://www.r-project.org/). Demographic characteristics were compared by using the *t* test and χ^2 test. WM-SA characteristics were compared between groups by using the Mann-Whitney *U* test.

Receiver operating characteristic (ROC) analysis curves were computed to calculate the area under the ROC curve for distinguishing CIS, OND, and HC groups on the basis of the frequency of both phase and T2 WM-SAs. To investigate whether the presence of phase-, T2, and overlapping phase T2 WM-SAs can aid in the differential diagnosis of patients with CIS from HCs and patients with OND, we conducted sensitivity, specificity, and accuracy analysis. We also examined whether the use of dichotomized variables (the presence of multiple phase lesions and a combination of multiple phase lesions with fulfillment of the McDonald 2005[30] and 2010[7] criteria for DIS) may further improve sensitivity and specificity in differentiating patients with CIS from those with OND. Analyses were repeated between patients with CIS who remained stable and those who progressed to CDMS after a 3-year follow-up. All *P* values were adjusted by using the false discovery rate at the *P* < .05 level.[31]

RESULTS

Demographic Characteristics

HC subject groups were age- and sex-matched to patients with CIS and OND (Table 1). Patients with CIS and OND had a mean disease duration of 2.8 ± 3.9 years and 12.3 ±11.2 years, respectively, and patients with CIS had a median Expanded Disability Status Scale score of 1.5 (interquartile range = 1). Patients with CIS had a significantly higher T2 WM-SA volume compared with HCs. Global and tissue-specific brain volumes were consistently smaller in the CIS and OND groups compared with the HC groups but did not reach statistical significance, with the exception of normalized WM volume, which was smaller in patients with CIS. Patients with CIS who converted to CDMS at follow-up did not differ significantly on demographic characteristics from those who did not (*P* > .05).

Presence, Prevalence, and Location of White Matter Signal Abnormalities

Table 2 reports the prevalence of WM-SAs visible on SWI-filtered phase and T2WI and WM-SAs overlapping between these 2 modalities. In total, 186 phase and 770 T2 WM-SAs (92 overlapping) were observed among patients with CIS, whereas HCs only showed 19 phase, 46 T2 WM-SAs, and zero overlapping WM-SAs

Table 1: Demographic characteristics of patients with clinically isolated syndrome and other neurologic disorders and healthy controls[a]

	CIS (n = 48)	HC (n = 47)	P	OND[b] (n = 30)	P[c]
Male/female	11:37	12:35	.766	7:23	.827
Age (yr) (mean)	40.7 ± 11.6	40.1 ± 10.7	.814	40.9 ± 15.6	.780
Age at diagnosis (yr) (mean)	38.3 ± 11.6	–	–	34.6 ± 17.1	–
Disease duration (yr) (mean)	2.8 ± 3.9	–	–	12.3 ± 11.2	–
Expanded Disability Status Scale (median ± IQR)	1.5 ± 1	–	–	–	–
Disease modifying therapy (No.) (%)					
No therapy	21, 43.8				
Interferon β 1a	19, 39.6	–	–	–	–
Glatiramer acetate	7, 14.5				
Other	1, 2.1				
Type of OND (No.) (%)[b]					
Degenerative				10 (33.3)	
Autoimmune	–	–	–	10 (33.3)	–
Vascular				10 (33.3)	
WM-SAV	5.1 ± 8.8	0.1 ± 0.3	<.001	3.4 ± 8.6	.042
Normalized brain volume	1532.6 ± 61.9	1556.4 ± 77.9	.103	1549.3 ± 101	.733
Normalized GM volume	785.8 ± 45.7	783.6 ± 45.1	.814	786.9 ± 82.5	.816
Normalized WM volume	746.9 ± 28.9	772.8 ± 49.8	.003	762.4 ± 37.6	.332
Normalized lateral ventricle volume	36.6 ± 15.2	30.5 ± 10.3	.032	36.2 ± 21.9	.151

Note:—CIS indicates clinically isolated syndrome; HC, healthy controls; IQR, interquartile range; OND, other neurological disorders; –, not applicable; WA-SAV, white matter signal abnormality volume.

[a] Values are presented as means. Volumetric measurements are presented in milliliters. Groups were compared using the χ^2 test and Student t test.

[b] Degenerative disease group (n = 10) included patients with Parkinson disease (n = 6), epilepsy (n = 2), cerebellum syndrome (n = 1), and dementia (n = 1); autoimmune disease group (n = 10) included patients with antiphospholipid syndrome (n = 4), systemic lupus erythematosus (n = 3), neurosarcoidosis (n = 1), acute disseminated encephalomyelitis (n = 1), and chronic fatigue syndrome (n = 1); neurovascular disease group (n = 10) included patients with migraine (n = 7), transitory ischemic attack (n = 1), headache (n = 1), and CNS vasculitis (n = 1).

[c] P value of OND vs HC.

Table 2: Location of white matter signal abnormalities visible on SWI-filtered phase, T2WI, and their overlaps between patients with clinically isolated syndrome, other neurologic disorders, and healthy controls[a]

	CIS (n = 48)		HC (n = 47)		OND (n = 30)		P	P
	(No.) (%)	Mean (SD) Median	(No.) (%)	Mean (SD) Median	(No.) (%)	Mean (SD) Median	CIS vs HC	CIS vs OND
Phase WM-SA								
Total	186 (100)	3.88 (5.18) 2	19 (100)	0.4 (0.85) 0	25 (100)	.83 (2.15) 0	.001	.0001
Periventricular	132 (71)	2.75 (3.26) 2	16 (84.2)	0.34 (0.7) 0	14 (56)	.47 (1.22) 0	.001	.0001
Juxtacortical	15 (8)	0.31 (0.55) 0	0 (0)	0 (0) 0	4 (16)	.13 (.43) 0	.001	.137
Infratentorial	0 (0)	0 (0) 0	0 (0)	0 (0) 0	0 (0)	0 (0) 0	1	1
Deep WM	39 (21)	0.81 (1.99) 0	3 (15.8)	0.06 (0.24) 0	7 (28)	.23 (.68) 0	.012	.232
T2 WM-SA								
Total	770 (100)	16.04 (14.27) 10.5	46 (100)	.98 (2.3) 0	243 (100)	8.1 (11.99) 4.5	.001	.0001
Periventricular	403 (52)	8.4 (5.68) 7.5	4 (9)	.09 (.28) 0	138 (57)	4.60 (4.92) 3	.001	.0001
Juxtacortical	53 (7)	1.10 (1.65) 1	5 (11)	.11 (.43) 0	15 (6)	.50 (1.28) 0	.001	.016
Infratentorial	14 (2)	0.29 (0.68) 0	0	0 (0) 0	1 (0)	.03 (.18) 0	.005	.083
Deep WM	300 (39)	6.25 (8.66) 2.5	37 (80)	.79 (2.1) 0	89 (37)	2.97 (6.63) 0	.001	.010
Overlap								
Total	92 (100)	1.92 (2.97) 1	0 (0) 0	0 (0) 0	12 (100)	.40 (1.4) 0	.001	.0001
Periventricular	70 (76)	1.46 (2.21) 1	0 (0) 0	0 (0) 0	5 (42)	.17 (.53) 0	.001	.0001
Juxtacortical	4 (4)	0.08 (0.28) 0	0 (0) 0	0 (0) 0	3 (25)	.10 (.40) 0	.082	.918
Infratentorial	0 (0)	0 (0) 0	0 (0) 0	0 (0) 0	0 (0)	0 (0) 0	1	1
Deep WM	18 (20)	0.38 (1.06) 0	0 (0) 0	0 (0) 0	4 (33)	.13 (.51) 0	.005	.245

[a] WM signal abnormality numbers were compared between groups using the Mann-Whitney U test. P values have been corrected for false discovery rate at the P < .05 level.

(all $P < .001$). This yielded a ratio of phase WM-SAs and T2 WM-SAs between CIS and HCs of 10:1 and 16:1, respectively. Most interesting, phase WM-SAs were, on average, more prevalent (4.7:1 ratio) among patients with CIS than among those with OND (CIS mean = 3.88 ± 5.2, OND mean = 0.83 ± 2.15, $P < .001$), whereas T2 WM-SAs were more prevalent at a 2:1 ratio for CIS versus OND (CIS mean = 16.04 ± 14.27 versus OND mean = 8.1 ± 11.99, $P < .001$). In subanalyses among patients with CIS who converted to CDMS versus those who did not within a 3-year follow-up period, converters had significantly more phase (CIS mean = 1.6 ± 1.8 versus CDMS mean = 6.2 ± 6.8, $P < .01$) but not T2 or T1 WM-SAs ($P > .05$).

In ROC curve analysis by using the frequency of phase, T2, and overlapping WM-SAs, the areas under the ROC curve for CIS versus HC were 0.782 (Fig 2A), 0.818, and 0.781, respectively. Phase WM-SAs had a moderate-to-high area under the curve in distinguishing CIS from OND (area under the curve = 0.755, Fig 2B). T2 WM-SAs and overlapping WM-SAs had respective areas under the curve of 0.739 and 0.725.

The most common location of phase WM-SAs across all study groups was the periventricular region (56%–84%), followed by the deep WM (16%–28%) and juxtacortical regions (0%–16%) (Table 2). No phase WM-SAs were observed infratentorially. While phase WM-SAs were relatively confined to the periven-
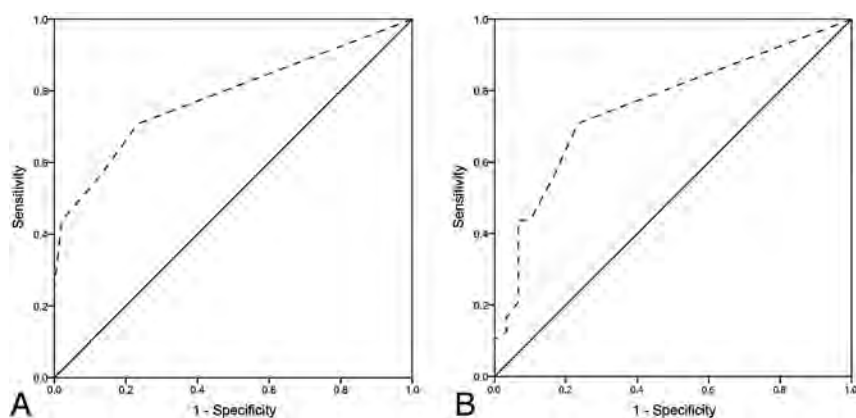
FIG 2. ROC curves for the number of phase white matter signal abnormalities in differentiating patients with clinically isolated syndrome versus healthy controls (*A*) and patients with CIS versus those with other neurologic diseases (*B*).

Table 3: Sensitivity and specificity for the presence of SWI-filtered phase, T2, and their overlapping white matter signal abnormalities among patients with clinically isolated syndrome, other neurologic disorders, and age- and sex-matched healthy controls[a]

	CIS vs HC			CIS vs OND		
	Sensitivity	Specificity	Accuracy	Sensitivity	Specificity	Accuracy
Phase WM-SA						
Total	70.8	76.6	73.7[b]	70.8	76.7	73.1[b]
Periventricular	66.7	76.6	71.6[b]	66.7	80	71.8[b]
Juxtacortical	27.1	100	63.2[b]	27.1	90	51.3
Infratentorial	0	100	—	0	100	—
Deep WM	27.1	93.8	60[c]	27.1	86.7	50
T2 WM-SA						
Total	93.9	68.8	81.4[b]	95.8	13.3	64.1
Periventricular	93.8	91.5	92.6[b]	93.8	13.3	62.8
Juxtacortical	52.1	93.6	72.6[b]	52.1	83.3	64.1[c]
Infratentorial	18.8	100	58.9[c]	18.8	96.7	48.7
Deep WM	81.3	74.5	77.9[b]	81.3	53.3	70.5
Overlapping						
Total	55.1	100	77.3b	56.3	90	69.2[b]
Periventricular	54.2	100	76.8[b]	54.2	90	67.9[b]
Juxtacortical	8.3	100	53.7[b]	8.3	93.3	41
Infratentorial	0	100	—	0	100	—
Deep WM	18.8	100	59[c]	18.8	93.3	47.4

Note:— indicates not applicable.
[a] Sensitivity and specificity were computed using cross-tabulations.
[b] $P < .001$.
[c] $P < .01$. P values have been corrected for false discovery rate at the $P < .05$ level.

tricular region, the occurrence of T2 WM-SAs was divided between the periventricular and deep WM areas. Of the 19 phase and 46 T2 WM-SAs observed in the HC group, no WM-SAs were visible on both sequences. Ninety-two of the 770 T2 WM-SAs (12%) in patients with CIS were also visible on SWI-filtered phase, while among patients with OND, 12 of the 243 T2 WM-SAs (5%) overlapped the SWI-filtered phase.

Sensitivity and Specificity Analysis

Sensitivity and specificity analysis of phase, T2, and overlapping phase T2 WM-SAs is shown in Table 3. The presence of phase WM-SAs was both a sensitive (70.8%) and specific (76.6%) method of differentiating patients with CIS from HCs. Because of the relatively high prevalence of T2 WM-SAs, the sensitivity was 93.9% but the specificity was lower at 68.8%. A high specificity (100%) but medium sensitivity (55.1%) was observed for WM-SAs visible on both T2 and SWI-filtered phase. Most interesting,

the presence of phase (sensitivity, 70.8%; specificity, 76.7%) and overlapping WM-SAs (sensitivity, 56.3%; specificity, 90%) differentiated relatively well patients with CIS and those with OND ($P < .001$), whereas the presence of T2 WM-SAs yielded high sensitivity (95.8%) but low specificity (13.3%). Additional analyses revealed that patients with OND with autoimmune origin other than CIS (a subset of the OND group, $n = 10$) could be accurately differentiated from patients with CIS when considering the presence of phase (sensitivity, 70.8%; specificity, 70%; accuracy, 70.7%) or overlapping phase T2 (sensitivity, 56.3%; specificity, 80%; accuracy, 60.3%), but not with T2 WM-SAs (sensitivity, 93.9%; specificity, 0%; accuracy, 77.9%).

The presence of ≥1 phase WM-SA was more sensitive and similarly specific (Table 3) compared with both the McDonald 2005 (Table 4) and the 2010 (Table 4) criteria for DIS when differentiating patients with CIS and those with OND. When we took into account the presence of multiple phase WM-SAs, the specificity of differentiating patients with CIS from those with OND improved up to 93.3% (Table 4), at the cost of lower sensitivity and accuracy. Combining the presence of multiple phase WM-SAs with the McDonald 2005 and 2010 criteria resulted in high specificity (90%) but lower sensitivity and accuracy.

Similar sensitivity, specificity, and accuracy were calculated between patients with CDMS and non-CDMS when taking into account the combination of McDonald 2005 and 2010 criteria and the presence of multiple phase WM-SAs (On-line Table 2).

DISCUSSION

In this study, the presence, prevalence, and location of phase WM-SAs were investigated in a sample of patients with CIS and OND. There are several important observations from our findings: 1) phase WM-SAs were more prevalent among patients with CIS than in HCs and patients with OND; 2) compared with T2 WM-SAs, phase WM-SAs were specific to patients with CIS and had high overall accuracy compared with individuals with OND and even individuals with OND of autoimmune origin; 3) the presence of >1 phase WM-SA increased the specificity in differentiating CIS from OND but was similar to the 2005 and 2010 McDonald criteria for DIS by using T2 WM-SAs; 4) the presence of multiple phase WM-SAs was associated with progression to

Table 4: Sensitivity and specificity for the presence of multiple SWI-filtered phase signal abnormalities and fulfillment of the McDonald 2005[30] and 2010[7] criteria for dissemination in space between patients with clinically isolated syndrome and other neurologic disorders[a]

	CIS vs. OND		
	Sensitivity	Specificity	Accuracy
≥2 Phase WM-SAs	56.3	83.3	66.7[b]
≥3 Phase WM-SAs	43.8	90	61.5[c]
≥4 Phase WM-SAs	43.8	93.3	62.8[b]
McDonald 2005 criteria for DIS	52.1	80	62.8[c]
McDonald 2010 criteria for DIS	62.5	76.7	67.9[c]
≥2 Phase + McDonald 2005 criteria for DIS	33.3	90	55.1
≥2 Phase + McDonald 2010 criteria for DIS	39.6	90	58.9[c]

Note:— $P < .05$. P values have been corrected for false discovery rate at the $P < .05$ level.

[a] Sensitivity and specificity were computed using cross-tabulations.

[b] $P < .001$.

[c] $P < .01$.

CDMS from CIS; 5) approximately half of phase WM-SAs were not detected by T2WI and may represent unique pathology; and 6) the presence of multiple phase WM SAs was associated with higher conversion to CDMS.

To our knowledge, this is the first study quantifying the occurrence of phase WM-SAs in an early disease course suggestive of MS, as well as OND, including those of autoimmune origin. Approximately three-quarters of phase WM-SAs were observed in the periventricular region, regardless of disease type, whereas T2 WM-SAs were commonly observed in both the periventricular and deep WM areas. This observation, coupled with there being no infratentorial phase WM-SAs, suggests that phase WM-SAs are either mostly present near the ventricles or are most readily detected periventricularly. No juxtacortical phase WM-SAs were observed in any of the HC subjects, yet 8% of patients with CIS and 7% of those with OND had phase WM-SAs near the neocortex. This finding suggests that the presence of juxtacortical phase WM-SAs may be specific to CNS disease, though confirmation is needed in a larger, healthy sample. In addition, zero WM-SAs were visible on both SWI-filtered phase and T2WI in the total sample of 47 HCs, making the presence of overlapping phase T2 WM-SAs another potential biomarker for CNS disease. The number of phase WM-SAs was significantly higher in patients with CIS versus HCs, as well as in patients with CIS versus those with OND. Evidently, the amount of phase WM-SAs was the highest among patients with CIS, with a ratio of 10:1 compared with the HC group. Similar results were observed for T2 WM-SAs. Approximately 50% of phase WM-SAs in patients with CIS were not visible on T2WI and might represent different pathology or WM-SAs at different development stages.[17,32] Inversely, 12% of T2 WM-SAs overlapped with phase WM-SAs, a number in line with but slightly lower than that previously observed (16%–18%) at higher field strengths and in patients at a more advanced disease stage.[24,33]

Even though this study demonstrates that the presence of phase WM-SAs is both sensitive (70.8%) and specific (76.6%) in distinguishing CIS and HCs, the benefit is not substantial compared with T2 WM-SAs. However, the presence of phase WM-SAs had a high sensitivity and specificity in differentiating patients

with CIS and OND, an observation that was even extended to differentiating patients with CIS from those with OND with autoimmune origin. These 2 findings were specific to phase WM-SAs because the presence of T2 WM-SAs had low specificity, limiting its usefulness. Accuracy, a combined measure of sensitivity and specificity, was also higher for phase WM-SAs. This result can be interpreted as the mere presence of phase WM-SAs being suggestive of CIS, whereas T2 WM-SAs can also be observed in other CNS disorders. Indeed, all subjects with OND of autoimmune origin had at least 1 T2 WM-SA.

A recent study showed marked phase shifts in WM-SAs of patients with MS before they appear on conventional MR imaging.[20] Yablonskiy et al[17] reported that the phase contrast observed in MS WM-SAs is dynamic and may be visible at early disease onset. However, others have reported that ringlike phase WM-SAs remained unchanged for several years.[13] Results from the present study indicate that the specificity in differentiating patients with CIS versus those with OND is increased by the presence of multiple phase WM-SAs, even exceeding the specificity of using McDonald 2005[30] and 2010[7] criteria for DIS. In fact, in subanalyses among patients with CIS who converted to CDMS versus those who did not within a 3-year follow-up, converters had significantly more phase, but not T2 or T1 WM-SAs. These results indicate that phase WM-SA, in addition to T2 WM-SAs, may be a valuable additional tool for diagnosis and conversion to CDMS of early patients with a single demyelinating episode. Compared with the McDonald 2005 and 2010 criteria, the presence of ≥3 phase WM-SAs was more specific in distinguishing CDMS and non-CDMS; and combining the presence of ≥2 phase WM-SAs with the McDonald criteria increased the specificity of identifying CDMS to >90%.

Previously, researchers have investigated other nonconventional MR imaging techniques[8,9] (eg, magnetization transfer,[6] diffusion tensor,[34] perfusion,[10] and MR spectroscopy[35]) to potentially increase the level of confidence in the differential diagnosis between MS and other conditions. However, there is no consensus at this time regarding their advantage in the differential diagnosis at first clinical onset. It is currently not entirely understood what phase shifts in WM-SAs constitute. Several properties have been proposed, all of which might have differing levels of effect on phase: iron, demyelination, deoxyhemoglobin, and inflammation, as well as tissue microstructure and fiber orientation.[11] In a recent autoimmune encephalomyelitis mouse-model study, phase WM-SAs correlated with all of these factors independently.[25] A majority of MS WM-SAs have a central vein as seen on MR venography,[36,37] and it stands to reason that some WM-SAs visible on SWI-filtered phase are the result of deoxygenated blood in those veins.

The current study included a group of patients with neurologic disorders other than CIS. Drawing conclusions from such a heterogeneous group is challenging. However, the group was included nonetheless to investigate whether there were any contrasting findings compared to patients with CIS. A subset of patients with OND with autoimmune origin confirmed our findings obtained in the whole sample, and even though the sample size was limited, the presence of phase WM-SAs could differentiate this group and patients with CIS, whereas the T2 WM-SAs could

not. Similarly, subanalyses of CDMS versus non-CDMS were also conducted on a limited sample size. Another limitation of the present study is that subtypes of phase WM-SAs based on their appearance were not investigated.[12-14] Furthermore, the subjects with CIS in the present study were not imaged at clinical onset and may, therefore, represent slightly more advanced patients, potentially influencing the findings. Longitudinal studies are needed to evaluate the value of phase lesions in diagnosing and monitoring patients with CIS and CDMS by dissemination in time and the potential effect of disease-modifying therapy.

CONCLUSIONS

This study showed that WM-SAs visible on SWI-filtered phase are relatively specific to patients with CIS, even compared with individuals with OND of autoimmune origin. This finding could render the imaging of phase WM-SAs a potential biomarker aiding in the differential diagnosis. Future longitudinal studies should reveal the source of phase contrast (iron, demyelination, deoxyhemoglobin, inflammation, and so forth) and thoroughly investigate its clinical significance in CNS disorders.

REFERENCES

1. Poloni G, Minagar A, Haacke EM, et al. **Recent developments in imaging of multiple sclerosis.** *Neurologist* 2011;17:185–204
2. Filippi M, Rocca MA, De Stefano N, et al. **Magnetic resonance techniques in multiple sclerosis: the present and the future.** *Arch Neurol* 2011;68:1514–20
3. Barkhof F. **The clinico-radiological paradox in multiple sclerosis revisited.** *Curr Opin Neurol* 2002;15:239–45
4. Barkhof F. **MRI in multiple sclerosis: correlation with Expanded Disability Status Scale (EDSS).** *Mult Scler* 1999;5:283–86
5. Miller DH, Barkhof F, Nauta JJ. **Gadolinium enhancement increases the sensitivity of MRI in detecting disease activity in multiple sclerosis.** *Brain* 1993;116(pt 5):1077–94
6. Rovaris M, Holtmannspotter M, Rocca MA, et al. **Contribution of cervical cord MRI and brain magnetization transfer imaging to the assessment of individual patients with multiple sclerosis: a preliminary study.** *Mult Scler* 2002;8:52–58
7. Polman CH, Reingold SC, Banwell B, et al. **Diagnostic criteria for multiple sclerosis: 2010 revisions to the McDonald criteria.** *Ann Neurol* 2011;69:292–302
8. Govoni M, Castellino G, Padovan M, et al. **Recent advances and future perspective in neuroimaging in neuropsychiatric systemic lupus erythematosus.** *Lupus* 2004;13:149–58
9. Triulzi F, Scotti G. **Differential diagnosis of multiple sclerosis: contribution of magnetic resonance techniques.** *J Neurol Neurosurg Psychiatry* 1998;64(suppl 1):S6–14
10. Zivadinov R, Bergsland N, Stosic M, et al. **Use of perfusion- and diffusion-weighted imaging in differential diagnosis of acute and chronic ischemic stroke and multiple sclerosis.** *Neurol Res* 2008;30:816–26
11. Yao B, Bagnato F, Matsuura E, et al. **Chronic multiple sclerosis lesions: characterization with high-field-strength MR imaging.** *Radiology* 2012;262:206–15
12. Hagemeier J, Heininen-Brown M, Poloni GU, et al. **Iron deposition in multiple sclerosis lesions measured by susceptibility-weighted imaging filtered phase: a case control study.** *J Magn Reson Imaging* 2012;36:73–83
13. Bian W, Harter K, Hammond-Rosenbluth KE, et al. **A serial in vivo 7T magnetic resonance phase imaging study of white matter lesions in multiple sclerosis.** *Mult Scler* 2013;19:69–75
14. Haacke EM, Makki M, Ge Y, et al. **Characterizing iron deposition in multiple sclerosis lesions using susceptibility weighted imaging.** *J Magn Reson Imaging* 2009;29:537–44
15. Zivadinov R, Heininen-Brown M, Schirda CV, et al. **Abnormal subcortical deep-gray matter susceptibility-weighted imaging filtered phase measurements in patients with multiple sclerosis: a case-control study.** *Neuroimage* 2012;59:331–39
16. Langkammer C, Krebs N, Goessler W, et al. **Susceptibility induced gray-white matter MRI contrast in the human brain.** *Neuroimage* 2012;59:1413–19
17. Yablonskiy DA, Luo J, Sukstanskii AL, et al. **Biophysical mechanisms of MRI signal frequency contrast in multiple sclerosis.** *Proc Natl Acad Sci U S A* 2012;109:14212–17
18. Schweser F, Deistung A, Lehr BW, et al. **Quantitative imaging of intrinsic magnetic tissue properties using MRI signal phase: an approach to in vivo brain iron metabolism?** *Neuroimage* 2011;54:2789–807
19. Hagemeier J, Geurts JJ, Zivadinov R. **Brain iron accumulation in aging and neurodegenerative disorders.** *Expert Rev Neurother* 2012;12:1467–80
20. Wiggermann V, Hernandez Torres E, Vavasour IM, et al. **Magnetic resonance frequency shifts during acute MS lesion formation.** *Neurology* 2013;81:211–18
21. Craelius W, Migdal MW, Luessenhop CP, et al. **Iron deposits surrounding multiple sclerosis plaques.** *Arch Pathol Lab Med* 1982;106:397–99
22. Ferguson B, Matyszak MK, Esiri MM, et al. **Axonal damage in acute multiple sclerosis lesions.** *Brain* 1997;120(pt 3):393–99
23. Trapp BD, Ransohoff R, Rudick R. **Axonal pathology in multiple sclerosis: relationship to neurologic disability.** *Curr Opin Neurol* 1999;12:295–302
24. Grabner G, Dal-Bianco A, Schernthaner M, et al. **Analysis of multiple sclerosis lesions using a fusion of 3.0 T FLAIR and 7.0 T SWI phase: FLAIR SWI.** *J Magn Reson Imaging* 2011;33:543–49
25. Nathoo N, Agrawal S, Wu Y, et al. **Susceptibility-weighted imaging in the experimental autoimmune encephalomyelitis model of multiple sclerosis indicates elevated deoxyhemoglobin, iron deposition and demyelination**. *Mult Scler* 2013;19:721–31
26. O'Connor K, Weinstock-Guttman B, Carl E, et al. **Patterns of dietary and herbal supplement use by multiple sclerosis patients.** *J Neurol* 2012;259:637–44
27. Foster M, Zivadinov R, Weinstock-Guttman B, et al. **Associations of moderate alcohol consumption with clinical and MRI measures in multiple sclerosis.** *J Neuroimmunol* 2012;243:61–68
28. Jenkinson M, Smith S. **A global optimisation method for robust affine registration of brain images.** *Med Image Anal* 2001;5:143–56
29. Zivadinov R, Rudick RA, De Masi R, et al. **Effects of IV methylprednisolone on brain atrophy in relapsing-remitting MS.** *Neurology* 2001;57:1239–47

30. Polman CH, Reingold SC, Edan G, et al. **Diagnostic criteria for multiple sclerosis: 2005 revisions to the "McDonald criteria."** *Ann Neurol* 2005;58:840–46

31. Benjamini Y, Hochberg Y. **Controlling the false discovery rate: a practical and powerful approach to multiple testing.** *Journal of the Royal Statistical Society Series B (Methodological)* 1995;57:289–300

32. Mehta V, Pei W, Yang G, et al. **Iron is a sensitive biomarker for inflammation in multiple sclerosis lesions.** *PLoS One* 2013;8:e57573

33. Eissa A, Lebel RM, Korzan JR, et al. **Detecting lesions in multiple sclerosis at 4.7 Tesla using phase susceptibility-weighting and T2-weighting.** *J Magn Reson Imaging* 2009;30:737–42

34. Rovaris M, Filippi M. **Diffusion tensor MRI in multiple sclerosis.** *J Neuroimaging* 2007;17(suppl 1):27S–30S

35. Richards TL. **Proton MR spectroscopy in multiple sclerosis: value in establishing diagnosis, monitoring progression, and evaluating therapy.** *AJR Am J Roentgenol* 1991;157:1073–78

36. Tan IL, van Schijndel RA, Pouwels PJ, et al. **MR venography of multiple sclerosis.** *AJNR Am J Neuroradiol* 2000;21:1039–42

37. Tallantyre EC, Morgan PS, Dixon JE, et al. **A comparison of 3T and 7T in the detection of small parenchymal veins within MS lesions.** *Invest Radiol* 2009;44:491–94

Prediction of Glioma Recurrence Using Dynamic ¹⁸F-Fluoroethyltyrosine PET

T. Pyka, J. Gempt, F. Ringel, S. Hüttinger, S. van Marwick, S. Nekolla, H.-J. Wester, M. Schwaiger, and S. Förster

ABSTRACT

BACKGROUND AND PURPOSE: Inter- and intratumor heterogeneity and the variable course of disease in patients with glioma motivate the investigation of new prognostic factors to optimize individual treatment. Here we explore the usefulness of standard static and more sophisticated dynamic ¹⁸F-fluoroethyltyrosine-PET imaging for the assessment of patient prognosis.

MATERIALS AND METHODS: Thirty-four consecutive patients with untreated, first-diagnosed, histologically proved glioma were included in this retrospective study. All patients underwent dynamic PET scans before surgery ($\pm$ standard treatment) and were followed up clinically and by MR imaging. Static and dynamic tumor-to-background ratio, TTP, and slope-to-peak were obtained and correlated with progression-free survival.

RESULTS: Twenty of 34 patients experienced progression, with a median progression-free survival of 28.0 ± 11.1 months. Dynamic TTP was highly prognostic for recurrent disease, showing a strong correlation with progression-free survival (hazard ratio, 6.050; 95% CI, 2.11–17.37; $P < .001$). Most interesting, this correlation also proved significant in the subgroup of low-grade glioma (hazard ratio, 5.347; 95% CI, 1.05–27.20; $P = .044$), but not when using established static imaging parameters, such as maximum tumor-to-background ratio and mean tumor-to-background ratio. In the high-grade glioma subgroup, both dynamic and static parameters correlated with progression-free survival. The best results were achieved by defining ROIs around "hot spots" in earlier timeframes, underlining the concept of intratumor heterogeneity.

CONCLUSIONS: ¹⁸F-fluoroethyltyrosine-PET can predict recurrence in patients with glioma, with dynamic analysis showing advantages over static imaging, especially in the low-grade subgroup.

ABBREVIATIONS: FET = ¹⁸F-fluoroethyltyrosine; LGG = low-grade glioma; HGG = high-grade glioma; HR = hazard ratio; PFS = progression-free survival; ROC = receiver operating characteristic analysis; TBR = tumor-to-background ratio

G lial cell tumors account for approximately 80% of all malignant primary brain tumors. In practice, their biologic behavior differs widely from nearly stationary to rapidly and invasively growing lesions. Naturally, the biologic aggressiveness of the tumor is of particular clinical interest, especially with respect to treatment planning; options range from wait and watch to extensive surgery, radiation, and/or chemotherapy. Optimal treatment

for the individual patient depends on a variety of factors and is still a matter of discussion.[1-3] Tumor grading based on histologic properties like cellular proliferation and the presence of necrosis, as described by the World Health Organization classification of brain tumors,[4] is an extensively studied prognostic factor and has, therefore, a major impact on therapeutic decisions. However, in many cases, it is preferable to gain prognostic information before potential surgery. For this purpose, stereotactic biopsies may be performed; nevertheless, these are still invasive procedures and may have sampling errors.

Therefore additional prognostic factors that can be obtained noninvasively have been described or are being investigated.[5,6] Particularly, numerous attempts have been made to use imaging techniques for prognostic stratification. Contrast enhancement in CT and MR imaging indicates disruption of the BBB, which is suggestive of aggressive biologic behavior. Contrast enhancement has been shown to correlate with histologic grading and has also been linked to patient outcome, especially in high-grade gliomas

(HGGs).[7] However, the method has several drawbacks; low-grade gliomas (LGGs) show contrast enhancement in only about 50% of cases; on the other hand, about one-third of nonenhancing gliomas are still classified as high-grade tumors.[8,9] Newer MR imaging–based techniques, such as perfusion imaging and MR spectroscopy, may contribute to better tumor characterization in the future but are still under clinical evaluation and have their limitations.[10,11]

Prediction of prognosis by assessing tumor glucose metabolism by using ^{18}F-fluoroethyltyrosine (FET)-PET has been proposed, but similar to contrast enhancement, this method is suitable primarily for high-grade tumors because FDG uptake in LGG is, in general, much lower and physiologic background uptake in the brain is considerable.[12] Amino acid PET tracers, on the contrary, are attractive for glioma imaging due to intratumoral upregulation of amino acid transport and low background activity.[13] FET generates a reliable strong signal in high-grade brain tumors and still has an uptake well above background in most low-grade tumors (Fig 1).[14] Another important advantage over FDG is the improved discrimination between malignant and benign lesions because no specific uptake of FET in inflammatory lesions is expected.[15] FET is already used in treatment planning and therapy monitoring,[16,17] and there have been suggestions that it might contribute to assessing patient prognosis.[18] A recent study showed the ability of FET-PET to identify malignant progression in LGG by both static and dynamic analysis of FET uptake.[19] With respect to prediction of tumor grade, dynamic evaluation of FET uptake is superior to static analysis.[20,21] This finding also supports the use of dynamic imaging for prognostication. The aim of this study was to establish the value of FET-PET imaging for predicting tumor progression and progression-free survival (PFS) and therefore to justify its use for optimal patient management.

MATERIALS AND METHODS

Patients
Thirty-four consecutive patients (12 women, 22 men; mean age, 41 years) were included in this study. All patients had first been diagnosed with glioma with no prior treatment and were subsequently referred to surgery, in some cases followed by an appropriate adjuvant treatment (see On-line Table 1 for individual patient data). Written informed consent was obtained before each PET scan as part of the clinical routine. Retrospective analysis of the data was approved by the ethics review board of the Technical University of Munich. Histopathologic diagnosis was established by standard light microscopic evaluation of the resected tumors stained with H&E according to the criteria of the latest World Health Organization brain tumor classification.

The primary end point of the study was tumor progression. Progression-free intervals were calculated starting from the baseline PET examination. All patients were followed up clinically. If no clinical signs of progression emerged, basic MR imaging follow-up intervals were 6 months for LGG and 3 months for HGG.[3] Progression was defined on conventional MR imaging.[22,23] In unclear cases, tumor progression was verified by stereotactic biopsy.

PET Studies
We obtained FET-PET scans before treatment with an ECAT Exact HR+ scanner (Siemens, Erlangen, Germany). To achieve standardized metabolic conditions, patients had to fast for a minimum of 6 hours before scanning. After a transmission scan with Germanium-68 sources (duration, 15 minutes), 190 MBq of FET was injected intravenously. Dynamic studies were acquired from 0 to 40 minutes after injection (128×128 matrix, 3D mode) and comprised 16 timeframes (7×10 seconds, 3×30 seconds, 2 minutes, 3×5 minutes, and 2×10 minutes). Data were reconstructed by filtered back-projection by using a Hann filter with a cutoff frequency of 0.34 Nyquist and corrected for scatter and attenuation.

Static Data
Maximum and mean tumor-to-background ratios (TBRmax, TBRmean) were calculated by using a 20- to 40-minute summed frame with a circular 1-cm region of interest around the spot of highest tracer uptake and a contralateral background region of interest according to standard criteria.[24]

Dynamic Data
Dynamic data analysis was performed by using a multimodal-multiparametric analytic imaging software (M3P Anima) developed in our institution.[25] Dynamic tumor activity was measured in a 90% isocontour region of interest around the hottest voxel as described previously.[20,21] Before this step, whether FET uptake in the tumor was high enough to allow adequate region-of-interest definition had to be determined. This decision depended, for example, on tumor localization and background homogeneity, but generally, a static TBR of 1.2–1.3 represented the lower threshold for accurate PET-based region-of-interest delineation. Cases that showed no clear tumor uptake above background were excluded from the dynamic analysis. Because a consensus for an optimal region-of-interest definition in dynamic FET uptake analysis does not yet exist, we investigated ROIs on the basis of different time-frames. For comparison, the reference region of interest was defined in averaged frames 11–13 (very early), 12–14 (early), 14–16 (late), and 11–16 (average) and was subsequently transferred to the whole time-series. As with static analysis, the data were normalized against background uptake, which was derived from a cortical region of interest in the opposite non-tumor-bearing hemisphere. In accordance with earlier publications,[20] background data were determined on a summed image (20–40 minutes after injection) to avoid biasing the rather subtle differences in tumor FET kinetics. On the basis of the normalized time-activity curves, we extracted the following dynamic parameters: peak TBR, defined as the highest TBR with time; TTP; and slope-to-peak, defined as the slope of region-of-interest activity from frame 10 to the peak frame (Fig 2).

Statistical Analysis
The above-mentioned parameters were tested for their ability to predict progression by using receiver operating characteristic analysis (ROC). Decision thresholds were considered optimal when the sum of paired values for sensitivity and specificity reached the maximum. In addition, for each method, the total area under the curve was calculated. Kaplan-Meier curves for PFS were estimated, and the distributions of PFS times were compared between groups by using the log-rank test. For relevant measures, hazard ratios (HRs) with 95% CI were estimated by using the Mantel-Haneszel approach. The patients were further divided

into LGG and HGG subgroups, for which the same tests used for the whole group were executed. The Statistical Package for the Social Sciences, Version 22 (IBM, Armonk, New York) and Prism 5 (GraphPad Software, San Diego, California) were used for statistical analysis. Univariate testing was used because the number of events did not allow a multivariate analysis. A 2-sided level of significance of 5% was used for all tests.

RESULTS

Thirteen of 21 patients (61.9%) with LGG and 11 of 13 patients (84.6%) with HGG showed sufficient FET uptake in the tumor to allow accurate region-of-interest definitions as described above. These relations represent the higher sensitivity of FET imaging for high-grade brain tumors. Twenty of 34 patients experienced progression, with a median progression-free interval of 28.0 ± 11.1 months. No deaths occurred before progression was determined; for this reason, progression-free interval and PFS are used synonymously. Kaplan-Meier analysis and log-rank tests revealed no significant differences in PFS between FET-enhancing and non-enhancing tumors with a hazard ratio of 1.44 (95% CI, 0.56–3.72). This finding also held true when dividing the collective into LGG and HGG subgroups. The respective hazard ratios were 1.275 (95% CI, 0.334–4.870) and 0.8223 (95% CI, 0.153–4.417). All FET-positive HGGs showed a static TBR above the published thresholds for high-grade tumors (TBRmax > 2.0, TBRmean > 1.6), and 7 of 21 low-grade tumors (33.3%) had this property.

As described above, dynamic data were evaluated in FET-enhancing tumors only. For this purpose, tumor ROIs based on different timeframes were investigated. Table 1 shows the area under the curve for ROC analyses of peak TBR, TTP, and slope-to-peak calculated in the respective
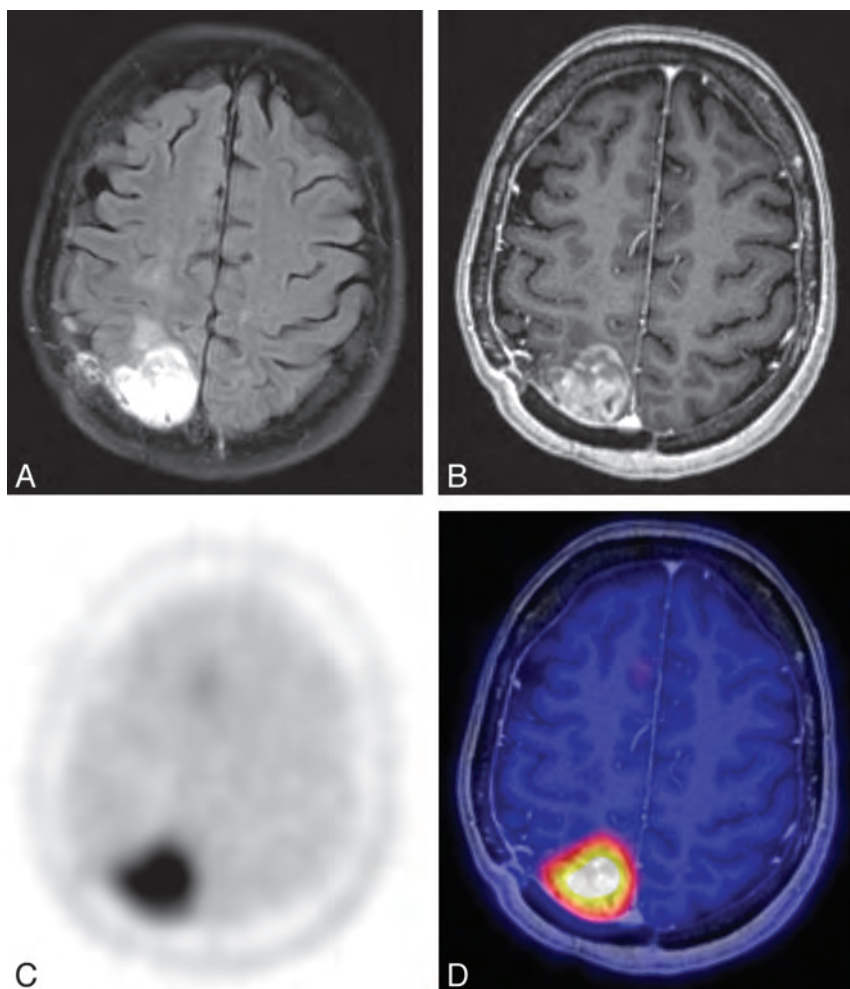
FIG 1. Example of combined FET-PET/MR imaging of a patient with HGG. *A*, T2-weighted FLAIR. *B*, T1-weighted image with Gd-DTPA. *C*, Static FET-PET. *D*, Fused image (*B* and *C*).
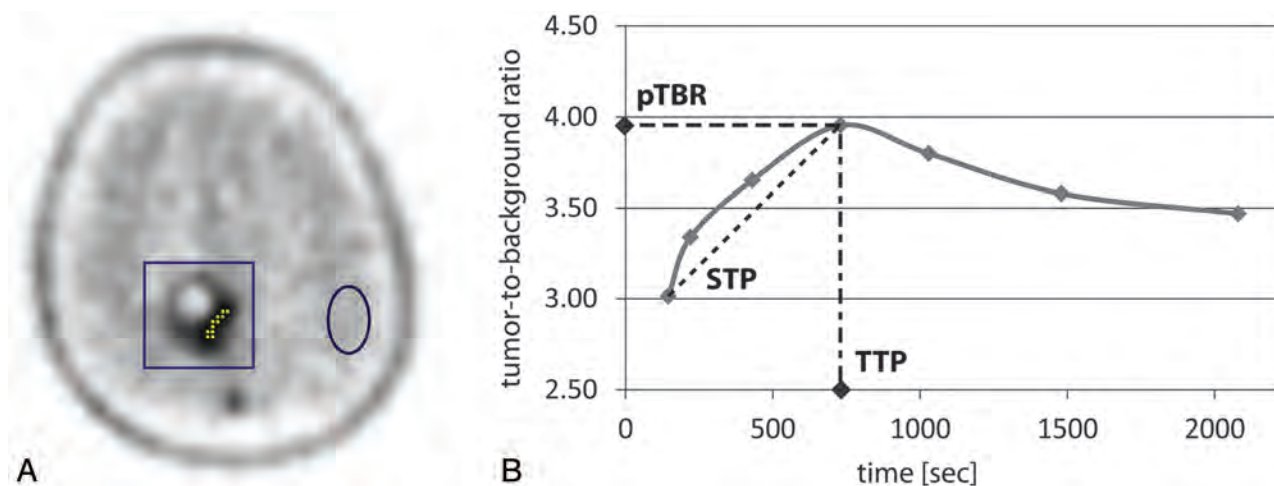
FIG 2. Dynamic FET-PET analysis in a patient with HGG. *A*, Region-of-interest definition with 90% isocontour tumor region of interest (*dots*) and background region of interest (*circle*). *B*, Corresponding time-activity curve with definitions of peak TBR, TTP, and slope-to-peak (STP).

tumor ROIs. These results suggested a region of interest based on early timeframes (frames 12–14 or 5–20 minutes) as the most suitable, and the subsequent analyses were performed by using this definition.

All examined parameters proved valuable for the prediction of PFS in the whole patient collective (Tables 2 and 3 and Fig 3). The property of early FET uptake kinetics as defined by a TTP < 20 minutes (ie, equal or less than frame 14 of 16) demonstrated the best statistical results in Kaplan-Meier/log-rank analysis (HR, 6.05; 95% CI, 2.11–17.37; P < .001; Fig 4). Peak TBR and slope-to-peak with thresholds determined by ROC analysis still showed significant results, but lower hazard ratios (HR, 3.39; P = .023 and HR, 4.73; P = .008). For comparison, static TBR was determined as described above, with results fairly similar to dynamic peak TBR and slope-to-peak (HR, 4.20; P = .010). No relevant differences were found between static TBRmean and TBRmax besides the generally higher values of the latter.

In the subgroup of patients with FET-positive LGG, 6 of 13 patients presented with tumor progression. TTP was by far the best parameter predicting PFS, with an HR of 5.347 (95% CI, 1.05–27.20; P = .044) in survival analysis. The remaining dynamic parameters, as well as static TBRmean and TBRmax, exhibited lower HRs, which were not statistically significant.

Among high-grade patients, our findings were also suggestive of a relation between progression and the examined uptake pa-

Table 1: Comparison of different ROI definitions for dynamic FET analysis

ROI Definition (Frames)	TTP[a]	Peak TBR[a]	Slope-to-Peak[a]
11–13 (Very early)	0.844 (.654–.100)	0.719 (.492–.945)	0.659 (.438–.881)
12–14 (Early)	0.848 (.642–1.00)	0.704 (.477–.930)	0.711 (.503–.919)
14–16 (Late)	0.719 (.494–.943)	0.711 (.482–.940)	0.563 (.333–.793)
11–16 (Average)	0.785 (.569–.100)	0.704 (.476–.931)	0.630 (.406–.854)

[a] Shown are area under the curve values for ROC regarding tumor progression.

Table 2: Evaluation of static and dynamic parameters regarding tumor progression

	ROC (AUC)	ROC Threshold
Dynamic		
Time-to-peak	0.848 (.642–1.00)	<20 Minutes
Peak TBR	0.704 (.477–.930)	>2.20
Slope-to-peak	0.711 (.503–.919)	$>7 \times 10^{-5}$/s
Static		
TBRmax	0.696 (.467–.925)	>2.50
TBRmean	0.696 (.456–.937)	>2.30

Note:—AUC indicates area under the curve.

Table 3: Kaplan-Meier analysis/log-rank test

	All	LGG	HGG
Dynamic			
TTP	P <.001	P = .043	P = .038
	HR, 6.05 (2.11–17.37)	HR, 5.35 (1.05–27.20)	HR, 4.45 (1.09–18.20)
Peak TBR	P = .023	P = .873	P = .022
	HR, 3.39 (1.19–9.68)	HR, 0.87 (0.15–5.08)	HR, 5.84 (1.29–26.4)
Slope-to-peak	P = .008	P = .301	P = .040
	HR, 4.73 (1.50–14.87)	HR, 2.54 (0.43–14.84)	HR, 4.86 (1.06–21.92)
Static			
TBRmax	P = .004	P = .847	P = .007
	HR, 4.20 (1.40–12.58)	HR, 0.84 (0.14–4.95)	HR, 8.19 (1.78–37.67)
TBRmean	P = .010	P = .847	P = .007
	HR, 4.20 (1.40–12.58)	HR, 0.84 (0.14–4.95)	HR, 8.19 (1.78–37.67)
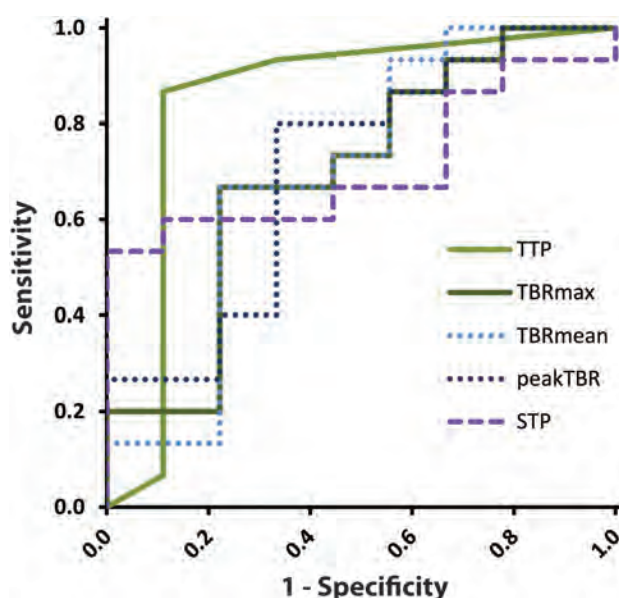
FIG 3. ROC curves for prediction of progression by using TBRmax, TBRmean, peak TBR (pTBR), slope-to-peak (STP), and time-to-peak (TTP).

rameters. Eleven of 13 patients had progressive disease during the follow-up period. Significant results were obtained for both static and dynamic parameters in the Kaplan-Meier analysis. Peak TBR, TBRmean, and TBRmax exhibited slightly better statistical properties than TTP and slope-to-peak (P = .022, .007, and .007 versus P = .038 and .040).

DISCUSSION

In this study, we wanted to clarify the possible role of dynamic FET-PET imaging in assessing the prognosis of patients with first-diagnosed glial cell tumors. The data presented show a correlation of several kinetic parameters and static TBR with PFS. The dynamic parameter TTP proved superior to static TBR, peak TBR, and slope-to-peak and yielded convincing statistic results in the overall patient collective (Tables 2 and 3 and Figs 3 and 4).

TTP also allowed prediction of PFS in the subgroup of low-grade tumors, whereas neither static TBR nor the other dynamic parameters showed a significant correlation with PFS in these patients. An earlier study also proposed a predictive value for static FET uptake in LGG; however, it had an unusually large proportion of patients without initial treatment, with only 3 patients undergoing complete tumor resection.[18] In HGG, on the contrary, we could demonstrate a correlation of PFS with dynamic and static parameters, with static TBR showing slightly better statistical properties in survival curve analysis. These details must be interpreted with care due to the lower number of patients and, in particular, long-time survivors in this subgroup. Similar positive results for static and dynamic FET imaging have been reported by a previous small-sized study focusing on glioblastoma.[26]
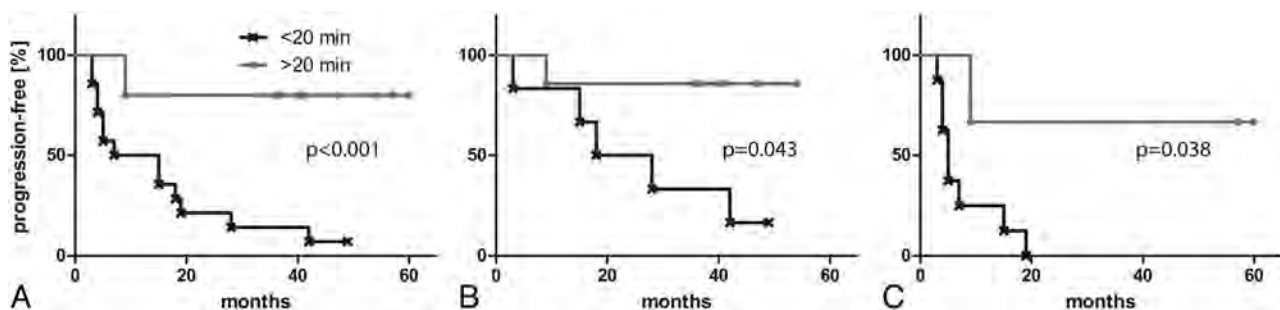
FIG 4. PFS of patients with early and late FET uptake kinetics according to TTP. *A*, All patients. *B*, Patients with LGG. *C*, Patients with HGG.

Our results indicate the presence of certain biologic characteristics in the early-enhancing tumors that go beyond those identified by the H&E staining based on the WHO grading system and that are linked to an unfavorable outcome. The nature of these characteristics has yet to be investigated but may be illuminated by studies that correlate areas identified by time-activity-curve-based analysis or, more demanding, kinetic modeling with new histopathologic markers.[27,28] Until now, whether increased expression of amino acid transporters in tumor cells contributes to rapid FET tracer uptake remains speculative. Another suggestion is an increased vascularity in highly malignant lesions, which would, at least in part, explain both the previously reported steep increase in activity in the beginning and the marked washout in the later timeframes.[20,21]

To obtain the above parameters, we investigated several tumor region-of-interest definitions on different summation timeframes. Time-activity curves deduced from ROIs defined on the earlier timeframes (ie, 5–20 minutes after injection) seem to characterize best the biologic behavior of the tumor, while ROIs defined on the later timeframes perform less well (Table 1). These results are in accordance with earlier publications on tumor grading, which also favored a region-of-interest definition on earlier timeframes.[20] It has already been shown that glial cell tumors exhibit a certain degree of inhomogeneity on the molecular level.[29] Assuming this intratumor variability, the importance of region-of-interest selection can be easily explained because ROIs based on the early timeframes can extract the "hot spots" of biologic aggressiveness, which are expected to show an earlier peak of FET uptake. In the future, a more thorough investigation of this relation should be performed by implementation of a voxelwise analysis of tracer kinetics.

The retrospective design is certainly a limitation of our study. As an additional limitation, the number of events and patients did not allow a multivariate analysis. Prospective studies and larger patient numbers will be necessary before the new predictive parameters presented can be introduced into routine clinical practice.

CONCLUSIONS

In this small, retrospective pilot study, dynamic FET imaging could predict prognosis in glioma and proved superior to static analysis for this purpose, especially in LGG, while both dynamic and static analyses appear useful in HGG. These results underline a previously suggested connection between FET uptake kinetics and tumor biology whose nature still needs to be disentangled.

REFERENCES

1. Viaccoz A, Lekoubou A, Ducray F. **Chemotherapy in low-grade gliomas.** *Curr Opin Oncol* 2012;24:694–701
2. Cloughesy T. **The impact of recent data on the optimization of standards of care in newly diagnosed glioblastoma.** *Semin Oncol* 2011;38(suppl 4):S11–20
3. Stupp R, Mason WP, van den Bent MJ, et al. **Radiotherapy plus concomitant and adjuvant temozolomide for glioblastoma.** *N Engl J Med* 2005;352:987–96
4. Louis DN, Ohgaki H, Wiestler OD, et al. **The 2007 WHO classification of tumours of the central nervous system.** *Acta Neuropathol* 2007;114:97–109
5. Chaudhry NS, Shah AH, Ferraro N, et al. **Predictors of long-term survival in patients with glioblastoma multiforme: advancements from the last quarter century.** *Cancer Invest* 2013;31:287–308
6. Weiler M, Wick W. **Molecular predictors of outcome in low-grade glioma.** *Curr Opin Neurol* 2012;25:767–73
7. Gutman DA, Cooper LA, Hwang SN, et al. **MR imaging predictors of molecular profile and survival: multi-institutional study of the TCGA glioblastoma data set.** *Radiology* 2013;267:560–69
8. Barker FG 2nd, Chang SM, Huhn SL, et al. **Age and the risk of anaplasia in magnetic resonance-nonenhancing supratentorial cerebral tumors.** *Cancer* 1997;80:936–41
9. Scott JN, Brasher PM, Sevick RJ, et al. **How often are nonenhancing supratentorial gliomas malignant? A population study.** *Neurology* 2002;59:947–49
10. Sanz-Requena R, Revert-Ventura A, Martí-Bonmatí L, et al. **Quantitative MR perfusion parameters related to survival time in high-grade gliomas.** *Eur Radiol* 2013;23:3456–65
11. Zonari P, Baraldi P, Crisi G. **Multimodal MRI in the characterization of glial neoplasms: the combined role of single-voxel MR spectroscopy, diffusion imaging and echo-planar perfusion imaging.** *Neuroradiology* 2007;49:795–803
12. Padma MV, Said S, Jacobs M, et al. **Prediction of pathology and survival by FDG PET in gliomas.** *J Neurooncol* 2003;64:227–37
13. Miyagawa T, Oku T, Uehara H, et al. **"Facilitated" amino acid transport is upregulated in brain tumors.** *J Cereb Blood Flow Metab* 1998;18:500–09
14. Jansen NL, Graute V, Armbruster L, et al. **MRI-suspected low-grade glioma: is there a need to perform dynamic FET PET?** *Eur J Nucl Med Mol Imaging* 2012;39:1021–29
15. Weckesser M, Langen K, Rickert C, et al. **O-(2-[(18)F]fluoroethyl)-**

L-tyrosine PET in the clinical evaluation of primary brain tumour. *Eur J Nucl Med Mol Imaging* 2005;32:422–29

16. Niyazi M, Geisler J, Siefert A, et al. **FET-PET for malignant glioma treatment planning.** *Radiother Oncol* 2011;99:44–48

17. Rachinger W, Goetz C, Pöpperl G, et al. **Positron emission tomography with O-(2-[18F]fluoroethyl)-l-tyrosine versus magnetic resonance imaging in the diagnosis of recurrent gliomas.** *Neurosurgery* 2005:57:505–11, discussion 505–11

18. Floeth FW, Pauleit D, Sabel M, et al. **Prognostic value of O-(2–18F-fluoroethyl)-L-tyrosine PET and MRI in low-grade glioma.** *J Nucl Med* 2007;48:519–27

19. Galldiks N, Stoffels G, Ruge MI, et al. **Role of O-(2–18F-fluoroethyl)-L-tyrosine PET as a diagnostic tool for detection of malignant progression in patients with low-grade glioma.** *J Nucl Med* 2013;54:2046–54

20. Pöpperl G, Kreth FW, Herms J, et al. **Analysis of 18F-FET PET for grading of recurrent gliomas: is evaluation of uptake kinetics superior to standard methods?** *J Nucl Med* 2006;47:393–403

21. Pöpperl G, Kreth FW, Herms J, et al. **FET PET for the evaluation of untreated gliomas: correlation of FET uptake and uptake kinetics with tumour grading.** *Eur J Nucl Med Mol Imaging* 2007;34:1933–42

22. van den Bent MJ, Wefel JS, Schiff D, et al. **Response assessment in neuro-oncology (a report of the RANO group): assessment of outcome in trials of diffuse low-grade gliomas.** *Lancet Oncol* 2011;12:583–93

23. Lutz K, Radbruch A, Wiestler B, et al. **Neuroradiological response criteria for high-grade gliomas.** *Clin Neuroradiol* 2011;21:199–205

24. Dunet V, Rossier C, Buck A, et al. **Performance of 18F-fluoro-ethyl-tyrosine (18F-FET) PET for the differential diagnosis of primary brain tumor: a systematic review and metaanalysis.** *J Nucl Med* 2012;53:207–14

25. van Marwick S, Beer A, Metz S, et al. **M3P-anima: a visualization and quantification concept for multimodal, multiparametric imaging.** In: *Proceedings of the 97th Annual Meeting of the Radiological Society of North America,* Chicago, Illinois. November 27–December 4, 2011

26. Thiele F, Ehmer J, Piroth MD, et al. **The quantification of dynamic FET PET imaging and correlation with the clinical outcome in patients with glioblastoma.** *Phys Med Biol* 2009;54:5525–39

27. Labussiere M, Wang XW, Idbaih A, et al. **Prognostic markers in gliomas.** *Future Oncol* 2010;6:733–39

28. Theeler BJ, Yung WK, Fuller GN, et al. **Moving toward molecular classification of diffuse gliomas in adults.** *Neurology* 2012;79:1917–26

29. Little SE, Popov S, Jury A, et al. **Receptor tyrosine kinase genes amplified in glioblastoma exhibit a mutual exclusivity in variable proportions reflective of individual tumor heterogeneity.** *Cancer Res* 2012;72:1614–20

Calvarial Fracture Patterns on CT Imaging Predict Risk of a Delayed Epidural Hematoma following Decompressive Craniectomy for Traumatic Brain Injury

J.F. Talbott, A. Gean, E.L. Yuh, and S.I. Stiver

ABSTRACT

BACKGROUND AND PURPOSE: The development of a delayed epidural hematoma as a result of decompressive craniectomy represents an urgent and potentially lethal complication in traumatic brain injury. The goal of this study was to determine the incidence of delayed epidural hematoma and whether patterns of skull fractures on the preoperative CT scan could predict risk of a delayed epidural hematoma.

MATERIALS AND METHODS: We retrospectively evaluated medical records and imaging studies for patients with acute traumatic brain injury who underwent a decompressive craniectomy during a 9-year period. We compared patterns of skull fractures contralateral to the side of the craniectomy with the occurrence of a postoperative delayed epidural hematoma.

RESULTS: In a series of 203 patients undergoing decompressive craniectomy for acute traumatic brain injury, the incidence of a delayed epidural hematoma complication was 6% (12 of 203). All 12 patients who developed a delayed epidural hematoma had a contralateral calvarial fracture on preoperative CT at the site where the delayed epidural hematoma subsequently formed. A contralateral calvarial fracture has perfect sensitivity (100%) for subsequent development of delayed epidural hematoma in our study population. Moreover, a contralateral calvarial fracture involving 2 or more bone plates had an especially high diagnostic odds ratio of 41 for delayed epidural hematoma.

CONCLUSIONS: Recognition of skull fracture patterns associated with delayed epidural hematoma following decompressive craniectomy may reduce morbidity and mortality by prompting early postoperative intervention in high-risk situations.

ABBREVIATIONS: DC = decompressive craniectomy; DEDH = delayed epidural hematoma; GOS = Glasgow Outcome Scale; ICP = intracranial pressure; TBI = traumatic brain injury

Decompressive craniectomy (DC) has been used with increasing frequency over the past few years to control raised intracranial pressure (ICP) that accompanies severe traumatic brain injury, malignant middle cerebral infarction, and other central nervous system conditions.[1-4] While DC is a potentially life-saving operation, the procedure is associated with a number of complications.[5-7] One potential devastating complication following DC is the development of an epidural hematoma remote to the craniectomy.[6,8-13] This hematoma has been termed a delayed epi-

dural hematoma (DEDH), as it is often first detected on the postoperative CT imaging studies. However, the hematoma may evolve during the decompression and present intraoperatively with external cerebral herniation through the craniectomy defect.[8,11,12] Although initially considered rare, the DEDH has become more common in the last decade with the resurgence of DC as a means to control raised ICP following traumatic brain injury (TBI). Clinical findings associated with DEDH include intraoperative brain swelling,[8] pupillary abnormalities,[14] increased ICP measurements, and acute neurologic deterioration.[5,15] The DEDH represents a potentially fatal complication and often requires a second surgical decompression.[10,15]

A frequent radiographic abnormality found in association with a DEDH is the presence of a calvarial skull fracture, contralateral to the craniectomy (Figs 1–3).[8-13,16] In the case series of Su et al,[8] contralateral calvarial fractures were present on the preoperative CT in 10 of 12 patients who developed a DEDH.[8] In the remaining 2 patients, a radiographically occult fracture was identified intraoperatively during DEDH evacuation. Despite the po-
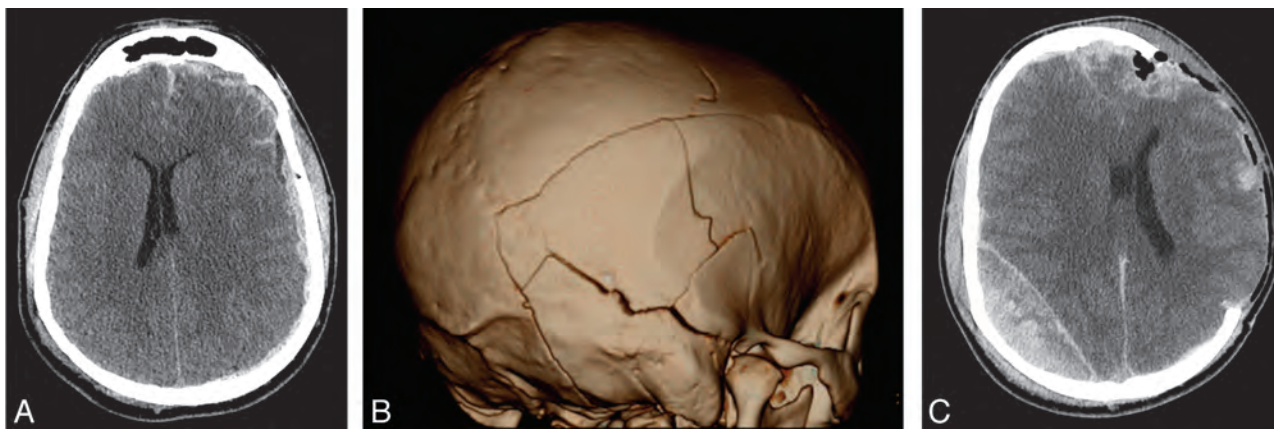
FIG 1. DEDH following decompressive hemicraniectomy for traumatic brain injury. *A*, Axial noncontrast CT at the level of the corona radiata before initial decompression demonstrates diffuse effacement of the cerebral sulci and small holohemispheric subdural hematoma on the left. Small bilateral frontal hemorrhagic contusions and scattered subarachnoid hemorrhage were also present. *B*, Three-dimensional volume-rendered image reconstructed from bone algorithm noncontrast head CT demonstrates complex calvarial fractures on the right involving the right temporal, occipital, and parietal bones. *C*, Noncontrast head CT performed after left decompressive hemicraniectomy shows interval development of a new, large, heterogeneously attenuated epidural hematoma in the right parietal region with new right to left midline shift and left frontotemporal external herniation.

tential high clinical significance of this finding, whether varying fracture patterns are associated with different rates of DEDH in patients undergoing DC has not been studied. Such descriptions would be important as preoperative CT findings implying high risk for DEDH could alert the surgeon to the risks of intraoperative brain swelling through the craniectomy defect and also suggest a need for early postoperative CT imaging to monitor for this potentially fatal complication.

The present study retrospectively evaluated a cohort of 203 patients undergoing DC for acute TBI over a 9-year period. We characterized contralateral calvarial skull fractures in all patients undergoing DC. We compared fracture patterns in patients who did versus those who did not develop DEDH. The goal of this study was to determine the incidence of DEDH after DC and whether skull fracture patterns on the preoperative CT scan can predict risk of a DEDH.

MATERIALS AND METHODS

The study was approved by the Committee on Human Subjects Research and was Health Insurance Portability and Accountability Act compliant. Patients who presented to our Level 1 trauma center with acute TBI and who underwent DC were retrospectively identified from our radiologic database of imaging reports using the search terms "craniectomy" and "hemicraniectomy." The search spanned a 9-year period between 2001 and 2010. Patients undergoing DC for nontraumatic indications or for penetrating trauma, including gunshot wounds, were excluded. Bifrontal decompressive craniectomies were also excluded. There were no age limitations. The study cohort included all patients undergoing DC who met inclusion criteria. The DC surgical procedure entailed removal of a large portion of frontal-temporal-parietal-occipital skull bone that measured approximately 12 by 15 cm. The underlying dura was opened in a stellate fashion to the bone edges, and the scalp flap was closed over the decompressed brain without a duroplasty.

CT studies consisting of thin section (0.625 to 1.25 mm) multidetector-row CT (Lightspeed VCT and CTi; GE Healthcare,

Milwaukee, Wisconsin) images with soft tissue and bone algorithm reconstructions were available for analysis on a PACS viewing station. CT imaging studies of the brain and calvaria were analyzed by 3 neuroradiologists with 4, 8, and over 20 years of experience. Review of the preoperative CT images was performed without knowledge of whether the patient developed a DEDH. The number and distribution of calvarial bone fractures on both sides of the skull were tabulated before review of the postoperative CT. Calvarial fractures were defined as those involving the parietal bone, squamosal temporal bone, calvarial sphenoid, calvarial occipital, and frontal bones. Skull base, nonsquamosal temporal bone, central sphenoid, and facial bone fractures were excluded from analysis. Preoperative CT images were scrutinized for epidural hematomas underlying calvarial skull fractures. In addition, the presence or absence of an acute subdural hematoma, signs of midline shift, and status of the basal cisterns were also recorded from the preoperative CT images. Cisterns were classified as open, effaced, or absent.[17] Postoperative CT images were examined for evidence of a DEDH, contralateral or remote to the craniectomy skull defect, after review of the preoperative CT images was complete. Whether the DC had been performed on the coup versus contre coup side of injury was noted. The relationship between DEDHs and calvarial skull fractures was noted. The DEDH volume, maximum diameter, and midline shift on the postoperative CT were recorded. Volume calculations for DEDHs were based on the Petersen and Espersen equation (one-half × anteroposterior diameter × transverse diameter × craniocaudal diameter in cm).[18,19] Calvarial fracture patterns contralateral to the side of DC were compared between patients who developed versus those who did not develop a DEDH.

Clinical records for the subgroup of patients with complications of a DEDH were reviewed in detail. Patient and injury characteristics, including the preoperative Glasgow Coma Scale, indications for postoperative CT scanning, and time interval from close of surgery to the postoperative CT were collected. Indications for a postoperative CT scan were classified as routine, ele-
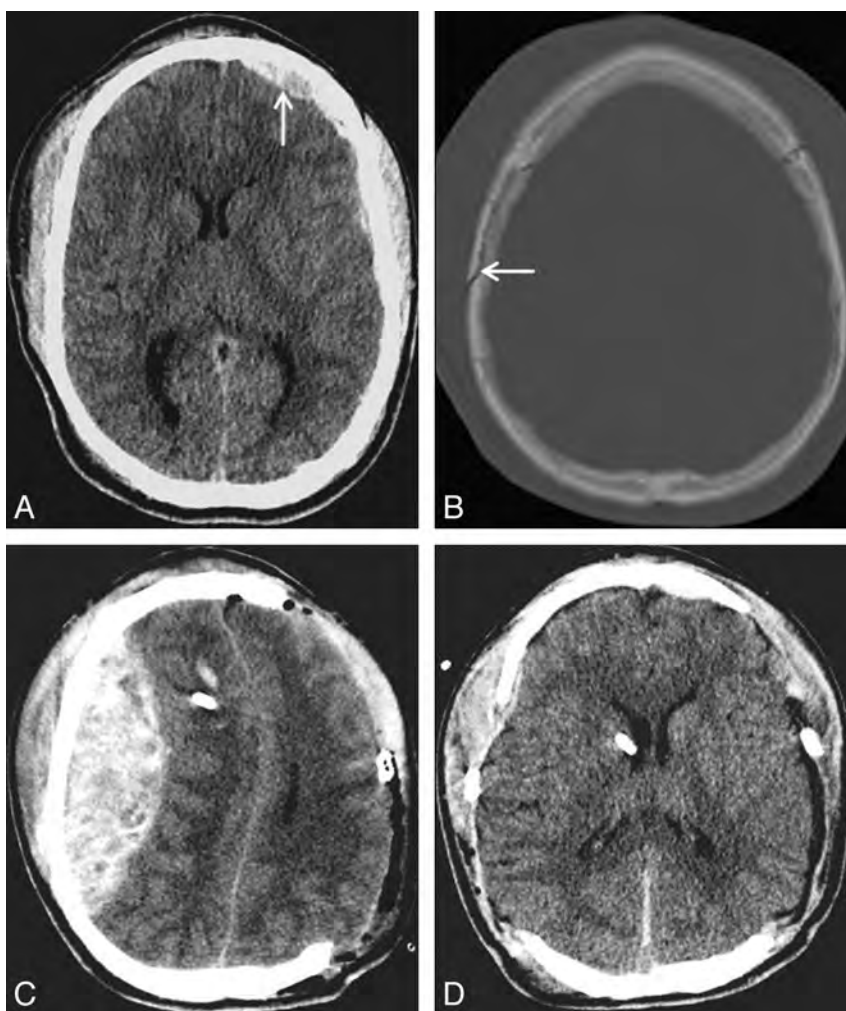
FIG 2. *A*, Axial noncontrast CT at the level of the internal capsules demonstrates a left frontal extra-axial hematoma (*arrow*). There is also diffuse sulcal effacement. *B*, Nondisplaced right-sided parietal calvarial fracture is present on the preoperative CT (*arrow*). Right frontal and temporal calvarial fractures were also present (not shown). Coronal suture diastasis is seen on the left. *C*, Following left-sided decompressive craniectomy, a large, predominantly parietal, DEDH developed adjacent to the patient's right parietal bone fracture. *D*, A decompressive craniectomy was subsequently performed on the right side with evacuation of DEDH and significant improvement in mass effect.

exact tests were used to determine whether there were significantly different rates of DEDH for different calvarial fracture patterns. A *P*-value < .05 was considered statistically significant. Statistical analyses were performed using SPSS version 18 statistical software (IBM, Armonk, New York).

RESULTS

Among 203 patients who underwent DC for acute nonpenetrating TBI, 12 patients (5.9%) developed a de novo DEDH remote to the craniectomy site. In all cases, the preoperative CT scan was devoid of any signs of a pre-existing epidural hematoma in the location where the DEDH later developed. Patient characteristics, injury mechanism, hospital course, and outcome results are summarized in On-line Table 1. This patient subgroup is predominantly composed of men (10 of 12, 83%) with a mean age of 32.3 ± 13.5 years (range 15–57 years). Two-thirds (8 of 12, 67%) of the patients with a DEDH met criteria for a severe TBI (preoperative Glasgow Coma Scale ≤ 8) with a mean preoperative Glasgow Coma Scale score of 7.0 ± 3.3. Mechanisms of injury involved high impact injuries without head protection in 10 of 12 (83%) patients. Assaults, mediated by generally lower energy contact forces, were observed in only 2 (17%) patients.

Preoperative CT imaging findings are summarized in On-line Table 2. The coup site was identified in 9 patients (75%), and the decompressive craniectomy was noted to have been performed on the contre coup side in these 9 patients. Subgaleal scalp swelling was bilateral in 3 (25%) of 12 patients, obscuring assignment of the craniectomy to the coup versus contre coup side. Acute subdural hematomas ipsilateral to the side of the decompressive craniectomy were present in all 12 patients who developed a DEDH. These acute subdural hematomas measured an average thickness of 5.8 ± 2.6 mm with midline shift of 6.4 ± 3.8 mm. In 9 of 12 (75%) patients, the subdural hematoma was categorized as "complex," as evidenced by signs of mass effect in proportion to the thickness of the subdural hematoma. Basal cisterns were compressed in 4 of 12 (33%) patients and completely obliterated in 7 of 12 (58%) patients undergoing DC. Together, signs of raised ICP as judged by midline shift greater than 5 mm and/or obliterated status of the basal cisterns were present in 11 of 12 (92%) patients.

The time interval from completion of the decompressive surgery to the postoperative CT imaging averaged 12.8 ± 17.1 hours. Indications for obtaining a follow-up CT after DC included elevated ICP (*n* = 5), new pupillary deficit (*n* = 3), and routine postoperative surveillance (*n* = 4). Imaging characteristics of the

vated ICP, or clinical findings of a fixed, dilated pupil. We collected information pertaining to hospital course and patient outcome including whether the patient underwent re-operation for evacuation of the DEDH, hospital length of stay, disposition from hospital, and the Glasgow Outcome Scale (GOS) at time of discharge. The GOS is assigned on a scale of 1 to 5, with ratings of 1 (death), 2 (persistent vegetative), 3 (severe disability), 4 (moderate disability), and 5 (good outcome).[20,21] Outcome was dichotomized into favorable (GOS 4 and 5) and unfavorable (GOS 1–3) outcomes.

Continuous data, conforming to a normal distribution curve, were described using mean values ± standard deviation. The Kolmogorov-Smirnov test was used to test whether a variable fitted a normal distribution curve. Categoric variables are presented as percentages. Sensitivity, specificity, and diagnostic odds ratios for calvarial fracture patterns were calculated from counts of the numbers of patients with positive and negative test results for an identifying criterion using standard statistical formulae. Fisher

FIG 3. *A*, Axial noncontrast CT at the level of the internal capsules demonstrates a left-sided frontoparietal subdural hematoma (*arrow*). There is also bilateral subarachnoid hemorrhage, diffuse sulcal effacement, left to right midline shift, and near complete effacement of the left lateral ventricle with early trapping of the right lateral ventricle. *B*, Nondisplaced right occipital calvarial fracture paralleling the ipsilateral lambdoid suture is also identified on the preoperative head CT. A right sided parietal calvarial fracture was also present (not shown). *C*, Following left-sided decompressive craniectomy, postoperative head CT reveals a large right-sided occipital DEDH in the posterior fossa, adjacent to right-sided occipital bone fracture, with severe mass effect on the cerebellum and brain stem and effacement of the fourth ventricle.

Sensitivity, specificity, and diagnostic odds ratio analyses of contralateral calvarial skull fractures for DEDHs after DC

	Any Contralateral Calvarial Fracture (*n* = 55)	Fractures Involving a Single Bone Plate (*n* = 33)	Fractures Involving ≥2 Bone Plates (*n* = 22)
Sensitivity	100%	25%	75%
Specificity	77%	83%	94%
Diagnostic odds ratio	Undefined[a]	1.8	41

[a] The sensitivity of the finding "any calvarial fracture" is 100%, therefore false negatives = 0 and odds ratio is undefined.

DEDHs are summarized in On-line Table 2. Postoperative DEDHs were remarkable for their large size (mean volume = 86.0 ± 67.2 mL; mean thickness 24.8 ± 9.8 mm) and the degree of associated midline shift (mean 9.5 ± 7.0 mm). The location of DEDHs was contralateral to the side of craniectomy in 10 of 12 (83%) of patients. In 2 patients, DEDHs were bilateral, underlying vertex fractures that crossed the midline.

The locations and patterns of skull fractures for all patients undergoing DC are summarized in On-line Table 3. Preoperative CT imaging identified a calvarial fracture contralateral to the planned craniectomy in 55 of 203 patients with DC (27%). In all 12 patients who developed a DEDH, a calvarial fracture(s) was present at the site where the DEDH formed. Fractures contralateral to the DC were confined to a single calvarial bone in 60% (33 of 55) and involved 2 or more calvarial bones in 40% (22 of 55) of patients. Sensitivity, specificity, and diagnostic odds ratio values for the different fracture patterns in relation to occurrence of DEDHs are summarized in the Table. Even though all 12 patients with DEDH had a skull fracture (sensitivity 100%) contralateral to the side of DC, only 3 of these fractures (25%) were limited to a single bone plate. In contrast, the sensitivity of fractures that spanned 2 or more bone plates was 75%. Statistical analysis demonstrated a highly significant association (*P* = .005; Fisher exact

test) between development of a DEDH and contralateral fractures involving 2 or more calvarial bones.

Reoperation was performed in 8 of the 12 (67%) patients who developed a DEDH. In 7 of these 8 patients, DEDHs exceeded the guidelines for surgical evacuation of epidural hematomas in closed TBI (volume over 30 mL with greater than 5 mm of midline shift).[22] Mean Glasgow Coma Scale in the reoperated group of patients was 7.3 ± 3.6 and mean time to acquisition of the postoperative CT was 7.0 ± 7.0 hours. In the reoperated group of 8 patients, the mean DEDH volume was 105.3 ± 65.3 mL, diameter thickness 27.9 ± 9.3 mm, and midline shift 11.4 ± 7.2 mm. One patient had a small DEDH without midline shift; however, intraparenchymal swelling with development of a dilated, fixed pupil on the side of the DEDH prompted a decompressive craniectomy together with evacuation of the small DEDH. This patient ultimately had a persistent vegetative outcome. Five patients underwent reoperation for DEDHs larger than 100 mL (mean volume 148.2 ± 31.6 mL, thickness 33 ± 5.9 mm, and midline shift 15 ± 4.9 mm). In the group of 12 patients with DEDH, 4 patients did not undergo reoperation. In 3 of these 4 patients, the volume of the DEDH was less than 30 mL. One patient, not reoperated upon, had a large DEDH (137 mL) with 13 mm midline shift, but the patient's neurologic condition was deemed nonsurvivable.

Outcome was analyzed for all 12 patients with a DEDH, managed operatively and nonoperatively. The mean hospital length of stay in this group was 45.6 ± 52.9 days. Two patients died within 48 hours of admission. At the time of hospital discharge, outcome was favorable (GOS 4 or 5) in 4 of 12 (33%), and unfavorable (GOS 1–3) in 8 of 12 (67%) patients. In the 8 patients undergoing reoperation for their DEDH, 5 survived (63%) and favorable outcome was achieved in 2 (2 of 8, 25%). Reoperation for the 5 patients with large DEDH over 100 mL yielded 2 survivors (2 of 5, 40%), with Glasgow Coma Scale outcomes of 4 and 3 at time of hospital discharge.

DISCUSSION

As randomized studies strive to define the role of DC in the management of acute TBI, complications directly related to this procedure have become increasingly important.[2,5-7,13,23-27] Complications of a DEDH arise from relief of the tamponade effect and hemorrhagic expansion of an injured meningeal artery, dural vein, or fractured diploe, upon opening of the skull. We observed a 6% incidence of DEDH following DC for acute TBI. This is comparable with the 4.5% incidence of DEDH reported by Matsuno et al.[10] Wen et al[13] recently published the largest cohort to date of 15 patients with TBI developing delayed extra-axial hemataoma contralateral to decompressive craniectomy, with a reported incidence of 6.8%, very similar to our incidence results. In our analysis of 203 preoperative CT scans, the finding of any contralateral calvarial skull fracture had a positive predictive value of 22% and perfect sensitivity (100%) for later development of a DEDH. Furthermore, the number of bone plates involved by the skull fracture was important. Specifically, if 2 or more calvarial bones are fractured on the side contralateral to craniectomy, the diagnostic odds ratio for developing DEDH is 41.

Our study of 12 patients with DEDH complications revealed a number of clinically significant observations. First, after removal of a large portion of the skull, the brain can accommodate large DEDHs with significant degrees of midline shift, without progression to brain death. In our study, only 2 of 12 patients with DEDH met clinical criteria for brain death. Second, patients can harbor DEDH of considerable size without clinical signs. In 2 patients, a DEDH measuring over 100 mL was first detected postoperatively by routine surveillance CT imaging. Third and most importantly, survival and good outcomes may be achieved by reoperation for evacuation of DEDHs. In our study, survival and outcomes following reoperation of even large DEDHs over 100 mL exceeded expectation given the large size and midline shift of these lesions. Confirmation of this trend with larger patient cohorts is warranted. Takeuchi et al[28] observed that CT scans can identify most new postoperative lesions even when performed within 1 hour after surgery for TBI. Thus, recognition of calvarial fracture patterns highly associated with DEDH may allow selection of patients for early postoperative CT scanning to reduce morbidity and mortality associated with DEDH complications after DC.

Our study has several limitations, including its retrospective study design. Over the 9-year span of the study, radiologic imaging protocols and patterns and standards of patient care may well have varied and are sources of potential bias and error. In addition, the small sample of only 12 DEDH lesions limited more detailed statistical analysis of this patient subgroup. Our study is also limited by the lack of long-term patient follow-up and outcome data.

CONCLUSIONS

The presence of a calvarial fracture contralateral to the anticipated side of craniectomy should alert the radiologist and neurosurgeon to the risk of a DEDH complication. This prepares the neurosurgeon for the possibility of intraoperative brain swelling through the craniectomy defect, and identifies high-risk patients in whom an early postoperative surveillance CT scan may be warranted to circumvent devastating neurologic injury from DEDH. Calvarial

fractures involving 2 or more bone plates are particularly highly predictive of DEDH. Recognition of skull fracture patterns associated with DEDH may help to identify patients at risk and prompt closer imaging monitoring to detect DEDH earlier.

REFERENCES

1. Hutchinson P. **Decompressive craniectomy for traumatic brain injury.** *Can J Neurol Sci* 2011;38:541–42
2. Hutchinson PJ, Kirkpatrick PJ. **Decompressive craniectomy in head injury.** *Curr Opin Crit Care* 2004;10:101–04
3. Di Rienzo A, Iacoangeli M, Rychlicki F, et al. **Decompressive craniectomy for medically refractory intracranial hypertension due to meningoencephalitis: report of three patients.** *Acta Neurochir (Wien)* 2008;150:1057–65
4. Hofmeijer J, Kappelle LJ, Algra A, et al. **Surgical decompression for space-occupying cerebral infarction (the Hemicraniectomy After Middle Cerebral Artery infarction with Life-threatening Edema Trial [HAMLET]): a multicentre, open, randomised trial.** *Lancet Neurol* 2009;8:326–33
5. Stiver SI. **Complications of decompressive craniectomy for traumatic brain injury.** *Neurosurg Focus* 2009;26:E7
6. Yang XF, Wen L, Shen F, et al. **Surgical complications secondary to decompressive craniectomy in patients with a head injury: a series of 108 consecutive cases.** *Acta Neurochir (Wien)* 2008;150:1241–47
7. Honeybul S. **Complications of decompressive craniectomy for head injury.** *J Clin Neurosci* 2010;17:430–35
8. Su TM, Lee TH, Chen WF, et al. **Contralateral acute epidural hematoma after decompressive surgery of acute subdural hematoma: clinical features and outcome.** *J Trauma* 2008;65:1298–302
9. Mohindra S, Mukherjee KK, Gupta R, et al. **Decompressive surgery for acute subdural haematoma leading to contralateral extradural haematoma: a report of two cases and review of literature.** *Br J Neurosurg* 2005;19:490–94
10. Matsuno A, Katayama H, Wada H, et al. **Significance of consecutive bilateral surgeries for patients with acute subdural hematoma who develop contralateral acute epi- or subdural hematoma.** *Surg Neurol* 2003;60:23–30
11. Meguro K, Kobayashi E, Maki Y. **Acute brain swelling during evacuation of subdural hematoma caused by delayed contralateral extradural hematoma: report of two cases.** *Neurosurgery* 1987;20:326–28
12. Feuerman T, Wackym PA, Gade GF, et al. **Intraoperative development of contralateral epidural hematoma during evacuation of traumatic extraaxial hematoma.** *Neurosurgery* 1988;23:480–84
13. Wen L, Li QC, Wang SC, et al. **Contralateral haematoma secondary to decompressive craniectomy performed for severe head trauma: a descriptive study of 15 cases.** *Brain Inj* 2013;27:286–92
14. Moon KS, Lee JK, Kim TS, et al. **Contralateral acute subdural hematoma occurring after removal of calcified chronic subdural hematoma.** *J Clin Neurosci* 2007;14:283–86
15. Su TM, Lee TH, Huang YH, et al. **Contralateral subdural effusion after decompressive craniectomy in patients with severe traumatic brain injury: clinical features and outcome.** *J Trauma* 2011;71:833–37
16. Lasierra JL, Fuentes CG, Vazquez DT, et al. **Contralateral extraaxial hematomas after urgent neurosurgery of a mass lesion in patients**

with traumatic brain injury. *Eur J Trauma Emerg Surg* 2013; 39:277–83

17. Maas AI, Hukkelhoven CW, Marshall LF, et al. **Prediction of outcome in traumatic brain injury with computed tomographic characteristics: a comparison between the computed tomographic classification and combinations of computed tomographic predictors.** *Neurosurgery* 2005;57:1173–82

18. Petersen OF, Espersen JO. **Extradural hematomas: measurement of size by volume summation on CT scanning.** *Neuroradiology* 1984; 26:363–67

19. Bullock MR, Chesnut R, Ghajar J, et al. **Appendix I: post-traumatic mass volume measurement in traumatic brain injury patients.** *Neurosurgery* 2006;58:S2–61

20. Wilson JT, Pettigrew LE, Teasdale GM. **Structured interviews for the Glasgow Outcome Scale and the extended Glasgow Outcome Scale: guidelines for their use.** *J Neurotrauma* 1998;15:573–85

21. Jennett B, Bond M. **Assessment of outcome after severe brain damage.** *Lancet* 1975;1:480–84

22. Bullock MR, Chesnut R, Ghajar J, et al. **Surgical management of acute epidural hematomas.** *Neurosurgery* 2006;58:S7–15

23. Hutchinson PJ, Kirkpatrick PJ. **Craniectomy in diffuse traumatic brain injury.** *N Engl J Med* 2011;365:375

24. Timmons SD, Ullman JS, Eisenberg HM. **Craniectomy in diffuse traumatic brain injury.** *N Engl J Med* 2011;365:373

25. Cooper DJ, Rosenfeld JV, Murray L, et al. **Decompressive craniectomy in diffuse traumatic brain injury.** *N Engl J Med* 2011; 364:1493–502

26. Plesnila N. **Decompression craniectomy after traumatic brain injury: recent experimental results.** *Prog Brain Res* 2007;161: 393–400

27. Sahuquillo J, Arikan F. **Decompressive craniectomy for the treatment of refractory high intracranial pressure in traumatic brain injury.** *Cochrane Database Syst Rev* 2006:CD003983

28. Takeuchi S, Takasato Y, Suzuki G, et al. **Postoperative computed tomography after surgery for head trauma.** *J Trauma Acute Care Surg* 2012;73:1254–60

Mechanical Embolectomy for Acute Ischemic Stroke in the Anterior Cerebral Circulation: The Gothenburg Experience during 2000–2011

A. Rentzos, C. Lundqvist, J.-E. Karlsson, V. Vilmarsson, K. Schnabel, and G. Wikholm

ABSTRACT

BACKGROUND AND PURPOSE: Intra-arterial treatment of proximal occlusions in the cerebral circulation have become an important tool in the management of acute ischemic stroke. Our goal was to evaluate the safety and efficacy of intra-arterial acute ischemic stroke treatment performed in our institution in consecutive patients with anterior circulation occlusion during 2000–2011.

MATERIALS AND METHODS: We identified, in our data base, 156 consecutive cases with anterior acute ischemic stroke treated intra-arterially during 2000–2011. Stroke severity was defined according to the National Institutes of Health Stroke Scale, the results of the procedure were defined according to the modified Thrombolysis in Cerebral Infarction score, and clinical outcome was defined according to the modified Rankin scale, with favorable outcome ≤2 at 90 days.

RESULTS: The mean admission NIHSS score was 19.4 (median, 20), with a mean time from stroke onset to groin puncture of 197 minutes (median, 171 minutes). The embolectomy tool of choice was the Amplatz GooseNeck snare (83%). Successful recanalization (modified TICI 2b +3) was seen in 74% of cases. A mRS ≤ 2 at 90 days was seen in 42% with a mortality rate of 17% and symptomatic intracerebral hemorrhage in 4%.

CONCLUSIONS: A high recanalization rate was obtained with the Amplatz GooseNeck snare without any device-related complications. Favorable outcome, mortality, and symptomatic intracerebral hemorrhage are comparable with results of newer embolectomy devices.

ABBREVIATIONS: AIS = acute ischemic stroke; mTICI = modified Thrombolysis in Cerebral Infarction; sICH = symptomatic intracerebral hemorrhage

Treatment with intravenous rtPA has proved successful in acute ischemic stroke within 4.5 hours of stroke onset.[1] However, in patients presenting with a high NIHSS score and proximal occlusions, intravenous treatment has been less successful, with low recanalization rates and increased mortality.[2-5] In the quest for more effective recanalization of proximal occlusions, research in intra-arterial treatment of acute ischemic stroke (AIS) has been ongoing for decades. It started with the intra-arterial injection of rtPA but made an important breakthrough in more recent years with the advent of stent-based embolectomy, especially with the Solitaire FR device (Covidien, Irvine, California), which had a huge impact in the intra-arterial treatment of AIS by substantially improving the recanalization rate. The success of this stent-based embolectomy approach continued with the production of other embolectomy devices such as Trevo (Stryker, Kalamazoo, Michigan) or Revive SE (Codman Neurovascular, Raynham, Massachusetts), which differ in characteristics but are based on the same principle as the Solitaire FR. At the same time, this breakthrough, along with increased competitiveness in the medical industry, brought an improvement of older embolectomy devices such as the Merci retriever (Concentric Medical, Mountain View, California) and the Penumbra System (Penumbra, Alameda, California). Our institution has been actively involved in intra-arterial treatment of AIS, performing intra-arterial thrombolysis and mechanical embolectomies since the beginning of the 1990s.

The Amplatz GooseNeck snare (Covidien) is a very common tool used in interventional radiology for extraction of foreign objects via the endovascular route, but it was first presented as an embolectomy tool in 1998.[6] Extracting a coherent but still softer material such as an embolus with the Amplatz GooseNeck snare involves slight moderation in the technique used for extracting foreign objects.[7] The aim of this retrospective study was to assess the safety and efficacy of these intra-arterial treatment methods in

Table 1: Group characteristics

Age (yr), mean (median)	64 ± 13.9 (67)
Sex	63% men, 37% women
Side of occlusion	60% left, 40% right
Site of occlusion	
Distal ICA	2
Distal ICA+M1	6 10 (6%)
Distal ICA+M2	2
Car-T	45 (29%)
M1	77 84 (54%)
M1+M2 and/or A2/A3	7
M2	13 17 (11%)
M2+other distal emboli	4
Cause of stroke	
Carotid stenosis	17 (11%)
Dissection	12 (8%)
Cardiac	95 (61%)
No identifiable cause	29 (19%)
Periprocedural stroke	3 (2%)
NIHSS score, mean (median)	19.4 ± 4.2 (20)

Note:—Car-T indicates carotid-T.

Table 2: Time intervals

	Mean ± SD (Median)
Stroke to groin puncture	197 ± 81 min (171 min)
Stroke to recanalization	289 ± 87 min (288 min)
Stroke to CT	100 ± 54 min (83 min)
CT to groin puncture	98 ± 65 min (79 min)
Procedure (1st-last image)	102 ± 87 min (92 min)

Table 3: Recanalization grade and functional outcome

mTICI	mRS
0 = 27 (17%)	0–1 = 37 (24%)
1 = 5 (3%)	≤2 = 65 (42%)
2a = 9 (6%)	3 = 29 (19%)
2b = 81 (52%)	4–5 = 35 (22%)
3 = 34 (22%)	6 = 27 (17%)

patients with severe anterior AIS. The patients were treated in our department during 2000–2011; most of the treatments were performed with the Amplatz GooseNeck snare.

MATERIALS AND METHODS

Intra-arterial AIS treatment has been performed in our institution since the early 1990s, initially in the form of intra-arterial thrombolysis and later mechanically, with the addition of embolectomy with the Amplatz GooseNeck snare. The criteria for intra-arterial AIS therapy included no intracerebral hemorrhage on the admission NCCT, NIHSS score of ≥14 when no CTA was performed, proved occlusion on CTA when performed, and treatment initiation within 6 hours. Hypoattenuation in more than one-third of the MCA would not exclude a patient from intra-arterial treatment except in cases in which hypoattenuation extended into most of the MCA territory. Patients admitted to our hospital who were eligible for intra-arterial treatment did not receive intravenous thrombolysis but were transported directly to the neurointerventional suite. In 2009, an intravenous bolus dose of rtPA before intra-arterial treatment was added to the protocol. Bridging therapy with a bolus dose and a continuous infusion of intravenous rtPA (0.9 mg/kg; maximum, 90 mg) was reserved for patients referred to us from other regional hospitals. As a rule, intra-arterial AIS treatment was performed with the patient under general anesthesia. For embolectomy, we mainly used the Amplatz GooseNeck snare but also the Solitaire FR revascularization device, the Merci retriever, and the Catch thrombectomy device (Balt, Montmorency, France). Intra-arterial injection of rtPA locally at the site of occlusion was mainly reserved as a complement to embolectomy or for more distally located emboli. Intra-arterial thrombolysis was rarely used as a primary method, and it was mainly performed earlier in the study period. Overall a combination of different tools was often used.

In our prospective data base, in which all patients treated in our unit are registered, 179 patients who had undergone intra-arterial treatment for anterior AIS since 1991 were identified. One hundred fifty-six such procedures (in 155 patients) met the following inclusion criteria: All patients presented with AIS with an

occlusion in a major artery as described in Tables 1–3. The time of symptom onset was known for all patients, and they had an NIHSS score of ≥14 when no CTA was performed or a proved occlusion on CTA. All pre- and postprocedural radiologic data were available and could be retrieved from the hospital archive. The functional status according to mRS was obtained by a vascular neurologist. In cases in which the mRS was obtained by a nonvascular neurologist or the score was not registered in the medical charts, 1 of our 2 experienced vascular neurologists would contact the patient or close relatives to confirm or obtain the mRS. The radiologic images were reviewed by 2 neurointerventionalists and trained neuroradiologists, and the entire process was under the supervision of a senior neurointerventionalist. In case of disagreement between the 2 reviewers, a repeat review with the supervisor was performed and a consensus-based solution was established. The vascular neurologists were blinded to the modified Thrombolysis in Cerebral Infarction (mTICI) score and the neurointerventionalists, to the mRS.

In the study protocol, we documented the NIHSS score at admission, use of intravenous rtPA, use of general anesthesia, extent of hypoattenuation in NCCT, location of the occlusion in CTA and DSA, use of embolectomy device, recanalization score according to the mTICI scale, complications, functional status according to the mRS at 3 months, all time intervals from stroke onset and NCCT examination to groin puncture, recanalization, and the last image of the procedure. In case of death in the 3-month period, the cause of mortality was established.

Statistical evaluations were performed with the Statistical Package for the Social Sciences, Version 22 (IBM, Armonk, New York) by using descriptive statistics (means, percentages, SDs) for the variables. The χ^2 or the Fisher exact test with a P level < .05 indicating a statistically significant difference was used for comparisons as appropriate.

Institutional review board approval was obtained to review the radiologic and clinical data.

RESULTS

Preprocedural Diagnostic Work-Up

From the 155 patients who fulfilled the study inclusion criteria, 10 had an NIHSS score of <14 but a proved occlusion in the CTA. NCCT of the head was the initial diagnostic method in all cases except 3. Among the 3 patients with no NCCT, 1 had MR imaging

Table 4: Findings on the preprocedural NCCT

	mTICI	mRS < 2	mRS 6
Hyperattenuated MCA sign 114/153 (74.5%)	2b + 3: 86 (75%)	44 (39%)	23 (20%)
Hypoattenuation less than one-third of MCA, 119 (78%)	0–2a: 31 (26%)	6 (19%)	10 (32%)
	2b + 3: 88 (74%)	49 (56%)	5 (6%)
Hypoattenuation more than one-third of MCA, 34 (22%)	0–2a: 15 (44%)	1 (15%)	6 (40%)
	2b + 3: 19 (56%)	8 (42%)	6 (32%)

and 2 had complications of carotid surgery and percutaneous coronary intervention, respectively.

Table 4 shows the findings of the preprocedural NCCT. Most (78%) had hypoattenuation in less than one-third of the MCA territory. If successful recanalization was achieved, a favorable outcome was seen in 56% of patients with hypoattenuation in less than one-third of the MCA territory and, remarkably, in 42% of patients with more than one-third hypoattenuation ($P = .67$). However, the mortality rate was 6% with less than one-third hypoattenuation and 32% with more than one-third hypoattenuation, respectively ($P = .02$). The cause of mortality in the second group, though, was mainly due to unrelated diseases and, in only 2 subjects, due to malignant infarction. The unrelated diseases were one of the following; uncontrolled pulmonary hypertension in a patient with cardiomyopathy, aspiration pneumonia, new stroke in the contralateral MCA in the following days, and perforation during the procedure.

When treatment was unsuccessful, the mortality rate was 32% in patients with hypoattenuation in less than one-third of the MCA territory, and it reached 40% in patients with hypoattenuation of more than one-third, most in this case attributed to malignant infarction and/or symptomatic intracerebral hemorrhage (sICH).

In 92 of the 153 cases, mainly those treated during the second half of the period (2006–2011), the diagnostic imaging protocol included a CTA besides the initial NCCT and the site of intracranial occlusion could be identified in all cases with CTA.

Intra-Arterial Treatment
Most patients were treated under general anesthesia except 14 cases treated under conscious sedation. In 2 cases, the treatment began with the patient under conscious sedation but was converted to general anesthesia. The treatment was initiated within 6 hours from the onset of symptoms in all cases except in 1 in which the treatment started 7 hours after the onset.

The Amplatz GooseNeck snare was used exclusively in 129 cases (83%) as the first device and as second or third device in 6 cases. In 25 cases, it was used to retrieve more distally located significant emboli. Successful recanalization was achieved with the Amplatz GooseNeck snare in 70% of the cases where it was the primary tool (90/129) while in all cases of successful recanalization ($n = 115$) the Amplatz GooseNeck snare was the embolectomy tool in 78% (90/115). No device-related complications could be identified with this snare. During 2000–2005, it was not always used as a first method by all neurointerventionalists because intra-arterial thrombolysis quite often was the first choice. The recanalization rate during this period was only 52%. When the Amplatz GooseNeck snare technique was established as the first method among all neurointerventionalists, the recanalization rate increased to 82% (during 2006–2011).

The Solitaire FR was used in 33 cases, with a recanalization rate of 42% (14/33), while the third most common device was the Merci retriever, used in 18 cases with a recanalization rate of 30% (6/18). However, these devices were mainly used after unsuccessful recanalization with the Amplatz GooseNeck snare and, only in a few cases, as first devices, usually during testing periods when these devices were new.

Intra-arterial thrombolysis with rtPA as the sole treatment method was used in 13 patients with a recanalization rate of 46% (6/13).

A combination of different devices was used in 31% (49/156). In 22 of the 49 cases, the occlusion was in the distal internal carotid or it was a carotid-T occlusion (occlusion in the distal internal carotid artery involving the A1 and M1 segments), while in 12 cases, a combination of devices was needed to extract residual emboli in the M2 and M3 segments or new emboli most often in the A1 and A2 segments.

Complications
Serious complications were seen in 8 cases (5%), with 4 being carotid-T occlusions and 4, M1 segment occlusions. The complications were perforations in 5 cases and dissections in 3 cases. Four patients died due to complications. Those who survived had mRS 2 ($n = 1$), 3 ($n = 2$), and 4 ($n = 1$).

In 4 of the 5 perforation cases, the cause was the microguidewire, and in 2, perforation occurred while trying to reach the occluded vessel via the contralateral circulation through the anterior communicating artery. One of these cases showed no visible subarachnoid hemorrhage in the postprocedural NCCT, despite a documented mild extravasation of contrast on DSA. In the fifth perforation case, a significant stenosis with poor filling of the vascular bed distal to the occlusion was detected in the M1 segment after a successful embolectomy. Attempted balloon dilation in this case resulted in a perforation of the MCA.

Two of the 3 dissections happened during embolectomy with the Merci retriever with subsequent bleeding seen in the postprocedural NCCT in 1 case. In the third case, the dissection was seen after a pass with the Solitaire FR through an M1 occlusion. A control DSA in this case revealed a possible stenosis and probable SAH, but no postprocedural NCCT was available for this patient.

Treatment of severe vasospasm in the M1 segment with local nimodipine infusion was used in 3 cases, with regression of the vasospasm in 2 cases, while in the third, the vasospasm after embolectomy with the Merci retriever was substantial and was so severe that only minimal flow could be seen distal to the vasospasm with no filling of the vascular bed.

Postprocedural Radiologic and Neurologic Results
In 150 cases, a postprocedural NCCT was available, with a mean acquisition time of 26 hours 31 minutes from the end of the DSA.

An mRS score was available in all 155 patients, with mRS ≤ 2 in 42% (65/155). In 115 cases with mTICI 2b/3, mRS ≤ 2 was seen in 51% (59/115). One patient had 2 stroke episodes and received intra-arterial therapy twice. Bad functional outcome (mRS 3–6) was as high as 85% in patients with unsuccessful recanalization, decreasing dramatically to 49% in patients with successful recanalization ($P < .01$). The mortality rate (mRS 6) after 3 months was 17%. Death related directly to the ischemic stroke and the endovascular procedure was observed in 17 patients (11%), while death from other causes was found in 10 patients (6%). Comparing the mortality rate in patients with unsuccessful and successful recanalization yielded a significant difference of 39% (16/41) and 10% (11/115), respectively ($P < .01$).

Dividing the patients into a group with a stroke onset–to–groin puncture time of <180 minutes and a group with a time of >180 minutes resulted in 80% recanalization rate and a 42.5% mRS ≤ 2 for the first group and a 67% recanalization rate ($P = .07$) and a 41% mRS ≤ 2 ($P = .8$) for the second group. The same analysis, except using 270 minutes as a cutoff point, yielded the same recanalization rate of 74% for both groups ($P = .98$) and an mRS ≤ 2 with only a slight difference, 43% for the group with stroke onset–to–groin puncture of <270 minutes and 41% for >270 minutes ($P = .47$).

The rate of sICH, as defined in the Safe Implementation of Thrombolysis in Stroke-Monitoring Study criteria was difficult to calculate due to lack of an early postprocedural NIHSS estimation in some patients. The presence of PH2 and review of the medical charts for a description of obvious deterioration in the patient's status were used with sICH estimated at 4%. The patients with sICH were equally distributed in the groups with stroke onset–to–groin puncture time under and over 180 minutes and equally distributed in groups showing hypoattenuation in less and more than one-third of the MCA territory. In 5 patients, SAH was identified and attributed to procedural complications as described earlier, except in 1 case in which a traumatic SAH was identified during review of the preprocedural NCCT.

Sixteen patients identified in 2000–2011 received bridging therapy. Successful recanalization was seen in 75%, while mRS ≤ 2 was seen in 31% ($P = .4$). Bleeding was seen in only 3 patients who received bridging therapy, and none were symptomatic.

A subanalysis of patients with carotid-T occlusion (45/156) shows that carotid-T occlusions have the lowest recanalization rate (55.5%) with a favorable outcome of 33% and a mortality rate of 22%. Patients presenting with M1 and/or M2 occlusions showed a higher recanalization rate (83%) compared with carotid-T occlusions ($P = .01$), an mRS ≤ 2 at 46%, and lower mortality rate (13%) than the average mortality rate of all patients in the study (17%).

DISCUSSION
Our study shows that a high recanalization rate can be achieved with the Amplatz GooseNeck snare, which can be used fast and safely for restoration of intracerebral circulation. The Amplatz GooseNeck snare technique was not established among neurointerventionalists in our department from the beginning, and commonly, intra-arterial thrombolysis was used as the first method. When the Amplatz GooseNeck snare became the standard embo-

lectomy method and the stroke logistics were restructured in our hospital leading to an increased proportion of patients receiving intra-arterial treatment, the recanalization rate reached 82% (2006–2011). During this time, a number of new devices were tried in our department, most commonly the Merci retriever first and later the Solitaire FR, the latter being, for the moment, our second device. The Amplatz GooseNeck snare is kept as the device of choice because newer devices have not shown any better results, are more expensive, and have shown a higher complication rate. Moreover, the catheterization time was not longer than in newer devices and may be faster, given that no incubation time is required after deployment and before the retrieval of the device (Fig 1).

Lastly, no procedural complications could be identified with the Amplatz GooseNeck snare, while a number of complications occurred with other devices or with the guidewire while trying to bypass the occlusion, something that it is not required with the Amplatz GooseNeck snare. However, the Solitaire FR, Merci retriever, and the other devices in our study were used as the first choice in only a few cases, usually during the test period for each device. As a rule, we used these devices only when recanalization was unsuccessful with the Amplatz GooseNeck snare. In most cases, these devices did not succeed either, leading to the low recanalization scores presented in the "Results." Studies in which these devices are the first choice show high recanalization rates and are more representative of the stent retrievers' true efficacy.[8]

The Amplatz GooseNeck snare reaches recanalization rates comparable with the newer stent retriever and, at the same time, offers advantages like cost-effectiveness and low complication rates, which make it a feasible and reliable embolectomy device, increasing the device choices available in the treatment of AIS.

Our study represents consecutively treated patients who received intra-arterial AIS treatment based mainly on clinical criteria of eligibility. Hypoattenuation in more than one-third of the MCA territory on NCCT was not an absolute contraindication. Many patients who would otherwise have been excluded by using the one-third hypoattenuation rule or even the ASPECTS as an absolute criterion were classified as eligible for intra-arterial treatment in our institution. The analysis of the preprocedural diagnostic work-up shows that there is a group of patients with hypoattenuation in more than one-third of the MCA territory who do benefit from successful recanalization. This patient group has a high mortality rate, but the causes of mortality in this group were, in most, not related to malignant infarct or sICH. Failing, however, to restore the circulation in this patient group leads to a slightly higher mortality rate and, more important, the causes of mortality are mostly related to malignant infarct and/or sICH. Using one-third of the MCA territory as the cutoff point for patient selection would have improved the total mRS of the group but, at the same time, would exclude many eligible patients with a poor prognosis who might benefit from the treatment, either reaching a good functional outcome or at least surviving. This highlights the necessity of improving our selection criteria.

The worst recanalization rate was seen in patients with carotid-T occlusion. A combination of different devices was often used in this type of occlusion. Good functional outcome was reached only after a successful recanalization in all but 1 of the

FIG 1. *A,* Occlusion of the left M1 segment with a 4-mm snare pushed out of the microcatheter just enough to open fully and take its built-in shape perpendicular to the catheter and vessel. *B,* The snare with the microcatheter is pushed forward to engulf the embolus, with a slight deformation of the snare loop indicating that the loop is surrounding the embolus. *C,* Careful partial withdrawal of the snare into the microcatheter is seen, leaving a small eye outside the catheter tip. *D,* The microcatheter with the snare is carefully pulled back, and a careful control injection is performed showing the embolus hanging from the catheter tip in the distal ICA (*arrow*), while the M1 and M2 segments are open (slightly different projection angle than in *A–C*). The snare and the microcatheter are again pulled back as 1 unit, and aspiration via the guide catheter is performed simultaneously.

patients with carotid-T, making recanalization the only possibility for a good outcome in these patients.

Our study shows that successful recanalization is essential to reaching independence and significantly decreases the mortality rate, while the 180- or 270-minute cutoff point from stroke onset to groin puncture does not significantly influence the recanalization rate, the neurologic outcome, or the occurrence of sICH.

Treating patients with occlusion of a major proximal artery with intravenous rtPA alone can be successful in some cases but usually leads to unsuccessful or delayed recanalization, followed by increased morbidity and mortality rates.[2-5] The efficacy of the mechanical embolectomy has never been validated through randomized trials until recently, when the results of the Interventional Management of Stroke III and Synthesis Expansion randomized studies were published.[9,10] Both studies compared intra-arterial treatment of AIS with intravenous thrombolysis alone but were not able to prove the superiority of the intra-arterial approach. However, in these studies, only intra-arterial thrombolysis and mostly older-generation devices were used, with a poor-to-moderate recanalization outcome. In addition, a preprocedural CTA to prove large-vessel occlusion was not performed in most patients; this procedure should be a prerequisite in such randomized trials.[11,12] There is, thus, a need for further investigation of the efficacy of the intra-arterial stroke treatment with a newer generation of devices such as stent retrievers and devices with proven good recanalization rates. Furthermore, unbiased comparison of the 2 methods requires that group characteristics and stroke severity be equal for both arms of treatment—that is, an NIHSS score between 10 and 24 points with proved

occlusion, excluding patients with a low NIHSS score where intra-arterial treatment is not indicated, and patients with >25 NIHSS points when intravenous thrombolysis is contraindicated.

While a satisfactory recanalization rate of occlusion in major arteries can be achieved with the Amplatz GooseNeck snare and the newer embolectomy devices,[13,14] further research is also needed to improve the selection of patients eligible for intra-arterial treatment. We recently added CT perfusion to our diagnostic protocol in an effort to better detect patients with an established infarct core and no or minimal penumbra to rescue and even patients with a large infarcted area who can eventually be at risk for sICH after a successful recanalization.[15] With this approach, we also hope to identify patients outside the present time window or with an unknown time of onset (eg, wake-up stroke) who may benefit from intra-arterial treatment.

Continuous effort to minimize the time between stroke onset and treatment initiation along with a rising public awareness of stroke symptoms would further contribute to a decrease in the morbidity and mortality rates.

CONCLUSIONS
Embolectomy with the Amplatz GooseNeck snare is safe and effective, reaching recanalization rates and functional outcome comparable with results of the newer embolectomy devices. Patients presenting with hypoattenuation in more than one-third of the MCA territory might benefit from intra-arterial treatment and should not be excluded. Successful recanalization is the most essential parameter for a good clinical outcome and survival of

these patients; improvement of the selection process of patients eligible for intra-arterial AIS treatment, good organization of the stroke unit, and rising public awareness will improve the clinical outcome in the future. However, there is a need of further validation of mechanical embolectomy, which will require new randomized studies.

REFERENCES

1. Wahlgren N, Ahmed N, Dávalos A, et al. **Thrombolysis with alteplase 3–4.5 h after acute ischaemic stroke (SITS-ISTR): an observational study.** *Lancet* 2008;372:1303–09
2. Bhatia R, Hill MD, Shobha N, et al. **Low rates of acute recanalization with intravenous recombinant tissue plasminogen activator in ischemic stroke: real-world experience and a call for action.** *Stroke* 2010;41:2254–58
3. Porelli S, Leonardi M, Stafa A, et al. **CT angiography in an acute stroke protocol: correlation between occlusion site and outcome of intravenous thrombolysis.** *Interv Neuroradiol* 2013;19:87–96
4. Smith WS, Lev MH, English JD, et al. **Significance of large vessel intracranial occlusion causing acute ischemic stroke and TIA.** *Stroke* 2009;40:3834–40
5. Rangaraju S, Owada K, Noorian AR, et al. **Comparison of final infarct volumes in patients who received endovascular therapy or intravenous thrombolysis for acute intracranial large-vessel occlusions.** *JAMA Neurol* 2013;70:831–36
6. Wikholm G. **Mechanical intracranial embolectomy: a report of two cases.** *Interv Neuroradiol* 1998;4:159–64
7. Wikholm G. **Transarterial embolectomy in acute stroke.** *AJNR Am J Neuroradiol* 2003;24:892–94
8. Broussalis E, Trinka E, Hitzl W, et al. **Comparison of stent-retriever devices versus the Merci retriever for endovascular treatment of acute stroke.** *AJNR Am J Neuroradiol* 2013;34:366–72
9. Broderick JP, Palesch YY, Demchuk AM, et al. **Endovascular therapy after intravenous t-PA versus t-PA alone for stroke.** *N Engl J Med* 2013;368:893–903
10. Ciccone A, Valvassori L, Nichelatti M, et al. **Endovascular treatment for acute ischemic stroke.** *N Engl J Med* 2013;368:904–13
11. Nogueira RG, Gupta R, Dávalos A. **IMS-III and SYNTHESIS expansion trials of endovascular therapy in acute ischemic stroke: how can we improve?** *Stroke* 2013;44:3272–74
12. Pierot L, Gralla J, Cognard C, et al. **Mechanical thrombectomy after IMS III, Synthesis, and MR-RESCUE.** *AJNR Am J Neuroradiol* 2013;34:1671–73
13. Saver JL, Jahan R, Levy EI, et al. **Solitaire flow restoration device versus the Merci retriever in patients with acute ischaemic stroke (SWIFT): a randomised, parallel-group, non-inferiority trial.** *Lancet* 2012;380:1241–49
14. Kwak JH, Zhao L, Kim JK, et al. **The outcome and efficacy of recanalization in patients with acute internal carotid artery occlusion.** *AJNR Am J Neuroradiol* 2014;35:747–53
15. Zhu G, Michel P, Aghaebrahim A, et al. **Computed tomography workup of patients suspected of acute ischemic stroke: perfusion computed tomography adds value compared with clinical evaluation, noncontrast computed tomography, and computed tomography angiogram in terms of predicting outcome.** *Stroke* 2013;44:1049–55

Evaluation of the Pontine Perforators of the Basilar Artery Using Digital Subtraction Angiography in High Resolution and 3D Rotation Technique

S. Lescher, T. Samaan, and J. Berkefeld

O⊷

ABSTRACT

BACKGROUND AND PURPOSE: Compromise of perforating branches of the basilar artery resulting in brain stem infarctions has been described as a major complication of intracranial stent placement for basilar artery stenosis or after implantation of endovascular flow diverters. Descriptions of pontine arteries are mainly based on examinations of injection specimens; however, there is a lack of consistent presentation of the small branches of the basilar artery in the imaging literature. Therefore, we retrospectively analyzed DSA images and 3D rotational angiography with a review of literature for an imaging definition of microvascular anatomy of the brain stem.

MATERIALS AND METHODS: We retrospectively analyzed 2k DSA images (detector format 32 × 32 cm; image matrix 2480 × 1920 pixels) and 3D rotational angiography reconstructions (5 second DSA, subtraction technique) obtained on Axiom Artis zee biplane neuroradiologic angiography equipment using standard protocol.

RESULTS: On 2D and 3D DSA images, small arterial side branches of the basilar artery can be demonstrated in each of the cases but with a wide variation in the visibility of these vessels. Compared with 2D DSA images, 3D DSA reconstructions allow superior visualization of the small branches of the basilar artery.

CONCLUSIONS: Our results demonstrate that 2D DSA and 3D-rotation techniques are able to reliably visualize the penetrating branches of the brain stem in vivo. No zone of basilar artery is free from important side branches. Collateral pathways between circumferential and perforating arteries are occasionally detectable. In the future, further refinement of imaging techniques is necessary to increase the reliability of small vessel angiography to use this data for risk assessment before stent placement and aneurysm treatment.

ABBREVIATIONS: 3DRA = 3D rotational angiography; 2k matrix DSA = detector format 32 × 32 cm; image matrix 2480 × 1920 pixels

Compromise of perforating branches of the basilar artery has been described as a major complication of intracranial angioplasty and stent placement or implantation of endovascular flow diverters.[1,2] Because of the small diameter of these side branches of 383 μm, visualization by different means of angiographic imaging like CT- or MR-based angiography is difficult and uncertain.[3]

High-resolution DSA images with 2k matrix (detector format 32 × 32 cm; image matrix 2480 × 1920 pixels) and especially flat detector CT with pixel sizes of 308 μm × 308 μm (2 × 2 binning), using a reconstructed section thickness of 0.1 mm and high-contrast resolution of CT and 3D reconstructions, provide a new basis to display these small vessels on recent flat detector neuroangiography systems.[4] We hypothesized that the 3D-rotation technique allows superior visualization of the small branches of the basilar artery than 2D DSA images do.

The microvascular anatomy of the vertebrobasilar junction and the distal basilar tip has been described in detail in the neurosurgical and neuroradiologic literature.[5-7] Remarkably, there are no comparable descriptions of the proximal and middle portion of the basilar artery in the imaging and neurosurgical literature. As such, anatomic knowledge is based on examinations of post mortem injection preparations.[8,9]

A continuation of patterns of the spinal cord vascular supply has been postulated for the brain stem with additional circumferential branches for the pons and cerebellum.[7]

The presence of perforating branches is known; however, in the past, angiographic imaging was far away from reliable pattern recognition and display of potential collateral pathways.

The lack of consistent descriptions in the imaging literature raised the question of whether the latest generations of flat detec-

tor neuroangiography allow for more reliable visualization of the pontine branches of the basilar artery with the use of 2k matrix DSA images and 3D rotational angiography.

Therefore, we retrospectively analyzed 2k DSA images and 3D rotational angiography reconstructions together with a review of the literature for an imaging definition of the microvascular anatomy.

MATERIALS AND METHODS

For retrospective analysis, we identified 41 consecutive cases with indications for selective vertebral angiography and 3D rotational angiography (3DRA) in a period from January 2011 until March 2013. Twenty-one datasets with minor image quality due to incomplete contrast filling or movement artifacts were excluded. Twenty datasets with adequate image quality were selected for further evaluation.

The protocol was authorized by the ethics committee of Frankfurt.

All angiograms and 3DRA data were obtained on an Axiom Artis zee biplane (Siemens, Erlangen, Germany) neuroradiologic angiography system. The angiographic system is equipped with a flat panel detector with 2480 × 1920 pixels (2k matrix) and a pixel pitch of 154 μm × 154 μm.

For the evaluation of pontine arteries, 2k DSA images using high-resolution technique and 3DRA runs of the basilar artery between the vertebrobasilar and the pontomesencephal junction were analyzed. Indications for DSA and especially 3DRA were justified by suspected pathologies like aneurysms (ruptured/unruptured), arteriovenous malformations, stenosis, infarctions, or vasculitis.

DSA with 2k Matrix

Compared to former angiographic systems equipped with an 1k image matrix of 1240 × 960 pixels, the newest generations of angiographic systems provide improved and higher spatial resolution using a 2k image matrix of 2480 × 1920 pixels and a flat detector zoom format of 32 × 32 cm in each plane. For retrospective evaluation of DSA images in standard Towne and lateral projections, we selected 20 consecutive cases with normal findings in the intracranial vertebrobasilar circulation and good image quality. DSA images were obtained using a standard program with a variable frame rate with 4 frames per second in the arterial phase, a small focus with a focal spot size of 0.3 mm, and edge enhancement reconstruction algorithm. A flat detector zoom format of 32 × 32 cm in each plane was used. In addition, 4–6 mL of non-ionic contrast material was applied via hand injection after selective catheterization of the dominant vertebral artery. The average effective dose of this examination was 2.7 mSv measured in an anthropomorphic Alderson-Rando phantom with thermoluminescence dosimetry.

Image evaluation was done retrospectively by consensus of 2 experienced reviewers who counted the number of visible side branches at each side of the basilar artery and distinguished between circumferential arteries and AICA variants. They described whether circumferential arteries were displayed in a segmental or more irregular network pattern and whether common trunks or anastomoses between adjacent branches were present.

The reviewers also looked for direct paramedian pontine perforators.

3D Rotation Technique

In the 20 patients with indications for 3DRA of the posterior circulation, we reconstructed the stored raw data of 3D DSA runs with a scan time of 5 seconds. A native rotational run was followed by contrast-enhanced images after mechanical intra-arterial injection of 20 mL of nonionic contrast material (Ultravist 240; Bayer-Schering, Berlin, Germany) into the dominant vertebral artery with a flow of 3 mL/s. Injection was started 2 seconds before the contrast-enhanced run. In each run, 133 images were obtained with a scan time of 5 seconds. The average effective dose of this examination was 0.9 mSv measured in an anthropomorphic Alderson-Rando phantom with thermoluminescence dosimetry. The spatial resolution of flat detector CT was reported to be 3.0 lp/mm with no binning and 1.5 lp/mm with 2 × 2 binning for high-resolution modes.[4,10]

The 3DRA raw data were transferred to a dedicated angiographic workstation (Siemens). The 3D datasets and CT-like images of subtraction angiograms were reconstructed using standard volume rendering and flat detector CT algorithms (DynaCT-arterial). MPR with section thicknesses of 0.1 mm and MIP with section thicknesses between 6 and 10 mm as well as volume rendering reconstructions with bicolored window and threshold settings were used for analysis of small vessels.

Datasets with a basilar artery stenosis and a midbrain AVM were analyzed as illustrative cases and additional proof of the value of our technique.

The number and pattern of pontine arteries was determined retrospectively by consensus of 2 reviewers. Analog to 2k DSA evaluation, the 2 reviewers counted the number of visible side branches at each side of the basilar artery and looked for direct paramedian midline perforators to determine origin and course of the small brain stem vessels. Especially in pathologic cases with stenotic lesion, we looked for potential collaterals between the small brain stem vessels according to rotating reconstructions. Perforators originating directly from the basilar artery were evaluated according to subtracted flat detector CT images.

RESULTS

Biplane 2k DSA Images in Standard Projections

Circumferential pontine arteries can be regularly demonstrated on DSA images of the basilar artery obtained with recent technology. The most common pattern is a segmental pattern of up to 10 circumferential arteries with slightly descending course around the pons. The origins from the dorsal surface of the basilar artery are best seen on lateral projection in an average distance of 1.5–3.5 mm between 2 "segmental" vessels and some variations between left and right. Common trunks bearing origins of several arteries, longitudinal anastomoses between different arteries, or midline perforators to the brain stem are occasionally seen.

3D and Flat Panel CT Angiography Reconstructions

Compared with DSA images, 3DRA and flat detector CT reconstructions are superior in demonstrating anatomic patterns of circumferential arteries and direct pontine perforators (Table).

The basic patterns derived from the analysis of 20 cases are up to 10 circumferential arteries on each side with a characteristic downward-curving route around the pons (Fig 1), which can be

Basic patterns of the small side branches of the basilar artery in 2k DSA and 3DRA imaging studies

	Number of Segmental Arteries Right			Number of Segmental Arteries Left			Direct Pontine Perforators			Collaterals[a]	Common Trunks of Circumferential Arteries	Pial Network
	0–3	4–7	8–10	0–3	4–7	8–10	Caudal	Medial	Rostral			
2k DSA	10	7	3	5	11	4	0	0	0	6	8	1
3DRA	6	13	1	5	13	2	20	20	20	11	10	6

[a]Collaterals are defined as small anastomosis with a descending course connecting 2 adjacent circumferential arteries.
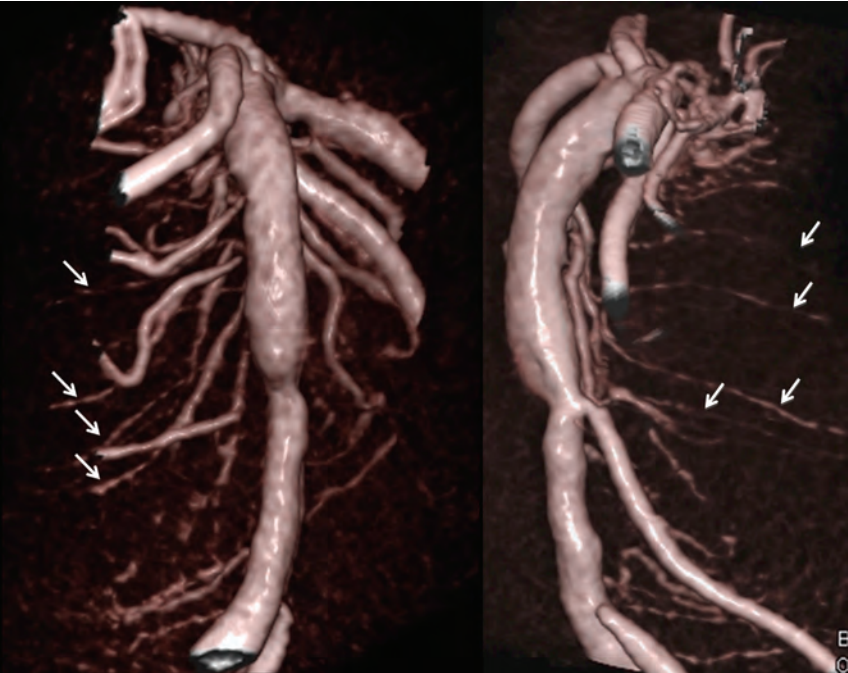
FIG 1. Segmental pattern and descending course of circumferential pontine arteries (*arrows*) on volume rendering reconstructions of a DynaCT dataset of the basilar artery in Towne and lateral projection.
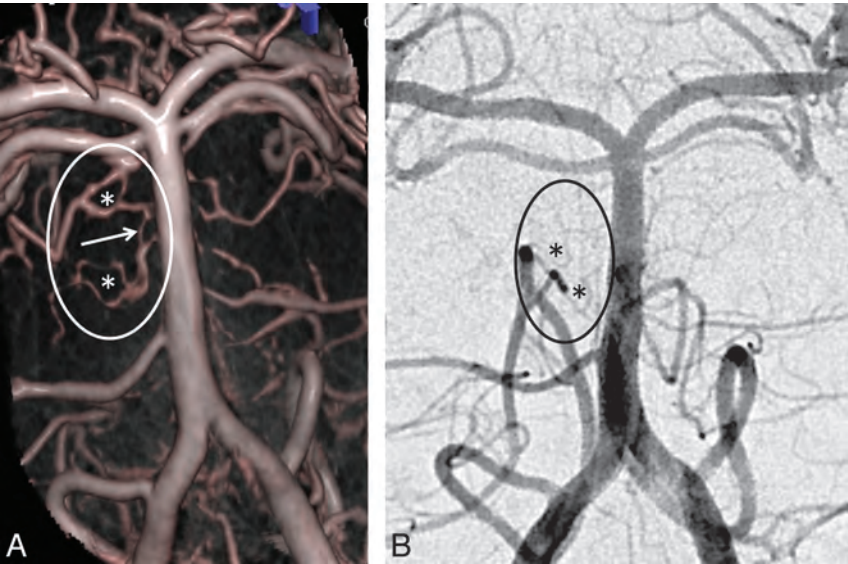
FIG 2. Another case shows a less regular pial network pattern (*) with connections (*arrow*) between adjacent arteries that are better demonstrated on DynaCT reconstructions (*A*), than on high resolution DSA with 2k matrix (*B*).

visualized more clearly in 3DRA compared with 2k DSA images. The number of the segmental arteries on each side of the basilar artery is the same in both 3DRA and 2k DSA images (Table). The distance between the origins of the circumferential branches ranged from 2.6–4.0 mm. Transversal flat detector CT reconstructions (DynaCT arterial mode) show that the circumferential arteries during their downward-curving route toward the tegmentum of the pons give off peripheral perforating branches extending to the pontine parenchyma. Asymmetries between left and right and variations in size have been revealed as common variation.

In 10 of 20 cases, several circumferential arteries arose from a common trunk (Table).

Descending course and tortuosities of circumferential arteries may mimic longitudinal anastomoses or arcade-like connections that are truly present in 6 cases with a more pial-like network and in a further 11 cases with longitudinal anastomoses between adjacent circumferential arteries close to the origin and in no cases in the dorsolateral periphery of the brain stem (Table; Fig 2). 3DRA dataset reconstructions are able to differentiate between true anastomosis and vessel overlap.

Analogous to the sulco-comissural arteries in the spinal cord[7,8] direct perforators to the pons could be identified as small paired vessels arising from the dorsal surface of the basilar artery and extending into the parenchyma. Direct pontine perforators could be identified on 3 levels (Fig 3): at the pontomesencephal junction (rostral), midbasilar (central), and vertebrobasilar junction (caudal). These 3 groups could be defined in all the evaluated images.

The AICA as the main branch of the midbasilar artery was seen in all cases. A large caliber of the AICA seems to be associated with smaller and less numerous other circumferential arteries.

Cases with Pathologies

In 2 cases with hemodynamically relevant stenosis of the basilar artery and the intradural part of the vertebral artery (V4), we identified small collaterals connecting circumferential arteries of the basilar artery bridging the stenosis (Fig 4).
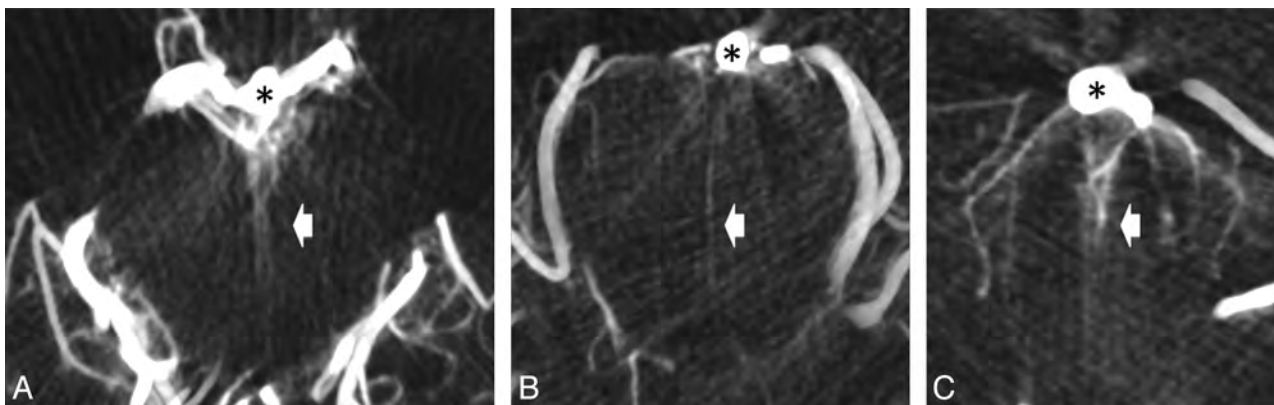
FIG 3. Axial cuts of DynaCT dataset with thin sections of 3 mm reconstructed from 3D rotational angiogram shows ventral pontine perforators (*bright arrows*) originating from the basilar artery (*) at the junction between mesencephalon and pons (*A*), at the midpontine level (*B*), and at the vertebrobasilar junction (*C*).
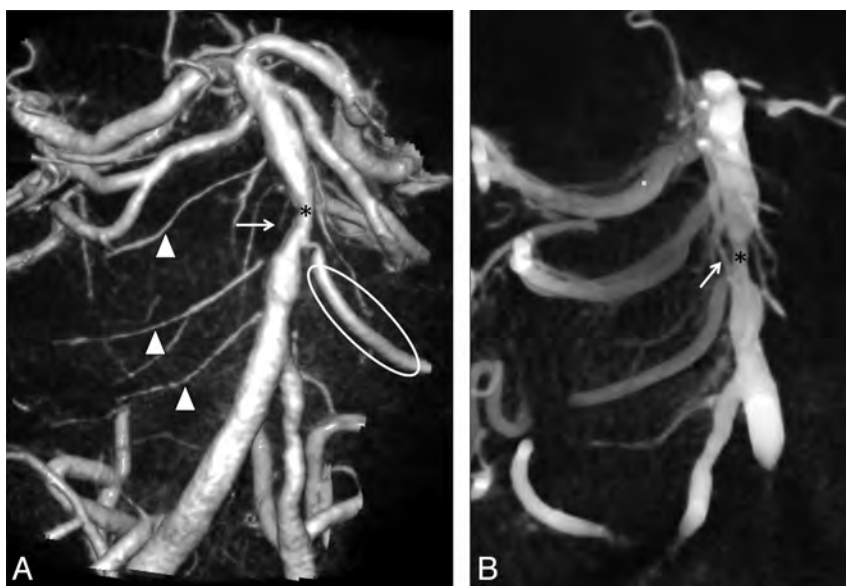
FIG 4. *A*, Volume rendering reconstructions of 3D rotational angiogram show a segmental pattern with several circumferential pontine arteries on the right side (*arrowheads*) and a dominant AICA (*ellipse*) and less other pontine branches on the left side in a patient with a midbasilar stenosis (*). *B*, Note the descending course and a small local collateral (*arrow*) bridging the stenosis (*) in MPR of DynaCT datasets in volume rendering technique (VRT) from the same 3DRA study.

curved and descending course of the circumferential arteries. The visualization of the smaller direct pontine perforators demanded thinner sections around 3 mm.

MPR with thick sections displayed the best results of the basic anatomic patterns of the small side branches of the basilar artery because of the general orientation of these penetrating vessels with their characteristic downward-curving route toward the pontine tegmentum. The con of using thicker reconstructed sections is a decline of spatial resolution in small vessel angiography. Some of the side branches cannot be displayed free from superimpositions, and the correct allocation to the left or right side is difficult.

Compared with the single frames of the 2k DSA series, the continuous acquisition of the 3D rotational angiography runs with a scan time of 5 seconds provides more reliable vessel detection (Figs 2 and 5). In 3D reconstructions, the small branches can be visualized free from superimpositions because of the increased number of projections and the longer acquisition time during pulsative vessel filling of these small branches.

Contrary to what might be expected from consideration of the total image acquisition count only, the patient radiation dose (reported in literature before) for a 3D rotational angiography acquisition is lower than for a biplanar DSA series.[11]

Venous contamination was widely excluded with early start and short scan durations of the scans and visual proof that small arteries originate directly from the basilar artery.

Imaging findings are coincident with previous anatomic descriptions based on examinations of injection specimens.[8,9] However, compared with the anatomic literature, angiographic detectability of the small vessels of the basilar artery seems to be incomplete. With existing angiography techniques and reconstruction tools, it is not possible to display all circumferential

In one case with an arteriovenous malformation, the circumferential and perforating brain stem arteries were clearly hypertrophic as they were part of the AVM-feeding vessels. In comparison to the other cases, the quantity of vessels was also considerably higher and they could be displayed more clearly (Fig 5).

DISCUSSION

Current neuroradiologic angiographic equipment is able to detect the main anatomic features of small pontine arteries. Volume rendering and CT-like reconstructions of 3D rotational datasets are superior to conventional DSA. A larger number of projections, like the subtraction technique with individual adjustment of threshold levels of flat panel CT and 3D reconstructions, increase the possibilities of image processing. In particular, transverse and parasagittal sections of volume rendering datasets with a section thickness between 5 to 10 mm include larger parts of the

FIG 5. Volume rendering reconstruction (*A*) and parasaggital cut of a DynaCT dataset (*B*) show multiple hypertrophied circumferential pontine arteries (*arrows*) involved as feeders in the supply of a mesencephalic AVM (*). Compared with the volume rendering reconstructions *A* and *B*, 2k DSA images of the same patient in standard projections, *C* and *D*, show fewer circumferential arteries (*arrows*) and those that are displayed are less well visualized.

arteries and anastomoses for an exact anatomic definition of this region as found in descriptions based on anatomic preparations.

In addition, our results give rise to the assumption that there are variations with deviations from the common segmental pattern: in several cases, we observed irregular settings with common trunks and anastomoses between adjacent branches resembling a pial network similar to findings at the spinal cord (Fig 2). Due to limitations in spatial resolution, anastomoses as potential pathways for local collaterals are only proved in occasional cases (Fig 2). In the presence of a basilar or vertebral artery stenosis, only 1 small collateral could be detected in each of the 2 cases (Fig 4). More circumferential arteries and anastomoses were seen in an AVM case with hypertrophy of arterial feeders (Fig 5).

Similar to the sulco-comissural arteries in the spinal cord, which enter the spinal cord only in greater intervals, we could regularly detect 3 groups of direct pontine perforators extending from the dorsal surface of the basilar artery entering the brain stem at the ventral surface (Fig 3).

The practical value of our findings is unknown at the moment. However, in the context of endovascular interventions, it be-

comes clear that almost no segment of the basilar artery is free from important side branches and display of these small vessels may contribute for risk assessment before angioplasty and stent placement. In the SAMMPRIS trial, most ischemic strokes after angiographically successful angioplasty and stent placement in the basilar artery in perforator territory.[12] In addition, perforator infarcts after treatment of fusiform aneurysms of the basilar artery raise doubts about sufficient consideration of vascular anatomy. In conclusion, efforts at reducing complications from endovascular treatments of aneurysm, infarctions, or stenosis with intracranial angioplasty and stent placement should focus on reducing the risks of regional perforator infarction.[12]

For the sake of completeness, some basilar artery pathologies have no important branch vessels in the involved segment, eg, sidewall aneurysms between the origins of the circumferential pontine arteries or aneurysms arising from the ventral surface of the basilar artery, which is free from side branches.

Limitations

Variation between the cases may be attributed to anatomic variants or a lack of detectability of the small vessels. Incomplete or delayed filling with contrast material and limitation in the resolution of smaller and terminal branches may be reasons for the incomplete display of anatomic features.[9,13,14] There are only a few descriptions of pontine arteries in the existing angiographic literature.[7] Only with the use of high-field MR imaging were Kang et al[15] able to detect similar patterns.

Incomplete contrast filling of the small branches in 2k DSA images depends on hand injection. Although details of technical safeguards for neuroangiography are seldom discussed in existing literature and contrast application via injector seems to be the standard in many institutes performing neuroangiography, in our opinion, hand injection in 2D DSA is safer and therefore the standard in our institute.[16-18] Contrast application via injector was only selected for 3D DSA. The caliber of the vertebral arteries varies quite often and hand injection may avoid complications, for example, dissection or vessel rupture.

CONCLUSIONS

Our study proves the concept that modern neuroangiographic imaging with 3DRA and flat detector CT reconstructions is able to display small pontine arteries with patterns described in the anatomic literature.

Potential furture developments should focus on a continuous improvement of image quality and further refinement of techno-

logical advances or concepts to increase reliability of small vessel angiography. Further development and improvement of applications are necessary. Limited spatial and contrast resolution of flat panel angiography as well as suboptimal protocols for injection of contrast materials are the main limitations of our approach. Possible avenues for future improvements should address the development of flat detectors with even higher resolution and faster and more flexible detector readout, allowing for faster scanning to improve image quality of small vessel angiograms.[4]

Remarkably, our findings were generated from historical datasets using standard clinical protocols. Dedicated angiographic protocols with optimization of scan time, iodine concentration, and injection parameters of contrast materials may provide future options to use this data for risk assessment of patients with arterial occlusive or stenotic disease or aneurysms before endovascular treatment with angioplasty and stent placement.

This was a proof of concept study about the feasibility to visualize the small side branches of the basilar artery by use of modern angiographic equipment and reconstructions tools. The sample size of this study is too low for an exact anatomic definition of this anatomic region. Currently, further research on small vessel angiography will be necessary and should address technical optimization to improve image quality as well as clinical validation in larger studies to become a routine procedure in neuroangiography. Future studies should be evaluated blinded to avoid exaggeration of the results and should compare different angiographic techniques.

REFERENCES

1. Piotin M, Blanc R, Kothimbakam R, et al. **Primary basilar artery stenting.** *AJR Am J Roentgenol* 2000;175:1367–69
2. Chimowitz MI, Lynn MJ, Derdeyn CP, et al. **Stenting versus aggressive medical therapy for intracranial arterial stenosis.** *N Engl J Med* 2011;365:993–1003
3. Lang J. *Clinical Anatomy of the Posterior Cranial Fossa and its Foramina.* Stuttgart: Thieme; 1991
4. Kalender WA, Kyriakou Y. **Flat-detector computed tomography (FD-CT).** *Eur Radiol* 2007;17:2767–79
5. Mercier PH, Brassier G, Fournier HD, et al. **Vascular microanatomy of the pontomedullary junction, posterior inferior cerebellar arteries, and the lateral spinal arteries.** *Interv Neuroradiol* 2008;14:49–58
6. Mercado R. Santos-Franco J, Ortiz-Velazquez I, et al. **Vascular anatomy of the foramen of Vicq d'Azyr: a microsurgical perspective.** *Minim Invasive Neurosurg* 2004;47:102–06
7. Lasjaunias P, Berenstein A, Ter Brugge KG. *Surgical Neuroangiography.* Berlin-Heidelberg: Springer-Verlag; 2001
8. Marinkovic S, Gibo H. **The surgical anatomy of the perforating branches of the basilar artery.** *Neurosurgery* 1993;33:80–87
9. Duvernoy HM. *Human Brain Stem Vessels.* Berlin Heidelberg: Springer-Verlag; 2010
10. Kyriakou Y, Struffert T, Dörfler A, et al. **Basic principles of flat detector computed tomography (FD-CT).** *Radiologe* 2009;49:811–19
11. Schueler B, Kallmes D, Cloft H. **3D cerebral angiography: radiation dose comparison with digital subtraction angiography.** *AJNR Am J Neuroradiol* 2005;25:1898–901
12. Derdeyn CP, Fiorella D, Lynn MJ, et al. **Mechanisms of stroke after intracranial angioplasty and stenting in the SAMMPRIS trial.** *Neurosurgery* 2013;72:777–95
13. Pai BS, Varma RG, Kulkarni RN, et al. **Microsurgical anatomy of the posterior circulation.** *Neurol India* 2007;55:31–41
14. Pais D, Arantes M, Casal D, et al. **Brain stem arteries in Canis familiaris–implications in experimental procedures.** *Braz J Morphol Sci* 2009;26:8–11
15. Kang CK, Park CA, Kim KN, et al. **Non-invasive visualization of basilar artery perforators with 7T MR angiography.** *JMRI* 2010;32:544–50
16. Yousem DM, Trinh BC. **Injection rates for neuroangiography: results of a survey.** *AJNR Am J Neuroradiol* 2001;22:1838–40
17. Fox AJ. **Technical aspects of neuroangiography: are risks and safeguards understood in the same way?** *AJNR Am J Neuroradiol* 2001;22:1809–10
18. Gailloud P, Murphy K. **Risk of cerebral angiographic complications, injection volumes, and rates.** *AJNR Am J Neuroradiol* 2002;23:893; author reply 893–94

Endovascular Treatment of Internal Carotid Artery Bifurcation Aneurysms: A Single-Center Experience and a Systematic Review and Meta-Analysis

S.F. Morales-Valero, W. Brinjikji, M.H. Murad, J.T. Wald, and G. Lanzino

ABSTRACT

BACKGROUND AND PURPOSE: Endovascular coiling of internal carotid artery bifurcation aneurysms can be challenging due to unfavorable morphologic features. With improvements in endovascular techniques, several series have detailed the results and complications of endovascular treatment of aneurysms at this location. We performed a systematic review and meta-analysis of published series on the endovascular treatment of ICA bifurcation aneurysms, including a tertiary referral center experience.

MATERIALS AND METHODS: We performed a comprehensive literature search for reports on contemporary endovascular treatment of ICA bifurcation aneurysms from 2000 to 2013, and we reviewed our experience. We extracted information regarding periprocedural complications, procedure-related morbidity and mortality, immediate angiographic outcome, long-term clinical and angiographic outcome, and retreatment rate. Event rates were pooled across studies by using random-effects meta-analysis.

RESULTS: Including our series of 37 patients, 6 studies with 158 patients were analyzed. Approximately 60% of the aneurysms presented as unruptured; 88.0% (95% CI, 68.0%–96.0%) of aneurysms showed complete or near-complete occlusion at immediate postoperative angiography compared with 82.0% (95% CI, 73.0%–88.0%) at last follow-up. The procedure-related morbidity and mortality were 3.0% (95% CI, 1.0%–7.0%) and 3.0% (95% CI, 1.0%–8.0%), respectively. The retreatment rate was 14.0% (95% CI, 8.0%–25.0%). Good neurologic outcome was achieved in 93.0% (95% CI, 86.0%–97.0%) of patients.

CONCLUSIONS: Endovascular treatment of ICA bifurcation aneurysms is feasible and effective and is associated with high immediate angiographic occlusion rates. However, retreatment rates and procedure-related morbidity and mortality are non-negligible.

Internal carotid artery bifurcation aneurysms represent between 2.4% and 4% of all intracranial aneurysms.[1-4] The presence of multiple perforators in this area along with the angle of origin (often skewed toward the MCA or the anterior cerebral artery primarily) can make treatment challenging.[3] Additionally, the increased hemodynamic stress at this level translates into a higher rate of recurrence compared with aneurysms in other locations.[4,5] Several studies have focused on the surgical management of ICA bifurcation aneurysms.[2,3,6-10] However, to our knowledge, there is limited evidence regarding their treatment by using endovascular techniques. To better understand the safety and efficacy of endovascular treatment for ICA bifurcation aneurysms, we report both our own experience and the results of a meta-analysis of the literature.

MATERIALS AND METHODS
Patient and Aneurysm Characteristics
After institutional review board approval, we performed a retrospective analysis of a prospectively collected data base of patients treated for intracranial aneurysms at our institution (Mayo Clinic, Rochester, Minnesota). All consecutive patients who underwent endovascular treatment of aneurysms located at the ICA bifurcation between February 1999 and November 2013 were identified. All patients provided approval for the use of their medical records for retrospective analysis. The following information was collected for each patient: demographic data, aneurysm characteristics, clinical presentation, and type of treatment. Among the aneurysm characteristics, size (maximum dimension as measured by 3D digital subtraction angiography) and rupture status were obtained. The patients presenting with subarachnoid hemorrhage were classified by using the Hunt and Hess scale score, and clinical outcomes were assessed by using the modified Rankin Scale.

Outcomes

Outcomes studied included periprocedural complications (<30 days), immediate angiographic outcome, clinical and angiographic outcomes at last follow-up, and retreatment. Studied periprocedural complications (within 30 days of treatment) included intraoperative rupture, thromboembolic events, parent artery and branch occlusion, stroke, vasospasm, and rebleeding.

The degree of aneurysm occlusion was stratified into 3 levels, according to the scale of Raymond et al (complete, near-complete, and incomplete occlusion).[11] This parameter was established immediately after the procedure and at last follow-up by the operator after reviewing the postoperative 3D-DSA images. Additionally, an experienced neuroradiologist not involved in the patient treatment reviewed the imaging and estimated the percentage of occlusion after the initial embolization and at last follow-up.

Literature Review

A comprehensive literature search of the data bases PubMed, Ovid MEDLINE, and Ovid EMBASE was designed and conducted by an experienced librarian with input from the authors. The key words "internal carotid artery," "intracranial aneurysm," "endovascular therapy," "coil," "bifurcation," and "terminus" were used in both "AND" and "OR" combinations. The search was limited to articles published from 2000 to November 2013 in the English language only. All studies reporting patients with ICA bifurcation aneurysms treated with endovascular therapy were selected. The inclusion criteria were the following: a series of >10 patients, with available data on periprocedural complications and clinical and angiographic follow-up. Two reviewers (S.F.M.-V. and W.B.) independently selected the included studies. For each study, we independently extracted the following information: rupture status, immediate and delayed angiographic occlusion rates, procedure-related morbidity and mortality, periprocedural stroke resulting in morbidity or mortality, intraoperative rupture rates, retreatment rates, and the rate of good neurologic outcome at last follow-up. For patients with ruptured aneurysms, we studied the rate of mortality attributed to complications of SAH, vasospasm rates, and rates of rerupture after coiling.

Statistical Analysis

We assessed the cumulative incidence (event rate) and 95% confidence interval for each outcome. Cumulative outcomes (ruptured and unruptured) were also calculated for all results. Perioperative complication rates and clinical outcomes were calculated separately for ruptured and unruptured aneurysms. For meta-analysis, event rates were pooled across studies by using a random-effects model.[12] Heterogeneity across studies was evaluated by using the I^2 statistic.[13] All statistical analyses were performed by using the meta-analysis software package Comprehensive Meta-Analysis (www.meta-analysis.com).

RESULTS
Institutional Series

Patient and Aneurysm Characteristics. Thirty-six consecutive patients (mean age, 50.7 years) with 37 ICA bifurcation aneurysms were included in the current series (22 female patients, 61.1%). The mean aneurysm size was 8.8 ± 5.1 mm. Specifically, there were 12 small aneurysms (≤5 mm), 20 medium aneurysms (6–15 mm), and 5 large aneurysms (16–25 mm). There were no giant aneurysms in our series. Thirteen patients (36.1%) had additional aneurysms in other locations. Nine patients (25%) presented with SAH. Of the 9 patients presenting with SAH, the Hunt and Hess scale score was 2 in 4 cases, 3 in 2 cases, and 5 in 3 cases. One of the patients presenting with SAH was found to have an additional unruptured aneurysm in the contralateral ICA bifurcation. Of the 27 patients with unruptured aneurysms, 3 (11.1%) were considered symptomatic (a visual field deficit in 1 patient and headache in 2 patients).

Aneurysm Treatment and Immediate Angiographic Outcome. Of the 37 aneurysms, 35 (94.6%) were initially treated with coiling and 2 (5.4%) were treated in a staged fashion with coiling and flow diversion. Balloon assistance was used in 6 patients undergoing coiling (17.1%), and stent assistance was not used in any patient. The patients treated with staged coiling and flow diversion had large aneurysms (a ruptured 21-mm aneurysm and an unruptured 23-mm aneurysm). Of the 37 treated aneurysms, 14 (38.8%) had complete occlusion and 23 (61.2%) had near-complete occlusion immediately after the procedure. No patients had incomplete occlusion. The mean percentage of occlusion was 80.8 ± 15% immediately after the procedure.

Periprocedural Complications

There were no cases of intraprocedural rupture or perforation and no cases of parent artery or branch occlusion. One of the patients treated with coiling for an unruptured ICA bifurcation aneurysm had a thromboembolic event 10 days after treatment, presenting with a transient neurologic deficit (dysarthria and word-finding difficulty). There were no intra- or periprocedural complications related to the use of the Pipeline Embolization Device (Covidien, Irvine, California). There was no mortality related to the endovascular procedure. As a result, in our institutional series, we had a combined procedure-related morbidity of 2.7% and no mortality.

Clinical Outcome

Of the 9 patients presenting with ruptured aneurysms, 2 died in-hospital of complications related to high-grade SAH (Hunt and Hess scale grade 5). Clinical follow-up was available for the 7 patients surviving discharge (mean, 60.6 months; range, 6.8–102 months). The mRS score at last clinical follow-up was zero in 3 patients, 1 in 3 patients, and 2 in 1 patient.

Clinical follow-up was available for 27 of 28 patients with unruptured aneurysms (mean, 44.4 months; range, 2–180 months). The mRS score at last clinical follow-up was zero in 8 patients (26.6%), 1 in 12 patients (44.5%), 2 in 4 patients (14.8%), 3 in 1 patient (3.7%), and 6 in 2 patients (5.9%). Of the 2 patients with mRS 6, one died of unrelated causes 4 months after treatment and 1 patient died after rupture of a recurrent giant ICA bifurcation aneurysm 30 months after coiling. She had a known recurrence, but given her advanced age and borderline medical condition, we had elected to manage it conservatively.

Table 1: Studies reporting endovascular treatment of ICA terminus aneurysms

Authors and Year	No. of Patients/ Aneurysms	Male/Female Ratio	Mean Age (yr) (Range)	Study Design	Ruptured Aneurysms (No.) (%)	Mean Angiographic Follow-Up (mo)
Geyik et al, 2007[14]	18/18	NR	31.9 (21–65)	R	NR	28
Uemura et al, 2008[16]	17/17	9:8	47 (24–77)	R	13 (76.5%)	12
van Rooij et al, 2008[4]	46/50	13:33	49.3 (23–76)	R	26 (52%)	16
Oishi et al, 2013[17]	25/25	11:14	60.9 (45–77)	P	2 (8%)	24
Zhou et al, 2013[15]	16/16	9:7	50.6 (34–66)	R	8 (50%)	12
Current study	36/37	14:22	50.7 (22–80)	R	9 (24.3%)	40

Note:—NR indicates not reported; R, retrospective; P, prospective.

Long-Term Angiographic Outcome

Angiographic follow-up was available for 88% of eligible patients (30/34). The average interval between initial treatment and last imaging follow-up was 39.5 months (range, 2–156.8 months). Of the 4 patients without available imaging follow-up, 2 were recently treated and had no indication of repeat imaging at the time of data collection and 2 had follow-up angiograms obtained at other institutions, which were not available for review. At last imaging follow-up, 14 of 30 patients (46.7%) had complete occlusion, 9 (30.0%) had near-complete occlusion, and 7 (23.3%) had incomplete occlusion. The mean percentage of occlusion was 85 ± 15.6% at last angiographic follow-up.

Recurrence and Retreatment

Overall, 34.3% (12/35) of aneurysms recurred after a mean of 13.3 months (range, 2–41 months). One recurrent aneurysm presented as rebleeding 2 months after the initial SAH and coiling; the remaining recurrent aneurysms were diagnosed during routine angiographic follow-up. By size, 41.7% of the small aneurysms recurred (5/12), as opposed to 25% of the medium aneurysms (5/20), and 2 of 3 large aneurysms. Nine aneurysms (25.7%) underwent retreatment: 6 with coiling, 2 with the Pipeline Embolization Device, and 1 with surgical clipping. Of the 3 patients with recurrent aneurysms that did not undergo retreatment, 2 aneurysms were not amenable to coiling and were thought to have a low risk of rupture and 1 patient was managed conservatively due to advanced age and a borderline medical condition. The 2 patients treated with the Pipeline Embolization Device included 1 with a 12-mm aneurysm initially treated with coiling and found to have recurred 28 months later and 1 with a large (23-mm) aneurysm initially treated with staged coiling and flow diversion found to have recurred during the 6-month angiographic follow-up. In this patient, further growth of the aneurysm was related to proximal delayed migration of the Pipeline Device. Retreatment with 2 additional telescoping Pipelines was complicated by a nondisabling stroke causing transient word-finding difficulties 1 week after treatment. The last angiographic follow-up on this patient 36 months after initial treatment showed complete obliteration. Similarly, the other patient initially treated with staged coiling and flow diversion showed complete obliteration of the aneurysm during the 12-month angiographic follow-up.

Systematic Review and Meta-Analysis

Search Results. The search criteria led to 171 citations. After screening the titles and abstracts, we identified 15 articles about treatment of ICA bifurcation aneurysms. Of these 15 articles, 5 were case reports and were excluded. Three studies included patients treated with surgery only and were excluded as well. Three large studies of endovascular treatment in various locations included patients with ICA bifurcation aneurysms, but only 1 reported disaggregated data and met our inclusion criteria.[14] Four series included exclusively patients with ICA bifurcation aneurysms undergoing endovascular treatment and were articles included in our analysis.[4,15-17] Thus, our search results yielded 5 published series on endovascular treatment of ICA bifurcation aneurysms.

Studies

Including the institutional series presented in this article, 6 studies encompassing 158 patients with 163 aneurysms were included in this meta-analysis (Table 1). Five studies with 145 aneurysms provided data regarding aneurysm rupture status; among them, 87 (60%) corresponded to unruptured aneurysms. All studies provided data on technical outcome, periprocedural complications, procedure-related morbidity and mortality, immediate and long-term angiographic outcomes, and clinical outcome.

Angiographic Outcomes

The rate of complete or near-complete occlusion immediately after the endovascular procedure was 88.0% (95% CI, 68.0%–96.0%) for all aneurysms. The occlusion rate for unruptured aneurysms was 84.0% (95% CI, 36.0%–98.0%), and for ruptured aneurysms, it was 69.0% (95% CI, 4.0%–99.0%). Long-term complete/near-complete occlusion rates were 82.0% (95% CI, 73.0%–88.0%) for all aneurysms. These data are summarized in Table 2.

Procedure-Related Complications

Overall, perioperative strokes resulting in morbidity or mortality occurred in 3.0% (95% CI, 1.0%–7.0%) of patients. Intraoperative rupture occurred in 3.0% (95% CI, 1.0%–7.0%) of patients. Procedure-related morbidity occurred in 4.0% (95% CI, 2.0%–14.0%), and procedure-related mortality occurred in 3.0% (95% CI, 1.0%–8.0%) of all patients. Procedure-related morbidity occurred in 6.0% (95% CI, 2.0%–14.0%) of patients with unruptured aneurysms and 9.0% (95% CI, 2.0%–36.0%) of patients with ruptured aneurysms. Procedure-related mortality occurred in 4.0% (95% CI, 1.0%–11.0%) of patients with unruptured aneurysms and 6.0% (95% CI, 2.0%–16.0%) of patients with ruptured aneurysms. These data are summarized in Table 2.

Long-Term Outcome

The mean duration of clinical follow-up among the included studies was 31.2 ± 9.7 months. The overall retreatment rate was

Table 2: Meta-analysis outcomes

	All Patients			Unruptured Aneurysm			Ruptured Aneurysm		
	Event Rate (95% CI)	I²	No. of Studies	Event Rate (95% CI)	I²	No. of Studies	Event Rate (95% CI)	I²	No. of Studies
Angiographic outcome									
Immediate complete/near-complete occlusion	88.0 (68.0–96.0)	80	6	84.0 (36.0–98.0)	79	2	69.0 (4.0–99.0)	84	4
Complete/near-complete occlusion at last follow-up	82.0 (73.0–88.0)	0	5	82.0 (66.0–92.0)	NA	2	67.0 (40.0–85.0)	NA	2
Perioperative clinical outcomes									
Procedure-related morbidity	4.0 (2.0–9.0)	0	6	6.0 (2.0–14.0)	0	5	9.0 (2.0–36.0)	50	5
Procedure-related mortality	3.0 (1.0–8.0)	0	6	4.0 (1.0–11.0)	0	5	6.0 (2.0–16.0)	0	5
Intraoperative rupture	3.0 (1.0–7.0)	0	6	3.0 (1.0–11.0)	0	5	7.0 (2.0–19.0)	0	5
Perioperative stroke resulting in morbidity or mortality	3.0 (1.0–7.0)	0	6	3.0 (1.0–11.0)	0	5	7.0 (3.0–17.0)	0	5
Long-term clinical outcomes									
Retreatment	14.0 (8.0–25.0)	37	6	14.0 (8.0–25.0)	37	6	22.0 (7.0–51.0)	45	4
Good neurologic outcome long-term	93.0 (86.0–97.0)	0	4	91.0 (82.0–96.0)	0	4	93.0 (79.0–98.0)	0	4

Note:—NA indicates not applicable.

Table 3: SAH patient-specific outcomes

	Event Rate (95% CI)	I²	No. of Studies
Mortality from SAH	14.0 (7.0–26.0)	0	5
Vasospasm	16.0 (4.0–46.0)	40	4
Reruptureafter coiling	6.0 (2.0–17.0)	0	5

14.0% (95% CI, 8.0%–25.0%). The retreatment rate for unruptured aneurysms was 14.0% (95% CI, 8.0%–25.0%), and for ruptured aneurysms, it was 22.0% (95% CI, 7.0%–51.0%). Overall, good long-term neurologic outcome was seen in 93.0% (95% CI, 86.0%–97.0%) of patients. Among patients with available long-term clinical follow-up, those with unruptured aneurysms had a good neurologic outcome rate of 91.0% (95% CI, 82.0%–96.0%), and those with ruptured aneurysms had a good neurologic outcome rate of 93.0% (95% CI, 79.0%–98.0%). These data are summarized in Table 2.

SAH-Specific Outcomes
Among patients included in the meta-analysis, mortality from SAH occurred in 14.0% (95% CI, 7.0–26.0%) of patients. Vasospasm occurred in 16.0% (95% CI, 4.0%–46.0%). Rerupture after coiling occurred in 6.0% (95% CI, 2.0%–17.0%). These data are summarized in Table 3.

Heterogeneity and Publication Bias
Heterogeneity was low for all outcomes except immediate complete/near-complete occlusion (I² = 80%). Therefore, variation in this event rate was noted across the available studies, whereas results were consistent for all the remaining outcomes. We were unable to determine the presence of publication bias due to the small number of included studies and the noncomparative nature of the available data.

DISCUSSION
Reporting our institutional experience with the endovascular treatment of ICA bifurcation aneurysms, we contribute to the literature with a relatively large contemporary series with the longest clinical and angiographic follow-up available to date, to our knowledge. Additionally, by combining our results with 5 previous studies, we are able to provide representative data and draw accurate conclusions regarding the safety and efficacy of endovascular treatment of ICA bifurcation aneurysms.

Most ICA terminus aneurysms in our meta-analysis were successfully embolized with a rate of complete or near-complete occlusion of 88% in the immediate postoperative setting. A potential limitation of endovascular treatment for aneurysms at bifurcation points is the possibility of coil compaction and subsequent aneurysm recurrence. Our data indicate that retreatment was necessary in 14% of patients undergoing endovascular treatment for ICA bifurcation aneurysms. However, complete or near-complete occlusion was seen in 82% of patients after long-term imaging follow-up.

Periprocedural complications following endovascular treatment of ICA terminus aneurysms are not negligible. Aneurysms at this location are at a high risk of ischemic stroke in the territory of the ipsilateral MCA (either from distal emboli during the procedure or clot formation at the level of the neck with impairment of distal MCA flow), a potential source of serious morbidity and mortality.[4,16,17] In our meta-analysis, perioperative morbidity rates were approximately 4% and mortality rates were 3%. Perioperative stroke was a major contributor to morbidity and mortality, occurring in approximately 3% of patients. Although good long-term neurologic outcome was achieved in >90% of patients regardless of aneurysm rupture status, the periprocedural complication rate reported is not trivial. Particularly worrisome is the procedure-related mortality of 4% for unruptured and 6% for ruptured ICA bifurcation aneurysms.

These findings stress the importance of proper patient selection because these aneurysms are often adequately and effectively treatable with surgical clip ligation. The high retreatment rate observed in our meta-analysis and in our own series is similar to that reported for aneurysms located in other bifurcation points. The retreatment rate reported for basilar bifurcation aneurysms ranges between 15% and 27.8%,[18-20] and for MCA bifurcation aneurysms, it has been reported in up to 7.6% of patients.[21] The increased hemodynamic stress at the level of arterial bifurcations has been linked to the development of aneurysms[5,22] and certainly has a role in the recurrence seen after endovascular treatment. Most interesting, some aneurysms were found to have recurred

even after stable follow-up imaging 6 or 12 months after initial treatment. This finding underscores the need for close angiographic follow-up in this patient population as stressed by other authors.[23]

Given that aneurysms located at the ICA bifurcation are relatively uncommon, the series included in our analysis had a small number of patients. Additionally, there was a wide range of angiographic outcomes among the different studies. By pooling the results of all available reports on endovascular treatment of ICA bifurcation aneurysms, our meta-analysis provides a more precise estimate of the safety and efficacy of this treatment technique for this particular group of aneurysms.

The surgical treatment of ICA bifurcation aneurysms is particularly challenging, due to their location at the highest point of the ICA and the presence of multiple perforators at this level that may be adherent to the back side of the aneurysm.[3] Results of endovascular treatment herein reported compare favorably with those observed after surgical treatment. Gupta el at[10] reported their experience with 89 patients with ruptured ICA bifurcation aneurysms and showed a good outcome in 68.6%. Although all of their patients presented with ruptured aneurysms, even patients with low-grade SAH (Hunt and Hess scale grades I and II) had a mortality rate of 6.3%, mainly due to intraoperative rupture and thromboembolic complications.[10] Miyazawa et al[2] reported a good outcome in 58.8% of patients with ruptured aneurysms and in all patients with unruptured aneurysms. In our study, good neurologic outcome was seen in >90% of patients, and >80% of patients had complete or near-complete occlusion of their aneurysms. These findings suggest that endovascular treatment could be considered a first-line treatment for ICA terminus aneurysms.

Treatment in a staged fashion by using coiling and flow diversion was used in 2 large aneurysms from our series. To our knowledge, this technique has not been reported previously for the treatment of ICA bifurcation aneurysms, and it proved effective in both cases. The safety and efficacy of flow diversion are well-documented for the treatment of sidewall aneurysms located in the proximal ICA.[24,25] However, this new technology has been increasingly used to treat aneurysms at other locations. A recent study reported 25 MCA bifurcation aneurysms treated by the Pipeline Embolization Device, showing complete occlusion in 84% of cases at last angiographic follow-up.[26] In our case, both patients with ICA bifurcation aneurysms and treated with staged coiling and flow diversion had complex and large lesions that were thought to have a high risk of recurrence if treated by conventional modalities. We consider that selected cases of aneurysms located at the ICA bifurcation represent a potential application of flow diverters. However, further evidence is required to confirm this assumption.

Limitations
Our study has methodologic limitations. Measurement of aneurysm occlusion by using both the 3-point scale of Raymond et al,[11] and the percentage occlusion scale can be subjective and subject to both inter- and intraobserver variability. For the meta-analysis, clinical and angiographic follow-up times were variable, the average ranging from 12 to 40 months. Thus, data on clinical and angiographic outcomes are limited by the heterogeneity in follow-up. In addition, many of the series analyzed and included in our analysis were cases collected for several years, and it is possible that complication rates have improved as a result of increased operator experience and skill and improved devices and technology. Using the Grading of Recommendations, Assessment, Development and Evaluation framework, we found that the quality of evidence (confidence in estimates) is limited because of imprecision, heterogeneity (only for the outcome of immediate complete/near-complete occlusion), and methodologic limitations of the studies included.[27-29]

Nevertheless, this meta-analysis provides useful data to share with patients and families when assessing the risks of endovascular treatment of ICA bifurcation aneurysms. Our study also provides a framework on which to base the treatment decision-making for these uncommon lesions and represents a benchmark against which future studies in this patient group can be compared. With 158 patients and 163 aneurysms, this study represents the largest study to date on the endovascular treatment of ICA terminus aneurysms.

CONCLUSIONS
Endovascular treatment of ICA bifurcation aneurysms is feasible and results in immediate complete or near-complete occlusion in 88% of patients. However, non-negligible complications can occur, and the procedure-related morbidity and mortality are 4% and 3%, respectively. ICA bifurcation aneurysms are subject to increased hemodynamic stress, which explains their tendency to recur (34.3% in our own series), requiring a retreatment rate of 14%. With close angiographic follow-up and adequate treatment of recurrences, most patients achieve a good neurologic outcome.

REFERENCES
1. Sakamoto S, Ohba S, Shibukawa M, et al. **Characteristics of aneurysms of the internal carotid artery bifurcation.** *Acta Neurochir (Wien)* 2006;148:139–43, discussion 143
2. Miyazawa N, Nukui H, Horikoshi T, et al. **Surgical management of aneurysms of the bifurcation of the internal carotid artery.** *Clin Neurol Neurosurg* 2002;104:103–14
3. Lehecka M, Dashti R, Romani R, et al. **Microneurosurgical management of internal carotid artery bifurcation aneurysms.** *Surg Neurol* 2009;71:649–67
4. van Rooij WJ, Sluzewski M, Beute GN. **Internal carotid bifurcation aneurysms: frequency, angiographic anatomy and results of coiling in 50 aneurysms.** *Neuroradiology* 2008;50:583–87
5. Ingebrigtsen T, Morgan MK, Faulder K, et al. **Bifurcation geometry and the presence of cerebral artery aneurysms.** *J Neurosurg* 2004;101:108–13
6. Perria L, Rivano C, Rossi GF, et al. **Aneurysms of the bifurcation of the internal carotid artery.** *Acta Neurochir (Wien)* 1968;19:51–68
7. Sengupta RP, Lassman LP, de Moraes AA, et al. **Treatment of internal carotid bifurcation aneurysms by direct surgery.** *J Neurosurg* 1975;43:343–51
8. Yaşargil MG, Boehm WB, Ho RE. **Microsurgical treatment of cerebral aneurysms at the bifurcation of the internal carotid artery.** *Acta Neurochir (Wien)* 1978;41:61–72
9. Da Pian R, Pasqualin A, Scienza R. **Direct microsurgical approach to aneurysms of the internal carotid bifurcation.** *Surg Neurol* 1980;13:27–37

10. Gupta SK, Khosla VK, Chhabra R, et al. **Internal carotid artery bifurcation aneurysms: surgical experience.** *Neurol Med Chir (Tokyo)* 2007;47:153–57, discussion 157–58

11. Raymond J, Guilbert F, Weill A, et al. **Long-term angiographic recurrences after selective endovascular treatment of aneurysms with detachable coils.** *Stroke* 2003;34:1398–403

12. DerSimonian R, Laird N. **Meta-analysis in clinical trials.** *Control Clin Trials* 1986;7:177–88

13. Higgins JP, Thompson SG, Deeks JJ, et al. **Measuring inconsistency in meta-analyses.** *BMJ* 2003;327:557–60

14. Geyik S, Yavuz K, Cekirge S, et al. **Endovascular treatment of basilar and ICA termination aneurysms: effects of the use of HydroCoils on treatment stability in a subgroup of patients prone to a higher recurrence rate.** *Neuroradiology* 2007;49:1015–21

15. Zhou Y, Yang PF, Hong B, et al. **Stent placement for the treatment of complex internal carotid bifurcation aneurysms: a review of 16 cases.** *Turk Neurosurg* 2013;23:232–40

16. Uemura A, Musacchio M, Cardoso M, et al. **Internal carotid bifurcation aneurysms: anatomical features and outcome of endovascular treatment.** *Neuroradiol J* 2008;21:574–78

17. Oishi H, Yamamoto M, Nonaka S, et al. **Endovascular therapy of internal carotid artery bifurcation aneurysms.** *J Neurointerv Surg* 2013;5:400–04

18. Chalouhi N, Jabbour P, Gonzalez LF, et al. **Safety and efficacy of endovascular treatment of basilar tip aneurysms by coiling with and without stent assistance: a review of 235 cases.** *Neurosurgery* 2012;71:785–94

19. Peluso JP, van Rooij WJ, Sluzewski M, et al. **Coiling of basilar tip aneurysms: results in 154 consecutive patients with emphasis on recurrent haemorrhage and re-treatment during mid- and long-term follow-up.** *J Neurol Neurosurg Psychiatry* 2008;79:706–11

20. Henkes H, Fischer S, Mariushi W, et al. **Angiographic and clinical results in 316 coil-treated basilar artery bifurcation aneurysms.** *J Neurosurg* 2005;103:990–99

21. Gory B, Rouchaud A, Saleme S, et al. **Endovascular treatment of middle cerebral artery aneurysms for 120 nonselected patients: a prospective cohort study.** *AJNR Am J Neuroradiol* 2014;35:715–20

22. Meng H, Wang Z, Hoi Y, et al. **Complex hemodynamics at the apex of an arterial bifurcation induces vascular remodeling resembling cerebral aneurysm initiation.** *Stroke* 2007;38:1924–31

23. Ferns SP, Sprengers ME, van Rooij WJ, et al. **Late reopening of adequately coiled intracranial aneurysms: frequency and risk factors in 400 patients with 440 aneurysms.** *Stroke* 2011;42:1331–37

24. Brinjikji W, Murad MH, Lanzino G, et al. **Endovascular treatment of intracranial aneurysms with flow diverters: a meta-analysis.** *Stroke* 2013;44:442–47

25. D'Urso PI, Lanzino G, Cloft HJ, et al. **Flow diversion for intracranial aneurysms: a review.** *Stroke* 2011;42:2363–68

26. Yavuz K, Geyik S, Saatci I, et al. **Endovascular treatment of middle cerebral artery aneurysms with flow modification with the use of the Pipeline embolization device.** *AJNR Am J Neuroradiol* 2014;35:529–35

27. Balshem H, Helfand M, Schunemann HJ, et al. **GRADE guidelines: 3. Rating the quality of evidence.** *J Clin Epidemiol* 2011;64:401–06

28. Guyatt GH, Oxman AD, Kunz R, et al. **GRADE guidelines: 6. Rating the quality of evidence–imprecision.** *J Clin Epidemiol* 2011;64:1283–93

29. Murad MH, Swiglo BA, Sidawy AN, et al. **Methodology for clinical practice guidelines for the management of arteriovenous access.** *J Vasc Surg* 2008;48:26S–30S

Enhancing Brain Lesions after Endovascular Treatment of Aneurysms

J.P. Cruz, T. Marotta, C. O'Kelly, M. Holtmannspötter, G. Saliou, R. Willinsky, T. Krings, and R. Agid

ABSTRACT

SUMMARY: Complications of endovascular therapy of aneurysms mainly include aneurysm rupture and thromboembolic events. The widespread use of MR imaging for follow-up of these patients revealed various nonvascular complications such as aseptic meningitis, hydrocephalus, and perianeurysmal brain edema. We present 7 patients from 5 different institutions that developed MR imaging–enhancing brain lesions after endovascular therapy of aneurysms, detected after a median time of 63 days. The number of lesions ranged from 4–46 (median of 10.5), sized 2–20 mm, and were mostly in the same vascular territory used for access. Three patients presented with symptoms attributable to these lesions. After a median follow-up of 21.5 months, the number of lesions increased in 2, was stable in 1, decreased in 3, and disappeared in 1. The imaging and clinical characteristics suggested a foreign body reaction. We could find no correlation to a specific device, but a possible source may be the generic hydrophilic coating.

ABBREVIATION: EVT = endovascular therapy

Endovascular therapy (EVT) is commonly used as a first-line therapy for intracranial aneurysms.[1,2] The complication rate of this procedure is relatively low[3] and mostly includes thromboembolic events and intraprocedure aneurysm rupture.[4] Less common nonvascular complications exist and include hydrocephalus and perianeurysmal edema.[5-7] There are isolated reports of foreign body emboli to the brain parenchyma after diagnostic and therapeutic cerebral angiograms, but only a few include the imaging characteristics of these lesions.[8-11] We describe a short series of nonischemic, enhancing parenchymal lesions appearing after EVT of intracranial aneurysms.

Case Series

We report cases from 5 different institutions. The authors at each of the 5 participating centers submitted the demographic data,

aneurysm characteristics, procedure type, devices used, and MR characteristics of the lesions as well as the imaging and clinical findings during follow-up. Analysis of the submitted data was performed by 2 of the authors (J.P.C. and R.A.).

A total of 7 cases of brain enhancing lesions after EVT were collected (6 women, 1 man) ranging from 32 to 71 years of age (median age 54). Six aneurysms were located in the anterior circulation and 1 in the posterior circulation. Three aneurysms were ruptured and 4 were unruptured.

The procedures included 2 conventional aneurysm coilings, 2 balloon-assisted coilings, 1 stent-assisted coiling, and 2 cases of flow-diverter stents. All patients had a single femoral access. A triaxial system was used in all but 2 patients, 1 of them with a posterior circulation aneurysm. Bare platinum coils were used in 3 of the 4 coiling procedures. Modified platinum coils were used in only 1 patient. None of the patients treated with flow diversion ($n = 2$) had adjuvant coiling. We could not identify 1 specific device that was predominantly used in all cases (On-line Table).

The median time from procedure to lesion detection on MR was 63 days (range 43–118 days, interquartile range = 35.5 days). Four patients (2 ruptured, 2 unruptured) had an early postprocedure MR (ie, within 7 days from the procedure); 3 showed few restricted DWI lesions in the vascular territory used for access (Fig 1) that disappeared in follow-up as expected for ischemic lesions after EVT.[12] All the other patients had the first postprocedure MR performed later as part of the routine follow-up. All but 1 patient had a contrast-enhanced MR imaging. The number of enhancing lesions per patient ranged from 4 to 46 (median 10.5, interquartile range = 33.5), the

FIG 1. A 54-year-old woman with a right supraclinoid ICA unruptured aneurysm treated with a flow diverter. Axial DWI on postoperative day (POD) 1 (*A*), contrast-enhanced T1-weighted and T2-FLAIR at 4 months (*B*), and 9 months after procedure (*C*). POD 1 MR image shows a few asymptomatic DWI lesions in the frontal lobe. Four-month follow-up MR shows subcortical enhancing lesions in both the frontal and parietal lobes, far more numerous than the DWI lesions seen in POD 1. The enhancing lesions and the perilesional edema persist in the 9-month follow-up MR imaging, which is not the expected evolution for ischemic lesions. Foreign body reaction was the presumed diagnosis after all clinical and laboratory work-up was negative for infection.

size of the lesions ranged from 2–20 mm in diameter. Most lesions showed solid enhancement. Rim enhancement was seen only in lesions larger than 5 mm. Lesions with rim enhancement were seen in 2 patients (2 lesions in each patient), and showed central restricted diffusion on DWI. Gradient recalled-echo signal dephasing was seen in 5 patients (total number of dephasing lesions = 14; range 1–4). Perilesional edema was seen in all patients, but varied in extent from lesion to lesion. All patients had subcortical lesions, but only 2 also showed deep gray matter lesions (1 anterior circulation and 1 posterior circulation aneurysm). The enhancing lesions were limited to the vascular territory of the artery used to access the aneurysm in 6 cases. In 1 case, the lesions were mostly in the expected vascular territory, with few isolated lesions elsewhere. The sample size did not allow for any subgroup analysis regarding procedure type and characteristics of the enhancing lesions.

Four patients had no neurologic symptoms related to the brain lesions (incidental finding on MR follow-up), 1 patient presented with paresthesias that were attributed to seizure-like activity, 1 patient had gait disturbances associated with posterior fossa lesions, and 1 had mild fluctuating central facial nerve palsy, mild arm weakness, and speech disturbances. Two of the asymptomatic patients had coexisting painless aseptic secretion and swelling at the arterial puncture site. None of the patients presented with hydrocephalus or with meningeal symptoms. In all patients, septic emboli were ruled out on clinical grounds and after an extensive work-up that included complete blood count, lumbar puncture, and echocardiography.

Treatment strategies for these lesions varied. Of the 4 neurologically asymptomatic patients, 2 received no treatment, 1 received empiric antibiotic therapy for 14 days, and 1 received both empiric antibiotics and steroids, with no changes in the imaging or clinical findings during follow-up. Of the 3 symptomatic patients, 1 received no treatment, 1 patient with presumed seizure-like activity received levetiracetam resulting in resolution of the symptoms, and 1 received combined antibiotic therapy for 6 months, but lesions persisted in next follow-up (Fig 2). In the patient treated with levetiracetam, the drug was discontinued after 6 weeks and the patient remained asymptomatic, but the brain

lesions remained unchanged. None of the patients underwent biopsy or surgical resection of the lesions.

Follow-up imaging including brain MR imaging and MRA was available for all 7 patients. Median follow-up was 21.5 months (range: 5–63 months, interquartile range = 11.25 months). Within the follow-up period, the enhancing lesions disappeared in 1 case, decreased in number in 3 cases (Fig 2), were unchanged in 1 case, and increased in number in 2 cases. Perilesional edema fluctuated during the follow-up period, but on last follow-up was better in 5 cases, stable in 1 case, and showed a mixed response in 1 case. None of the cases showed continuing or new restricting lesions on DWI. The 4 rim-enhancing lesions evolved to a solid pattern of enhancement (Fig 3). Of the 14 lesions with gradient recalled-echo signal dephasing, 1 disappeared, 3 showed interval decrease in size, and the rest remained unchanged. All patients but 1, including those initially symptomatic, had no neurologic symptoms attributable to the brain lesions at their last clinical appointment. None of the patients developed new or worsening symptoms.

DISCUSSION

It is reasonable to believe that the enhancing brain lesions we describe represent an embolic phenomenon as they were restricted in all but 1 case to the vascular territory of the catheterized arteries. In addition, lesions were predominately located in the cortico-subcortical region where small emboli are more likely to get lodged.

Clinically silent emboli are a common known occurrence of diagnostic cerebral angiograms and neuroendovascular procedures, occuring in approximately 13%–53% of cases.[12,13] Inadvertent foreign body emboli is a far less known complication, first described in 1960.[14] Subsequent reports mostly focused on this phenomenon as a cause of postprocedural ischemia.[11] More recently, hydrophilic polymer emboli have been reported as a cause of brain infarction after EVT.[10,15] In a more recent report, intraprocedural foreign body emboli of one of the water-soluble polymers used for hydrophilic coating (polyvinylpyrrolidone or PVP) have been associated with posttreatment delayed ipsilateral
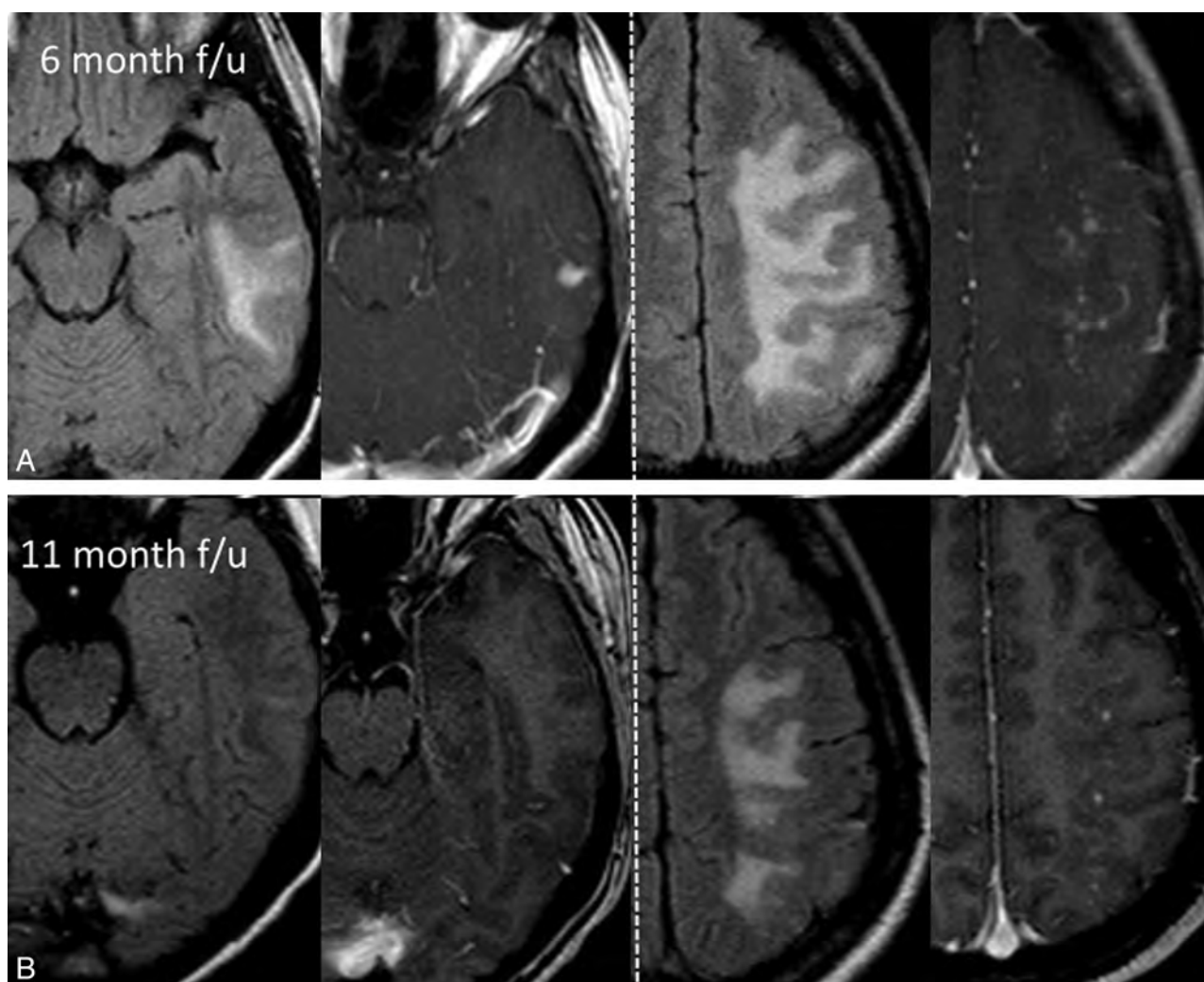
FIG 2. A 32-year-old woman with an unruptured left MCA aneurysm treated with balloon-assisted coiling. Axial FLAIR and axial T1-weighted contrast-enhanced MR images at 6 months (*A*) and 11 months (*B*) follow-up show multiple enhancing cortico-subcortical lesions in the distal MCA territory surrounded by vasogenic edema. Combined antibiotic therapy was initiated after (*A*) with only partial improvement in the next follow-up. Note how the middle temporal gyrus lesion disappears over time while the middle frontal lesions only decrease in number.

intraparenchymal hemorrhage after flow diversion.[16] The first reported brain parenchymal foreign body reaction presenting as MR imaging–enhancing lesions after EVT was published by Fealey et al[8] in a 58-year-old woman with a ruptured right ICA aneurysm. This patient presented 9 months after uneventful coiling with seizures and 3 associated rim-enhancing brain lesions in the postcentral gyrus. After empiric antibitotic treatment with no change in the brain lesions, a brain biopsy was performed. The pathology specimen revealed granulomatous foreign body reaction and trapped filaments of hydrophilic coating polymer. Similar lesions were found in the arterial access site of the other 2 patients described in this case report.

It is likely that the number of diagnosed cases of brain foreign body granulomas after neuroendovascular procedures is increasing in recent years as MR and MRA widely replace the use of DSA for follow-up of aneurysms after EVT. Surprisingly, recent trials that have used MR imaging for follow-up do not comment on the presence or absence of enhancing lesions.[2] Specifically, the 2 recent trials that used modified platinum coils where nonvascular complications were first described made no mention regarding subacute enhancing brain lesions in their published data.[17,18]

In our case series, the lesions were diagnosed on MR relatively late (after a median time of 63 days) and only a few lesions were restricted on DWI; thus, acute or subacute ischemia is not considered a plausible diagnosis. In patients for whom early postprocedure MR imaging was available, there were a few isolated DWI restricting lesions, but no early enhancing lesions were documented. All of our patients had perilesional edema, which prompted a more complete brain MR imaging protocol, and underwent extensive clinical and laboratory work-up to rule out an infectious etiology (ie, septic emboli). Moreover, the rare reports of brain abscesses after coiling, all presented with positive biochemical markers of CNS infection or isolated pathogen on CSF cultures.[19-21] The 4 lesions in our series that showed diffusion restriction and rim enhancement could be in keeping with aseptic abscesses, which have been described in foreign body reaction after surgery.[22-24] All these lesions evolved from a rim-enhancing pattern to a solid enhancement pattern in follow-up and the diffusion restriction disappeared (Fig 3). This appearance could represent evolution from an aseptic abscess to the more chronic form of a foreign body granuloma.
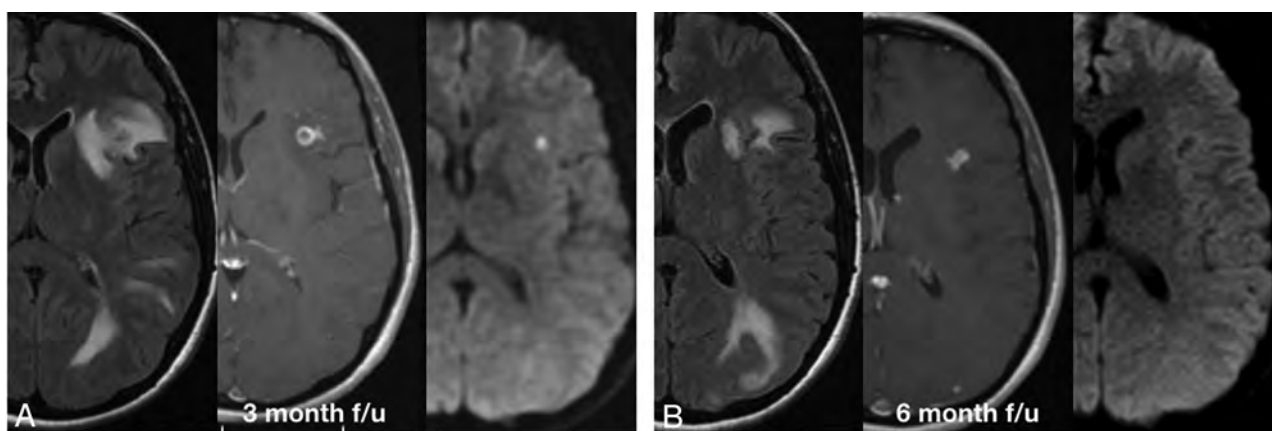
FIG 3. A 51-year-old woman with an asymptomatic intradural left cavernous ICA aneurysm treated with a flow diverter. Axial contrast-enhanced T1-weighted, T2-FLAIR, and DWI brain MR images at 3 months (*A*) and 6 months (*B*). *A*, Representation of 1 of the rim-enhancing lesions in the frontal operculum, with significant perilesional edema and restricted diffusion. An infectious cause was ruled out on clinical grounds and a foreign body reaction was considered as the most possible cause. The patient received 6 weeks of combined oral antibiotic therapy and remained asymptomatic. *B*, At 6-month follow-up, the lesions show a solid pattern of enhancement, with no restricted diffusion and only partial improvement of the edema. This was considered to represent the evolution of an aseptic abscess into a foreign body granuloma. The lesions and the surrounding edema decrease slowly in size but at 2-year follow up still exist (not shown).

Local foreign body reaction at the puncture site was described (2.8%–5.0%) in the cardiology literature after radial access by using long hydrophilic coated sheaths.[25-27] Two of our patients presented with aseptic secretion and local inflammation at the puncture site that did not respond to the initial antibiotic treatment, and eventually resolved spontaneously over a few months. Pathologic specimen was not obtained in these cases; however, the clinical picture corresponds to a foreign body skin reaction. Whether this makes the host more prone to developing a foreign body reaction to hydrophilic coating in the brain is unclear.

Our small case series is limited to EVT for aneurysms, which does not mean that this phenomenon cannot be seen in other neurovascular procedures. It is possible that all of our cases are aneurysmal due to the need to navigate distally toward the aneurysm and use coaxial catheters with friction between coaxial catheters and between the coils, stents, and the microcatheter lumen during these procedures. This might increase the risk of hydrophilic coating dislodgement. Aneurysm coiling is also the most common procedure in the institutions participating in this report and all participating institutions use MRA for follow-up, allowing depiction of asymptomatic lesions.

There are several limitations to this series. First, we report a limited series of incidental cases and not a systematic review of all cases performed, thus the exact incidence of this complication cannot be established. We can presume that it is a rare occurrence given that cases were submitted from 5 different referral neurovascular centers with an average of 95 aneurysms per center per year. One of the patients presented 5 years ago and the rest in the last 3 years with no other diagnosed cases in this time period. The timing of the initial and follow-up MR imaging varies widely from case to case and between institutions. Thus, a conclusion regarding the exact timing of lesion development is limited. In addition, none of our cases are proved by surgical biopsy, as lesion resection was not considered necessary, and the diagnosis was made on the basis of clinical and imaging features.

CONCLUSIONS

Enhancing brain lesions are a rare complication after aneurysm EVT. We did not find this complication exclusive to the use of any particular device. Imaging and clinical characteristics suggest a foreign body reaction such as aseptic abscess and granuloma. We suggest that the cause of these lesions might be shedding of hydrophilic coating from endovascular devices into the blood stream.

REFERENCES

1. Molyneux AJ, Kerr RS, Birks J, et al. **Risk of recurrent subarachnoid haemorrhage, death, or dependence and standardised mortality ratios after clipping or coiling of an intracranial aneurysm in the International Subarachnoid Aneurysm Trial (ISAT): long-term follow-up.** *Lancet Neurol* 2009;8:427–33
2. Spetzler RF, McDougall CG, Albuquerque FC, et al. **The Barrow ruptured aneurysm trial: 3-year results.** *J Neurosurg* 2013;119:146–57
3. Pierot L, Wakhloo AK. **Endovascular treatment of intracranial aneurysms: current status.** *Stroke* 2013;44:2046–54
4. Pierot L, Cognard C, Spelle L, et al. **Safety and efficacy of balloon remodeling technique during endovascular treatment of intracranial aneurysms: critical review of the literature.** *AJNR Am J Neuroradiol* 2012;33:12–15
5. Fanning NF, Willinsky RA, ter Brugge KG. **Wall enhancement, edema, and hydrocephalus after endovascular coil occlusion of intradural cerebral aneurysms.** *J Neurosurg* 2008;108:1074–86
6. Horie N, Kitagawa N, Morikawa M, et al. **Progressive perianeurysmal edema induced after endovascular coil embolization. Report of three cases and review of the literature.** *J Neurosurg* 2007;106:916–20
7. Marchan EM, Sekula RF, Jr, Ku A, et al. **Hydrogel coil-related delayed hydrocephalus in patients with unruptured aneurysms.** *J Neurosurg* 2008;109:186–90
8. Fealey ME, Edwards WD, Giannini C, et al. **Complications of endo-**

vascular polymers associated with vascular introducer sheaths and metallic coils in 3 patients, with literature review. *Am J Surg Pathol* 2008;32:1310–16

9. Mehta RI, Mehta RI, Fishbein MC, et al. **Intravascular polymer material after coil embolization of a giant cerebral aneurysm.** *Hum Pathol* 2009;40:1803–07

10. Mehta RI, Mehta RI, Solis OE, et al. **Hydrophilic polymer emboli: an under-recognized iatrogenic cause of ischemia and infarct.** *Mod Pathol* 2010;23:921–30

11. Shannon P, Billbao JM, Marotta T, et al. **Inadvertent foreign body embolization in diagnostic and therapeutic cerebral angiography.** *AJNR Am J Neuroradiol* 2006;27:278–82

12. Bendszus M, Koltzenburg M, Burger R, et al. **Silent embolism in diagnostic cerebral angiography and neurointerventional procedures: a prospective study.** *Lancet* 1999;354:1594–97

13. Hill MD, Martin RH, Mikulis D, et al. **Safety and efficacy of NA-1 in patients with iatrogenic stroke after endovascular aneurysm repair (ENACT): a phase 2, randomised, double-blind, placebo-controlled trial.** *Lancet Neurol* 2012;11:942–50

14. Silberman J, Cravioto H, Feigin, I. **Foreign body emboli following cerebral angiography.** *Trans Am Neurol Assoc* 1960;85:123–25

15. Barnwell SL, D'Agostino AN, Shapiro SL, et al. **Foreign bodies in small arteries after use of an infusion microcatheter.** *AJNR Am J Neuroradiol* 1997;18:1886–89

16. Hu YC, Deshmukh VR, Albuquerque FC, et al. **Histopathological assessment of fatal ipsilateral intraparenchymal hemorrhages after the treatment of supraclinoid aneurysms with the Pipeline embolization device.** *J Neurosurg* 2014;120:365–74

17. Coley S, Sneade M, Clarke A, et al. **Cerecyte coil trial: procedural safety and clinical outcomes in patients with ruptured and unruptured intracranial aneurysms.** *AJNR Am J Neuroradiol* 2012;33:474–80

18. White PM, Lewis SC, Gholkar A, et al. **Hydrogel-coated coils versus bare platinum coils for the endovascular treatment of intracranial aneurysms (HELPS): a randomised controlled trial.** *Lancet* 2011;377:1655–62

19. AL-Okaili, R, Patel SJ. **Brain abscess after endovascular coiling of a saccular aneurysm: case report.** *AJNR Am J Neuroradiol* 2002;23:697–99

20. Jenkinson MD, Javadpour M, Nixon T, et al. **Intracerebral abscess formation following embolisation of an internal carotid artery aneurysm using Guglielmi detachable coils.** *Acta Neurochir (Wien)* 2003;145:703–05; discussion 705–06

21. Kirollos RW, Bosma JJ, Radhakrishnan J, et al. **Endovascularly treated cerebral aneurysm using Guglielmi detachable coils acting as a nidus for brain abscess formation secondary to salmonella bacteremia: case report.** *Neurosurgery* 2002;51:234–37; discussion 237–38

22. Jang SW, Kim SJ, Kim SM, et al. **MR spectroscopy and perfusion MR imaging findings of intracranial foreign body granuloma: a case report.** *Korean J Radiol* 2010;11:359–63

23. Kothbauer KF, Jallo GI, Siffert J, et al. **Foreign body reaction to hemostatic materials mimicking recurrent brain tumor. Report of three cases.** *J Neurosurg* 2001;95:503–06

24. Yoon MA, Kim E, Kwon BJ, et al. **Muslinoma and muslin-induced foreign body inflammatory reactions after surgical clipping and wrapping for intracranial aneurysms: imaging findings and clinical features.** *J Neurosurg* 2010;112:640–47

25. Cogliano MA, Tolerico PH. **Nonhealing wound resulting from a foreign body to a radial arterial sheath and sterile inflammation associated with transradial catheterization and hydrophilic sheaths.** *Catheter Cardiovasc Interv* 2004;63:104–05

26. Ziakas A, Karkavelas G, Mochlas S. **Sterile inflammation after transradial catheterization using a hydrophilic sheath: a case report.** *Int J Cardiol* 2005;99:495–96

27. Kozak M, Adams DR, Ioffreda MD, et al. **Sterile inflammation associated with transradial catheterization and hydrophilic sheaths.** *Catheter Cardiovasc Interv* 2003;59:207–13

Dynamic CT for Parathyroid Disease: Are Multiple Phases Necessary?

P. Raghavan, C.R. Durst, D.A. Ornan, S. Mukherjee, M. Wintermark, J.T. Patrie, W. Xin, A.L. Shada, J.B. Hanks, and P.W. Smith

ABSTRACT

BACKGROUND AND PURPOSE: A 4D CT protocol for detection of parathyroid lesions involves obtaining unenhanced, arterial, early, and delayed venous phase images. The aim of the study was to determine the ideal combination of phases that would minimize radiation dose without sacrificing diagnostic accuracy.

MATERIALS AND METHODS: With institutional review board approval, the records of 29 patients with primary hyperparathyroidism who had undergone surgical exploration were reviewed. Four neuroradiologists who were blinded to the surgical outcome reviewed the imaging studies in 5 combinations (unenhanced and arterial phase; unenhanced, arterial, and early venous; all 4 phases; arterial alone; arterial and early venous phases) with an interval of at least 7 days between each review. The accuracy of interpretation in lateralizing an abnormality to the side of the neck (right, left, ectopic) and localizing it to a quadrant in the neck (right or left upper, right or left lower) was evaluated.

RESULTS: The lateralization and localization accuracy (90.5% and 91.5%, respectively) of the arterial phase alone was comparable with the other combinations of phases. There was no statistically significant difference among the different combinations of phases in their ability to lateralize or localize adenomas to a quadrant ($P = .976$ and .996, respectively).

CONCLUSIONS: Assessment of a small group of patients shows that adequate diagnostic accuracy for parathyroid adenoma localization may be achievable by obtaining arterial phase images alone. If this outcome can be validated prospectively in a larger group of patients, then the radiation dose can potentially be reduced to one-fourth of what would otherwise be administered.

ABBREVIATIONS: NPV = predictive value; PPV = positive predictive value

Primary hyperparathyroidism is defined as hypercalcemia secondary to overproduction of parathyroid hormone by ≥ 1 parathyroid gland.[1] Excessive unregulated parathyroid hormone production by a parathyroid adenoma or hyperplasia results in increased renal absorption of calcium, increased synthesis of $1,25(OH)_2D_3$, phosphaturia, and accelerated bone resorption.[2] Primary hyperparathyroidism can only be cured by surgical exci-

sion of the abnormal parathyroid tissue, which, in approximately 90% of patients, is a solitary adenoma. With the advent of improved preoperative imaging and the use of intraoperative parathyroid hormone monitoring, standard cervical (or "4-gland") exploration has given way to "minimally invasive" or directed parathyroidectomy for the treatment of single-gland disease in the hands of most experienced parathyroid surgeons.[3] Directed parathyroidectomy allows a smaller surgical incision and a more limited cervical dissection, thereby decreasing the risk of recurrent laryngeal nerve injury, permanent hypoparathyroidism, and postoperative pain; decreasing the cost and duration of hospital stay; and, in some patients, avoiding general anesthesia.[3]

Preoperative localization may be achieved with sonography, technetium Tc99m sestamibi imaging (with or without SPECT/CT), and/or dynamic 4D CT. On a standard, nondynamic contrast-enhanced CT of the neck with scan delays approximately 80 seconds after injection, however, differentiation between parathyroid lesions and adjacent small lymph nodes may not be possible. Reported sensitivities of standard neck CT range from 46% to 87% for localization of parathyroid adenoma.[4] 4D CT, intro-

Indicates article with supplemental on-line tables.

Indicates article with supplemental on-line figures.

duced by Rodgers et al,[3] involves obtaining precontrast, arterial, venous, and delayed images of the neck after administration of a bolus of intravenous contrast. 4D CT has been reported to be superior to sonography and sestamibi scanning, with sensitivities in excess of 90% for lateralizing a parathyroid adenoma to one side of the neck and in excess of 85% for localizing an abnormal gland to the correct quadrant of the neck.[5,6] In comparison, the sensitivity for precise localization to a quadrant of the neck ranges from 33% to 65% by using sestamibi and 29%–57% for sonography.[3]

The principle behind 4D CT is that the hypervascularity of parathyroid lesions results in rapid enhancement (detectable in the arterial phase) and washout of contrast (detectable on venous and delayed phases) compared with lymph nodes, which enhance to a lesser degree and retain contrast through the venous and delayed phases. Despite the appearance of numerous articles on the subject in the literature, there is not yet a consensus on what constitutes an optimal dynamic CT study: Some authors advocate 2 phases (unenhanced, arterial), some advocate 3 phases (unenhanced, arterial, venous), some advocate 2.5 phases (unenhanced and arterial phase of the neck followed by a venous phase of the lower neck and entire chest, with a single contrast bolus), while others support 4 phases (unenhanced, arterial, venous, and delayed).[3,5,7-10] Given the variability in techniques reported in the literature, our objective was to determine the optimal dynamic CT protocol necessary for accurate detection of these lesions in a selected cohort of patients undergoing surgical exploration for primary hyperparathyroidism.

MATERIALS AND METHODS

This study was approved by our institutional review board. Data were collected retrospectively and de-identified in compliance with Health Insurance Portability and Accountability Act regulations.

Patient Selection

Between May 2008 and March 2010, 103 patients underwent surgical exploration for primary hyperparathyroidism. Of these, 29 patients met the following inclusion criteria:

1) Laboratory data (blood parathyroid hormone, calcium, inorganic phosphorus, and $1,25[OH]_2D_3$ levels) consistent with primary hyperparathyroidism.
2) Preoperative 4D CT was performed either because of equivocal sonography and sestamibi imaging findings or to facilitate surgical planning.

The clinical records of all patients were reviewed to identify sonography and sestamibi results. Eighteen patients underwent sonography, and 16 underwent sestamibi scanning. Of the 18 patients who underwent sonographic examinations in the clinic, 11 had findings that were negative or equivocal. Three accurately predicted the site of the lesion, and 4 incorrectly predicted the site of the lesion. The sensitivity for all 4 quadrants was 37%, and the specificity was 92%. Of the 16 patients in whom sestamibi imaging was performed, 7 studies had negative or equivocal findings. Seven lesions were accurately identified, and 2 were incorrectly identified. The sensitivity of sestamibi for all 4 quadrants was 37%, and the specificity was 95%. Six patients were re-operative

Table 1: Sequences that readers were allowed to use for interpretation each week

Week No.	Sequences
1	Unenhanced, arterial
2	Unenhanced, arterial, venous
3	Unenhanced, arterial, venous, delayed
4	Arterial
5	Arterial, venous

candidates. Each of these 6 patients underwent a preoperative sestamibi scan, and 4 of the 6 underwent preoperative sonography.

CT Study

Imaging was performed with a 32-section multidetector CT scanner. The scanning parameters were 120 kVp, 50–400 mA range, 1-second rotation speed, pitch of 0.968, detector configuration section width of 1.25 mm, total beam width of 40 mm, and table translation speed of 38.75 mm per gantry rotation; 1.25-mm thick sections were reconstructed at a window width of 350 HU and a 40-HU window center with the detail reconstruction kernel. An unenhanced phase was first obtained. Twenty-five seconds before commencement of the arterial phase, 120 mL of iodinated contrast material (iohexol, Omnipaque 350; GE Healthcare, Piscataway, New Jersey) was injected at 4 mL/s via a pressure injector. A third venous phase was obtained 50 seconds after the commencement of injection, and a fourth delayed phase was obtained 80 seconds after the beginning of injection. All scans were obtained from the carina to the angle of the mandible.

The volume CT dose index for the unenhanced phase was 26.45 mGy. For the other phases, it was 25.41 mGy. The dose-length product (milligray $\times$ centimeter) for the unenhanced phase was 590.49, and for the other phases, it was 567.28.

Image Analysis

Four board-certified neuroradiologists (P.R., S.M., D.A.O., C.D.) with between 1 and 6 years' experience in neuroimaging, retrospectively reviewed each study. Each reader was blinded to the original radiology interpretation, surgical records, and pathology findings. During a 5-week period, the readers were asked to assess each study by using 5 different combinations of the available 4D CT sequences. The order and number of sequences available for interpretation each week were designed to determine whether additional sequences would improve the reader's accuracy in identification of a parathyroid lesion. All readers reviewed the same subset of sequences according to the schedule in Table 1. However, the order of patients was scrambled for each reader so that the readers would not be able to discuss their findings. Two methods were used to limit memory bias. First, the readers were asked to allow 1 week between each assessment. Second, the patients were de-identified, and the reading order was randomly generated and re-scrambled each week.

A lesion that demonstrated enhancement in the arterial phase and was present in one of the locations described below was considered compatible with a parathyroid lesion. The readers were asked to classify the lesions according to their anatomic location: left upper quadrant, left lower quadrant, right upper quadrant, or right lower quadrant with respect to a transverse plane through the middle of the thyroid gland and the midline, or ectopic when

Table 2: Results of localization analysis by sequence combination

Week	Sequences	Accuracy % (95% CI)	Sensitivity % (95% CI)	Specificity % (95% CI)	PPV % (95% CI)	NPV % (95% CI)
1	U, A	91.2 (86.5–94.4)	82.1 (74.8–88.1)	94.1 (91.5–96.1)	81.6 (74.2–87.6)	94.3 (91.7–96.3)
2	U, A, V	90.9 (86.6–93.9)	82.9 (75.6–88.7)	93.4 (90.7–95.5)	80.0 (72.6–86.2)	94.5 (91.9–96.4)
3	U, A, V, D	90.5 (86.1–93.6)	82.1 (74.8–88.1)	93.2 (90.4–95.4)	79.3 (71.8–85.6)	94.3 (91.6–96.2)
4	A	91 (87.1–93.9)	83.6 (76.4–89.3)	93.4 (90.7–95.5)	80.1 (72.7–86.3)	94.7 (92.2–96.6)
5	A, V	91.6 (87.4–94.4)	84.3 (77.2–89.9)	93.9 (91.2–95.9)	81.4 (74.1–87.4)	94.9 (92.4–96.8)

Note:—U indicates unenhanced; A, arterial; V, venous; D, delayed.

located in the mediastinum. If a lesion was encountered in an unusual location, such as in the retropharyngeal space, the readers were asked to indicate this. Note that the quadrants were named on the basis of anatomic position on imaging and not the embryologic origin of the gland. This classification is described as "localization" below. Because there is potential for confusion due to the difference in radiographic anatomic location and embryologic anatomic location, each lesion was also classified on the basis of its general location, either left, right, or mediastinal. This classification is termed "lateralization" below.

The attenuation of each lesion was measured in Hounsfield units for each phase of contrast. For comparison, the Hounsfield unit of a representative lymph node and thyroid tissue was measured for each phase of contrast. To measure the attenuation, we coregistered the 4 phases. Then, a region of interest was drawn to incorporate as much of the suspected lesion as possible while excluding the edge of the tissue to limit extraneous pixel values due to volume averaging. The region of interest was copied to the other 3 phases, and the accuracy of the region-of-interest positioning was verified.

The surgical records were reviewed to identify the locations of the abnormal glands. Intraoperative parathyroid hormone levels and pathologic analysis were used to verify that the suspected lesion was, in fact, an abnormal gland (adenoma or hyperplasia).

Statistical Analyses

Analysis of Measurement Agreement. The surgical findings (pathologically abnormal gland, the removal of which resulted in a drop in serum parathormone levels) were considered the reference standard. Measurement agreement was evaluated for both the neuroradiologists' interpretations of the presence/absence of parathyroid lesions by using localization categorization and for neuroradiologists' interpretations of the presence/absence of parathyroid lesions by using lateralization categorization. Measurement agreement was assessed in terms of the sensitivity and the specificity of the neuroradiologically based interpretations relative to the surgical findings and in terms of the positive predictive value (PPV) and the negative predictive value (NPV) of the neuroradiologically based interpretations. Ninety-five percent confidence interval construction for each of the aforementioned summary measures was based on the exact methods of Agresti and Coull.[11] Area under the receiver operating curve was estimated on the basis of the predictions of binomial generalized estimating equation regression models (On-line Tables 1 and 3).

Analysis of Neuroradiologic Interpretation Accuracy. The accuracy of the neuroradiologists' interpretations of the presence/absence of parathyroid lesions by using localization and lateraliza-

tion categorization in relationship to the surgical findings was assessed by binomial generalized estimating equation regression models.[12] Two regression analyses were conducted. One regression analysis evaluated the accuracy of the neuroradiologists' localization categorizations, while the other evaluated the accuracy of the neuroradiologists' lateralization categorizations. For each regression analysis, the outcome variable was a binary indicator variable that was assigned the value 1 if the neuroradiologist's parathyroid lesion interpretation (present, absent) agreed with the surgical findings, and the value zero was assigned if the 2 findings disagreed. Each regression model included a single categoric predictor variable that identified the 5 4D CT sequence subsets (Table 1). Because the 4 neuroradiologists' parathyroid lesion interpretations could not be assumed to be independent for the same patient, the variance-covariance matrices of the generalized estimating equation regression models were estimated via the Huber-White sandwich variance-covariance estimator to account for inter-reader parathyroid lesion-interpretation correlation in the hypothesis testing and the confidence interval construction processes.[13] Accuracy was defined as the percentage agreement between the neuroradiologists' interpretations and the surgical findings with respect to the presence/absence of parathyroid lesions. Ninety-five percent confidence interval construction for neuroradiologic interpretation accuracy was based on the generalized estimating equation version of the Wald confidence interval construction method. The GENMOD Procedure of the statistical software package SAS, Version 9.3 (SAS Institute, Cary, North Carolina) was used to conduct the aforementioned generalized estimating equation analyses.

Interreader Agreement. Interreader agreement was assessed in 2 ways for both the localization categorizations and the lateralization categorizations. "Complete" interreader agreement required that all 4 readers have the same interpretation with respect to the presences/absence of parathyroid lesions, while "consensus" interreader agreement required that at least 3 of the 4 readers have the same interpretation with respect to the presence/absence of parathyroid lesions. For both criteria, interreader agreement was summarized as the percentage of image assessments in which the criterion was met.

See On-line Tables 1–6 for additional information.

RESULTS
Patients
Twenty-four of the 29 patients in this study were female. The mean age was 56.1 ± 12.8 years with a minimum of 14 years and a maximum of 74 years. The median age was 57 years. The 25th percentile age was 50 years, and the 75th percentile age was 67 years.

Table 3: Results of lateralization analysis by sequence combination

Week	Sequences	Accuracy % (95% CI)	Sensitivity % (95% CI)	Specificity % (95% CI)	PPV % (95% CI)	NPV % (95% CI)
1	U, A	91.1 (85.8–94.6)	89.5 (82.7–94.3)	92.0 (87.6–95.2)	86.0 (78.8–91.5)	94.1 (90.1–96.8)
2	U, A, V	91.7 (87.1–94.7)	91.9 (85.7–96.1)	91.5 (87.1–94.8)	85.7 (78.6–91.2)	95.3 (91.6–97.7)
3	U, A, V, D	90.8 (86.5–93.8)	90.3 (83.7–94.9)	91.1 (86.5–94.5)	84.8 (77.6–90.5)	94.4 (90.5–97.1)
4	A	90.5 (85.4–94)	88.7 (81.8–93.7)	91.5 (87.1–94.8)	85.3 (78–90.8)	93.6 (89.5–96.5)
5	A, V	92. (87.5–95.3)	92.7 (86.7–96.6)	92 (87.6–95.2)	86.5 (79.5–91.8)	95.8 (92.2–98.1)

Note:—U indicates unenhanced; A, arterial; V, venous; D, delayed.
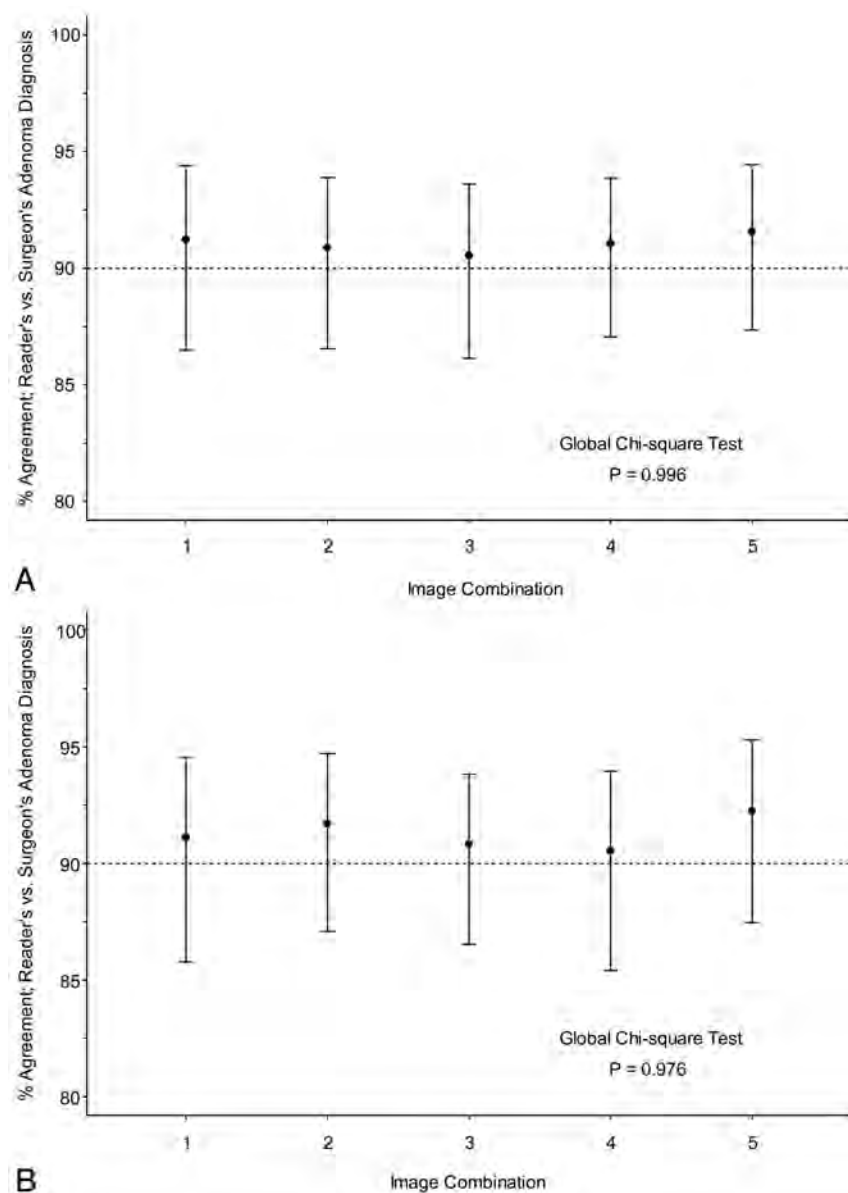
FIG 1. *A*, Accuracy of radiologic interpretation of parathyroid lesions by using localization categorization. *B*, Accuracy of radiographic interpretation of parathyroid lesions by using lateralization categorization. Imaging combinations are given in Table 1.

Surgical/Pathologic Analysis

Of the 29 patients, 3 had no parathyroid lesion at surgery. Five patients had multiglandular disease, 3 of which were hyperplastic and 2 of which were adenomatous. Twenty-one patients had single glandular disease: Twenty were adenomatous and 1 was hyperplastic. The mean weight of the abnormal glands was 539 mg, (median, 520 ± 429.8 mg; range, 6–2200 mg).

4D CT Interpretation

Sensitivities for identifying the specific location of a parathyroid lesion were >80% for each of the imaging combinations, while the specificities were relatively consistent between 93% and 94% as seen in Table 2. The lateralization analysis yielded improved sensitivities, ranging from 88.7% to 92.7% as seen in Table 3. However, the specificity for lateralization dipped to 91.1%–92% because of the 40% decrease in possible locations where an abnormal gland could be classified. Regardless of whether one used the localization or lateralization classification, there was no statistically significant difference between the diagnostic assessment for each combination of phases and the surgical findings with *P* values of .996 and .976, respectively, as seen in Fig 1. The consistency from week to week was, in part, due to a complete interreader agreement of 78% for localization and 77% for lateralization and a consensus interreader agreement of 95% by localization and 95% for lateralization (On-line Tables 1–6, On-line Figs 1 and 2).

Reader-to-surgeon agreement by using localization categorization ranged from 85.2% to 90.2%, with an average of 88.1% (Fig 1*A*). For lateralization, agreement ranged from 84.6% to 91.7%, with an average of 87.7% (Fig 1*B*). This agreement is summarized in Tables 2 and 3.

As seen in Fig 2, the attenuation of parathyroid lesions was similar to that of lymph nodes on noncontrast imaging. On administration of intravenous contrast, there is a greater increase in attenuation in the parathyroid lesions compared with lymph nodes, 108 and 32 HU, respectively. During the venous phase, the contrast in the parathyroid lesions begins to wash out, while the contrast of lymph nodes continues to increase. On delayed imaging, the attenuation of parathyroid lesions approaches that of lymph nodes.

DISCUSSION

Our data indicate that the accuracy, sensitivity, and specificity for localization and lateralization of the arterial phase alone were
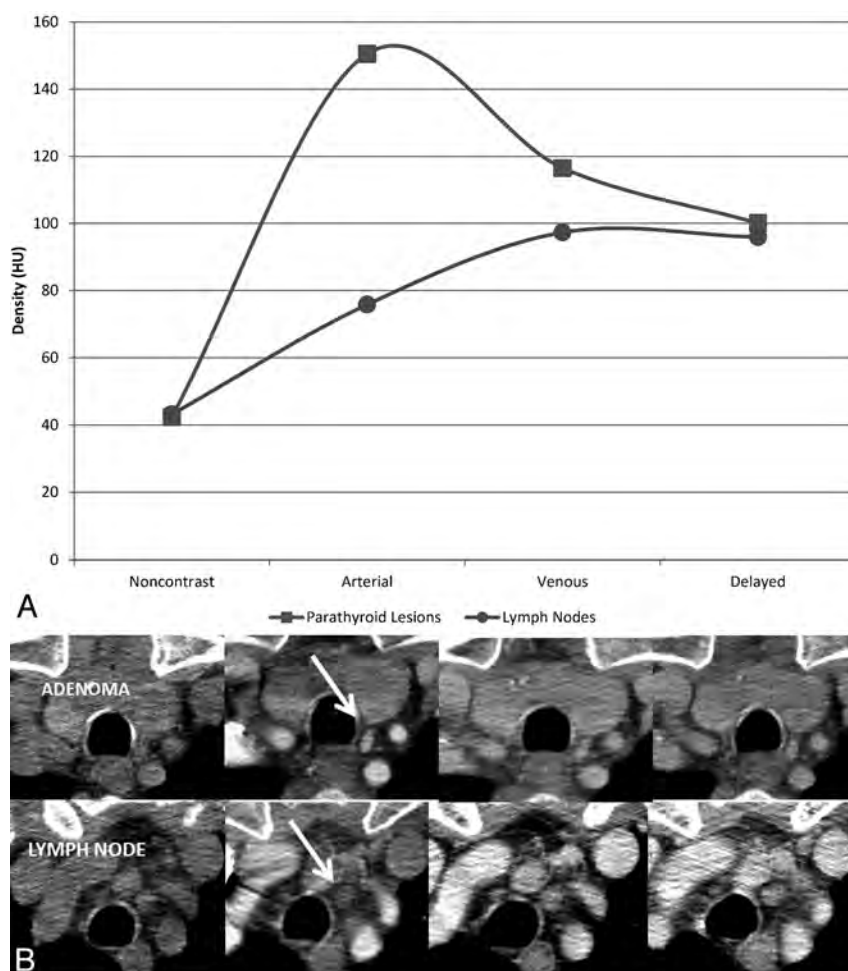
FIG 2. Comparison of the attenuation of true-positive parathyroid lesions and lymph nodes across the 4 phases of contrast. *A*, The time-attenuation curve illustrates that the greatest difference in attenuation between a parathyroid adenoma and a lymph node is in the arterial phase. In the example in *B*, showing axial unenhanced, arterial, venous, and delayed phase CT images from left to right, note that the parathyroid adenoma enhances intensely in the arterial phase, while the lymph node does not (*arrow*). The 2 demonstrate similar densities in the venous and delayed phases.

comparable with the full complement of 4 phases in our cohort of patients. Our sensitivities for lateralization and localization are also similar to those reported by Rodgers et al[3] (sensitivity for lateralization, 88%; for localization, 70%), Chazen et al[5] (93%, 92%), Starker et al[6] (93.9%, 85.7%), and Beland et al[7] (localization 82%). They are also comparable with a recent article by Hunter et al,[14] who, in a study of 4D CT in 143 patients with single-gland disease, reported lateralization and localization accuracies of 93.7% and 86.6%, respectively. The high accuracy of the arterial phase alone is not a surprising finding, given that the greatest difference in attenuation between an adenoma and small lymph nodes is in the arterial phase. This is illustrated in the time-attenuation curve in Fig 2.

All the parathyroid lesions in our series demonstrated arterial phase hyperenhancement. Most adenomas share 2 distinctive features, rapid arterial phase enhancement and location in typical anatomic areas, both of which can be characterized on arterial phase imaging. There may, however, be instances in which additional phases are necessary. For example, a case may be made for an unenhanced phase to enable differentiation of an intrinsically hyperattenuated exophytic thyroid nodule from an enhancing parathyroid lesion. An unenhanced phase would also be of use in patients whose adenomas are not separable by a fat plane from the thyroid. Unenhanced phases would not be expected to be helpful if the thyroid itself is diseased and is not inherently hyperattenuated, a phenomenon not infrequently encountered. In addition, in patients with a history of thyroidectomy, this phase could be omitted. Additional phases are likely of value in the detection of intrathyroidal adenomas. These, however, are uncommon and account for <1% of all adenomas.[15]

Hunter et al[16] proposed a logistic regression model that incorporates information from a triple-phase 4D CT scan of the neck to provide improved discriminatory ability compared with a dual-phase 4D CT scan when used to distinguish parathyroid adenomas and local mimics. Their data indicate that a model using an unenhanced, arterial phase had an accuracy of 94.7% compared with 96.9% in a model built from 3 phases. While statistically significant and interesting, the clinical utility of a 1.9% gain in accuracy would have to be evaluated in a prospective study. Such a model also has the limitation of requiring a stand-alone calculator, an endeavor that is not trivial in routine clinical practice. Furthermore, not all parathyroid adenomas enhance intensely in the arterial phase. These include lipoadenomas and cystic adenomas, both rare lesions.[17,18] It may be argued that the fat content of the former and the cystic nature of the latter should be detectable in any phase and the performance of multiple phases confers no benefit.

As discussed in a recent review of the subject, concerns about the radiation exposure associated with 4D CT do exist.[19] Mahajan et al[20] calculated a 10.4-mSv patient effective dose for 4D CT, while in a study by Madorin et al,[21] it was 5.56 mSv, highlighting that the differences in radiation dosage between these studies reflect the variability in dynamic parathyroid CT protocols between institutions. However, although the effective dose to the thyroid is significantly higher with 4D CT than with scintigraphy, the lifetime attributable risk of thyroid cancer in the typical demographic that presents with hyperparathyroidism (women older than 50 years) is 3 times lower than the 2009 population incidence of thyroid cancer (14 per 100,000).[22] The thyroid cancer risk does, however, exceed the current thyroid cancer incidence in younger patients (females 30 years of age or younger or males 20 years of age or younger). It is, therefore, prudent to use 4D CT judiciously,

especially in younger patients. Substituting the 4D study with a single arterial phase in such patients can reduce radiation dose without substantially sacrificing accuracy.

Our study has some important limitations. The sample size (29 patients) is relatively small, and our readers were asked to interpret the same studies 5 times, though in varying combinations of phases. This requirement may impart an element of memory bias, which would favor interpretations performed in the later weeks of the study. We attempted to minimize this by allowing at least 1 week between each assessment and by ensuring that the patients were de-identified and the reading order was re-scrambled each week. Additionally, we structured the study so that those phases that were hypothesized to yield the least confidence (single-phase interpretation, 2-phase interpretation, and so forth) were performed at the beginning of the study to ensure that memory bias would be less of an issue while interpreting these phases. Also due to the small sample size, factors such as streak artifacts from the contrast bolus, distorted anatomy due to previous surgery, and slips and remnants of thyroid tissue were not encountered to a degree significant enough to confound interpretation.

CONCLUSIONS

Our preliminary data suggest that in routine practice, multiple phases may not be necessary for the localization of parathyroid lesions. In most cases, a single arterial phase CT study may be sufficient, conveying the important advantage of reduction in radiation dose, especially in younger patients. There are instances in which additional phases may be of benefit, but their relatively low prevalence may not warrant subjecting every patient with a suspected parathyroid adenoma to the full complement of phases and the radiation dose that this entails. A full 4D CT study could be considered a problem-solving tool in those cases in which single-phase imaging is equivocal.

REFERENCES

1. Rodgers SE, Lew JI, Solorzano CC. **Primary hyperparathyroidism.** *Curr Opin Oncol* 2008;20:52–58
2. DeLellis RA, Mazzaglia P, Mangray S. **Primary hyperparathyroidism: a current perspective.** *Arch Pathol Lab Med* 2008;132:1251–62
3. Rodgers SE, Hunter GJ, Hamberg LM, et al. **Improved preoperative planning for directed parathyroidectomy with 4-dimensional computed tomography.** *Surgery* 2006;140:932–40, discussion 940–41
4. Gotway MB, Higgins CB. **MR imaging of the thyroid and parathyroid glands.** *Magn Reson Imaging Clin N Am* 2000;8:163–82, ix
5. Chazen JL, Gupta A, Dunning A, et al. **Diagnostic accuracy of 4D-CT for parathyroid adenomas and hyperplasia.** *AJNR Am J Neuroradiol* 2012;33:429–33
6. Starker LF, Mahajan A, Bjorklund P, et al. **4D parathyroid CT as the initial localization study for patients with de novo primary hyperparathyroidism.** *Ann Surg Oncol* 2011;18:1723–28
7. Beland MD, Mayo-Smith WW, Grand DJ, et al. **Dynamic MDCT for localization of occult parathyroid adenomas in 26 patients with primary hyperparathyroidism.** *AJR Am J Roentgenol* 2011;196:61–65
8. Linda DD, Ng B, Rebello R, et al. **The utility of multidetector computed tomography for detection of parathyroid disease in the setting of primary hyperparathyroidism.** *Can Assoc Radiol J* 2012;63:100–08
9. Kutler DI, Moquete R, Kazam E, et al. **Parathyroid localization with modified 4D-computed tomography and ultrasonography for patients with primary hyperparathyroidism.** *Laryngoscope* 2011;121:1219–24
10. Harari A, Zarnegar R, Lee J, et al. **Computed tomography can guide focused exploration in select patients with primary hyperparathyroidism and negative sestamibi scanning.** *Surgery* 2008;144:970–76, discussion 976–79
11. Agresti A, Coull BA. **Approximate is better than "exact" for interval estimation of binomial proportions.** *The American Statistician* 1998;52:119–26
12. Hardin JW, Hilbe JM. *Generalized Estimating Equations.* Boca Raton: Chapman and Hall/CRC; 2003
13. Huber PJ. **The behavior of maximum likelihood estimates under nonstandard conditions.** In: Le Cam LM, Neyman J, eds. *Proceedings of the Fifth Berkeley Symposium on Mathematical Statistics and Probability.* Vol 1. Berkeley: University of California Press; 1967
14. Hunter GJ, Schellingerhout D, Vu TH, et al. **Accuracy of four-dimensional CT for the localization of abnormal parathyroid glands in patients with primary hyperparathyroidism.** *Radiology* 2012;264:789–95
15. Mazeh H, Kouniavsky G, Schneider DF, et al. **Intrathyroidal parathyroid glands: small, but mighty (a Napoleon phenomenon).** *Surgery* 2012;152:1193–200
16. Hunter GJ, Ginat DT, Kelly HR, et al. **Discriminating parathyroid adenoma from local mimics by using inherent tissue attenuation and vascular information obtained with four-dimensional CT: formulation of a multinomial logistic regression model.** *Radiology* 2014;270:168–75
17. Chow LS, Erickson LA, Abu-Lebdeh HS, et al. **Parathyroid lipoadenomas: a rare cause of primary hyperparathyroidism.** *Endocr Pract* 2006;12:131–36
18. Sillery JC, DeLone DR, Welker KM. **Cystic parathyroid adenomas on dynamic CT.** *AJNR Am J Neuroradiol* 2011;32:E107–09
19. Hoang JK, Sung WK, Bahl M, et al. **How to perform parathyroid 4D CT: tips and traps for technique and interpretation.** *Radiology* 2014;270:15–24
20. Mahajan A, Starker LF, Ghita M, et al. **Parathyroid four-dimensional computed tomography: evaluation of radiation dose exposure during preoperative localization of parathyroid tumors in primary hyperparathyroidism.** *World J Surg* 2012;36:1335–39
21. Madorin CA, Owen R, Coakley B, et al. **Comparison of radiation exposure and cost between dynamic computed tomography and sestamibi scintigraphy for preoperative localization of parathyroid lesions.** *JAMA Surg* 2013;148:500–03
22. Surveillance Research Program. National Cancer Institute SEER*Stat software. Version 1983–2009. seer.cancer.gov/seerstat. Accessed October 1, 2013

Ossification of the Vascular Pedicle in Microsurgical Fibular Free Flap Reconstruction of the Head and Neck

C.M. Glastonbury, A. van Zante, and P.D. Knott

ABSTRACT

BACKGROUND AND PURPOSE: The fibular free flap, often used for osseous reconstruction following extirpation of head and neck malignancies, has been associated with heterotopic periosteal ossification. We aimed to determine the frequency and radiologic characteristics of this process and describe its clinical correlates.

MATERIALS AND METHODS: Surgical records for 2 years and neck imaging reports for 10 years were evaluated to identify patients with fibular free flap reconstruction and CT and/or PET/CT imaging available for review. The images were evaluated for the quality, type, and contour of ossification, and the reports were reviewed for associated clinical findings and radiologic impressions.

RESULTS: Of 32 patients with posttreatment CT or PET/CT imaging, ossification was evident in 16 patients (50%) as early as 1 month following fibular free flap reconstruction. In 8 patients, it mimicked a new bone; in 5, it appeared as linear attenuation; in 2, as multiple short segments; and in 1 patient, a mixed appearance was found. No associated FDG uptake was seen on PET/CT. On MR imaging, these findings were extremely subtle or not appreciable. In only 1 patient was new bone associated with symptoms.

CONCLUSIONS: Periosteal ossification of the vascular pedicle is commonly evident on CT following fibular free flap, even as early as 1 month after reconstruction, though the finding is not typically noted on imaging. While symptoms related to new bone are uncommon, they may mimic recurrent tumor. The location and pattern of ossification and the absence of a soft-tissue mass or FDG uptake are useful distinguishing imaging features.

ABBREVIATIONS: FFF = fibular free flap; HNSCC = head and neck squamous cell carcinoma

Microsurgical free flaps are commonly used for reconstruction of surgical defects in patients with head and neck malignancies. Such flaps allow cosmetic and functional improvement following resection of neoplasms, and they may additionally provide protection for vulnerable tissues before radiation therapy.[1,2] Following resection of all or part of the mandible or maxilla, osteocutaneous flaps may be used for reconstruction, with the most frequent choice being the fibular free flap (FFF).[2] After fibula bone harvest, the distal aspect of the bone is osteotomized and contoured to fit the facial bone defect, while the vascular pedicle is carefully preserved and then anastomosed to available neck vessels in either the ipsilateral or contralateral neck.[3]

Posttreatment imaging evaluation after free flap reconstruction is often complex, with loss of reliably symmetric anatomic landmarks and altered signal intensity (MR imaging) or attenuation (CT) of both native and flap tissues, particularly with denervation changes in the muscular component of myogenous flaps. Concurrently, the clinical examination after reconstruction can be difficult, both in the early postoperative edematous phase and the more delayed phase, especially when radiation is also delivered.

While the imaging features of microsurgical free flaps[4-6] have been described and imaging features suggesting recurrent tumor have also been delineated,[7,8] we have observed an unusual finding on neck CT scans of new bone developing in patients with prior fibular free flap placement. This new bone has been described in the surgical literature, predominantly in case reports, and has been ascribed to heterotopic ossification arising from fibula periosteum, which is preserved as part of the vascular pedicle during microvascular reconstruction.[9-16] It has been described as a potential clinical pitfall, presenting as a new hard neck mass and mimicking recurrent disease. We sought to determine the frequency, timing, and radiologic characteristics of heterotopic
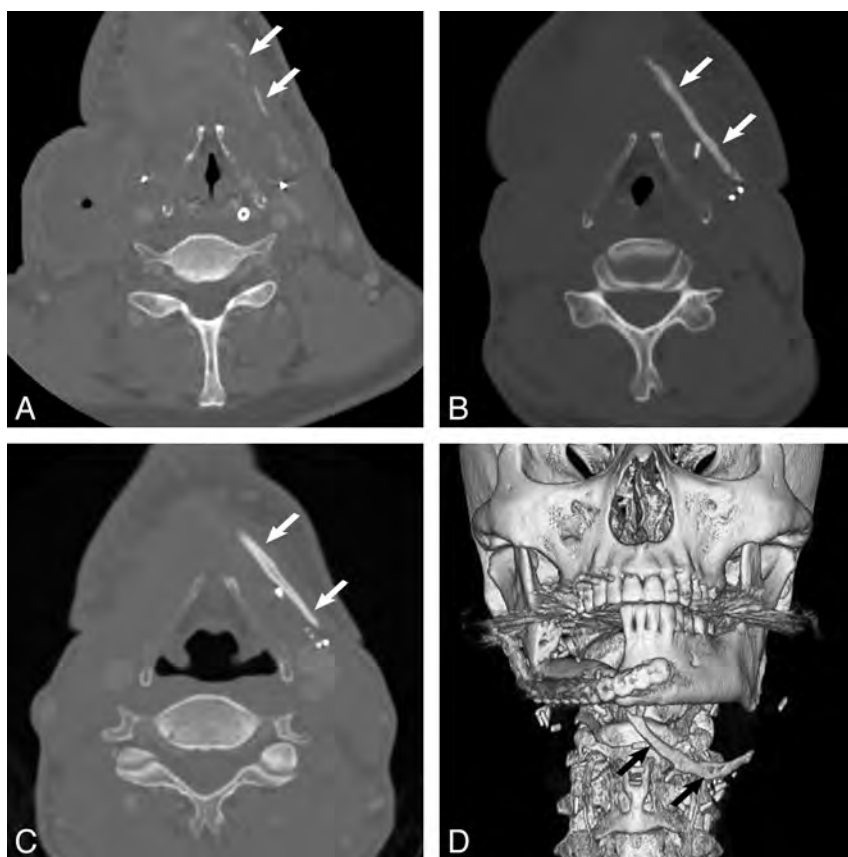
FIG 1. Axial contrast-enhanced neck CT scans and 3D reformat performed in a 59-year-old-man who underwent fibular free flap reconstruction for osteomyelitis complicating segmental mandibulectomy (patient 3). Imaging performed at 1 month (*A*), 2 months (*B*), and 12 months (*C*) shows progressive ossification in the left neck from linear segmental densities to a linear attenuation to a linear structure with features characteristic of bone (*arrows*). The new bone is of greater attenuation than enhancing vessels and is less attenuated than adjacent vascular clips. *D*, 3D reformation from a CT scan at 9 months when the pedicle ossification (*arrows*) was first mentioned in the imaging report.

MR imaging. The images were evaluated for the size and type of ossification (linear or curved, continuous or multisegmented) and quality (dense or bonelike with cortical bone and marrow evident). If MR imaging was available, it was reviewed in a retrospective fashion to determine whether ossification could be identified. If multiple imaging studies were performed, these were reviewed sequentially to determine any changes in the development of ossification such as ongoing growth or resorption.

Evaluation of flaps by CT is performed as a postcontrast CT examination with 3-mm sections and sagittal and coronal reformations. Images are also reviewed on bone window algorithm images generated from the same data. All PET/CT at our institution for patients with head and neck pathology is routinely performed with intravenous contrast (unless contraindicated) and is reformatted with dedicated 3-mm neck CT sections. Neck MR imaging is performed on either a 1.5T or 3T magnet with 4-mm axial and coronal T1 and T2 fat saturated sequences and postcontrast axial and coronal T1 fat saturated sequences unless gadolinium is contraindicated.

The patient' clinical records were reviewed for the indication for FFF reconstruction, and the clinical notes were reviewed to determine whether concerning symptoms or a mass was evident clinically. The imaging reports were also reviewed to determine whether ossification had been reported.

ossification after flap placement and the frequency with which it was described in CT, MR imaging, and PET/CT imaging reports or was clinically concerning.

MATERIALS AND METHODS

The surgical records of a single head and neck reconstructive surgeon were evaluated to identify patients who had FFF reconstructive surgery and neck imaging available. In addition, all CT, PET/CT, and MR imaging radiology reports at our institution from July 2004 to July 2013 were searched for the terms "free flap," "flap reconstruction," "fibula flap," and "fibular flap" by using Illuminate (Softek, Version 2.0; http://www.softekinc.com/illuminate/) to identify imaging studies of patients with FFF neck reconstruction and imaging performed postoperatively. Institutional review board approval was obtained with consent waived for this retrospective evaluation of clinical notes and imaging records.

The inclusion criteria for the study were those patients with FFF reconstruction at our institution who had at least 1 postoperative CT or PET/CT study available for review. Any neck MR imaging examinations, if available for this cohort, were also reviewed.

The pertinent neck imaging examinations were reviewed by a Certificate of Added Qualification– certified neuroradiologist to determine the presence of ossification on CT, PET/CT, and/or

RESULTS
Patients and Imaging

Using the search methods described, we identified 50 patients who had an FFF placed for facial bony reconstruction. Of this group, 14 were excluded because they had no postoperative imaging available, and 4, because only postoperative neck MR imaging was available. Of the remaining 32 patients, 8 were women and 24 were men. They ranged in age from 29 to 78 years, with a mean age of 60.2 years. Eighteen patients had at least 1 posttreatment neck CT (with or without contrast) available for review, including 2 patients with only early postoperative scans at 1 and 3 weeks, respectively. Eighteen patients had at least 1 posttreatment PET/CT available for review, with 3 patients having both modalities performed. Of the group of 32 with CT of the neck and/or PET/CT, 16 also had neck MR imaging.

In 16 of the 32 patients (50%), heterotopic periosteal ossification was identified. The new bone appeared as bone attenuation and was denser than intravascular iodinated contrast and less dense than metallic clips. The Table describes this study group and its findings. Of those with ossification, 2 were
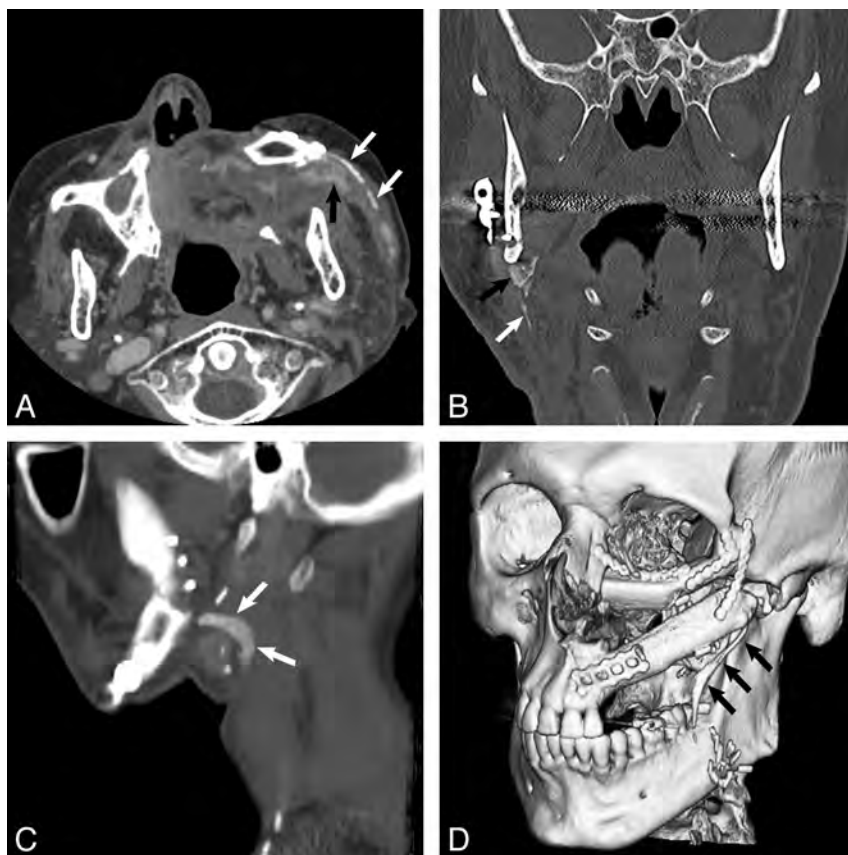
FIG 2. Different patterns of heterotopic ossification. Axial contrast-enhanced CT (*A*) in a 77-year-old man (patient 4) 5 months after FFF reconstruction shows multiple linear densities (*white arrows*); we classify this pattern as multisegmented ossification. Note that pedicle ossification is clearly denser than the adjacent enhancing flap vessels (*black arrow*). Coronal face CT (*B*) in a 72-year-old man (patient 9) 5 months after reconstruction shows vertical linear ossification (*white arrow*) with a more superior triangular bonelike component (*black arrow*). Sagittal reformat from neck CT (*C*) in a 51-year-old man (patient 6) 10 months after reconstruction for recurrent HNSCC shows curved bonelike ossification (*arrows*). 3D reformat (*D*) in a 37-year-old man (patient 2) 9 months after reconstruction following resection of a maxillary osteoblastic osteosarcoma shows a linear bonelike structure (*arrows*).

age thickness and length were 3 mm and 3.7 cm, respectively. For attenuated ossification components, the average thickness and length were 2.5 mm and 2.7 cm, respectively.

In the 6 patients with ossification and multiple CT or PET/CT scans, the ossification was seen to thicken and progress and/or stabilize; it was not seen to resorb or resolve in any case, with the maximum time to imaging of 20 months postreconstruction. The earliest imaging findings were noted on CT or PET/CT scans obtained at 1 month in 3 patients who all had subsequent confirmatory imaging scans. All patients who had ossification had evidence of it on their earliest available CT or PET/CT, and 2 of the linear bonelike structures began as linear densities on the earliest scan.

None of the 16 ossification cases showed a soft-tissue mass in association with the new bone and none of the 8 cases with PET/CT showed FDG uptake above that of background activity associated with the bone. In the 9 ossification cases that also had MR imaging, it was extremely difficult to confidently identify the ossification, even in reviewing the scans alongside the CT scans with abnormal findings and even in cases with thicker bonelike growths.

One patient from the original group of 32 was only imaged at 3 weeks postoperatively and showed no evidence of ossification, but dense tram-track-like vascular calcification of the peroneal artery was present, which was clearly identifiable and distinguishable from the ossification seen in other cases (Fig 3).

women and 14 were men. These patients ranged in age from 37 to 78 years (mean, 62.3 years) at the time of FFF reconstruction. Eight (50%) had surgery for primary or recurrent head and neck squamous cell carcinoma (HNSCC); 2 (12.5%) each, for failed prior reconstruction, metastatic disease, and osteoradionecrosis; 1 (6.25%), for osteomyelitis; and 1, for osteosarcoma. Fourteen of 16 (87.5%) cases were mandibular reconstructions, with the 2 maxillary reconstructions performed for osteoblastic osteosarcoma and failed previous flap after subtotal maxillectomy, respectively.

Patterns of Ossification

In 8 patients (50%), pedicle ossification mimicked development of a "new bone" with cortical and marrow densities evident on CT (Figs 1 and 2). Five of these were linear bonelike structures, 2 of 8 bonelike densities were curved, and 1 of 8 was a rectangular segment of bone. In 5 patients (31%), the ossification appeared as long dense linear segments, and in 2 patients (13%), as multiple short segments of linear density. One patient had a mixed appearance with a long segment of linear density and a short triangular bonelike component. For the bonelike components, the aver-

Radiology and Clinical Reports

On review of the CT imaging reports, the presence of new bone or new density was mentioned in only 1 of the patients. The possibility of a retained foreign body was raised in a neck CT scan obtained at 9 months after FFF because the attenuated structure was retrospectively noted to be present 1 month postreconstruction (Fig 1). Clinical examination of this patient revealed a firm mass in the neck that followed the course of the vascular pedicle. The patient subsequently underwent neck surgery for an unrelated issue, and this tissue was resected, demonstrating well-organized lamellar bone (Fig 4). This was the only patient with a clinical neck mass or reported symptoms referable to the ossification.

DISCUSSION

A fibular free flap is a vascularized osteocutaneous flap used for reconstruction of composite surgical defects of the head and neck. In our practice, it is most often used for reconstruction following segmental mandibulectomy or hemimandibulectomy for squa-

mous cell carcinoma, but it may also be used after resection of other head and neck, jaw, or facial neoplasms and for reconstruction following jaw osteoradionecrosis. The flap can provide up to 25 cm of cortical bone in addition to cutaneous cover and is adequate bone for osseointegrated (dental) implants, which are usually placed later in a second-stage surgery. The bone is fixed in place with reconstruction plates while microvascular anastomosis is performed.[1-3]

We found 16 cases of ossification of the vascular pedicle among 32 patients (50%) with FFF and at least 1 posttreatment CT or PET/CT scan, suggesting that this is not an uncommon finding. While flap ossification is described as rare in the literature, it has also been variably reported as occurring in 17%–65% of neck CT scans and on orofacial panoramic films in 27% of cases in different surgical studies.[9,11,16] One craniofacial article reported more frequent occurrence of heterotopic ossification in FFF reconstructions performed for maxilla resections.[12] Multiple theories have been proposed to account for this new bone formation, including active fracture repair at the osteotomy site, growth factors, mechanical tension, inflammation, and increased blood flow allowing osteoprogenitor recruitment.[12,14,16] These factors
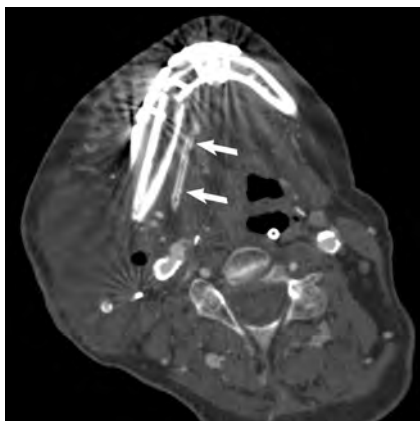
FIG 3. Axial nonenhanced CT in a 73-year-old man 3 weeks after FFF reconstruction shows tram-track vascular calcification in the wall of the peroneal artery (*arrows*), a pattern typical of atherosclerosis. This appears distinctly different from the attenuated, linear, continuous, or multisegmented patterns that were observed in patients with periosteal ossification. Pedicle ossification is not evident on this scan, and the patient had no further CT or PET/CT follow-up at our institution.
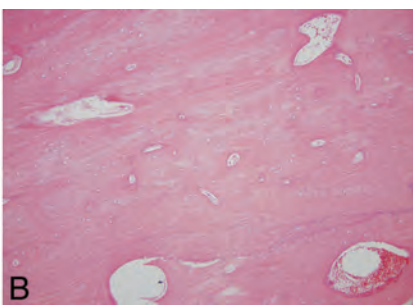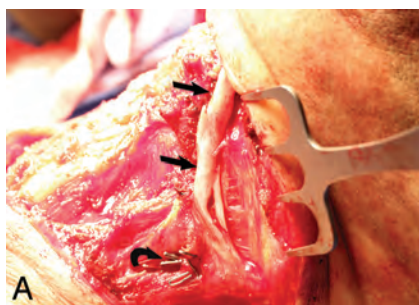
FIG 4. Operative and histopathology images from same patient as in Fig 1 (patient 3). Intraoperative photograph (*A*) at 13 months following fibula microvascular transfer demonstrates pronounced heterotopic calcification of the fibula periosteum (*arrows*). Also note surgical clips (*curved arrow*) that were placed on side branches during the fibula transfer. Histologic section of this resected bone (*B*) with hematoxylin and eosin stain at magnification of 200X shows mature lamellar bone without marrow elements. This bone is microscopically indistinguishable from native bone, such as the hyoid.

may all influence the development of bone formation, but the key underlying characteristic of the FFF is the presence of periosteum from the fibula to which the peroneal vascular pedicle is attached.

During harvest of the fibula, virtually the entire bone is taken (up to 25 cm), while only the distal one-half or one-third of the bone is typically used for reconstruction of the facial bone defect. The proximal one-half to two-thirds of the fibular bone is discarded; however, the contiguous periosteum of the discarded proximal bone is preserved because the vascular pedicle is intimately associated with it and cannot be easily dissected from it. In cases in which the pedicle must reach distant recipient neck vessels, such as in the contralateral neck or to the transverse cervical vessels, the osseous component of the flap may be short and the pedicle with the overlying attached periosteum may be relatively long. This segment of fibular periosteum remains with the FFF and is implanted in the neck, either along the native bone or over the vessels to protect the anastomosis. A recent surgical study had a prospective arm in which 20 patients had a modified harvesting procedure with removal of this fibular periosteum before vascular anastomosis, and none of these patients developed flap ossification in the 18 months following FFF reconstruction.[16] Radiation therapy has also been described as a potential factor in the induction of periosteal ossification but does not appear to influence the onset or extent of flap ossification in either the literature or this current study.[12]

Of the group of 32 patients with FFF and imaging available for review, 2 of 8 women (25%) and 14 of 24 men (58%) developed ossification. The literature does not report a similar sex bias for the occurrence of ossification, and with our small numbers, we are unsure of the reason for this more common frequency in men. While hormones have been proposed as potentially having a role, ossification has been reported in males and females in wide age ranges from pubescence to adults, including postmenopausal women, as is the case with our 2 patients.[9-13,16]

Reported clinical manifestations of pedicle ossification include trismus, severe pain with mastication or head turning, submandibular swelling, or a hard palpable mass, though it is evident in the literature that such clinical findings are present in less than one-third of patients with imaging evidence of ossification and only 1 of our 16 patients was symptomatic.[10,14-16] These clinical symptoms may mimic or raise clinical concern for recurrent tumor. The development of ossification in our patients was all within the 2-year postreconstruction period, when the concern for local tumor recurrence in HNSCC cases is greatest.

In symptomatic cases, the ossified pedicle and its surrounding periosteal tissues may be excised. In asymptomatic cases, there appears to be no surgical indication for resection. That heterotopic ossification of the vascular pedicle is largely asymptomatic undoubtedly accounts for its rare description in the literature. In all except 1 of our patients,

flap ossification was not noted in the radiology report, even when attaining several centimeters in size. The radiologist noting the possibility of a foreign body suggests that radiologists may also not be aware of this phenomenon. The attenuated linear pattern of early new bone may be mistaken for vascular clips, though these are distinctly denser than bone. Mature bone is also less attenuated than contrast-enhancing flap vasculature and appears distinctly different from the tram-track pattern of vascular calcification.

We were only able to identify pedicle ossification on neck MR imaging with careful retrospective review, suggesting that CT (or PET/CT) may be of greater value than MR imaging when a hard mass develops in patients with prior FFF reconstruction.

This retrospective study is limited in that fibular free flap reconstruction at our institution is not routinely followed by CT or PET/CT. In addition, follow-up imaging studies were not always performed at our institution and/or available for review or performed in a defined timeframe. Thus, it is not possible to determine the exact frequency or timing of heterotopic ossification in this setting, though our results agree with the current surgical literature and suggest that it is a reasonably common and stable finding, evident even in the early months following reconstruction.

CONCLUSIONS

Ossification of the vascular pedicle arising from the periosteum associated with a fibular free flap reconstruction is a reasonably common finding on CT examinations of the neck as early as 1 month following reconstruction. This finding is not associated with FDG avidity on PET/CT examinations and is typically very subtle or imperceptible on MR imaging. It may uncommonly present with trismus, pain, or a palpable mass and can be readily differentiated on CT from peroneal artery atherosclerosis, retained surgical material, and, perhaps more important, from recurrent disease by the surgical history, the contour and attenuation of the ossification, and the lack of an associated soft-tissue mass.

REFERENCES

1. Wong CH, Wei FC. **Microsurgical free flap in head and neck reconstruction.** *Head Neck* 2010;32:1236–45
2. Hayden RE, Mullin DP, Patel AK. **Reconstruction of the segmental mandibular defect: current state of the art.** *Curr Opin Otolaryngol Head Neck Surg* 2012;20:231–36
3. Wehage IC, Fansa H. **Complex reconstructions in head and neck cancer surgery: decision making.** *Head Neck Oncol* 2011;3:14
4. Learned KO, Malloy KM, Loevner LA. **Myocutaneous flaps and other vascularized grafts in head and neck reconstruction for cancer treatment.** *Magn Reson Imaging Clin N Am* 2012;20:495–513
5. Hudgins PA. **Flap reconstruction in the head and neck: expected appearance, complications, and recurrent disease.** *Eur J Radiol* 2002;44:130–38
6. Chong J, Chan LL, Langstein HN, et al. **MR imaging of the muscular component of myocutaneous flaps in the head and neck.** *AJNR Am J Neuroradiol* 2001;22:170–74
7. Hudgins PA, Burson JG, Gussack GS, et al. **CT and MR appearance of recurrent malignant head and neck neoplasms after resection and flap reconstruction.** *AJNR Am J Neuroradiol* 1994;15:1689–94
8. Tomura N, Watanabe O, Hirano Y, et al. **MR imaging of recurrent head and neck tumours following flap reconstructive surgery.** *Clin Radiol* 2002;57:109–13
9. DeConde AS, Vira D, Blackwell KE, et al. **Neck mass due to pedicle ossification after oromandibular reconstruction.** *Laryngoscope* 2011;121:2095–99
10. Smith RB, Funk GF. **Severe trismus secondary to periosteal osteogenesis after fibula free flap maxillary reconstruction.** *Head Neck* 2003;25:406–11
11. Karagozoglu KH, Winters HA, Forouzanfar T, et al. **Periosteal ossification of the vascular pedicle after reconstruction of continuity defects of the mandible and the maxilla with fibular free flaps: a retrospective study.** *Br J Oral Maxillofac Surg* 2013;51:965–67
12. Myon L, Ferri J, Genty M, et al. **Consequences of bony free flap's pedicle calcification after jaw reconstruction.** *J Craniofac Surg* 2012;23:872–77
13. Acartürk TO, Aslaner EE. **Periosteal ossification from the vascular pedicle of a free fibular flap.** *J Craniofac Surg* 2011;22:e29–32
14. González-García R, Manzano D, Ruiz-Laza L, et al. **The rare phenomenon of vascular pedicle ossification of free fibular flap in mandibular reconstruction.** *J Craniomaxillofac Surg* 2011;39:114–18
15. Autelitano L, Colletti G, Bazzacchi R, et al. **Ossification of vascular pedicle in fibular free flaps: a report of four cases.** *Int J Oral Maxillofac Surg* 2008;37:669–71
16. Tarsitano A, Sgarzani R, Betti E, et al. **Vascular pedicle ossification of free fibular flap: is it a rare phenomenon? Is it possible to avoid this risk?** *Acta Otorhinolaryngol Ital* 2013;33:307–10

Qualitative and Quantitative Performance of ^{18}F-FDG-PET/MRI versus ^{18}F-FDG-PET/CT in Patients with Head and Neck Cancer

S. Partovi, A. Kohan, J.L. Vercher-Conejero, C. Rubbert, S. Margevicius, M.D. Schluchter, C. Gaeta, P. Faulhaber, and M.R. Robbin

ABSTRACT

BACKGROUND AND PURPOSE: MR imaging and PET/CT are integrated in the work-up of head and neck cancer patients. The hybrid imaging technology ^{18}F-FDG-PET/MR imaging combining morphological and functional information might be attractive in this patient population. The aim of the study was to compare whole-body ^{18}F-FDG-PET/MR imaging and ^{18}F-FDG-PET/CT in patients with head and neck cancer, both qualitatively in terms of lymph node and distant metastases detection and quantitatively in terms of standardized uptake values measured in ^{18}F-FDG-avid lesions.

MATERIALS AND METHODS: Fourteen patients with head and neck cancer underwent both whole-body PET/CT and PET/MR imaging after a single injection of ^{18}F-FDG. Two groups of readers counted the number of lesions on PET/CT and PET/MR imaging scans. A consensus reading was performed in those cases in which the groups disagreed. Quantitative standardized uptake value measurements were performed by placing spheric ROIs over the lesions in 3 different planes. Weighted and unweighted κ statistics, correlation analysis, and the Wilcoxon signed rank test were used for statistical analysis.

RESULTS: κ statistics for the number of head and neck lesion lesions counted (pooled across regions) revealed interreader agreement between groups 1 and 2 of 0.47 and 0.56, respectively. Intrareader agreement was 0.67 and 0.63. The consensus reading provided an intrareader agreement of 0.63. For the presence or absence of metastasis, interreader agreement was 0.85 and 0.70. The consensus reading provided an intrareader agreement of 0.72. The correlations between the maximum standardized uptake value in ^{18}F-FDG-PET/MR imaging and ^{18}F-FDG-PET/CT for primary tumors and lymph node and metastatic lesions were very high (Spearman $r = 1.00$, 0.93, and 0.92, respectively).

CONCLUSIONS: In patients with head and neck cancer, ^{18}F-FDG-PET/MR imaging and ^{18}F-FDG-PET/CT provide comparable results in the detection of lymph node and distant metastases. Standardized uptake values derived from ^{18}F-FDG-PET/MR imaging can be used reliably in this patient population.

ABBREVIATIONS: SUV = standardized uptake value; SUV_{max} = maximum standardized uptake value

H ead and neck cancers are relatively common malignancies in the United States,[1,2] with an incidence estimated between 10 and 20 cases per 100,000 per year.[3] Multimodal complex therapy

protocols are established, which include chemotherapy, radiation therapy, and surgical resection.[4] Accurate staging and re-staging are essential for selection of the appropriate treatment approach in individual patients.

Human whole-body combined or hybrid PET/MR imaging has been recently introduced in the clinical arena. The rationale for PET/MR imaging in head and neck cancer is based on the role of MR imaging and PET/CT in the work-up of this patient population. In head and neck cancer, MR imaging is an attractive technique due to its superior soft-tissue contrast and lower occurrence of metallic dental implant artifacts.[5] PET/CT, however, is capable of depicting regional adenopathy, small tumors, and distant metastases in a whole-body approach. PET/CT is an established technique for staging, re-staging, and treatment-response assessment in head and neck cancer.[6,7] PET/MR imaging, however, might also be attractive for head and neck cancer imaging because it combines the superior soft-tissue and functional

Table 1: Baseline characteristics of patients

Patient	Sex	Age (yr)	Histopathology	Treatment Prior to PET/MRI Study
1	Male	53	Squamous cell carcinoma of the tongue	Radiation therapy and chemotherapy
2	Male	46	Adenocarcinoma of the salivary gland	Chemotherapy
3	Male	66	Squamous cell carcinoma of the tongue	Radiation therapy and chemotherapy
4	Male	67	Squamous cell carcinoma of the oropharynx	Radiation therapy and chemotherapy
5	Male	51	Adenocarcinoma of the salivary gland	Chemotherapy
6	Male	63	Squamous cell carcinoma of the tongue and pharyngeal wall	Radiation therapy and chemotherapy
7	Male	54	Squamous cell carcinoma of the tonsil	No therapy
8	Female	49	Squamous cell carcinoma of the tongue	Radiation therapy and chemotherapy
9	Male	66	Squamous cell carcinoma of the tonsil	Radiation therapy and chemotherapy
10	Male	54	Squamous cell carcinoma of the tonsil	Radiation therapy and chemotherapy
11	Male	57	Squamous cell carcinoma of the tongue	Radiation therapy and chemotherapy
12	Male	42	Squamous cell carcinoma of the tongue	No therapy
13	Male	54	Squamous cell carcinoma of the oropharynx	Radiation therapy and chemotherapy
14	Male	44	Squamous cell carcinoma of the nasopharynx	No therapy

information of MR imaging with the ability of PET to deliver information about metabolism on a cellular level.[8,9]

Uptake of PET tracer can be visualized and quantified by using standardized uptake values (SUVs). Early comparisons of SUVs between PET/MR imaging and PET/CT from our group and others in healthy tissue of oncology patient population have shown good agreement.[10,11] The logical next step is to analyze correlations of SUV in a variety of pathologic conditions in order to use the values derived from PET/MR imaging data reliably in patients for quantification of studies.

The purpose of this prospective study was to systematically analyze lymph node and distant metastases detection qualitatively on whole-body ^{18}F-FDG-PET/MR imaging versus ^{18}F-FDG-PET/CT in patients with head and neck cancer. A further aim of this study was to compare SUVs of ^{18}F-FDG-avid lesions as a quantitative measure of tracer uptake in whole-body ^{18}F-FDG-PET/MR imaging versus ^{18}F-FDG-PET/CT.

MATERIALS AND METHODS
Patient Population
The Health Insurance Portability and Accountability Act–compliant study was approved by the local ethics committee. All patients gave written informed consent before enrollment in the study. Fourteen patients with head and neck cancer (13 men; mean age, 54.7 ± 8.2 years) were included in the study. The baseline characteristics of the patients are listed in Table 1. The patients were referred for a clinically indicated ^{18}F-FDG-PET/CT and then underwent a ^{18}F-FDG-PET/MR imaging. Two of the 14 patients underwent PET/MR imaging first followed by PET/CT. PET/CT was performed 63 ± 6 minutes and PET/MR imaging was conducted 100 ± 34 minutes after ^{18}F-FDG injection. The mean injected dose of ^{18}F-FDG was 11.7 ± 1.4 mCi.

Only patients with head and neck cancer 18 years or older who were referred by their physicians for clinical PET/CT were eligible for the study. All consecutive patients who gave written informed consent were included in the analysis. Exclusion criteria were as follows: 1) patients who were not able to give informed consent (cognitive impairment), 2) pregnant women, 3) implanted metallic or electronic devices, 4) hip or other joint replacements, and 5) a history of kidney disease, with high creatinine levels or a low glomerular filtration rate.

PET/CT Studies
The PET/CT studies were performed, as previously described, according to a standard clinical protocol.[12] In short, a large-bore PET/CT with time-of-flight technology was used (Gemini TF PET/CT; Philips Healthcare, Best, the Netherlands). PET/CT images were acquired in 9–10 bed positions, with 90–120 seconds per bed position. For attenuation-correction and anatomic localization purposes, a low-dose CT protocol without contrast administration was acquired (parameters: 120 kV; 100 mAs; dose modulation; pitch 0.813; slice thickness 5 mm). The overall imaging time for PET/CT was 17 ± 2 minutes.

PET/MR Imaging Studies
^{18}F-FDG-PET/MR imaging was performed on a combined current-generation time-of-flight PET and a 3T MR imaging system (Ingenuity TF PET/MR; Philips Healthcare). PET/MR images were acquired in 9–11 bed positions, with 120–150 seconds per bed position to compensate for radiotracer decay in those cases in which PET/MR imaging was performed after PET/CT. The MR imaging component was performed with an integrated radiofrequency coil and a multistation protocol. In the protocol, the slab size was 6 cm and the maximum FOV was 46 cm. For attenuation correction, a whole-body free-breathing 3D T1-weighted spoiled gradient-echo sequence (sequence parameters: TE, 2.3 ms; TR, 4 ms; 10° flip angle) was acquired. The automatic attenuation-correction procedure was performed according to a previously published method, leading to a 3-segment model with differentiation of air, lung, and soft tissue.[13] The overall time for PET/MR imaging was 29 ± 31 minutes.

Data Analysis
Qualitative reading and quantitative measurements were performed with commercially available software (MIM, Version 5.2; MIM Software, Cleveland, Ohio).

For the qualitative reading, a 2-step approach was used. Initially, 2 independent groups of readers (1 radiologist and 1 nuclear medicine physician per group) read the 28 examinations (14 PET/CT and 14 PET/MR imaging) in a blinded and randomized fashion. After an initial assessment on interreader agreement, a consensus reading was performed in those cases in which the 2 groups disagreed. This second step was also performed in a randomized and blinded fashion
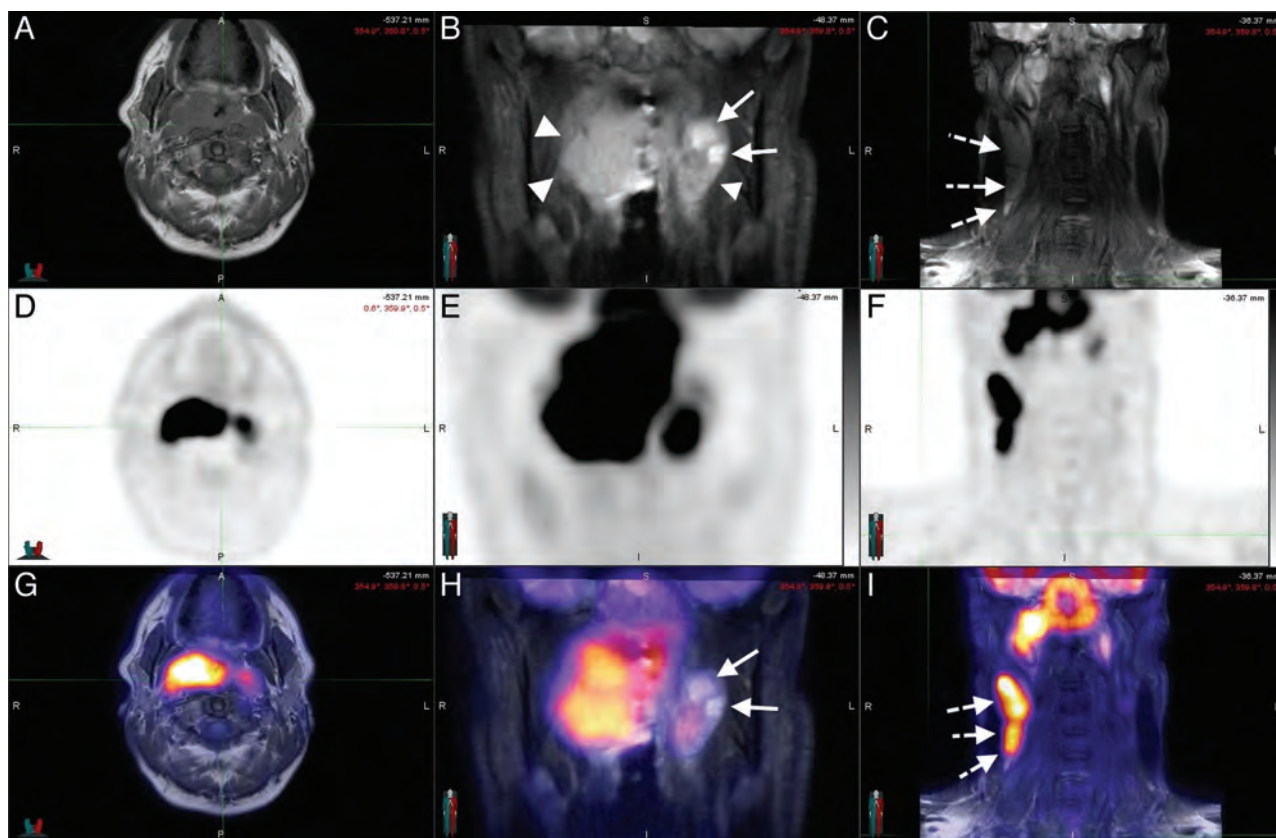
FIG 1. A 44-year-old man with squamous cell carcinoma of the nasopharynx. Axial T1 (*A*) and coronal STIR (*B* and *C*) sequences, with corresponding PET (*D–F*) and the fusion of both (*G–I*), in a patient with nasopharyngeal carcinoma. The neoplastic tissue (*arrowheads*) is easily identifiable in STIR sequences (*B*) in which the cystic component can be visualized (*arrows*). The T1-weighted sequences allow a good assessment of the fat planes. Metastatic lymph nodes (*dotted arrows*) can be assessed morphologically (*C*) and functionally (*I*). Notice the concordance of the cystic areas of the lesion with an area of lower ^{18}F-FDG uptake as expected.

and included 18 examinations, corresponding to 9 patients. Clinical follow-up based on patient charts confirmed the presence or absence of head and neck cancer.

Quantitative analysis of the detected lesions was performed by an experienced board-certified nuclear medicine physician (J.L.V.-C.) through the placement of spheric ROIs over the lesions in 3 different planes (axial, sagittal, and coronal). Maximum SUVs of the lesions, both in PET/CT and PET/MR imaging, were recorded.

Statistical Analysis

Unless otherwise specified, continuous data are reported as mean ± SD. For the first reading, inter- and intrareader agreement was assessed for the number of lesions by using weighted κ statistics. For the first reading, inter- and intrareader agreement was also assessed for the presence or absence of distant metastases (metastases yes or no) by using an unweighted κ statistics. Interreader agreement for PET/CT and PET/MR imaging was evaluated between groups 1 and 2. Intrareader agreements for groups 1 and 2 were evaluated between PET/MR imaging and PET/CT. For the second reading, intrareader agreement for the number of lesions was assessed between PET/MR imaging and PET/CT by using a weighted κ statistics. In this reading, the number of lesions ranged from 0 to 9, and they were categorized as 0, 1, 2, 3, 4, 5 or more. For the second reading, intrareader agreement for the presence or absence of distant metastases (metastases yes or no) was evaluated as well between PET/MR imaging and

PET/CT by using an unweighted κ statistics. For interpretation of the κ statistics, we applied the established criteria of Landis and Koch[14]: κ values in the range of <0.0, $0.0-0.20$, $0.21-0.40$, $0.41-0.60$, $0.61-0.80$, and >0.80 represented poor, slight, fair, moderate, substantial, and almost perfect, respectively.

For the assessment of maximum standardized uptake value (SUV$_{max}$), a clinical (primary tumor, lymph node, and distant metastases) and a localization (for distant metastases: bone, liver, and lung lesions) based assessment were performed. Spearman correlation coefficients between SUV$_{max}$ in PET/MR imaging and PET/CT were calculated. Differences between SUV$_{max}$ in PET/MR imaging and PET/CT were tested by using the Wilcoxon signed rank test. Interpretation of the Spearman correlation coefficients was performed per established standards as previously described[10]: A value ≤0.35 represented a weak correlation; a value between 0.36 and 0.67 represented a moderate correlation; a value between 0.68 and 1.0 represented a high correlation, where a value of ≥0.90 represented a very high correlation. For differences in the Wilcoxon signed rank test, $P < .05$ was considered significant.

RESULTS

Three representative PET/MR imaging cases of head and neck cancer of the study are shown in Fig 1 and On-line Figs 1 and 2.

Qualitative Reading

Agreement on the Number of Lesions (Pooled across Regions). For the first reading, interreader agreements between groups 1 and 2 were moderate for both imaging modalities: Weighted κ values were 0.47 (95% CI, 0.30–0.63) and 0.56 (95% CI, 0.34–0.78) for PET/MR imaging and PET/CT, respectively. For the first reading, intrareader agreements between PET/MR imaging and PET/CT were substantial for both groups: Weighted κ values were 0.67 (95% CI, 0.45–0.88) and 0.63 (95% CI, 0.45–0.80) for groups 1 and 2, respectively.

For the second reading, intrareader agreement between PET/MR imaging and PET/CT was substantial (0–5 or more lesions): The weighted κ was 0.63 (95% CI, 0.47–0.79).
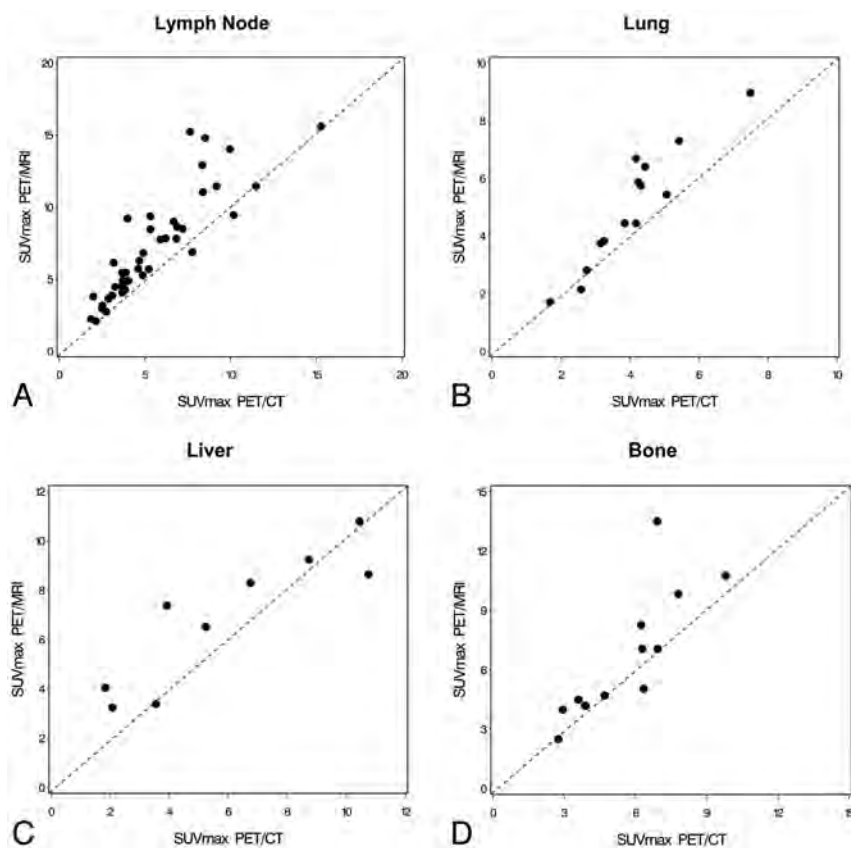
Agreement on the Presence or Absence of Metastases. For the first reading, interreader agreement between groups 1 and 2 was

Table 2: Statistical analysis of differences and correlation between SUV$_{max}$ from PET/CT and PET/MRI

	Primary Tumor Lesions (*n* = 4)	Lymph Node Lesions (*n* = 45)	Distant Metastasis Lesions (*n* = 38)
Spearman *r*	1.00	0.93	0.92
PET/CT	15.69 ± 8.61	5.42 ± 2.83	5.30 ± 2.56
PET/MRI	15.88 ± 5.01	7.10 ± 3.61	6.35 ± 2.92
Difference[a]	0.20 ± 3.97	1.67 ± 1.76	1.05 ± 1.42
P value[b]	.875	<.0001	<.0001

[a] Difference is SUV$_{max}$ PET/MRI minus SUV$_{max}$ PET/CT.
[b] *P* value from the Wilcoxon signed rank test.

Table 3: Statistical analysis of differences and correlation between SUV$_{max}$ from PET/CT and PET/MRI regarding the location of distant metastasis

	Bone Lesions (*n* = 12)	Liver Lesions (*n* = 9)	Lung Lesions (*n* = 15)
Spearman *r*	0.89	0.88	0.93
PET/CT	5.67 ± 2.14	5.92 ± 3.43	4.13 ± 1.41
PET/MRI	6.78 ± 3.28	6.83 ± 2.73	5.12 ± 2.07
Difference[a]	1.11 ± 1.96	0.91 ± 1.56	0.99 ± 0.88
P value[b]	.034	.098	.0006

[a] Difference is SUV$_{max}$ PET/MRI minus SUV$_{max}$ PET/CT.
[b] *P* value from the Wilcoxon signed rank test.

almost perfect for PET/MR imaging and was substantial for PET/CT: Unweighted κ values were 0.85 (95% CI, 0.56–1.00) and 0.70 (95% CI, 0.33–1.00) for PET/MR imaging and PET/CT, respectively. For the first reading, intrareader agreement between PET/MR imaging and PET/CT was substantial for group 1 and almost perfect for group 2: Unweighted κ values were 0.69 (95% CI, 0.30–1.00) and 0.84 (95% CI, 0.55–1.00) for groups 1 and 2, respectively.

For the second reading, intrareader agreement between PET/MR imaging and PET/CT was substantial: The unweighted κ value was 0.72 (95% CI, 0.38–1.00).

Quantitative Analysis

The statistical analysis of the clinical-based assessment of the SUV$_{max}$ values is shown in Table 2. The scatterplot for visualization of SUV$_{max}$ correlation of ^{18}F-FDG-avid lymph node lesions is shown in Fig 2. Because there were only 4 primary tumors, a scatterplot for the primary tumors was not created. Very high correlations between SUV$_{max}$ in PET/MR imaging and PET/CT could be found for primary tumors and lymph node and metastatic lesions (Spearman *r* = 1.00, 0.93, and 0.92, respectively). The absolute values were higher in PET/MR imaging compared with PET/CT for primary tumor and lymph node and metastatic lesions. This increase in SUV$_{max}$ for PET/MR imaging versus PET/CT was statistically significant for lymph node and metastatic lesions (*P* < .0001 for both), whereas the difference did not reach the significance level for the primary tumor lesions (*P* = .875).

The SUV$_{max}$ values are strongly based on the attenuation-correction maps, and the attenuation-correction maps are dependent on the anatomic location. The primary tumor and the lymph node lesions are both in the head and neck region. Because the metastases are in different anatomic areas, however, a location-based SUV$_{max}$ analysis was performed, and the results are demonstrated in Table 3. The scatterplots for visualization of SUV$_{max}$ correlations of ^{18}F-FDG-avid metastatic lesions in the

FIG 2. Scatterplots as visualization of the correlations demonstrating SUV$_{max}$ values in PET/CT and PET/MR imaging for ^{18}F-FDG-avid lymph node (*A*), lung (*B*), liver (*C*), and bone (*D*) lesions.

lung, liver, and bone are shown in Fig 2. High correlations between SUV_{max} in PET/MR imaging and PET/CT could be found for bone and liver lesions (Spearman $r = 0.89$ and 0.88, respectively), whereas a very high correlation was found for lung lesions (Spearman $r = 0.93$). The absolute SUV_{max} values were higher in PET/MR imaging compared with PET/CT for bone, liver, and lung lesions. These increases in SUV_{max} for PET/MR imaging versus PET/CT were statistically significant for bone and lung lesions ($P = .034$ and $P = .0006$, respectively), whereas the difference did not reach the significance level for the liver lesions ($P = .098$).

DISCUSSION

With a dedicated reading session, including radiology and nuclear medicine physicians, detection of lymph node and distant metastases by using whole-body ^{18}F-FDG-PET/MR imaging in patients with head and neck cancer was equal to PET/CT. Regarding the lesion-based analysis, the intrareader agreement was substantial for the first and second readings, and the inter-reader agreement (first reading) was moderate. Regarding the analysis of the presence or absence of metastatic disease, the intrareader agreement for the first and second readings was substantial to almost perfect, and the interreader agreement (first reading) was almost perfect.

Very high correlations between SUV_{max} from ^{18}F-FDG-avid lesions in PET/MR imaging versus PET/CT were found. In the quantitative analysis part, we evaluated SUV correlation per type of lesion (primary tumor or lymph node or distant metastases) and per anatomic localization. As mentioned previously, it is important to conduct a localization-based analysis due to the crucial role of attenuation correction and its dependency on the anatomic region. In both analyses, very high correlations were demonstrated, thus allowing the reliable use of the values in patients with head and neck cancer for quantification of tracer uptake and lesion assessment.

Furthermore, the high number of distant metastases detected demonstrates the crucial role of a whole-body approach for staging and re-staging in this patient population.

PET/MR imaging is promising for head and neck cancer imaging because these tumors frequently require both PET/CT and MR imaging during patient work-up. Evidence from this study and from recently published studies reveals head and neck cancer as one of the future indications for PET/MR imaging.[15]

In one of the initial human feasibility studies with 8 patients with head and neck cancer, the simultaneous PET/MR imaging brain prototype was used after standard-of-care PET/CT imaging.[16] For attenuation correction, a previously published combined atlas registration and pattern-recognition approach was applied.[17] The authors reported an excellent image quality with minor streak artifacts in the PET datasets of PET/MR imaging not affecting the assessment of the malignancy. When comparing the tracer uptake of the tumor in PET/MR imaging versus PET/CT, a higher ^{18}F-FDG uptake was detected in PET/MR imaging. A high correlation coefficient was found for the mean and maximum metabolic ratios of the tumors between both imaging technologies.[16] Our study differs from this early PET/MR imaging feasibility investigation using the brain prototype. This prototype had a limited craniocaudal FOV of 19 cm, hence enabling visualization

only to the level II neck lymph node regions.[16] We used a whole-body approach, which is of clinical relevance in patients with head and neck cancer. According to a screening study in preoperative patients with head and neck cancer, 17% had distant metastatic disease.[18] A whole-body PET/MR imaging approach also helps in visualizing second primary malignancies, which is important in this patient population.[19,20]

A recently published feasibility study using ^{18}F-FDG-PET/MR imaging for initial staging of 20 patients having head and neck squamous cell carcinoma confirmed the possibility of applying the hybrid imaging technology to this patient population without compromising image quality.[21] ^{18}F-FDG-PET/MR imaging was compared, in this study, with a traditional ^{18}F-FDG-PET scanner. Malignancies could be detected with PET/MR imaging, PET alone, and MR imaging alone in 17, 16, and 14 of the 20 cases investigated. Significantly more ^{18}F-FDG-avid lymph nodes were detected in PET/MR imaging versus PET. Furthermore, the SUVs in tumor and the cerebellum were significantly higher when comparing PET/MR imaging versus stand-alone PET.[21] This observation is in accordance with our study in which the absolute SUV_{max} were higher in PET/MR imaging versus PET/CT as well. In comparison with their study, the current study compared whole-body ^{18}F-FDG-PET/MR imaging versus ^{18}F-FDG-PET/CT instead of a stand-alone PET. We included, in this study, the 2 most common histopathologic types of head and neck cancer, namely squamous cell carcinoma and adenocarcinoma.

Absolute SUV_{max} values were higher in PET/MR imaging compared with PET/CT. The higher SUV_{max} reached statistical significance in the lymph node and metastatic lesions. In primary tumors, the SUV difference was minimal, not reaching statistical significance, but this can be explained by the small number of primary lesions ($n = 4$) and thus low statistical power. When analyzing the metastatic lesions per region, again this study found higher SUV_{max} in PET/MR imaging versus PET/CT, reaching statistical significance for bone and lung but not liver lesions. We explain the results by the measurement of PET/MR imaging after PET/CT in most patients (12 of 14) leading to an increased tracer uptake with time. However, different attenuation-correction techniques may also contribute to these findings. With regard to the SUV analysis, it is crucial to do correlative studies between PET/MR imaging and PET/CT. In the previously published study of our group comparing SUVs from ^{18}F-FDG-PET/MR imaging with ^{18}F-FDG-PET/CT in healthy tissue, high correlations for SUV_{max} and SUV_{mean} were found.[10] In certain tissues, the absolute SUV_{max} and SUV_{mean} differed significantly, but when a good correlation was shown between PET/MR imaging and PET/CT as the standard method, the values from PET/MR imaging could be used reliably in the clinical settings for follow-up comparisons. Attenuation-correction solutions based on MR imaging data are one of the major challenges for PET/MR imaging.[22] Attenuation correction has an impact on both SUV_{max} and SUV_{mean}.

According to our experience with PET/MR imaging, workflow and associated time constraints frequently pose a challenge in PET/MR imaging. In this study, the PET/CT examination lasted 17 ± 2 minutes and the PET/MR imaging study took 29 ± 31 minutes. This study and others demonstrate that that the scan-

ning time in PET/MR imaging is slightly longer compared with PET/CT.[21] This may change in the future when a full diagnostic MR imaging protocol is integrated into the PET/MR imaging workflow.

The study has limitations. First, only 14 patients with head and neck cancer were enrolled in this prospective study. Second, we did not have a uniform diagnostic MR imaging protocol. Besides the whole-body T1-weighted sequence for attenuation correction, we acquired, in 12 of the 14 patients, extra MR images, but the protocol was not unified. Third, the first 12 of the 14 patients with head and neck cancer underwent PET/CT, followed by PET/MR imaging. Only the last 2 patients had PET/MR imaging first. A randomization approach during the entire study would have been better from a scientific perspective, but when we started the clinical PET/MR imaging program, we decided, due to ethical reasons, to give the clinically referred PET/CT examination priority, followed by the PET/MR imaging study.

CONCLUSIONS

The detection of adenopathy and distant metastatic disease is reliable with whole-body ^{18}F-FDG-PET/MR imaging compared with state-of-the art ^{18}F-FDG-PET/CT imaging in head and neck cancer. This is reflected by the moderate-to-substantial inter- and intrareader agreements with regard to head and neck lesion detection (pooled across regions) and by the substantial to almost perfect inter- and intrareader agreements with regard to detection of the presence or absence of metastatic disease. Very high correlations between SUVs in PET/MR imaging versus PET/CT of ^{18}F-FDG-avid lesions were demonstrated, thus enabling the reliable use of SUVs in this patient population. Head and neck cancer is one of the promising indications for PET/MR imaging.

REFERENCES

1. Ferlay J, Shin HR, Bray F, et al. **Estimates of worldwide burden of cancer in 2008: GLOBOCAN 2008.** *Int J Cancer* 2010;127:2893–917
2. Curado MP, Hashibe M. **Recent changes in the epidemiology of head and neck cancer.** *Curr Opin Oncol* 2009;21:194–200
3. Guntinas-Lichius O, Wendt T, Buentzel J, et al. **Head and neck cancer in Germany: a site-specific analysis of survival of the Thuringian cancer registration database.** *J Cancer Res Clin Oncol* 2010;136:55–63
4. Tulunay-Ugur OE, McClinton C, Young Z, et al. **Functional outcomes of chemoradiation in patients with head and neck cancer.** *Otolaryngol Head Neck Surg* 2013;148:64–68
5. Eiber M, Souvatzoglou M, Pickhard A, et al. **Simulation of a MR-PET protocol for staging of head-and-neck cancer including Dixon MR for attenuation correction.** *Eur J Radiol* 2012;81:2658–65
6. Ishikita T, Oriuchi N, Higuchi T, et al. **Additional value of integrated PET/CT over PET alone in the initial staging and follow up of head and neck malignancy.** *Ann Nucl Med* 2010;42:77–82
7. Iyer NG, Clark JR, Singham S, et al. **Role of pretreatment 18FDG-PET/CT in surgical decision-making for head and neck cancers.** *Head Neck* 2010;32:1202–08
8. Jeong HS, Baek CH, Son YI, et al. **Use of integrated [18F]-FDG PET/CT to improve the accuracy of initial cervical nodal evaluation in patients with head and neck squamous cell carcinoma.** *Head Neck* 2007;29:203–10
9. Ng SH, Yen TC, Chang JT, et al. **Prospective study of [18F]fluorodeoxyglucose positron emission tomography and computed tomography and magnetic resonance imaging in oral cavity squamous cell carcinoma with palpably negative neck.** *J Clin Oncol* 2006;24:4371–76
10. Kershah S, Partovi S, Traughber BJ, et al. **Comparison of standardized uptake values in normal structures between PET/CT and PET/MRI in an oncology patient population.** *Mol Imaging Biol* 2013;15:776–85
11. Heusch P, Buchbender C, Beiderwellen K, et al. **Standardized uptake values for [18F] FDG in normal organ tissues: comparison of whole-body PET/CT and PET/MRI.** *Eur J Radiol* 2013;82:870–76
12. Partovi S, Kohan A, Gaeta C, et al. **Image quality assessment of automatic three-segment MR attenuation correction vs. CT attenuation correction.** *Am J Nucl Med Mol Imaging* 2013;3:291–99
13. Schulz V, Torres-Espallardo I, Renisch S, et al. **Automatic, three-segment, MR-based attenuation correction for whole-body PET/MR data.** *Eur J Nucl Med Mol Imaging* 2011;38:138–52
14. Landis JR, Koch GG. **The measurement of observer agreement for categorical data.** *Biometrics* 1977;33:159–74
15. Buchbender C, Heusner TA, Lauenstein TC, et al. **Oncologic PET/MRI. Part 1. Tumors of the brain, head and neck, chest, abdomen, and pelvis.** *J Nucl Med* 2012;53:928–38
16. Boss A, Stegger L, Bisdas S, et al. **Feasibility of simultaneous PET/MR imaging in the head and upper neck area.** *Eur Radiol* 2011;21:1439–46
17. Hofmann M, Steinke F, Scheel V, et al. **MRI-based attenuation correction for PET/MRI: a novel approach combining pattern recognition and atlas registration.** *J Nucl Med* 2008;49:1875–83
18. de Bree R, Deurloo EE, Snow GB, et al. **Screening for distant metastases in patients with head and neck cancer.** *Laryngoscope* 2000;110(pt 1):397–401
19. Jones AS, Morar P, Phillips DE, et al. **Second primary tumors in patients with head and neck squamous cell carcinoma.** *Cancer* 1995;75:1343–53
20. Priante AV, Castilho EC, Kowalski LP. **Second primary tumors in patients with head and neck cancer.** *Curr Oncol Rep* 2011;13:132–37
21. Platzek I, Beuthien-Baumann B, Schneider M, et al. **PET/MRI in head and neck cancer: initial experience.** *Eur J Nucl Med Mol Imaging* 2013;40:6–11
22. Keereman V, Mollet P, Berker Y, et al. **Challenges and current methods for attenuation correction in PET/MR.** *MAGMA* 2013;26:81–98

Orbital Lymphoproliferative Disorders (OLPDs): Value of MR Imaging for Differentiating Orbital Lymphoma from Benign OPLDs

K. Haradome, H. Haradome, Y. Usui, S. Ueda, T.C. Kwee, K. Saito, K. Tokuuye, J. Matsubayashi, T. Nagao, and H. Goto

ABSTRACT

BACKGROUND AND PURPOSE: Accurate discrimination of orbital lymphoma from benign orbital lymphoproliferative disorders is crucial for treatment planning. We evaluated MR imaging including DWI and contrast-enhanced MR imaging for differentiating orbital lymphoma from benign orbital lymphoproliferative disorders.

MATERIALS AND METHODS: Forty-seven histopathologically proved orbital lymphoproliferative disorders (29 orbital lymphomas and 18 benign orbital lymphoproliferative disorders) were evaluated. Two board-certified radiologists reviewed visual features on T1-weighted, fat-suppressed T2-weighted, diffusion-weighted, and contrast-enhanced MR images. For quantitative evaluation, ADC and contrast-enhancement ratio of all lesions were measured and optimal cutoff thresholds and areas under curves for differentiating orbital lymphoma from benign orbital lymphoproliferative disorders were determined using receiver operative characteristic analysis; corresponding sensitivities and specificities were calculated.

RESULTS: Multivariate logistic regression analysis showed that ill-defined tumor margin ($P = .003$) had a significant association with orbital lymphoma whereas the "flow void sign" ($P = .005$) and radiologic evidence of sinusitis ($P = .0002$) were associated with benign orbital lymphoproliferative disorders. The mean ADC and contrast-enhancement ratio of orbital lymphomas were significantly lower than those of benign orbital lymphoproliferative disorders ($P < .01$). An ADC of less than 0.612×10^{-3} mm^2/s and a contrast-enhancement ratio of less than 1.88 yielded areas under curves of 0.980 and 0.770, sensitivity of 94.1% and 95.5%, and specificities of 93.3% and 80.0% for predicting orbital lymphoma, respectively.

CONCLUSIONS: Some characteristic MR imaging features and quantitative DWI and contrast-enhanced MR imaging are useful in further improving the accuracy of MR imaging for differentiation of orbital lymphoma from benign orbital lymphoproliferative disorders.

ABBREVIATIONS: AUC = area under curve; CER = contrast-enhancement ratio; ICC = interclass correlation coefficient; MALT = extranodal marginal zone lymphoma of mucosa-associated lymphoid tissue; OLPD = orbital lymphoproliferative disorder

Orbital lymphoproliferative disorders (OLPDs) frequently present as an orbital mass lesion (24%–49%) in the adult and comprise a wide spectrum of diseases ranging from benign to malignant lesions.[1] Orbital lymphoma is the most common orbital neoplasm representing 55% of cases in adults.[2] Most orbital lymphomas are primary, low-grade, B-cell, non-Hodgkin lymphomas, and the most common subtype is extranodal marginal zone lymphoma of mucosa-associated lymphoid tissue (MALT).[3] Other OLPDs comprise several benign, noninfectious, chronic inflammatory diseases, including IgG4-related ophthalmic disease, reactive lymphoid hyperplasia, and idiopathic orbital inflammation.[4] Among them, IgG4-related ophthalmic disease is becoming increasingly recognized and accounts for approximately half of benign OPLDs on the basis of recent surveillance.[5] The discrimination of orbital lymphoma from benign OLPDs is crucial because of the different therapeutic implications: the former is amenable to low-dose radiation therapy, whereas the latter are expected to show a good response to corticosteroid therapy.[6] The utility of conventional anatomic MR imaging for this purpose is limited, however, because orbital lymphoma and benign OLPDs frequently share similar imaging features.[7,8] Recently, some researchers have reported quantitative DWI with ADC measurements to be potentially useful for discriminating orbital lymphoma from other orbital tumors.[9-15] However, these studies in-

cluded other neoplastic and nonneoplastic lesions such as cavernous hemangiomas, neurogenic tumors, and metastases, and the value of DWI for discrimination of lymphoma and OLPDs remains unclear. The purpose of this study was to assess the value of MR imaging including DWI and contrast-enhanced MR imaging for the discrimination of primary orbital lymphoma from benign OLPDs.

MATERIALS AND METHODS

Patients

The institutional review board of Tokyo Medical University approved this retrospective study. Written informed consent from patients was waived.

A total of 187 patients with an orbital mass lesion and whom had undergone surgical biopsy for pathologic diagnosis were identified in our hospital's database within a consecutive period of 5 years (between January 2008 and September 2013). From these pathologically-proved cases, we retrospectively searched for eligible candidates for this study using the search terms "lymphoproliferative disorder including malignant lymphoma, IgG4-related ophthalmic disease, reactive lymphoid hyperplasia, and idiopathic orbital inflammation," and 77 patients were identified. Of these 77 patients, 30 patients were excluded because of 1) non-availability of both DWI and contrast (gadolinium)-enhanced MR imaging ($n = 16$), 2) administration of corticosteroid therapy before MR imaging ($n = 10$), 3) a case of secondary lymphoma ($n = 1$), 4) a case with inconclusive pathology ($n = 1$), and 5) two cases with a single small lesion at the conjunctiva that did not allow for accurate ADC measurement. Finally, 47 patients (28 men and 19 women; mean age and standard deviation 66.6 ± 14.4 years; age range, 27–88 years) with 47 lesions (29 orbital lymphomas and 18 benign OLPDs) were enrolled in this study. Benign OLPDs consisted of IgG4-related ophthalmic disease ($n = 14$) and reactive lymphoid hyperplasia ($n = 4$). In the cohort, 27 patients had undergone both DWI and contrast-enhanced MR examinations, 5 patients had undergone only DWI, and 15 patients had undergone only contrast-enhanced MR imaging. All patients received the MR imaging before surgical biopsy.

MR Imaging

All MR examinations were performed using a 1.5T scanner (Avanto; Siemens, Erlangen, Germany) equipped with high-performance gradients (maximum gradient strength of 45 mT/m; peak slew rate of 200 mT/m/ms) and a 12-channel phased-array head coil allowing for parallel image acquisition.

Unenhanced MR images included 1) transverse and coronal T2-weighted fat-suppressed turbo spin-echo sequences (TR/TE of 3500 ms/96 ms, echo-train length of 7, section thickness of 3 mm, an intersection gap of 0.3 mm (10%), a field of view of 150 × 150 mm², matrix of 320 × 320, number of excitations of 2); 2) a transverse T1-weighed spin-echo sequence (TR/TE of 450 ms/12 ms, flip angle of 90, section thickness of 3 mm, an intersection gap of 0.3 mm (10%), field of view of 150 × 150 mm², matrix of 512 × 512, number of excitations of 2); and 3) a transverse diffusion-weighted sequence with b-values of 0 and 1000 seconds/mm² (TR/TE of 6836 ms/68 ms, section thickness of 2 mm, an intersection gap of 0.2 mm (10%), a field of view of 280 × 280 mm²,

matrix of 256 × 208, number of excitations of 6–8). Parallel imaging acquisition with a reduction factor of 2 was applied for DWI. Diffusion motion probing gradients were applied in 3 orthogonal directions and trace images were obtained using the manufacturer's software. Voxel-based ADC maps were created by means of a commercial workstation on the MR console using a linear regression analysis of the function $S = S_0 \times \exp(-b \times ADC)$, where S is the signal intensity after the applied motion probing gradients and S_0 is the signal intensity at $b = 0$ seconds/mm². Two b-values (0 and 1000 seconds/mm²) were used for the ADC calculation. After intravenous administration of an extracellular gadolinium-based contrast agent (0.2 mL/kg), transverse, coronal, and sagittal contrast-enhanced fat-saturated T1-weighted sequences (TR/TE of 632 ms/12 ms, flip angle of 90, section thickness of 3 mm, intersection gap of 0.3 mm [10%], a field of view of 150 × 150 mm², matrix of 512 × 512, number of excitations of 2) were obtained.

Qualitative MR Imaging Features Analysis

All MR images were reviewed by 2 board-certified radiologists with 19 and 9 years of experience, respectively, who were blinded to the clinical information and histologic results, using a PACS. Consensus between the 2 readers was reached by means of an additional joint reading session. The following items were evaluated: 1) the laterality (unilateral/bilateral), 2) the shape of the margins (well-defined, ill-defined [infiltrative], and lobulated) and signal intensity on T1-weighted, T2-weighted, and diffusion-weighted images relative to cerebral cortex (hypo-, iso-, or hyperintense),[10,11] 3) the homogeneity and degree of contrast enhancement relative to extraocular muscles, 4) the presence of a signal void from a vessel in the lesion on T2-weighted images, referred to as the "flow void sign," and 5) findings indicative of sinusitis; for this purpose, the readers comprehensively considered the following criteria: 1) significant paranasal mucosal thickness (>4 mm), 2) fluid level, and 3) the presence of a retention cyst at each paranasal cavity.[16]

Quantitative DWI and Contrast-Enhanced MR Imaging Analyses

Regions of interest for ADC measurements and contrast-enhancement ratio (CER) calculation were determined by an ophthalmologist assisted by a radiologist with 20 years of clinical experience. Both observers were blinded to the pathologic results. On all lesions, a circular region of interest was placed over the entire lesion on "diffusion-weighted" images obtained with a b-value of 0 seconds/mm², while avoiding artifacts and in reference to the other sequences. This region of interest was then copied and pasted onto the ADC maps and the corresponding ADCs were measured. ADC measurements were repeated 3 times for each lesion and the mean was calculated for further statistical analysis. To calculate the CER, the signal intensities of the lesions and temporal muscle were measured for each patient on transverse fat-saturated contrast-enhanced T1-weighted images. The signal intensity of the temporal muscle was measured by a circular region of interest while avoiding the artifacts. The CERs were calculated as follows:

$SI_{lesion}/SI_{temporal\ muscle}$, where SI_{lesion} and $SI_{temporal\ muscle}$ are the signal intensity of the lesion and the temporal muscle on contrast-enhanced

Table 1: Patient characteristics and pathologic findings of OLPD cases

	Orbital Lymphoma (n = 29)	Benign OLPDs (n = 18)	P Value
Age	72.2 ± 11.3 (47–88)	57.6 ± 14.7 (27–80)	P = .001[a]
Sex	Male 18, Female 11	Male 10, Female 8	P = .763
Histologic subtypes	MALT lymphoma 21 (72)	IgG4-related ophthalmic disease 14 (78)	
	DLBCL 4 (14)	RLH 4 (22)	
	Follicular lymphoma 3 (10)		
	Mantle cell lymphoma 1 (3)		
Laterality	Bilateral 12 (41)	Bilateral 15 (83)	P = .006[a]
	Unilateral 17 (59)	Unilateral 3 (17)	

Note:—Data in parentheses are ranges for age and percentages for histologic subtypes and laterality. DLBCL indicates diffuse large B-cell lymphoma; RLH, reactive lymphoid hyperplasia.
[a] There were significant differences in age and laterality between the 2 groups.

Table 2: MR imaging characteristics

	Orbital Lymphoma (n = 29)	Benign OLPDs (n = 18)	P Value
Shape	Well-defined 7 (24)	Well-defined 10 (56)	P = .0006[a]
	Ill-defined 21 (72)	Ill-defined 3 (17)	
	Lobulated 1 (3)	Lobulated 5 (17)	
Signal intensity			
T1WI	Iso 28 (97)	Iso 18 (100)	P = .2548
	Low 1 (3)		
T2WI	Iso 27 (93)	Iso 16 (89)	P = .6147
	Low 2 (7)	Low 2 (11)	
DWI	High 17 (100)	High 14 (93)	P = .2794
		Iso 1 (7)	
Homogeneity and degree of contrast enhancement	Homogeneous 23 (85)	Homogeneous 15 (100)	P = .2787
	Inhomogeneous 4 (15)		
		High 2 (13)	P = .0519
	Iso 27 (100)	Iso 13 (87)	
Presence of "flow void sign"	17 (59)	17 (94)	P = .0084[a]
Findings suggestive of sinusitis	8 (28)	16 (89)	P < .001[a]

Note:—Data in parentheses are percentages.
[a] There were significant differences in shape of the lesions, presence of the "flow void sign," and findings suggestive of sinusitis between the 2 groups.

MR images, respectively.[17] To confirm the reproducibility of both ADC and CRE measurements for the intraobserver agreement analysis, 3 repeated measurements were conducted with a week interval between each set of measurements.

Pathologic Diagnosis
Pathologic diagnosis of all OLPDs was established using histopathologic features including immunohistochemical staining, flow cytometric analysis, and gene rearrangement analysis according to the latest World Health Organization[18] criteria in 2008. Flow cytometric and gene rearrangement analyses were used to identify a monoclonal immunoglobulin band for the diagnosis of orbital lymphoma. For the diagnosis of IgG4-related ophthalmic disease, the following 2 main criteria were adopted: 1) serum IgG4 concentration >135 mg/dl, and 2) >40% of IgG4 positive plasma cells and >10 cells/high-power field in the biopsy sample.[18] The distributions of B- and T-cells in a lesion were evaluated by immunohistochemical staining, where a normal distribution of these cells was considered to indicate reactive lymphoid hyperplasia.

Statistical Analysis
All OLPDs were divided into 2 groups: orbital lymphoma and benign OLPDs. The differences in mean age and sex distinction between the 2 groups were assessed by a t-test and a Fisher exact test, respectively. The results of the qualitative MR features between the 2 groups were compared using a χ^2 test. The parameters found to have statistical significance by univariate analysis were entered into a multivariate logistic regression model to elucidate the useful findings for predicting orbital lymphoma or benign OLPDs. Differences in mean lesion ADCs and CERs between the 2 groups were assessed using a t-test with a Welch correction. Receiver operating characteristic analysis with multiple logistic regression was used to calculate areas under the ROC curve (AUC) and optimal cutoff thresholds of ADC and CER for differentiating orbital lymphoma from benign OLPDs, along with corresponding sensitivities, specificities, and positive and negative predictive values. The intrarater reliability was calculated by an interclass correlation coefficient (ICC) using a random effect analysis of variance. Agreement between the 2 readers with regard to the assessment of qualitative MR features was analyzed using the κ statistic. Differences in mean region of interest size in ADC and CER measurements between the 2 groups were analyzed using the Mann-Whitney test. The P values < .05 were considered to indicate a significant difference.

RESULTS
Patient Characteristics, Pathologic Findings, Disease Distribution
Patient characteristics, pathologic subtypes, and disease distribution are summarized in Table 1. Age of the patients with orbital lymphoma was significantly higher than those with benign OLPDs (P = .001) whereas no significant difference in sex distribution was observed between the 2 groups (P = .763). Most orbital lymphomas and benign OLPDs were MALT lymphoma (21/29, 72%) and IgG4-related ophthalmic disease (14/18, 78%), respectively. Most orbital lymphomas had unilateral involvement (17/29, 59%), whereas most benign OLPDs had bilateral involvement (15/18, 83%).

Qualitative MR Imaging Features
The qualitative MR imaging features of orbital lymphoma and benign OLPDs are summarized in Table 2. Most orbital lymphomas and benign OLPDs appeared as ill-defined masses (21/29, 72%) and well-defined masses (10/18, 56%), respectively, and a significant difference was observed between the 2 groups (P = .0006). The lesion signal of orbital lymphoma and benign OLPDs on unenhanced MR imaging was similar, and most lesions showed isointensity on T1-weighted and T2-weighted images and
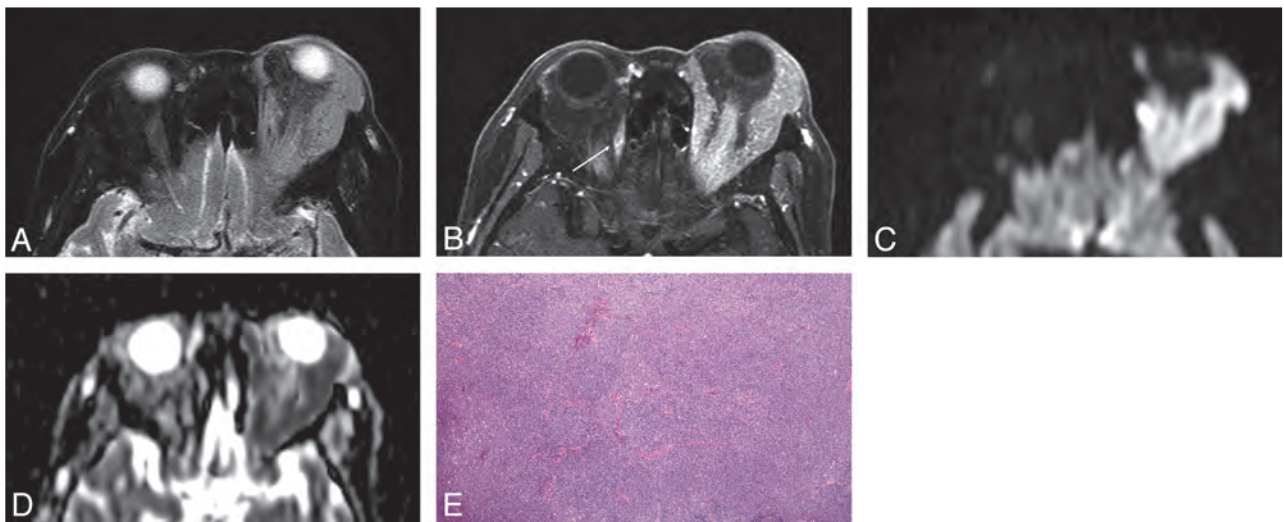
FIG 1. Orbital lymphoma (MALT lymphoma) in a 79-year-old woman. *A*, Transverse fat-saturated T2-weighted image; *B*, Transverse postcontrast fat-saturated T1-weighted image; *C*, Transverse DWI; *D*, ADC map; and *E*, Hematoxylin and eosin (HE)-stained biopsied specimen of the orbital tumor at low power field. An infiltrative mass involves the left lacrimal gland and extraocular muscles, appears isointense compared with the brain cortex on a fat-saturated T2-weighted MR image (*A*), and shows homogeneous contrast enhancement, similar to that of the right extraocular muscle (*arrow*) (*B*). The mass appears as strongly hyperintense on DWI (*C*) and hypointense on the ADC map (*D*). Notably, noninvolved extraocular muscles do not show hyperintensity similar to that of the mass on DWI (*C*). Lesion ADC and CER were 0.56×10^{-3} mm^2/s and 1.69, respectively. HE-stained biopsied specimen (*E*) demonstrated numerous small-to-medium-sized atypical lymphocytes around reactive lymph follicles, with greater high cellular attenuation, however, interstitial fibrosis or edematous change was not prominent.
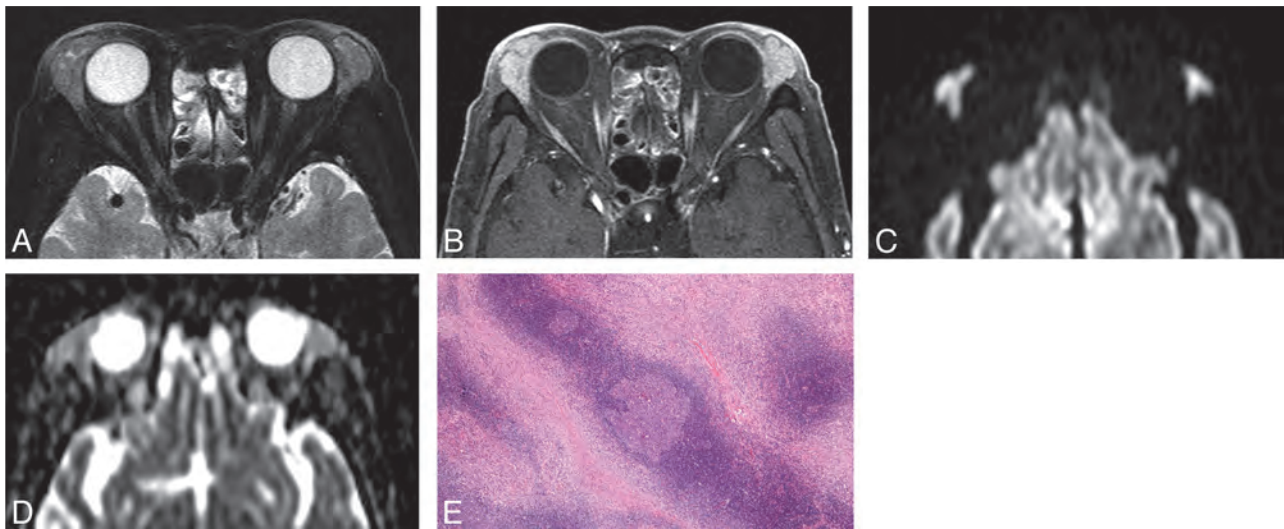
FIG 2. IgG4-related ophthalmic disease in a 67-year-old woman. *A*, Transverse fat-saturated T2-weighted image; *B*, transverse postcontrast fat-saturated T1-weighted image; *C*, transverse DWI; *D*, ADC map; and *E*, Hematoxylin and eosin (HE)-stained biopsied specimen of the lacrimal gland at low power field. The mass-like enlarged lacrimal glands are isointense compared with the brain cortex on the fat-saturated T2-weighted image (*A*) and show homogeneous contrast enhancement, similar to that of the extraocular muscles (*B*). The lesions appear mildly hyperintense on DWI (*C*) and slightly hypointense on the ADC map (*D*). Lesion ADC and CER were 0.94/0.75 (right/left) $\times 10^{-3}$ mm^2/s and 2.05/2.07 (right/left), respectively. HE-stained biopsied specimen (*E*) showed a large germinal center with accompanying lymphoplasmacytic infiltration and abundant interstitial fibrosis with edematous changes. On immunochemical stained section analysis (not shown), many IgG4-positive plasma cell (>40%) were identified, and this is compatible with IgG4-related ophthalmic disease.

hyperintensity on diffusion-weighted images, relative to cerebral cortex (Figs 1–3). In the 2 benign OLPDs showing hypointensity on T2-weighted images, abundant fibrotic components (sclerosed type) were histopathologically identified. After gadolinium-based contrast administration, most orbital lymphomas and all benign OLPD lesions showed homogeneous contrast enhancement (23/27, 85% for orbital lymphomas and 15/15, 100% for benign OLPDs) and their signal intensities were similar to those of the nonaffected external ocular muscles (Figs 1–3). The "flow

void sign" (Fig 4) was identified significantly more frequently ($P = .008$) in benign OLPDs (17/18, 94%) than in orbital lymphoma (17/29, 59%). Radiologic sinusitis findings were also seen significantly more often ($P < .001$) in benign OLPDs (16/18, 89%) than in orbital lymphoma (8/29, 28%). Upon multivariate logistic regression analysis, ill-defined tumor margin ($P = .003$) was a significant predictor of orbital lymphoma, whereas the "flow void sign" ($P = .005$) and radiologic sinusitis ($P = .0002$) were predictors of benign OLPDs. The reader agreement for the
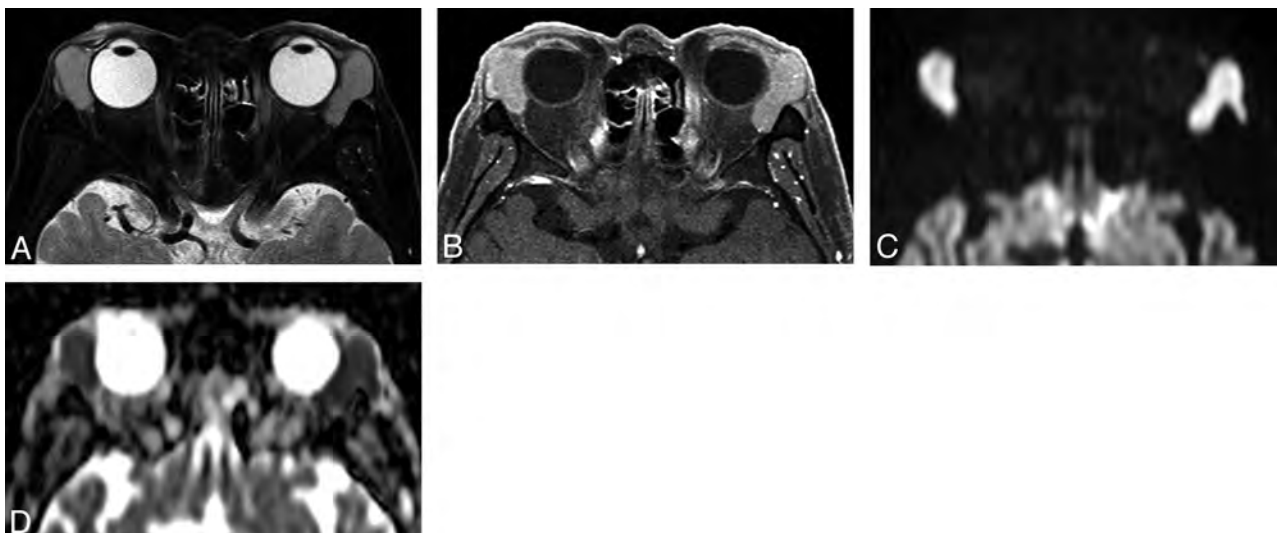
FIG 3. Orbital lymphoma (mantle cell lymphoma) in a 71-year-old man. *A*, Transverse fat-saturated T2-weighted image; *B*, transverse fat-saturated postcontrast T1-weighted image; *C*, transverse DWI; and *D*, ADC map. The lesions involve the bilateral lacrimal glands, appear isointense compared with the brain cortex on fat-saturated T2-weighted image (*A*), and show homogeneous contrast enhancement, similar that of the extraocular muscles (*B*). The lesions are strongly hyperintense on the DWI (*C*) and hypointense on the ADC map (*D*). Lesion ADC and CER were 0.47/0.48 (right/left) $\times 10^{-3}$ mm²/s and 1.49/1.46 (right/left), respectively. The low ADC and CER values could suggest orbital lymphoma though the imaging features are similar to that of IgG4-related ophthalmic disease (Fig 2).
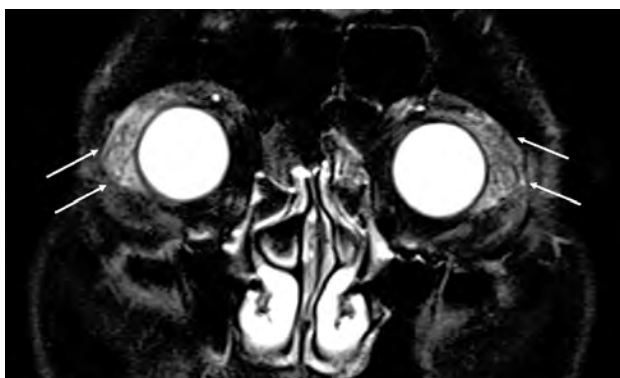
FIG 4. Reactive lymphoid hyperplasia in a 65-year-old man. *A*, Coronal fat-saturated T2-weighted image. A number of vessel signal voids are observed in the bilaterally enlarged lacrimal glands on T2-weighted image ("flow void sign") (*arrows*).

assessment of qualitative MR imaging features was good to excellent (0.627–1.00): shape, 0.856; T1WI signal, 0.849; T2WI signal, 0.877; DWI signal, 1.00; degree of contrast enhancement, 0.916; homogeneity of contrast enhancement, 0.627; flow void sign, 0.787; radiologic sinusitis, 0.872. Additional joint reading sessions had to be conducted to obtain the consensus in up to a maximum of 4 cases for each qualitative MR imaging feature.

Quantitative DWI and Contrast-Enhanced MR Imaging Analyses

The ADCs and CERs of orbital lymphoma and benign OLPDs, including their histologic subtypes, are summarized in Tables 3 and 4. The mean ADC and CER of orbital lymphoma (0.544×10^{-3} mm²/s and 1.70) were significantly lower ($P < .01$) than those of benign OLPDs (0.812×10^{-3} mm²/s and 2.07) (Fig 5). The standard deviation of the ADC of orbital lymphomas was lower (± 0.051) compared with that of benign OLPDs (± 0.246), and ADCs of only 2 benign OLPDs overlapped with those of orbital lymphomas in the

ADC range, whereas CERs of both entities showed considerable overlap though a significant difference was observed in their mean CERs (Fig 5). Based upon the ROC analysis, an optimal ADC threshold of less than 0.612×10^{-3} mm²/s yielded an AUC, sensitivity, and specificity of 0.980, 94.1%, and 93.3%, and a positive and negative predictive value of 94.1% and 93.3% for predicting orbital lymphoma. Meanwhile, an optimal CER threshold of less than 1.88 yielded an AUC, sensitivity, and specificity of 0.770, 95.5%, and 80.0%, and a positive and negative predictive value of 87.5% and 92.3% for diagnosing orbital lymphoma. In benign OLPDs, a lower ADC and CER below each optimal threshold (false-positive lesion) were observed with 1 lesion in the ADC and 3 lesions in the CER, respectively. The 1 benign OLPD lesion showing a lower ADC demonstrated pathologically a relatively higher cellular attenuation, less edematous change, and a mild to moderate fibrosis. In the 3 benign OLPD lesions showing a lower CER, fibrotic changes were less prominent than in the other benign OLPDs, whereas the orbital lymphomas showing a higher CER (>2.0) had a tendency to have higher vascularization on pathology. Intraobserver reliabilities were almost perfect in the repeated ADC and CER measurements: ADC in orbital lymphoma (ICC = 0.98, $P < .001$), ADC in benign OLPDs (ICC = 0.99, $P < .001$), CER in orbital lymphoma (ICC = 0.97, $P < .001$), and CER in benign OLPDs (ICC = 0.98, $P < .001$). The region of interest sizes for ADC and CER measurements ranged from 34.6 to 221.4 mm² (mean, 69.6 mm²) and from 22.1 to 268.2 mm² (mean, 85.2 mm²), respectively. The mean region of interest sizes for both ADC and CER measurements in benign OLPDs (59.3 mm² in ADC, 61.6 mm² in CER) were smaller than those in orbital lymphomas (78.7 mm² in ADC, 98.3 mm² in CER) though no significant differences were observed.

DISCUSSION

In agreement with previous results,[10,11,14] we found that the mean ADC of orbital lymphomas (0.544×10^{-3} mm²/s) was signifi-

cantly lower ($P < .001$) than that of benign OLPDs (0.812×10^{-3} mm²/s). It is thought to reflect a higher cellularity in orbital lymphoma lesions because of numerous uniformly small-sized atypical lymphocyte infiltrations.[19,20] Moreover, interstitial edematous changes in benign OLPDs, which lead to increased ADC, could also contribute to a significant difference in the ADCs. It is important to note that previous studies mainly included other benign and malignant orbital neoplastic lesions rather than inflammatory orbital lesions.[9-15] Sepahdari et al [10] reported that an ADC of less than 1.0×10^{-3} mm²/s was optimal for predicting malignancy and Politi et al [11] indicated that a threshold of 0.775×10^{-3} mm²/s was optimal for predicting orbital lymphoma. Therefore, their reported optimal ADC may be unfit for differentiating orbital lymphoma from benign OLPDs because these ADC values are higher than the ADCs of the majority of benign OLPDs found in this study. In contrast to these previous studies, the present study focused on the differentiation of orbital lymphoma from benign OLPDs and we found that a lower ADC threshold of 0.612×10^{-3} mm²/s is more optimal for discriminating between these 2 entities with sufficiently high diagnostic capability (AUC of 0.980). In addition, it should be noted that ADC measurements can be affected by the MR acquisition parameters and magnetic field strength. In the study by Sepahdari et al,[10] patients were examined at different magnetic field strengths (1.5T and 3T). Image distortion due to susceptibility artifacts, which could affect the ADC measurement error, occurs more easily with high field strength. Orbital lesions are frequently in close proximity to normal orbital organs such as the eyeball, which could cause an ROI measurement error because of contamination from the nonlesional signal in the scanning section. Moreover, orbital lesions are sometimes of small size. For example, if a lesion is localized in the lacrimal gland, it is usually smaller than other orbital lesions. Thus, scanning with thinner section thickness is crucial to reduce the effect of the partial-volume effect on the ADC measurements. In the present study, we used a high b-value (1000 seconds/mm²) and a thinner section thickness (2 mm) for DWI to minimize perfusion and partial volume effects. Thus, our ADC values were globally lower than those found in previous investigations. In the present study, orbital lymphomas had highly homogeneous ADCs with a low standard deviation, which is in line with previously reported data,[11] and ADCs of only 2 benign OLPD lesions had values

Table 3: ADCs of each group of OLPDs

	Mean ADC ± SD	ADC range	*P* Value
Orbital lymphoma (*n* = 17)	0.54 ± 0.05	0.44–0.64	*P* < .001[a]
MALT lymphoma (*n* = 12)		0.47–0.64	
DLBCL (*n* = 2)		0.44–0.56	
Follicular lymphoma (*n* = 2)		0.53–0.57	
Mantle cell lymphoma (*n* = 1)		0.47	
Benign OLPDs (*n* = 15)	0.81 ± 0.18	0.58–1.24	
IgG4-related ophthalmic disease (*n* = 12)		0.58–1.24	
RLH (*n* = 3)		0.73–0.85	

Note:—There were significant differences in ADC between the 2 groups. SD indicates standard deviation; DLBCL diffuse large B-cell lymphoma; RLH, reactive lymphoid hyperplasia.

Table 4: CERs of each group of OLPDs

	Mean CER ± SD	CER Range	*P* Value
Orbital lymphoma (*n* = 27)	1.70 ± 0.25	1.27–2.24	*P* = .0096[a]
MALT lymphoma (*n* = 20)		1.27–2.24	
DLBCL (*n* = 3)		1.36–1.71	
Follicular lymphoma (*n* = 3)		1.76–1.94	
Mantle cell lymphoma (*n* = 1)		1.55	
Benign OLPDs (*n* = 15)	2.07 ± 0.46	1.27–3.03	
IgG4-related ophthalmic disease (*n* = 11)		1.27–3.03	
RLH (*n* = 4)		1.66–2.14	

[a] There were significant differences in CER between the 2 groups. SD indicates standard deviation; DLBCL, diffuse large B-cell lymphoma; RLH, reactive lymphoid hyperplasia.
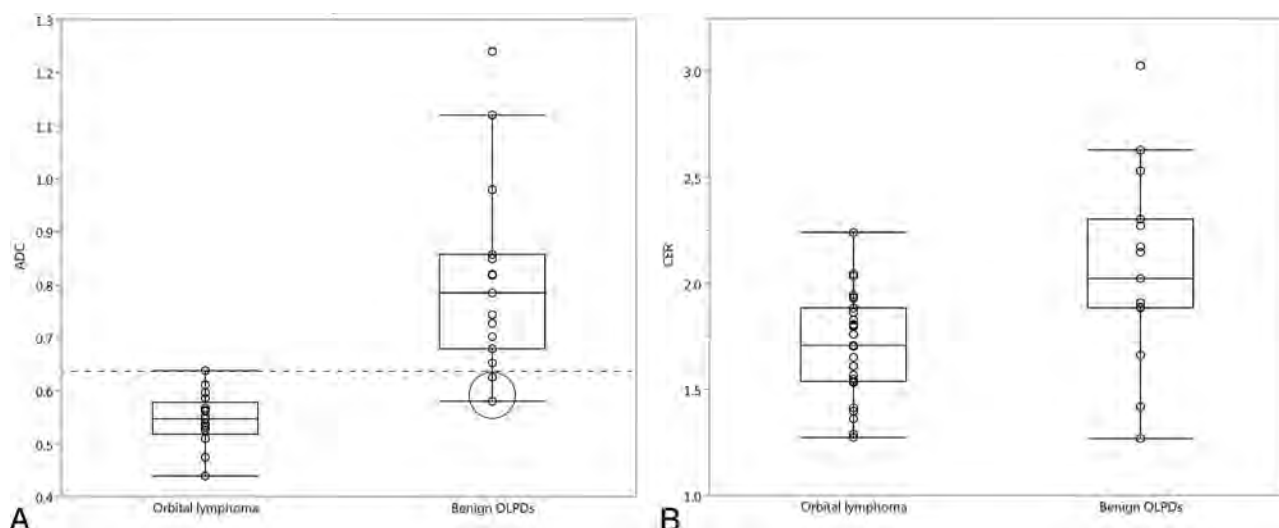
FIG 5. ADCs and CERs of orbital lymphoma and benign OPLDs. *A* and *B*, Scatterplot and box-and-whisker plot show the distribution of ADCs and CERs, and each mean value in the orbital lymphoma and benign OLPDs lesions. The mean ADC and CER of orbital lymphomas are significantly lower than those of benign OLPDs ($P < .01$). The standard deviation of the ADC of orbital lymphomas was lower (±0.051) compared with that of benign OLPDs (±0.246), and ADCs of only 2 benign OLPDs (encircled) overlapped with those of orbital lymphomas in the ADC range.

that overlapped with the orbital lymphoma lesions. The mean CER of orbital lymphoma (1.70) was significantly lower ($P = .0096$) than that of benign OLPDs (2.07), which could be used as an additional valuable index for the diagnosis of orbital lymphoma. Abundant fibrotic components and higher vascularization in benign OLPDs compared with orbital lymphoma may be responsible for the higher CER of benign OLPDs. However, CERs of both entities showed considerable overlap though a significant difference was observed in the mean CER between the 2 entities. We also confirmed the reproducibility of the measured ADC and CER values with almost perfect ICC as previously reported.[21] Ill-defined tumor margin had a significant association with orbital lymphoma in present study. In addition, some characteristic conventional MR imaging features were found to be potentially useful for the differential diagnosis of OLPDs in the present study. The presence of a vessel signal void on T2-weighted MR imaging ("flow void sign") (Fig 4) was observed significantly more frequently ($P = .008$) in benign OLPDs (17/18, 94%) than in orbital lymphoma (17/29, 59%), probably because of the hypervascular nature of the former.[22,23] As 1 report indicated, an extension of inflammatory changes to the mucosa of nasal and paranasal cavities can occur in IgG4-related disease;[24] we also found that imaging findings indicative of sinusitis were seen significantly more frequently ($P < .001$) in benign OLPDs (16/18, 89%) than in orbital lymphoma (8/29, 28%). In addition to the intrinsic limitation of a retrospective study, this study had other limitations that should be noted. First, the number of included patients was relatively low. Further large-scale studies are needed to confirm the present results. Second, in addition to the confirmation of intraobserver reliability with regard to the ADC and CER measurement, assessing interobserver agreement of radiologist versus ophthalmologist would be of interest. Third, further optimization of b-values for DWI in this application may be needed. One researcher adopted a low b-value of 500 seconds/mm^2.[25] Although low high b-values may provide higher signal-to-noise ratio and reduce eddy current artifacts, the inclusion of perfusion effects in ADC measurements could limit their value for discriminating orbital lymphoma from IgG4-related ophthalmic disease because the measured ADCs of both entities showed considerable overlap because of the variation of the lesion vascularity.[25] Therefore, we believe that the use of a high b-value of 1000 seconds/mm^2 is crucial for accurately distinguishing orbital lymphoma from benign OLPDs with DWI.

CONCLUSIONS

Some characteristic conventional MR imaging features and quantitative evaluations with DWI and contrast-enhanced MR imaging are useful for discriminating orbital lymphoma from benign OLPDs.

ACKNOWLEDGMENTS

REFERENCES

1. Goto H. *Review of Ocular Tumor in Practical Ophthalmology.* Vol. 24. Tokyo, Japan: Bunkodo; 2008:5–7
2. Valvassori GE, Sabnis SS, Mafee RF, et al. **Imaging of orbital lymphoproliferative disorders.** *Radiol Clin North Am* 1999;37:135–50
3. Jenkins C, Rose G, Bunce C, et al. **Histological features of ocular adnexal lymphoma (REAL classification) and their association with patient morbidity and survival.** *Br J Ophthalmol* 2000;84:907–13
4. Espinoza GM. **Orbital inflammatory pseudotumors: etiology, differential diagnosis, and management.** *Curr Rheumatol Rep* 2010;12:443–47
5. Takahira M, Ozawa Y, Kawano M, et al. **Clinical aspects of IgG4-related orbital inflammation in a case series of ocular adnexal lymphoproliferative disorders.** *Int J Rheumatol* 2012;2012:635473
6. Garner A. **Orbital lymphoproliferative disorders.** *Br J Ophthalmol* 1992;76:47–48
7. Priego G, Majos C, Climent F, et al. **Orbital lymphoma: imaging features and differential diagnosis.** *Insights Imaging* 2012;3:337–44
8. Akansel G, Hendrix L, Erickson BA, et al. **MRI patterns in orbital malignant lymphoma and atypical lymphocytic infiltrates.** *Eur J Radiol* 2005;53:175–81
9. Kapur R, Sepahdari AR, Mafee MF, et al. **MR imaging of orbital inflammatory syndrome, orbital cellulitis, and orbital lymphoid lesions: the role of diffusion-weighted imaging.** *AJNR Am J Neuroradiol* 2009;30:64–70
10. Sepahdari AR, Aakalu VK, Setabutr P, et al. **Indeterminate orbital masses: restricted diffusion at MR imaging with echo-planar diffusion-weighted imaging predicts malignancy.** *Radiology* 2010;256:554–64
11. Politi LS, Forghani R, Godi C, et al. **Ocular adnexal lymphoma: diffusion-weighted MR imaging for differential diagnosis and therapeutic monitoring.** *Radiology* 2010;256:565–74
12. Roshdy N, Shahin M, Kishk H, et al. **MRI in diagnosis of orbital masses.** *Curr Eye Res* 2010;35:986–91
13. Razek AA, Elkhamary S, Mousa A. **Differentiation between benign and malignant orbital tumors at 3-T diffusion MR-imaging.** *Neuroradiology* 2011;53:517–22
14. Sepahdari AR, Kapur R, Aakalu VK, et al. **Diffusion-weighted imaging of malignant ocular masses: initial results and directions for further study.** *AJNR Am J Neuroradiol* 2012;33:314–19
15. Sepahdari AR, Politi LS, Aakalu VK, et al. **Diffusion-weighted imaging of orbital masses: multi-institutional data support a 2-ADC threshold model to categorize lesions as benign, malignant, or indeterminate.** *AJNR Am J Neuroradiol* 2014;35:170–75
16. Bhattacharyya N. **The role of CT and MRI in the diagnosis of chronic rhinosinusitis.** *Curr Allergy Asthma Rep* 2010;10:171–74
17. Lee KC, Moon WK, Chung JW, et al. **Assessment of lymph node metastases by contrast-enhanced MR imaging in a head and neck cancer model.** *Korean J Radiol* 2007;8:9–14
18. World Health Organization. *Classification of Tumors of Heamatopoietic and Lymphoid Tissues.* Lyon, France: International Agency for Research on Cancer; 2008
19. Guo AC, Cummings TJ, Dash RC, et al. **Lymphomas and high-grade astrocytomas: comparison of water diffusibility and histologic characteristics.** *Radiology* 2002;224:177–83
20. Wu X, Pertovaara H, Dastidar P, et al. **ADC measurements in diffuse large B-cell lymphoma and follicular lymphoma: a DWI and cellularity study.** *Eur J Radiol* 2013;82:e158–64
21. Kwee TC, Takahara T, Luijten PR, et al. **ADC measurements of lymph nodes: inter- and intra-observer reproducibility study and an overview of the literature.** *Eur J Radiol* 2010;75:215–20
22. Go H, Kim JE, Kim YA, et al. **Ocular adnexal IgG4-related disease: comparative analysis with mucosa-associated lymphoid tissue lymphoma and other chronic inflammatory conditions.** *Histopathology* 2012;60:296–312
23. Asai S, Okami K, Nakamura N, et al. **Sonographic appearance of the submandibular glands in patients with immunoglobulin G4-related disease.** *J Ultrasound Med* 2012;31:489–93
24. Moteki H, Yasuo M, Hamano H, et al. **IgG4-related chronic rhinosinusitis: a new clinical entity of nasal disease.** *Acta Otolaryngol* 2011;131:518–26
25. Hiwatashi A, Yoshiura T, Togao O, et al. **Diffusivity of intraorbital lymphoma vs. IgG4-related disease: 3D turbo field echo with diffusion-sensitised driven-equilibrium preparation technique.** *Eur Radiol* 2014;24:581–86

Impaired White Matter Development in Extremely Low-Birth-Weight Infants with Previous Brain Hemorrhage

X. Ou, C.M. Glasier, R.H. Ramakrishnaiah, S.B. Mulkey, Z. Ding, T.L. Angtuaco, A. Andres, and J.R. Kaiser

ABSTRACT

BACKGROUND AND PURPOSE: Brain hemorrhage is common in premature infants. The purpose of the study is to evaluate white matter development in extremely low-birth-weight infants with or without previous brain hemorrhage.

MATERIALS AND METHODS: Thirty-three extremely low-birth-weight infants were prospectively enrolled and included in this institutional review board–approved study. Another 10 healthy term infants were included as controls. The medical records of the extremely low-birth-weight infants were reviewed for sonography diagnosis of intraventricular hemorrhage. All infants had an MR imaging examination at term-equivalent age for detection of previous hemorrhage, and their white matter was scored and compared among different groups. DTI measured fractional anisotropy values were also compared voxelwise by tract-based spatial statistics.

RESULTS: Compared with controls, the white matter score was not significantly different in extremely low-birth-weight infants without blood deposition on MR imaging ($P = .17$), but was significantly worse in extremely low-birth-weight infants with blood deposition on MR imaging but no intraventricular hemorrhage diagnosis by sonography ($P = .02$), in extremely low-birth-weight infants with grade 1 or 2 intraventricular hemorrhage on sonography ($P = .003$), and in extremely low-birth-weight infants with grade 3 or 4 intraventricular hemorrhage on sonography ($P = .0001$). Extremely low-birth-weight infants without blood deposition on MR imaging did not show any white matter regions with significantly lower fractional anisotropy values than controls. Extremely low-birth-weight infants with blood deposition on MR imaging, but no intraventricular hemorrhage diagnosis, did show white matter regions with significantly lower fractional anisotropy values, and extremely low-birth-weight infants with intraventricular hemorrhage diagnosis had widespread white matter regions with lower fractional anisotropy values.

CONCLUSIONS: Previous brain hemorrhage is associated with abnormal white matter in extremely low-birth-weight infants at term-equivalent age, and sonography is not sensitive to minor hemorrhages that are sufficient to cause white matter injury.

ABBREVIATIONS: ELBW = extremely low-birth-weight; FA = fractional anisotropy; IVH = intraventricular hemorrhage; TBSS = tract-based spatial statistics

P reterm birth and associated low birth weight remains a prevalent condition despite advances in obstetric and neonatal care. Of particular concern are infants born with extremely low birth weight (ELBW, birth weight ≤ 1000 g). In addition to the

necessity for prolonged neonatal intensive care, poor neurodevelopmental outcome is quite common in surviving ELBW infants.[1,2] Neurologic and developmental deficits have been associated with neonatal brain injury in preterm infants, especially injury to the cerebral white matter.[3,4] White matter abnormalities are common in very preterm infants[5,6] and can range from macroscopic injury such as cystic periventricular leukomalacia, which can be detected by sonography, to microstructural abnormalities that can only be measured by sensitive MR imaging methods such as DTI,[7-9] and can persist from the neonatal age to adolescence, and then to adulthood.[10,11]

Intraventricular hemorrhage (IVH) is the most common form of brain hemorrhage in very preterm infants, and is frequently accompanied by white matter injury[12] such as periventricular hemorrhagic infarction.[13] IVH is conventionally graded 1 to 4, ranging from subependymal germinal hemorrhage not extending

Table 1: MRI findings for the 9 ELBW infants with normal ultrasounds with blood product deposition noted on MRI at term-equivalent age

Subject	Location	Findings
1	Occipital horn of the left lateral ventricle	Minimal non-acute blood products
2	Bilateral choroid plexus	Minimal non-acute blood products
3	Bilateral cerebellar hemispheres	Old hemorrhage
4	Subependymal regions of the lateral ventricles	Old hemorrhage
5	Subependymal regions and cerebellum	Old hemorrhage
6	Bilateral frontal white matter and cerebellum	Old hemorrhage
7	Ependyma of the posterior right lateral ventricle	Minimal non-acute blood products
8	Subependymal of the posterior right lateral ventricle	Minimal non-acute blood products
9	Left subependymal region	Minimal non-acute blood products

into ventricles to extended intraparenchymal hemorrhage with periventricular hemorrhagic infarction. While the adverse neurodevelopmental consequences of severe IVH (grade 3 or 4) are well recognized, the consequences of low-grade (grade 1 or 2) IVH need further study. For example, 1 study reported a higher percentage of neurodevelopmental impairment compared with controls in very preterm infants with grade 1 or 2 IVH,[14] whereas another study observed adverse neurodevelopmental outcome[15] only when IVH was accompanied by white matter lesions. Because cystic periventricular leukomalacia rarely accompanies low-grade IVH, microstructural white matter injury will need further study. In addition, other types of brain hemorrhage, such as intracerebellar hemorrhages, though less frequent, may occur with or without IVH in preterm infants, and may also affect developing white matter.

While sonography is the standard method for the diagnosis of IVH and can detect overt white matter lesions, MR imaging provides better spatial resolution and higher contrast. Specific MR imaging pulse sequences such as susceptibility-weighted imaging and DTI are very sensitive to hemorrhage and white matter integrity, respectively, and can reveal pathology not apparent on sonography. While the ROI method is a conventional way to compare DTI parameters, such as the fractional anisotropy (FA) among subject groups, the recently developed tract-based spatial statistics (TBSS) method can provide a voxelwise statistical analysis of DTI parameters in the whole brain and is ROI-independent, thus nonsubjective. DTI-TBSS has shown great sensitivity in detecting white matter abnormalities in ELBW infants at term-equivalent age.[7,16]

We hypothesized that any form of previous brain hemorrhage, including intracerebellar hemorrhage and all grades of IVH, may be associated with white matter microstructural abnormalities at term-equivalent age. To test our hypothesis, we performed MR imaging examinations at term-equivalent age in ELBW infants, reviewed sonography diagnosis of IVH, divided them into different groups according to the extent of hemorrhage, and compared their white matter development respectively to healthy term infants.

MATERIALS AND METHODS
Subjects
ELBW infants with birth weight 401–1000 g (gestational age <30 weeks) from the University of Arkansas for Medical Sciences and

the Arkansas Children's Hospital neonatal intensive care units were recruited for MR imaging examinations. Parents of ELBW infants who were stable at near term-equivalent age were approached, and informed consent was obtained from those who agreed to participate in the MR imaging study. All procedures complied with local institutional review board regulations. ELBW infants with complex congenital anomalies, central nervous system malformations, chromosomal abnormalities, or hydrops fetalis were excluded. The medical records of the ELBW infants were reviewed for cranial sonography diagnosis of IVH. Most of the ELBW infants had 2 cranial ultrasounds during the first week of life; if an abnormality was noted, serial cranial ultrasounds were performed during the initial hospitalization. Other ELBW infants had additional sonography screenings after the first week of life for other clinical reasons. In total, 39 ELBW infants were enrolled and completed an MR imaging examination. Among them, 1 infant did not have a valid DTI scan due to motion artifact and was therefore excluded from the analysis; 5 infants had moderate-to-severe ventricular dilation (4 of them had an sonography diagnosis of grade 3 or 4 IVH) on MR imaging examination and were also excluded because of the concern of large white matter structural distortion and the difficulty for image registration in the DTI-TBSS analysis. For the remaining 33 ELBW infants, 7 had grade 3 or 4 IVH (6 were diagnosed during the first week and 1 was diagnosed during the first month), 8 had grade 1 or 2 IVH (7 diagnosed during the first week and 1 diagnosed during the first month), 9 had no sonography diagnosis of IVH but showed blood product deposition on MR imaging at term-equivalent age (Table 1), and another 9 had no sonography diagnosis of IVH and also had no blood product deposition on MR imaging. In addition, 10 term healthy infants were recruited from another longitudinal clinical trial at our institution that follows healthy pregnant woman and their neonates. The parents consented soon after delivery for MR imaging examination of their neonates, and the MR imaging data served as control data to the MR imaging of ELBW infants. The postmenstrual ages at MR imaging were similar between the ELBW and the control infants. The subject characteristics, as well as the gestational age (based on menstrual dating) and postmenstrual age at MR imaging for the ELBW and control infants are listed in Table 2.

MR Imaging Examinations
All ELBW infants had MR imaging examinations without sedation at term-equivalent age. The infants were fed in the MR imaging suite 30 minutes before the scan, swaddled in warm sheets, and immobilized using a MedVac Infant Immobilizer (CFI Medical Solutions, Fenton, Michigan). The MR imaging examinations were performed on a 1.5T Achieva MR imaging scanner (Philips Health Care, Best, the Netherlands) with 60 cm bore size, 33 mT/m gradient amplitude, and 100 mT/m/ms maximum slew rate. A pediatric 8-channel sensitivity encoding head coil was

Table 2: Gestational and postmenstrual ages for control and ELBW infants

	Number of Subjects	Gestational Age (weeks)	Postmenstrual Age at MRI (weeks)	P Value of Postmenstrual Age Compared with Controls[a]
Controls (term infants)	n = 10	39.0 ± 0.9	41.2 ± 1.0	N/A
ELBW infants without blood product deposition on MRI	n = 9	25.2 ± 1.2	40.1 ± 1.0	.05
ELBW infants with blood product deposition on MRI but no IVH diagnosis	n = 9	25.2 ± 1.4	40.4 ± 1.1	.18
ELBW infants with grades 1 or 2 IVH diagnosis	n = 8	24.7 ± 1.2	41.1 ± 3.7	.51
ELBW infants with grades 3 or 4 IVH diagnosis	n = 7	25.3 ± 1.3	40.4 ± 2.7	.16

[a] $P > .05$ for the age comparison between any ELBW groups.

used. A neonatal brain MR imaging protocol was used, which includes sagittal T1-weighted 3D (acquisition matrix 1 mm × 1 mm × 1.5 mm) reconstructed to 3 planes, axial T2-weighted, axial diffusion-weighted, and axial T2*-weighted gradient-echo or SWI sequences (switched from gradient-echo to SWI at the early stage of this study for better sensitivity to blood product deposition). In addition, a single-shot spin-echo-planar imaging sequence with acquisition voxel size 2 mm × 2 mm × 3 mm and diffusion weighting gradients ($b = 700$ seconds/mm^2) uniformly distributed in 15 directions was used to acquire DTI data. At approximately 2 weeks of age, the controls had a no-sedation MR imaging with the same experimental procedures and same T2-weighted, DTI, and T1-weighted 3D sequences.

White Matter Abnormality Scoring
The conventional MR images (including T1–3D, axial T2, DWI, and gradient-echo or SWI) for all control and ELBW infants were transmitted to a PACS and were evaluated by 2 neuroradiologists (C.M.G., > 28 years of experience; and R.H.R., > 5 years of experience in neuroradiology practice) who were blinded to the grouping information of the ELBW infants. They independently determined whether there was blood product deposition on the T2* gradient-echo or susceptibility-weighted images. Either "positive" or "negative" was recorded in the data sheet, with no grading of mild/moderate/severe. The radiologists also independently scored the white matter abnormality for each infant, using a method similar to that of Woodward et al.[4] The scoring method consisted of 6 components: white matter signal intensity on T1 and T2, volume of periventricular white matter, presence of cysts, ventricular dilation, abnormality on DWI, and corpus callosum thickness, with each component scored from 1 to 4, corresponding to normal, mildly, moderately, and severely affected, respectively. The overall white matter abnormality score was the sum of the 6 sub-category scores, and the scores from the 2 neuroradiologists were averaged. A normal brain would have a score of 6. The higher the score, the more severe were the white matter abnormalities. The average white matter abnormality score for each ELBW group and for the controls were calculated and compared. In addition, to investigate whether previous brain hemorrhage was a factor in white matter abnormality score at term-equivalent age in the ELBW infants, a 1-way ANOVA was used.

DTI-TBSS Analysis
The FA maps for each subject were computed from the scanner-carried software (Fibertrak, Philips) and were exported to a workstation with the FMRIB Software Library for TBSS analysis (V1.2, http://fsl.fmrib.ox.ac.uk/fsl/fslwiki/TBSS/UserGuide) by an MR

imaging physicist with >5 years of experience in DTI data analysis. The FA images were first preprocessed. Each FA dataset was aligned to every other one to identify the most representative set that had the least amount of total warping; this one subsequently served as the target FA. Nonlinear transforms were then performed to register each FA dataset to the target. Standard nonlinear transformation program in TBSS V1.2 was used, except for modification to reflect registration of all FA to the target FA from our own data but not to the Montreal Neurological Institute 152 template. Afterward, all FA images were merged, averaged, and entered into the FA skeletonization program to create a mean FA skeleton in which a threshold of FA ≥ 0.15 was selected. Ventriculomegaly did not affect the TBSS registration and skeletonization because infants with moderate to severe ventricular dilation (as defined by conventional MR imaging white matter grading) were already excluded. Nevertheless, the registration and the skeletonization were carefully reviewed section by section to ensure no misregistration. Finally, randomization with threshold-free cluster enhancement was used to perform voxelwise comparison of FA values in each ELBW group versus the control group collectively.

Statistics
For the comparison of ages and white matter abnormality scores between groups, values were reported as mean ± standard deviation and a Wilcoxon rank sum test was performed by Matlab software (MathWorks, Natick, Massachusetts) to determine if there was difference. $P < .05$ was regarded as significant. In addition, Cohen κ coefficients were used to measure the interrater agreement of white matter scoring and hemorrhage determination by the 2 neuroradiologists. The κ coefficients were interpreted as follows[17]: 0.41–0.60, moderate agreement; 0.61–0.80, substantial agreement; 0.81–0.99, almost perfect agreement; and 1, perfect agreement. For the effects of previous hemorrhage on white matter abnormality scores in ELBW infants, a 1-way ANOVA was performed by Matlab. For the DTI-TBSS analysis, $P < .05$ after multiple comparisons correction controlling for family wise error was used for the voxelwise comparison in FSL to detect regions with significant difference in FA values.

RESULTS
There was no difference in birth gestational age between the ELBW infant groups and no difference in postmenstrual age at MR imaging between the ELBW infant groups. The postmenstrual age at MR imaging was similar in controls and the ELBW infants groups (Table 2).
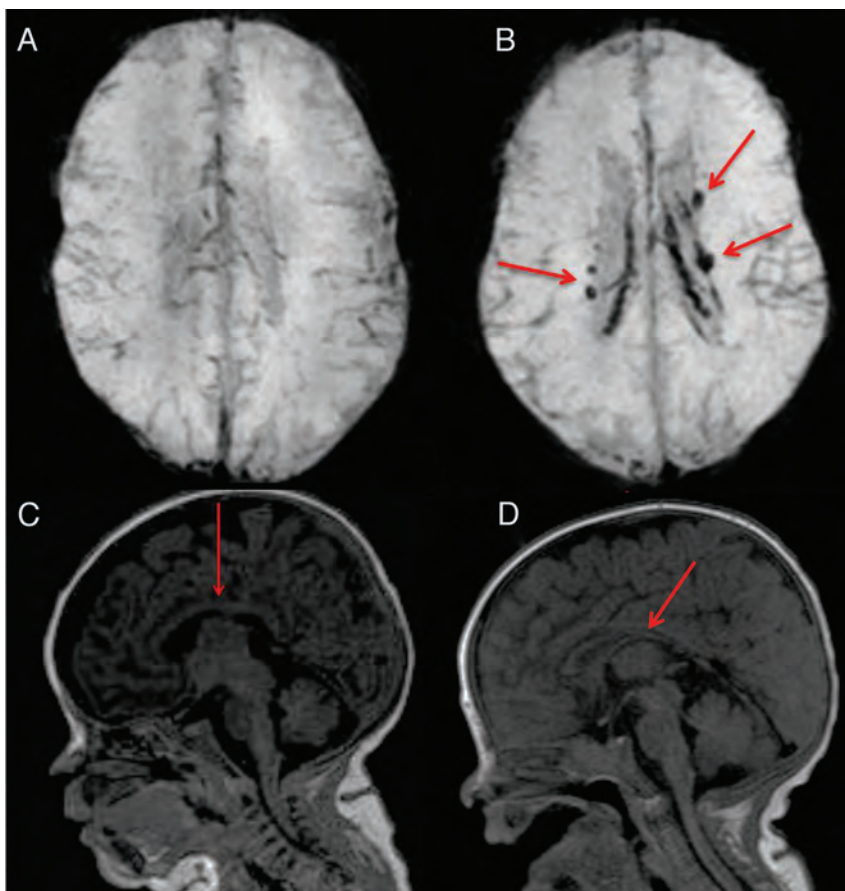
FIG 1. Examples of conventional MR imaging findings: *A*, SWI shows brain without blood deposition in an ELBW infant; *B*, SWI shows brain with blood deposition (*arrows* show the old blood product) in an ELBW infant with sonography IVH diagnosis; *C*, normal thickness of corpus callosum (*arrow*) in an ELBW infant; *D*, moderate thinning of corpus callosum (*arrow*) in an ELBW infant.

Table 3: White matter abnormality scores for the control and ELBW infants

	White Matter Abnormality Score	P Value (Compared with Controls)
Controls (term infants)	6.0 ± .0	N/A
ELBW infants without blood product deposition on MRI	6.2 ± .3	.17
ELBW infants with blood product deposition on MRI but no IVH diagnosis	6.7 ± .9	.02
ELBW infants with grades 1 or 2 IVH diagnosis	7.5 ± 1.7	.003
ELBW infants with grades 3 or 4 IVH diagnosis	8.6 ± 1.3	.0001

and white matter grading (for the component of corpus callosum thickness). White matter abnormality scores for the control and ELBW infants are reported in Table 3. The white matter abnormality score was 6.0 ± 0.0 for the controls, 6.2 ± 0.3 for the ELBW infants without old blood deposition on MR imaging at term-equivalent age, 6.7 ± 0.9 for ELBW infants with old blood on MR imaging but no IVH diagnosis by sonography, 7.5 ± 1.7 for ELBW infants with grade 1 or 2 IVH, and 8.6 ± 1.3 for ELBW infants with grade 3 or 4 IVH. Compared with controls, the white matter abnormality score for ELBW infants without old blood on MR imaging was not significantly different ($P = .17$), but was significantly different in the other ELBW infant groups ($P = .02, .003,$ and $.0001$, respectively). A box-plot of the white matter abnormality score for the 4 ELBW infant groups is shown in Fig 2. One-way ANOVA of these data revealed a significant effect ($P < .001$) of previous hemorrhage on white matter abnormality score by MR imaging at term-equivalent age.

Figure 3 shows the DTI-TBSS results for the ELBW and control infants. Compared with controls, ELBW infants without old blood deposition on MR imaging at term-equivalent age did not show any white matter region with significantly lower FA values ($P < .05$, corrected). ELBW infants with old blood on MR imaging but no IVH diagnosis after birth showed a few regions with significantly lower FA values ($P < .05$, corrected). These regions were limited mostly to the splenium of the corpus callosum and the optic radiation. ELBW infants with grade 1 or 2 IVH diagnosis by sonography had widespread regions with lower FA values ($P < .05$, corrected), including the optic radiation, the genu, body, and splenium of the corpus callosum, the cingulum, and the frontal corona radiata. ELBW infants with grade 3 or 4 IVH had similar but even more extensive white matter regions with decreased FA ($P < .05$, corrected), involving association, projection, and callosal fibers.

DISCUSSION

Our results demonstrate that previous hemorrhage in the brain had a significant effect on white matter development in ELBW infants at term-equivalent age. Compared with controls, ELBW infants with no apparent history of brain hemorrhage (as reflected by no blood product deposition on MR imaging) did not have a significant difference in white matter abnormality score or DTI-measured FA values in any brain regions; on the other hand, ELBW infants with signs of previous brain hemorrhage had significantly worse white matter scores and significantly lower FA values in many brain regions. Many of the ELBW infants without

The interrater agreement by the 2 neuroradiologists on blood product deposition identified on MR imaging was perfect ($\kappa = 1$). The interrater agreement was substantial on white matter abnormality scores ($\kappa = 0.71$). Specifically, perfect agreement on presence of cysts ($\kappa = 1$) and on abnormality on DWI ($\kappa = 1$), almost perfect agreement on volume of periventricular white matter ($\kappa = 0.83$), substantial agreement on ventricular dilation ($\kappa = 0.80$) and on white matter signal intensity on T1 and T2 ($\kappa = 0.69$), and moderate agreement on corpus callosum thickness ($\kappa = 0.52$). Figure 1 shows examples of blood product deposition

cranial sonography IVH diagnosis but with positive MR imaging findings of previous hemorrhage at term-equivalent age showed only minimal blood product deposition near the lateral ventricles on MR imaging. This could represent a minor intracranial hem-

FIG 2. Boxplot of the white matter abnormality scores for the 4 ELBW infant groups show that the more previous brain hemorrhage, the more white matter abnormality at term-equivalent age. A score of 6 means normal white matter. Any score greater than 6 means abnormality. The line in the middle for each box is the median score for each group, and the box contains scores in 25–75 percentiles. Minimum/maximum scores in each group are also marked. A 1-way ANOVA revealed the significant effect ($P < .001$) of brain hemorrhage on white matter abnormality score at term-equivalent age in ELBW infants. ELBW_NO: 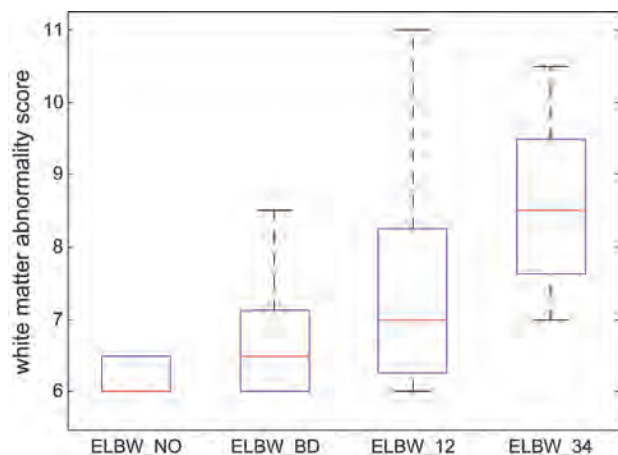ELBW infants without old blood product deposition on MR imaging at term-equivalent age; ELBW_BD: ELBW infants with old blood product on MR imaging but no IVH diagnosis by sonography; ELBW_12: ELBW infants with grades 1 or 2 IVH diagnosis; ELBW_34: ELBW infants with grades 3 or 4 IVH diagnosis.
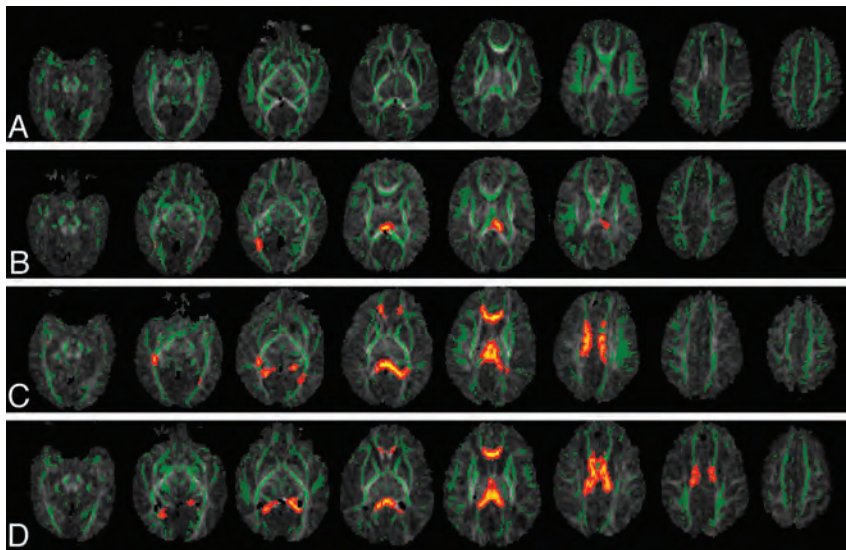
FIG 3. DTI-TBSS results show that the more previous brain hemorrhage, the more white matter microstructural abnormalities (as reflected by more regions with lower FA compared with controls). Green represents the average white matter skeleton overlaid on FA images, orange/yellow represent white matter regions with significantly lower FA values (when compared with control infants, $P < .05$, fully corrected for multiple comparisons) in A, ELBW infants with no old blood product deposition on MR imaging at term-equivalent age, B, ELBW infants with old blood product deposition on MR imaging but no sonography IVH diagnosis after birth, C, ELBW infants with old blood product deposition on MR imaging and previous sonography diagnosis of grades 1 or 2 IVH, and D, ELBW infants with old blood product deposition on MR imaging and previous sonography diagnosis of grades 3 or 4 IVH.

orrhage, which was not detected by early sonography screenings. Assuming that infants with blood on MR imaging and not on sonography had smaller hemorrhage compared with those infants with a sonography diagnosis of IVH, our results demonstrated an inverse relationship between white matter development at term-equivalent age and degrees of previous hemorrhage in the brain, because a higher degree of hemorrhage corresponded to a worse white matter score and more regions with lower FA values.

While the association of IVH with poor neurodevelopmental outcome has been previously documented, many studies focused on severe IVH (grade 3–4) only. For example, a large multicenter study showed that grade 3–4 IVH was significantly associated with neurodevelopmental morbidity in ELBW infants at 18–22 months corrected age, whereas grade 1–2 IVH was not considered.[18] In another large study of infants born at <28 weeks gestation, the risk of developing cerebral palsy at 2 years of age was only slightly higher (9% versus 6%) for infants with isolated IVH (corresponding to grade 1 or 2) compared with those with normal neonatal sonography findings; however, this risk was much higher (39%) in those with ventriculomegaly.[19] In contrast, another study focusing on low-grade IVH showed that ELBW infants with grade 1 or 2 IVH had significantly lower mean Bayley Scales of Infant Development-II Mental Developmental Index scores and higher rates of neurodevelopmental impairment or major neurologic abnormality at 20 months corrected age compared with ELBW infants with normal cranial ultrasounds.[20] Furthermore, another study showed that 9% of ELBW infants with normal neonatal ultrasounds developed cerebral palsy and 25% had Mental Developmental Index scores <70 at 18–22 months age.[21] These studies suggest that all grades of IVH may be a risk factor of poor neurodevelopmental outcome in ELBW infants, and normal cranial sonography findings do not necessarily correlate with normal neurodevelopment.

The percentage of missed brain hemorrhage diagnosis by cranial sonography was high in our study (27%). This was likely because of these being minimal hemorrhages that would be undetectable by sonography, and less likely (though still possible) due to hemorrhages that occurred during the interval between the last sonography screening and the MR imaging examination at term-equivalent age as most hemorrhages occur during the first few days of life for premature infants and our sonography screening covered at least the first week of life. Cerebellar hemorrhage by MR imaging was also observed in 3 ELBW infants without hemorrhage noted on sonography, which is a less recognized area of brain injury[22] but has recently been shown to be associated with long-term neurodevelopmental disabilities in premature infants.[22,23] Overall, as our study indicated, MR imaging (particularly the T2*-weighted sequences) was more sensitive to brain hemorrhage and may reveal pathologic

findings that cannot be diagnosed by cranial sonography. There is currently no large-scale study (compared with sonography studies with large sample sizes) to evaluate the association of MR imaging findings of hemorrhage at term-equivalent age and neurodevelopmental outcome at later age; MR imaging is not routinely performed and not a standard of care in ELBW infants in most centers. Our results showed that the ELBW infants with normal ultrasounds but with blood product deposition on MR imaging also had significant white matter abnormalities at term-equivalent age. Because white matter development is known to be most predictive of neurodevelopmental outcome,[3,4] our MR imaging findings of additional ELBW infants with hemorrhagic injury and white matter abnormalities indicate that MR imaging screening at term-equivalent age in ELBW infants may be beneficial to identify those infants with a higher risk of poor neurodevelopmental outcome.

The exact mechanism of the observed association between earlier brain hemorrhage and later white matter abnormality at term-equivalent needs to be determined. It is believed that some white matter injuries are the direct result of IVH.[13] The germinal matrix destruction caused by IVH may induce deficits of white matter microstructural development because the germinal matrix provides precursor cells that become oligodendroglia and astrocytes, which are important for myelination. More severe IVH may also cause periventricular venous congestion, which generates ischemia and results in periventricular hemorrhagic infarction in white matter.[13] Other factors such as free radical formation induced by iron from red blood cells and cellular effects by cytokines may also link hemorrhage to white matter injury.[24]

One limitation of our study is that we excluded ELBW infants with moderate to severe ventricular dilation at term-equivalent age in the DTI-TBSS analysis to avoid imaging registration artifacts. Most of these ELBW infants had grades 3 or 4 IVH diagnosed by sonography within the first week of life. Our sample for the grade 3 or 4 IVH group therefore did not include all available subjects. Because severe ventricular dilation worsens the white matter score (if we include these ELBW infants, the white matter abnormality scores for the grade 3 or 4 IVH group were higher: 10.2 ± 3.1, $P < .0001$ compared with controls) and DTI has shown white matter microstructural abnormalities in infants with ventriculomegaly,[25] we do not feel the exclusion of these infants altered the conclusions of our study. Meanwhile, our DTI-TBSS analysis provided a nonsubjective region-specific quantitative measure of white matter; this is a great addition to (and maybe more sensitive than) the semiquantitative but more clinically feasible white matter scoring. For better sensitivity to small hemorrhages in ELBW infants, we switched from gradient-echo ($n = 12$, 67% with positive findings) to SWI sequences ($n = 21$, 76% with positive findings). Reviewing several MR imaging datasets with both gradient-echo and SWI sequences acquired during the transition showed that gradient-echo may be adequate for the determination of whether there was blood product deposition; however, it is still possible that there were small hemorrhages omitted by the gradient-echo images. Another limitation is the relatively small sample size in this study. Nevertheless, our results achieved statistical significance ($P < .05$ for TBSS, after multiple comparison correction). Finally, lack of data correlating MR imaging-revealed hemorrhage and white matter injury to neurodevelopmental outcome is another limitation that cannot be addressed in

this study. Further study is needed to determine whether hemorrhage noted by MR imaging at term-equivalent age is a valid predictor of long-term neurodevelopmental outcome.

CONCLUSIONS

In this study, we showed that previous hemorrhage in the brain had significant effects on white matter development in ELBW infants at term-equivalent age. Compared with controls, ELBW infants with no blood product deposition in the brain did not have a significant difference in white matter abnormality score or microstructural development measured by DTI, whereas ELBW infants with signs of previous brain hemorrhage had significantly worse white matter scores and lower FA values in many regions in the brain. Notably, cranial sonography after birth was not sensitive to amounts of hemorrhage that were sufficient to cause white matter injury at term-equivalent age. Our results suggest that MR imaging at term-equivalent age may add value in determining neurodevelopmental outcome in ELBW infants who have normal ultrasounds.

REFERENCES

1. Marlow N, Wolke D, Bracewell MA, et al. **Neurologic and developmental disability at six years of age after extremely preterm birth.** *N Engl J Med* 2005;352:9–19
2. Wood NS, Marlow N, Costeloe K, et al. **Neurologic and developmental disability after extremely preterm birth.** *N Engl J Med* 2000;343:378–84
3. Perlman JM. **White matter injury in the preterm infant: an important determination of abnormal neurodevelopment outcome.** *Early Hum Dev* 1998;53:99–120
4. Woodward LJ, Anderson PJ, Austin NC, et al. **Neonatal MRI to predict neurodevelopmental outcomes in preterm infants.** *N Engl J Med* 2006;355:685–94
5. Larroque B, Marret S, Ancel PY, et al. **White matter damage and intraventricular hemorrhage in very preterm infants: the EPIPAGE study.** *J Pediatr* 2003;143:477–83
6. Volpe JJ. **Cerebral white matter injury of the premature infant—more common than you think.** *Pediatrics* 2003;112:176–80
7. Anjari M, Srinivasan L, Allsop JM, et al. **Diffusion tensor imaging with tract-based spatial statistics reveals local white matter abnormalities in preterm infants.** *Neuroimage* 2007;35:1021–27
8. Volpe JJ. **Brain injury in premature infants: a complex amalgam of destructive and developmental disturbances.** *Lancet Neurol* 2009; 8:110–24
9. Perlman JM, Risser R, Broyles RS. **Bilateral cystic periventricular leukomalacia in the premature infant: associated risk factors.** *Pediatrics* 1996;97:822–27
10. Eikenes L, Lohaugen GC, Brubakk AM, et al. **Young adults born**

preterm with very low birth weight demonstrate widespread white matter alterations on brain DTI. *Neuroimage* 2011;54:1774–85

11. Skranes J, Vangberg TR, Kulseng S, et al. **Clinical findings and white matter abnormalities seen on diffusion tensor imaging in adolescents with very low birth weight.** *Brain* 2007;130:654–66

12. Kuban K, Sanocka U, Leviton A, et al. **White matter disorders of prematurity: association with intraventricular hemorrhage and ventriculomegaly.** *J Pediatr* 1999;134:539–46

13. Volpe JJ. *Neurology of the Newborn*, 4th ed. Philadelphia: W.B. Saunders; 2001

14. Klebermass-Schrehof K, Czaba C, Olischar M, et al. **Impact of low-grade intraventricular hemorrhage on long-term neurodevelopmental outcome in preterm infants.** *Childs Nerv Syst* 2012;28:2085–92

15. O'Shea TM, Allred EN, Kuban KCK, et al. **Intraventricular hemorrhage and developmental outcomes at 24 months of age in extremely preterm infants.** *J Child Neurol* 2012;27:22–29

16. Smith SM, Jenkinson M, Johansen-Berg H, et al. **Tract-based spatial statistics: voxelwise analysis of multi-subject diffusion data.** *Neuroimage* 2006;31:1487–505

17. Landis JR, Koch GG. **Measurement of observer agreement for categorical data.** *Biometrics* 1977;33:159–74

18. Vohr BR, Wright LL, Dusick AM, et al. **Neurodevelopmental and functional outcomes of extremely low birth weight infants in the** National Institute of Child Health and Human Development Neonatal Research Network, 1993–1994. *Pediatrics* 2000;105:1216–26

19. Kuban KCK, Allred EN, O'Shea TM, et al. **Cranial ultrasound lesions in the NICU predict cerebral palsy at age 2 years in children born at extremely low gestational age.** *J Child Neurol* 2009;24:63–72

20. Patra K, Wilson-Costello D, Taylor HG, et al. **Grades I-II intraventricular hemorrhage in extremely low birth weight infants: effects on neurodevelopment.** *J Pediatr* 2006;149:169–73

21. Laptook AR, O'Shea TM, Shankaran S, et al. **Adverse neurodevelopmental outcomes among extremely low birth weight infants with a normal head ultrasound: prevalence and antecedents.** *Pediatrics* 2005;115:673–80

22. Volpe JJ. **Cerebellum of the premature infant: rapidly developing, vulnerable, clinically important**. *J Child Neurol* 2009;24:1085–104

23. Limperopoulos C, Bassan H, Gauvreau K, et al. **Does cerebellar injury in premature infants contribute to the high prevalence of long-term cognitive, learning, and behavioral disability in survivors?** *Pediatrics* 2007;120:584–93

24. Bassan H. **Intracranial hemorrhage in the preterm infant: understanding it, preventing it.** *Clin Perinatol* 2009;36:737–62

25. Gilmore JH, Smith LC, Wolfe HM, et al. **Prenatal mild ventriculomegaly predicts abnormal development of the neonatal brain.** *Biol Psychiatry* 2008;64:1069–76

Biotin-Responsive Basal Ganglia Disease: Neuroimaging Features before and after Treatment

H. Kassem, A. Wafaie, S. Alsuhibani, and T. Farid

ABSTRACT

BACKGROUND AND PURPOSE: Biotin-responsive basal ganglia disease is an autosomal recessive neurometabolic disorder presenting with subacute encephalopathy that can cause death if left untreated. The purpose of this study is to assess the neuroimaging and clinical features of the disease before and after treatment with biotin.

MATERIALS AND METHODS: We retrospectively reviewed the clinical, laboratory, and neuroimaging features of 15 genetically-proved Middle Eastern cases of biotin-responsive basal ganglia disease. Brain MR imaging was done at the onset of symptoms in all cases and within 2–8 weeks after biotin and thiamine therapy in 14 patients. The MR imaging datasets were analyzed according to lesion location, extent, and distribution.

RESULTS: Brain MR imaging showed bilateral lesions in the caudate nuclei with complete or partial involvement of the putamen and sparing of the globus pallidus in all cases. In 80%, discrete abnormal signals were observed in the mesencephalon, cerebral cortical-subcortical regions, and thalami. In 53%, when the disease was advanced, patchy deep white matter affection was found. The cerebellum was involved in 13.3%. The signal abnormality of the mesencephalon, cortex, and white matter disappeared after treatment whereas the caudate and putamen necrosis persisted in all patients, including those who became asymptomatic.

CONCLUSIONS: Biotin-responsive basal ganglia disease is a treatable underdiagnosed disease. It should be suspected in pediatric patients with unexplained encephalopathy whose brain MR imaging shows bilateral and symmetric lesions in the caudate heads and putamen, with or without involvement of mesencephalon, thalami, and cortical-subcortical regions, as the therapeutic trial of biotin and thiamine can be lifesaving.

ABBREVIATIONS: BBGD = biotin-responsive basal ganglia disease; MELAS = mitochondrial myopathy, encephalopathy, lactic acidosis, and strokelike episodes; MERRF = myoclonic epilepsy associated with ragged red fibers; WE = Wernicke encephalopathy

Biotin-responsive basal ganglia disease (BBGD) was first described by Ozand et al in 10 patients of Arab ancestry in 1998.[1] Subsequently, cases have been reported in patients of different ethnicities including those of Portuguese, Indian, Japanese, and German origin.[2-6]

BBGD is an autosomal recessive neurometabolic disorder. It is

characterized by subacute encephalopathy with confusion, seizure, dysarthria, and dystonia following a history of febrile illness. If left untreated with biotin, the disease can progress to severe quadriparesis and even death.[7]

Biotin is a water-soluble vitamin belonging to the B complex and acts as a co-enzyme for the 4 important carboxylases in humans.[3] Biotin-dependent carboxylases catalyze the fixation of bicarbonate in organic acids and play crucial roles in the metabolism of fatty acids, amino acids, and glucose. The carboxylase activities decrease substantially when there is biotin deficiency.[8] The etiology of biotin deficiency is believed to be caused by a genetic defect in the transporter system of biotin across the blood-brain barrier.[1] In 2005, it was demonstrated that homozygous mutation in *SLC19A3* is the genetic defect that causes BBGD.[9]

BBGD responds to the administration of high doses of biotin, which ensures some biotin transport into brain by nonspecific diffusion.[10] It also increases the expression of the *SLC19A3* gene, thus restoring some function of the mutated receptor.[11,12] Recently, thiamine has been added to biotin in the treatment regi-

FIG 1. MR imaging of the brain in a male patient, 4 years old, with subacute encephalopathy. Axial FLAIR before (*A–D*) and 4 weeks after (*E–H*) treatment with biotin and thiamine. *A*, Abnormal areas of increased signal intensity in the cerebellum. *B* and *C*, Abnormal high signal and swelling of the caudate nuclei showing small central focal necrosis with involvement of putamina and medial thalami. *D*, Focal high cortical and subcortical signals at both frontal and parietal lobes. Follow-up MR imaging after treatment (*E–H*) shows resolution of the abnormal signal in the cerebellar, cortical, and subcortical areas. The caudate nuclei and putamina are evolved from swelling into atrophy and necrosis with persistent abnormal signal intensity.

men of BBGD based on the hypothesis that the impairment of thiamine transport in the brain also has a critical role in this disorder. This combination of biotin and thiamine proved to prevent the recurrence of encephalopathy crisis.[7,9]

It is important to recognize this disease because its symptoms may be reversed and the progression of its clinical course can be prevented simply by the administration of biotin and thiamine.[1,7]

The purpose of this study is to assess the clinical and neuroimaging features of the disease on MR imaging before and after treatment with biotin and thiamine.

MATERIALS AND METHODS

We retrospectively reviewed the clinical, laboratory, and neuroimaging features of 15 genetically proved cases of biotin-responsive basal ganglia disease. The patients were 9 females and 6 males with an age range (at the time of symptom onset) of 2 to 11 years (mean: 6 years). MR imaging of the brain was done in all cases at the onset of symptoms. Follow-up MR imaging within 2–8 weeks after the administration of high doses of biotin (5–10 mg/kg/d) and thiamine (100–300 mg/d) was done in 14 patients.

All patients were of Arab (Middle East) ancestry, and 73% had consanguineous parents. Recessive genetic defect was detected in all cases. All cases were found to have the same homozygous mutation in exon 5 of the *SLC19A3* gene and their parents were heterozygous for this mutation. The molecular genetic analysis of the *SLC19A3* gene was performed in the Center for Human Genetics (Bioscientia, Ingelheim, Germany). The blood and CSF

chemical tests for organic and inorganic toxic compounds, carboxylases, and biotinidase values were normal in all patients.

All patients presented with subacute or acute encephalopathy leading to seizures, extrapyramidal symptoms, quadriparesis, or quadriplegia and coma.

The MR imaging was performed in all patients using the Signa LX 1.5T machine (GE Healthcare, Milwaukee, Wisconsin). Our brain MR imaging protocol included sagittal spin-echo T1WI (TR 535 milliseconds, TE 13 milliseconds), axial and coronal FSE T2WI (TR 3500 milliseconds, TE 182 milliseconds), axial FLAIR (TR 9000 milliseconds, TI 2500 milliseconds, TE 104 milliseconds), axial spin-echo T1WI (TR 535 milliseconds, TE 13 milliseconds), and axial DWI ($b=0-1000$). Postgadolinium axial and coronal T1WI were performed in 9 cases.

Spectroscopy (^{1}H-MR) was performed in 6 cases at the time of onset of symptoms and before starting the biotin therapy. After therapy MR spectroscopy was done in only 1 of these 6 cases. MR spectroscopy was performed through point-resolved proton spectroscopy sequences with TE of 35 and 144 msec. The voxels were positioned in axial T2WI on areas showing an abnormal signal at the basal ganglia and parieto-occipital cortical-subcortical regions of either the left or right side. Voxels were $2 \times 2 \times 2$ cm in size. NAA was assigned at 2.02 parts per million, Cho at 3.2 ppm, Cr at 3.03 ppm, and lactate at 1.3 ppm. Metabolite ratios (NAA/Cr and Cho/Cr) were also measured. All data processing was performed by software provided by the scanner manufacturer.
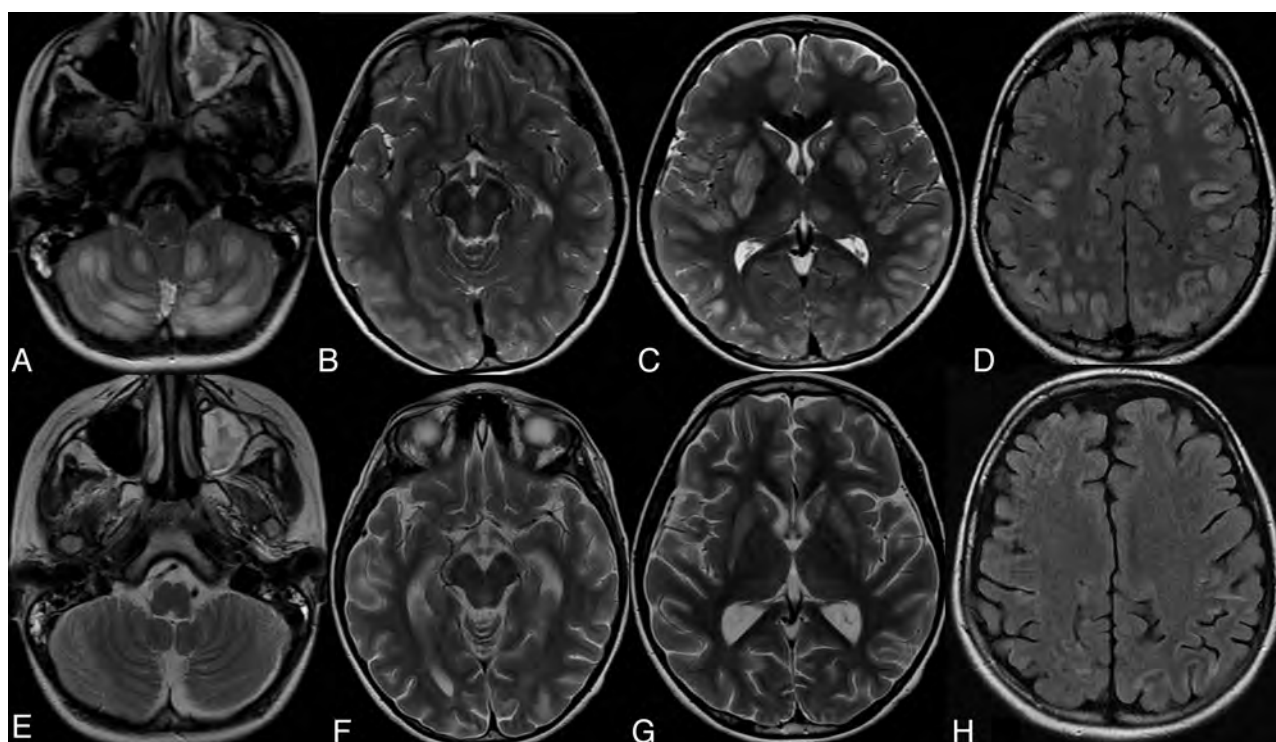
FIG 2. Brain MR imaging of a female patient, 8 years old, presenting with subacute encephalopathy and focal seizures. Axial T2WI (*A–C*) and FLAIR (*D*) before and 3 weeks after (*E–H*) treatment with biotin and thiamine. *A*, Abnormal areas of increased signal intensity in the cerebellum with involvement of the dentate nuclei. *B*, Increased signal intensity in the mesencephalon involving the red nuclei and periaquiductal gray matter. *C*, Swelling and increased signal intensity in the caudate nuclei, putamina, and medial thalami with small focal necrosis in the caudate heads. *D*, Widespread focal cortical and subcortical high signal areas at both cerebral hemispheres (could represent transient edema attributed to recent seizures and not necessarily the disease). Follow-up MR imaging after treatment (*E–H*) shows resolution of the cerebellar and mesencephalic lesions with notable regression of the thalamic, cortical, and subcortical lesions. The caudate nuclei and putamina show persistent signal abnormality and have evolved from swelling into atrophy.

Spinal cord MR imaging was done in 7 cases. The MR imaging spine protocol included sagittal T1WI (TR 397 milliseconds, TE 12 milliseconds) and T2WI (TR 3700 milliseconds, TE 103 milliseconds). Axial T2WI (TR 4220 milliseconds, TE 101 milliseconds) was performed at cervical and dorsal levels.

Image Analysis

MR examinations of the brain and spine and MR spectroscopy datasets were reviewed by 2 experienced radiologists in consensus with an emphasis on the involvement or sparing of the mesencephalon, cerebellum, caudate nuclei, globus pallidi, putamina, thalami, cortical-subcortical regions, and deep white matter before and after treatment as well as the presence of lactate doublet, NAA peak, and NAA/Cr ratio on MR spectroscopy.

The study was approved by the ethical committees of our institutions.

RESULTS

Our study enrolled 15 patients (their clinical and neuroimaging data are shown in the On-line Table). Eleven cases (73%) had positive consanguinity. On presentation, 13 patients (86.7%) had subacute onset in the form of encephalopathy, ataxia, and seizures, whereas only 2 patients (13.3%) presented by acute crisis with severe neurologic deficit, generalized dystonia, quadriplegia, and coma. Pre-existing trigger factor (febrile illness or trauma) was found in 7 cases (46.7%).

The brain MR imaging showed bilateral and symmetric lesions in the caudate heads in all of our patients with complete or partial involvement of the putamen (Figs 1–4). The globus pallidi were spared in all patients. In 12 cases (80%), discrete abnormal signal changes were observed in the mesencephalon (Fig 2), cortical-subcortical regions, and the medial dorsal nuclei of the thalami (Figs 1–3). In 8 cases (53%), when the disease was advanced, patchy deep white matter affection was found. The cerebellum along the cerebellar cortex and vermis was involved in only 2 patients (13.3%) (Figs 1 and 2). The affected brain regions showed variable swelling and vasogenic edema during the acute/subacute phase. No cytotoxic edema was found. No pattern of diffusion restriction on diffusion-weighted images or significant contrast enhancement was detected.

The MR imaging of patients under treatment showed evolution of the basal ganglia from swelling into atrophy and necrosis in all cases with resolution of the abnormal high signals of the cortex and subcortical regions. Resolution of the cerebellar abnormal signal was also observed in the 2 patients who showed cerebellar involvement. However, the abnormal signals of the caudate and putamen persisted in all patients (Figs 1–4).

Pretherapy ^{1}H-MR spectroscopy showed consistent elevation of lactate within the affected regions and decrease in NAA peak and NAA/Cr ratio in all cases. Disappearance of the lactate peak after biotin/thiamine therapy was noted in the single obtained posttherapy MR spectroscopy (Fig 4).
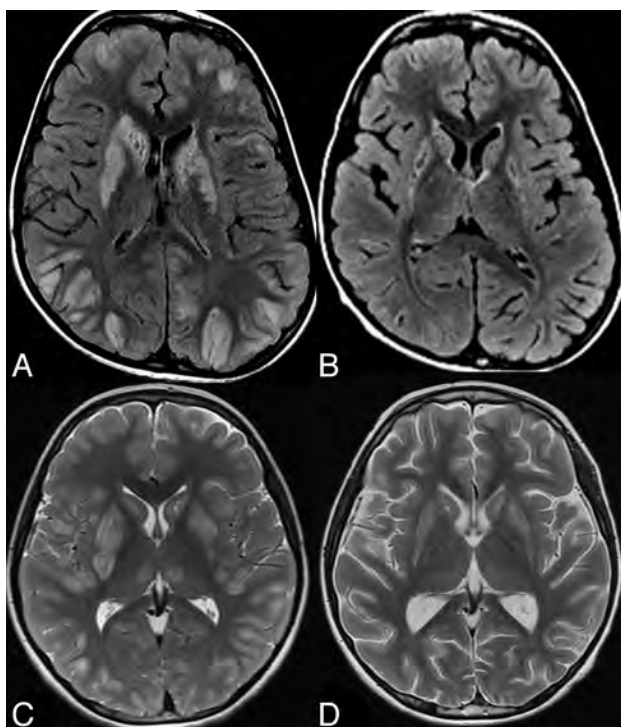
FIG 3. Brain MR imaging in 2 different patients with BBGD (*A* and *B*, axial FLAIR for patient 1; *C* and *D*, axial T2WI for patient 2). In the 2 patients, the pretreatment images (*A*, *C*) demonstrate bilateral swelling and increased signal in the caudate nuclei and putamina with abnormal signal in the cortex and gray-white matter junction at multiple locations. Involvement of the medial thalami is also noted in patient 2 (*C*). Follow-up after treatment (*B*, *D*) shows disappearance of the abnormal signal in the cortical and subcortical lesions with resolution of the thalamic lesions in patient 2, who developed mild brain atrophy. The basal ganglia became atrophic with persistent abnormal signal intensity.

The spinal MR imaging done for 7 cases at the onset of symptoms showed normal appearance of the spinal cord.

All patients received a combination of biotin and thiamine. Twelve cases (80%) had a good (favorable) outcome with no clinical sequelae. Two patients (13.3%) had mild to moderate sequelae (unfavorable outcome) in the form of dystonia and dysarthria that did not interefere with daily life or school activities. One patient (6.7%) died from severe encephalopathy, coma, cardiac arrest, and rhabdomyolysis. The high signal abnormality of the mesencephalon and cerebral/cerebellar cortical and subcortical areas disappeared after treatment whereas the caudate and putamen necrosis persisted in the 14 cases that underwent follow-up.

DISCUSSION

BBGD is an autosomal recessive neurometabolic disorder.[7] It was first described in 1998 in 10 patients from the Middle East.[1] Recently, the disease was recognized as a panethnic condition that usually occurs in preschool and school-aged children.[2,4]

The typical clinical presentation of patients with BBGD is recurrent subacute episodes of encephalopathy, often triggered by febrile illness or mild trauma and characterized by confusion, seizures, dystonia, external ophthalmoplegia, and dysphagia, eventually leading to coma and even death. Less frequently, patients with BBGD present with a chronic or slowly progressive condition characterized by dystonia, seizures, and psychomotor delay.[13]

The neurologic history of most our patients (86.7%) was in the form of subacute encephalopathy similar to the first 10 patients described by Ozand et al.[1] However, 2 patients (13.3%) presented with acute crisis with severe neurologic deficit, generalized dystonia, quadriplegia, and coma. A pre-existing trigger factor (febrile illness or trauma) was found in 46.7% of our cases.

Early diagnosis of BBGD is crucial because early administration of biotin and thiamine results in partial or complete improvement within days. Delay or lack of treatment may result in death or severe neurologic sequelae, including dystonia and quadriparesis. Moreover, patients require counseling regarding life-long treatment.[13]

In the original report by Ozand et al,[1] the MR imaging findings consisted of bilateral necrosis in the basal ganglia, particularly at the central part of the caudate heads and part or all of the putamen with severe edema during the acute/subacute crisis in addition to white matter involvement at the gray–white matter junction. Subsequent reports confirmed these findings and added the involvement of the thalami, cerebellum, and brain stem.[2,5] Our results supported the findings of these previous reports regarding the MR imaging distribution of lesions in all cases. In addition, the globus pallidi were spared in all patients in agreement with most of previous reports.[1,2,13]

Alfadhel et al[7] emphasized diffuse involvement of the cortical and subcortical white matter in the acute phase and atrophy and necrosis of the basal ganglia in the chronic phase in all cases. The thalami and brain stem were involved in one-third of their patients. In the present study, we demonstrated discrete abnormal signal changes in the mesencephalon, cerebral cortical-subcortical regions, and in the medial dorsal nuclei of the thalami in 80% of cases. In 53%, when the disease was advanced, patchy deep white matter affection was found. The cerebellum along the cerebellar cortex and vermis was involved in only 13.3% of our cases compared with one-third of the patients of Alfadhel et al.[7]

Follow-up of our patients under treatment confirmed the evolution of the basal ganglia from swelling into atrophy and necrosis with resolution of the abnormal high signals of the cerebral cortex and subcortical areas together with regression of the cerebellar abnormal signal in patients who showed cerebellar involvement. However, the abnormal signal lesions of the caudate and putamen persisted. These findings are in absolute agreement with earlier reports.[1-4,7,13]

Despite the extensive abnormal findings observed on the brain MR imaging, 80% of our patients with biotin-responsive encephalopathy remained asymptomatic under treatment. This observation suggests that enough tissue may be preserved in the target areas of the disease, to permit neurologic function.[1]

Interestingly, in the report by Alfadhel et al,[7] 1 patient demonstrated spinal cord involvement with increased T2 signal intensity particularly at the cervical region, which was not reported on earlier studies. They thought that the spinal cord involvement could be part of the disease and advised performing spinal MR imaging for all patients with BBGD. However, 7 of our patients were investigated by spinal MR imaging and none showed spinal cord involvement, which strongly argues against spinal cord involvement as a part of the disease. The absence of spinal cord lesions in
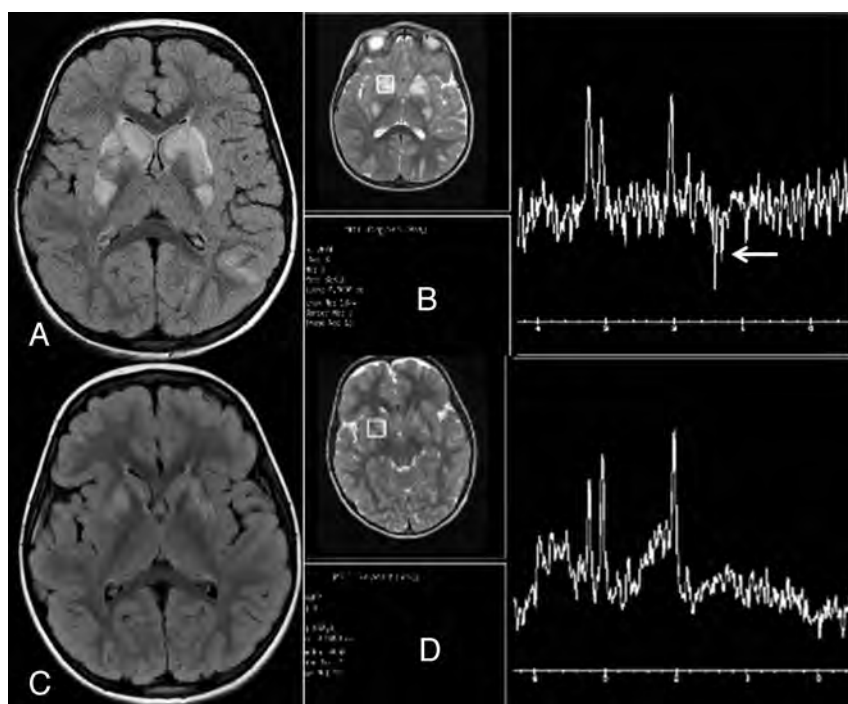
FIG 4. Female patient, 2.5 years old, with BBGD. Pretherapy axial FLAIR (*A*) shows high signal and swelling of the caudate nuclei with partial involvement of the putamina. *B*, Pretherapy single voxel MR spectroscopy at the right basal ganglia at 144 ms shows abnormal inverted lactate doublet (*arrow*) indicating lactate elevation and decreased NAA peak. *C*, Posttherapy axial FLAIR shows regressive changes of the abnormal signal and swelling in the basal ganglia. *D*, Posttherapy single voxel MR spectroscopy at the right basal ganglia at 144 ms shows disappearance of the lactate doublet with subtle improvement of NAA peak.

our patients is consistent with all previously described cases, except the 1 reported by Alfadhel et al.[7]

Spectroscopy (¹H-MR) was performed in 6 of our cases at time of onset of symptoms and before initiation of therapy. It depicted lactate peaks and decreased NAA in all cases. The lactate doublet could be interpreted as sign of ongoing apoptosis. It has disappeared in the single posttherapy MR spectroscopy. Decreased NAA could be explained by early brain injury and neuronal loss.[13] We found no appreciable differences between the MR spectrum in basal ganglia and in parieto-occipital cortical-subcortical lesions. As increased CNS lactate can be found in other pathologic processes including mitochondrial diseases,[14] these findings are considered nonspecific.[13]

In our study, because assessment of the response to therapy was limited clinically to the reversibility of symptoms and radiologically to the regression of the swelling and vasogenic edema of the affected regions, none of our patients had follow-up MR spectroscopy except 1. Interestingly, in this patient (Fig 4), the lactate peak has almost disappeared reflecting that MR spectroscopy could provide additional information as a monitor of response to therapy. The short half-time of lactate could be valuable as an early indicator of response to treatment in the future.

Bilateral and symmetrical basal ganglia lesions are caused by different systemic or metabolic conditions that share some findings with BBGD. However, the dramatic response to biotin therapy and persistence of caudate and putaminal signal abnormality without neurologic sequelae are characteristic features of BBGD. Wernicke encephalopathy (WE) is an example of these diseases. It

can involve the medial dorsal nucleus in thalami, periventricular regions of the third ventricle, brain stem, central gray matter, basal ganglia, and cerebellum similar to BBGD. However, the main MR imaging differences between the two are that in BBGD, the mammillary bodies are spared when usually involved in WE and the supra- and infratentorial cortical involvement in BBGD is more extensive compared with WE.[15]

Mitochondrial disorders can also mimic BBGD because of similarity in deep gray matter involvement. They include Leigh disease, MELAS (mitochondrial myopathy, encephalopathy, lactic acidosis, and strokelike episodes), and MERRF (myoclonic epilepsy associated with ragged red fibers). Like BBGD, Leigh disease typically causes symmetric putaminal involvement, which may be associated with abnormalities of caudate nuclei, thalami, and brain stem; however, it less frequently involves the cerebral cortex and rarely involves the white matter.[16] In MELAS, the multiple cortical and subcortical infarctlike lesions that cross vascular boundaries are a distinctive feature.[16] In MERRF, the imaging findings are nonspecific. The cerebral and cerebellar white matter is reported to show patchy T2 prolongation on MR imaging. Cerebral and cerebellar atrophy are almost always present. Involvement of the deep gray matter nuclei with degeneration and calcification of dentate and globus pallidus are the most common manifestations.[17] On the contrary, in BBGD the globus pallidus is usually not affected.[1,2,13,18] This also differentiates the disease from toxic causes of encephalopathy such as carbon monoxide poisoning, which has propensity to affect the globus pallidus.[19]

Although the disease described responds to biotin, biotinidase deficiency is absent. The brain imaging findings are also different from those seen in biotinidase deficiency, in which the neuroradiologic changes indicate diffuse low attenuation of the white matter followed by progressive marked cerebral atrophy.[20]

In contrast to the swelling of the caudate heads and putamen in patients with BBGD, the main radiologic feature in juvenile Huntington disease is caudate atrophy and increased proton attenuation and T2 signal in the atrophic caudate nuclei and putamina.[21] In patients with acute destructive lesions of the basal ganglia, ie, the so-called benign form of infantile bilateral striatal necrosis, the basal ganglia lesions might return to normal[22] while they persist after treatment in BBGD.[4]

Generally, BBGD should be thought of in any pediatric patient with neurologic symptoms and bilateral and symmetrical affection of caudate nuclei and putamina in MR imaging. Biotin and thiamine treatment is then suggested until either BBGD is excluded or 1 of the other differential diseases has been clearly identified.[23]

In our study, 12 cases (80%) had a good (favorable) outcome with no clinical sequelae, whereas 3 patients had an unfavorable outcome, 2 (13.3%) had dystonia and dysarthria, and 1 patient (6.7%) died from severe encephalopathy because of delayed diagnosis and treatment. These data suggested better outcome results when compared with Alfadhel et al[7] who had 4 of 18 (22%) patients who died, 6 (33.3%) patients who showed mild to moderate neurologic deficit, and 2 (11%) cases in which the patients had severe neurologic deficits.

The gap between the age of disease onset and the date of starting treatment by biotin and thiamine correlates directly with the neurologic outcome. Two of our 15 patients who had delayed diagnosis displayed neurologic deficits and another patient died for the same reason; the remaining patients who were diagnosed early and received immediate treatment achieved good outcomes and became asymptomatic.

It is important to check for the presence of BBGD in children with acute onset extrapyramidal symptoms as it can be managed without further neurologic deterioration.[3] Because there is no known biochemical marker for the disease, the only way to confirm the diagnosis is the detection of a mutation in the *SLC19A3* gene.[6]

CONCLUSIONS

BBGD is a treatable underdiagnosed condition. Children with unexplained encephalopathy and bilateral signal alterations of the caudate nucleus and putamen in MR imaging should be suspected of having the disease and a therapeutic trial with biotin and thiamine seems to be mandatory as the prognosis depends on the time interval between the diagnosis and initiation of therapy.

REFERENCES

1. Ozand PT, Gascon GG, Al Essa M, et al. **Biotin-responsive basal ganglia disease: a novel entity.** *Brain* 1998;121:1267–79
2. El-Hajj TI, Karam PE, Mikati MA. **Biotin-responsive basal ganglia disease: case report and review of the literature.** *Neuropediatrics* 2008;39:268–71
3. Bindu PS, Noone ML, Nalini A, et al. **Biotin-responsive basal ganglia disease: a treatable and reversible neurological disorder of childhood.** *J Child Neurol* 2009;24:750–52
4. Debs R, Depienne C, Rastetter A, et al. **Biotin-responsive basal ganglia disease in ethnic Europeans with novel SLC19A3 mutations.** *Arch Neurol* 2010;67:126–30
5. Yamada K, Miura K, Hara K, et al. **A wide spectrum of clinical and brain MRI findings in patients with SLC19A3 mutations.** *BMC Med Genet* 2010;11:171–79
6. Reihle C, von Kalle T, Severien C, et al. **Biotin-responsive basal gan-**
glia disease in a 10-year-old German girl without SLC19A3 gene mutation. In: *39th Annual Meeting of the Society of Neuropediatrics,* Innsbruck, Austria. April 25–28, 2013
7. Alfadhel M, Almuntashri M, Jadah RH, et al. **Biotin-responsive basal ganglia disease should be renamed biotin-thiamine-responsive basal ganglia disease: a retrospective review of the clinical, radiological and molecular findings of 18 new cases.** *Orphanet J Rare Dis* 2013;8:83–87
8. Zempleni J, Hassan YI, Wijeratne SS. **Biotin and biotinidase deficiency.** *Expert Rev Endocrinol Metab* 2008;3:715–24
9. Zeng WQ, Al-Yamani E, Acierno JS Jr., et al. **Biotin-responsive basal ganglia disease maps to 2q36.3 and is due to mutations in SCL19A3.** *Am J Hum Genet* 2005;77:16–26
10. Spector R, Mock D. **Biotin transport through the blood-brain barrier.** *J Neurochem* 1987;48:400–04
11. Vlasova TI, Stratton SL, Wells AM, et al. **Biotin deficiency reduces expression of SLC19A3, a potential biotin transporter, in leukocytes from human blood.** *J Nutr* 2005;135:42–47
12. Rodriguez-Melendez R, Zempleni J. **Regulation of gene expression by biotin (review).** *J Nutr Biochem* 2003;14:680–90
13. Tabarki B, Al-Shafi S, Al-Shahwan S, et al. **Biotin-responsive basal ganglia disease revisited: clinical, radiologic, and genetic findings.** *Neurology* 2013;80:261–67
14. Lin DD, Crawford TO, Barker PB. **Proton MR spectroscopy in the diagnostic evaluation of suspected mitochondrial disease.** *AJNR Am J Neuroradiol* 2003;24:33–41
15. Zuccoli G, Santa Cruz D, Bertolini M, et al. **MR imaging findings in 56 patients with Wernicke encephalopathy: nonalcoholics may differ from alcoholics.** *AJNR Am J Neuroradiol* 2009;30:171–76
16. Cheon JE, Kim IO, Hwang YS, et al. **Leukodystrophy in children: a pictorial review of MR imaging features.** *Radiographics* 2002;22:461–76
17. Barkovich AJ, Good WV, Koch TK, et al. **Mitochondrial disorders: analysis of their clinical and imaging characteristics.** *AJNR Am J Neuroradiol* 1993;14:1119–37
18. Roig M, Calopa M, Rovira A, et al. **Bilateral striatal lesions in childhood.** *Pediatr Neurol* 1993;9:349–58
19. Hegde AN, Mohan S, Lath N, et al. **Differential diagnosis for bilateral abnormalities of the basal ganglia and thalamus.** *Radiographics* 2011;31:5–30
20. Bousounis DP, Camfield PR, Wolf B. **Reversal of brain atrophy with biotin treatment in biotinidase deficiency.** *Neuropediatrics* 1993;24:214–17
21. Ho VB, Chuang HS, Rovira MJ, et al. **Juvenile Huntington disease: CT and MR features.** *AJNR Am J Neuroradiol* 1995;16:1405–12
22. Roig M, Macaya A, Munell F, et al. **Acute neurologic dysfunction associated with destructive lesions of the basal ganglia: a benign form of infantile bilateral striatal necrosis.** *J Pediatr* 1990;117:578–81
23. Distelmaier F, Huppke P, Pieperhoff P, et al. **Biotin-responsive basal ganglia disease: a treatable differential diagnosis of Leigh syndrome.** *JIMD Rep* 2014;13:53–57

MRI Characteristics of Ependymoblastoma: Results from 22 Centrally Reviewed Cases

J. Nowak, C. Seidel, F. Berg, T. Pietsch, C. Friedrich, K. von Hoff, S. Rutkowski, and M. Warmuth-Metz

ABSTRACT

BACKGROUND AND PURPOSE: Ependymoblastoma is a malignant embryonal tumor that develops in early childhood and has a dismal prognosis. Categorized by the World Health Organization as a subgroup of CNS-primitive neuroectodermal tumor, ependymoblastoma is histologically defined by "ependymoblastic rosettes." Because it is so rare, little is known about specific MR imaging characteristics of ependymoblastoma. We systematically analyzed and discussed MR imaging features of ependymoblastoma in a series of 22 consecutive patients.

MATERIALS AND METHODS: Ependymoblastoma cases were obtained from the database of the German multicenter HIT trials between 2002 and 2013. All cases within this study were centrally reviewed for histopathology, MR imaging findings, and multimodal therapy. For systematic analysis of initial MR imaging scans at diagnosis, we applied standardized criteria for reference image evaluation of pediatric brain tumors.

RESULTS: Ependymoblastomas are large tumors with well-defined tumor margins, iso- to hyperintense signal on T2WI, and diffusion restriction. Contrast enhancement is variable, with a tendency to mild or moderate enhancement. Subarachnoid spread is common in ependymoblastoma but can be absent initially. There was a male preponderance (1.75:1 ratio) for ependymoblastoma in our cohort. Mean age at diagnosis was 2.1 years.

CONCLUSIONS: With this study, we add the largest case collection to the limited published database of MR imaging findings in ependymoblastoma, together with epidemiologic data. However, future studies are needed to systematically compare MR imaging findings of ependymoblastoma with other CNS-primitive neuroectodermal tumors and ependymoma, to delineate imaging criteria that might help distinguish these pediatric brain tumor entities.

ABBREVIATIONS: EBL = ependymoblastoma; PNET = primitive neuroectodermal tumor

According to the 2007 World Health Organization Classification of Tumors of the CNS, ependymoblastoma (EBL) is a grade IV embryonal tumor that can be categorized as a subgroup of primitive neuroectodermal tumor (PNET).[1] The group of CNS-PNET can be further subdivided into CNS-neuroblastoma, CNS-ganglioneuroblastoma, NOS (not otherwise specified), and medulloepithelioma. EBLs are highly aggressive tumors that occur mainly in young children, with rapid growth and craniospinal dissemination. The MR imaging appearance of EBL has been described in the literature as a large, well-demarcated but heterogeneous mass with variable contrast enhancement.[2] Most of the tumors are located supratentorially, followed by infratentorial and spinal sites.[3] Locations outside the CNS are exceptionally rare, with published cases of congenital sacrococcygeal or ovarian tumors.[4,5]

First described by Bailey and Cushing[6,7] in 1926 as an ependymal-derived entity, the exact definition of EBL has since generated some controversy among neuropathologists. Rubinstein[8] later characterized EBLs as primitive neuroepithelial tumors of high cellularity that show numerous and characteristic "ependymoblastic rosettes."

We want to contribute to this ongoing discussion with the first

FIG 1. Typical MR imaging of EBL (patient 11), presenting as large hemispheric tumor mass. Note the well-delineated tumor margins and absence of surrounding edema. MR signal intensity is high in T2WI (*A*) and iso- to hypointense in T1WI (*B*). The tumor shows moderate enhancement of some parts after gadolinium administration (*C*). ADC map shows low signal (*D*, see also Fig 5*B*). Single-voxel MR spectroscopy (*E*) of the tumor with a choline:NAA ratio of 5:1, indicating high cellularity. There is a small peak for lactate at 1.3 ppm. A signal for lipids was not detected in this case (3T Trio; Siemens, Erlangen, Germany).

systematic analysis of imaging characteristics of EBL. Differentiation from other primitive embryonal tumors (such as other CNS-PNET variants and medulloblastoma) by means of diagnostic imaging is challenging. Due to the rarity of this tumor, a systematic analysis of MR imaging features of EBL has not yet been performed. To determine specific diagnostic features, we report on imaging characteristics of 22 consecutive EBL cases that were collected from the prospective German Society of Pediatric Oncology and Hematology multicenter trials HIT91, HIT-SKK92, and HIT2000 (HIT is a German abbreviation for brain tumor), with central review for neuropathology, neuroradiology, and therapy.[3,9,10]

MATERIALS AND METHODS
Study Population
EBL cases were obtained from the database of the German multicenter HIT trials.[11] Cases with histolopathologic diagnosis of EBL, confirmed by central review in the Neuropathological Brain Tumor Reference Center of the German Society of Neuropathology and Neuroanatomy (T.P.), were included. Patients were diagnosed with EBL between the years 2002 and 2013. Two patients were initially diagnosed with EBL and were excluded because they showed negative immunohistochemistry for LIN28A, which has been recently proposed as a molecular marker for embryonal tumors with multilayered rosettes.[12] We further excluded older cases where MR imaging (film copies) had not yet been digitized for image analysis. One patient from an external center was excluded because we lacked the initial MR imaging scans before surgery. A minimum of T1WI, T2WI, and contrast-enhanced T1WI in at least 2 different planes and without severe motion artifacts was required for cranial MR imaging scans in our study. Finally, 22 patients with sufficient preoperative cranial MR imaging scans were identified.

Image Analysis
For image analysis of our EBL cases, we used standardized MR imaging criteria according to the established routine evaluation of our Neuroradiological Reference Center for the HIT studies (as demonstrated in the On-line Table). Tumor diameter was measured in 3 dimensions (craniocaudal, left-right, anteroposterior; in cm), and tumor volume was calculated according to a common approximation formula ($a \times b \times c \times 0.5$; in cm³). Tumor location was recorded (supratentorial, infratentorial, brain stem/diencephalon; related to cortex or ventricles, basal ganglia, or intra-

ventricular location). T1- and T2-signal intensity of the tumor in relation to the signal intensity of the cerebral and cerebellar cortex was analyzed. We searched for possible cysts within the tumor, their localization (periphery, or other location) and size (small/large cysts, with a diameter >1 cm being considered as large). Furthermore, we registered hemorrhagic changes, the homogeneity of the solid tumor and the delineation of the tumor mass from the adjacent tissue (well or ill-defined). We analyzed possible peritumoral edema and the extent of edema. Another criterion was the pattern of gadolinium enhancement within the tumors (intensity, percentage of enhancing volume, homogeneity), and possible restriction of EBL in DWI. We recorded tumor staging with possible macroscopic meningeal dissemination (stage M2–M3, according to the Chang classification of CNS-PNET[13]) at the time of diagnosis. Finally, CT scans (with focus on calcifications and tumor attenuation) and MR spectroscopy data were analyzed when provided by the external referring centers. With respect to the multicenter approach, MR imaging studies were obtained with MR scanners of different manufacturers at 0.5–3 T field strength. Image reading was performed by 2 neuroradiologists (M.W.-M. and J.N.) in consensus.

RESULTS
Study Population
A total of 22 consecutive patients with EBL (mean age at diagnosis 2.1 years, range 0.3–3.4 years) were analyzed for this study. There was a male preponderance with a 1.75:1 ratio (14 patients were male and 8 were female).

Image Analysis
Most EBLs were located supratentorially (16 of 22 cases, Fig 1), whereas 4 tumors were found infratentorially (Fig 2) and 2 tumors occurred in the brain stem/diencephalon. The MR imaging appearance of brain stem EBL has been recently described in detail by our group.[14] Mean tumor volume was 114.7 cm³ (range 3–262 cm³). Cysts could be seen in 50% of the tumors (11 of 22), of which 6 tumors (55%) showed cysts in the tumor periphery. Regarding cyst size, only 2 of 11 tumors (18%) showed large cysts (as illustrated in Fig 3). In 17 of 22 EBL cases (77%), there were signs of intratumoral hemorrhage. There was also a tendency of inhomogeneous signal appearance in T1WI and T2WI: 17 tumors (77%) showed inhomogeneous or predominantly inhomogeneous signal, and only 2 tumors showed a homogeneous signal (9%; 3 tumors = 14% with predominantly homogeneous signal),
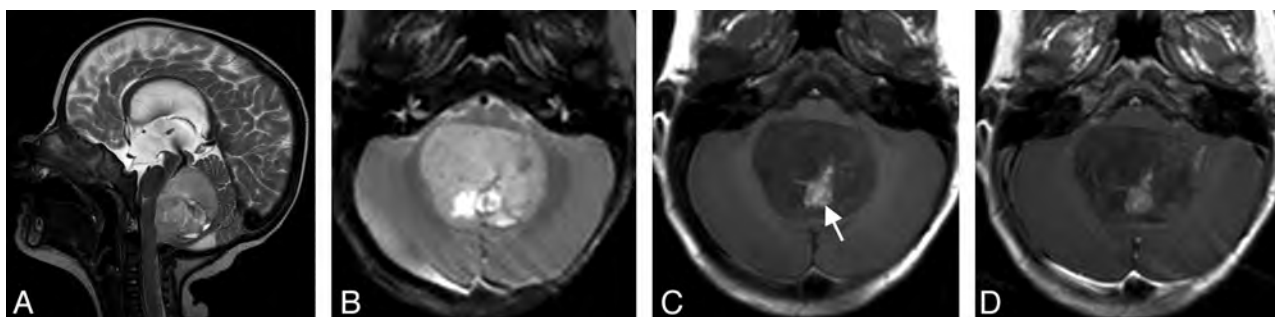
FIG 2. Infratentorial EBL (patient 7) of the fourth ventricle with marked displacement of the brain stem (*A*). T2 signal is predominantly inhomogeneous. No surrounding edema is present (*B*). Methemoglobin as a sign of intratumoral hemorrhage (*white arrow* in *C*). This tumor does not enhance after contrast administration (*D*) (1.5T Symphony; Siemens).
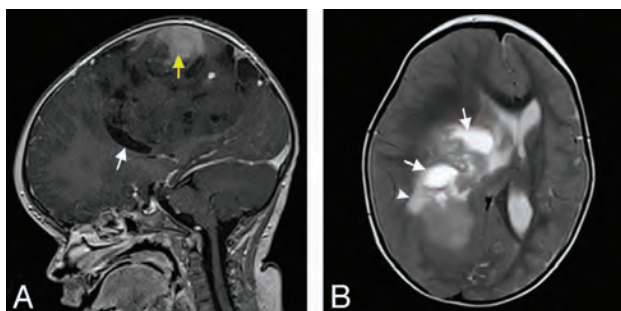
FIG 3. Hemispheric EBL (patient 6) with inhomogeneous signal and moderate contrast enhancement (*yellow arrow* in *A*). Cystic components of variable size are present in the tumor (*white arrows* in *A* and *B*). Small peritumoral edema can be found in T2WI (*white arrowhead* in *B*). Note there is significant mass effect with midline shift. Tumor margins are less defined in some areas compared with patient 11 (Fig 1) (1.5T Symphony; Siemens).

as demonstrated in Fig 4. This is also reflected by the particular analysis of T1 and T2 signal intensity. In T1WI, the predominant signal was hypo- (9 of 22, 41%) to isointense (27%). In the remaining 7 tumors (32%), different signal intensities (hypo-/iso-/hyperintense) could be found in T1WI, mainly due to partial hemorrhage and/or calcifications. In T2WI, hypo- to hyperintense signal intensities (ie, all types of signal intensities) were present in 19 of 22 cases (86%), reflecting inhomogeneous signal. The predominant T2 signal was isointense (12 cases, 55%) or hyperintense (10 cases, 45%). None of the tumors showed a predominant low (hypointense) signal intensity in T2WI. However, all analyzed tumors had sharp (19 of 22, 86%) or predominantly sharp (3 of 22, 14%) tumor margins (Fig 1) against the adjacent structures. Surrounding edema was present in only 2 of the cases with EBL (9%). DWI was available in 14 of 22 patients; in the remaining 8 cases, DWI was either not acquired or not submitted for central neuroradiologic review. All 14 tumors with available DWI showed high signal suspecting diffusion restriction, which could be confirmed by low ADC in 11 cases (Fig 1*D*, Fig 5*B*). In 3 cases, there was no ADC map available. Here, high signal in DWI with corresponding relatively low signal intensity in T2WI (not hyperintense) was considered as restricted diffusion. Hence, all 14 tumors (100%) with available DWI showed diffusion restriction. There were 17 tumors (77%) that presented with enhancement after intravenous gadolinium administration, with 6 tumors (35%) showing mild, 8 tumors (47%) moderate, and 3 tumors (18%) strong contrast enhancement. Enhancement was predom-
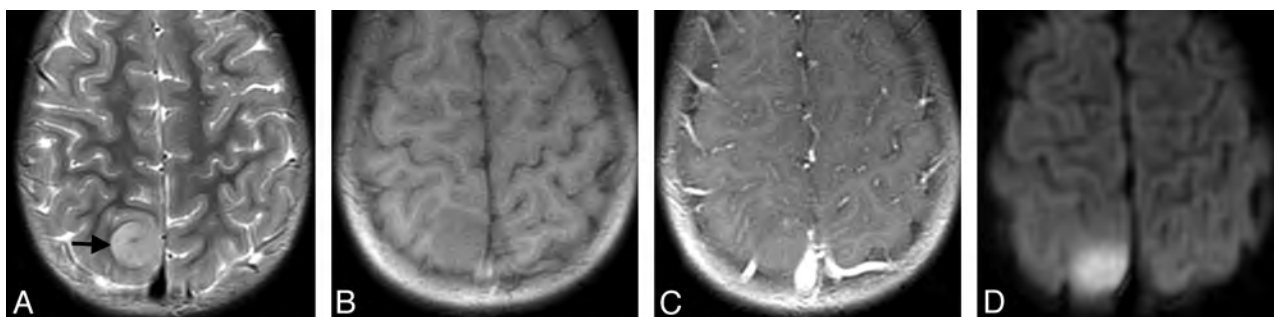
inantly homogeneous in most enhancing tumors (13 cases, 76%), and completely homogeneous in 1 case (6%). A total of 2 tumors (12%) showed predominantly inhomogeneous contrast enhancement, and 1 tumor (6%) showed (completely) inhomogeneous enhancement. One tumor was found with 51%–75% gadolinium enhancement of the solid tumor component. Most EBLs (16 of 17, 94%) showed 26%–50% (7 cases) or 1%–25% (9 cases) solid tumor enhancement.

More than two-thirds of our EBL cases (17 of 22, or 77%) did not show imaging evidence of meningeal dissemination (indicating macroscopic dissemination) at presentation. In addition, we lacked spinal MR imaging scans for 4 cases and hence CNS macroscopic dissemination status remained unclear. At presentation, 6 of 7 patients (86%) with complete intracranial and spinal MR imaging datasets did not have positive imaging signs (M2 and/or M3) of meningeal dissemination. One patient had M3 stage (spinal CNS dissemination). Another patient presented with a solitary M2 stage (intracranial dissemination). However, spinal datasets were incomplete in this patient (according to our internal standard of MR acquisition parameters; see Discussion), in another 2 patients with proposed M3 stage, and in 2 patients with proposed M2 and M3 stage (intracranial and spinal dissemination). In the remaining patients, the exact status of possible CNS spread remained unclear from our neuroradiologic perspective. Single-voxel MR spectroscopy data were available for only 3 patients (14%), and showed an increase in the choline:NAA ratio up to 5:1, compared with normal brain tissue (Fig 1*E*). Additional CT scans were submitted in 5 of our 22 cases (23%), with EBL showing different solid components from hypoattenuation (minimum of 20 Hounsfield units) to hyperattenuation (maximum of 41 Hounsfield units), compared with cortex (Fig 6*B*, -*D*). In 3 cases (60%), there were calcifications within the tumors (60%). Typical histopathologic appearance of EBL is demonstrated in Fig 7.

DISCUSSION
Study Population
With this series comprising 22 MR imaging studies of EBL, we present detailed imaging characteristics of this rare pediatric CNS tumor entity. In addition to imaging features, our study also provides epidemiologic information of EBL. We found a male to female ratio of 1.75:1 in our patient collective. In all CNS-PNETs, this ratio has been reported with 1.4:1, according to the annual report of the German Childhood Cancer Registry.[15] The mean age

FIG 4. Small parasagittal EBL (patient 15) with predominantly homogeneous, isointense MR signal in T2WI (*A*, *black arrow*) and T1WI (*B*). Note there is diffusion restriction (*D*), but no intratumoral contrast enhancement (*C*) (1.5T Signa Excite; GE Healthcare, Milwaukee, Wisconsin).
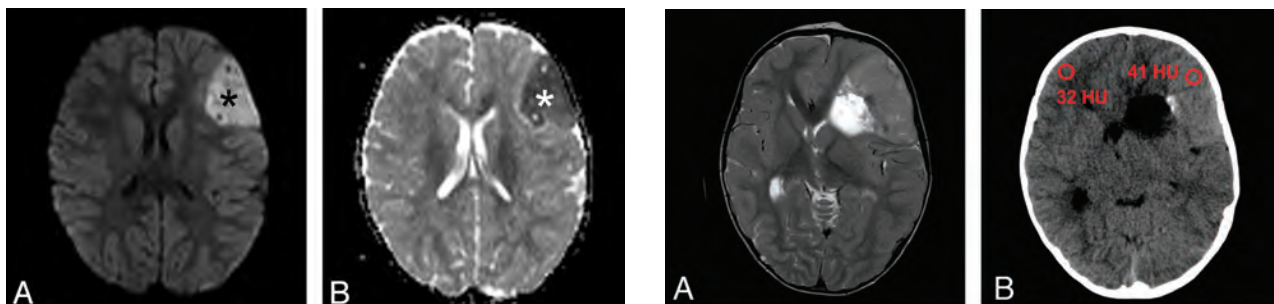
FIG 5. Left hemispheric EBL of patient 5 showing restricted diffusion (*black asterisk* in *A*) with corresponding low signal in ADC map (*white asterisk* in *B*), reflecting diffusion restriction and high cellularity. This finding was observed in every patient with EBL of our cohort (3T Verio; Siemens).

at diagnosis for all CNS-PNETs in this registry was 4 years 0 months, whereas mean age at diagnosis of EBL was 2.1 years in our study. Thus, it seems that there might be a male preponderance for EBL and other CNS-PNETs (with a slightly stronger tendency for EBL in males), and a younger age at diagnosis in EBL, compared with other CNS-PNETs. There are currently no data available in the literature about mean age at diagnosis, incidence, or sex and race predisposition of EBL. According to the Surveillance, Epidemiology and End-Results database, neither sex nor race was a predictor for CNS-PNET development.[16]

Image Analysis

To date, only very limited MR imaging data are available from few case reports.[3,17-21] Histologically designated as a subgroup of CNS-PNET, EBL seems to share imaging features with (other) CNS-PNETs. On MR imaging scans, EBL and other CNS-PNETs appear as large, heterogeneous tumor masses with iso- to hyperintense signal to gray matter on T2WI, pointing to increased cellularity.[22,23] This is further supported by restricted diffusion (100% of our EBL cases) and decreased ADC, which has been reported for other CNS-PNETs as well.[24] In addition, necrosis and hemorrhage are common in CNS-PNET and in our EBL cases (77%). The solid tumor component of CNS-PNET has been described with avid heterogeneous gadolinium enhancement in the literature.[25] For EBL, we found mild to moderate enhancement in most cases (6 and 8 of 22, respectively). Only 3 cases showed strong enhancement, whereas 5 patients did not show any contrast enhancement. Surrounding edema seems to be only minimal in both EBL (9% in our study) and other CNS-PNETs.[23] Calcifi-
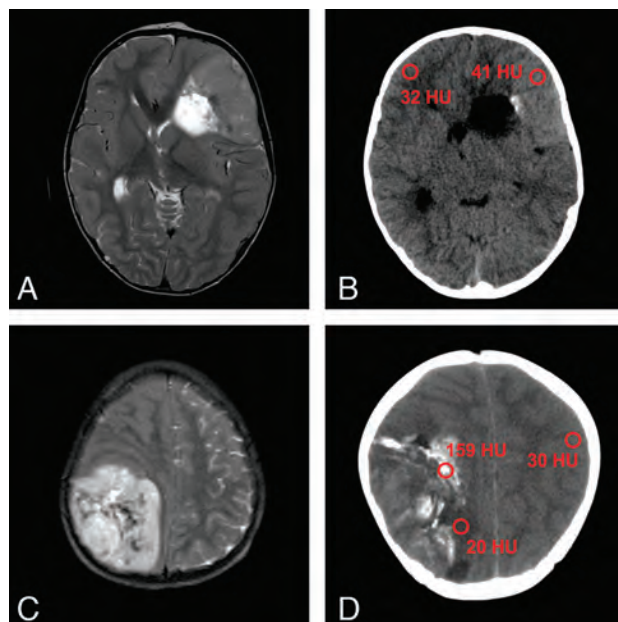
FIG 6. T2WI of 2 EBLs with corresponding CT scans of patient 12 (*A*, *B*) and patient 19 (*C*, *D*). Note almost T2 isointense signal of the tumor in (*A*) with slight hyperattenuation in the corresponding CT image (*B*). This tumor is indicative of higher cellularity, compared with the EBL shown in (*C*) and (*D*). Calcifications such as in (*D*) can complicate the detection of components with high cellularity. Region of interest in red showing Hounsfield units of tumors, normal cortex, and calcifications (*A*, 1.5T Signa Excite, GE Healthcare; *B*, Sensation 16, Siemens; *C*, 0.5T NT Intera, Philips Healthcare, Best, the Netherlands; *D*, Lightspeed Plus, GE Healthcare).

cations are seen in up to 70% of CNS-PNETs, with iso- to hyperattenuating appearance in CT.[22,26] This is relatively consistent with our EBL cases (60% calcifications), though we analyzed only 5 tumors with available CT scans. MR spectroscopy findings in CNS-PNET are characterized by marked elevation of taurine and choline levels with low creatine.[26,27] We are the first to demonstrate MR spectroscopy findings in EBL, with a high choline:NAA ratio pointing to increased cell turnover, similar to CNS-PNET. It is not yet clear whether MR spectroscopy might be useful to distinguish CNS-PNET variants from EBL and other brain tumors in the clinical setting. Considering evolving techniques such as perfusion MR imaging and DTI, we lack data to further characterize EBL. Perfusion MR imaging in CNS-PNET showed increased relative CBV values that might result from vascular endothelial hyperplasia and increased permeability, as seen in other high-grade
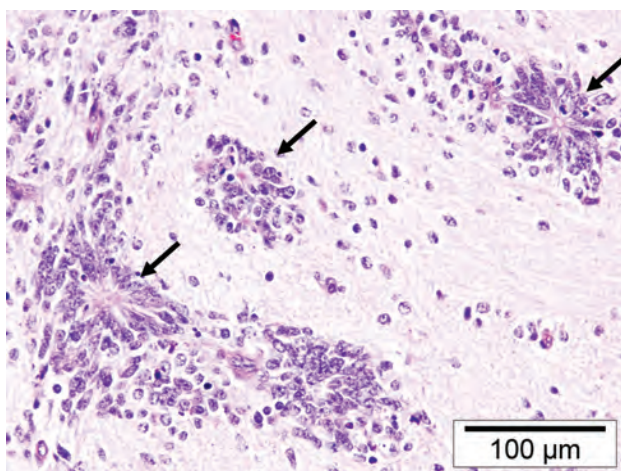
FIG 7. Typical histopathologic finding of EBL (patient 1) with ependymoblastic rosettes (*black arrows*).

tumors.[28] Furthermore, DTI has been applied for the evaluation of postradiation white matter changes in children with brain tumors including CNS-PNET, medulloblastoma, atypical teratoid/rhabdoid tumor, and high-grade gliomas.[29]

A limitation of our study might be that most of the MR imaging cases were provided by external centers because of the multicentric nature of the HIT studies. Only 2 of 22 patients were treated in our clinic. Thus, cranial MR imaging datasets were of different quality, according to field strength (0.5–3T) and image acquisition parameters. To address the issue of heterogeneous MR imaging quality, all 22 cases were centrally reviewed regarding MR imaging findings by the Reference Center for Neuroradiology (M.W.-M.).

EBL and other CNS-PNETs are highly malignant tumors, with aggressive growth and subarachnoid spread. It has been shown that about 40% of patients with supratentorial CNS-PNET or medulloblastoma show meningeal dissemination at presentation.[22] Spinal MR imaging is therefore strongly recommended and important for treatment and prognosis. Similar to cranial MR imaging, a difficulty in our study was the diverging image quality (section thickness, pulsation artifacts, sequence parameters) of the available spinal MR imaging scans. A total of 11 patients did not meet all quality criteria of our Reference Center, and hence diagnostic value of possible CNS spread of EBL within our study was limited. Being focused on tumor imaging in EBL, we do not provide data regarding possible M0 or M1 stage at presentation.

Histopathologic Diagnosis of EBL

The exact histopathologic diagnosis of EBL has its own controversial history. Bailey and Cushing[6] first proposed EBL as a specific diagnostic entity in 1926, characterized by the presence of "ependymal spongioblasts" (tumor cells with cytoplasmic processes that form "pseudorosettes"), separating EBL from ependymoma.[30] However, they later abandoned the term EBL, retaining "ependymoma" as the preferred designation. Rubinstein[8] reintroduced EBL as a malignant CNS tumor entity of young children in 1970, characterized by undifferentiated morphology and the presence of multilayered proliferative rosettes with a lumen (ependymoblastic rosettes). Recently, a primitive

tumor termed an embryonal tumor with abundant neuropil and true rosettes (ETANTR) has been proposed as a novel CNS tumor entity by some authors.[31] They argue that combined features of EBL and neuroblastoma, containing multilayered ependymoblastic rosettes ("true" rosettes), define a separate novel histologic tumor entity with poor outcome.[7,31,32] However, this largely overlaps with the original descriptions by Rubinstein,[8] probably representing the identical phenotype and diagnosis. Recent molecular studies further clearly demonstrate that tumors diagnosed as EBL, ETANTR, or embryonal tumors with multilayered rosettes carry identical, highly specific chromosomal alterations (amplification at 19q and/or gain of chromosome 2).[33] EBL and the proposed "novel" entities therefore represent a single embryonal tumor entity (defined as EBL according to the 2007 World Health Organization classification).[1,12,33,34] Consequently, all 22 tumors of our case collection were designated EBL by central neuropathologic review (T.P.). We intend to contribute to this ongoing discussion with the first systematic analysis of imaging characteristics of EBL.

CONCLUSIONS

The case series presented here is the largest collection of MR imaging data for EBL to date. Imaging appearance of EBL seems to share features with other pediatric embryonal CNS tumors. However, a systematic analysis that compares imaging findings of EBL with (other) CNS-PNETs and ependymoma is needed to evaluate possible differences in image appearance of these entities.

REFERENCES

1. Louis DN, Ohgaki H, Wiestler OD, et al. *WHO Classification of Tumours of the Central Nervous System*. Lyon, France: IARC Press; 2007
2. Osborn AG. *Osborn's Brain: Imaging, Pathology, and Anatomy*. Salt Lake City: Amirsys; 2013:573–75
3. Gerber NU, von Hoff K, von Bueren AO, et al. **Outcome of 11 children with ependymoblastoma treated within the prospective HIT-trials between 1991 and 2006.** *J Neurooncol* 2011;102:459–69
4. Morovic A, Damjanov I. **Neuroectodermal ovarian tumors: a brief overview.** *Histol Histopathol* 2008;23:765–71
5. Santi M, Bulas D, Fasano R, et al. **Congenital ependymoblastoma arising in the sacrococcygeal soft tissue: a case study.** *Clin Neuropathol* 2008;27:78–82
6. Bailey P, Cushing H. *A Classification of the Tumors of the Glioma*

Group on a Histogenetic Basis With a Correlated Study of Prognosis. Philadelphia: JB Lippincott Co.; 1926

7. Judkins AR, Ellison DW. **Ependymoblastoma: dear, damned, distracting diagnosis, farewell!*.** *Brain Pathol* 2010;20:133–39

8. Rubinstein LJ. **The definition of the ependymoblastoma.** *Arch Pathol* 1970;90:35–45

9. Rutkowski S, von Bueren A, von Hoff K, et al. **Prognostic relevance of clinical and biological risk factors in childhood medulloblastoma: results of patients treated in the prospective multicenter trial HIT'91.** *Clin Cancer Res* 2007;13:2651–57

10. von Hoff K, Hinkes B, Gerber NU, et al. **Long-term outcome and clinical prognostic factors in children with medulloblastoma treated in the prospective randomised multicentre trial HIT'91.** *Eur J Cancer* 2009;45:1209–17

11. Friedrich C, von Bueren AO, von Hoff K, et al. **Treatment of young children with CNS-primitive neuroectodermal tumors/pineoblastomas in the prospective multicenter trial HIT 2000 using different chemotherapy regimens and radiotherapy.** *Neuro Oncol* 2013; 15:224–34

12. Korshunov A, Sturm D, Ryzhova M, et al. **Embryonal tumor with abundant neuropil and true rosettes (ETANTR), ependymoblastoma, and medulloepithelioma share molecular similarity and comprise a single clinicopathological entity.** *Acta Neuropathol* 2014;128:279–89

13. Laurent JP, Chang CH, Cohen ME. **A classification system for primitive neuroectodermal tumors (medulloblastoma) of the posterior fossa.** *Cancer* 1985;56:1807–09

14. Nowak J, Seidel C, Pietsch T, et al. **Ependymoblastoma of the brainstem: MRI findings and differential diagnosis.** *Pediatr Blood Cancer* 2014;61:1132–34

15. German Childhood Cancer Registry. Annual Report 2011. http://www.kinderkrebsregister.de/fileadmin/kliniken/dkkr/pdf/jb/jb2010/jb2010_2_Diagnosen.pdf. Accessed March 3, 2014

16. Smoll NR, Drummond KJ. **The incidence of medulloblastomas and primitive neurectodermal tumours in adults and children.** *J Clin Neurosci* 2012;19:1541–44

17. Cervoni L, Celli P, Trillo G, et al. **Ependymoblastoma: a clinical review.** *Neurosurg Rev* 1995;18:189–92

18. Dorsay TA, Rovira MJ, Ho VB, et al. **Ependymoblastoma: MR presentation. A case report and review of the literature.** *Pediatr Radiol* 1995;25:433–35

19. Nejat F, Kazmi SS, Ardakani SB. **Congenital brain tumors in a series of seven patients.** *Pediatr Neurosurg* 2008;44:1–8

20. Ng SH, Ko SF, Chen YL, et al. **Ependymoblastoma: CT and MRI demonstration.** *Chin J Radiol* 2002;27:21–25

21. Ortiz J, Otero A, Bengoechea O, et al. **Divergent ependymal tumor (ependymoblastoma/anaplastic ependymoma) of the posterior fossa: an uncommon case observed in a child.** *J Child Neurol* 2008;23:1058–61

22. Chawla A, Emmanuel JV, Seow WT, et al. **Paediatric PNET: pre-surgical MRI features.** *Clin Radiol* 2007;62:43–52

23. Newton H, Jolesz F. *Handbook of Neuro-Oncology Neuroimaging.* New York: Elsevier; 2008

24. Gauvain KM, McKinstry RC, Mukherjee P, et al. **Evaluating pediatric brain tumor cellularity with diffusion-tensor imaging.** *AJR Am J Roentgenol* 2001;177:449–54

25. Poussaint TY. **Magnetic resonance imaging of pediatric brain tumors: state of the art.** *Top Magn Reson Imaging* 2001;12:411–33

26. Borja MJ, Plaza MJ, Altman N, et al. **Conventional and advanced MRI features of pediatric intracranial tumors: supratentorial tumors.** *AJR Am J Roentgenol* 2013;200:W483–503

27. Kovanlikaya A, Panigrahy A, Krieger MD, et al. **Untreated pediatric primitive neuroectodermal tumor in vivo: quantitation of taurine with MR spectroscopy.** *Radiology* 2005;236:1020–25

28. Law M, Kazmi K, Wetzel S, et al. **Dynamic susceptibility contrast-enhanced perfusion and conventional MR imaging findings for adult patients with cerebral primitive neuroectodermal tumors.** *AJNR Am J Neuroradiol* 2004;25:997–1005

29. Hua C, Merchant TE, Gajjar A, et al. **Brain tumor therapy-induced changes in normal-appearing brainstem measured with longitudinal diffusion tensor imaging.** *Int J Radiat Oncol Biol Phys* 2012; 82:2047–54

30. Godfraind C. **Classification and controversies in pathology of ependymomas.** *Childs Nerv Syst* 2009;25:1185–93

31. Eberhart CG, Brat DJ, Cohen KJ, et al. **Pediatric neuroblastic brain tumors containing abundant neuropil and true rosettes.** *Pediatr Dev Pathol* 2000;3:346–52

32. Gessi M, Giangaspero F, Lauriola L, et al. **Embryonal tumors with abundant neuropil and true rosettes: a distinctive CNS primitive neuroectodermal tumor.** *Am J Surg Pathol* 2009;33:211–17

33. Korshunov A, Remke M, Gessi M, et al. **Focal genomic amplification at 19q13.42 comprises a powerful diagnostic marker for embryonal tumors with ependymoblastic rosettes.** *Acta Neuropathol* 2010; 120:253–60

34. Ceccom J, Bourdeaut F, Loukh N, et al. **Embryonal tumor with multilayered rosettes: diagnostic tools update and review of the literature.** *Clin Neuropathol* 2014;33:15–22

Interhypothalamic Adhesion: A Series of 13 Cases

M.T. Whitehead and G. Vezina

ABSTRACT

SUMMARY: Interhypothalamic adhesion is a newly described disease entity, characterized by an abnormal parenchymal band connecting the medial margins of the hypothalami across the third ventricle. Additional anomalies, including cleft palate, gray matter heterotopia, cerebellar hypoplasia, optic atrophy, hippocampal under-rotation, and white matter lesions, may coexist. The purpose of this clinical report is to describe the imaging findings from a series of 13 patients with interhypothalamic adhesions discovered on brain MR imaging.

ABBREVIATIONS: IHA = interhypothalamic adhesion; SPGR = spoiled gradient-recalled-echo

An interhypothalamic adhesion (IHA) is a horizontally oriented parenchymal band connecting the hypothalami across the third ventricle. Its architecture resembles that of a normal interthalamic adhesion. Although there are no known cases with histologic correlation, it may represent a choristoma. IHA could be considered a form fruste holoprosencephaly because additional midline abnormalities may be present in these patients.[1] Indeed, failed hypothalamic separation of varying degrees is a constant feature of the classic holoprosencephaly spectrum.[2]

After institutional review board approval and waiver, all cases of IHA encountered by the neuroradiology service during a 1-year period from 2 separate academic children's hospitals were retrospectively reviewed. We present MR imaging findings from 13 separate patients with interhypothalamic adhesions.

MATERIALS AND METHODS

Case Series

Thirteen patients were documented, with a mean age of 4 ± 3 years (range, 3 days to 15 years) and a balanced sex distribution (On-line Table). MR imaging examinations from each patient were analyzed by 2 board-certified neuroradiologists (M.T.W.

and G.V.); a consensus was reached in each case. All scans were obtained on either a 1.5 or 3T MR imaging scanner (Signa HDxt; GE Healthcare, Milwaukee, Wisconsin) and included at least the following pulse sequences: sagittal spoiled gradient-recalled-echo (SPGR) T1WI reformatted into axial and coronal planes, axial T2WI, axial T2 FLAIR, axial DWI, and coronal fat-saturated T2WI. In each patient, the signal intensity of the IHA was evaluated in the following planes and sequences: axial (T2WI, T2 FLAIR, and SPGR T1WI), coronal (SPGR T1WI and fat-saturated T2WI), and sagittal (SPGR T1WI). All examinations were of diagnostic quality. No exclusionary criteria prevented accurate evaluation.

The mean interhypothalamic adhesion volume was 29.4 ± 30.1 mL (range, 2.1–187.2 mL), assuming an ellipsoid with 3 orthogonal caliper-based measurements acquired from the sagittal SPGR T1WI and coronal and axial reformats representing the axes (volume = d1 × d2 × d3 × pi/6) where d = diameter. IHA locations involved portions of the expected area of the dorsomedial ($n = 10$), ventromedial ($n = 7$), arcuate ($n = 6$), paraventricular ($n = 5$), and preoptic ($n = 3$) nuclei; IHA locations were categorized on the basis of pre-existing literature.[3] In all cases, the IHA was isointense to gray matter on all sequences and connected the medial walls of the hypothalami horizontally. Additional brain abnormalities were detected in 12 of 13 patients; midline anomalies were present in 12 of 13 patients. Intravenous gadolinium was administered in 6 patients; none of the interhypothalamic adhesions demonstrated contrast enhancement. Pituitary hypoplasia was present in 1 patient. The pituitary gland and stalk were normal in all remaining patients.

Case 1. A 9-month-old boy status post cleft palate repair was referred to exclude congenital brain anomalies. Brain MR imaging
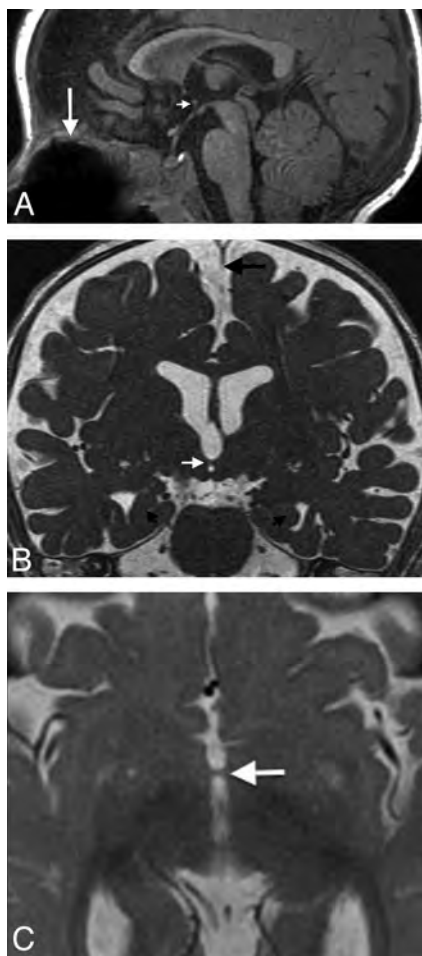
FIG 1. *A*, Sagittal fast-spoiled gradient recalled brain volume T1WI (TR/TE/TI, 10/4/450 ms) showing a parenchymal band representing an interhypothalamic adhesion in the third ventricle between the anterior commissure and mammillary body (*small arrow*). The pituitary infundibulum, adenohypophysis, and neurohypophysis are normal. Note metallic susceptibility artifacts in the roof of the oral cavity from prior cleft palate repair (*large arrow*). *B*, Coronal FIESTA with phase cycling (TR/TE, 10/4 ms) demonstrates an IHA traversing the third ventricle (*white arrow*), oblique axes of the hippocampal heads representing under-rotation (*small black arrows*), and incomplete formation of the falx cerebri (*large black arrow*). *C*, Axial T2WI (TR/TE, 5000/85 ms) shows an IHA connecting the medial hypothalamic margins across the third ventricle (*arrow*).

revealed an interhypothalamic adhesion in addition to olfactory bulb hypoplasia, hippocampal under-rotation, and falx cerebri hypoplasia (Fig 1). An IHA connected the hypothalami in the expected area of the dorsomedial hypothalamic nuclei.

Case 2. A 2-month-old preterm female, delivered early for intrauterine growth retardation due to maternal lupus and hypertension, underwent a term-equivalent brain MR imaging. It demonstrated an IHA, mild hippocampal under-rotation, and mild cerebral white matter hypoplasia. The IHA was located in the anterior/inferior third ventricle. It was centered in the expected area of the dorsomedial/ventromedial hypothalamic nuclear junction but extended inferiorly to abut the median eminence in the expected area of the arcuate nucleus.

Case 3. A 4-year-old boy underwent brain MR imaging for headaches and vomiting. Medical history was remarkable for Leber congenital amaurosis, small body habitus, facial dysmorphia,

hearing loss, developmental delay, and hypotonia. Findings of a chromosomal microarray were normal. Brain MR imaging depicted an IHA, optic pathway atrophy, and an old frontal lobe white matter injury. The IHA traversed the anterior/inferior third ventricle, partially inseparable from the forniceal columns and spanning to the third ventricular floor. It was centered in the expected area of the dorsomedial and ventromedial hypothalamic nuclei and extended inferiorly to the region of the arcuate nucleus.

Case 4. A 6-month-old term-gestation boy, with a history of global hypotonia, failure to thrive, cyanosis, and upper respiratory tract infection, presented for brain MR imaging evaluation. A chromosomal microarray showed areas of homozygosity consistent with parental consanguinity. Metabolic work-up demonstrated normal urine organic acid levels, plasma amino acid levels, creatine kinase levels, and lactate/pyruvate ratios. Imaging revealed an IHA in the anterior/inferior third ventricle and underrotation of the left hippocampus. Centered at the level of the superior margin of the brain stem, the IHA was located anterior to the forniceal columns in the region of the dorsomedial and ventromedial hypothalamic nuclei. A follow-up brain MR imaging at 11 months showed no change apart from normal myelination progression.

Case 5. A 5-year-old boy with developmental delay, seizures, and presumed Dandy-Walker malformation continuum diagnosed on prenatal sonography underwent brain MR imaging. An IHA was present in the anterior/inferior third ventricle, partially integrated into the forniceal columns. It was centered in the expected area of the dorsomedial and ventromedial hypothalamic nuclei and extended inferiorly to the region of the arcuate nucleus. Additional abnormalities included cerebellar hypoplasia/dysplasia, brain stem hypoplasia, Blake pouch cyst, falx cerebri deficiency, malformations of occipital development, hippocampal dysgenesis, and periventricular nodular heterotopia (Fig 2). A follow-up brain MR imaging performed at 9 years of age showed no change.

Case 6. An 8-month-old girl presented with lethargy and seizures after an upper respiratory tract infection. She was found to have hyponatremia, presumed secondary to polydipsia. MR imaging demonstrated an IHA and hippocampal under-rotation. The IHA was located midway between the anterior commissure and tuber cinereum, just posterior to the lamina terminalis. It was centered at the expected junction of the paraventricular and dorsomedial hypothalamic nuclei.

Case 7. A 7-year-old boy was imaged for emesis and headaches. Brain MR imaging showed an interhypothalamic adhesion centered in the anterior/inferior third ventricle (Fig 3*A*). The IHA was partially integrated into the forniceal columns and mammillary bodies, centered at the upper margin of the mesencephalon but spanning to the tuber cinereum. It was centered in the area of the dorsomedial and ventromedial hypothalamic nuclei and extended inferiorly to the arcuate nucleus. Additional abnormalities included cerebral white matter hypoplasia, remote bifrontal white matter injury, and hippocampal dysgenesis and under-rotation. An unusually deep sulcus was present, extending through the left anterior precuneus and posterior cingulate gyrus into the margin
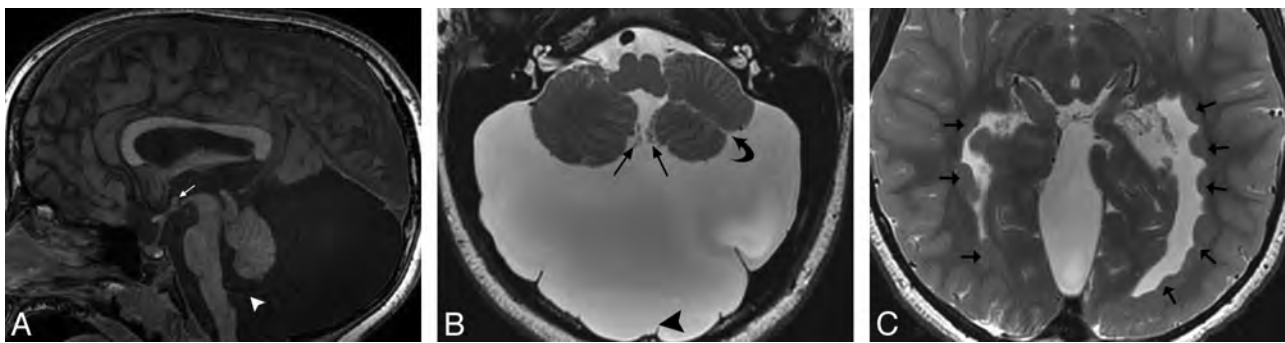
FIG 2. *A*, Sagittal SPGR T1WI (TR/TE/IR, 8/3/450 ms) demonstrating a nodular structure isointense to gray matter consistent with an IHA (*white arrow*) located at the level of the upper midbrain in the anterior/inferior third ventricle, spanning to the third ventricular floor. A Blake pouch cyst is present, enlarging the posterior fossa and communicating with the fourth ventricle via a widened foramen of Magendie (*white arrowhead*) and without accompanying vermian malrotation. Note also generalized vermian and brain stem hypoplasia. *B*, Axial T2 fast-spoiled gradient recalled image (TR/TE, 3049/99 ms) shows a large retrocerebellar cystic lesion markedly enlarging the posterior fossa, associated with an incomplete falx cerebelli (*arrowhead*). Choroid plexus is seen extending from the foramen of Magendie along its anteromedial walls (*straight arrows*), consistent with a Blake pouch cyst. The cerebellum is dysplastic with irregular foliation and a left cerebellar hemispheric cleft (*curved arrow*). *C*, Axial T2 fast-spoiled gradient recalled scan (TR/TE, 3049/99 ms) depicts periventricular nodular heterotopia along the lateral ventricular atria and occipital and temporal horns (*arrows*).
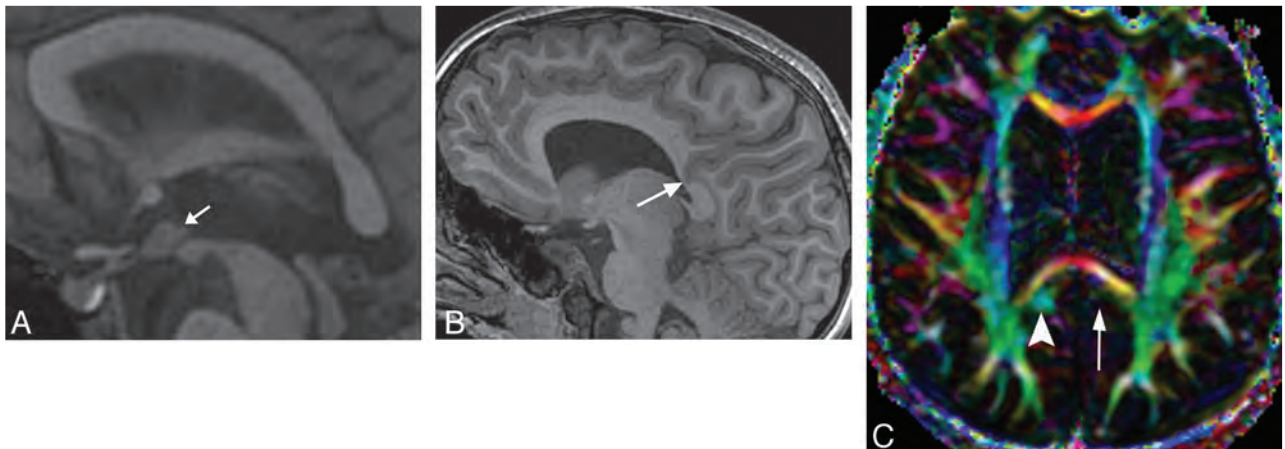
FIG 3. *A*, Sagittal SPGR T1WI (TR/TE/IR, 8/3/450 ms) demonstrating a nodular structure isointense to gray matter consistent with IHA (*arrow*) located at the level of the upper midbrain in the inferior third ventricle, extending to the tuber cinereum. *B*, Sagittal SPGR T1WI (TR/TE/IR, 8/3/450 ms) demonstrates an unusual deep parietal sulcus extending through the cingulate gyrus and distorting the callosal splenium architecture (*arrow*). *C*, Axial directionally encoded color map of DTI data (15 directions of encoding; TR/TE, 10,000/82 ms) shows absence of the normal green hue of the left cingulum isthmus (*long arrow*). Note the normal right cingulum isthmus (*arrowhead*).

of the callosal splenium, associated with focal thinning of the splenium (Fig 3*B*, -*C*).

Case 8. A 14-year-old girl was referred to brain MR imaging for delirium. An IHA was centered across the anterior third ventricle at the level of the superior midbrain margin, abutting the lamina terminalis. The IHA spanned portions of the area where one would expect to locate the preoptic, paraventricular, and dorsomedial hypothalamic nuclei. The brain was otherwise normal.

Case 9. A 4-month-old girl underwent brain MR imaging for infantile spasms. She had no other significant medical history. An IHA was present in the anterior third ventricle, centrally located among the lamina terminalis, forniceal columns, optic chiasm, and anterior commissure in the region of the paraventricular nucleus. Parieto-occipital white matter hypoplasia and hippocampal under-rotation were also evident.

Case 10. A 26-month-old girl with a history of Chiari II malformation status post myelomeningocele repair presented for MR

imaging to exclude hydrocephalus. The patient was also status post cranioplasty for unicoronal synostosis. An IHA was seen in the anterior third ventricle midway between the median eminence and anterior commissure (Fig 4*A*) in the approximate location of the paraventricular nucleus. Parenchymal stigmata of Chiari II malformation were present, including a small posterior fossa, tectal beaking, and mild corpus callosum dysgenesis (Fig 4*B*). In addition, partial rhombencephalosynapsis (Figs 4*A*, -*B*) and moderate ventriculomegaly were present. The hippocampi were under-rotated.

Case 11. A 3-day-old term boy was referred for evaluation of a prenatally diagnosed intracranial cyst. Brain MR imaging demonstrated an IHA connecting the expected areas of the dorsomedial, ventromedial, and arcuate nuclei (Fig 5*A*). A large midline meningeal cyst, septum pellucidum fenestration, and corpus callosum dysgenesis were present (Fig 5*A*). Periventricular nodular heterotopia (Fig 5*B*), a thickened thalamic mass intermedia, under-ro-

FIG 4. *A*, Sagittal SPGR T1WI (TR/TE/IR, 11/5/500 ms) demonstrating a small nodular structure representing an IHA located in the midanterior third ventricle in the expected area of the paraventricular nucleus (*arrowhead*). Parenchymal stigmata of a Chiari II malformation include a small posterior fossa, tectal beaking (*curved arrow*), and mild corpus callosum dysgenesis. In addition, partial rhombencephalosynapsis is present with loss of the normal architecture of the posterior vermis (*straight arrow*). *B*, Coronal fat-saturated T2WI (TR/TE, 3931/100 ms) shows continuous transverse cerebellar hemispheric folia and fissures extending across the midline, representing absence of the posterior vermis and partial rhombencephalosynapsis.
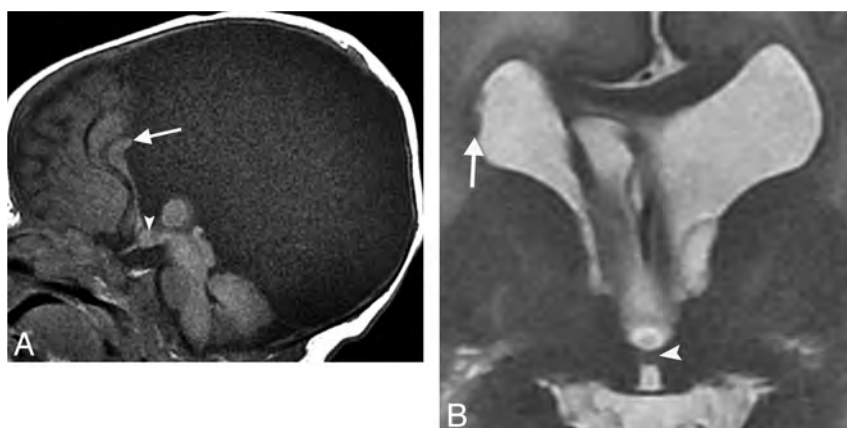
FIG 5. *A*, Sagittal T1WI (TR/TE, 400/9 ms) depicting a nodular structure occupying the anterior/inferior third ventricle, consistent with an IHA (*arrowhead*). A large interhemispheric meningeal cyst is associated with corpus callosal dysgenesis (*arrow*). *B*, Coronal T2WI (TR/TE, 2217/103 ms) shows a horizontal parenchymal band adjoining the medial thalami, representing an IHA (*arrowhead*), and periventricular nodular heterotopia (*arrow*).

tation and dysgenesis of the hippocampi, and hydrocephalus were also evident.

Case 12. A 3-year-old girl presented for evaluation of developmental delay and encephalopathy. Brain MR imaging revealed a tiny IHA connecting the region of the preoptic and paraventricular hypothalamic nuclei. With the exception of a 10-mm complicated pineal cyst, the remainder of the brain was normal for age.

Case 13. A 15-year-old boy was referred for evaluation of anosmia. His medical history was positive for congenital digital hypoplasia. Brain MR imaging showed an IHA encompassing nearly the entire medial surface area of the hypothalamus. The bases of the mammillary bodies were apposed. The corpus callosum was mildly thickened, and the pituitary gland was hypoplastic. Olfactory bulbs and tracts were aplastic. A subependymal nodular heterotopian was present in the right parietal lobe.

DISCUSSION

An interhypothalamic adhesion is a newly described entity characterized by an abnormal band of tissue adjoining the medial hypothalami to one another across the third ventricle.[1] The appearance of the interhypothalamic adhesion is quite characteristic, always visible in the sagittal plane as an additional small ovoid structure between the fornices and lamina terminalis, centered near the level of the midbrain cranial margin (Fig 6). Anatomically, this location corresponds to the anterior and tuberalis regions of the periventricular hypothalamus. Although there are no known cases with histologic correlation, interhypothalamic adhesion may represent a choristoma or a focal area of failed hypothalamic separation.

The hypothalamus borders much of the anteroinferior third ventricle (Fig 6). The normal anatomic boundaries of the hypothalamus are the hypothalamic sulcus (superior), roof of the suprasellar cistern (inferior), an imaginary line between the intraventricular foramina and mid-optic chiasm (rostral), and mammillary body/midbrain tegmentum junction (caudal).[4] Various nuclei and white matter tracts are the foundation of this functionally diverse and critical organ. Although current imaging techniques are incapable of defining the precise boundaries of the hypothalamic zones and nuclei, Lemaire et al[3] have devised a scheme for segmentation based on universally visible anatomic landmarks.

The interhypothalamic adhesion is a band of tissue that structurally connects, at the very least, the periventricular hypothalamic zones and, potentially, portions of the hypothalamic nuclei. In most patients (10/13), the IHA traversed the expected area of the dorsomedial and/or ventromedial hypothalamic nuclei. The arcuate or paraventricular nuclei appeared involved in 6 patients. The IHA involved the preoptic nucleus area in 3 patients. One patient with Kallmann syndrome (case 13) had pituitary hypoplasia. None of the other patients in this cohort had a documented history of endocrinopathy, hypotension, thermoregulatory abnormality, obesity, or abnormal fear response; the pituitary gland was structurally normal in all other patients.

Holoprosencephaly represents a spectrum of failed prosencephalon separation. The range of classic holoprosencephaly includes 3 subtypes in decreasing order of severity: alobar, semilobar, and lobar.[5-7] The mildest form of classic holoprosencephaly manifests with partial forebrain and diencephalic union. The hypothalamus is incompletely separated in the mildest of forms of
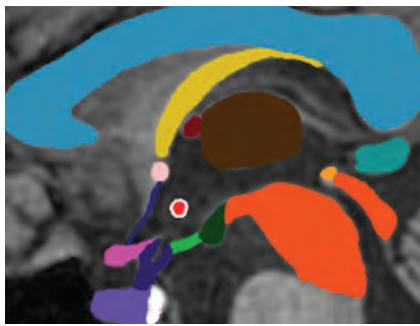
FIG 6. Midline sagittal graphic depicting the hypothalamus and neighboring structures. With the exception of the mammillary bodies (dark green) and tuber cinereum (bright green), the hypothalami are not visible at midline. The location of the IHA (bright red/white margin) is typical, centered in the anterior/inferior third ventricle. Choroid plexus is present in the anterior/superior third ventricle (dark red). The corpus callosum (light blue), fornix (yellow), thalamus (brown), midbrain (dark orange), posterior commissure (bright orange), pineal gland (teal), lamina terminalis (dark blue), anterior commissure (light pink), optic chiasm (dark pink), pituitary stalk (dark purple), adenohypophysis (light purple), and neurohypophysis (white) are represented.

classic holoprosencephaly. A retrospective study by Simon et al[2] demonstrated hypothalamic union in all patients with holoprosencephaly in their cohort. An isolated interhypothalamic adhesion could represent form fruste holoprosencephaly, and as such, its presence should prompt a search for additional midline anomalies.[1] Additional manifestations of holoprosencephaly may include ocular anomalies, cleft lip, cleft palate, absent septum pellucidum, falx cerebri hypoplasia, under-rotation of the hippocampi, and/or corpus callosum dysgenesis.[8-11] Hippocampal abnormalities were present in 9 of 13 patients, and hypoplasia of the falx cerebri was present in 2 patients. Symmetric hypoplasia of the optic bulbs was present in 2 patients.

Rhombencephalosynapsis is a midline cerebellar anomaly that can coexist with holoprosencephaly[12]; partial rhombencephalosynapsis associated with Chiari II malformation was present in 1 patient. Additional midline anomalies outside the typical holoprosencephaly disease spectrum were also encountered in this case series. Some of these midline abnormalities included corpus callosum dysgenesis, cysts (Blake pouch, pineal, meningeal), Kallmann syndrome, brain stem hypoplasia, and malformations of cerebral and cerebellar development.

Care should be taken to distinguish normal regional anatomy from an IHA. Choroid plexus occupying the anterior/superior third ventricle can mimic an IHA; however, its appearance is characteristic (Fig 6). Coronal images can exclude a hypothalamic connection. A small third ventricle with apposing lateral walls could conceivably be mistaken for IHA; thin-section coronal and/or axial images are useful for making the distinction. Further-

more, small interhypothalamic adhesions could be easily missed without thin-section images.

The differential diagnosis for IHA includes hypothalamic hamartoma and glioma. Both hamartoma and IHA are isointense to gray matter. However, a hamartoma is sessile or pedunculated in morphology, often extending into the third ventricle but not connecting the medial hypothalami to one another. Gliomas are of different signal intensity than gray matter and may enhance after contrast material administration. If this diagnosis is in question, gadolinium should be administered and postcontrast images should be acquired for clarification.

CONCLUSIONS

Interhypothalamic adhesions are parenchymal bands of tissue connecting the medial hypothalami across the third ventricle. Accompanying structural abnormalities range from mild hippocampal under-rotation to severe malformations of brain development. Midline anomalies are coexistent in most patients, supporting a type of form fruste holoprosencephaly. Therefore, midline structures should be scrutinized carefully on discovery of an interhypothalamic adhesion.

REFERENCES

1. Whitehead MT, Angel JD. **Interhypothalamic adhesion in a 9 month-old male with cleft palate.** *Case Rep Radiol* 2013;2013:197415
2. Simon EM, Hevner R, Pinter JD, et al. **Assessment of the deep gray nuclei in holoprosencephaly.** *AJNR Am J Neuroradiol* 2000;21: 1955–61
3. Lemaire J, Nezzar H, Sakka L, et al. **Maps of the adult human hypothalamus.** *Surg Neurol Int* 2013;4(suppl 3):S156–63
4. Nieuwenhuys R, Voogd J, van Huijzen C. *The Human Central Nervous System.* 4th ed. Berlin: Springer-Verlag; 2008:289–90
5. Tortori-Donati P, Rossi A, Biancheri R. **Brain malformations.** In: Tortori-Donati P, Rossi A, eds. *Pediatric Neuroradiology: Brain, Head, Neck and Spine.* Berlin: Springer-Verlag; 2009:86–94
6. Swaiman K, Ashwal S, Ferriero DM, et al. *Swaiman's Pediatric Neurology: Principles and Practice.* 5th ed. China: Elsevier Saunders; 2012:151–84
7. Dias M, Partington M. **Normal and abnormal embryology of the brain.** In: Winn HR, ed. *Youmans Neurological Surgery.* 6th ed. Philadelphia: Elsevier Saunders; 2011:1883–97
8. Cohen MM Jr. **Holoprosencephaly: clinical, anatomic, and molecular dimensions.** *Birth Defects Res A Clin Mol Teratol* 2006;76:658–73
9. Gawrych E, Janiszewska-Olszowska J, Walecka A, et al. **Lobar holoprosencephaly with a median cleft: case report.** *Cleft Palate Craniofac J* 2009;46:549–54
10. Huang J, Wah IY, Pooh RK, et al. **Molecular genetics in fetal neurology.** *Semin Fetal Neonatal Med* 2012;17:341–46
11. Sato N, Hatakeyama S, Shimizu N, et al. **MR evaluation of the hippocampus in patients with congenital malformations of the brain.** *AJNR Am J Neuroradiol* 2001;22:389–93
12. Ishak GE, Dempsey JC, Shaw DW, et al. **Rhombencephalosynapsis: a hindbrain malformation associated with incomplete separation of midbrain and forebrain, hydrocephalus and a broad spectrum of severity.** *Brain* 2012;135(pt 5):1370–86

MR Myelography for Identification of Spinal CSF Leak in Spontaneous Intracranial Hypotension

J.L. Chazen, J.F. Talbott, J.E. Lantos, and W.P. Dillon

ABSTRACT

BACKGROUND AND PURPOSE: CT myelography has historically been the test of choice for localization of CSF fistula in patients with spontaneous intracranial hypotension. This study evaluates the additional benefits of intrathecal gadolinium MR myelography in the detection of CSF leak.

MATERIALS AND METHODS: We performed a retrospective review of patients with spontaneous intracranial hypotension who underwent CT myelography followed by intrathecal gadolinium MR myelography. All patients received intrathecal iodine and off-label gadolinium-based contrast followed by immediate CT myelography and subsequent intrathecal gadolinium MR myelography with multiplanar T1 fat-suppressed sequences. CT myelography and intrathecal gadolinium MR myelography images were reviewed by an experienced neuroradiologist to determine the presence of CSF leak. Patient records were reviewed for demographic data and adverse events following the procedure.

RESULTS: Twenty-four patients met both imaging and clinical criteria for spontaneous intracranial hypotension and underwent CT myelography followed by intrathecal gadolinium MR myelography. In 3/24 patients (13%), a CSF leak was demonstrated on both CT myelography and intrathecal gadolinium MR myelography, and in 9/24 patients (38%), a CSF leak was seen on intrathecal gadolinium MR myelography ($P = .011$). Four of 6 leaks identified independently by intrathecal gadolinium MR myelography related to meningeal diverticula. CT myelography did not identify any leaks independently. There were no reported adverse events.

CONCLUSIONS: Present data demonstrate a higher rate of leak detection with intrathecal gadolinium MR myelography when investigating CSF leaks in our cohort of patients with spontaneous intracranial hypotension. Although intrathecal gadolinium is an FDA off-label use, all patients tolerated the medication without evidence of complications. Our data suggest that intrathecal gadolinium MR myelography is a well-tolerated examination with significant benefit in the evaluation of CSF leak, particularly for patients with leak related to meningeal diverticula.

ABBREVIATIONS: CTM = CT myelography; MRM = intrathecal gadolinium MR myelography; SIH = spontaneous intracranial hypotension

Spontaneous intracranial hypotension (SIH) is a debilitating condition with protean symptoms, which is often misdiagnosed at initial presentation.[1,2] The most common cause of SIH is a spinal CSF leak. Patients often have an underlying connective tissue disorders, though underproduction or increased absorption of CSF, dural elasticity, and minor trauma, including disk herniation, may all be contributing factors.[3,4] A reduction in CSF volume leads to compensatory dilation of venous structures in the brain, which may result in headache and subdural collections via meningeal traction.[5,6] Severe untreated cases of SIH can lead to coma and stroke.[7]

CT myelography (CTM) has historically been considered the study of choice for the detection and localization of CSF leak, though a criterion standard test is difficult to establish, given the varied etiologies for SIH.[8] Recent literature has questioned whether CTM is the most sensitive technique for the detection and localization of CSF leaks.[9,10] More recent techniques have been described, including dynamic CTM, digital subtraction myelography, heavily T2-weighted spinal MR imaging, and intrathecal gadolinium MR myelography (MRM). Both dynamic CT and digital subtraction myelography have been advocated in cases
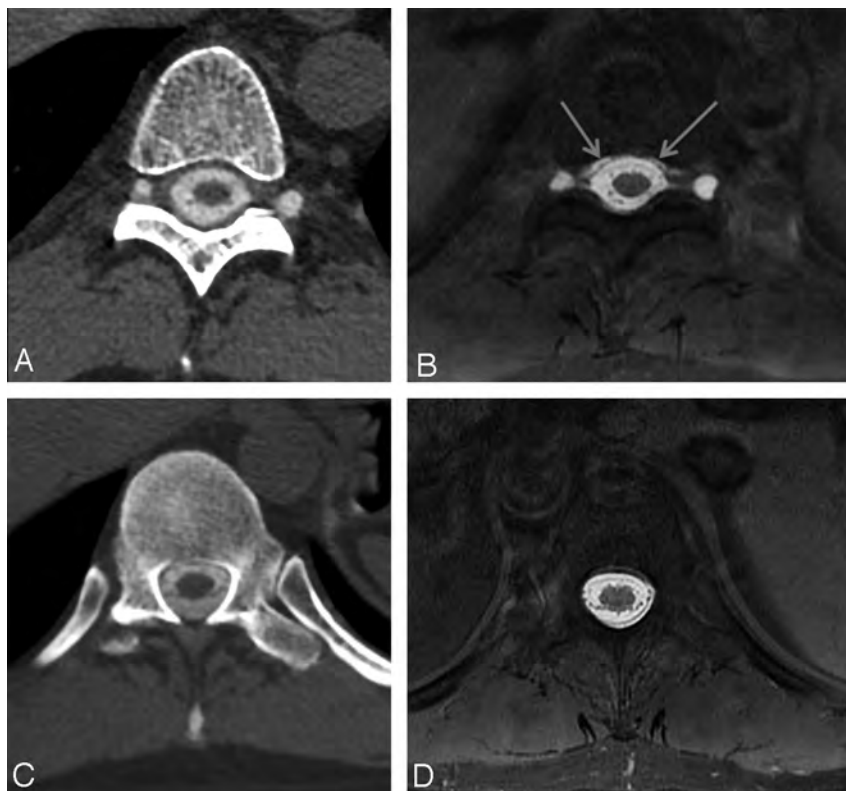
Leak Detection by Modality
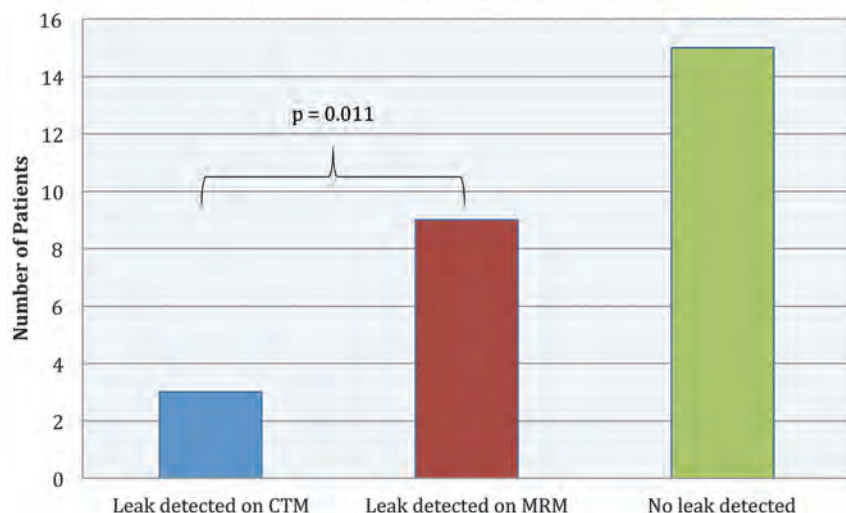
FIG 1. Bar graph illustrating the rate of leak detection by CTM and MRM. A statistically significant difference was observed between CTM and MRM by a 2-tailed paired *t* test (*P* = .011).

FIG 2. Patient 4. A 52-year-old former fire fighter with a 1-year history of postural headaches. Axial CTM (*A* and *C*) and axial T1 fat-suppressed images from MRM (*B* and *D*) following intrathecal administration of iodinated contrast and gadolinium. Multiple spinal diverticula are seen along with an extradural contrast collection (*arrows*, *B*) not evident on a concurrent CTM examination.

with significant spinal extra-arachnoid fluid collections on pre-procedural spinal MR imaging.[11] MRM with intrathecal gadolinium has been shown to have a high rate of leak detection and appears safe in small doses used for myelography.[12]

The mainstay of treatment for SIH is autologous epidural blood patch, initially effective in about one-third of patients.[13]

Directed epidural blood patch at the site of CSF fistula with CT guidance has been shown to be effective.[14] Targeted therapy may improve clinical outcomes with evidence of benefit when the blood patch is performed as close as possible to the site of CSF fistula.[13] Therefore, diagnostic techniques that precisely localize a CSF leak are important for guiding therapy, particularly for treatments such as fibrin glue injection and surgical repair.[2]

Our study evaluates the relative benefit of intrathecal gadolinium MRM compared with CTM in detecting and localizing CSF leaks in patients with previously confounding diagnostic work-up to guide treatment in patients with SIH.

MATERIALS AND METHODS

A waiver of informed consent was obtained from our Committee on Human Research for this retrospective review, consistent with the Health Insurance Portability and Accountability Act. A search of the radiology information system between May 2007 and April 2013 yielded 30 patients who had lumbar puncture and intrathecal instillation of iodine- and gadolinium-based contrast followed by CTM and subsequent MRM. Many patients in our cohort had prior unrevealing diagnostic work-up for symptoms of SIH and were referred to our institution for further evaluation.

All patients with contrast brain MRI as well as CTM and MRM studies were reviewed for evidence of SIH by a single attending neuroradiologist (W.P.D.) with >20 years of experience and a Certificate of Added Qualification in neuroradiology. Patients were included if they had clinical and imaging evidence of SIH, and all patients met the modified criteria of Schievink et al[15] for SIH, including orthostatic headache, brain MR imaging with pachymeningeal enhancement and/or brain sagging, and absence of recent lumbar puncture or other attributable intervention. Multiplanar images from CTM and MRM were reviewed to determine whether a CSF leak was present. A CSF leak on CTM or MRM was defined as an extra-arachnoid collection of contrast unrelated to the needle puncture. Patients were excluded if they did not meet the modified criteria of Schievink et al for SIH or if complete demographic or imaging information was unavailable.

A combined CTM and MRM imaging procedure was performed as follows: Informed consent was obtained after the discussion of off-label use of gadolinium in the intrathecal space. All studies were performed by using a CT-guided lumbar puncture with a 22-ga spinal needle. Opening pressure was measured in the decubitus position. A mixture of 10-mL Omnipaque (iohexol, 240 mg/mL; GE Healthcare, Princeton, New Jersey) and 0.3-mL Magnevist (gadopentetate dimeglumine, 0.5 mol/L; Schering, Berlin, Germany) was then instilled intrathecally, and the spinal needle was removed. After repositioning the patient on a gurney to facilitate passage of contrast throughout the spinal canal, including Trendelenburg positioning, the patient was transferred back to the CT scanner table for CTM.

CT of the spinal axis was performed on a LightSpeed VCT 64-detector row scanner (GE Healthcare, Milwaukee, Wisconsin) with a rotation time of 0.8 seconds, detector coverage of 40 mm, pitch of 0.98:1, section thickness of 0.625 mm, and 100 kV with auto-mA, and noise index of 10.8. Multiplanar reformations were generated for review. The patient was then transferred to the MR imaging suite.

MR imaging of the spinal axis was performed on a 3T Discovery MR imaging scanner (GE Healthcare) an average of 45 minutes following the CT myelogram. T1-weighted sagittal, coronal, and axial imaging was acquired by a using modified 3-point Dixon fat-suppression technique at 4-mm section thickness with no skip. We used the following MR imaging parameters: TR, 400–750 ms; echo train length, 3–5; bandwidth, 50 Hz; TE, 10–50 ms ("minimum full" was selected by the technologist depending on TR and echo train length). FOV for axial imaging was 16 cm; for sagittal thoracic and lumbar imaging, 24 cm; and for sagittal cervical imaging, 20 cm. Matrix size was 320–384 in the frequency-encoding direction and 192–256 in the phase direction.

Excel for Mac 2011, Version 14.0 (Microsoft, Redmond, Washington) was used for all statistical analyses. Categoric variables are presented as frequencies and percentages, while continuous variables are presented as means and SDs. The difference in leak detection between CTM and MRM was calculated by using a 2-tailed paired t test of the means, with significance set at $P < .05$. A 2-tailed test was chosen because the null hypothesis was that neither CTM nor MRM was the more sensitive test; if either had been more sensitive, the null hypothesis would be voided. A paired test was chosen because the same patients underwent both studies.

RESULTS

Thirty patients were identified with CTM and MRM procedures performed during the study period from May 2007 through April 2013. Twenty-four patients met inclusion criteria, including clinical and brain MR imaging findings of SIH. The mean age was 51 years (range, 20–85 years), and 58% of patients were male. The mean opening pressure at lumbar puncture was 7.8 ± 3.9 cm H_2O (range, 0–14.5 cm H_2O).

In 15 of 24 patients (63%), no CSF leak was found on either CTM or MRM. In 3 of 24 patients (13%), a CSF leak was demonstrated on both CTM and MRM, and in 6 of 24 patients (25%), a CSF leak was seen only on MRM. MRM (9/24, 38%) was more sensitive than CTM (3/24, 13%) for the detection of
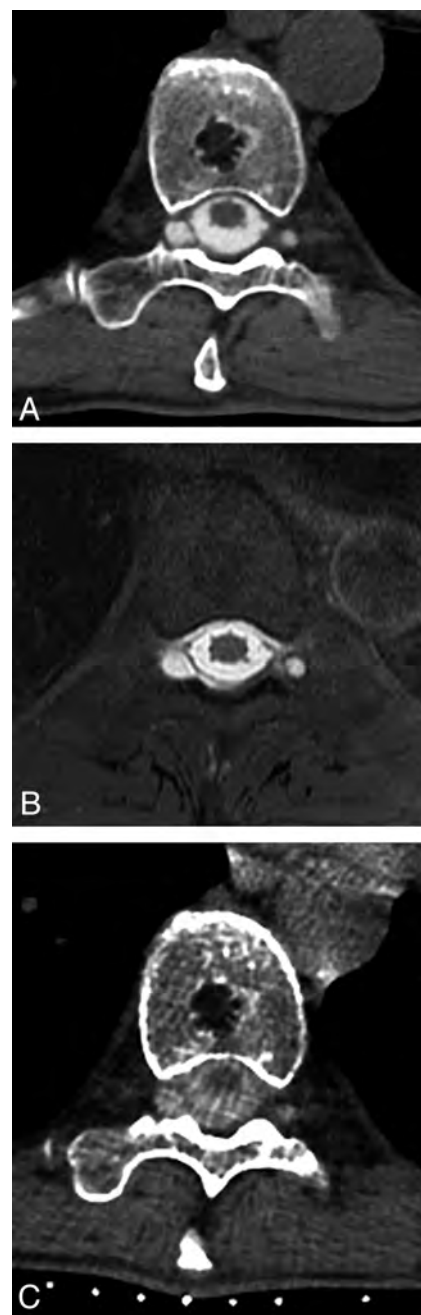
FIG 3. Patient 2. A 62-year-old man with headache and recurrent subdural hemorrhage following evacuation, found to have imaging findings of SIH. Axial CTM (*A*) and MRM (*B*) images at the T9–T10 level. Spinal diverticula are evident on both examinations. The MRM demonstrates an extra-arachnoid contrast collection and ill-defined increased T1 signal surrounding the enlarged right spinal diverticula. Subsequent CT performed for epidural blood patch planning with a localization grid in place (*C*) shows the spinal diverticula; the extra-arachnoid contrast collection is not evident. The patient reported symptomatic relief following directed blood patch and was without headache as of the 2-month follow-up note.

CSF leak ($P = .011$). No patients had a leak seen exclusively on CTM (Fig 1).

The MRM examination followed the CTM examination by an average of 45 ± 21 minutes. Most leaks involved the midthoracic region with extra-arachnoid collections seen in most (7/9) patients with leaks (Table, Figs 2 and 3). Among the 3 patients with
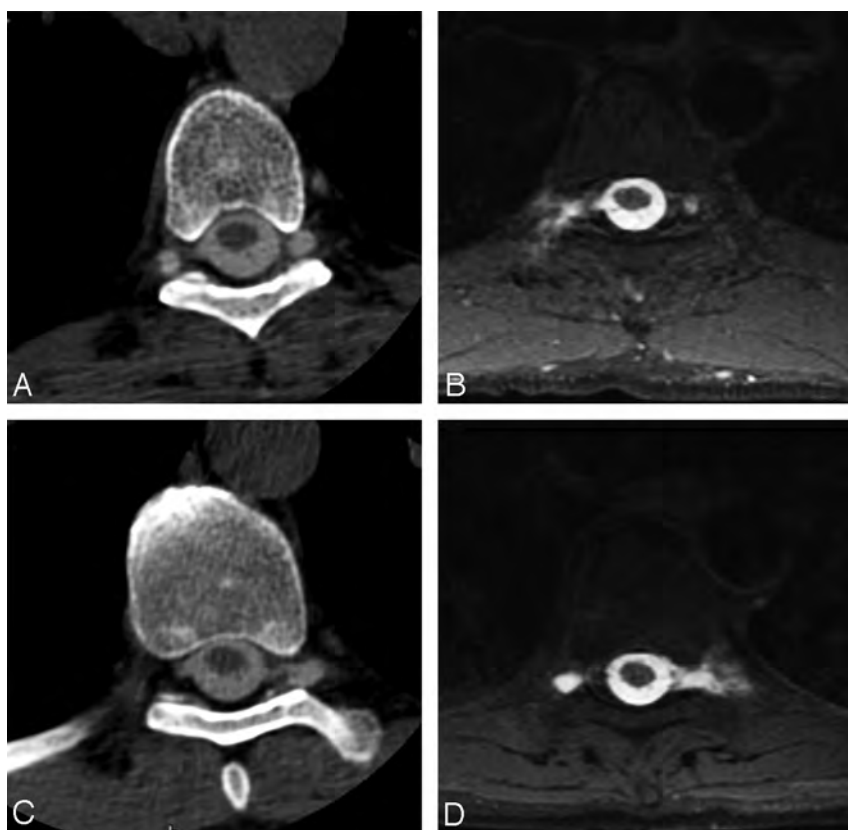
FIG 4. Patient 7. A 55-year-old man with a history of lethargy, fatigue, and hearing loss. Axial CTM (A and C) and axial MRM (B and D) images. CT shows bilateral spinal diverticula. MR image demonstrates prominent contrast leakage from the right-sided T5–T6 (B) and left T10–T11 (D) diverticula, with gadolinium extending into the adjacent paraspinal musculature. The patient underwent targeted epidural blood patches of both leaking spinal diverticula.

leaks detected on CTM, 2 had a disk herniation likely resulting in a dural tear; the third patient had marfanoid features and leak attributable to dural ectasia. All 6 patients with leaks detected only on MRM had multiple spinal meningeal diverticula (Figs 4 and 5). One patient had a significant epidural collection spanning C3–L1 on MRM and required digital subtraction myelography for leak localization. CT-guided epidural blood patch was performed on all 9 patients with detectable leak and on the same day as CTM and MRM studies when possible (4/9 patients).

DISCUSSION

MRM was more sensitive than CTM for the detection of CSF leak in our cohort of patients with SIH. A CSF leak was identified in 9 of 24 (38%) patients on MRM but in only 3 of 24 (13%) patients with CTM ($P = .011$). CTM did not identify any leaks that were not found on MRM.

Most interesting, 4 of 6 patients in whom a leak was identified on MRM, but not CTM, had leaks in close proximity to spinal meningeal diverticula (Figs 4 and 5). The association between SIH and spinal meningeal diverticula is well-established.[16] There is evidence that targeted therapy as close as possible to the site of CSF leak is beneficial; and targeted blood patches, fibrin glue therapy, and surgical ligation of spinal meningeal diverticula have been described with good results.[13,14] Present data suggest that MRM may be particularly helpful for the detection of CSF leak

and guiding treatment for this subpopulation of patients with CSF leak associated with spinal meningeal diverticula.

The sensitivity of CTM for the detection of leaks in patients with clinical symptoms of SIH is difficult to determine given the lack of a robust criterion standard. Patients may demonstrate intracranial hypotension without discrete CSF leak, suggesting that etiologies for the SIH syndrome are varied. In addition to a frank dural tear, SIH may relate to abnormal thecal sac compliance or imbalance between epidural and CSF pressures;[17] the cause of SIH in patients with negative CTM and MRM findings remains unresolved in most cases. Occult CSF leaks resulting from slow-flow CSF venous fistula may represent an additional etiology for SIH, which would be difficult to identify at imaging, though secondary signs such as early radiotracer within the bladder have been described. Opening pressure is often low but may be within normal limits.[18] Underlying dural and connective tissue abnormalities are hypothesized to contribute to the abnormal CSF egress.[19] Thus, the potential etiologies for SIH are numerous, and the significant number of patients in our cohort without evidence of leak on multiple imaging examinations may reflect slow-flow leaks occult on both CTM and MRM.

We postulate that the overall relatively low rate of leak detection in our cohort is due to patient selection, because many patients in our study were referred to our large tertiary care center when prior outside nuclear or CT localization techniques were unrevealing, thus selecting out patients with more conspicuous leaks. However, our finding of a higher rate of leak detection with MRM compared with CTM is in accordance with recently published studies.[11] We found a leak at MRM in 9 of 24 patients (38%) with clinical symptoms and imaging findings of SIH, similar to findings in a recent study by Akbar et al,[10] which detected a leak on MRM in 5 of 24 patients (21%) with negative CTM findings. Despite our cohort of diagnostically challenging patients, we recognize the benefit of MRM and advocate MRM examinations early in the diagnostic work-up.

Increased leak detection with MRM over CTM may, in part, be related to the longer imaging half-life of gadolinium in soft tissues. While iodinated contrast will peak and wash out of soft-tissues rapidly, gadolinium has been shown to maintain sufficient concentrations for T1 shortening for hours after intravenous administration—a property that has been exploited in many fields, including hepatic imaging.[20] As a result, even though delayed imaging with CTM may still have sufficient contrast inside the subarachnoid space, extradural contrast that has leaked out of the thecal sac may be more difficult to see with CTM than MRM

because of these different soft-tissue characteristics. It is unclear how the mixture of iodinated contrast with gadolinium affects imaging parameters in our cohort, though there is evidence that iodinated contrast increases T1 and T2 shortening on MR imaging, possibly increasing signal of the contrast mixture on T1 fat-suppressed sequences.[21]

All patients in our study were able to complete both lumbar puncture and subsequent imaging studies. No adverse reactions were observed. In a cohort of 100 patients receiving Gd-DTPA, no adverse events were reported outside of postprocedural headache.[22] Gd-DTPA has been advocated as the safest agent for in-trathecal administration.[22] While there are limited data on the toxic effects of intrathecal gadolinium-based contrast agents, a 2010 report described the onset of adverse symptoms 6 hours following accidental intrathecal gadolinium contrast administration at a dose 20× that used in our study.[23] Twenty-four-hour telephone follow-up and subsequent clinical notes did not reveal adverse events attributable to the MRM procedure in our cohort. Despite the apparent safety, physicians need to be mindful that intrathecal gadolinium is an FDA off-label use and should weigh the risks and benefits of the procedure carefully in each patient.

In our experience, CTM and MRM are complementary examinations. While CTM did not independently identify extradural collections, the rapid acquisition following intrathecal contrast administration may provide diagnostic benefits for high-flow leaks and facilitate subsequent targeted treatment.[24] CTM provides additional anatomic information, for example, bone detail that is better appreciated. Additionally, high-flow spinal CSF leaks may benefit from dynamic CTM because a large-volume leak can obscure a leak site.[13] Although there are benefits of CTM and MRM performed concurrently, some patients may benefit from MRM performed first followed by CTM, as necessary, to minimize radiation exposure. There is a trade-off with this approach and the possibility of subjecting patients to 2 lumbar puncture procedures.

Limitations of our study include those inherent in a retrospective design and single-center experience with a relatively small number of patients. A possible confounding factor is the delayed nature of MRM in this cohort, which was performed an average of 45 minutes following CTM, likely allowing additional time for contrast to diffuse into small leaks. However, in patients receiving same-day CT-guided blood patches, leaks evident only on the MRM were not
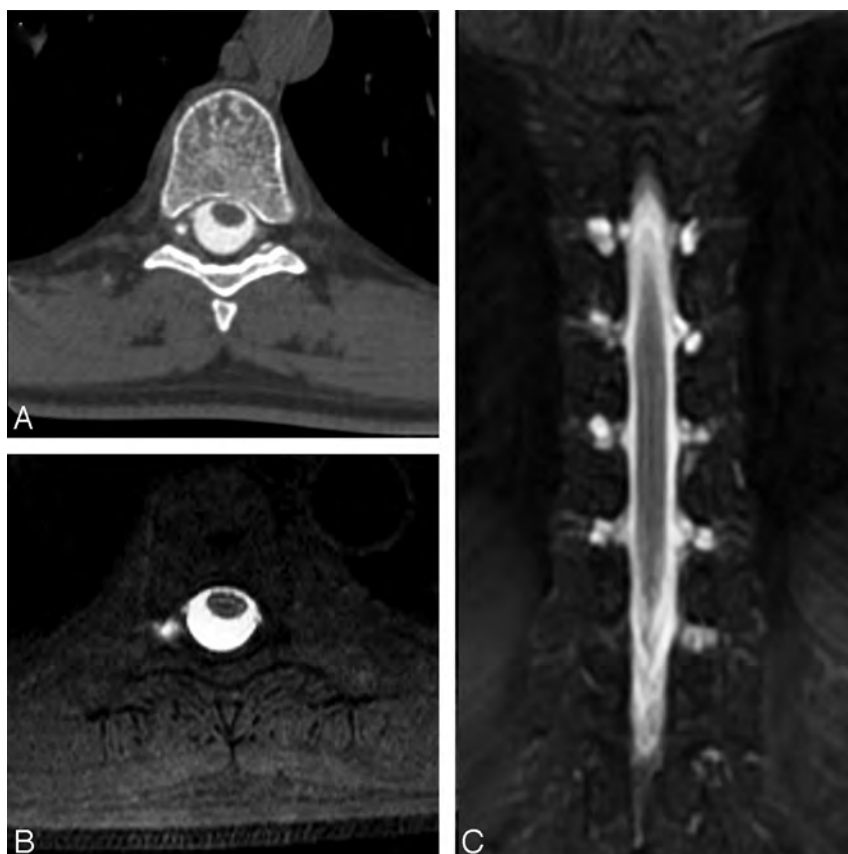
FIG 5. Patient 8. A 55-year-old man with postural headache and low CSF pressure on lumbar puncture. Axial CTM (*A*), axial MRM (*B*), and coronal MRM (*C*) images. Coronal MRM shows multiple spinal diverticula. However, only the right T7–T8 spinal diverticula, seen on the CTM (*A*), shows evidence of contrast leakage on axial MRM (*B*), evident by ill-defined T1 shortening surrounding the cyst. This lesion was treated with directed epidural blood patch with symptomatic improvement for 5 years following treatment.

Patients with CSF leak detected on CTM or MRM[a]

Patient No.	Age (yr)	Sex	Opening Pressure (cm H$_2$O)	Leak Detected on CTM	Leak Detected on MR Myelogram	Time Difference (h:min)	Extent of Extra-Arachnoid Contrast	Same-Day Blood Patch	Suspected CSF Leak Etiology
1	66	Female	5	No	Yes	0:37	T6–T12	No	Unclear; spinal diverticula C6–C7 through L2–L3
2	62	Male	7	No	Yes	1:14	T9–L1	Yes	Bilateral T9–T10 spinal diverticula
3	27	Male	10	Yes	Yes	0:55	L2–L5	No	Dural ectasia; marfanoid features
4	52	Male	7	No	Yes	1:14	T6–T12	Yes	Bilateral T9–T10 and left T11–T12 spinal diverticula
5	32	Female	0	No	Yes	0:29	C3–L1	No	No source of leak detected; T2–T3 leak seen on subsequent fluoroscopic subtraction myelogram
6	37	Female	6	Yes	Yes	5:14	T10–L1	Yes	T11–T12 disk osteophyte; blood patch performed before MRM
7	55	Male	8	No	Yes	0:49	T5–T6 and T9–T10	No	Right T5–T6 and left T9–T10 spinal diverticula
8	55	Male	6	No	Yes	0:12	T7–T8	Yes	Right T7–T8 spinal diverticula
9	58	Female	0	Yes	Yes	0:46	C7–T4	No	T1–T2 secondary to disk protrusion and dural tear

[a] The time difference reflects the time stamp difference between CTM acquisition and the beginning of MRM. A same-day blood patch was performed when logistically possible and a clear source of leak was identified.

seen on delayed CT imaging (Fig 3). Follow-up studies with MRM followed by delayed CTM would be necessary to confirm this observation. This study is also limited by the lack of a criterion standard for leak confirmation. While many of our patients received targeted epidural blood patches with symptomatic improvement, no leaks were confirmed surgically.

CONCLUSIONS

Our data build on the growing body of evidence that MRM is more sensitive than CTM for the detection of CSF leaks in SIH.[5,6] This finding is important because treatment with either directed blood patch, fibrin glue injections, or surgery requires preprocedural knowledge of the site of CSF leak. Although intrathecal administration remains an FDA off-label use of gadolinium, all patients in our study tolerated intrathecal gadolinium without complications. MRM is most useful in patients without obvious high-flow leaks who may be better evaluated by dynamic CTM or fluoroscopic myelography. Perhaps most important, MRM was superior to CTM for identifying CSF leaks related to meningeal diverticula. MRM is a well-tolerated examination that appears complementary to CTM with significant benefit in the diagnosis of CSF leaks.

REFERENCES

1. Renowden SA, Gregory R, Hyman N, et al. **Spontaneous intracranial hypotension.** *J Neurol Neurosurg Psychiatry* 1995;59:511–15
2. Schievink WI. **Misdiagnosis of spontaneous intracranial hypotension.** *Arch Neurol* 2003;60:1713–18
3. Schievink WI. **Spontaneous spinal cerebrospinal fluid leaks and intracranial hypotension.** *JAMA* 2006;295:2286–96
4. Rapport RL, Hillier D, Scearce T, et al. **Spontaneous intracranial hypotension from intradural thoracic disc herniation: case report.** *J Neurosurg* 2003;98(3 suppl):282–84
5. Mokri B. **Spontaneous cerebrospinal fluid leaks: from intracranial hypotension to cerebrospinal fluid hypovolemia—evolution of a concept.** *Mayo Clin Proc* 1999;74:1113–23
6. George U, Rathore S, Pandian JD, et al. **Diffuse pachymeningeal enhancement and subdural and subarachnoid space opacification on delayed postcontrast fluid-attenuated inversion recovery imaging in spontaneous intracranial hypotension: visualizing the Monro-Kellie hypothesis.** *AJNR Am J Neuroradiol* 2011;32:E16
7. Pleasure SJ, Abosch A, Friedman J, et al. **Spontaneous intracranial hypotension resulting in stupor caused by diencephalic compression.** *Neurology* 1998;50:18545–47
8. Wang EW, Vandergrift WA 3rd, Schlosser RJ. **Spontaneous CSF leaks.** *Otolaryngol Clin North Am* 2011;44:845–56, vii
9. Albes G, Weng H, Horvath D, et al. **Detection and treatment of spinal CSF leaks in idiopathic intracranial hypotension.** *Neuroradiology* 2012;54:1367–73
10. Akbar JJ, Leutmer PH, Schwartz KM, et al. **The role of MR myelography with intrathecal gadolinium in localization of spinal CSF leaks in patients with spontaneous intracranial hypotension.** *AJNR Am J Neuroradiol* 2012;33:535–40
11. Luetmer PH, Schwartz KM, Eckel LJ, et al. **When should I do dynamic CT myelography? Predicting fast CSF leaks in patients with spontaneous intracranial hypotension.** *AJNR Am J Neuroradiol* 2012;33:690–94
12. Albayram S, Kilic F, Ozer H, et al. **Gadolinium-enhanced MR cisternography to evaluate dural leaks in intracranial hypotension syndrome.** *AJNR Am J Neuroradiol* 2008;29:116–21
13. Sencakova D, Mokri B, McClelland RL. **The efficacy of epidural blood patch in spontaneous CSF leaks.** *Neurology* 2001;57:1921–23
14. Kranz PG, Gray L, Taylor JN. **CT-guided epidural blood patching of directly observed or potential leak sites for the targeted treatment of spontaneous intracranial hypotension.** *AJNR Am J Neuroradiol* 2011;32:832–38
15. Schievink WI, Dodick DW, Mokri B, et al. **Diagnostic criteria for headache due to spontaneous intracranial hypotension: a perspective.** *Headache* 2011;51:1442–44
16. Medina JH, Abrams K, Falcone S, et al. **Spinal imaging findings in spontaneous intracranial hypotension.** *AJR Am J Roentjenol* 2010;195:459–64
17. Franzini A, Messina G, Chiapparini L, et al. **Treatment of spontaneous intracranial hypotension: evolution of the therapeutic and diagnostic modalities.** *Neurol Sci* 2013;34(suppl 1):S151–55
18. Mokri B. **Spontaneous intracranial hypotension.** *Curr Pain Headache Rep* 2001;5:284–91
19. Grimaldi D, Mea E, Chiapparini L, et al. **Spontaneous low cerebrospinal pressure: a mini review.** *Neurol Sci* 2004;25(suppl 3):S135–37
20. Aime S, Caravan P. **Biodistribution of gadolinium-based contrast agents, including gadolinium deposition.** *J Magn Reson Imaging* 2009;30:1259–67
21. Hergan K, Doringer W, Längle M, et al. **Effects of iodinated contrast agents in MR imaging.** *Eur J Radiol* 1995;21:11–17
22. Algin O, Turkbey B. **Intrathecal gadolinium-enhanced MR cisternography: a comprehensive review.** *AJNR Am J Neuroradiol* 2013;34:14–22
23. Park KW, Im SB, Kim BT, et al. **Neurotoxic manifestations of an overdose intrathecal injection of gadopentetate dimeglumine.** *J Korean Med Sci* 2010;25:505–08
24. Wendl CM, Schambach F, Zimmer C, et al. **CT myelography for the planning and guidance of targeted epidural blood patches in patients with persistent spinal CSF leakage.** *AJNR Am J Neuroradiol* 2012;33:541–44

Distinguishing Imaging Features between Spinal Hyperplastic Hematopoietic Bone Marrow and Bone Metastasis

Y. Shigematsu, T. Hirai, K. Kawanaka, S. Shiraishi, M. Yoshida, M. Kitajima, H. Uetani, M. Azuma, Y. Iryo, and Y. Yamashita

ABSTRACT

BACKGROUND AND PURPOSE: Systematic investigations of the distinguishing imaging features between spinal hyperplastic hematopoietic bone marrow and bone metastasis have not been reported, to our knowledge. The purpose of this study was to determine the distinguishing imaging features of the 2 entities.

MATERIALS AND METHODS: We retrospectively reviewed the radiologic images of 8 consecutive male patients (age range, 52–78 years; mean, 64 years) with suspected spinal metastasis on MR imaging and FDG-PET, which was later confirmed as hyperplastic hematopoietic bone marrow. MR imaging, FDG-PET, CT, and bone scintigraphy images were qualitatively and/or quantitatively evaluated. Imaging findings in 24 patients with spinal metastasis were compared, and differences were statistically analyzed.

RESULTS: All 8 vertebral hyperplastic hematopoietic bone marrow lesions were hypointense on T1- and T2-weighted images; lesions contiguous with the adjacent vertebra were significantly more often seen in hyperplastic hematopoietic bone marrow than in metastasis ($P = .035$). T2 signal intensity of the lesion was significantly different between the 2 entities ($P = .033$). FDG-PET showed slightly higher uptake in all hyperplastic hematopoietic bone marrow lesions; their maximum standard uptake value was significantly lower than that of metastatic lesions ($P = .037$). CT attenuation of hyperplastic hematopoietic bone marrow was equal to or slightly higher than that of adjacent normal-appearing vertebra; the CT appearances of hyperplastic hematopoietic bone marrow and metastasis were significantly different ($P < .01$). Bone scintigraphy showed normal uptake for all vertebrae with hyperplastic hematopoietic bone marrow; the uptake was significantly different from that of metastasis ($P < .01$).

CONCLUSIONS: If a lesion was isointense to hyperintense to normal-appearing marrow on MR imaging or had a maximum standard uptake value of >3.6, the lesion was considered metastatic. A normal appearance on CT or bone scintigraphy excluded metastasis.

ABBREVIATIONS: HHBM = hyperplastic hematopoietic bone marrow; 99mTc-MDP = technetium Tc99m methylene diphosphonate; SUV$_{max}$ = maximum standard uptake value

Among oncologic diagnostic modalities, FDG-PET and FDG-PET/CT are used increasingly for the staging of malignancies.[1] FDG-PET/CT is highly sensitive and specific for the detection of bone metastasis.[2] MR imaging is also highly sensitive for detecting bone metastasis and is widely used for determining the presence of bone lesions.[3] Meta-analysis showed that FDG-PET and MR imaging are significantly more accurate than CT and bone scintigraphy for the diagnosis of bone metastasis.[4]

Hyperplastic hematopoietic bone marrow (HHBM) is a proliferation (hyperplasia) of hematopoietic cells in response to in-creased peripheral demand or hypofunction of blood cells. One or multiple cell lines (eg, erythroid, megakaryocytic, myeloid cells) may be hyperplastic, depending on the stimulus. In adults, it is identified by the reconversion from fatty yellow to red marrow.[5] Conditions that may lead to such reconversion include heavy smoking, long-distance running, obesity, chronic anemia, and the use of hematopoietic growth factors.[5-9] Spinal HHBM mimicking bone metastasis on FDG-PET and MR imaging scans significantly affects patient management.[10] We encountered several patients with spinal HHBM in whom both FDG-PET and MR imaging revealed abnormalities and CT-guided biopsy was required for pathologic confirmation. Although the discrimination of spinal HHBM and bone metastasis is clinically important, no systematic investigations of the distinguishing imaging features of the 2 entities have been reported, to our knowledge. The purpose of this study was to determine the features of PET, MR imaging, bone scintigraphy, and CT for differentiating spinal HHBM and bone metastasis.

Table 1: Summary of characteristics of patients with spinal HHBM

Case No.	Age	Sex	Clinical Diagnosis (TNM stage)	Symptom	Location of Spinal Lesions	Biopsy Site	Brinkman Index	Hemoglobin (g/dL)
1	57	Male	Lung ca. (T1N0)	None	T2–L3	T5	684	12.4↓
2	54	Male	Lung ca. (T2N1)	None	T11–L3	T11	750	11.4↓
3	59	Male	Esop. ca. (T3N2)	None	C2–T12, S1	T11	780	10.9↓
4	73	Male	Esop. ca. (T1N0)	None	T9–11	T11	1060	12.6↓
5	78	Male	Esop. ca. (T3N2)	None	C2–T9, L1,3	L1	0	11.9↓
6	70	Male	Esop. ca. (T2N0)	None	L3	L3	900	11.6↓
7	70	Male	Lumbar spondylosis	LBP	C6–T12	T12	1075	14.1
8	52	Male	Lumbar spondylosis	LBP	C9–L5	L3	640	13.7↓

Note:—Lung ca. indicates lung cancer; Esop. ca., esophageal cancer; LBP, low back pain; C, cervical spine; T, thoracic spine; L, lumbar spine; S, sacral spine; ↓, anemia.

MATERIALS AND METHODS

Patients

Our institutional review board approved this retrospective study and waived patient informed consent. Between August 2006 and January 2012, we encountered 8 patients with spinal HHBM pathologically diagnosed after CT-guided spinal bone biopsy (Table 1). All patients were men, ranging in age from 52 to 78 years (mean, 64.1 years). Six had known malignancies (esophageal squamous cell carcinoma, $n = 4$; pulmonary squamous cell carcinoma, $n = 1$; pulmonary adenocarcinoma, $n = 1$); none reported back pain. The other 2 patients had low back pain; their lumbar MR imaging scans revealed spinal vertebral lesions mimicking bone metastasis. Subsequent FDG-PET/CT studies failed to rule out a neoplastic condition. Seven patients had moderate anemia and a Brinkman index, which is defined as the number of cigarettes smoked per day times smoking years, of >600. All 8 patients were referred for CT-guided biopsy of the spinal lesions detected on both FDG-PET/CT and MR imaging. The CT-guided vertebral bone biopsy was performed for a vertebra that showed the highest uptake on FDG-PET. Five patients had undergone bone scintigraphy by using technetium Tc99m methylene diphosphonate (99mTc-MDP), and none had received granulocyte colony-stimulating factors or anticancer drugs. For all 8 patients, at least 6-month follow-up medical records showed no symptoms suggesting spinal bone metastasis.

During the same period, 26 patients diagnosed with spinal bone metastasis based on CT-guided bone biopsy findings were included in this study. Two were undergoing chemotherapy and were excluded from this study. Therefore, 24 patients (14 men and 10 women) ranging in age from 30 to 84 years (mean, 65.4 years) with biopsy-proved spinal bone metastases were included. Their primary malignant tumors were lung cancer ($n = 4$), hepatocellular carcinoma ($n = 4$), malignant lymphoma ($n = 4$), leiomyosarcoma ($n = 2$), renal cell carcinoma ($n = 2$); and prostatic ($n = 2$), uterine- ($n = 1$), gall bladder- ($n = 1$), urinary bladder ($n = 1$), gastric ($n = 1$), and breast ($n = 1$) cancer and primary unknown adenocarcinoma ($n = 1$). All 24 underwent CT, 21 underwent MR imaging studies, 12 underwent FDG-PET, and 13 underwent bone scintigraphy. In each patient, the imaging studies were performed within 1 week of each other as a rule.

### MR Imaging, FDG-PET, CT, and Bone Scintigraphy

All MR imaging studies were performed on 1 of 2 MR imaging units (Achieva; Philips Healthcare, Best, the Netherlands; or Magnetom Trio; Siemens, Erlangen, Germany) by using spine coils at 3T. The spinal MR imaging protocol included 3-mm-section sagittal and 4-mm-section axial T1- and T2-weighted spin-echo sequences. When possible, STIR diffusion-weighted and postcontrast T1-weighted imaging studies were performed. In patients who underwent diffusion-weighted imaging, we calculated the apparent diffusion coefficient values of the lesion. In patients who had undergone FDG-PET, we acquired spinal MR imaging scans to cover the entire spine with areas of abnormal uptake. For postcontrast T1-weighted imaging, we intravenously administered 0.1-mL gadopentetate dimeglumine (Magnevist; Bayer-Schering, Berlin, Germany) per kilogram of body weight.

In whole-body FDG-PET/CT, data were acquired with a dedicated combined FDG-PET/CT system (Gemini GXL; Philips Healthcare). Patients fasted for 6 hours before scanning; the blood glucose levels were <150 mg/dL in all patients. An hour before imaging, 185–222 mBq of ^{18}F-FDG (4 millibecquerel per kilogram of body weight) were injected intravenously. Whole-body images covering the skull base to the midthigh level were acquired with the patient in a supine position. Before PET, we obtained unenhanced CT images on an integrated 16-section scanner (tube voltage, 120 kV[peak]; tube current, 80 mA; rotation time, 0.5 seconds; pitch, 0.938; collimation, 16 × 1.5 mm). Then we performed whole-body PET emission scanning. The PET images were reconstructed by using the CT images for attenuation correction. Axial, coronal, and sagittal multiplanar images of the spine were reconstructed.

CT studies were performed without contrast material administration on a 64–detector row CT system (Brilliance 64; Philips Healthcare) with a 0.5-second gantry rotation speed, an x-ray tube voltage of 120 kV, and an x-ray tube current of 300 mA. The collimation was 64 × 0.625 mm, the beam pitch was 0.515, and the table speed was 20.6 mm per rotation. The helical data were reconstructed in the axial plane with a 0.5-mm section thickness at 0.3-mm intervals before storage and transfer to a workstation (M900QUADRA; Amin, Tokyo, Japan). The multiplanar reformation images, including coronal and sagittal images, were reconstructed at a voxel size of 0.4 × 0.4 × 0.7 mm.

For bone scintigraphy, double-head γ camera detectors (Skylight; ADAC Laboratories, Milpitas, California) equipped with a low-energy, general purpose, parallel-hole collimator were used. After the IV injection of 555 mBq (15 mCi) of 99mTc-MDP 3–4 hours earlier, we obtained whole-body images at a scan speed of 12 cm/min in the anterior and posterior projections. Additional static planar images were acquired at the discretion of the attending nuclear physician.
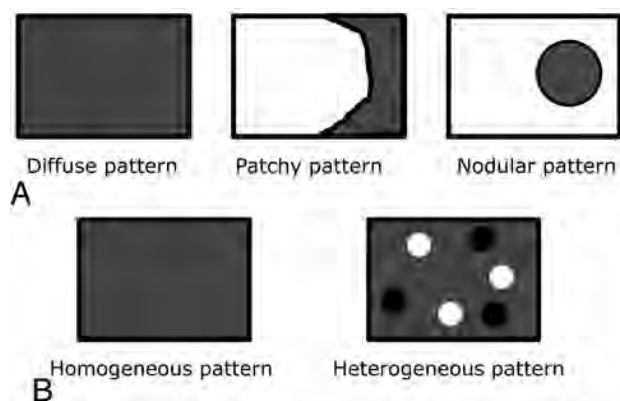
FIG 1. *A*, Schema of the distribution pattern of a lesion in a single vertebral body. "Diffuse pattern" indicates involvement of the entire region in a single vertebral body; "patchy pattern," involvement of the partial region in a single vertebral body; and "nodular pattern," involvement of the nodular area in a single vertebral body. *B*, Schema of the appearance of homogeneity of a lesion in a single vertebral body. Lesions were considered homogeneous if no evidence of necrosis, cyst, hemorrhage, or fracture was seen on T1- and T2-weighted images. If ≥1 of these features or mixed signal intensity (ie, high and low signal intensity on the MR images) was present, the vertebral lesion was considered heterogeneous.

Image Analysis

All image assessments and measurements were performed on a PACS workstation. PET/CT images were independently evaluated by 2 nuclear medicine physicians (S.S. and M.Y., with 15 and 6 years of nuclear medicine experience, respectively) who were blinded to the final diagnosis. Divergent evaluations were reviewed to reach consensus. The PET and MR imaging scans were carefully compared for accurate anatomic identification of the lesions. For quantitative analysis, a circular region of interest was placed over the biopsy-proved vertebral bone lesion on the PET images. The maximum standardized uptake value (SUV_{max}) of vertebral lesions with the greatest uptake was recorded from a 1-cm^2 region of interest in the center of the lesion; SUV_{max} in each region of interest was calculated automatically.

Bone scintigraphy images were interpreted independently by the same 2 readers blinded to the final diagnosis. They reviewed divergent evaluations to reach consensus. The lesional uptake was qualitatively graded as high, equivalent, or low with respect to adjacent normal-appearing vertebrae. High or low uptake was considered abnormal.

On MR imaging, 2 neuroradiologists (T.H. and Y.S., with 22 and 19 years of neuro-MR imaging experience, respectively) blinded to the final diagnosis independently compared the signal intensity of biopsy-proved spinal vertebral body lesions with adjacent normal-appearing spinal vertebrae and graded it as hypo-, iso-, or hyperintense. The distribution pattern of a main lesion in a single vertebra was also recorded as diffuse, patchy, or nodular (Fig 1*A*). The vertebral lesions were classified as homogeneous or heterogeneous on the basis of MR imaging findings (Fig 1*B*). Lesions were considered homogeneous if no evidence of necrosis, cyst, hemorrhage, or fracture was seen on T1- and T2-weighted images. If ≥1 of these features or mixed signal intensity (ie, high and low signal intensity) on the MR images was present, the vertebral lesion was considered heterogeneous. The readers also as-

sessed the location of other spinal vertebral lesions with the same signal intensity as the biopsy-proved spinal HHBM.

The same neuroradiologists also independently rated the CT appearance of each vertebral body lesion by using a 4-point grading system: grade 1 = normal appearance with normal or subtle high attenuation, grade 2 = osteolytic lesions, grade 3 = osteoblastic lesions, and grade 4 = mixed osteolytic and osteoblastic lesions. When grade 2, 3, or 4 vertebral lesions were observed, their appearance was graded as abnormal. When the grades assigned by the 2 readers were different, the final grade was determined by consensus. For the quantitative assessment of CT attenuation, 1 neuroradiologist (Y.S., 19 years of neuro-CT experience) placed a 1-cm^2 region of interest in the lesion center and on an adjacent normal-appearing vertebral body by referring to the corresponding MR images.

Statistical Analysis

To compare findings in patients with HHBM and bone metastasis, we used the Mann-Whitney and Fisher exact tests. Differences in the CT attenuation between HHBM lesions and adjacent normal-appearing vertebrae were analyzed with the Wilcoxon signed rank test. A *P* value < .05 was considered statistically significant.

RESULTS
MR Imaging Findings

HHBM. HHBM was more likely to be seen in the thoracic region (Table 1). In 7 of 8 patients with vertebral HHBM, the lesions were contiguous with the adjacent vertebral body (Fig 2 and Table 1). The other patient had a diffuse lesion in only 1 vertebra. The HHBM lesions were hypointense compared with adjacent normal-appearing vertebrae on both T1- and T2-weighted images in all 8 patients (Fig 2 and Table 2). The vertebral HHBM distribution pattern was diffuse in 5 patients, patchy in 2, and nodular in 1. The HHBM lesion in all patients had a homogeneous appearance. On STIR sequences acquired in 4 patients, the signal intensity was slightly hyperintense in 3 and isointense in 1 (Fig 2). In 2 patients, we performed contrast-enhanced studies; in both, the HHBM lesions were slightly more enhanced than the normal-appearing adjacent vertebral bone marrow. Two patients underwent diffusion-weighted imaging; in both, the lesions were hyperintense and their ADC values were 0.56 and 0.47 × 10^{-3}mm^2/s, respectively (Fig 2). The ADC values in normal-appearing vertebrae of the same patients were 0.78 and 0.57 × 10^{-3}mm^2/s, respectively.

Bone Metastasis. The 21 vertebral lesions in 21 patients were pathologically confirmed as spinal bone metastasis and were hypointense on T1-weighted images (Fig 3). In 13 of 21 patients with bone metastasis, the lesions were contiguous with the adjacent vertebral body. Lesions contiguous with the adjacent vertebral body were present significantly more often in HHBM than in bone metastasis (*P* = .035). On T2-weighted images, 12 lesions were hypointense, 6 were isointense, and 3 were hyperintense (Fig 3). When the signal intensity was divided into 2 categories (hypointensity versus iso- to hyperintensity), there was no significant difference in the T1 signal intensity of the lesions between patients with HHBM and those with bone metastasis (Table 2). On the other hand, there was a significant difference in the T2 signal
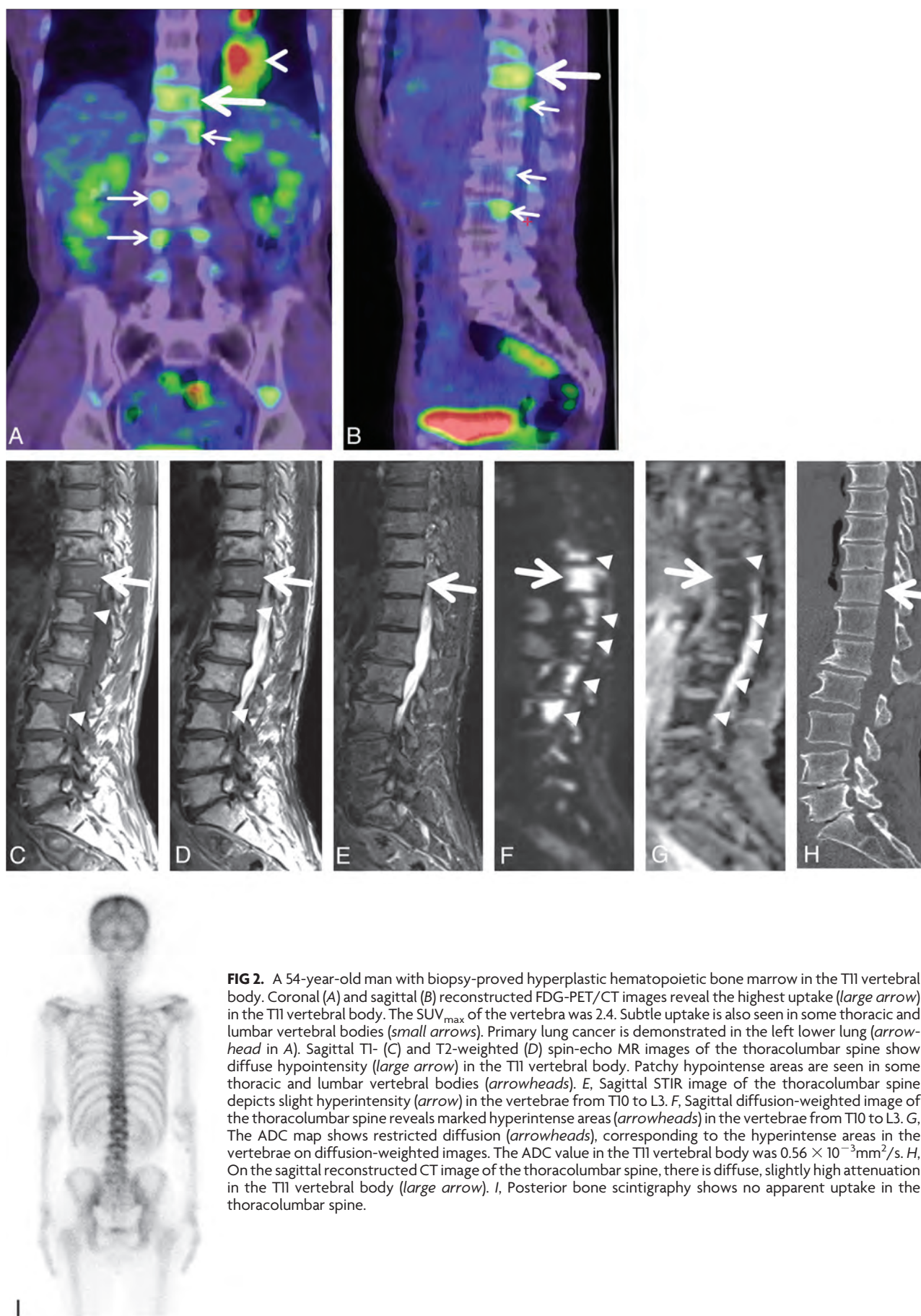
FIG 2. A 54-year-old man with biopsy-proved hyperplastic hematopoietic bone marrow in the T11 vertebral body. Coronal (*A*) and sagittal (*B*) reconstructed FDG-PET/CT images reveal the highest uptake (*large arrow*) in the T11 vertebral body. The SUV$_{max}$ of the vertebra was 2.4. Subtle uptake is also seen in some thoracic and lumbar vertebral bodies (*small arrows*). Primary lung cancer is demonstrated in the left lower lung (*arrowhead* in *A*). Sagittal T1- (*C*) and T2-weighted (*D*) spin-echo MR images of the thoracolumbar spine show diffuse hypointensity (*large arrow*) in the T11 vertebral body. Patchy hypointense areas are seen in some thoracic and lumbar vertebral bodies (*arrowheads*). *E*, Sagittal STIR image of the thoracolumbar spine depicts slight hyperintensity (*arrow*) in the vertebrae from T10 to L3. *F*, Sagittal diffusion-weighted image of the thoracolumbar spine reveals marked hyperintense areas (*arrowheads*) in the vertebrae from T10 to L3. *G*, The ADC map shows restricted diffusion (*arrowheads*), corresponding to the hyperintense areas in the vertebrae on diffusion-weighted images. The ADC value in the T11 vertebral body was 0.56 × 10^{-3}mm^2/s. *H*, On the sagittal reconstructed CT image of the thoracolumbar spine, there is diffuse, slightly high attenuation in the T11 vertebral body (*large arrow*). *I*, Posterior bone scintigraphy shows no apparent uptake in the thoracolumbar spine.

Table 2: Summary of visual assessments of vertebral lesions on MRI[a]

	T1WI			T2WI			Distribution Pattern			Appearance	
	Hyper	Iso	Hypo	Hyper	Iso	Hypo	Diffuse	Patchy	Nodular	Homo	Hetero
HHBM (n = 8)	0	0	8	0	0	8	5	2	1	8	0
Metastasis (n = 21)	0	0	21	3	6	12	20	0	1	15	6

Note:—Hyper indicates hyperintensity; Iso, isointensity; Hypo, hypointensity; Homo, homogeneous; Hetero, heterogeneous.
[a] When the signal intensity was divided into 2 categories (hypointensity vs iso- to hyperintensity), there was no significant difference in the T1 signal intensity of the lesions between patients with HHBM and those with bone metastasis. On the other hand, there was a significant difference in the T2 signal intensity of the lesions between the 2 groups (Fisher exact test, $P = .033$). There was no significant difference in the distribution pattern and appearance of the lesions between patients with HHBM and those with bone metastasis.
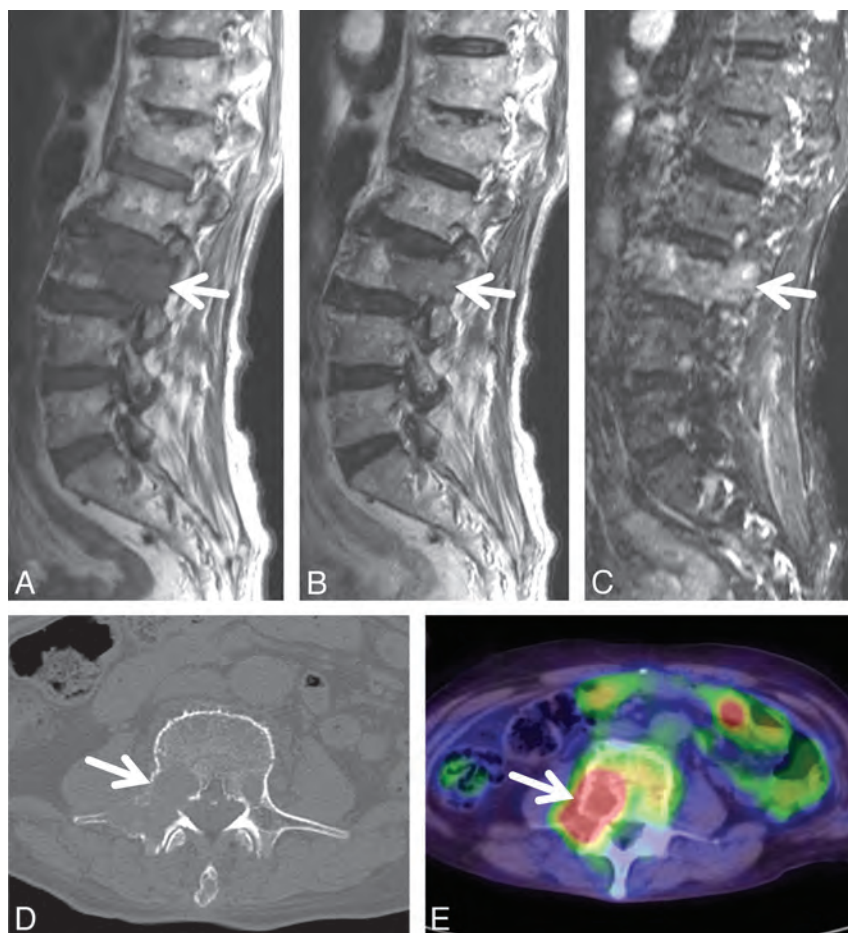
FIG 3. An 84-year-old man with lung cancer and biopsy-proved metastatic bone tumor in the L3 vertebral body. Sagittal T1- (A) and T2-weighted (B) spin-echo MR images of the lumbar spine show diffuse hypointensity (arrow) in the L3 vertebra. There are no vertebral lesions adjacent to the L3 lesion. C, Sagittal STIR image of the lumbar spine depicts hyperintensity (arrow) in the same vertebra. D, On the axial CT image at the level of the L3 lumbar vertebra, there is an osteolytic area in the vertebral body (arrow). E, Axial FDG-PET/CT image at the level of the L3 lumbar vertebra reveals a high uptake area in the vertebral body (arrow). SUV_{max} of the vertebral lesion was 12.4.

intensity of the lesion between the 2 groups ($P = .033$, Table 2). The lesional distribution pattern was diffuse in 20 patients and nodular in 1; 15 lesions had a homogeneous and 6 a heterogeneous appearance. There was no significant difference in the distribution pattern and appearance of the lesions between patients with HHBM and those with bone metastasis (Table 2).

FDG-PET Findings

HHBM. In all 8 patients with pathologically confirmed HHBM, the vertebral lesions showed a relatively high uptake compared with adjacent normal-appearing vertebrae (Fig 2). The mean SUV_{max} of biopsy-proved HHBM was 2.72 ± 0.57; it ranged from 2.09 to 3.6 (Figs 2 and 4).

Bone Metastasis. In 12 patients, FDG-PET studies were performed before biopsy. The mean SUV_{max} of the biopsy-proved spinal bone metastases was 6.46 ± 4.90 (range, 1.97–17.67) (Figs 3 and 4). There was a statistically significant difference in the SUV_{max} between patients with HHBM and those with bone metastasis ($P = .037$, Fig 4).

CT Findings

HHBM. In all 8 patients with HHBM, the affected vertebrae were ranked grade 1 (subtle high attenuation, $n = 7$; normal, $n = 1$) (Fig 2 and Table 3). Their mean CT attenuation was 189.8 ± 49.0 HU, significantly higher than that of adjacent normal-appearing vertebrae (93.7 ± 37.0 HU, $P = .0078$) (Fig 5).

Bone Metastasis. Of the 24 vertebral lesions pathologically proved as spinal bone metastasis, 17 were ranked as osteolytic (grade 2), and 5, as osteoblastic (grade 3) (Fig 3). The other 2 were grades 1 and 4. With regard to the CT appearance of normal (grade 1) and abnormal (grades 2–4) patterns, HHBM and metastasis differed significantly ($P < .01$, Table 3).

Bone Scintigraphy Findings

HHBM. Of the 8 patients with HHBM, 5 had undergone bone scintigraphy before bone biopsy (Table 4). The uptake was equivalent in the 5 HHBM lesions and the adjacent normal-appearing vertebrae (Fig 2).

Bone Metastasis. In 13 of the 24 patients with bone metastasis, bone scintigraphy was performed before biopsy. The uptake was higher in all 13 lesions than in the adjacent normal-appearing vertebrae. Qualitative uptake assessment yielded significantly different results for HHBM and bone metastasis ($P < .01$, Table 4).
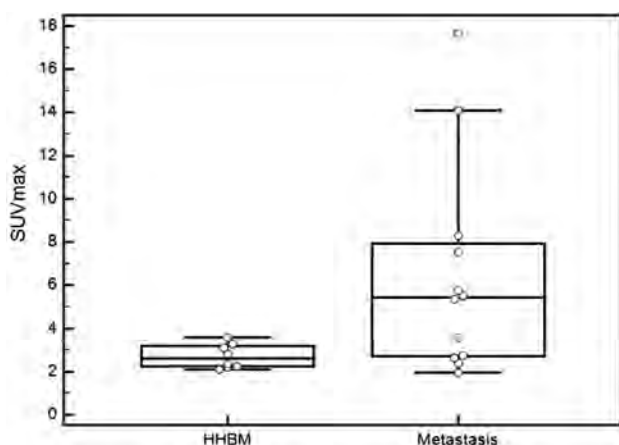
FIG 4. Comparison of SUV_{max} between HHBM and bone metastasis. The SUV_{max} of the biopsy-proved vertebral lesions is shown. A significant difference is seen between HHBM and bone metastasis (Mann-Whitney test, $P = .037$). The horizontal short lines indicate 95% CI for the median.

Table 3: Summary of visual inspections of vertebral lesions on CT[a]

	CT Appearance[b]			
	Grade 1	Grade 2	Grade 3	Grade 4
HHBM (n = 8)	8	0	0	0
Bone metastasis (n = 24)	1	17	5	1

[a] When the CT appearance was divided into 2 categories (grade 1 vs grades 2–4), HHBM and metastasis differed significantly (Fisher exact test, $P < .01$).
[b] CT appearance of each vertebral body lesion was classified using the 4-point grading system: grade 1, normal appearance with normal or subtle high attenuation; grade 2, osteolytic lesions; grade 3, osteoblastic lesions; and grade 4, mixed osteolytic and osteoblastic lesions.
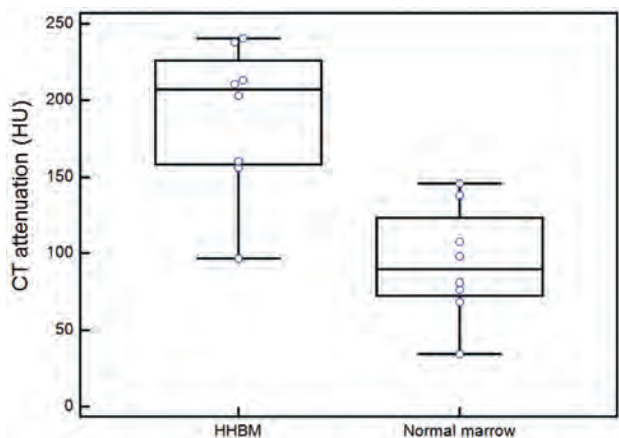
FIG 5. Comparison of CT attenuation between HHBM and normal-appearing bone marrow. The mean CT attenuation of HHBM was significantly higher than that of adjacent normal-appearing vertebrae (Wilcoxon signed rank test, $P = .0078$). The horizontal short lines indicate 95% CI for the median.

DISCUSSION

Spinal HHBM lesions with abnormalities on both FDG-PET and MR imaging are clinically problematic, especially at the staging of malignant neoplasms, because the diagnosis affects patient management. Therefore, an understanding of the typical imaging findings of HHBM is important. To our knowledge, we are the first to report the characteristic findings of HHBM on systematic studies of MR imaging, FDG-PET, CT, and bone scintigraphy.

Table 4: Summary of visual inspections for abnormal uptake on bone scintigraphy

	Abnormal Uptake[a]	
	None	Present
HHBM (n = 5)	5	0
Bone metastasis (n = 13)	0	13

[a] The uptake assessment between the HHBM and bone metastasis was significantly different (Fisher exact test, $P < .01$).

MR imaging findings on HHBM have been documented.[5-10] Typically, the MR imaging signal of HHBM is compatible with that of normal red marrow—that is, there is a moderate-to-marked decrease in signal intensity on T1- and T2-weighted spin-echo images and an intermediate-to-moderate increase in signal intensity on fat-saturated T2-weighted images.[5] Although STIR findings have not been described, they can be expected to be similar to those on fat-saturated T2-weighted images. In all of our patients with HHBM, the signal intensity was similar to that in earlier reports. Our results indicate that HHBM and bone metastasis significantly differ on T2 signal intensity. On T2-weighted images, in 9 (43%) of 21 patients with cancer, we were able to differentiate HHBM and bone metastasis. Thus, the T2 signal intensity of the lesion would be useful for differentiating the 2 entities. Although HHBM and bone metastasis did not significantly differ in the lesional distribution pattern and appearance in a single vertebra, a heterogeneous vertebral lesion was seen in only 6 (29%) of 21 patients with cancer.

Under normal conditions, red marrow is generally distributed in a homogeneous pattern within the vertebral body. Occasionally, red marrow can be more cellular near the vertebral endplate and in the anterior aspect of the vertebral bodies on MR imaging.[11] Then, fatty marrow can become prominent around the vertebral basilar veins on MR imaging.[11] As a rule, these variations in the MR imaging appearance should involve all vertebral bodies of the same subject in a similar manner. In spinal HHBM, on the other hand, we found that the distribution pattern of vertebral HHBM was diffuse, patchy, or nodular and that the HHBM lesions often involved adjacent vertebrae. The same MR imaging appearance of adjacent vertebral bodies may be a feature of spinal vertebral HHBM, though this can also be seen in metastatic spinal tumors.

As did others,[5,12] we found that areas involved by HHBM may be contrast-enhanced. This makes it difficult to distinguish HHBM and metastatic bone lesions. We found no earlier reports on the appearance of HHBM on diffusion-weighted images. Our study revealed that spinal HHBM lesions manifested restricted diffusion, but this result was derived from only 2 patients. Some metastatic spinal tumors may show restricted diffusion on diffusion-weighted images.[13] In our study, patients with bone metastasis did not undergo diffusion-weighted imaging. Therefore, the usefulness of diffusion-weighted imaging for discriminating bone metastasis is not understood. Further studies by using large population data are required to clarify this issue.

In our patients with HHBM, the qualitative assessment of FDG-PET scans showed a relatively high uptake by HHBM lesions compared with adjacent normal-appearing vertebrae. Our quantitative study demonstrated that mean SUV_{max} for HHBM was significantly lower than that for vertebral metastasis. Although a relatively high uptake by HHBM on FDG-PET scans has
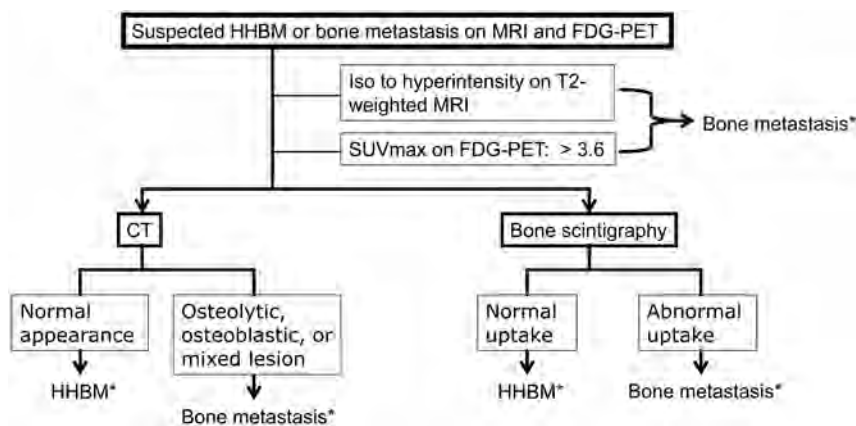
FIG 6. A proposed diagnostic scheme to be followed by practitioners/radiologists when faced with the problem of differentiating HHBM from bone metastasis. *Asterisk* indicates that bone biopsy might be still needed in indeterminate cases.

been described in some case studies,[11,14] to our knowledge, there are no reports on the SUV$_{max}$ of HHBM. Our results indicate that quantitative assessment by using SUV$_{max}$ is useful for differentiating HHBM and bone metastasis. If the SUV$_{max}$ of a vertebral lesion exceeds 3.6, the possibility of HHBM appears to be low (Fig 4).

Our quantitative analysis of CT showed that CT attenuation of HHBM was significantly higher than that of normal bone marrow. We also found that the CT appearance of HHBM was significantly different from that of bone metastasis. To our knowledge, such findings have not been reported elsewhere. We suggest that this observation is important for the CT diagnosis of HHBM; osteolytic, osteoblastic, or mixed lesions should not be misdiagnosed as HHBM (Fig 5).

On bone scintigraphs, we observed no abnormal uptake in areas involved in HHBM. Because there was a significant difference in the uptake between HHBM and bone metastasis, bone scintigraphy can be useful for a differential diagnosis. Because the uptake of 99mTc-MDP mainly reflects osteoblastic activity, it is surprising that HHBM with slightly higher attenuation on CT images did not show a high uptake on bone scintigraphs. The slightly higher attenuation of HHBM on CT may be due to high cellularity in the vertebrae. This theory is compatible with diffusion restriction of HHBM in our study.

Our study has some limitations. First, it was retrospective, the number of consecutive patients with HHBM was small, and all were men. Because heavy smoking and chronic anemia can lead to HHBM,[5-9] their history of smoking and anemia may have affected the etiology of HHBM in our patients. Second, we did not use other imaging techniques for differentiating HHBM from bone metastasis, such as MR imaging with in-phase and opposed-phase techniques[15] or contrast-enhanced MR imaging by using iron oxide.[16] Third, the tumor type of bone metastasis may have affected our results. It is well-known that lymphoma often shows little abnormality on bone scintigraphy and CT. We included only 4 cases with lymphoma in this study. Because lymphomas usually indicate high SUV$_{max}$,[17] FDG-PET may be useful for differentiating HHBM from lymphoma.

Fourth, we did not perform CT-guided biopsy for all vertebral lesions indicating abnormal signal or uptake on MR imaging and

FDG-PET. In each case, only 1 vertebral bone biopsy was performed for a vertebra that showed the highest uptake at FDG-PET. Due to the invasiveness of CT-guided biopsy, our approach is considered a reasonable strategy for evaluating the vertebral lesions. In our institution, no patients have been misdiagnosed by using this CT-guided biopsy approach for vertebral lesions.

CONCLUSIONS

We found that if a lesion was isointense to hyperintense to normal-appearing marrow in other vertebral bodies on MR imaging or had a SUV$_{max}$ of >3.6, it was considered metastatic (Fig 6). If not, then a normal appearance on CT or bone scintigraphy excluded metastasis (Fig 6). HHBM was more likely to be seen in asymptomatic patients and in the thoracic spine; contiguous lesions with the adjacent vertebral body were more often seen in HHBM than in bone metastasis. Bone biopsy might still be needed in indeterminate cases. To put our findings to the absolute test, a prospective study is required in the future.

REFERENCES

1. Mittra E, Quon A. **Positron emission tomography/computed tomography: the current technology and applications.** *Radiol Clin North Am* 2009;47:147–60
2. Cheng X, Li Y, Xu Z, et al. **Comparison of ^{18}F-FDG PET/CT with bone scintigraphy for detection of bone metastasis: a meta-analysis.** *Acta Radiol* 2011;52:779–87
3. Wu LM, Gu HY, Zheng J, et al. **Diagnostic value of whole-body magnetic resonance imaging for bone metastases: a systematic review and meta-analysis.** *J Magn Reson Imaging* 2011;34:128–35
4. Yang HL, Liu T, Wang XM, et al. **Diagnosis of bone metastases: a meta-analysis comparing ^{18}FDG PET, CT, MRI and bone scintigraphy.** *Eur Radiol* 2011;21:2604–17
5. Vande Berg BC, Lecouvet FE, Galant C, et al. **Normal variants and frequent marrow alterations that simulate bone marrow lesions at MR imaging.** *Radiol Clin North Am* 2005;43:761–70, ix
6. Deutsch AL, Mink JH, Rosenfelt FP, et al. **Incidental detection of hematopoietic hyperplasia on routine knee MR imaging.** *AJR Am J Roentgenol* 1989;152:333–36
7. Shellock FG, Morris E, Deutsch AL, et al. **Hematopoietic bone marrow hyperplasia: high prevalence on MR images of the knee in asymptomatic marathon runners.** *AJR Am J Roentgenol* 1992;158:335–38
8. Poulton TB, Murphy WD, Duerk JL, et al. **Bone marrow reconversion in adults who are smokers: MR imaging findings.** *AJR Am J Roentgenol* 1993;161:1217–21
9. Caldemeyer KS, Smith RR, Harris A, et al. **Hematopoietic bone marrow hyperplasia: correlation of spinal MR findings, hematologic parameters, and bone mineral density in endurance athletes.** *Radiology* 1996;198:503–08
10. Bordalo-Rodrigues M, Galant C, Lonneux M, et al. **Focal nodular hyperplasia of the hematopoietic marrow simulating vertebral metastasis on FDG positron emission tomography.** *AJR Am J Roentgenol* 2003;180:669–71
11. Ricci C, Cova M, Kang YS, et al. **Normal age-related patterns of cellular and fatty bone marrow distribution in the axial skeleton: MR imaging study.** *Radiology* 1990;177:83–88
12. Amano Y, Hayashi H, Kumazaki T. **Gd-DTPA enhanced MRI of reactive hematopoietic regions in marrow.** *J Comput Assist Tomogr* 1994;18:214–17

13. Herneth AM, Philipp MO, Naude J, et al. **Vertebral metastases: assessment with apparent diffusion coefficient.** *Radiology* 2002; 225:889–94

14. Elstrom RL, Tsai DE, Vergilio JA, et al. **Enhanced marrow [18F]fluorodeoxyglucose uptake related to myeloid hyperplasia in Hodgkin's lymphoma can simulate lymphoma involvement in marrow.** *Clin Lymphoma* 2004;5:62–64

15. Kaplan KR, Mitchell DG, Steiner RM, et al. **Polycythemia vera and myelofibrosis: correlation of MR imaging, clinical, and laboratory findings.** *Radiology* 1992;183:329–34

16. Daldrup-Link HE, Rummeny EJ, Ihssen B, et al. **Iron-oxide-enhanced MR imaging of bone marrow in patients with non-Hodgkin's lymphoma: differentiation between tumor infiltration and hypercellular bone marrow.** *Eur Radiol* 2002;12:1557–66

17. Tsukamoto N, Kojima M, Hasegawa M, et al. **The usefulness of (18)F-fluorodeoxyglucose positron emission tomography ((18)F-FDG-PET) and a comparison of (18)F-FDG-PET with (67)gallium scintigraphy in the evaluation of lymphoma: relation to histologic subtypes based on the World Health Organization classification.** *Cancer* 2007;110:652–59

Tapering of the Cervical Spinal Canal in Patients with Distended or Nondistended Syringes Secondary to Chiari Type I Malformation

Z. Zhu, S. Sha, X. Sun, Z. Liu, H. Yan, W. Zhu, Z. Wang, and Y. Qiu

ABSTRACT

BACKGROUND AND PURPOSE: Steeper tapering of the cervical spinal canal as documented in recent studies is thought to have a role in the pathophysiology of Chiari malformation-associated syringomyelia. This study aimed to determine whether taper ratio of the cervical spinal canal differs between patients with distended and nondistended syringes.

MATERIALS AND METHODS: Seventy-seven adolescents (10–18 years) were divided into 2 groups: 44 with distended syrinx and 33 with nondistended syrinx. On T2-weighted MR images, anteroposterior diameter of the spinal canal was measured at each cervical level, and a linear trend line was fit by least squares regression to calculate the taper ratio. Taper ratios were compared between the 2 groups and further evaluated with respect to age and sex.

RESULTS: In the nondistended group ND, the taper ratios for C1–C7, C1–C4, and C4–C7 averaged -0.73 ± 0.57, -1.61 ± 0.98, and -0.04 ± 0.54, respectively, all of which were significantly steeper than those observed in the distended group ($P = .001$, .004, and .033, respectively). Regarding the average diameters plotted by cervical level, the narrowest region of the canal was found to occur at C4 in both groups. In addition, no significant differences in taper ratio were noted between males and females, or between older ($>$14 years) and younger patients ($\leq$14 years).

CONCLUSIONS: Taper ratios of the cervical spinal canal were found to be different between patients with distended and nondistended syringes, indicating a reciprocal interaction between the syrinx and the cervical spine anatomy.

ABBREVIATIONS: CMI = Chiari malformation type I; SM = syringomyelia; D = distended; ND = nondistended; S/C = syrinx/cord

Chiari malformation type I (CMI) is the leading cause of syringomyelia (SM), a debilitating disorder that can give rise to neurologic impairments including motor weakness and sensory disturbance.[1-3] To date, the exact pathogenesis responsible for SM associated with CMI remains incompletely understood. Although numerous theories and hypotheses have been proposed to explicate the mechanisms underlying such pathologic entity,[4-7] none thoroughly elucidated the clinical and radiologic findings within the disease spectrum.

According to a prevailing concept, altered CSF flow at the craniovertebral junction is one of the essential elements in the

pathophysiology of SM and hypothetically causes the neurologic signs and symptoms associated with CMI.[8-11] Pinna et al[12] reported that the elongation of the systolic flow might prolong the condition of elevated spinal subarachnoid pressure in patients with CMI. Using computational flow analysis in an idealized 3D model of the subarachnoid space, Roldan et al[13] and Linge et al[11] found that the peak CSF velocities increased progressively from the foramen magnum to C4 or C5. These findings, coupled with the mesodermal dysgenesis theory as evidenced by hypoplasia of the posterior cranial fossa,[14,15] imply an abnormal cervical spinal canal anatomy in patients with CMI. In an attempt to verify this hypothesis, Hirano et al[16] and Hammersley et al[17] investigated tapering of the upper cervical spinal canal, and as steeper taper ratio was found in patients with CMI as compared with healthy controls, they speculated that such bony variations might increase the pressure gradients between the cranial and caudal ends of the spinal canal, resulting in dysfunctional CSF flow and thus favoring the formation of a syrinx.

Despite the elegance of the work of Hirano et al[16] and Hammersley et al,[17] which added an interesting twist to the pathomechanism of SM, their theory fails to account for the influence of a syrinx upon

morphology of the cervical spinal canal. Clinically, it is observed that patients with a distended syrinx tend to have regional enlargement of the spinal canal. We, therefore, set out to determine whether taper ratio of the cervical spinal canal differs between patients with distended and nondistended syringes secondary to CMI.

MATERIALS AND METHODS

Our institutional review board approved this study and waived the requirement for written informed consent for the retrospective review of MR images and patient data.

Subjects

A 5-year retrospective review (between January 2008 and January 2013) was performed at our center on 170 consecutive patients with CMI-associated SM. The inclusion criteria were as follows: 1) age 10–18 years and 2) syrinx located within the cervicothoracic region. Patients with hydrocephalus, history of spinal trauma, changes of the sagittal cervical alignment (kyphosis or straightening), associated intraspinal anomalies, or congenital spinal deformity were excluded. A subset of 77 patients including 46 males and 31 females were ultimately enrolled for analyses.

All patients underwent MR scanning of the entire spinal cord with a 1.5T MR imaging system (Gyroscan Intera; Philips Medical Systems, Best, the Netherlands). As a routine imaging protocol, sagittal images were obtained using T1-weighted (TR/TE, 717/10 ms; flip angle, 90°; field of view, 200 mm; matrix, 168 × 315; NEX, 3) and T2-weighted (TR/TE, 2038/100 ms; flip angle, 90°; field of view, 200 mm; matrix, 168 × 315; NEX, 3) spin-echo techniques with 3-mm sections and 2.5-mm intersection gaps. Based on the syrinx/cord (S/C) ratio defined as the maximal anteroposterior diameter of the syrinx divided by the anteroposterior diameter of the spinal cord at the same level on the transverse MR images (TR/TE, 2038/100 ms; flip angle, 90°; field of view, 300 mm; matrix, 248 × 306; NEX, 3), patients were subdivided into those with distended (S/C > 0.5) and nondistended (S/C ≤ 0.5) syringes.[18,19]

Radiographic Measurements

In line with the methods described previously,[16,17] the anteroposterior diameter of the cervical spinal canal was measured on T2-weighted MR images for each level at the midpoint of the vertebral body (in the case of C1, at the midportion of the anterior arch), along a line perpendicular to the spinal axis extending from the anterior to the posterior edge of the subarachnoid space (Fig 1). The diameters of the spinal canal were plotted against the cervical level. Then a linear trend line was fitted by least squares regression with an algorithm resident in the Excel spreadsheet (Microsoft, Redmond, Washington) (Fig 2), and the slope of this line was recorded as taper ratio (mm/level).

Location of the syrinx was recorded as the proximal and distal levels. The extent of tonsillar descent was evaluated on T1-weighted MR images and classified into 3 grades[20]: grade I, where the tonsil extended below the foramen magnum but did not reach the C1 arch; grade II, where the tonsil reached the C1 arch; and grade III, where the tonsil extended below the C1 arch. Anteroposterior diameter of the foramen magnum as defined by the distance between the basion and the opisthion[21] was also measured.
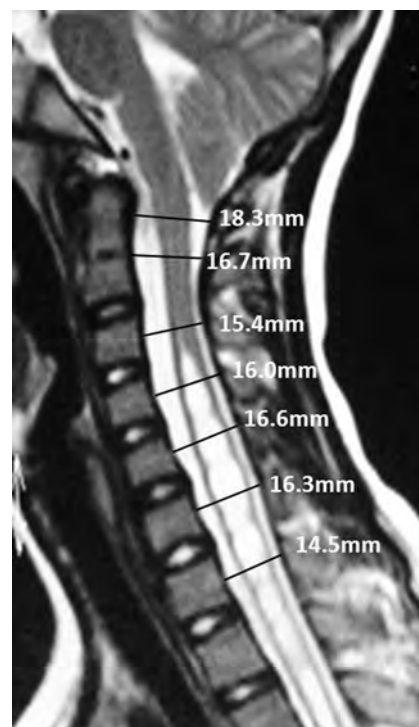
FIG 1. Sagittal T2-weighted MR image illustrating the measurement of the anteroposterior spinal canal diameter at 7 cervical levels.

Statistical Analysis

Data analysis was performed using SPSS 19.0 software (IBM, Armonk, New York). For comparisons of demographic data between the 2 groups, the Student t test and χ^2 analysis were applied for testing of continuous and categoric variables, respectively. The Fisher exact test was used for small data subsets ($n < 5$). The relationship between taper ratio and the anteroposterior diameter of the foramen magnum was assessed using the Spearman correlation test. Differences in taper ratios of the spinal canal (C1–C7, C1–C4, and C4–C7) for the 2 groups were tested for significance by the Kruskal-Wallis test with significance set at .05.

RESULTS

Of the 77 patients, 44 were classified as having distended syrinx (group D), and 33 were assigned into the nondistended group (group ND). Table 1 summarizes the clinical and radiographic characteristics of patients in the 2 groups. The average age was 14.0 ± 2.0 years (range: 10–18 years) for group D and 14.6 ± 1.9 years (range: 10–18 years) for group ND. In group D, 25 patients were identified with grade I tonsillar ectopia, 16 with grade II, and 3 with grade III; in group ND, the corresponding values were 17, 15, and 1, respectively. Concerning the syrinx location, the proximal level varied from C2 to C5 in group D and from C2 to C6 in group ND, whereas the distal level for the 2 groups ranged, respectively, from C6 to T4 and from C6 to T3. None of the above-mentioned parameters were found to be statistically different between the 2 groups ($P > .05$).

Taper ratios for C1–C7 averaged −0.34 ± 0.54 (range: −2.03– 0.81) and −0.73 ± 0.57 (range: −1.88−0.98) mm/levels, respectively, in groups D and ND ($P = .001$). Regarding the other 2

segments (C1–C4 and C4–C7), taper ratios were also noted to be significantly steeper in group ND than in group D ($P = .004$ and .033, respectively; Fig 3).

Figure 4 illustrates the average anteroposterior diameters of spinal canal plotted by cervical level. In group D, spinal canal diameters averaged 17.2 ± 2.5 mm (range: 12.7–22.5 mm) at C1 and 15.3 ± 2.1 mm (range: 11.9–20.5 mm) at C7, whereas the average diameter at C1 and C7 in group ND was 19.0 ± 3.4 mm (range: 11.2–24.7 mm) and 14.5 ± 2.5 mm (range: 11.2–22.8

mm), respectively. In addition, the narrowest diameter was found to occur at the C4 level in both groups.

Taper ratios for C1–C7 were also analyzed with respect to age, sex, and the extent of tonsillar descent in each group (Table 2); however, no significant differences were noted between males and females, or between older (>14 years) and younger patients (≤14 years), or between patients with different grades (I, II, and III) of tonsillar ectopia ($P > .05$). In addition, taper ratio of the cervical spinal canal was found to be marginally significantly correlated with the anteroposterior diameter of the foramen magnum (Spearman correlation, −.221; $P = .053$).

DISCUSSION

Syringomyelia has been reported to accompany CMI 20%–85% of the time and, if left untreated, may lead to progressive deterioration of the spinal cord function.[22-24] Despite decades of research, the maintenance, propagation and, in particular, the pathogenesis of SM in association with CMI remain virtually obscure. As highlighted in the literature, dysfunctional CSF hydrodynamics arising from overcrowding of the caudal cranial fossa and downward displacement of the cerebellar tonsils may, in essence, be held responsible for the development of SM, with steeper pressure differentials across the foramen magnum or spinal levels precipitating accentuated pulsatile CSF subarachnoid waves during systole and diastole.[8-11] No consensus, however, has hitherto been reached as to what primarily contributes to this pressure gradient.

Recently, the cervical spinal anatomy as a key component in the pathogenesis of CMI-associated SM has received in-
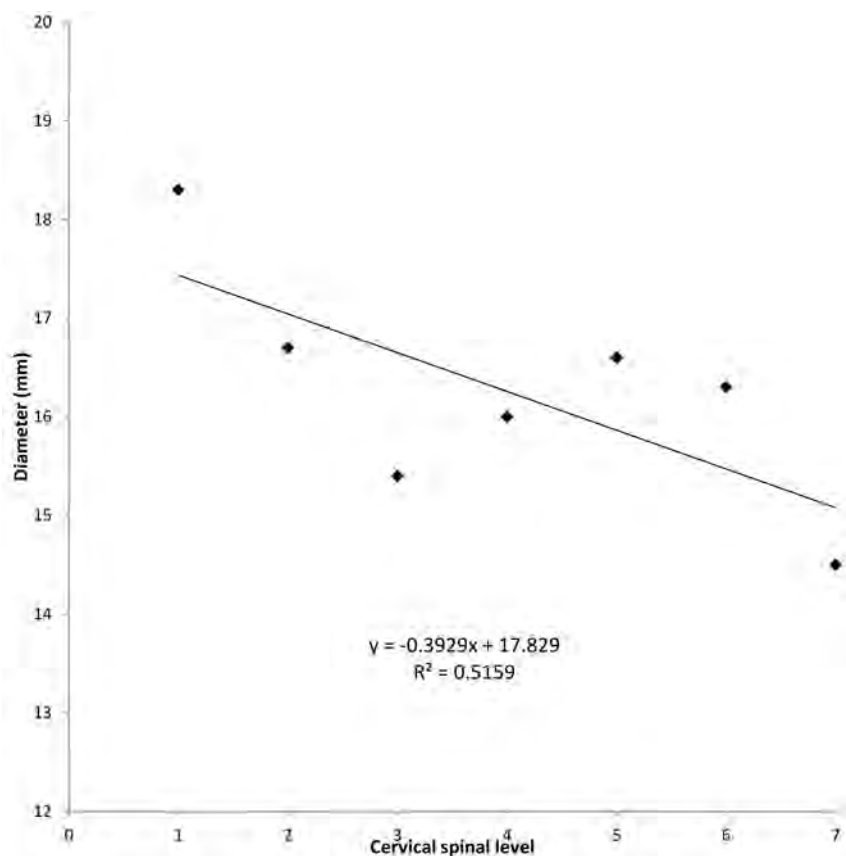
FIG 2. Plot of diameters of the cervical spinal canal for the patient in Fig 1 and the fitting of a trend line. The slope is −0.39 mm/level, with the negative sign indicating the taper toward C7.

Table 1: Clinical and radiographic characteristics of patients in the 2 groups

	Group D	Group ND	P
Number	44	33	
Age (years)	14.0 ± 2.0 (10–18)	14.6 ± 1.9 (10–18)	NS
Sex (male/female)	26/18	20/13	NS[a]
Extent of tonsillar descent			NS[a]
Grade I	25	17	
Grade II	16	15	
Grade III	3	1	
Syrinx location			NS[b]
Proximal level	C2–C5	C2–C6	
Distal level	C6–T4	C6–T3	
Syrinx/cord ratio	0.70 ± 0.10 (0.51–0.88)	0.39 ± 0.09 (0.19–0.50)	<.001
Taper ratio (mm/level)			
C1–C7	−0.34 ± 0.54 (−2.03–0.81)	−0.73 ± 0.57 (−1.88–0.98)	.001[c]
C1–C4	−0.98 ± 0.87 (−2.47–1.70)	−1.61 ± 0.98 (−3.66–0.85)	.004[c]
C4–C7	0.24 ± 0.50 (−0.85–1.65)	−0.04 ± 0.54 (−0.97–1.36)	.033[c]

Note:—NS indicates statistical nonsignificance.
[a] χ^2 test.
[b] Fisher exact test.
[c] Kruskal–Wallis test or otherwise Student t test.
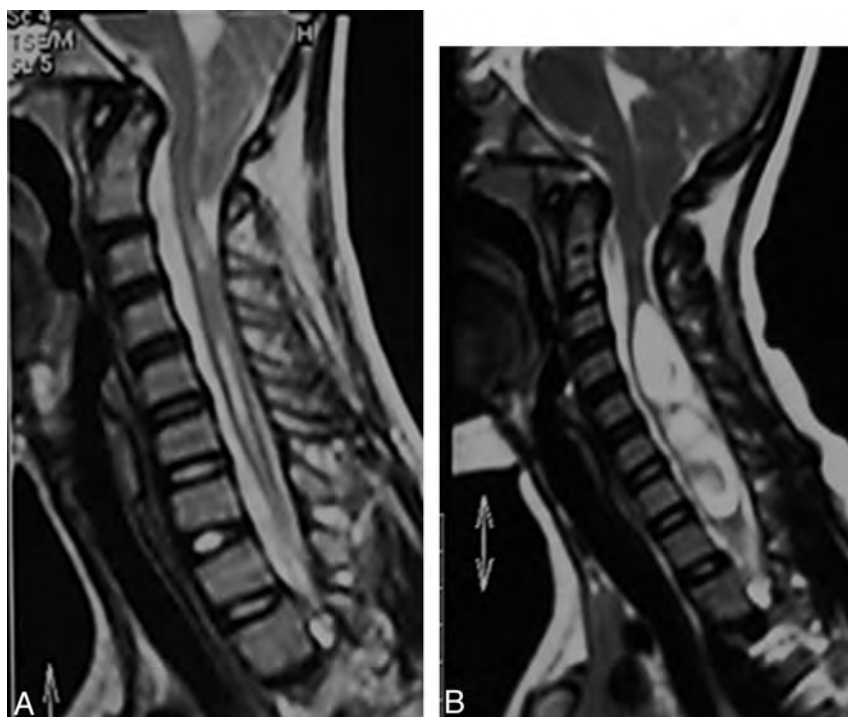
FIG 3. Two adolescents with Chiari malformation and syringomyelia. *A*, A 13-year-old male with nondistended syrinx. The taper ratios for C1–C7, C1–C4, and C4–C7 are −1.52, −2.76, and −0.22, respectively. *B*, A 12-year-old female with distended syrinx. The taper ratios for C1–C7, C1–C4, and C4–C7 are 0.79, 0.63, and 0.50, respectively.

FIG 4. Average anteroposterior diameters of the cervical spinal canal plotted by cervical level in the 2 groups.

cervical spinal canal anatomy in CMI, and brought to light an interesting and under-recognized phenomenon that may contribute to a better understanding of the pathophysiology of SM. Unfortunately, the small sample size, to some extent, restrained the validity of their findings. Bearing in mind the documented correlation between age 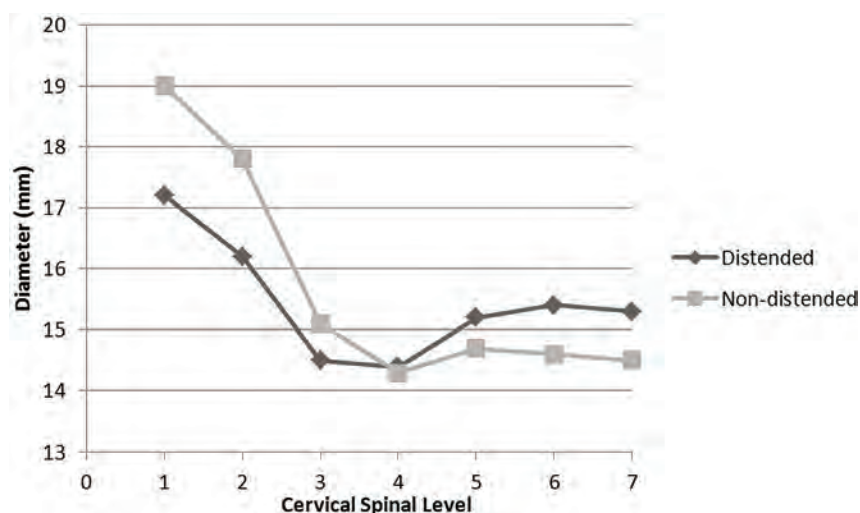and taper ratio,[17] confounding bias might also be potentially induced by their relatively wide age range (from 4 to 60 years of age). To mitigate this bias and further clarify their findings, we analyzed the sagittal profiles of the cervical spinal canal on a larger but homogeneous cohort of adolescents with CMI. In addition, given that patients with a distended syrinx are more inclined to have a regional enlargement of the spinal canal than those with less extensive cavitation, we sought to determine whether disparities in the spinal geometry exist between the 2 subgroups.

In our series, the average taper ratios of the cervical spinal canal in patients with distended and nondistended syringes were both steeper than in the healthy controls reported previously (-0.2 ± 0.3 mm/level, on average),[16] corroborating the conjecture of an abnormal development of the cervical spine in patients with CMI. Based on established hydrodynamics principles, the intrathoracic pressures are transmitted toward the spinal and cranial compartments and further to the subarachnoid space.[25,26] Hence, one can hypothesize that in patients with CMI, the physiologic pressure transmission that normally exists between the intrathoracic and CSF compartments is exaggerated as a consequence of the steeper tapering of spinal canal, which, in turn, exacerbates the pressure differentials between the cranial and spinal compartments as well as their possibility of equalization, both of which are already altered by the herniated cerebellar tonsils. Intuitively, the elevated pressure differential may precipitate hyperkinetic CSF flow, and once a critical threshold is surpassed, a syrinx could be created. In addition, the anteroposterior diameter of the cervical spinal canal was found to be narrowest at C4 in both groups (Fig 4), corresponding with the results of prior studies that the peak CSF velocity increased progressively from the foramen magnum to C4 in patients with CMI.[11,13,27] In light of these findings and the well-recognized association of syrinx with cervical canal stenosis,[28,29] the pivotal role of cer-

creasing concern.[16,17] Hirano et al,[16] in their retrospective review of 21 patients, noted a statistically steeper taper ratio of the upper cervical spinal canal in patients with CMI and SM. Concerning patients with CMI but no syrinx, however, taper ratio was found to be similar to that of their age- and sex-matched control subjects. These authors, therefore, surmised that steeper tapering of the spinal canal, in conjunction with obstruction of the subarachnoid space at the level of foramen magnum, could substantially increase the pressure gradient and subsequently accelerate the CSF velocities, leading to syrinx formation. Of note, their studies took an important first step in trying to elucidate the role of the

Table 2: Analyses of the taper ratio for C1–C7 with respect to age and gender

	Group D		Group ND	
	N	Taper Ratio	N	Taper Ratio
Age				
≤14 years	28	−0.26 ± 0.55	12	−0.77 ± 0.46
>14 years	16	−0.49 ± 0.53	21	−0.71 ± 0.63
P		.380		.750
Sex				
Male	26	−0.39 ± 0.56	20	−0.72 ± 0.70
Female	18	−0.27 ± 0.53	13	−0.75 ± 0.27
P		.358		.883
Extent of tonsillar descent				
Grade I	25	−0.34 ± 0.62	17	−0.79 ± 0.50
Grade II	16	−0.29 ± 0.46	15	−0.61 ± 0.63
Grade III	3	−0.56 ± 0.38	1	−1.37
P		.525		.335

Note:—Statistical significance was tested using the Kruskal–Wallis test.

vical spinal canal dimensions in determining CSF circulatory features seems to be evident.

Theoretically, CSF circulatory disturbances may not only be associated with syrinx formation but also could influence the progression of SM, because its maintenance rests upon CSF being forced into the spinal cord by pulsatile pressure waves.[6,30] Based on this assumption, the steeper the tapering is, the more abnormal the CSF dynamics and thus the larger the syrinx should be. Our results, however, demonstrated that patients with nondistended syrinx (S/C ratio ≤0.5) had steeper taper ratios than those with distended syrinx (S/C ratio > 0.5). In a previous study of 22 patients with CMI, Hammersley et al[17] demonstrated that the taper ratio for C1–C7 was similar between patients with CMI plus syrinx and those with CMI only; however, the fact that only 2 patients were included in the latter group made this finding somewhat less convincing. Given that the local bone growth may be influenced by the size of the spinal cord in early development, as evidenced by the experimental work from Holtzer,[31] a plausible explanation for our results is that the regional enlargement of the spinal cord caused by SM may exert an impact upon the development of the cervical spinal canal during skeletal maturation. Clarke et al[9] reported that as a syrinx forms and enlarges, characteristics of the spinal subarachnoid space are altered, resulting in the CSF flow profile being stabilized or reverting to closer to normal, which indirectly supports our findings.

The correlation between age/sex and taper ratio has been documented in healthy adults and patients with CMI.[16,32] Hirano et al[16] reported that each increasing year of age was associated with a 0.03 mm/level decrease in the taper ratio in patients with CMI. In the present study, however, no significant difference in taper ratio was noted between older patients (>14 years) and younger patients (≤14 years) (Table 2), which presumably reflected the small sample sizes of the subgroups and also the narrow age range of subjects. We also looked into the possible relationship between sex and spinal canal diameters; however, no statistical correlation was found. Notably, a marginally significant correlation was demonstrated between taper ratio and the anteroposterior diameter of the foramen magnum ($r = -.221$, $P = .053$), and this probably reflects the close anatomic relationship between the cervical spinal canal and the foremen magnum. In addition, no significant

differences in taper ratio were found between patients with different grades of cerebellar tonsillar descent.

Importantly, the current study has for the first time unraveled the disparities in cervical spinal anatomy between patients with CMI with different syrinx morphologies, which, we anticipate, will shed further light on the integral role of cervical spinal canal dimensions in the pathophysiology of CMI-associated syringomyelia. Limitations of our study lie in its cross-sectional design and the lack of a control group. Consequently, future longitudinal studies involving both patients with CMI and healthy adolescents are warranted to expand our understanding of the reciprocal interactions between syringomyelia and the cervical spinal canal geometry. Subjects of this study were limited to adolescents to mitigate potential confounding bias. Tapering of the cervical spinal canal in the pediatric and adult population, therefore, still merits further investigation. In addition, the fact that more clinically severe syrinx cases are more likely to present for medical evaluation at an earlier time than those with less severe syrinx tends to induce a selection bias. Moreover, whether the relationship between syrinx size and spinal canal tapering observed in this study is an early developmental finding that remains relatively static or an evolving dynamic process has yet be explored by future studies.

CONCLUSIONS

Patients with nondistended syrinx have steeper tapering of the cervical spinal canal than those with distended syrinx, indicating a reciprocal interaction between the syrinx and the cervical spine anatomy. The integral role of spinal canal dimensions in the pathogenesis of syringomyelia, however, has yet to be explored by longitudinal studies involving both patients with CMI and healthy controls.

REFERENCES

1. Qiu Y, Zhu Z, Wang B, et al. **Radiological presentations in relation to curve severity in scoliosis associated with syringomyelia.** *J Pediatr Orthop* 2008;28:128–33
2. Sha S, Zhu Z, Sun X, et al. **Effectiveness of brace treatment of Chiari malformation-associated scoliosis after posterior fossa decompression: a comparison with idiopathic scoliosis.** *Spine* 2013;38:E299–305
3. Qiu Y, Zhu F, Wang B, et al. **Clinical etiological classification of scoliosis: report of 1289 cases.** *Orthop Surg* 2009;1:12–16
4. Gardner WJ. **Hydrodynamic factors in Dandy-Walker and Arnold-Chiari malformations.** *Childs Brain* 1977;3:200–12
5. Williams B. **The distending force in the production of communicating syringomyelia.** *Lancet* 1970;2:41–42
6. Heiss JD, Patronas N, DeVroom HL, et al. **Elucidating the pathophysiology of syringomyelia.** *J Neurosurg* 1999;91:553–62
7. Josephson A, Greitz D, Klason T, et al. **A spinal thecal sac constriction model supports the theory that induced pressure gradients in the cord cause edema and cyst formation.** *Neurosurgery* 2001;48:636–45
8. Clarke EC, Fletcher DF, Stoodley MA, et al. **Computational fluid dynamics modelling of cerebrospinal fluid pressure in Chiari malformation and syringomyelia.** *J Biomech* 2013;46:1801–09
9. Clarke EC, Stoodley MA, Bilston LE. **Changes in temporal flow characteristics of CSF in Chiari malformation type I with and without syringomyelia: implications for theory of syrinx development.** *J Neurosurg* 2013;118:1135–40
10. Hentschel S, Mardal KA, Lovgren AE, et al. **Characterization of cyclic**

CSF flow in the foramen magnum and upper cervical spinal canal with MR flow imaging and computational fluid dynamics. *AJNR Am J Neuroradiol* 2010;31:997–1002

11. Linge SO, Haughton V, Lovgren AE, et al. **CSF flow dynamics at the craniovertebral junction studied with an idealized model of the subarachnoid space and computational flow analysis.** *AJNR Am J Neuroradiol* 2009;31:185–92

12. Pinna G, Alessandrini F, Alfieri A, et al. **Cerebrospinal fluid flow dynamics study in Chiari I malformation: implications for syrinx formation.** *Neurosurg Focus* 2000;8:E3

13. Roldan A, Wieben O, Haughton V, et al. **Characterization of CSF hydrodynamics in the presence and absence of tonsillar ectopia by means of computational flow analysis.** *AJNR Am J Neuroradiol* 2009;30:941–46

14. Stovner LJ, Bergan U, Nilsen G, et al. **Posterior cranial fossa dimensions in the Chiari I malformation: relation to pathogenesis and clinical presentation.** *Neuroradiology* 1993;35:113–18

15. Nishikawa M, Sakamoto H, Hakuba A, et al. **Pathogenesis of Chiari malformation: a morphometric study of the posterior cranial fossa.** *J Neurosurg* 1997;86:40–47

16. Hirano M, Haughton V, Munoz del Rio A. **Tapering of the cervical spinal canal in patients with Chiari I malformations.** *AJNR Am J Neuroradiol* 2012;33:1326–30

17. Hammersley J, Haughton V, Wang Y, et al. **Tapering of the cervical spinal canal in patients with scoliosis with and without the Chiari I malformation.** *AJNR Am J Neuroradiol* 2012;33:1752–55

18. Zhu Z, Qiu Y, Wang B, et al. **Abnormal spreading and subunit expression of junctional acetylcholine receptors of paraspinal muscles in scoliosis associated with syringomyelia.** *Spine* 2007;32:2449–54

19. Qiu Y, Zhu Z, Wang B, et al. **Abnormal spread of junctional acetylcholine receptor of paraspinal muscles in scoliosis associated with syringomyelia.** *Stud Health Technol Inform* 2006;123:117–22

20. Ono A, Ueyama K, Okada A, et al. **Adult scoliosis in syringomyelia associated with Chiari I malformation.** *Spine* 2002;27:E23–28

21. Schady W, Metcalfe RA, Butler P. **The incidence of craniocervical bony anomalies in the adult Chiari malformation.** *J Neurol Sci* 1987;82:193–203

22. Dyste GN, Menezes AH, VanGilder JC. **Symptomatic Chiari malformations. An analysis of presentation, management, and long-term outcome.** *J Neurosurg* 1989;71:159–68

23. Tubbs RS, McGirt MJ, Oakes WJ. **Surgical experience in 130 pediatric patients with Chiari I malformations.** *J Neurosurg* 2003;99:291–96

24. Park JK, Gleason PL, Madsen JR, et al. **Presentation and management of Chiari I malformation in children.** *Pediatr Neurosurg* 1997;26:190–96

25. Hamilton WF, Woodbury RA, Harper HT. **Physiologic relationships between intrathoracic, intraspinal, and arterial pressures.** *JAMA* 1936;107:853–56

26. Herlihy WF. **Revision of the venous system; the role of the vertebral veins.** *Med J Aust* 1947;1:661–72

27. Shah S, Haughton V, del Rio AM. **CSF flow through the upper cervical spinal canal in Chiari I malformation.** *AJNR Am J Neuroradiol* 2011;32:1149–53

28. Martin BA, Labuda R, Royston TJ, et al. **Spinal subarachnoid space pressure measurements in an in vitro spinal stenosis model: implications on syringomyelia theories.** *J Biomech Eng* 2010;132:111007

29. Kato N, Tanaka T, Nagashima H, et al. **Syrinx disappearance following laminoplasty in cervical canal stenosis associated with Chiari malformation–case report.** *Neurol Med Chir (Tokyo)* 2010;50:172–74

30. Oldfield EH, Muraszko K, Shawker TH, et al. **Pathophysiology of syringomyelia associated with Chiari I malformation of the cerebellar tonsils. Implications for diagnosis and treatment.** *J Neurosurg* 1994;80:3–15

31. Holtzer O. **Experimental analysis of development of spinal column.** *J Exp Zool* 1952;121:121–47

32. Tatarek NE. **Variation in the human cervical neural canal.** *Spine J* 2005;5:623–31

Target® Detachable Coil

See package insert for complete indications, contraindications, warnings and instructions for use.

INTENDED USE / INDICATIONS FOR USE
Target Detachable Coils are intended to endovascularly obstruct or occlude blood flow in vascular abnormalities of the neurovascular and peripheral vessels.

Target Detachable Coils are indicated for endovascular embolization of:
- Intracranial aneurysms
- Other neurovascular abnormalities such as arteriovenous malformations and arteriovenous fistulae
- Arterial and venous embolizations in the peripheral vasculature

CONTRAINDICATIONS
None known.

POTENTIAL ADVERSE EVENTS
Potential complications include, but are not limited to: allergic reaction, aneurysm perforation and rupture, arrhythmia, death, edema, embolus, headache, hemorrhage, infection, ischemia, neurological/intracranial sequelae, post-embolization syndrome (fever, increased white blood cell count, discomfort), TIA/stroke, vasospasm, vessel occlusion or closure, vessel perforation, dissection, trauma or damage, vessel rupture, vessel thrombosis. Other procedural complications including but not limited to: anesthetic and contrast media risks, hypotension, hypertension, access site complications.

WARNINGS
- Contents supplied STERILE using an ethylene oxide (EO) process. Do not use if sterile barrier is damaged. If damage is found, call your Stryker Neurovascular representative.
- For single use only. Do not reuse, reprocess or resterilize. Reuse, reprocessing or resterilization may compromise the structural integrity of the device and/or lead to device failure which, in turn, may result in patient injury, illness or death. Reuse, reprocessing or resterilization may also create a risk of contamination of the device and/or cause patient infection or cross-infection, including, but not limited to, the transmission of infectious disease(s) from one patient to another. Contamination of the device may lead to injury, illness or death of the patient.
- After use, dispose of product and packaging in accordance with hospital, administrative and/or local government policy.
- **This device should only be used by physicians who have received appropriate training in interventional neuroradiology or interventional radiology and preclinical training on the use of this device as established by Stryker Neurovascular.**
- Patients with hypersensitivity to 316LVM stainless steel may suffer an allergic reaction to this implant.
- MR temperature testing was not conducted in peripheral vasculature, arteriovenous malformations or fistulae models.
- The safety and performance characteristics of the Target Detachable Coil System (Target Detachable Coils, InZone Detachment Systems, delivery systems and accessories) have not been demonstrated with other manufacturer's devices (whether coils, coil delivery devices, coil detachment systems, catheters, guidewires, and/or other accessories). Due to the potential incompatibility of non Stryker Neurovascular devices with the Target Detachable Coil System, the use of other manufacturer's device(s) with the Target Detachable Coil System is not recommended.
- To reduce risk of coil migration, the diameter of the first and second coil should never be less than the width of the ostium.
- In order to achieve optimal performance of the Target Detachable Coil System and to reduce the risk of thromboembolic complications, it is critical that a continuous infusion of appropriate flush solution be maintained between a) the femoral sheath and guiding catheter, b) the 2-tip microcatheter and guiding catheters, and c) the 2-tip microcatheter and Stryker Neurovascular guidewire and delivery wire. Continuous flush also reduces the potential for thrombus formation on, and crystallization of infusate around, the detachment zone of the Target Detachable Coil.
- Do not use the product after the "Use By" date specified on the package.
- Reuse of the flush port/dispenser coil or use with any coil other than the original coil may result in contamination of, or damage to, the coil.
- Utilization of damaged coils may affect coil delivery to, and stability inside, the vessel or aneurysm, possibly resulting in coil migration and/or stretching.
- The fluoro-saver marker is designed for use with a Rotating Hemostatic Valve (RHV). If used without an RHV, the distal end of the coil may be beyond the alignment marker when the fluoro-saver marker reaches the microcatheter hub.
- If the fluoro-saver marker is not visible, do not advance the coil without fluoroscopy.
- Do not rotate delivery wire during or after delivery of the coil. Rotating the Target Detachable Coil delivery wire may result in a stretched coil or premature detachment of the coil from the delivery wire, which could result in coil migration.
- Verify there is no coil loop protrusion into the parent vessel after coil placement and prior to coil detachment. Coil loop protrusion after coil placement may result in thromboembolic events if the coil is detached.
- Verify there is no movement of the coil after coil placement and prior to coil detachment. Movement of the coil after coil placement may indicate that the coil could migrate once it is detached.
- Failure to properly close the RHV compression fitting over the delivery wire before attaching the InZone® Detachment System could result in coil movement, aneurysm rupture or vessel perforation.
- Verify repeatedly that the distal shaft of the catheter is not under stress before detaching the Target Detachable Coil. Axial compression or tension forces could be stored in the 2-tip microcatheter causing the tip to move during coil delivery. Microcatheter tip movement could cause the aneurysm or vessel to rupture.
- Advancing the delivery wire beyond the microcatheter tip once the coil has been detached involves risk of aneurysm or vessel perforation.
- The long term effect of this product on extravascular tissues has not been established so care should be taken to retain this device in the intravascular space.

Damaged delivery wires may cause detachment failures, vessel injury or unpredictable distal tip response during coil deployment. If a delivery wire is damaged at any point during the procedure, do not attempt to straighten or otherwise repair it. Do not proceed with deployment or detachment. Remove the entire coil and replace with undamaged product.

- After use, dispose of product and packaging in accordance with hospital, administrative and/or local government policy.

CAUTIONS / PRECAUTIONS
- Federal Law (USA) restricts this device to sale by or on the order of a physician.
- Besides the number of InZone Detachment System units needed to complete the case, there must be an extra InZone Detachment System unit as back up.
- Removing the delivery wire without grasping the introducer sheath and delivery wire together may result in the detachable coil sliding out of the introducer sheath.
- Failure to remove the introducer sheath after inserting the delivery wire into the RHV of the microcatheter will interrupt normal infusion of flush solution and allow back flow of blood into the microcatheter.
- Some low level overhead light near or adjacent to the patient is required to visualize the fluoro-saver marker; monitor light alone will not allow sufficient visualization of the fluoro-saver marker.
- Advance and retract the Target Detachable Coil carefully and smoothly without excessive force. If unusual friction is noticed, slowly withdraw the Target Detachable Coil and examine for damage. If damage is present, remove and use a new Target Detachable Coil. If friction or resistance is still noted, carefully remove the Target Detachable Coil and microcatheter and examine the microcatheter for damage.
- If it is necessary to reposition the Target Detachable Coil, verify under fluoroscopy that the coil moves with a one-to-one motion. If the coil does not move with a one-to-one motion or movement is difficult, the coil may have stretched and could possibly migrate or break. Gently remove both the coil and microcatheter and replace with new devices.
- Increased detachment times may occur when:
  – Other embolic agents are present.
  – Delivery wire and microcatheter markers are not properly aligned.
  – Thrombus is present on the coil detachment zone.
- Do not use detachment systems other than the InZone Detachment System.
- Increased detachment times may occur when delivery wire and microcatheter markers are not properly aligned.
- Do not use detachment systems other than the InZone Detachment System.

Stryker Neurovascular
47900 Bayside Parkway
Fremont, CA 94538-6515

stryker.com/neurovascular

Date of Release: JUN/2014

EX_EN_US

Trevo® XP ProVue Retrievers

See package insert for complete indications, complications, warnings, and instructions for use.

INDICATIONS FOR USE
The Trevo Retriever is intended to restore blood flow in the neurovasculature by removing thrombus in patients experiencing ischemic stroke within 8 hours of symptom onset. Patients who are ineligible for intravenous tissue plasminogen activator (IV t-PA) or who fail IV t-PA therapy are candidates for treatment.

COMPLICATIONS
Procedures requiring percutaneous catheter introduction should not be attempted by physicians unfamiliar with possible complications which may occur during or after the procedure. Possible complications include, but are not limited to, the following: air embolism; hematoma or hemorrhage at puncture site; infection; distal embolization; pain/headache; vessel spasm, thrombosis, dissection, or perforation; emboli; acute occlusion; ischemia; intracranial hemorrhage; false aneurysm formation; neurological deficits including stroke; and death.

COMPATIBILITY
3x20 mm retrievers are compatible with Trevo® Pro 14 Microcatheters (REF 90231) and Trevo® Pro 18 Microcatheters (REF 90238). 4x20 mm retrievers are compatible with Trevo® Pro 18 Microcatheters (REF 90238). Compatibility of the Retriever with other microcatheters has not been established. Performance of the Retriever device may be impacted if a different microcatheter is used. The Merci® Balloon Guide Catheters are recommended for use during thrombus removal procedures. Retrievers are compatible with the Abbott Vascular DOC® Guide Wire Extension (REF 22260).

WARNINGS
- Contents supplied STERILE, using an ethylene oxide (EO) process. Nonpyrogenic.
- To reduce risk of vessel damage, adhere to the following recommendations:
  – Take care to appropriately size Retriever to vessel diameter at intended site of deployment.
  – Do not perform more than six (6) retrieval attempts in same vessel using Retriever devices.
  – Maintain Retriever position in vessel when removing or exchanging Microcatheter.
- To reduce risk of kinking/fracture, adhere to the following recommendations:
  – Immediately after unsheathing Retriever, position Microcatheter tip marker just proximal to shaped section. Maintain Microcatheter tip marker just proximal to shaped section of Retriever during manipulation and withdrawal.
  – Do not rotate or torque Retriever.
  – Use caution when passing Retriever through stented arteries.
- Do not resterilize and reuse. Structural integrity and/or function may be impaired by reuse or cleaning.
- The Retriever is a delicate instrument and should be handled carefully. Before use and when possible during procedure, inspect device carefully for damage. Do not use a device that shows signs of damage. Damage may prevent device from functioning and may cause complications.
- Do not advance or withdraw Retriever against resistance or significant vasospasm. Moving or torquing device against resistance or significant vasospasm may result in damage to vessel or device. Assess cause of resistance using fluoroscopy and if needed resheath the device to withdraw.
- If Retriever is difficult to withdraw from the vessel, do not torque Retriever. Advance Microcatheter distally, gently pull Retriever back into Microcatheter, and remove Retriever and Microcatheter as a unit. If undue resistance is met when withdrawing the Retriever into the Microcatheter, consider extending the Retriever using the Abbott Vascular DOC guidewire extension (REF 22260) so that the Microcatheter can be exchanged for a larger diameter catheter such as a DAC® catheter. Gently withdraw the Retriever into the larger diameter catheter.
- Administer anti-coagulation and anti-platelet medications per standard institutional guidelines.

PRECAUTIONS
- Prescription only – device restricted to use by or on order of a physician.
- Store in cool, dry, dark place.
- Do not use open or damaged packages.
- Use by "Use By" date.
- Exposure to temperatures above 54°C (130°F) may damage device and accessories. Do not autoclave.
- Do not expose Retriever to solvents.
- Use Retriever in conjunction with fluoroscopic visualization and proper anti-coagulation agents.
- To prevent thrombus formation and contrast media crystal formation, maintain a constant infusion of appropriate flush solution between guide catheter and Microcatheter and between Microcatheter and Retriever or guidewire.
- Do not attach a torque device to the shaped proximal end of DOC® Compatible Retriever. Damage may occur, preventing ability to attach DOC® Guide Wire Extension.

Concentric Medical
301 East Evelyn
Mountain View, CA 94041

EC REP

EMERGO Europe
Molenstraat 15
2513 BH, The Hague
The Netherlands

CE 0459

Stryker Neurovascular
47900 Bayside Parkway
Fremont, CA 94538-6515

stryker.com/neurovascular
stryker.com/emea/neurovascular

Date of Release: JUN/2014

EX_EN_GL

Target® Nano™

DETACHABLE COILS

Beyond Soft

The softest coil technology* available, combined with Target Coil's consistently smooth deployment and exceptional microcatheter stability, results in an experience that is beyond soft. Designed to treat small spaces, the Target Nano Coil's incredible softness delivers increased conformability and shape adjustment.

Target Nano Coils–**Smooth and Stable** has never been so soft.

For more information, please visit www.strykerneurovascular.com/Target

stryker®
Neurovascular

*Testing performed by Stryker Neurovascular. n=3. Data are on file at Stryker Neurovascular and will be made available upon request. Bench test results may not necessarily be indicative of clinical performance.

Stroke: *Our Only Focus. Our Ongoing Promise.*